

# BOTTOM-UP SYNTHESIS OF CARBON NANOSTRUCTURES

A Dissertation

Presented to the Faculty of the Graduate School

of Cornell University

In Partial Fulfillment of the Requirements for the Degree of

Doctor of Philosophy

by

Hasan Arslan

August 2014

© 2014 Hasan Arslan

## BOTTOM-UP SYNTHESIS OF CARBON NANOSTRUCTURES

Hasan Arslan, Ph. D.

Cornell University 2014

Nanostructured forms of graphene with well-defined structures, including graphene nanoribbons (GNRs) and graphene quantum dots, have attracted interest as high performance semiconductors and luminescent probes. Top-down approaches, including patterning graphene or unzipping carbon nanotubes (CNTs), have provided access to GNRs and allowed their electronic properties to be measured, but these methods do not provide atomically precise control over the GNR width and edge structure. Bottom-up approaches, in which GNRs are synthesized from specific molecular precursors, promise to provide such control but have so far not produced sufficiently long, dispersed ribbons deposited on insulating substrates. We developed a solution based bottom-up synthesis of GNRs, which relies on a benzannulation reaction at each carbon-carbon triple bond of poly(phenylene ethynylene)s (PPEs) followed by oxidative dehydrogenation for graphitization. PPEs are attractive GNR precursors because their polymerization is well established, tolerates a broad range of functional groups, and provides high molecular weight materials. They can be applied to small molecules which are intriguing and previously unavailable polycyclic aromatic hydrocarbons (PAHs). Resulting contorted and highly dispersible PAHs exhibit strongly red shifted absorption spectra and their bandgaps can be tuned by extended conjugation. Benzannulation reaction used in the synthesis of carbon nanostructures is highly regioselective. The main determining factor in regioselectivity is the electronics of the dienophile. This knowledge will allow rational design of regioselective synthesis of carbon nanostructures.

## BIOGRAPHICAL SKETCH

Hasan Arslan was born in 1987 in Elmali, Turkey, a small town in Taurus Mountains by Mediterranean Sea. He learned to read and write at the age of five in the small village school where both his parents, his mother Fatma Arslan, and his father Bayram Arslan taught elementary school. When he was eleven, the family moved to Antalya, a large coastal city, where he attended the middle school. Hasan excelled among his peers and placed in the top 200 in the National High School Entrance Exam, allowing him the admission to the prestigious Izmir Science High School, the top ranked public high school in the country. There, Hasan learned about scientific methodology and received a very extensive scientific education. It was here that he realized his passion for chemistry. He took place in chemistry Olympiads and was involved with chemistry projects. As a result, he received numerous national and international recognitions and awards, including a gold medal at 36<sup>th</sup> International Chemistry Olympiads in Kiel, Germany in 2004, where he represented Turkey. Motivated to explore more, he attended Middle East Technical University in Ankara, Turkey between 2004 and 2009, where he studied chemistry. During his undergraduate career, he was involved with research in several groups and his love for chemistry only grew stronger. He graduated from college in 2009 as Valedictorian and joined Cornell University as a chemistry graduate student. He joined Professor William Dichtel's group as one of his early students. As a member of a young research group, he had the privilege and the responsibility of starting a new project, which was challenging and rewarding. His research mostly focused on developing new synthetic strategies to build carbon nanostructures using a bottom-up approach, with particular emphasis on graphene nanoribbons (GNRs) and related small molecules. Hasan graduated as a Ph.D. student from Cornell in July 2014 and will continue his work as a postdoctoral fellow in Northwestern University with Professor J. Fraser Stoddart.



Dedicated to  
My mother Fatma Arslan,  
My loving girlfriend Christine Gleave,  
And my late father Bayram Arslan.

## ACKNOWLEDGMENTS

I would like to thank Professor William Dichtel for giving me the opportunity to work in his group and take up a challenge of starting a research project from scratch. Over the years, I learned a lot from him; from how to run a column to the essentials of giving an effective talk. Most importantly, he helped me become an independent scientist, who can see the contemporary problems we face in chemistry, and seek creative solutions. I could not have done it without his patience and guidance. I would like to also thank my special committee members Professor Geoffrey Coates and Jiwoong Park for the advice and support they gave me over the years.

As a synthetic chemist who makes exotic molecules, the most important technique I have used is NMR spectroscopy. I have to thank Dr. Ivan Keresztes with his tremendous help with the NMR experiments and structural assignments of some very critical molecules in my graduate career. Without his genius, I would not be able to look at the characterization of the complex systems the way I do now. I should also mention Professor Frank Schroeder for his very challenging but equally instructional class that taught me most of the NMR knowledge I have today.

I would like to also thank my collaborators, Professor Paulette Clancy, and Jonathan Saathoff from the Department of Chemical Engineering, and Professor Lynn Loo and Dr. Jia Gao from the Department of Chemical Engineering at Princeton University, who helped us make significant progress with our understanding of graphene nanoribbons.

I was also lucky to have excellent group members. Dr. Fernando Uribe-Romo, and Dr Brian Smith have been great colleagues to work with. Sam Hein has been an excellent lab mate making very important discoveries, carrying the benzannulation chemistry in new directions. I would like to thank Dr. Jason Mann, who was a very close friend of mine, for getting my sense of humor and sharing it. He also taught me a lot of the laboratory techniques that made me a synthetic organic chemist. I have to especially acknowledge Cathy DeBlase for her kindness, for being a great friend throughout the years, and arranging the first date with my girlfriend

Christine Gleave, which changed my life dramatically for the better over the last few years.

I have to thank my family, especially my mother Fatma Arslan, who always supported me throughout my Ph.D. Without her encouragement, I probably would have thrown in the towel long time ago. Finally, I have to thank my girlfriend and love of my life Christine Gleave for always being there for me through the hardest times of the grad school. She made me a better person, helped me adopt a healthier life style, raised my spirit and nurtured me with her love. I could not have possibly done this without her.

The work in this thesis was funded by the National Science Foundation (Grant No. CHE-1124754), the Beckman Young Investigator Program of the Arnold and Mabel Beckman Foundation, the Doctoral New Investigator Program of the ACS Petroleum Research Fund (Grant No. 52019-DNI7), the Cottrell Scholar Program of the Research Corporation for Science Advancement, and a Sloan Research Fellowship from the Alfred P. Sloan Foundation. The research presented in this thesis made use of the Cornell Center for Materials Research (CCMR) facilities with support from the NSF Materials Research Science and Engineering Centers (MRSEC) program (Grant No. DMR-0520404).

## TABLE OF CONTENTS

Biographical Sketch		iii
Dedication		iv
Acknowledgements		v
Table of Contents		vii
List of Figures		viii
List of Tables		xxvi
CHAPTER ONE	General Methods to Prepare Hindered Oligo- and Poly(arylenes)	1
CHAPTER TWO	Highly Efficient Benzannulation of Poly(Phenylene Ethynylene)s	25
CHAPTER THREE	Accessing Extended and Partially Fused Hexabenzocoronenes Using a Benzannulation / Cyclodehydrogenation Approach	74
CHAPTER FOUR	Origins of the Regioselectivity in the Asao–Yamamoto Benzannulation of Diaryl Acetylenes	201
CHAPTER FIVE	Design and Bottom-Up Synthesis of Dispersible, Structurally Precise Graphene Nanoribbons	336

## LIST OF FIGURES

### CHAPTER ONE

Figure 1.1	General strategies for the synthesis of sterically congested aromatic systems. <b>A.</b> Suzuki cross-coupling reaction <b>B.</b> Diels-Alder reaction between cyclopentadienones and alkynes <b>C.</b> alkyne cyclotrimerization <b>D.</b> Asao-Yamamoto benzannulation	2
Figure 1.2	Proposed mechanism of the Yamamoto benzannulation. Adapted from Ref. 52. Copyright (2003) American Chemical Society.	5
Figure 1.3	General synthetic strategies to prepare oligo( <i>o</i> -phenylene)s. <b>A.</b> An iterative Suzuki cross-coupling-triflation synthesis of <i>o</i> -arylenes. <b>B.</b> Cu-mediated oxidative coupling of lithiated precursors to form oligomers and polymers. <b>C.</b> Several end functionalized hexa- <i>o</i> -phenylenes. <b>D.</b> Redox switching of the conformational behavior of $\text{oP}^8(\text{NO}_2)_2$ . A and C were reproduced from Ref. 18. Copyright (2013) American Chemical Society. B and D were reproduced from Ref. 13 with permission from The Nature Publishing Group.	7
Figure 1.4	Synthesis of poly( <i>o</i> -arylene)s <i>via</i> polymerization of [2.2.1] Oxabicyclic Alkenes and Subsequent Dehydration. Reproduced from Ref. 62. Copyright (2014) American Chemical Society.	10
Figure 1.5	Synthesis of polyphenylene <b>7</b> , <i>via</i> Suzuki coupling and its graphitization to GNR <b>8</b> <i>via</i> Scholl oxidation. Reproduced from Ref. 23. Copyright (2008) American Chemical Society.	11
Figure 1.6	Diels-Alder polymerization for the synthesis of GNRs <b>A.</b> Diels-Alder Polymerization of <b>9</b> , and subsequent graphitization to GNR <b>11</b> . <b>B.</b> An AFM image of long (100–200nm) GNRs on highly ordered pyrolytic graphite. Reproduced from Ref. 22 with permission of The Nature Publishing Group.	12
Figure 1.7	Synthesis of a 9th generation polyphenylene dendrimer. Adapted from Ref. 39. Copyright (2013) American Chemical Society.	15
Figure 1.8	Synthesis of contorted HBC. Ramirez reaction used in olefination step ( <b>14</b> to <b>15</b> ) provides rapid access to the precursor <b>17</b> of contorted HBC <b>18</b> . Reproduced from Ref. 90 with permission of The Royal Society of Chemistry.	16

Figure 1.9	Synthesis of contorted aromatic systems due to steric congestion <b>A.</b> Neighboring <i>t</i> Bu groups are preventing the formation of complete fusion. Reproduced from Ref. 20 with permission of The John Wiley and Sons. <b>B.</b> Benzannulation of the appropriately substituted phenylene ethynylenes give sterically congested phenylenes that also form contorted aromatics. Reproduced from Ref. 86 with permission of The Royal Society of Chemistry.	17
------------	-----------------------------------------------------------------------------------------------------------------------------------------------------------------------------------------------------------------------------------------------------------------------------------------------------------------------------------------------------------------------------------------------------------------------------------------------------------------------	----

## CHAPTER TWO

Scheme 2.1	Benzannulation of each alkyne of a substituted poly(phenylene ethynylene) <b>1</b> provides the polyphenylene <b>3</b> .	26
Figure 2.1	A model study of the benzannulation strategy. a, The terphenyl-containing dialkyne <b>4</b> , a molecular compound similar in structure to PPE <b>1</b> , was subjected to the Cu(OTf) <sub>2</sub> -catalyzed benzannulation. b, MALDI-TOF mass spectra of dialkyne <b>4</b> and benzannulated product <b>5</b> . inset: Structure of a possible naphthyl ketone side product based on previous reports of the benzannulation reaction, <sup>[14]</sup> which is observed only as a trace impurity in the mass spectrum.	28
Figure 2.2	Refractive index SEC traces of PPE <b>1</b> (blue) and polyphenylene <b>3</b> (red trace).	30
Figure 2.3	Illustration of the three most common conformations in the simulation of several repeat units of polymer <b>3</b> in the presence of 1,2-dichlorobenzene solvent. Truncated polymer structures are shown with their <i>n</i> -nonyl side-chains omitted for clarity.	30
Figure 2.4	Characterization of the benzannulation of PPE <b>1</b> . a, UV/visible absorption, and b, photoemission spectra of the PPE <b>1</b> (blue trace), benzannulated polymer <b>3</b> (red trace), the dialkyne <b>4</b> (green trace), and its benzanulation product <b>5</b> (brown trace). The steric congestion of <b>3</b> reduces the effective conjugation length, shifting the absorbance of the polymer to higher energy.	33
Figure 2.5	Partial <sup>13</sup> C NMR spectra (CDCl <sub>3</sub> , 100 MHz, rt) of a <sup>13</sup> C-enriched sample of <b>1</b> (a, blue spectrum) that was benzannulated to provide <sup>13</sup> C-enriched <b>3</b> (b, red spectrum). The resonances of the enriched carbons (*) shift to the aromatic region of the spectrum, and no resonances corresponding to residual alkynes are observed. Inset: Partial <sup>13</sup> C NMR spectrum of <b>3</b> (CD <sub>2</sub> Cl <sub>4</sub> , 125 MHz, 135 °C) obtained at increased temperature shows resolution and coupling of the two inequivalent <sup>13</sup> C-enriched resonances.	35

## APPENDIX ONE

Figure A1.1	$^1\text{H}$ NMR of <b>S3</b> (300 MHz, $\text{CDCl}_3$ , 298 K)	53
Figure A1.2	$^{13}\text{C}$ NMR of <b>S3</b> (75 MHz, $\text{CDCl}_3$ , 298 K).	53
Figure A1.3	$^1\text{H}$ NMR of <b>S4</b> (300 MHz, $\text{CDCl}_3$ , 298 K)	54
Figure A1.4	$^{13}\text{C}$ NMR of <b>S4</b> (75 MHz, $\text{CDCl}_3$ , 298 K).	54
Figure A1.5	$^1\text{H}$ NMR of <b>4</b> (400 MHz, $\text{CDCl}_3$ , 298 K).	55
Figure A1.6	$^{13}\text{C}$ NMR of <b>4</b> (100 MHz, $\text{CDCl}_3$ , 298 K).	55
Figure A1.7	$^1\text{H}$ NMR of <b>5</b> (500 MHz, $\text{CDCl}_3$ , 298 K).	56
Figure A1.8	$^{13}\text{C}$ NMR of <b>5</b> (125 MHz, $\text{CDCl}_3$ , 298 K).	56
Figure A1.9	$^1\text{H}$ NMR of polymer <b>1</b> (400 MHz, $\text{CDCl}_3$ , 323 K)	57
Figure A1.10	$^{13}\text{C}$ NMR of polymer <b>1</b> (100 MHz, $\text{C}_2\text{D}_2\text{Cl}_4$ , 393 K).	57
Figure A1.11	$^1\text{H}$ NMR of polymer <b>3</b> (400 MHz, $\text{CDCl}_3$ , 298 K).	58
Figure A1.12	$^{13}\text{C}$ NMR of polymer <b>3</b> (75 MHz, $\text{CDCl}_3$ , 298 K).	58
Figure A1.13	$^1\text{H}$ NMR of $^{13}\text{C}$ - <b>S2</b> (300 MHz, $\text{CDCl}_3$ , 298 K).	59
Figure A1.14	$^{13}\text{C}$ NMR of $^{13}\text{C}$ - <b>S2</b> (75 MHz, $\text{CDCl}_3$ , 298 K).	59
Figure A1.15	$^1\text{H}$ NMR of $^{13}\text{C}$ - <b>S3</b> (300 MHz, $\text{CDCl}_3$ , 298 K).	60
Figure A1.16	$^{13}\text{C}$ NMR of $^{13}\text{C}$ - <b>S3</b> (100 MHz, $\text{CDCl}_3$ , 298 K).	60
Figure A1.17	$^1\text{H}$ NMR of $^{13}\text{C}$ - <b>S4</b> (400 MHz, $\text{CDCl}_3$ , 298 K).	61
Figure A1.18	$^{13}\text{C}$ NMR of $^{13}\text{C}$ - <b>S4</b> (100 MHz, $\text{CDCl}_3$ , 298 K).	61
Figure A1.19	$^1\text{H}$ NMR of $^{13}\text{C}$ - <b>1</b> (400 MHz, $\text{CDCl}_3$ , 298 K).	62
Figure A1.20	$^{13}\text{C}$ NMR of $^{13}\text{C}$ - <b>1</b> (100 MHz, $\text{CDCl}_3$ , 298 K).	62
Figure A1.21	$^1\text{H}$ NMR of $^{13}\text{C}$ - <b>3</b> (300 MHz, $\text{CDCl}_3$ , 298 K).	63
Figure A1.22	$^{13}\text{C}$ NMR of $^{13}\text{C}$ - <b>3</b> (100 MHz, $\text{CDCl}_3$ , 298 K).	63
Figure A1.23	Comparison of the $^{13}\text{C}$ NMR of $^{13}\text{C}$ - <b>3</b> (100 MHz, $\text{CDCl}_3$ , 298 K, blue trace) and <b>3</b> (75 MHz, $\text{CDCl}_3$ , 298 K, red trace).	64
Figure A1.24	Partial $^1\text{H}$ NMR of $^{13}\text{C}$ - <b>3</b> (500 MHz, 1,1,2,2- $\text{C}_2\text{D}_2\text{Cl}_4$ ) at various temperatures.	64
Figure A1.25	Partial $^{13}\text{C}$ NMR of $^{13}\text{C}$ - <b>3</b> (125 MHz, 1,1,2,2- $\text{C}_2\text{D}_2\text{Cl}_4$ ) at various temperatures.	65
Figure A1.26	2D-INADEQUATE spectrum of $^{13}\text{C}$ - <b>3</b> (125 MHz, 1,1,2,2- $\text{C}_2\text{D}_2\text{Cl}_4$ , 408 K).	65
Figure A1.27	FTIR spectra of polymer <b>1</b> and polymer <b>3</b> .	66
Figure A1.28	FTIR spectra of compounds <b>4</b> and <b>5</b> .	67
Figure A1.29	Thermogravimetric analysis of polymer <b>1</b> .	68
Figure A1.30	Thermogravimetric analysis of polymer <b>3</b>	68
Figure A1.31	Size-exclusion chromatograms of polymer <b>1</b> (blue) and polymer <b>3</b>	69

	(red), as detected by their light-scattering intensity.	
Figure A1.32	Size-exclusion chromatograms of polymer <b>1</b> (blue) and polymer <b>3</b> (red), as detected by changes in refractive index of the THF mobile phase.	69
Figure A1.33	Numbered dihedrals were calculated to differentiate distinct conformers. Dihedrals of the same color would be expected to have the same angular preferences. The shown planar structure is the default starting position for the simulations.	71
Figure A1.34	Illustration of the most common monomer conformations in the simulated polyphenylene <b>3</b> . Each conformer has two eight letter codes because each should give roughly equivalent structures due to symmetry. Carbons linking phenyl groups are shown in pink to assist viewing. The full 12 units of each polymer are not shown.	72

### CHAPTER THREE

Figure 3.1	A series of dialkyne compounds <b>1a-d</b> provide partially fused HBC derivatives <b>4a-d</b> and fully fused products <b>5a</b> and <b>5d</b> using a two-step benzannulation/cyclodehydrogenation protocol.	76
Figure 3.2	<b>A.</b> The benzannulation of <b>1a</b> with <b>2-<sup>13</sup>C<sub>2</sub></b> provides the labelled derivative <b>3a-<sup>13</sup>C<sub>2</sub></b> , indicating that the reaction is regioselective. <b>B.</b> Partial <sup>13</sup> C NMR of <b>3a-<sup>13</sup>C<sub>2</sub></b> . <b>C.</b> Regiochemistry of the benzannulation reaction consistent with this experiment.	77
Figure 3.3	<b>A.</b> Rearrangement during the Scholl oxidation observed by King et al. <sup>30</sup> <b>B.</b> The expected (observed) and possible rearranged (not observed) products for the oxidation of <b>3b</b> .	80
Figure 3.4	Partial <sup>1</sup> H NMR spectrum of the aromatic and <i>t</i> Bu regions of <b>4b</b> .	81
Figure 3.5	MALDI-TOF MS spectra taken of the oxidation of <b>3d</b> as a function of reaction time. Four carbon-carbon bonds are formed in fewer than 20 minutes, while full oxidation occurs after longer reaction times.	83
Figure 3.6	DFT-optimized structures of partially and fully fused compounds <b>4a</b> and <b>5a</b> , respectively. The <i>n</i> -C <sub>9</sub> H <sub>19</sub> chains were truncated to –CH <sub>3</sub> groups in the calculations.	85
Figure 3.7	<b>A.</b> UV/vis and <b>(B)</b> fluorescence spectra of contorted compounds <b>4a-c</b>	87
Figure 3.8	Cyclic voltammetry (0.1 M Bu <sub>4</sub> NPF <sub>6</sub> in CH <sub>2</sub> Cl <sub>2</sub> ; Pt button electrode) of <b>4a-4c</b> .	89



## APPENDIX TWO

Figure A2.1	$^1\text{H}$ NMR of <b>S2</b> (300 MHz, $\text{CDCl}_3$ , 300 K).	114
Figure A2.2	$^{13}\text{C}$ NMR of <b>S2</b> (75 MHz, $\text{CDCl}_3$ , 300 K).	114
Figure A2.3	$^1\text{H}$ NMR of <b>S3</b> (300 MHz, $\text{CDCl}_3$ , 300 K).	115
Figure A2.4	$^{13}\text{C}$ NMR of <b>S3</b> (75 MHz, $\text{CDCl}_3$ , 300 K).	115
Figure A2.5	$^1\text{H}$ NMR of <b>1a</b> (400 MHz, $\text{CDCl}_3$ , 298 K).	116
Figure A2.6	$^{13}\text{C}$ NMR of <b>1a</b> (100 MHz, $\text{CDCl}_3$ , 298 K).	116
Figure A2.7	$^1\text{H}$ NMR of <b>S4</b> (300 MHz, $\text{CDCl}_3$ , 298 K).	117
Figure A2.8	$^{13}\text{C}$ NMR of <b>S4</b> (75 MHz, $\text{CDCl}_3$ , 298 K).	117
Figure A2.9	$^1\text{H}$ NMR of <b>1b</b> (300 MHz, $\text{CDCl}_3$ , 300 K).	118
Figure A2.10	$^{13}\text{C}$ NMR of <b>1b</b> (75 MHz, $\text{CDCl}_3$ , 300 K).	118
Figure A2.11	$^1\text{H}$ NMR of <b>1c</b> (500 MHz, $\text{CDCl}_3$ , 328 K).	119
Figure A2.12	$^{13}\text{C}$ NMR of <b>1c</b> (125 MHz, $\text{CDCl}_3$ , 328 K).	119
Figure A2.13	$^1\text{H}$ NMR of <b>S5</b> (400 MHz, $\text{CDCl}_3$ , 297 K).	120
Figure A2.14	$^{13}\text{C}$ NMR of <b>S5</b> (100 MHz, $\text{CDCl}_3$ , 297 K).	120
Figure A2.15	$^1\text{H}$ NMR of <b>1d</b> (400 MHz, $\text{CDCl}_3$ , 295 K).	121
Figure A2.16	$^{13}\text{C}$ NMR of <b>1d</b> (100 MHz, $\text{CDCl}_3$ , 295 K).	121
Figure A2.17	$^1\text{H}$ NMR spectrum of <b>S6-<math>^{13}\text{C}_2</math></b> (400 MHz, $\text{CDCl}_3$ , 298 K).	122
Figure A2.18	$^{13}\text{C}$ NMR spectrum of <b>S6-<math>^{13}\text{C}_2</math></b> (100 MHz, $\text{CDCl}_3$ , 298 K).	122
Figure A2.19	$^1\text{H}$ NMR spectrum of <b>S7-<math>^{13}\text{C}_2</math></b> (400 MHz, $\text{CDCl}_3$ , 298 K).	123
Figure A2.20	$^{13}\text{C}$ NMR spectrum of <b>S7-<math>^{13}\text{C}_2</math></b> (100 MHz, $\text{CDCl}_3$ , 298 K).	123
Figure A2.21	$^1\text{H}$ NMR spectrum of <b>2-<math>^{13}\text{C}_2</math></b> (400 MHz, $\text{CDCl}_3$ , 298 K).	124
Figure A2.22	$^{13}\text{C}$ NMR spectrum of <b>2-<math>^{13}\text{C}_2</math></b> (100 MHz, $\text{CDCl}_3$ , 298 K).	124
Figure A2.23	$^1\text{H}$ NMR of <b>3a</b> (500 MHz, $\text{CDCl}_3$ , 298 K).	125
Figure A2.24	$^{13}\text{C}$ NMR of <b>3a</b> (125 MHz, $\text{CDCl}_3$ , 298 K).	125
Figure A2.25	$^1\text{H}$ NMR spectrum of <b>3a-<math>^{13}\text{C}_2</math></b> (500 MHz, $\text{CDCl}_3$ , 298 K).	126
Figure A2.26	Partial $^1\text{H}$ NMR spectra (500 MHz, $\text{CDCl}_3$ , 298K) of <b>3a</b> and <b>3a-<math>^{13}\text{C}_2</math></b> that indicate $^{13}\text{C}$ - $^1\text{H}$ coupling at the labeled position.	126
Figure A2.27	$^{13}\text{C}$ NMR spectrum of <b>3a-<math>^{13}\text{C}_2</math></b> (125 MHz, $\text{CDCl}_3$ , 298 K).	127
Figure A2.28	$^1\text{H}$ NMR of <b>3b</b> (400 MHz, $\text{CDCl}_3$ , 297 K).	128
Figure A2.29	$^{13}\text{C}$ NMR of <b>3b</b> (100 MHz, $\text{CDCl}_3$ , 297 K).	128

Figure A2.30	$^1\text{H}$ NMR of <b>3c</b> (400 MHz, $\text{CDCl}_3$ , 295 K).	129
Figure A2.31	$^{13}\text{C}$ NMR of <b>3c</b> (100MHz, $\text{CDCl}_3$ , 295 K).	129
Figure A2.32	$^1\text{H}$ NMR of <b>3d</b> (400 MHz, $\text{CDCl}_3$ , 295 K).	130
Figure A2.33	$^{13}\text{C}$ NMR of <b>3d</b> (100MHz, $\text{CDCl}_3$ , 295 K).	130
Figure A2.34	$^1\text{H}$ NMR of <b>4a</b> (500 MHz, $\text{CDCl}_3$ , 295 K).	131
Figure A2.35	$^{13}\text{C}$ NMR of <b>4a</b> (125 MHz, $\text{CDCl}_3$ , 295 K).	131
Figure A2.36	$^1\text{H}$ NMR of <b>4b</b> (500 MHz, $\text{CDCl}_3$ , 295 K).	132
Figure A2.37	$^{13}\text{C}$ NMR of <b>4b</b> (125 MHz, $\text{CDCl}_3$ , 295 K).	132
Figure A2.38	$^1\text{H}$ NMR of <b>4c</b> (500 MHz, $\text{CDCl}_3$ , 298 K).	133
Figure A2.39	$^{13}\text{C}$ NMR of <b>4c</b> (125 MHz, $\text{CDCl}_3$ , 298 K).	133
Figure A2.40	$^1\text{H}$ NMR of <b>5a</b> (300 MHz, $o\text{-C}_6\text{D}_4\text{Cl}_2$ , 353 K).	134
Figure A2.41	$^1\text{H}$ NMR of <b>5a</b> (300 MHz, $o\text{-C}_6\text{D}_4\text{Cl}_2$ , 353 K), aromatic region.	134
Figure A2.42	$^{13}\text{C}$ NMR of <b>5a</b> (75 MHz, 2:1 $\text{CS}_2\text{:CD}_2\text{Cl}_2$ , 298 K).	135
Figure A2.43	$^1\text{H}$ NMR spectrum of <b>5a-<math>^{13}\text{C}_2</math></b> (500 MHz, 1,2- $\text{C}_2\text{H}_2\text{Cl}_4$ , 408 K).	136
Figure A2.44	$^1\text{H}$ NMR spectrum of <b>5a-<math>^{13}\text{C}_2</math></b> (500 MHz, 1,2- $\text{C}_2\text{H}_2\text{Cl}_4$ , 408 K). 1H signal assignment of aromatic region.	136
Figure A2.45	$^{13}\text{C}$ NMR spectrum of <b>5a-<math>^{13}\text{C}_2</math></b> . (125 MHz, 1,2- $\text{C}_2\text{H}_2\text{Cl}_4$ , 408 K)	137
Figure A2.46	Full COSY spectrum of <b>3a</b> (500 MHz, 500 MHz, $\text{CDCl}_3$ , 295 K).	139
Figure A2.47	Partial COSY spectrum of <b>3a</b> showing the aromatic region (500 MHz, 500 MHz, $\text{CDCl}_3$ , 295 K).	140
Figure A2.48	Full ROESY spectrum of <b>3a</b> (500 MHz, 500 MHz, $\text{CDCl}_3$ , 295 K).	141
Figure A2.49	Partial ROESY spectrum of <b>3a</b> showing the aromatic region (500 MHz, 500 MHz, $\text{CDCl}_3$ , 295 K).	142
Figure A2.50	Full HSQC spectrum of <b>3a</b> (500 MHz, 125 MHz, $\text{CDCl}_3$ , 295 K).	143
Figure A2.51	Partial HSQC spectrum of <b>3a</b> showing the aromatic region (500 MHz, 125 MHz, $\text{CDCl}_3$ , 295 K).	143
Figure A2.52	Full HMBC spectrum of <b>3a</b> (500 MHz, 125 MHz, $\text{CDCl}_3$ , 295 K).	144
Figure A2.53	Partial HMBC spectrum of <b>3a</b> showing the aromatic region (500 MHz, 125 MHz, $\text{CDCl}_3$ , 295 K).	144
Figure A2.54	Full COSY spectrum of <b>4a</b> (500 MHz, 500 MHz, $\text{CDCl}_3$ , 295 K).	146
Figure A2.55	Partial COSY spectrum of <b>4a</b> showing the aromatic region (500 MHz, 500 MHz, $\text{CDCl}_3$ , 295 K).	147
Figure A2.56	Full ROESY spectrum of <b>4a</b> (500 MHz, 500 MHz, $\text{CDCl}_3$ , 295 K).	148
Figure A2.57	Partial ROESY spectrum of <b>4a</b> showing the aromatic region (500 MHz, 500 MHz, $\text{CDCl}_3$ , 295 K).	149
Figure A2.58	Full HSQC spectrum of <b>4a</b> (500 MHz, 125 MHz, $\text{CDCl}_3$ , 295 K).	150

Figure A2.59	Partial HSQC spectrum of <b>4a</b> showing the aromatic region (500 MHz, 125 MHz, CDCl <sub>3</sub> , 295 K).	150
Figure A2.60	Full HMBC spectrum of <b>4a</b> (500 MHz, 125 MHz, CDCl <sub>3</sub> , 295 K).	151
Figure A2.61	Partial HMBC spectrum of <b>4a</b> showing the aromatic region (500 MHz, 125 MHz, CDCl <sub>3</sub> , 295 K).	151
Figure A2.62	Full COSY spectrum of <b>4b</b> (500 MHz, 500 MHz, CDCl <sub>3</sub> , 298 K).	153
Figure A2.63	Partial COSY spectrum of <b>4b</b> showing the aromatic region (500 MHz, 500 MHz, CDCl <sub>3</sub> , 298 K).	154
Figure A2.64	Full ROESY spectrum of <b>4b</b> (500 MHz, 500 MHz, CDCl <sub>3</sub> , 298 K).	155
Figure A2.65	Partial ROESY spectrum of <b>4b</b> showing the aromatic region (500 MHz, 500 MHz, CDCl <sub>3</sub> , 298 K).	156
Figure A2.66	Full HSQC spectrum of <b>4b</b> (500 MHz, 125 MHz, CDCl <sub>3</sub> , 298 K).	157
Figure A2.67	Partial HSQC spectrum of <b>4b</b> showing the aromatic region (500 MHz, 125 MHz, CDCl <sub>3</sub> , 298 K).	157
Figure A2.68	Full HMBC spectrum of <b>4b</b> (500 MHz, 125 MHz, CDCl <sub>3</sub> , 298 K).	158
Figure A2.69	Partial HMBC spectrum of <b>4b</b> showing the aromatic region (500 MHz, 125 MHz, CDCl <sub>3</sub> , 298 K).	158
Figure A2.70	Full COSY spectrum of <b>4c</b> (500 MHz, 500 MHz, CDCl <sub>3</sub> , 296 K).	160
Figure A2.71	Partial COSY spectrum of <b>4c</b> showing the aromatic region (500 MHz, 500 MHz, CDCl <sub>3</sub> , 296 K).	161
Figure A2.72	Full ROESY spectrum of <b>4c</b> (500 MHz, 500 MHz, CDCl <sub>3</sub> , 296 K).	162
Figure A2.73	Partial ROESY spectrum of <b>4c</b> showing the aromatic region (500 MHz, 500 MHz, CDCl <sub>3</sub> , 296 K).	163
Figure A2.74	Full HSQC spectrum of <b>4c</b> (500 MHz, 125 MHz, CDCl <sub>3</sub> , 296 K).	164
Figure A2.75	Partial HSQC spectrum of <b>4c</b> showing the aromatic region (500 MHz, 125 MHz, CDCl <sub>3</sub> , 298 K).	164
Figure A2.76	Full HMBC spectrum of <b>4c</b> (500 MHz, 125 MHz, CDCl <sub>3</sub> , 296 K).	165
Figure A2.77	Partial HMBC spectrum of <b>4c</b> showing the aromatic region (500 MHz, 125 MHz, CDCl <sub>3</sub> , 296 K).	165
Figure A2.78	Full COSY spectrum of <b>5a</b> - <sup>13</sup> C <sub>2</sub> (500 MHz, 500 MHz, 1,2-C <sub>2</sub> H <sub>2</sub> Cl <sub>4</sub> , 408 K).	167
Figure A2.79	Partial COSY spectrum of <b>5a</b> - <sup>13</sup> C <sub>2</sub> showing the aromatic region (500 MHz, 500 MHz, 1,2-C <sub>2</sub> H <sub>2</sub> Cl <sub>4</sub> , 408 K).	168
Figure A2.80	Full ROESY spectrum of <b>5a</b> - <sup>13</sup> C <sub>2</sub> (500 MHz, 500 MHz, 1,2-C <sub>2</sub> H <sub>2</sub> Cl <sub>4</sub> , 408 K).	169
Figure A2.81	Partial ROESY spectrum of <b>5a</b> - <sup>13</sup> C <sub>2</sub> showing the aromatic region (500 MHz, 500 MHz, 1,2-C <sub>2</sub> H <sub>2</sub> Cl <sub>4</sub> , 408 K).	170
Figure A2.82	Full HSQC spectrum of <b>5a</b> - <sup>13</sup> C <sub>2</sub> (500 MHz, 125 MHz, 1,2-C <sub>2</sub> H <sub>2</sub> Cl <sub>4</sub> , 408 K).	171
Figure A2.83	Partial HSQC spectrum of <b>5a</b> - <sup>13</sup> C <sub>2</sub> showing the aromatic region (500 MHz, 125 MHz, 1,2-C <sub>2</sub> H <sub>2</sub> Cl <sub>4</sub> , 408 K).	171
Figure A2.84	Full HMBC spectrum of <b>5a</b> - <sup>13</sup> C <sub>2</sub> (500 MHz, 125 MHz, 1,2-C <sub>2</sub> H <sub>2</sub> Cl <sub>4</sub> , 408 K).	172

Figure A2.85	Partial HMBC spectrum of <b>5a</b> - $^{13}\text{C}_2$ showing the aromatic region (500 MHz, 125 MHz, 1,2- $\text{C}_2\text{H}_2\text{Cl}_4$ , 408 K).	172
Figure A2.86	UV/Vis absorption spectra of the compounds <b>4a</b> (green) and <b>5a</b> - $^{13}\text{C}_2$ (pink).	173
Figure A2.87	UV/Vis photoemission spectra of the compounds <b>4a</b> (green, $\lambda_{\text{ex}} = 344 \text{ nm}$ ) and <b>5a</b> (pink, $\lambda_{\text{ex}} = 389 \text{ nm}$ ).	173
Figure A2.88	Illustration of the dihedral angles measured in the optimized structures to represent torsion	174
Figure A2.89	Two possible conformations of <b>4a</b> : twisted (left), and anti (right). The <i>n</i> -nonyl chains were truncated to methyl groups.	174
Figure A2.90	Cyclic voltammograms of <b>4a</b> (green) and <b>5a</b> (pink)	199

## CHAPTER FOUR

Scheme 4.1	The Asao-Yamamoto benzannulation of diarylalkynes with 2-phenylethynylbenzaldehydes provides two possible regioisomers when $\text{X} \neq \text{H}$ and $\text{Ar}^1 \neq \text{Ar}^2$ .	202
Scheme 4.2	The benzannulation of diyne <b>5</b> by $^{13}\text{C}$ -labeled benzaldehyde <b>1</b> - $^{13}\text{C}_2$ provides the oligo(arylene) product as a single isotopomer.	204
Scheme 4.3	<b>A.</b> Proposed mechanism of the Yamamoto benzannulation. <b>B.</b> The observed regioselectivity is consistent with asynchronous bond formation with developing positive charge on one of the two alkyne carbons.	205
Figure 4.1	Partial $^1\text{H}$ NMR spectra (400 MHz, $\text{CDCl}_3$ , 298 K) of <b>8</b> (top) and the single regioisomer (400 MHz, $\text{CDCl}_3$ , 298 K) of <b>8</b> - $^{13}\text{C}$ derived from the benzannulation of <b>2</b> with <b>1</b> - $^{13}\text{C}_2$ (bottom). The single isotopomer exhibits strong $^1\text{H}$ - $^{13}\text{C}$ coupling only at the labeled position, which was unambiguously assigned as Hd based on multidimensional NMR experiments.	210
Figure 4.2	Partial $^1\text{H}$ NMR spectra (400 MHz, $\text{CDCl}_3$ , 298 K) of <b>9</b> (top) and the two regioisomers (500 MHz, $\text{CDCl}_3$ , 298 K) of <b>9</b> - $^{13}\text{C}$ derived from the benzannulation of <b>3</b> with <b>1</b> - $^{13}\text{C}_2$ (bottom). The mixture of two isotopomers gives rise to $^1\text{H}$ - $^{13}\text{C}$ coupling to both Ha and Hd with nearly equal integration ratios.	210

## APPENDIX THREE

Figure A3.1	$^1\text{H}$ NMR of <b>1-F</b> (400 MHz, $\text{CDCl}_3$ , 298 K).	231
Figure A3.2	$^{13}\text{C}$ NMR of <b>1-F</b> (100 MHz, $\text{CDCl}_3$ , 298 K).	231
Figure A3.3	$^1\text{H}$ NMR of <b>2</b> (500 MHz, $\text{CDCl}_3$ , 298 K).	232
Figure A3.4	$^{13}\text{C}$ NMR of <b>2</b> (125 MHz, $\text{CDCl}_3$ , 298 K).	232

Figure A3.5	$^1\text{H}$ NMR of <b>8</b> (500 MHz, $\text{CDCl}_3$ , 298 K).	233
Figure A3.6	$^{13}\text{C}$ NMR of <b>8</b> (125 MHz, $\text{CDCl}_3$ , 298 K).	233
Figure A3.7	$^1\text{H}$ NMR of <b>8a</b> - $^{13}\text{C}$ (400 MHz, $\text{CDCl}_3$ , 298 K).	234
Figure A3.8	$^{13}\text{C}$ NMR of <b>8a</b> - $^{13}\text{C}$ (75 MHz, $\text{CDCl}_3$ , 298 K).	234
Figure A3.9	$^1\text{H}$ NMR of <b>8c-F</b> (500 MHz, $\text{CDCl}_3$ , 298 K).	235
Figure A3.10	$^{13}\text{C}$ NMR of <b>8c-F</b> (125 MHz, $\text{CDCl}_3$ , 298 K).	235
Figure A3.11	$^1\text{H}$ NMR of <b>3</b> (400 MHz, $\text{CDCl}_3$ , 298 K).	236
Figure A3.12	$^{13}\text{C}$ NMR of <b>3</b> (100 MHz, $\text{CDCl}_3$ , 298 K).	236
Figure A3.13	$^1\text{H}$ NMR of <b>9</b> (500 MHz, $\text{CDCl}_3$ , 298 K).	237
Figure A3.14	$^{13}\text{C}$ NMR of <b>9</b> (125 MHz, $\text{CDCl}_3$ , 298 K).	237
Figure A3.15	$^1\text{H}$ NMR of <b>9a</b> - $^{13}\text{C}$ and <b>9b</b> - $^{13}\text{C}$ (400 MHz, $\text{CDCl}_3$ , 298 K).	238
Figure A3.16	$^{13}\text{C}$ NMR of <b>9a</b> - $^{13}\text{C}$ and <b>9b</b> - $^{13}\text{C}$ (75 MHz, $\text{CDCl}_3$ , 298 K).	238
Figure A3.17	$^1\text{H}$ NMR of <b>8c-F</b> (500 MHz, $\text{CDCl}_3$ , 298 K).	239
Figure A3.18	$^{13}\text{C}$ NMR of <b>8c-F</b> (125 MHz, $\text{CDCl}_3$ , 298 K).	239
Figure A3.19	$^1\text{H}$ NMR of <b>4</b> (500 MHz, $\text{CDCl}_3$ , 298 K).	240
Figure A3.20	$^{13}\text{C}$ NMR of <b>4</b> (125 MHz, $\text{CDCl}_3$ , 298 K).	240
Figure A3.21	$^1\text{H}$ NMR of <b>10</b> (500 MHz, $\text{CDCl}_3$ , 298 K).	241
Figure A3.22	$^{13}\text{C}$ NMR of <b>10</b> (125 MHz, $\text{CDCl}_3$ , 298 K).	241
Figure A3.23	$^1\text{H}$ NMR of <b>10a</b> - $^{13}\text{C}$ (400 MHz, $\text{CDCl}_3$ , 298 K).	242
Figure A3.24	$^{13}\text{C}$ NMR of <b>10a</b> - $^{13}\text{C}$ (125 MHz, $\text{CDCl}_3$ , 298 K).	242
Figure A3.25	$^1\text{H}$ NMR of <b>10c-F</b> (500 MHz, $\text{CDCl}_3$ , 298 K).	243
Figure A3.26	$^{13}\text{C}$ NMR of <b>10c-F</b> (125 MHz, $\text{CDCl}_3$ , 298 K).	243
Figure A3.27	$^1\text{H}$ NMR of <b>11d-F</b> (500 MHz, $\text{CDCl}_3$ , 298 K).	244
Figure A3.28	$^{13}\text{C}$ NMR of <b>11d-F</b> (125 MHz, $\text{CDCl}_3$ , 298 K).	244
Figure A3.29	$^1\text{H}$ NMR of <b>6</b> (600 MHz, $\text{CDCl}_3$ , 298 K).	245
Figure A3.30	$^{13}\text{C}$ NMR of <b>6</b> (125 MHz, $\text{CDCl}_3$ , 298 K).	245
Figure A3.31	$^1\text{H}$ NMR of <b>12a-F</b> and <b>12b-F</b> (600 MHz, $\text{CDCl}_3$ , 298 K).	246
Figure A3.32	$^{13}\text{C}$ NMR of <b>12a-F</b> and <b>12b-F</b> (150 MHz, $\text{CDCl}_3$ , 298 K).	246
Figure A3.33	$^1\text{H}$ NMR of <b>13a-F</b> and <b>13b-F</b> (600 MHz, $\text{CDCl}_3$ , 298 K).	247
Figure A3.34	$^{13}\text{C}$ NMR of <b>13a-F</b> and <b>13b-F</b> (125 MHz, $\text{CDCl}_3$ , 298 K).	247
Figure A3.35	Full COSY spectrum of <b>8</b> (500 MHz, 500 MHz, $\text{CDCl}_3$ , 298 K).	249
Figure A3.36	Partial COSY spectrum of <b>8</b> showing the aromatic region (500	250

	MHz, 500 MHz, CDCl <sub>3</sub> , 298 K).	
Figure A3.37	Full NOESY spectrum of <b>8</b> (500 MHz, 500 MHz, CDCl <sub>3</sub> , 298 K).	251
Figure A3.38	Partial NOESY spectrum of <b>8</b> showing the aromatic region (500 MHz, 500 MHz, CDCl <sub>3</sub> , 298 K).	252
Figure A3.39	Full HSQC spectrum of <b>8</b> (500 MHz, 125 MHz, CDCl <sub>3</sub> , 298 K).	253
Figure A3.40	Partial HSQC spectrum of <b>8</b> showing the aromatic region (500 MHz, 125 MHz, CDCl <sub>3</sub> , 298 K).	254
Figure A3.41	Full HMBC spectrum of <b>8</b> (500 MHz, 125 MHz, CDCl <sub>3</sub> , 298 K).	255
Figure A3.42	Partial HMBC spectrum of <b>8</b> showing the aromatic region (500 MHz, 125 MHz, CDCl <sub>3</sub> , 298 K).	256
Figure A3.43	Full COSY spectrum of <b>8c-F</b> (500 MHz, 500 MHz, CDCl <sub>3</sub> , 298 K).	258
Figure A3.44	Partial COSY spectrum of <b>8c-F</b> showing the aromatic region (500 MHz, 500 MHz, CDCl <sub>3</sub> , 298 K).	259
Figure A3.45	Full NOESY spectrum of <b>8c-F</b> (500 MHz, 500 MHz, CDCl <sub>3</sub> , 298 K).	260
Figure A3.46	Partial NOESY spectrum of <b>8c-F</b> showing the aromatic region (500 MHz, 500 MHz, CDCl <sub>3</sub> , 298 K).	261
Figure A3.47	Full HSQC spectrum of <b>8c-F</b> (500 MHz, 125 MHz, CDCl <sub>3</sub> , 298 K).	262
Figure A3.48	Partial HSQC spectrum of <b>8c-F</b> showing the aromatic region (500 MHz, 125 MHz, CDCl <sub>3</sub> , 298 K).	263
Figure A3.49	Full HMBC spectrum of <b>8c-F</b> (500 MHz, 125 MHz, CDCl <sub>3</sub> , 298 K).	264
Figure A3.50	Partial HMBC spectrum of <b>8c-F</b> showing the aromatic region (500 MHz, 125 MHz, CDCl <sub>3</sub> , 298 K).	265
Figure A3.51	Full COSY spectrum of <b>9</b> (500 MHz, 500 MHz, CDCl <sub>3</sub> , 298 K).	267
Figure A3.52	Partial COSY spectrum of <b>9</b> showing the aromatic region (500 MHz, 500 MHz, CDCl <sub>3</sub> , 298 K).	268
Figure A3.53	Full NOESY spectrum of <b>9</b> (500 MHz, 500 MHz, CDCl <sub>3</sub> , 298 K).	269
Figure A3.54	Partial NOESY spectrum of <b>9</b> showing the aromatic region (500 MHz, 500 MHz, CDCl <sub>3</sub> , 298 K).	270
Figure A3.55	Full HSQC spectrum of <b>9</b> (500 MHz, 125 MHz, CDCl <sub>3</sub> , 298 K).	271
Figure A3.56	Partial HSQC spectrum of <b>9</b> showing the aromatic region (500 MHz, 125 MHz, CDCl <sub>3</sub> , 298 K).	272
Figure A3.57	Full COSY spectrum of <b>9c-F (blue) and 9d-F (green)</b> (500 MHz, 500 MHz, CDCl <sub>3</sub> , 298 K).	274
Figure A3.58	Partial COSY spectrum of <b>9c-F (blue) and 9d-F (green)</b> showing the aromatic region (600 MHz, 600 MHz, CDCl <sub>3</sub> , 298 K).	275
Figure A3.59	Full NOESY spectrum of <b>9c-F (blue) and 9d-F (green)</b> (600 MHz, 600 MHz, CDCl <sub>3</sub> , 298 K).	276
Figure A3.60	Partial NOESY spectrum of <b>9c-F (blue) and 9d-F (green)</b> showing the aromatic region (600 MHz, 600 MHz, CDCl <sub>3</sub> , 298 K).	277
Figure A3.61	Full HSQC spectrum of <b>9c-F (blue) and 9d-F (green)</b> (500 MHz, 125 MHz, CDCl <sub>3</sub> , 298 K).	278

	125 MHz, CDCl <sub>3</sub> , 298 K).	
Figure A3.62	Partial HSQC spectrum of <b>9c-F (blue) and 9d-F (green)</b> showing the aromatic region (500 MHz, 125 MHz, CDCl <sub>3</sub> , 298 K).	279
Figure A3.63	Full HMBC spectrum of <b>9c-F (blue) and 9d-F (green)</b> (500 MHz, 125 MHz, CDCl <sub>3</sub> , 298 K).	280
Figure A3.64	Partial HMBC spectrum of <b>9c-F (blue) and 9d-F (green)</b> showing the aromatic region (500 MHz, 125 MHz, CDCl <sub>3</sub> , 298 K).	281
Figure A3.65	Full COSY spectrum of <b>10</b> (500 MHz, 500 MHz, CDCl <sub>3</sub> , 298 K).	283
Figure A3.66	Partial COSY spectrum of <b>10</b> showing the aromatic region (500 MHz, 500 MHz, CDCl <sub>3</sub> , 298 K).	284
Figure A3.67	Full ROESY spectrum of <b>10</b> (500 MHz, 500 MHz, CDCl <sub>3</sub> , 298 K).	285
Figure A3.68	Partial ROESY spectrum of <b>10</b> showing the aromatic region (500 MHz, 500 MHz, CDCl <sub>3</sub> , 298 K).	286
Figure A3.69	Full HSQC spectrum of <b>10</b> (500 MHz, 125 MHz, CDCl <sub>3</sub> , 298 K).	287
Figure A3.70	Partial HSQC spectrum of <b>10</b> showing the aromatic region (500 MHz, 125 MHz, CDCl <sub>3</sub> , 298 K).	288
Figure A3.71	Full HMBC spectrum of <b>10</b> (500 MHz, 125 MHz, CDCl <sub>3</sub> , 298 K).	289
Figure A3.72	Partial HMBC spectrum of <b>10</b> showing the aromatic region (500 MHz, 125 MHz, CDCl <sub>3</sub> , 298 K).	290
Figure A3.73	Full COSY spectrum of <b>10c-F</b> (500 MHz, 500 MHz, CDCl <sub>3</sub> , 298 K).	292
Figure A3.74	Partial COSY spectrum of <b>10c-F</b> showing the aromatic region (500 MHz, 500 MHz, CDCl <sub>3</sub> , 298 K).	293
Figure A3.75	Full ROESY spectrum of <b>10c-F</b> (500 MHz, 500 MHz, CDCl <sub>3</sub> , 298 K).	294
Figure A3.76	Partial ROESY spectrum of <b>10c-F</b> showing the aromatic region (500 MHz, 500 MHz, CDCl <sub>3</sub> , 298 K).	295
Figure A3.77	Full HSQC spectrum of <b>10c-F</b> (500 MHz, 125 MHz, CDCl <sub>3</sub> , 298 K).	296
Figure A3.78	Partial HSQC spectrum of <b>10c-F</b> showing the aromatic region (500 MHz, 125 MHz, CDCl <sub>3</sub> , 298 K).	297
Figure A3.79	Full HMBC spectrum of <b>10c-F</b> (500 MHz, 125 MHz, CDCl <sub>3</sub> , 298 K).	298
Figure A3.80	Partial HMBC spectrum of <b>10c-F</b> showing the aromatic region (500 MHz, 125 MHz, CDCl <sub>3</sub> , 298 K).	299
Figure A3.81	Full COSY spectrum of <b>11d-F</b> (500 MHz, 500 MHz, CDCl <sub>3</sub> , 298 K).	301
Figure A3.82	Partial COSY spectrum of <b>11d-F</b> showing the aromatic region (500 MHz, 500 MHz, CDCl <sub>3</sub> , 298 K).	302
Figure A3.83	Full ROESY spectrum of <b>11d-F</b> (500 MHz, 500 MHz, CDCl <sub>3</sub> , 298 K).	303
Figure A3.84	Partial ROESY spectrum of <b>11d-F</b> showing the aromatic region (500 MHz, 500 MHz, CDCl <sub>3</sub> , 298 K).	304
Figure A3.85	Full HSQC spectrum of <b>11d-F</b> (500 MHz, 125 MHz, CDCl <sub>3</sub> , 298 K).	305

Figure A3.86	Partial HSQC spectrum of <b>11d-F</b> showing the aromatic region (500 MHz, 125 MHz, CDCl <sub>3</sub> , 298 K).	306
Figure A3.87	Full HMBC spectrum of <b>11d-F</b> (500 MHz, 125 MHz, CDCl <sub>3</sub> , 298 K).	307
Figure A3.88	Partial HMBC spectrum of <b>11d-F</b> showing the aromatic region (500 MHz, 125 MHz, CDCl <sub>3</sub> , 298 K).	308
Figure A3.89	Full COSY spectrum of <b>12b-F (blue) and 12a-F (green)</b> (500 MHz, 500 MHz, CDCl <sub>3</sub> , 298 K).	310
Figure A3.90	Partial COSY spectrum of <b>12b-F (blue) and 12a-F (green)</b> showing the aromatic region (600 MHz, 600 MHz, CDCl <sub>3</sub> , 298 K).	311
Figure A3.91	Full ROESY spectrum of <b>12b-F (blue) and 12a-F (green)</b> (600 MHz, 600 MHz, CDCl <sub>3</sub> , 298 K).	312
Figure A3.92	Partial ROESY spectrum of <b>12b-F (blue) and 12a-F (green)</b> showing the aromatic region (600 MHz, 600 MHz, CDCl <sub>3</sub> , 298 K).	313
Figure A3.93	Full HSQC spectrum of <b>12b-F (blue) and 12a-F (green)</b> (600 MHz, 150 MHz, CDCl <sub>3</sub> , 298 K).	314
Figure A3.94	Partial HSQC spectrum of <b>12b-F (blue) and 12a-F (green)</b> showing the aromatic region (600 MHz, 150 MHz, CDCl <sub>3</sub> , 298 K).	315
Figure A3.95	Full HMBC spectrum of <b>12b-F (blue) and 12a-F (green)</b> (600 MHz, 150 MHz, CDCl <sub>3</sub> , 298 K).	316
Figure A3.96	Partial HMBC spectrum of <b>12b-F (blue) and 12a-F (green)</b> showing the aromatic region (600 MHz, 150 MHz, CDCl <sub>3</sub> , 298 K).	317
Figure A3.97	COSY spectrum of <b>13a-F (blue) and 13b-F (green)</b> (600 MHz, 600 MHz, CDCl <sub>3</sub> , 298 K).	319
Figure A3.98	ROESY spectrum of <b>13a-F (blue) and 13b-F (green)</b> (600 MHz, 600 MHz, CDCl <sub>3</sub> , 298 K).	320
Figure A3.99	HSQC spectrum of <b>13a-F (blue) and 13b-F (green)</b> (600 MHz, 150 MHz, CDCl <sub>3</sub> , 298 K).	321
Figure A3.100	HMBC spectrum of <b>13a-F (blue) and 13b-F (green)</b> (600 MHz, 150 MHz, CDCl <sub>3</sub> , 298 K).	322

## CHAPTER FIVE

Figure 5.1	<b>a.</b> Strategy used to transform PPEs (purple) into GNRs (green) featuring the benzannulation of the alkyne subunits followed by Scholl oxidation. <b>b.</b> GNRs described in this manuscript: <b>GNR-C<sub>9</sub>H<sub>19</sub></b> (top) is a first generation system with <i>n</i> -nonyl that confers insufficient dispersibility; <b>GNR-OH<sub>x</sub>g</b> (bottom) is fully dispersible and features an armchair edge structure.	339
Scheme 5.1	Synthesis of poly-( <i>p</i> -phenylene-ethynylene)s (PPEs) and their subsequent transformation into benzannulated polyphenylenes (BPPs).	340



Figure 5.2	<b>a.</b> A partial $^{13}\text{C}$ NMR (125 MHz, $\text{DMSO}-d_6$ , 353 K) spectrum of <b>PPE-OHxg</b> - $^{13}\text{C}$ indicates intense resonances corresponding to the alkyne carbons and the oligo-(ethylene-oxide) side chains. Signals corresponding to 1,3-butadiyne moieties are expected between 74 and 82 ppm and are not observed. <b>b.</b> Partial Raman spectra ( $I_{\text{ex}} = 785 \text{ nm}$ ) indicating the alkyne stretch of <b>PPE-OHxg</b> (blue) and <b>PPE-OHxg</b> - $^{13}\text{C}$ (purple).	343
Figure 5.3	Partial $^{13}\text{C}$ CP-MAS (100 MHz, 8.0 kHz MAS, rt) spectra of (a) <b>PPE-OHxg</b> - $^{13}\text{C}$ , (b) <b>BPP-OHxg</b> - $^{13}\text{C}(2,3)$ and (c) <b>BPP-OHxg</b> - $^{13}\text{C}(I)$ . The two isotopically labeled <b>BPP-OHxg</b> spectra both indicate efficient benzannulation of the corresponding PPE and indicate different chemical shift environments of the isotopically enriched carbons. Filled symbols indicate spinning side bands, stars indicate $^{13}\text{C}$ labeling.	345
Scheme 5.2	Scholl oxidation of model compound.	348
Scheme 5.3	Scholl oxidation of BPPs to GNRs.	349
Figure 5.4	Spectroscopic characterization of GNR-OHxg. <b>a.</b> Raman spectrum ( $I_{\text{ex}} = 488 \text{ nm}$ ) displays the <i>D</i> , <i>G</i> , and the corresponding 2 <i>D</i> and 2 <i>G</i> overtones and <i>D</i> + <i>G</i> combination vibrational features. <b>b.</b> Partial FT-IR spectrum of <b>BPP-OHxg</b> and <b>GNR-OHxg</b> indicate decreased intensity of the aromatic C-H stretching mode relative to the OHxg C-H stretching mode upon cyclodehydrogenation. <b>c.</b> A high resolution XPS C 1s spectrum was fit to three GL functions corresponding to the OHxg side chains (orange), graphitized carbon (blue) and a weak $\pi$ -type satellite peak (purple).	351
Figure 5.5	High-field (188 MHz, MAS rate of 15 kHz, $-5^\circ\text{C}$ ) $^{13}\text{C}$ CP-MAS spectra of natural abundance <b>GNR-OHxg</b> ( <b>a</b> ), and $^{13}\text{C}$ MAS spectra of isotopically enriched <b>GNR-OHxg</b> - $^{13}\text{C}(I)$ ( <b>b</b> ) and <b>GNR-OHxg</b> - $^{13}\text{C}(2,3)$ ( <b>c</b> ), indicating the presence of carbons in oligo ethylene oxide and aromatic chemical environments. Filled symbols indicate spinning side bands, stars indicate $^{13}\text{C}$ labeling.	352
Figure 5.6	Near-infrared (NIR) photoemission spectrum (DMF, $I_{\text{ex}} = 450 \text{ nm}$ ) of <b>GNR-OHxg</b> . The $I_{\text{max}}$ of 0.88 eV corresponds well to the calculated bandgap.	354
Figure 5.7	<b>a.</b> Repeating unit of the <b>GNR-OCH<sub>3</sub></b> model used for the DFT calculation of the band structure and density of states (DOS) of the <b>GNR-OHxg</b> . <b>b.</b> Calculated band structure and DOS of <b>GNR-OCH<sub>3</sub></b> near the Fermi level, indicating a bandgap of 0.83 eV.	356
Figure 5.8	<b>a.</b> Representative AFM micrograph of isolated <b>GNR-OHxg</b>	358

polymer chains deposited onto mica. **b.** A histogram of the particle height distribution produces average heights consistent with individual GNRs.

#### APPENDIX FOUR

Figure A4.1	Size-exclusion chromatogram of polymers with $D_{p,theor} = \infty$ (entry A Table S1), as detected by their differential refractive index on the THF mobile phase.	393
Figure A4.2	Size-exclusion chromatogram of polymers with $D_{p,theor} = \infty$ (entry A Table S1), as detected by their light scattering intensity.	393
Figure A4.3	Size-exclusion chromatogram of polymers with $D_{p,theor} = 80$ (entry B Table S1), as detected by their differential refractive index on the THF mobile phase.	394
Figure A4.4	Size-exclusion chromatogram of polymers with $D_{p,theor} = 80$ (entry B Table S1), as detected by their light scattering intensity.	394
Figure A4.5	Size-exclusion chromatogram of polymers with $D_{p,theor} = 40$ (entry C Table S1), as detected by their differential refractive index on the THF mobile phase.	395
Figure A4.6	Size-exclusion chromatogram of polymers with $D_{p,theor} = 40$ (entry C Table S1), as detected by their light scattering intensity.	395
Figure A4.7	Size-exclusion chromatogram of isotopically enriched polymers with $D_{p,theor} = 80$ (entry D Table S1), as detected by their differential refractive index on the THF mobile phase.	396
Figure A4.8	Size-exclusion chromatogram of isotopically enriched polymers with $D_{p,theor} = 80$ (entry D Table S1), as detected by their light scattering intensity.	396
Figure A4.9	Size-exclusion chromatogram of isotopically enriched polymers with $D_{p,theor} = 80$ (entry E Table S#), as detected by their light scattering and differential refractive index on the THF mobile phase.	397
Figure A4.10	SEC detail of <b>PPE-OHxg</b> (entry D) before, after precipitation, and the resulting residue, as detected by the differential refractive index response.	399
Figure A4.11	SEC detail of <b>BPP-OHxg</b> (entry D') before, after precipitation, and the resulting residue, as detected by the differential refractive index response.	400
Figure A4.12	UV-Visible photoabsorption spectra of <b>PPE-OHxg</b> , <b>BPP-OHxg</b> (1,2-dichloroethane) and <b>GNR-OHxg</b> (NMP).	401
Figure A4.13	UV-vis photoemission spectra of <b>PPE-OHxg</b> , <b>BPP-OHxg</b> (1,2-dichloroethane) and <b>GNR-OHxg</b> (NMP). Spectra recorded with a $\lambda_{ex} = 350$ nm at an optical density $A = 0.10$ .	401
Figure A4.14	UV-vis-NIR photoabsorption spectrum of <b>GNR-C<sub>9</sub>H<sub>19</sub></b> (black trace) in CS <sub>2</sub> .	402
Figure A4.15	UV-vis photoemission spectrum of <b>GNR-C<sub>9</sub>H<sub>19</sub></b> (black trace) in 1,2-dichlorobenzene (oDCB). Spectrum recorded with a $\lambda_{ex} = 400$ nm.	403

Figure A4.16	UV-Visible photoabsorption spectra of <b>7</b> (purple trace) and <b>8</b> (orange trace) in CHCl <sub>3</sub> .	403
Figure A4.17	Photoemission spectra of <b>7</b> (purple trace) and <b>8</b> (orange trace) in CHCl <sub>3</sub> . Spectra recorded with a $\lambda_{\text{ex}} = 285$ nm and 400 nm, respectively, at an optical density A = 0.10.	404
Figure A4.18	Near-IR photoabsorption spectrum of <b>GNR-OHxg</b> in DMF. Spectra recorded at a concentration of <i>ca.</i> 0.5 mg mL <sup>-1</sup> .	404
Figure A4.19	NIR photoemission spectra of <b>GNR-OHxg</b> in DMF vs. photon wavelength. Spectra recorded with a $\lambda_{\text{ex}} = 450$ nm and a concentration of <i>ca.</i> 0.5 mg mL <sup>-1</sup> .	405
Figure A4.20	NIR photoemission spectra of <b>GNR-OHxg</b> in DMF vs. photon energy. Spectra recorded with a $\lambda_{\text{ex}} = 450$ nm and a concentration of <i>ca.</i> 0.5 mg mL <sup>-1</sup> .	405
Figure A4.21	NIR photoemission spectrum of <b>GNR-C<sub>9</sub>H<sub>19</sub></b> in CS <sub>2</sub> vs. photon wavelength. Spectra recorded with a $\lambda_{\text{ex}} = 823$ nm.	406
Figure A4.22	NIR photoemission spectrum of <b>GNR-C<sub>9</sub>H<sub>19</sub></b> in CS <sub>2</sub> vs. photon energy. Spectra recorded with a $\lambda_{\text{ex}} = 823$ nm.	406
Figure A4.23	Integrated total emission intensity vs. optical density plot of anthracene in cyclohexane (yellow), <b>PPE-OHxg</b> (blue) and <b>BPP-OHxg</b> (red) in 1,2-dichloroethane, <b>GNR-OHxg</b> (green) in NMP, <b>7</b> (purple) <b>8</b> (orange) in CHCl <sub>3</sub> .	407
Figure A4.24	Raman spectrum of <b>PPE-OHxg</b> natural abundance (green) and <sup>13</sup> C enriched at the alkynes (blue). Note the shift from 2200 to 2112 cm <sup>-1</sup> of the -C≡C- symmetric stretching mode as result of the change in mass. $\lambda_{\text{ex}} = 785$ nm.	409
Figure A4.25	Featureless Raman spectrum of <b>BPP-OHxg</b> natural abundance. $\lambda_{\text{ex}} = 488$ nm.	409
Figure A4.26	Raman spectrum of <b>GNR-OHxg</b> natural abundance. $\lambda_{\text{ex}} = 488$ nm.	410
Figure A4.27	Raman spectrum of <b>GNR-OHxg</b> - <sup>13</sup> C( <i>I</i> ). $\lambda_{\text{ex}} = 488$ nm.	410
Figure A4.28	Raman spectrum of <b>GNR-OHxg</b> - <sup>13</sup> C( <i>2,3</i> ). $\lambda_{\text{ex}} = 488$ nm.	411
Figure A4.29	Raman spectrum of CS <sub>2</sub> extract of <b>GNR-C<sub>9</sub>H<sub>19</sub></b> . $\lambda_{\text{ex}} = 488$ nm. Signals at 520 and 998 cm <sup>-1</sup> correspond to Si and SiO <sub>2</sub> from substrate, respectively.	411
Figure A4.30	FTIR spectra of natural abundance <b>PPE-OHxg</b> , <b>BPP-OHxg</b> and <b>GNR-OHxg</b> in transmittance mode (offset by 20% for clarity).	412
Figure A4.31	FTIR spectra of CS <sub>2</sub> extract of <b>GNR-C<sub>9</sub>H<sub>19</sub></b> in transmittance mode.	412
Figure A4.32	XPS spectrum of <b>BPP-OHxg</b> . Note the sole presence of Si 1s (substrate), Au (substrate), C 1s and O 1s.	413
Figure A4.33	XPS spectrum of <b>GNR-OHxg</b> . Note the sole presence of Si 1s (substrate), Au (substrate), C 1s and O 1s.	413
Figure A4.34	XPS C 1s spectrum of <b>BPP-OHxg</b> .	414
Figure A4.35	XPS C 1s spectrum of <b>GNR-OHxg</b> .	414
Figure A4.36	XPS O 1s spectrum of <b>BPP-OHxg</b> .	415
Figure A4.37	XPS O 1s spectrum of <b>GNR-OHxg</b> .	415
Figure A4.38	Refined C 1s XPS overlay spectra of <b>GNR-OHxg</b> and <b>BPP-OHxg</b> .	416

Figure A4.39	Refined O 1s XPS overlay spectra of <b>GNR-OHxg</b> and <b>BPP-OHxg</b> .	416
Figure A4.40	$^{13}\text{C}$ CPMAS NMR spectrum of <b>PPE-OHxg</b> (natural abundance).	417
Figure A4.41	$^{13}\text{C}$ CPMAS NMR spectrum of <b>PPE-OHxg-<math>^{13}\text{C}</math></b> .	417
Figure A4.42	$I$ vs. $t_{\text{CP}}$ plot of <b>PPE-OHxg-<math>^{13}\text{C}</math></b> .	418
Figure A4.43	$^{13}\text{C}$ MAS NMR spectrum of <b>PPE-OHxg-<math>^{13}\text{C}</math></b> .	418
Figure A4.44	$^{13}\text{C}$ CPMAS NMR spectrum of <b>BPP-OHxg</b> (natural abundance).	419
Figure A4.45	$^{13}\text{C}$ CPMAS NMR spectrum of <b>BPP-OHxg-<math>^{13}\text{C}(I)</math></b> .	419
Figure A4.46	$^{13}\text{C}$ MAS NMR spectrum of <b>BPP-OHxg-<math>^{13}\text{C}(I)</math></b> .	420
Figure A4.47	$I$ vs. $t_{\text{CP}}$ plot of <b>BPP-OHxg-<math>^{13}\text{C}(I)</math></b> .	420
Figure A4.48	$I$ vs. $t_{\text{ID}}$ plot of <b>BPP-OHxg-<math>^{13}\text{C}(I)</math></b> .	421
Figure A4.49	$^{13}\text{C}$ CPMAS NMR spectrum of <b>BPP-OHxg-<math>^{13}\text{C}(2,3)</math></b> .	421
Figure A4.50	$^{13}\text{C}$ MAS NMR spectrum of <b>BPP-OHxg-<math>^{13}\text{C}(2,3)</math></b> .	422
Figure A4.51	$I$ vs. $t_{\text{CP}}$ plot of <b>BPP-OHxg-<math>^{13}\text{C}(2,3)</math></b> .	422
Figure A4.52	$I$ vs. $t_{\text{ID}}$ plot of <b>BPP-OHxg-<math>^{13}\text{C}(2,3)</math></b> .	423
Figure A4.53	$^{13}\text{C}$ CPMAS NMR spectrum of <b>GNR-OHxg</b> (natural abundance).	423
Figure A4.54	$^{13}\text{C}$ CPMAS NMR spectrum of <b>GNR-OHxg-<math>^{13}\text{C}(I)</math></b> .	424
Figure A4.55	$^{13}\text{C}$ MAS NMR spectrum of <b>GNR-OHxg-<math>^{13}\text{C}(I)</math></b> .	424
Figure A4.56	$^{13}\text{C}$ CPMAS NMR spectrum of <b>GNR-OHxg-<math>^{13}\text{C}(2,3)</math></b> .	425
Figure A4.57	$^{13}\text{C}$ MAS NMR spectrum of <b>GNR-OHxg-<math>^{13}\text{C}(2,3)</math></b> .	425
Figure A4.58	$^{13}\text{C}$ MAS NMR spectra of <b>PPE-C<sub>9</sub>H<sub>19</sub>-<math>^{13}\text{C}</math></b> (blue) <b>BPP-C<sub>9</sub>H<sub>19</sub>-<math>^{13}\text{C}</math></b> (2,3) (red) and <b>GNR-C<sub>9</sub>H<sub>19</sub>-<math>^{13}\text{C}</math></b> (2,3) (black).	426
Figure A4.59	<b>PPE-OHxg</b> (blue trace). Loss of HxgO side chains corresponds to a 56.7% mass loss. <b>BPP-OHxg</b> (red trace) Loss of HxgO side chains corresponds to at 47.7% loss. <b>GNR-OHxg</b> (black trace) HxgO side chains corresponds to a 48.2% mass loss.	427
Figure A4.60	<b>GNR-C<sub>9</sub>H<sub>19</sub></b>	427
Figure A4.61	AFM micrograph of <b>BPP-OHxg</b> mica substrate.	428
Figure A4.62	AFM micrograph of <b>GNR-OHxg</b> from DMF dropcast on mica substrate.	429
Figure A4.63	Particle height histogram of <b>GNR-OHxg</b> DMF dropcast deposited over mica as obtained from Figure S64.	430
Figure A4.64	Arbitrary views of the <b>GNR-OMe</b> ( $P2/m$ ) unit cell model. Axes are indicated.	433
Figure A4.65	Band structure and density of states plot of <b>GNR-OMe</b> ( $P2/m$ ) model using LDA-CA-PZ functional.	435
Figure A4.66	Band structure and density of states plot of <b>GNR-OMe</b> ( $P2/m$ ) model using GGA-PBE functional.	435
Figure A4.67	Band structure and density of state plot of <b>GNR-OMe</b> ( $P2/m$ ) model using GGA-PW91 functional.	436
Figure A4.68	Arbitrary views of the <b>GNR-OMe</b> ( $P1$ ) model.	436

Figure A4.69	Band structure and density of state plot of <b>GNR-OMe</b> (P1) model using GGA-PBE functional.	439
Figure A4.70	Arbitrary views of the <b>GNR-H</b> ( <i>Pmmm</i> ) model.	439
Figure A4.71	Band structure and density of states plot of <b>GNR-H</b> ( <i>Pmmm</i> ) model using GGA-PBE XC functional.	440
Figure A4.72	Arbitrary views of the <b>GNR-Me</b> (P1) model.	441
Figure A4.73	Atomic coordinates of <b>GNR-Me</b> (P1) model	442
Figure A4.74	<sup>1</sup> H NMR spectrum of <b>S2</b> . 25 °C, CDCl <sub>3</sub> .	443
Figure A4.75	<sup>13</sup> C NMR spectrum of <b>S2</b> . 25 °C, CDCl <sub>3</sub> .	443
Figure A4.76	<sup>1</sup> H NMR spectrum of <b>S3</b> . 25 °C, CDCl <sub>3</sub> .	444
Figure A4.77	<sup>13</sup> C NMR spectrum of <b>S3</b> . 25 °C, CDCl <sub>3</sub> .	444
Figure A4.78	<sup>1</sup> H NMR spectrum of <b>S4</b> . 25 °C, dioxane- <i>d</i> <sub>8</sub> /D <sub>2</sub> O/DCI 99:0.7:0.3 (v/v/v).	445
Figure A4.79	<sup>13</sup> C NMR spectrum of <b>S4</b> . 25 °C, dioxane- <i>d</i> <sub>8</sub> /D <sub>2</sub> O/DCI 99:0.7:0.3 (v/v/v).	445
Figure A4.80	<sup>1</sup> H NMR spectrum of <b>S7</b> . 25 °C, dmso- <i>d</i> <sub>6</sub> .	446
Figure A4.81	<sup>13</sup> C NMR spectrum of <b>S7</b> . 25 °C, dmso- <i>d</i> <sub>6</sub> .	446
Figure A4.82	<sup>1</sup> H NMR spectrum of <b>S7-<sup>13</sup>C<sub>4</sub></b> . 25 °C, dmso- <i>d</i> <sub>6</sub> .	447
Figure A4.83	<sup>13</sup> C NMR spectrum of <b>S7-<sup>13</sup>C<sub>4</sub></b> . 25 °C, dmso- <i>d</i> <sub>6</sub> .	447
Figure A4.84	<sup>1</sup> H NMR spectrum of <b>4</b> . 80 °C, dmso- <i>d</i> <sub>6</sub> .	448
Figure A4.85	<sup>13</sup> C NMR spectrum of <b>4</b> . 80 °C, dmso- <i>d</i> <sub>6</sub> .	448
Figure A4.86	<sup>1</sup> H NMR spectrum of <b>4-<sup>13</sup>C<sub>4</sub></b> . 25 °C, dmso- <i>d</i> <sub>6</sub> .	449
Figure A4.87	<sup>13</sup> C NMR spectrum of <b>4-<sup>13</sup>C<sub>4</sub></b> . 25 °C, dmso- <i>d</i> <sub>6</sub> .	449
Figure A4.88	<sup>1</sup> H NMR spectrum of <b>PPE-OHxg</b> . Entry A Table A4.1 ( <i>D<sub>p</sub></i> = ∞). 80 °C, dmso- <i>d</i> <sub>6</sub> .	450
Figure A4.89	<sup>1</sup> H NMR spectrum of <b>PPE-OHxg</b> . Entry B Table A4.1 ( <i>D<sub>p</sub></i> = 80). 80 °C, dmso- <i>d</i> <sub>6</sub> .	450
Figure A4.90	<sup>1</sup> H NMR spectrum of <b>PPE-OHxg</b> . Entry C Table A4.1 ( <i>D<sub>p</sub></i> = 40). 80 °C, dmso- <i>d</i> <sub>6</sub> .	451
Figure A4.91	<sup>13</sup> C NMR spectrum of <b>PPE-OHxg</b> . 80 °C, dmso- <i>d</i> <sub>6</sub> .	451
Figure A4.92	<sup>1</sup> H NMR spectrum of <b>PPE-OHxg-<sup>13</sup>C</b> . 80 °C, dmso- <i>d</i> <sub>6</sub> .	452
Figure A4.93	<sup>13</sup> C NMR spectrum of <b>PPE-OHxg-<sup>13</sup>C</b> . 80 °C, dmso- <i>d</i> <sub>6</sub> .	452
Figure A4.94	<sup>1</sup> H NMR spectrum of <b>6-<sup>13</sup>C<sub>2</sub></b> . 25 °C, CDCl <sub>3</sub> .	453
Figure A4.95	<sup>13</sup> C NMR spectrum of <b>6-<sup>13</sup>C<sub>2</sub></b> . 25 °C, CDCl <sub>3</sub> .	453
Figure A4.96	<sup>1</sup> H NMR spectrum of <b>BPP-OHxg</b> . 80 °C, dmso- <i>d</i> <sub>6</sub> .	454
Figure A4.97	<sup>13</sup> C NMR spectrum of <b>BPP-OHxg</b> . 80 °C, dmso- <i>d</i> <sub>6</sub> .	454
Figure A4.98	<sup>1</sup> H NMR spectrum of <b>BPP-OHxg-<sup>13</sup>C(I)</b> . At 135 °C in C <sub>2</sub> D <sub>2</sub> Cl <sub>4</sub> .	455
Figure A4.99	<sup>13</sup> C NMR spectrum of <b>BPP-OHxg-<sup>13</sup>C(I)</b> . At 135 °C in C <sub>2</sub> D <sub>2</sub> Cl <sub>4</sub> .	455
Figure A4.100	<sup>1</sup> H NMR spectrum of <b>BPP-OHxg-<sup>13</sup>C(2,3)</b> . 25 °C, CDCl <sub>3</sub> .	456

Figure A4.101	$^{13}\text{C}$ NMR spectrum of <b>BPP-OHxg-<math>^{13}\text{C}(2,3)</math></b> . 25 °C, $\text{CDCl}_3$ .	456
Figure A4.102	$^1\text{H}$ NMR spectrum of <b>S8</b> . 60 °C, $\text{dms}\text{-}d_6$ .	457
Figure A4.103	$^{13}\text{C}$ NMR spectrum of <b>S8</b> . 60 °C, $\text{dms}\text{-}d_6$ .	457
Figure A4.104	COSY spectrum of <b>S8</b> . 60 °C, $\text{dms}\text{-}d_6$ .	458
Figure A4.105	ROESY spectrum of <b>S8</b> . 60 °C, $\text{dms}\text{-}d_6$ .	458
Figure A4.106	HSQC spectrum of <b>S8</b> . 60 °C, $\text{dms}\text{-}d_6$ .	459
Figure A4.107	HMBC spectrum of <b>S8</b> . 60 °C, $\text{dms}\text{-}d_6$ .	459
Figure A4.108	$^1\text{H}$ NMR spectrum of <b>7</b> . 25 °C, $\text{dms}\text{-}d_6$ .	460
Figure A4.109	$^{13}\text{C}$ NMR spectrum of <b>7</b> . 25 °C, $\text{dms}\text{-}d_6$ .	460
Figure A4.110	COSY spectrum of <b>7</b> . 25 °C, $\text{dms}\text{-}d_6$ .	461
Figure A4.111	ROESY spectrum of <b>7</b> . 25 °C, $\text{dms}\text{-}d_6$ .	461
Figure A4.112	HSQC spectrum of <b>7</b> . 25 °C, $\text{dms}\text{-}d_6$ .	462

## LIST OF TABLES

Table A1.1	Molecular weight Determination of Polymers <b>1</b> and <b>3</b> .	69
Table A1.2	Common polyphenylene <b>3</b> Dihedral Monomers	71
Table A2.1	Calculated HOMOs and LUMOs of compounds <b>4a-d</b> and <b>5a-d</b>	175
Table A2.2	Cartesian coordinates of DFT computed geometries	177
Table A2.3	Optical and electrochemical bandgaps of the compounds <b>4a-4c</b> and <b>5a</b>	199
Table 4.1	Benzannulation of diaryl alkynes with <b>1</b> .	207
Table 4.2	Benzannulation of diaryl alkynes with <b>1</b> - <sup>13</sup> C <sub>2</sub> and <b>1-F</b> .	208
Table A3.1	Calculated relative energies of carbocations <b>8a'</b> , <b>-10a'</b> , <b>12a'</b> , <b>13a'</b> and <b>8b'</b> , <b>-10b'</b> , <b>12b'</b> , <b>13b'</b>	323
Table A3.2	Cartesian coordinates of DFT computed geometries	325
Table 5.1	Average molecular weights ( $M_n$ , $M_w$ ), dispersities ( $D_M$ ), and average degrees of polymerization ( $D_p$ ) of <b>PPE-OHxg</b> and <b>BPP-OHxg</b> samples, as determined from SEC/MALS in THF as mobile phase.	342
Table A4.1	Molecular weight determinations of synthesized polymers as determined by SEC-MALLS. $D_p$ was calculated from $M_w$ .	397
Table A4.2	Average Molecular weight and degree of polymerization of <b>PPE-OHxg</b> as determined by end group intensity from <sup>1</sup> H NMR	399
Table A4.3	Slope and correlation coefficient of the linear fit and quantum yields for the synthesized compounds.	407
Table A4.4	Statistics of <b>GNR-OHxg</b> DMF dropcast deposited over mica as obtained from Figure S64.	430
Table A4.5	Calculated electronic bandgaps.	432
Table A4.6	Atomic coordinates of <b>GNR-OMe</b> ( <i>P2/m</i> ) model.	433
Table A4.7	Atomic coordinates of <b>GNR-OMe</b> ( <i>P1</i> ) model.	437
Table A4.8	Atomic coordinates of <b>GNR-H</b> ( <i>Pmmm</i> ) model.	439
Table A4.9	Atomic coordinates of <b>GNR-Me</b> () model	441

## CHAPTER ONE

### GENERAL METHODS TO PREPARE HINDERED OLIGO- AND POLY(ARYLENES)

#### **1.1 Abstract**

Despite extensive research into the properties and applications of conjugated molecules and polymers, sterically crowded aromatic systems have received less attention because of synthetic limitations. However, recent studies demonstrate that these systems exhibit distinct properties and serve as precursors to nanographene structures with designable shape and functionality. Here, we discuss the most recent advances in the preparation of these materials, including *ortho*-arylene foldamers, graphene nanoribbon (GNR) and polycyclic hydrocarbon (PAH) precursors, and polyphenylene dendrimers. These targets require efficient reactions that tolerate high steric demands – especially polymeric systems, for whom incomplete conversions or side reactions represent unremovable defects. We highlight the most common and effective synthetic strategies that are able to produce sterically crowded architectures.

#### **1.2 Introduction**

Conjugated polymers exhibit many desirable properties, including semiconducting behavior, visible and near-infrared light absorption and emission, delocalized excitons, and accessible redox processes.<sup>1-3</sup> These properties motivate their continued study and incorporation into many optoelectronic, sensing, and energy storage devices. The most established classes of conjugated polymers, such as poly(*p*-phenylene)s,<sup>4-6</sup> polythiophenes,<sup>7,8</sup> and poly(phenylene ethynylene)s,<sup>9,10</sup> are often synthesized using transition-metal catalyzed processes, which tolerate diverse substituents and remarkable structural variation. The linkages that comprise these polymer



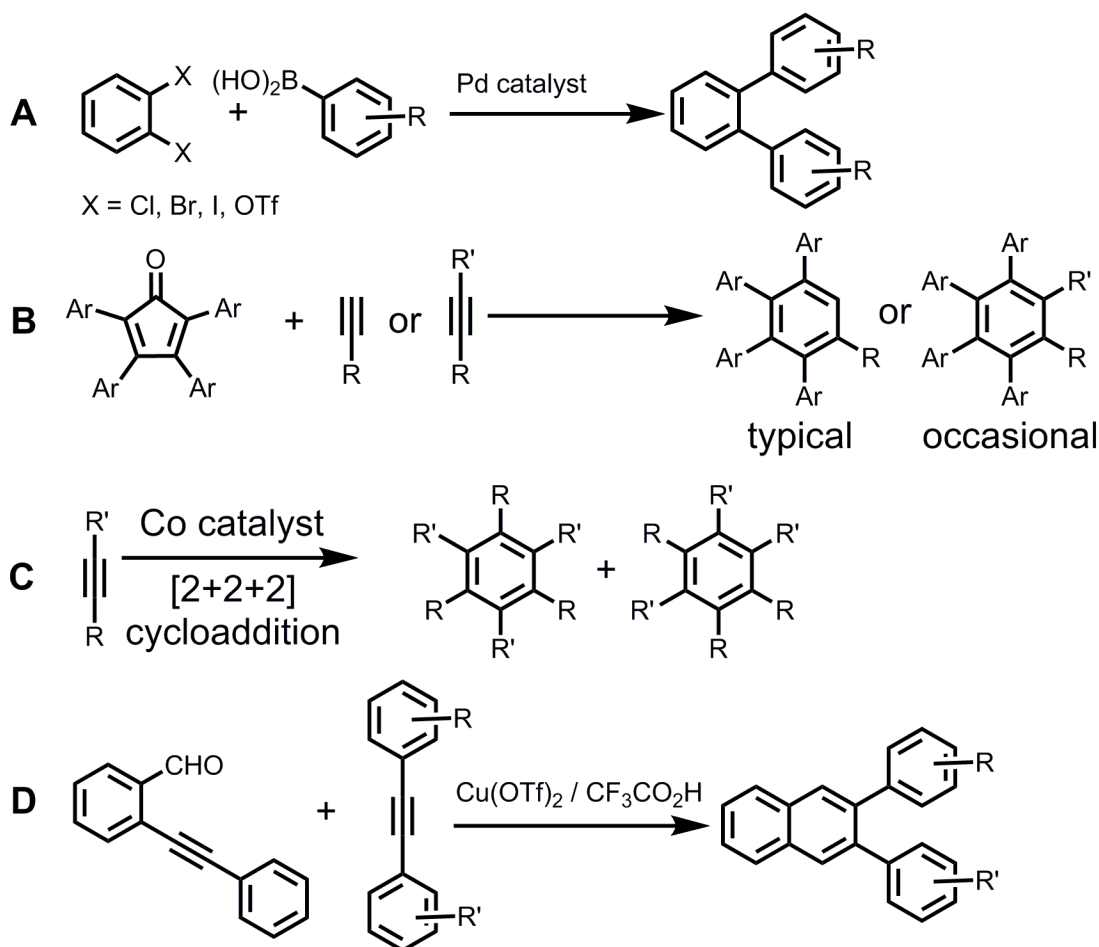


**Figure 1.1.** General strategies for the synthesis of sterically congested aromatic systems. **A.** Suzuki cross-coupling reaction **B.** Diels-Alder reaction between cyclopentadienones and alkynes **C.** alkyne cyclotrimerization **D.** Asao-Yamamoto benzannulation

backbones project in opposite directions from the aromatic systems (e.g., 1,4-phenyl; 2,5-thiophenyl), and this lack of steric hindrance facilitates efficient polymerizations. In contrast, ortho-linked analogues, such as poly(*o*-phenylene)s, are more difficult to synthesize. Highly congested aromatic polymers and molecular compounds have recently attracted increased attention for their unique conformational behavior,<sup>11-19</sup> the distinct electronic properties and shape complementarity to fullerenes of contorted polycyclic aromatic hydrocarbons,<sup>20,21</sup> and applications as precursors to nanostructured analogues of graphene.<sup>22-32</sup> New methods of efficiently accessing these compounds are now emerging, joining established strategies, including transition metal-catalyzed cross-couplings,<sup>23,24</sup> cycloadditions between

tetra(aryl)cyclopentadienones and alkynes,<sup>22,33</sup> and alkyne cyclotrimerizations.<sup>34-36</sup> These methods all tolerate the steric demands associated with crowded architectures. This chapter briefly introduces these methods and describes their recent application to the synthesis of congested aromatic architectures.

### ***1.3 Overview of General Synthesis Strategies For Congested Aromatic Systems***

The synthesis of congested aromatic polymers and molecular compounds requires transformations that proceed efficiently on sterically hindered substrates. Functional group tolerance, regio- and/or stereoselectivity if applicable, and ease of accessing the reactants are also important considerations. Finally, it should be noted that polymerization or polymer modification strategies require particularly efficient reactions to be of practical use – either to ensure high molecular weight polymers or avoid defects along the chain from incomplete or undesired reactions. Each transformation highlighted in this section fulfills many of the above criteria and represents a useful starting point for designing new syntheses. Their application to specific aromatic architectures follows later in this chapter.

Transition metal-catalyzed cross-coupling reactions revolutionized organic synthesis, including the field of conjugated polymers, and their importance was recognized with the 2010 Nobel Prize in Chemistry. These reactions, including the Sonogashira coupling of aryl halides and terminal alkynes<sup>9,10</sup> and the Stille coupling of aryl halides and organotin compounds,<sup>37</sup> have been widely applied to prepare traditional conjugated polymers. The Suzuki reaction, which couples an aryl halide and an aryl boronate species, has been used most extensively to prepare *ortho*-linked aromatic systems (Figure 1.1A)<sup>5</sup>. Nevertheless, the reactivity of *ortho*-linked systems remains lower than *meta*- and *para*-linked aromatic systems. The Suzuki reaction has been employed extensively to prepare congested molecular compounds and oligo(*o*-

phenylene)s,<sup>15-19,38</sup> but high molecular weight poly(*o*-phenylene)s have not yet been demonstrated.

The Diels-Alder reaction of tetraarylcyclopentadienones with terminal alkynes is remarkably versatile as it has been broadly applied to prepare densely substituted linear and branched poly(phenylene)s (Figure 1.1B).<sup>22,31,39-46</sup> Triisopropylsilyl (TIPS)-protected alkynes do not undergo the Diels-Alder reaction with tetraarylcyclopentadienones under typical reaction conditions. However, the terminal alkynes that form upon deprotection of the TIPS groups are highly reactive. This difference in reactivity allows building huge dendritic structures with high monodispersity.<sup>39,46</sup> These shape persistent dendrimers can be used to decorate chromophores<sup>39,42,45,47</sup> or can be graphitized by oxidation to large nanographenes.<sup>29,31,32</sup> Moreover, it is possible to synthesize GNR precursors using bifunctional alkynes and cyclopentadienone derivatives.<sup>22,41,43</sup> The reaction is commonly used for the synthesis of hexaarylbenzenes, which are often oxidized to the corresponding hexabenzocoronenes or related PAHs under Scholl oxidation conditions.<sup>48</sup>

The cyclotrimerization of alkynes (Figure 1.1C) also provides tri- or hexasubstituted benzenes in a single convergent step.<sup>34,48,49</sup> This reaction is catalyzed by many transition metals, and a cobalt catalyst, such as CpCo(CO)<sub>2</sub> or Co<sub>2</sub>(CO)<sub>8</sub>, is usually the catalyst of choice. The reaction offers impressive steric tolerance, as exemplified by the synthesis of a dendrimer with a hexasubstituted benzene core from the corresponding alkyne bearing two dendrons.<sup>50</sup> The cyclotrimerization of aromatic diynes has been used to form hyperbranched polyarylenes with unique light-emitting properties.<sup>51</sup> One notable limitation of the reaction is that unsymmetric alkynes give rise to two possible regioisomers, often with little or no selectivity.

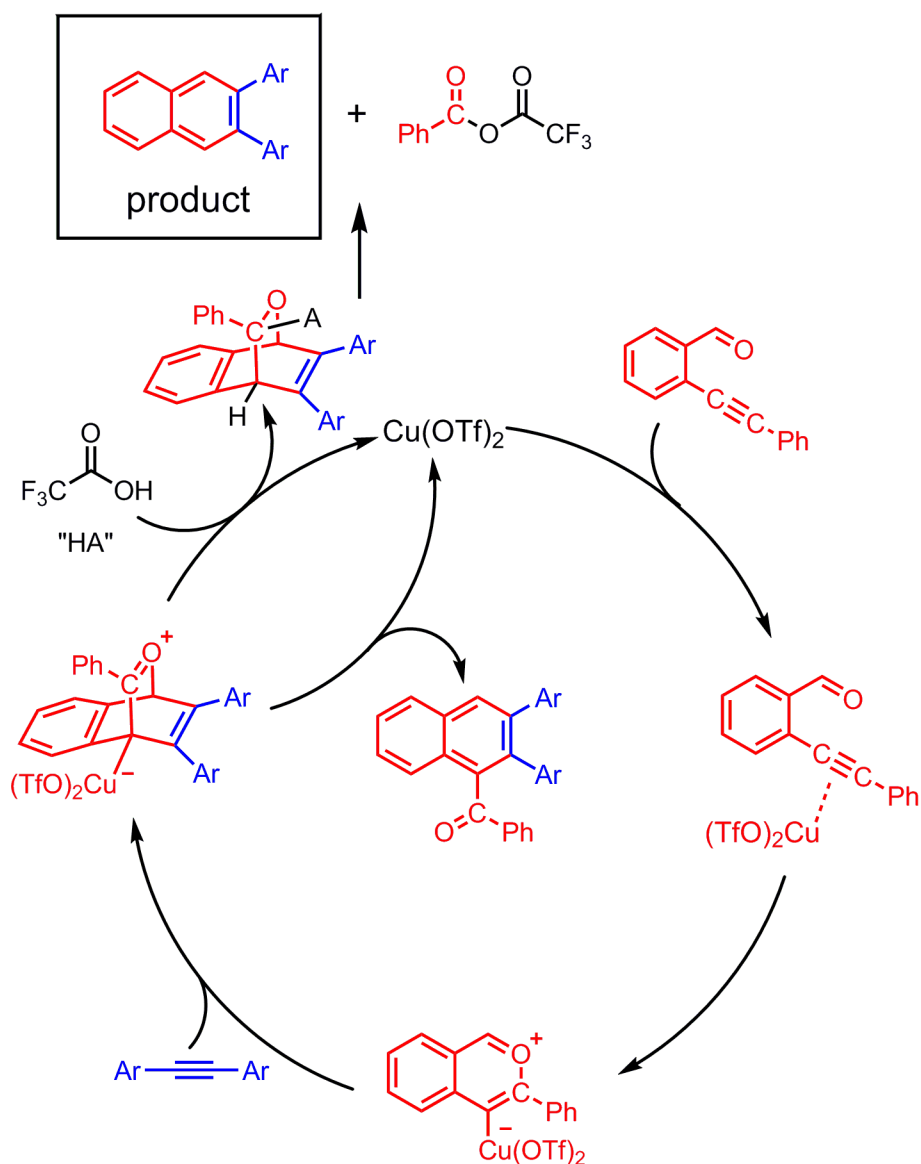


**Figure 1.2.** Proposed mechanism of the Yamamoto benzannulation. Adapted from Ref. 52. Copyright (2003) American Chemical Society.

Finally, the Asao-Yamamoto benzannulation reaction transforms diarylacetylenes into 2,3-diarylnaphthalene moieties with excellent efficiency, tolerance of bulky substituents, and often complete regioselectivity (Figure 1.1D).<sup>52</sup> As will be described later in this thesis, we used this reaction to modify the relatively unreactive alkynes along a poly(phenylene ethynylene) backbone to provide a poly(arylene) with alternating *ortho* and *para* linkages. The benzannulation reaction was the first reported example of such a transformation along a

conjugated polymer backbone, which provides a means to transform readily available PPEs to otherwise inaccessible poly(arylene)s.<sup>53</sup> The reaction was proposed<sup>52</sup> to proceed through the formation of a Cu-bound pyrylium intermediate, which reacts with the alkyne in a formal [4+2] reaction, followed by rearomatization (Figure 1.2). Two current limitations of this reaction are notable: a ketone side product is formed in the absence of a strong Brønsted acid, and the efficiency of the reaction drops significantly when electron withdrawing groups are present on the diarylalkyne. Both of these features limit the substrate scope.

#### **1.4 Poly- and Oligo(*o*-Arylene)s**

Although meta- and para-linked polyphenylenes have been studied extensively, poly(*o*-phenylene)s were almost completely unexplored until recent work by Hartley<sup>14-19</sup> and Aida<sup>11-13</sup>. The close proximity of the phenyl substituents along the polymer backbone complicates the synthesis of high molecular weight polymers by standard oxidative or cross-coupling methods used for poly(*p*-phenylene)s. In the 1960s, Kovacic reported a chloro-substituted poly(*o*-phenylene) through the oxidative polymerization of chlorobenzene, but the resulting samples had low molecular weights and are thought to have contained larger PAH defects.<sup>54-56</sup> The first structurally well-defined *ortho*-linked polyarylenes were poly(2,3-quinoxaline)s reported by Ito and coworkers.<sup>57,58</sup> Simpkins systematically synthesized a series of oligo-*o*-phenylenes using iterative Suzuki coupling reactions and showed that the resulting hexamer folded into a tight helical structure in the solid state.<sup>59</sup> The groups of Hartley and Aida have since developed complementary methods to prepare oligo(*o*-phenylene)s, both as discrete species and as mixtures of oligomers (Figure 1.3). These synthetic advances enabled studies of the solution and solid-state behaviors of these materials, which have provided improved insight into their conformational and electronic delocalization.

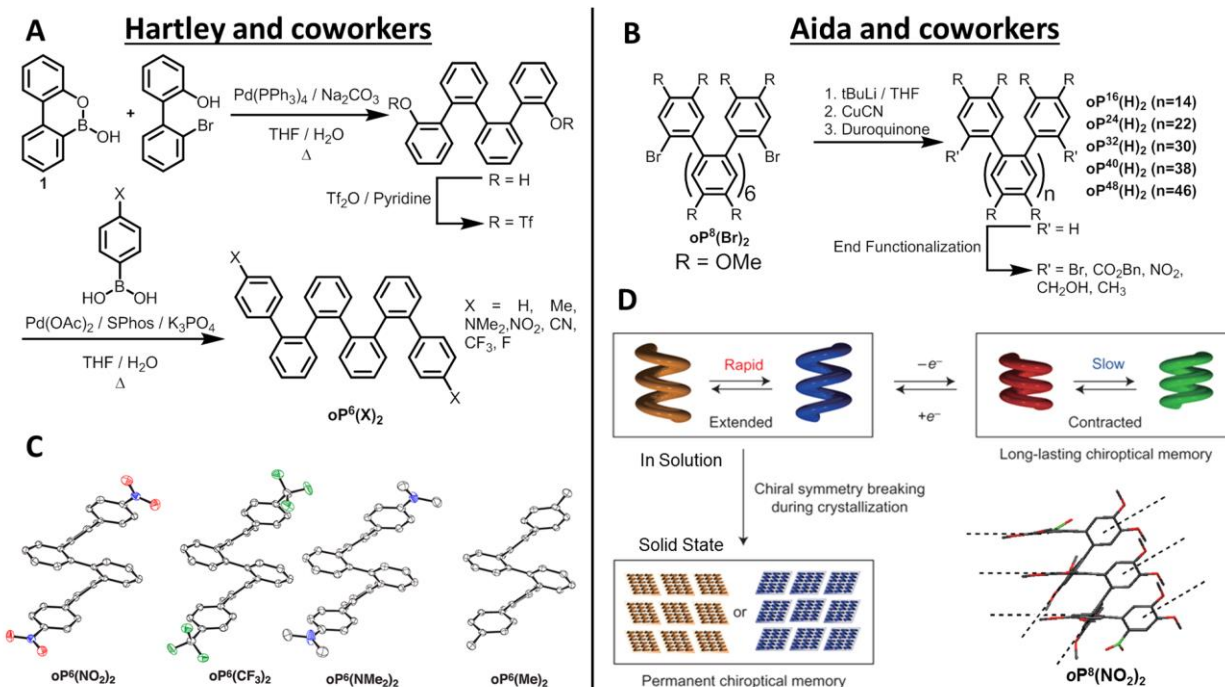


**Figure 1.3.** General synthetic strategies to prepare oligo(*o*-phenylene)s. **A.** An iterative Suzuki cross-coupling-triflation synthesis of *o*-arylenes. **B.** Cu-mediated oxidative coupling of lithiated precursors to form oligomers and polymers. **C.** Several end functionalized hexa-*o*-phenylenes. **D.** Redox switching of the conformational behavior of  $\text{oP}^8(\text{NO}_2)_2$ . A and C were reproduced from Ref. 18. Copyright (2013) American Chemical Society. B and D were reproduced from Ref. 13 with permission from The Nature Publishing Group.

Hartley *et al.* synthesized oligo-*o*-phenylenes using iterative Suzuki coupling and triflation steps, starting with the 9,10-boroxaphenanthrene **1**, and substituted derivatives (Figure 1.3A).<sup>14-19</sup> Oligomers up to dodecamers were described, although this strategy appears amenable for higher oligomers as well. This iterative approach allows different monomers to be incorporated at any step such that functional groups may be positioned specifically along the oligomer backbone or end groups. Similar iterative cross-coupling strategies were recently used to make oligo-*o-o-p*-phenylenes<sup>38</sup> and oligo(naphthalene-2,3-diyl)s.<sup>60</sup>

Aida *et al.* employed a Cu-mediated oxidative coupling of dilithiated *o*-phenylenes to prepare higher molecular weight oligo(*o*-phenylene)s (Figure 1.3B).<sup>11,13</sup> Using an octamer as a precursor to larger oligomers (up to 48-mers) proved important, because smaller precursors

produced undesired cyclic side products. The resulting mixture of oligomers was resolved into specific species using preparative size exclusion chromatography, which enabled precise characterization of their identity and length-dependent behaviors. Intriguing effects on the racemization of these helical compounds based on the substituents on the terminal arene group were observed, suggesting a rich and complex conformational landscape for these newly accessible systems.

Studies of high-quality oligo(*o*-phenylene) samples indicate that these polymers adopt specific helical conformations.<sup>15,16,18,19</sup> Numerous examples by Simpkins,<sup>59</sup> Hartley (Figure 1.3C),<sup>18</sup> and Aida (Figure 1.3D)<sup>13</sup> adopt one-handed helices with a pitch of three phenylene units. Hartley found that unsubstituted *o*-phenylenes adopt two different helical conformations: an “open” helix with large dihedral angles (130°) throughout the backbone, approximating a more planar structure, or a “closed” helix with small dihedral angles (70°) that is more tightly packed.<sup>19</sup> Most *o*-phenylenes crystallize in the closed form, but a hexamer exhibits closed helix character in the middle of the molecule and open helix character at the ends.<sup>16</sup> The open helical conformation is preferred for poly(2,3-quinoxaline)s reported by Ito, presumably because of the increased size of the quinoxaline repeat unit.<sup>57,61</sup>

In contrast to their solid-state structures, *o*-phenylene oligomers are conformationally dynamic in solution, with both open and closed conformations possible. Aida *et al.* reported **oP<sup>8</sup>(NO<sub>2</sub>)<sub>2</sub>**, an octamer that crystalizes with chiral-symmetry breaking (i.e., the resulting crystals are enriched in one of the two possible enantiomers).<sup>13</sup> Upon dissolution, the helices quickly racemize, indicating their dynamic bond rotations. In contrast, the radical cation of **oP<sup>8</sup>(NO<sub>2</sub>)<sub>2</sub>** exhibits a tighter helix in the solid-state, which suggests charge delocalization over the entire molecule. In solution, this species racemized 450 times slower compared to the neutral species

(Figure 1.3D). The dynamic nature of *o*-phenylene folding generally gives rise to complex NMR spectra, and Aida demonstrated that specific end groups lock the helical conformation, as evidenced by their simplified NMR spectra. This effect appears to be steric since both electron-donating and electron-withdrawing substituents induced the behavior. The racemization rate also slowed with increasing oligomer size. In contrast, Hartley observed different conformational behavior in a series of hexamers. The perfect closed helix was the major component, followed by open at one end, and lastly open at both ends. Electron-withdrawing substituents gave higher ratios of perfect helices, which was attributed to the increased strength of their stacking interactions. Perfect helical conformations were not observed in any of these systems in CD<sub>3</sub>CN. The two oligomers most obviously differ in their methoxy or hydrogen substituents along the oligomer backbone, respectively. Differences in their conformational behavior almost certainly derive from this structural feature, although the nature of these effects is not yet clear. The conformation of *o*-arylenes is sensitive to both steric and electronic perturbation, which might be exploited in stimuli-responsive systems in the future.

The nature of conjugation and electronic delocalization in *o*-phenylenes is of great interest given the inability of the aromatic rings to adopt planar conformations. Hartley demonstrated that the effective conjugation lengths of oligo(*o*-phenylene)s are 8-9 repeat units, considerably longer than previously thought. It should be noted that the effect of conjugation is small relative to other conjugated polymers with similar effective conjugation lengths due to twisting of the backbone. The evidence for hole delocalization in **oP<sup>8</sup>(NO<sub>2</sub>)<sub>2</sub>** described above is also suggestive of the effective conjugation of *o*-phenylenes.

Ito and coworkers recently pioneered a new approach to synthesize poly(*o*-arylene)s, which utilizes monomers that serve as masked aryne equivalents.<sup>62</sup> [2.2.1] oxabicyclic alkenes



were polymerized using a Pd catalyst (Figure 1.4). The resulting polymer was aromatized by dehydration using HCl. Optimized polymerization conditions provide polymers with  $M_w = 5500$  and  $PDI = 1.2$  from alkene **2a**, corresponding to degrees of polymerization of up to 38. This method is significant because previous attempts to polymerize arynes resulted in only cyclic compounds and because of the compatibility of several aromatic systems, including masked anthracenes (**2d**) and triphenylenes (**2e**). Further optimization of this method and conversion of the resulting polymers to graphene nanoribbons (see below) are anticipated.

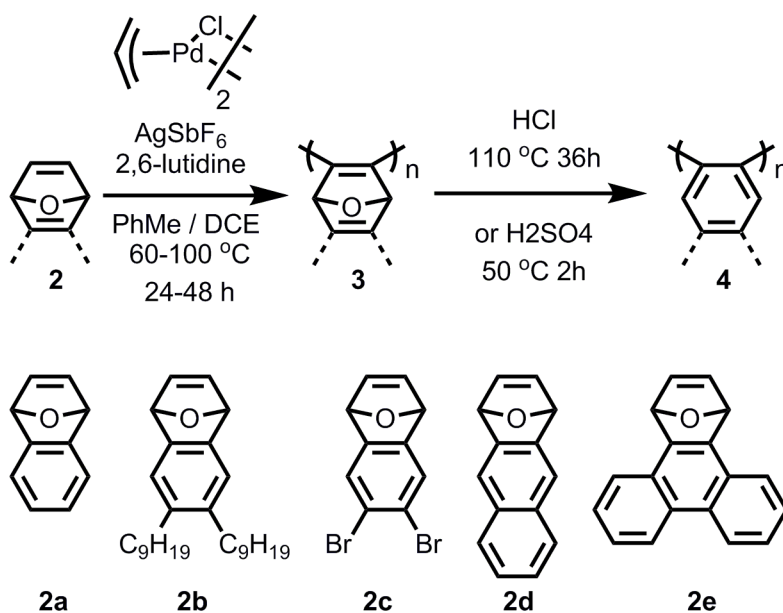


**Figure 1.4.** Synthesis of poly(*o*-arylene)s *via* polymerization of [2.2.1] Oxabicyclic Alkenes and Subsequent Dehydration. Reproduced from Ref. 62. Copyright (2014) American Chemical Society.

With the recent development of robust syntheses of *o*-arylene oligomers, their unique optoelectronic properties and helical conformations may result in new applications. For example, Aida employed an octameric *o*-phenylene to direct the ordering of discotic liquid crystals.<sup>13</sup> Also, *o*-phenylenes will serve as precursors to GNRs if they can be cyclodehydrogenated cleanly and efficiently.

### 1.5 Graphene Nanoribbon Precursors

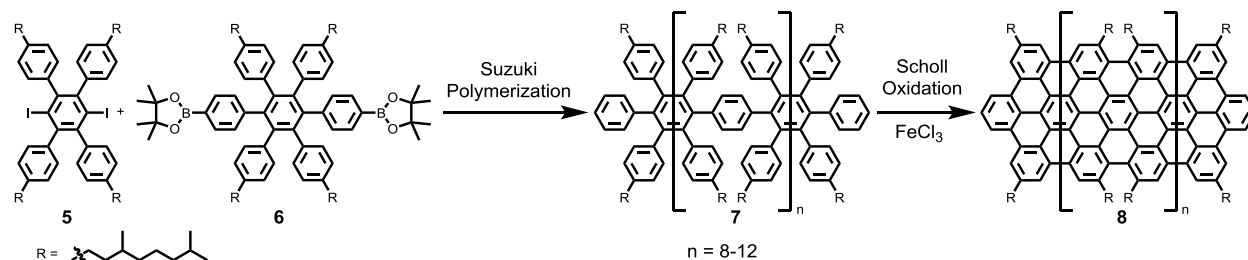


**Figure 1.5.** Synthesis of polyphenylene **7**, *via* Suzuki coupling and its graphitization to GNR **8** *via* Scholl oxidation. Reproduced from Ref. 23. Copyright (2008) American Chemical Society.

With the emergence of graphene as high-performance electronic material, methods to rationally synthesize nanostructured graphenes with control of their electronic, optical, and physical properties have attracted investment. Of particular importance are GNRs, which are thin strips of graphene (width  $<10$  nm). The finite width of GNRs give them their semiconducting properties by opening a bandgap due to quantum confinement effects. GNRs have been primarily fabricated by top-down approaches, such as patterning of graphene by lithography<sup>63-67</sup> or unzipping carbon nanotubes (CNTs).<sup>68-71</sup> However, these methods do not provide sufficient control over the width or edge structure, and produce GNRs with a large variation between individual ribbons.

As an alternative, bottom-up syntheses have been developed, which involve polymerizing small molecules to form polyphenylenes that can be oxidized to GNRs.<sup>22-24,26,41,72-77</sup> In this method, the polymerization step provides good control over the width, edge structure, and functionality of resulting GNRs. One approach to this bottom-up strategy is to polymerize aryl halides on metal surfaces *via* thermal activation. Certain metal surfaces, such as Au(111), catalyze the homolytic cleavage of aryl-halide bonds and allow the polymerization of the resulting radicals. Elevated temperature induces cyclodehydrogenation and planarization to form

GNRs.<sup>73-75</sup> This method provides excellent structural control, and atomic-scale characterization by scanning probe microscopy has been achieved. However, only a small amount of material is obtained and GNRs remain bound to their metal growth substrate. Bottom-up syntheses are also conducted in solution, which provides bulk samples of the resulting ribbons. Moreover, dispersible samples in solution enable facile deposition on a range of surfaces, which will be necessary for device fabrication and characterization. In an early example of a solution-based GNR synthesis, Müllen and coworkers described a Suzuki coupling polymerization using the monomers **5** and **6** to give polyphenylene **7** (Figure 1.5).<sup>23</sup> **7** was subsequently graphitized to GNR **8** by the Scholl oxidation. The oxidation worked efficiently, but the degree of polymerization was low (DP = 8-12), leading to the formation of only oligomeric species. The low DP can be attributed to high steric demands imparted by the *o*-substituents relative to the iodines. This method requires improvements, as sufficiently long ribbons are needed for GNRs to be useful for device fabrication.

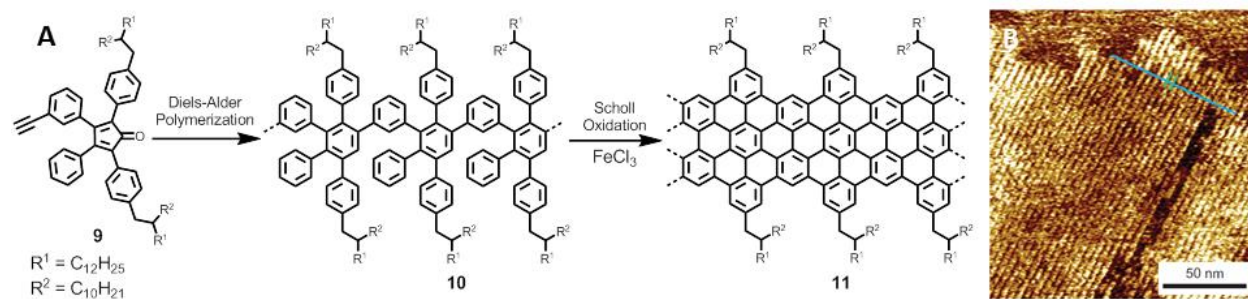


**Figure 1.6.** Diels-Alder polymerization for the synthesis of GNRs **A.** Diels-Alder Polymerization of **9**, and subsequent graphitization to GNR **11.** **B.** An AFM image of long (100–200nm) GNRs on highly ordered pyrolytic graphite. Reproduced from Ref. 22 with permission of The Nature Publishing Group.

More recently, Müllen and coworkers presented a new polymerization strategy to address the challenge of increasing the GNR length. Diels-Alder reactions of cyclopentadienone derivatives with terminal alkynes form highly branched and sterically crowded phenylenes. This

strategy was used to make graphitic ribbons by an AA-BB type step-growth polymerization more than a decade ago.<sup>41,43</sup> This idea has been refined recently to carry out an AB type step-growth polymerization to eliminate any stoichiometric imbalance, resulting in large polyphenylenes with  $M_w = 370 \pm 40 \text{ kg} \cdot \text{mol}^{-1}$  and polydispersity index (PDI) = 4.9 (Figure 1.6).<sup>22</sup> Subsequent Scholl oxidation gave highly dispersible GNRs, with lengths greater than 200 nm. Drop-cast samples were imaged by atomic force microscopy (AFM) to confirm the expected long lengths of the ribbons (Figure 1.6B).

In summary, advances in the bottom-up synthesis of graphene nanoribbons now provide access to large amounts of structurally precise materials. Their electronic properties are now being evaluated with an eye towards field-effect transistors and sensor platforms.

## **1.6 Polyphenylene Dendrimers**

Dendrimers are discrete macromolecules that branch at each monomer repeat unit. This structure enforces a globular shape and distinct interior and exterior microenvironments. Their structural precision has inspired a wide variety of fundamental studies of their ability to mediate energy and electron transfer between donors and acceptors, immobilize catalysts at the periphery or core, and release molecular payloads, such as drug molecules, in response to various stimuli.<sup>78-80</sup> For example, Fréchet and coworkers reported a water soluble dendrimer that acted as a singlet oxygen photosensitizer.<sup>81</sup> Polyphenylene dendrimers are a rigid and shape-persistent subclass that organize arbitrary groups in the core, scaffold, or the periphery.<sup>82</sup> Their rigid, unique 3D structures with large spaces differentiate them from more flexible backbones, whose conformational mobility can lead to backfolding of the arms into the interior. Polyphenylene dendrimers have been used to produce energy transfer systems containing densely attached chromophores. As such, aggregation, excimer formation, and self-quenching of the

polyphenylene dendrimers decorated with chromophores is very limited compared to flexible dendrimers.<sup>39,42,45,47</sup> Other desirable properties of such dendritic structures are conjugation, monodispersity, and processability. For example, photoresponsive polyphenylene dendrimers of different sizes with azobenzene linkages have been synthesized and exhibited photo-switchable conformation changes.<sup>40</sup> This switching behavior can be used for energy transfer and guest encapsulation and release.<sup>47</sup>

The most common strategy to build these dendrimers is the iterative Diels-Alder reaction of terminal alkynes with cyclopentadienones containing triisopropylsilyl (TIPS) protected alkynes.<sup>44,46,82</sup> Upon reaction, TIPS groups are removed, providing terminal alkynes available for further polymerization. The reaction is irreversible due to the extrusion of CO and formation of a stable benzene ring. Most recently, Müllen *et al.* reported a 9th generation polyphenylene dendrimer **G9** with molecular weight in the megadalton range with good structural precision (Figure 1.7).<sup>39</sup> The large chromophore core and AB<sub>2</sub> building blocks with extended arms resulted in dendrimer arms with no backfolding. This, combined with the isolation of deprotected alkynes from degradation conditions, made it possible to synthesize very large dendrimers with few defects. Polyphenylene dendrimers are also useful precursors of nanographene structures. Cyclodehydrogenation of 3D polyphenylenes gives 2D graphitic sheets.<sup>26,27,29-32</sup> Precise control over the size, composition and functional groups provide these molecular analogs of graphene with unique photophysical and catalytic properties. For instance, nitrogen doped nanographenes were recently used for electrocatalytic oxygen reduction.<sup>83,84</sup>

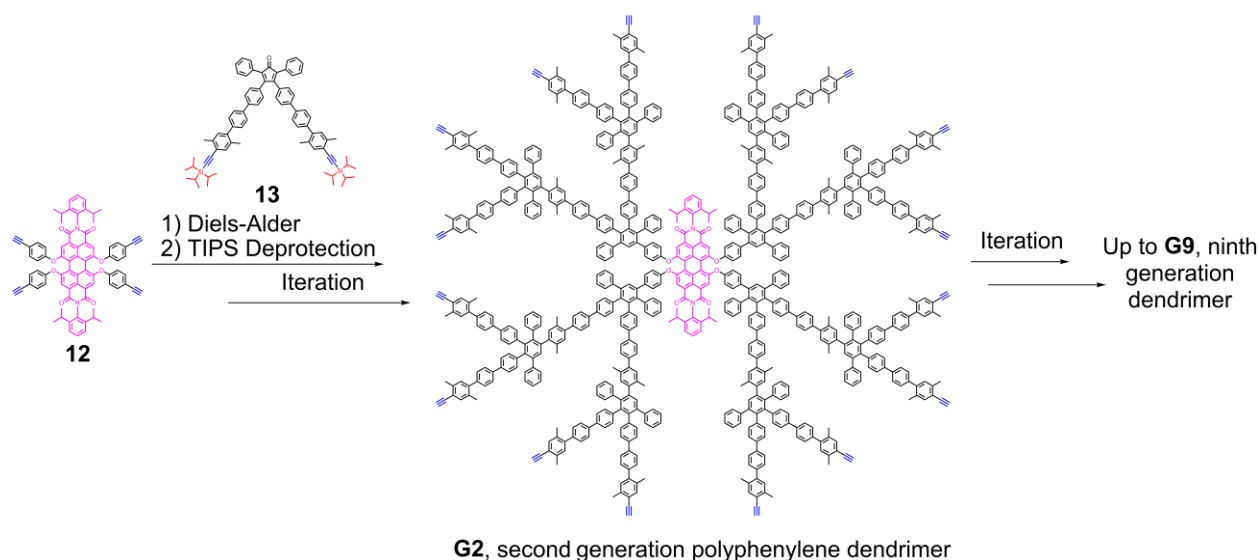


**Figure 1.7.** Synthesis of a 9th generation polyphenylene dendrimer. Adapted from Ref. 39. Copyright (2013) American Chemical Society.

### 1.7 Contorted Polycyclic Aromatic Hydrocarbons

Advances in the synthesis of sterically hindered phenylenes led to the discovery of various contorted PAHs (cPAHs), which exhibit distinct properties from their planar counterparts. cPAHs lack the large surface contacts found in planar PAHs because of their curved surfaces, which are induced by steric congestion. The optical and electronic properties of cPAHs are also affected by this curvature.<sup>85,86</sup> For example, strong Van der Waals interactions are not observed in contorted PAHs, resulting in significantly higher solubility in organic solvents than that of planar PAHs.<sup>87</sup> Nuckolls *et al.* have shown that such PAHs are readily processable and useful in organic electronic devices.<sup>85,88-93</sup> Contorted PAHs have demonstrated their utility in organic photovoltaic devices, in which a co-crystalline region formed between the contorted PAH and fullerene phases.<sup>90-93</sup> Nuckolls *et al.* developed a method to synthesize contorted hexabenzocoronenes (HBCs) and related cPAHs using the Ramirez reaction as the key step (Figure 1.8).<sup>90</sup>

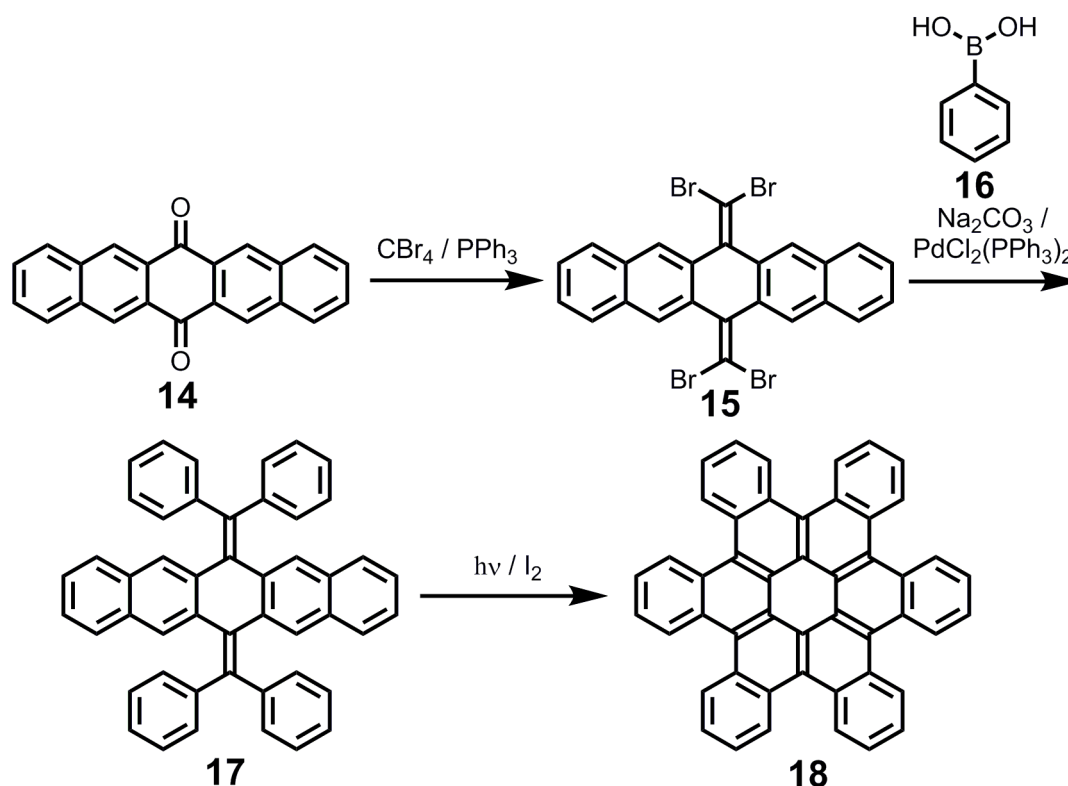


**Figure 1.8.** Synthesis of contorted HBC. Ramirez reaction used in olefination step (**14** to **15**) provides rapid access to the precursor **17** of contorted HBC **18**. Reproduced from Ref. 90 with permission of The Royal Society of Chemistry.

Durola *et al.* showed that such contorted aromatics can be accessed using bulky groups, such as *t*Bu (Figure 1.9A).<sup>20,21</sup> The sterically crowded three-fold symmetric compound **21** was synthesized using a Suzuki reaction. When oxidized under typical Scholl oxidation conditions, the compound is only partially fused and forms a propeller-shaped molecule **22** due to steric repulsion between the neighboring *t*Bu groups. Using a similar strategy, we recently employed a Yamamoto benzannulation to make sterically congested phenylenes from readily synthesized phenylene ethynylenes (Figure 1.9B).<sup>86</sup> **25** was oxidized to the partially fused, cPAH **26**, because of the steric crowding of the *t*Bu substituents on the terminal benzene rings. **26** and analogous PAHs synthesized are highly soluble in common organic solvents with strong absorbance in the visible region of the electromagnetic spectrum.

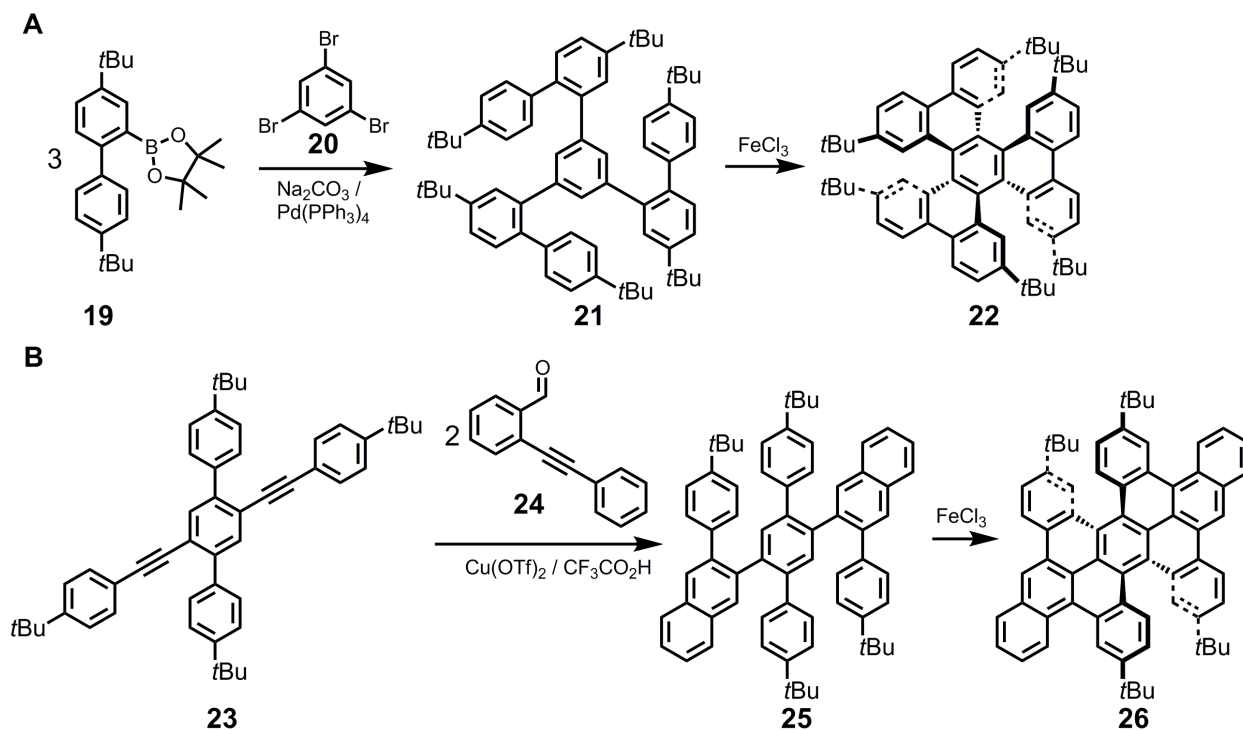


**Figure 1.9.** Synthesis of contorted aromatic systems due to steric congestion **A.** Neighboring *t*Bu groups are preventing the formation of complete fusion. Reproduced from Ref. 20 with permission of The John Wiley and Sons. **B.** Benzannulation of the appropriately substituted phenylene ethynylenes give sterically congested phenylenes that also form contorted aromatics. Reproduced from Ref. 86 with permission of The Royal Society of Chemistry.

## 1.8 Conclusions

In this introduction, we discussed the contemporary methods to synthesize *ortho*-arylene foldamers, GNR precursors, large polyphenylene dendrimers, and small PAH precursors. These hindered oligo- and poly(arylene)s exhibit specific conformational behaviors and are desirable precursors to nanographene structures. The synthetic methods of Suzuki polycondensation, Diels-Alder polymerization, alkyne cyclotrimerization, and Yamamoto benzannulation provide these hindered materials in high efficiency. Developing such methods to expand the toolbox for the synthesis of sterically crowded materials will increase access to new materials, which will find use especially in emerging organic electronic device applications.



## REFERENCES

- (1) Mullen, K.; Reynolds, J. R.; Masuda, T. *Conjugated Polymers : A Practical Guide to Synthesis*; Royal Society of Chemistry: Cambridge, 2014.
- (2) Skotheim, T. A.; Reynolds, J. R. *Handbook of Conducting Polymers*; 3rd ed.; CRC Press: Boca Raton, FL, 2007.
- (3) Inzelt, G. *Conducting Polymers*; Springer: Heidelberg, 2008.
- (4) Remmers, M.; Müller, B.; Martin, K.; Räder, H.-J.; Köhler, W. *Macromolecules* **1999**, *32*, 1073.
- (5) Sakamoto, J.; Rehahn, M.; Wegner, G.; Schlüter, A. D. *Macromol. Rapid Commun.* **2009**, *30*, 653.
- (6) Grimsdale, A. C.; Leok Chan, K.; Martin, R. E.; Jokisz, P. G.; Holmes, A. B. *Chem. Rev.* **2009**, *109*, 897.
- (7) Fichou, D. *Handbook of Oligo- and Polythiophenes*; Wiley: Weinheim, 1999.
- (8) McCullough, R. D. *Adv. Mater.* **1998**, *10*, 93.
- (9) Bunz, U. H. F. *Macromol. Rapid Commun.* **2009**, *30*, 772.
- (10) Weder, C. *Poly(arylene ethynylene)s : From Synthesis to Application*; Springer: Heidelberg, 2005.
- (11) Ando, S.; Ohta, E.; Kosaka, A.; Hashizume, D.; Koshino, H.; Fukushima, T.; Aida, T. *J. Am. Chem. Soc.* **2012**, *134*, 11084.
- (12) Kajitani, T.; Suna, Y.; Kosaka, A.; Osawa, T.; Fujikawa, S.; Takata, M.; Fukushima, T.; Aida, T. *J. Am. Chem. Soc.* **2013**, *135*, 14564.
- (13) Ohta, E.; Sato, H.; Ando, S.; Kosaka, A.; Fukushima, T.; Hashizume, D.; Yamasaki, M.; Hasegawa, K.; Muraoka, A.; Ushiyama, H.; Yamashita, K.; Aida, T. *Nature Chem.* **2011**, *3*, 68.

- (14) Hartley, C. S. *J. Org. Chem.* **2011**, 76, 9188.
- (15) Hartley, C. S.; He, J. *J. Org. Chem.* **2010**, 75, 8627.
- (16) He, J.; Crase, J. L.; Wadumethrige, S. H.; Thakur, K.; Dai, L.; Zou, S.; Rathore, R.; Hartley, C. S. *J. Am. Chem. Soc.* **2010**, 132, 13848.
- (17) He, J.; Mathew, S. M.; Cornett, S. D.; Grundy, S. C.; Hartley, C. S. *Org. Biomol. Chem.* **2012**, 10, 3398.
- (18) Mathew, S. M.; Engle, J. T.; Ziegler, C. J.; Hartley, C. S. *J. Am. Chem. Soc.* **2013**, 135, 6714.
- (19) Mathew, S. M.; Hartley, C. S. *Macromolecules* **2011**, 44, 8425.
- (20) Pradhan, A.; Dechambenoit, P.; Bock, H.; Durola, F. *Angew. Chem. Int. Ed.* **2011**, 50, 12582.
- (21) Pradhan, A.; Dechambenoit, P.; Bock, H.; Durola, F. *J. Org. Chem.* **2013**, 78, 2266.
- (22) Narita, A.; Feng, X.; Hernandez, Y.; Jensen, S. A.; Bonn, M.; Yang, H.; Verzhbitskiy, I. A.; Casiraghi, C.; Hansen, M. R.; Koch, A. H. R.; Fytas, G.; Ivasenko, O.; Li, B.; Mali, K. S.; Balandina, T.; Mahesh, S.; De Feyter, S.; Müllen, K. *Nature Chem.* **2014**, 6, 126.
- (23) Yang, X.; Dou, X.; Rouhanipour, A.; Zhi, L.; Räder, H. J.; Müllen, K. *J. Am. Chem. Soc.* **2008**, 130, 4216.
- (24) Dössel, L.; Gherghel, L.; Feng, X.; Müllen, K. *Angew. Chem. Int. Ed.* **2011**, 50, 2540.
- (25) Yan, X.; Li, B.; Li, L.-s. *Acc. Chem. Res.* **2012**, 46, 2254.
- (26) Chen, L.; Hernandez, Y.; Feng, X.; Müllen, K. *Angew. Chem. Int. Ed.* **2012**, 51, 7640.
- (27) Li, L.-s.; Yan, X. *The Journal of Physical Chemistry Letters* **2010**, 1, 2572.
- (28) Yan, X.; Cui, X.; Li, B.; Li, L.-s. *Nano Lett.* **2010**, 10, 1869.
- (29) Yan, X.; Cui, X.; Li, L.-s. *J. Am. Chem. Soc.* **2010**, 132, 5944.

- (30) Yan, X.; Li, L.-s. *J. Mater. Chem.* **2011**, *21*, 3295.
- (31) Simpson, C. D.; Brand, J. D.; Berresheim, A. J.; Przybilla, L.; Räder, H. J.; Müllen, K. *Chemistry – A European Journal* **2002**, *8*, 1424.
- (32) Simpson, C. D.; Mattersteig, G.; Martin, K.; Gherghel, L.; Bauer, R. E.; Räder, H. J.; Müllen, K. *J. Am. Chem. Soc.* **2004**, *126*, 3139.
- (33) Gagnon, E.; Halperin, S. D.; Métivaud, V.; Maly, K. E.; Wuest, J. D. *J. Org. Chem.* **2009**, *75*, 399.
- (34) Pisula, W.; Kastler, M.; Wasserfallen, D.; Pakula, T.; Müllen, K. *J. Am. Chem. Soc.* **2004**, *126*, 8074.
- (35) Herwig, P.; Kayser, C. W.; Müllen, K.; Spiess, H. W. *Adv. Mater.* **1996**, *8*, 510.
- (36) Fechtenkötter, A.; Tchebotareva, N.; Watson, M.; Müllen, K. *Tetrahedron* **2001**, *57*, 3769.
- (37) Carsten, B.; He, F.; Son, H. J.; Xu, T.; Yu, L. *Chem. Rev.* **2011**, *111*, 1493.
- (38) Manabe, K.; Kimura, T. *Org. Lett.* **2013**, *15*, 374.
- (39) Nguyen, T. T.; Baumgarten, M.; Rouhanipour, A.; Rader, H. J.; Lieberwirth, I.; Mullen, K. *J. Am. Chem. Soc.* **2013**, *135*, 4183.
- (40) Grebel-Koehler, D.; Liu, D.; De Feyter, S.; Enkelmann, V.; Weil, T.; Engels, C.; Samyn, C.; Müllen, K.; De Schryver, F. C. *Macromolecules* **2003**, *36*, 578.
- (41) Wu, J.; Gherghel, L.; Watson, M. D.; Li, J.; Wang, Z.; Simpson, C. D.; Kolb, U.; Müllen, K. *Macromolecules* **2003**, *36*, 7082.
- (42) Weil, T.; Reuther, E.; Müllen, K. *Angew. Chem. Int. Ed.* **2002**, *41*, 1900.
- (43) Shifrina, Z. B.; Averina, M. S.; Rusanov, A. L.; Wagner, M.; Müllen, K. *Macromolecules* **2000**, *33*, 3525.

- (44) Morgenroth, F.; Müllen, K. *Tetrahedron* **1997**, *53*, 15349.
- (45) Maus, M.; De, R.; Lor, M.; Weil, T.; Mitra, S.; Wiesler, U.-M.; Herrmann, A.; Hofkens, J.; Vosch, T.; Müllen, K.; De Schryver, F. C. *J. Am. Chem. Soc.* **2001**, *123*, 7668.
- (46) Wiesler, U.-M.; Mullen, K. *Chem. Commun.* **1999**, 2293.
- (47) Nguyen, T. T.; Turp, D.; Wang, D.; Nolscher, B.; Laquai, F.; Mullen, K. *J. Am. Chem. Soc.* **2011**, *133*, 11194.
- (48) Seyler, H.; Purushothaman, B.; Jones, D. J.; Holmes, A. B.; Wong, W. W. H. *Pure Appl. Chem.* **2012**, *84*, 1047.
- (49) Häußler, M.; Lam, J. W. Y.; Zheng, R.; Peng, H.; Luo, J.; Chen, J.; Law, C. C. W.; Tang, B. Z. *C. R. Chim.* **2003**, *6*, 833.
- (50) Hecht, S.; Fréchet, J. M. J. *J. Am. Chem. Soc.* **1999**, *121*, 4084.
- (51) Häußler, M.; Liu, J.; Lam, J. W. Y.; Qin, A.; Zheng, R.; Tang, B. Z. *J. Polym. Sci., Part A: Polym. Chem.* **2007**, *45*, 4249.
- (52) Asao, N.; Nogami, T.; Lee, S.; Yamamoto, Y. *J. Am. Chem. Soc.* **2003**, *125*, 10921.
- (53) Arslan, H.; Saathoff, J. D.; Bunck, D. N.; Clancy, P.; Dichtel, W. R. *Angew. Chem. Int. Ed.* **2012**, *51*, 12051.
- (54) Kovacic, P.; Uchic, J. T.; Hsu, L.-C. *Journal of Polymer Science Part A-1: Polymer Chemistry* **1967**, *5*, 945.
- (55) Kovacic, P.; Ramsey, J. S. *Journal of Polymer Science Part A-1: Polymer Chemistry* **1969**, *7*, 111.
- (56) Hsing, C.-F.; Jones, M. B.; Kovacic, P. *Journal of Polymer Science: Polymer Chemistry Edition* **1981**, *19*, 973.
- (57) Ito, Y.; Ihara, E.; Murakami, M.; Shiro, M. *J. Am. Chem. Soc.* **1990**, *112*, 6446.

- (58) Suginome, M.; Collet, S.; Ito, Y. *Org Lett* **2002**, *4*, 351.
- (59) Blake, A. J.; Cooke, P. A.; Doyle, K. J.; Gair, S.; Simpkins, N. S. *Tetrahedron Lett.* **1998**, *39*, 9093.
- (60) Koyanagi, M.; Eichenauer, N.; Ihara, H.; Yamamoto, T.; Suginome, M. *Chem. Lett.* **2013**, *42*, 541.
- (61) Suginome, M.; Collet, S.; Ito, Y. *Org. Lett.* **2002**, *4*, 351.
- (62) Ito, S.; Takahashi, K.; Nozaki, K. *Journal of the American Chemical Society* **2014**, *136*, 7547.
- (63) Chen, Z.; Lin, Y.-M.; Rooks, M. J.; Avouris, P. *Physica E: Low-dimensional Systems and Nanostructures* **2007**, *40*, 228.
- (64) Han, M. Y.; Özyilmaz, B.; Zhang, Y.; Kim, P. *Phys. Rev. Lett.* **2007**, *98*, 206805.
- (65) Tapaszto, L.; Dobrik, G.; Lambin, P.; Biro, L. P. *Nat Nano* **2008**, *3*, 397.
- (66) Bai, J.; Duan, X.; Huang, Y. *Nano Lett.* **2009**, *9*, 2083.
- (67) Wassei, J. K.; Kaner, R. B. *Acc. Chem. Res.* **2013**, *46*, 2244.
- (68) Kosynkin, D. V.; Higginbotham, A. L.; Sinitskii, A.; Lomeda, J. R.; Dimiev, A.; Price, B. K.; Tour, J. M. *Nature* **2009**, *458*, 872.
- (69) Jiao, L.; Zhang, L.; Wang, X.; Diankov, G.; Dai, H. *Nature* **2009**, *458*, 877.
- (70) Xie, L.; Wang, H.; Jin, C.; Wang, X.; Jiao, L.; Suenaga, K.; Dai, H. *J. Am. Chem. Soc.* **2011**, *133*, 10394.
- (71) James, D. K.; Tour, J. M. *Acc. Chem. Res.* **2012**, *46*, 2307.
- (72) Vo, T. H.; Shekhirev, M.; Kunkel, D. A.; Orange, F.; Guinel, M. J. F.; Enders, A.; Sinitskii, A. *Chem. Commun.* **2014**, *50*, 4172.

- (73) Bronner, C.; Stremlau, S.; Gille, M.; Brauße, F.; Haase, A.; Hecht, S.; Tegeder, P. *Angew. Chem. Int. Ed.* **2013**, *52*, 4422.
- (74) Cai, J.; Ruffieux, P.; Jaafar, R.; Bieri, M.; Braun, T.; Blankenburg, S.; Muoth, M.; Seitsonen, A. P.; Saleh, M.; Feng, X.; Mullen, K.; Fasel, R. *Nature* **2010**, *466*, 470.
- (75) Talirz, L.; Söde, H.; Cai, J.; Ruffieux, P.; Blankenburg, S.; Jafaar, R.; Berger, R.; Feng, X.; Müllen, K.; Passerone, D.; Fasel, R.; Pignedoli, C. A. *J. Am. Chem. Soc.* **2013**, *135*, 2060.
- (76) Vo, T. H.; Shekhirev, M.; Kunkel, D. A.; Morton, M. D.; Berglund, E.; Kong, L.; Wilson, P. M.; Dowben, P. A.; Enders, A.; Sinitskii, A. *Nat Commun* **2014**, *5*.
- (77) Müllen, K. *ACS Nano* **2014**, *8*, 6531.
- (78) Astruc, D.; Boisselier, E.; Ornelas, C. *Chem. Rev.* **2010**, *110*, 1857.
- (79) Grayson, S. M.; Fréchet, J. M. J. *Chem. Rev.* **2001**, *101*, 3819.
- (80) Killops, K. L.; Campos, L. M.; Hawker, C. J. *J. Am. Chem. Soc.* **2008**, *130*, 5062.
- (81) Oar, M. A.; Serin, J. M.; Dichtel, W. R.; Fréchet, J. M. J.; Ohulchanskyy, T. Y.; Prasad, P. N. *Chem. Mater.* **2005**, *17*, 2267.
- (82) Bauer, R.; Grimsdale, A.; Müllen, K. In *Functional Molecular Nanostructures*; Schlüter, A. D., Ed.; Springer Berlin Heidelberg: 2005; Vol. 245, p 253.
- (83) Li, Q.; Noffke, B. W.; Wang, Y.; Menezes, B.; Peters, D. G.; Raghavachari, K.; Li, L.-s. *J. Am. Chem. Soc.* **2014**, *136*, 3358.
- (84) Li, Q.; Zhang, S.; Dai, L.; Li, L.-s. *J. Am. Chem. Soc.* **2012**, *134*, 18932.
- (85) Whalley, A. C.; Plunkett, K. N.; Gorodetsky, A. A.; Schenck, C. L.; Chiu, C.-Y.; Steigerwald, M. L.; Nuckolls, C. *Chem. Sci.* **2011**, *2*, 132.
- (86) Arslan, H.; Uribe-Romo, F. J.; Smith, B. J.; Dichtel, W. R. *Chem. Sci.* **2013**, *4*, 3973.
- (87) Kawasumi, K.; Zhang, Q.; Segawa, Y.; Scott, L. T.; Itami, K. *Nature Chem.* **2013**, *5*, 739.

- (88) Xiao, S.; Kang, S. J.; Wu, Y.; Ahn, S.; Kim, J. B.; Loo, Y.-L.; Siegrist, T.; Steigerwald, M. L.; Li, H.; Nuckolls, C. *Chem. Sci.* **2013**, *4*, 2018.
- (89) Xiao, S.; Myers, M.; Miao, Q.; Sanaur, S.; Pang, K.; Steigerwald, M. L.; Nuckolls, C. *Angew. Chem. Int. Ed.* **2005**, *44*, 7390.
- (90) Chiu, C.-Y.; Kim, B.; Gorodetsky, A. A.; Sattler, W.; Wei, S.; Sattler, A.; Steigerwald, M.; Nuckolls, C. *Chem. Sci.* **2011**, *2*, 1480.
- (91) Tremblay, N. J.; Gorodetsky, A. A.; Cox, M. P.; Schiros, T.; Kim, B.; Steiner, R.; Bullard, Z.; Sattler, A.; So, W.-Y.; Itoh, Y.; Toney, M. F.; Ogasawara, H.; Ramirez, A. P.; Kymissis, I.; Steigerwald, M. L.; Nuckolls, C. *ChemPhysChem* **2010**, *11*, 799.
- (92) Kang, S. J.; Kim, J. B.; Chiu, C.-Y.; Ahn, S.; Schiros, T.; Lee, S. S.; Yager, K. G.; Toney, M. F.; Loo, Y.-L.; Nuckolls, C. *Angew. Chem. Int. Ed.* **2012**, *51*, 8594.
- (93) Schiros, T.; Kladnik, G.; Prezzi, D.; Ferretti, A.; Olivieri, G.; Cossaro, A.; Floreano, L.; Verdini, A.; Schenck, C.; Cox, M.; Gorodetsky, A. A.; Plunkett, K.; Delongchamp, D.; Nuckolls, C.; Morgante, A.; Cvetko, D.; Kymissis, I. *Adv. Energy Mater.* **2013**, *3*, 894.

## CHAPTER TWO

### HIGHLY EFFICIENT BENZANNULATION OF POLY(PHENYLENE ETHYNYLENE)S

#### 2.1 *Abstract*

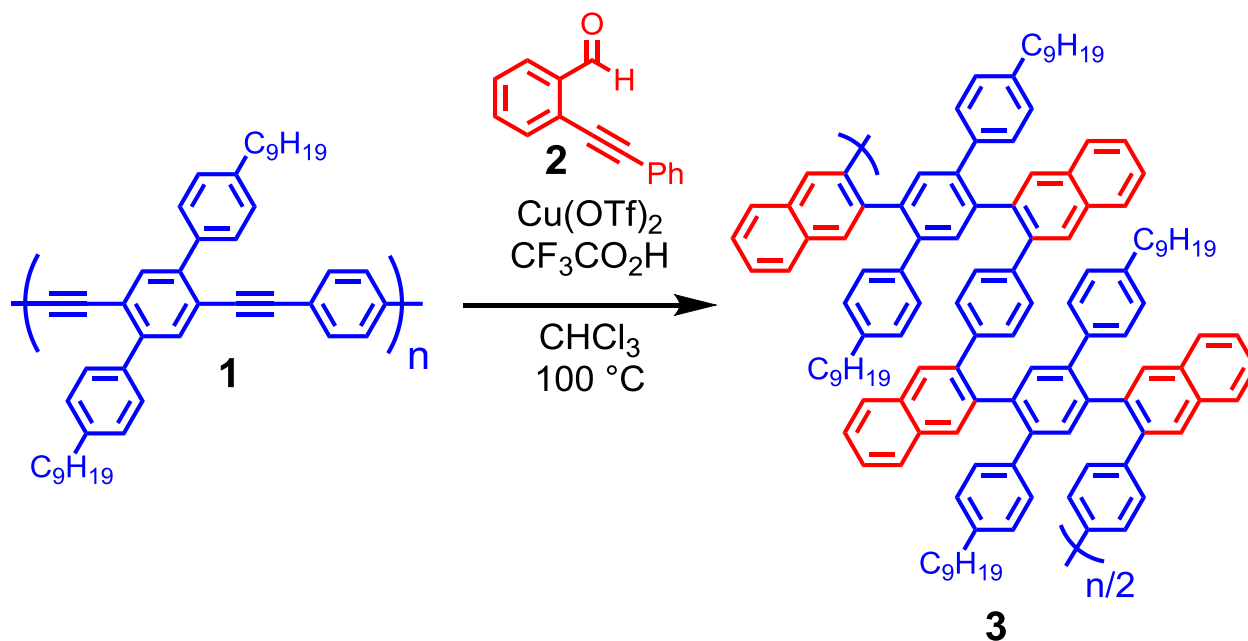
Sterically congested poly(arylene)s can be synthesized by performing a benzannulation reaction at each carbon-carbon triple bond of a poly(phenylene ethynylene), one of the most easily synthesized and versatile classes of conjugated polymers. The benzannulation reaction is highly specific and efficient, as determined by an isotopic labelling study and several complementary spectroscopic methods. The work in this chapter was previously published in *Angewandte Chemie International Edition* ([Arslan, H.; Saathoff, J. D.; Bunck, D. N.; Clancy, P.; Dichtel, W. R. *Angew. Chem. Int. Ed.*, **2012**, *51*, 12051.] - Reproduced by permission of John Wiley and Sons)

#### 2.2 *Introduction*

Macromolecules linked by single bonds between aromatic substituents, or poly(phenylene)s, have attracted great interest for use in organic light-emitting diodes (OLEDs)<sup>[1]</sup> and other optoelectronic devices,<sup>[2]</sup> as structurally rigid dendrimers,<sup>[3]</sup> for isolating<sup>[4]</sup> or organizing chromophores,<sup>[5]</sup> and as soluble precursors of nanostructured forms of graphene.<sup>[6]</sup> High molecular weight *para*- and *meta*-linked poly(phenylene)s are synthesized through transition metal-catalyzed cross-coupling approaches, some proceeding through chain-growth mechanisms.<sup>[7]</sup> Only a few oligomeric *o*-linked phenylenes have been reported,<sup>[8]</sup> due to poor cross-coupling efficiency during the polymerization. Longer *o*-poly(phenylene)s are interesting because they can adopt specific helical conformations induced by steric interactions along the polymer backbone<sup>[8,9]</sup> and can be oxidized to soluble, structurally precise graphene



nanoribbons.<sup>[10]</sup> New strategies for accessing *o*-poly(phenylene)s, particularly those that tolerate additional aromatic substituents, are therefore of great utility.



**Scheme 2.1.** Benzannulation of each alkyne of a substituted poly(phenylene ethynylene) **1** provides the polyphenylene **3**.

Here we report a versatile and efficient approach to prepare high molecular weight polymers containing *o*-substituted arylene linkages through a cycloaddition reaction at each alkyne function of a poly(phenylene ethynylene) (PPE). PPEs are attractive precursors because of the structural versatility, functional group tolerance, and efficiency of their polymerizations. However, their alkynes are notably unreactive and have only been reduced to methylene<sup>[11]</sup> or *cis*-vinylene groups prior to this study.<sup>[12]</sup> This benzannulation strategy (Scheme 2.1) is the first report of an efficient cycloaddition performed along a conjugated polymer backbone<sup>[13]</sup> and tolerates bulky aromatic substituents adjacent to the alkynes, suggesting that it will be applicable for a broad range of crowded aromatic architectures.

### 2.3 *Benzannulation of the Model System*

Yamamoto reported a  $\text{Cu}(\text{OTf})_2$ -catalyzed benzannulation of diphenylacetylene with *o*-(phenylethynyl)benzaldehyde **2** to produce 2,3-diphenylnaphthalene,<sup>[14]</sup> but this transformation has not previously been employed for polymer modification. We first evaluated its feasibility for PPE benzannulation using dialkyne **4** (Figure 2.1), a model compound similar in structure to PPE **1**. Compound **4** reacts rapidly (in as little as 30 min) and efficiently with **2** in the presence of catalytic amounts of  $\text{Cu}(\text{OTf})_2$  and excess trifluoroacetic acid ( $\text{CF}_3\text{CO}_2\text{H}$ ) at 100 °C to provide the doubly benzannulated product **5** in 98% isolated yield. Yamamoto found that some alkyne-containing substrates form up to ~10% of a naphthyl ketone side product (Figure 1b, inset) under the  $\text{Cu}(\text{OTf})_2$ -catalyzed benzannulation conditions, although this side reaction was not observed for the substrate diphenyl acetylene.<sup>[14]</sup> If present in our system, this side reaction would induce defects along the poly(phenylene) backbone. Fortunately, **4** forms little or no naphthyl ketone side products (<1%), as judged by the high isolated yield of **5**, as well as by NMR and Fourier transform infrared (FTIR) spectroscopies (see Appendix), and thin-layer chromatography.

A comparison of the MALDI-TOF mass spectra of the **4** and **5** also indicates the high efficiency of the reaction. After benzannulation, a strong signal for the doubly benzannulated product **5** is observed. The weak signal in the spectrum at 773.6 mass units corresponds to a fragmentation product of **5**. The only signals corresponding to trace benzannulation side products are weaker: the naphthyl ketone at 990.6 mass units and monoannulated product at 784.6 mass units. These byproducts were formed in trace amounts and were not observed by other analytical methods. In summary, this model study confirms the promise of this reaction for polymer modification.

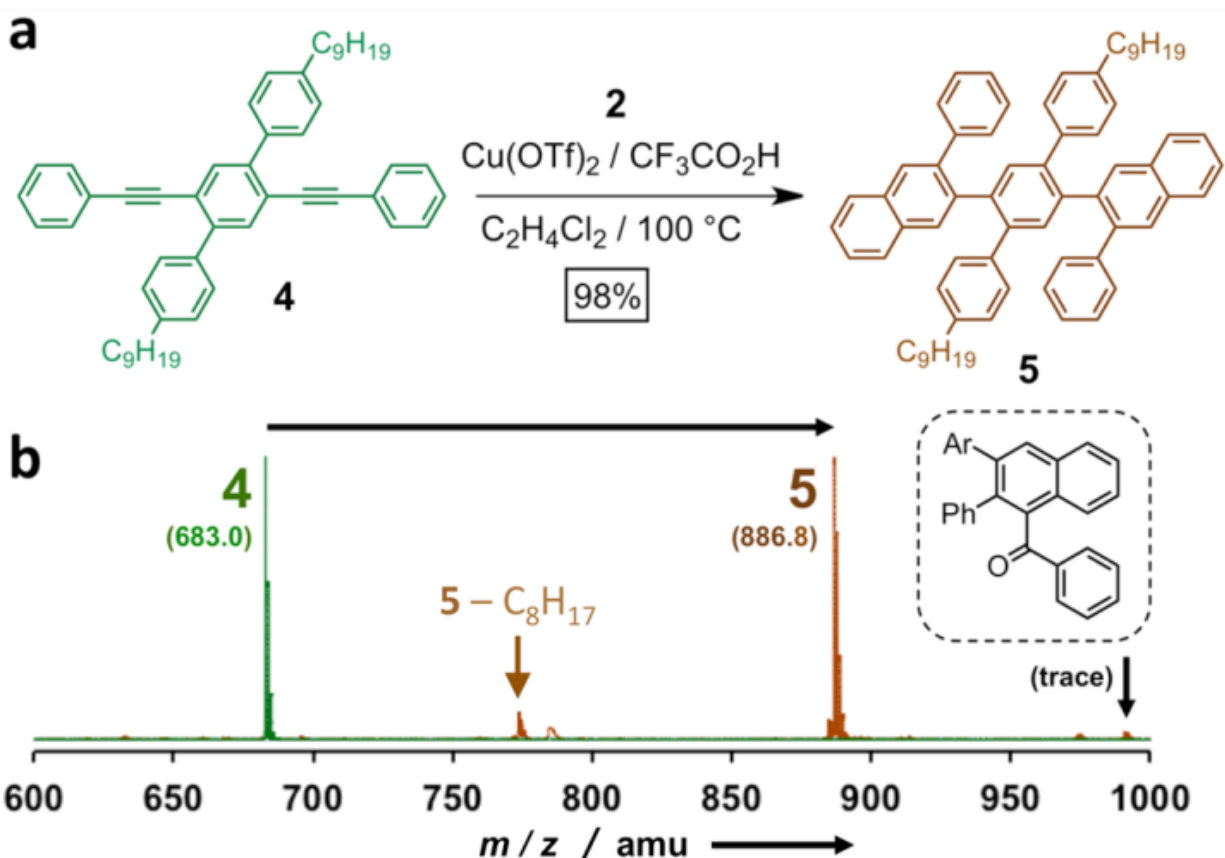


**Figure 2.1.** A model study of the benzannulation strategy. a, The terphenyl-containing dialkyne **4**, a molecular compound similar in structure to PPE **1**, was subjected to the Cu(OTf)<sub>2</sub>-catalyzed benzannulation. b, MALDI-TOF mass spectra of dialkyne **4** and benzannulated product **5**. inset: Structure of a possible naphthyl ketone side product based on previous reports of the benzannulation reaction,<sup>[14]</sup> which is observed only as a trace impurity in the mass spectrum.

#### 2.4 Benzannulation of Poly(Phenylene Ethynylene) **1** and Characterization

The *p*-terphenyl-*alt*-phenyl PPE **1** was obtained by copolymerizing the appropriate terphenyl dialkyne monomer and 1,4-diiodobenzene under Sonogashira cross-coupling conditions. A substoichiometric amount of a monofunctional aryl iodide, 4-iodoanisole, was used to control the polymer's molecular weight and end-group identity. Nevertheless, **1** is insoluble in the reaction mixture at molecular weights approaching 100 kDa and partially precipitates during the polymerization. As a result, we obtained a bimodal molecular weight distribution ( $M_n = 7.85$  kDa; PDI = 3.53;  $D_p = 12$ ) by size exclusion chromatography (SEC), consisting of a low

molecular weight main peak with a high molecular weight shoulder (Figure 2.2). These molecular weights were determined by multi-angle light scattering, a direct measure of the polymer mass that does not rely on comparisons to polymer standards of questionable applicability. Despite its broad molecular weight distribution, we did not separate **1** into high and low molecular weight fractions because we found that the shorter chains were easily removed by precipitation after the benzannulation step. We estimate the  $D_p$  of the high molecular weight fraction of **1** to be approximately 59, making it an appropriate system in which to evaluate our synthetic approach.

PPE **1** was benzannulated under similar conditions as the model compound **5** [3 equiv. **2** per alkyne, 3 equiv.  $\text{CF}_3\text{CO}_2\text{H}$ , 0.05 equiv.  $\text{Cu}(\text{OTf})_2$ ], after which polyphenylene **3** was isolated by precipitation from  $\text{CH}_2\text{Cl}_2$  into acetone, followed by Soxhlet extraction using acetone as the liquid phase. SEC analysis of the acetone-insoluble material showed a monomodal distribution of chain sizes whose molecular weight and polydispersity ( $M_n = 39.6$  kDa,  $\text{PDI} = 1.65$ ,  $D_p = 49$ ) correspond to the benzannulation of the higher molecular weight portion of **1**. Steric hindrance along the polymer backbone prevents **3** from adopting a planar conformation and it is far more soluble in organic solvents than **1**. Despite its higher molecular weight, polyphenylene **3** is retained longer by the SEC columns relative to its PPE precursor **1**, which we attribute to the polymer adopting a more compact solvated structure as a consequence of its steric demands (Figure 2.2). As a result, the polymer chains of **3** adopt smaller hydrodynamic volumes than random-coil polymer chains of comparable molecular weight. This explanation is consistent with recent findings that oligomeric *o*-phenylenes adopt specific helical conformations as a consequence of their crowded structure.<sup>[8,15]</sup>

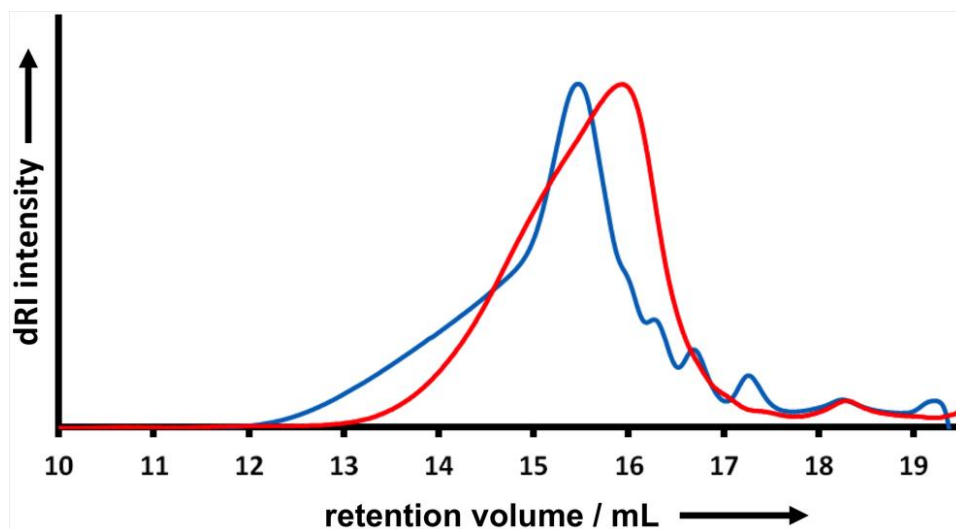


**Figure 2.2** Refractive index SEC traces of PPE 1 (blue) and polyphenylene 3 (red trace).

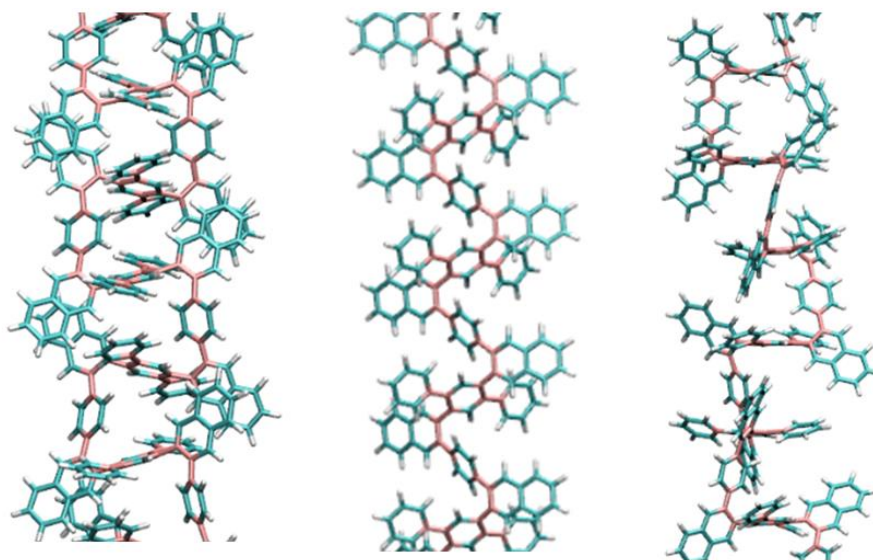


**Figure 2.3.** Illustration of the three most common conformations in the simulation of several repeat units of polymer **3** in the presence of 1,2-dichlorobenzene solvent. Truncated polymer structures are shown with their *n*-nonyl side-chains omitted for clarity.

A Molecular Dynamics (MD) simulation also finds that polyphenylene **3** adopts a compact structure in organic solvent. MD provides an atomically explicit representation of the dynamics of the system under the influence of inter- and intramolecular forces. A 24-unit

polymer chain of **3** was simulated among 11,740 1,2-dichlorobenzene solvent molecules using the OPLS-AA force field<sup>[16]</sup> within the LAMMPS software package<sup>[17]</sup> (see Appendix for complete details). The resulting structure of the polymer was highly contorted with several distinct conformations at each monomer unit, which contribute to the solvated polymer's compact solution structure. We investigated the disposition of eight different dihedral angles within the polymer that we determined to affect the polymer conformations. Preferred angles were found by locating peaks in histograms generated by the data; Gaussian distributions were fitted to each peak to estimate an average angle value as well as a standard deviation (see Appendix Table A1.2). The three most common conformations of **3** are shown in Figure 2.3, which have lengths of 5.8, 9.6, and 7.2 Å per monomer unit, respectively. Even though **3** does not fold into a single or small number of well-defined conformers, as do *o*-phenylene oligomers, many of the rotations of its aromatic rings are correlated, as evidenced by their specific ranges of energetically favorable dihedral angles. These simulations are consistent with the otherwise anomalous shift to higher SEC retention times when **1** is benzannulated to **3**.

The efficiency of the benzannulation of PPE **1** was characterized using a full complement of spectroscopic measurements. The inability of adjacent aromatic rings in **3** to adopt coplanar conformations induces a significant blue shift in its UV/Vis absorption spectrum relative to its PPE precursor **1**. The  $\lambda_{\text{max}}$  of **3** is shifted 140 nm lower than that of **1** (Figure 2.4a) and its spectrum is strikingly similar to that of benzannulated model compound **5** (Figure 2.4a). In addition, the absorption spectrum of model compound **4** shows an intense band with defined vibrational structure from 325-375 nm (Figure 2.4a). If the benzannulation were inefficient, residual alkyne-containing subunits would cause **3** to absorb in this region or at longer wavelengths, yet **3** does not absorb strongly within this spectral range.

Trends observed in the photoemission spectra of **1**, **3**, **4**, and **5** are also consistent with the interpretation that efficient benzannulation of **1** occurred (Figure 2.4b). The emission of PPE **1** shows well-known components of both isolated and aggregated PPE emission with local maxima at 426 nm and 447 nm, respectively.<sup>[18]</sup> Upon benzannulation, the maximum emission shifts blue by 22 nm but also broadens significantly. Emission over a similarly broad wavelength range was observed by Hartley and coworkers in a series of *o*-phenylene oligomers, which was attributed to emission from two different conformational states.<sup>[8a]</sup> Fourier transform infrared (FTIR) spectroscopy of **3** showed increased sp<sup>2</sup> C–H stretches at 3030 cm<sup>-1</sup> from the newly installed naphthalene rings (Appendix Figure A1.27), as well as significant changes in the 500-1500 cm<sup>-1</sup> region that suggest major modifications to the structure of **3** relative to its PPE precursor **1**. In summary, UV/Vis, fluorescence, and FTIR spectroscopies are each consistent with efficient benzannulation of PPE **1**.

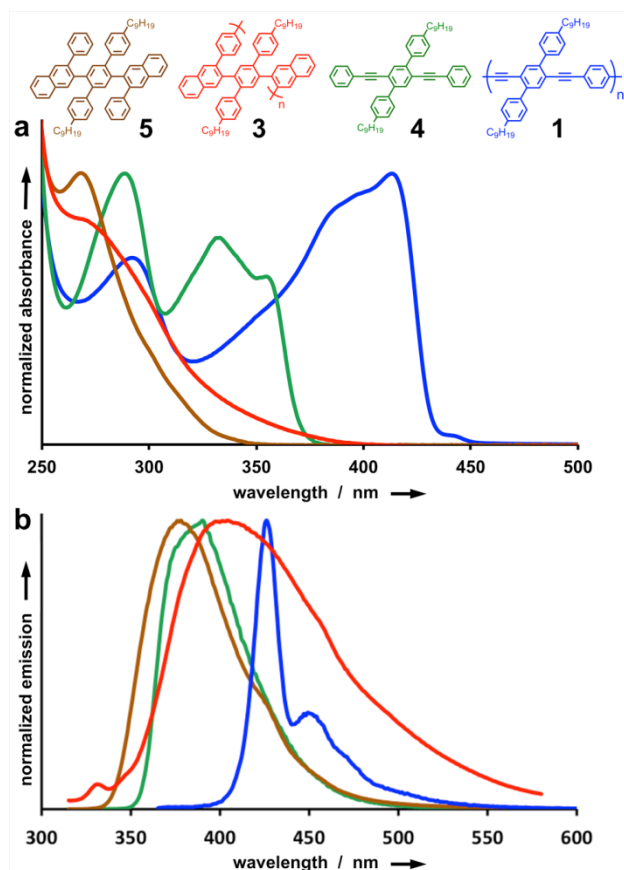


**Figure 2.4.** Characterization of the benzannulation of PPE **1**. a, UV/visible absorption, and b, photoemission spectra of the PPE **1** (blue trace), benzannulated polymer **3** (red trace), the dialkyne **4** (green trace), and its benzannulation product **5** (brown trace). The steric congestion of **3** reduces the effective conjugation length, shifting the absorbance of the polymer to higher energy.

Finally, an isotopic labeling study also provided direct evidence for the high efficiency of the benzannulation reaction. A sample of PPE **1** with  $^{13}\text{C}$ -enriched alkyne carbons was prepared by employing trimethylsilylacetylene- $^{13}\text{C}_2$  in the synthesis of its dialkyne monomer. The most intense resonances of its  $^{13}\text{C}$  NMR spectrum (Figure 2.5a) are centered at 92.8 ppm and correspond to the two  $^{13}\text{C}$ -enriched alkyne carbons. The three small resonances at 128.3, 129.3 and 131.5 ppm correspond to aromatic carbons with naturally abundant amounts of  $^{13}\text{C}$  and occur at identical chemical shifts as the three most intense aromatic resonances in the spectrum



of unlabeled **1** (Appendix Figure A1.10). After benzannulation, the  $^{13}\text{C}$ -enriched alkyne signals were shifted cleanly to a broad peak centered at 139.5 ppm, and no residual alkyne resonances are visible above the baseline (Figure 2.5b). Both the  $^{13}\text{C}$ -labeled and unlabeled  $^1\text{H}$  and  $^{13}\text{C}$  NMR spectra of the benzannulated polymer obtained at room temperature show peak broadening as a consequence of hindered rotation about the newly installed 2,3-disubstituted naphthalene moieties, consistent with the above MD simulations.  $^{13}\text{C}$  NMR spectra obtained in  $\text{C}_2\text{D}_2\text{Cl}_4$  sharpen at higher temperatures, such that the non-equivalent  $^{13}\text{C}$ -enriched signals are resolved. These resonances are shown in a partial spectrum obtained at 135 °C as an inset of Figure 5b, and complete spectra obtained in ten degree increments between 25–135 °C are provided in the Appendix (Figures A1.24– A1.25). These resolved resonances are coupled to one another, as determined by a 2D-INADEQUATE experiment (Appendix Figure A1.26). These isotopic labeling experiments, in concert with the spectroscopic and SEC characterization of the polymer **3**, unambiguously demonstrate that this unprecedented transformation of PPE **1** proceeds specifically and efficiently.

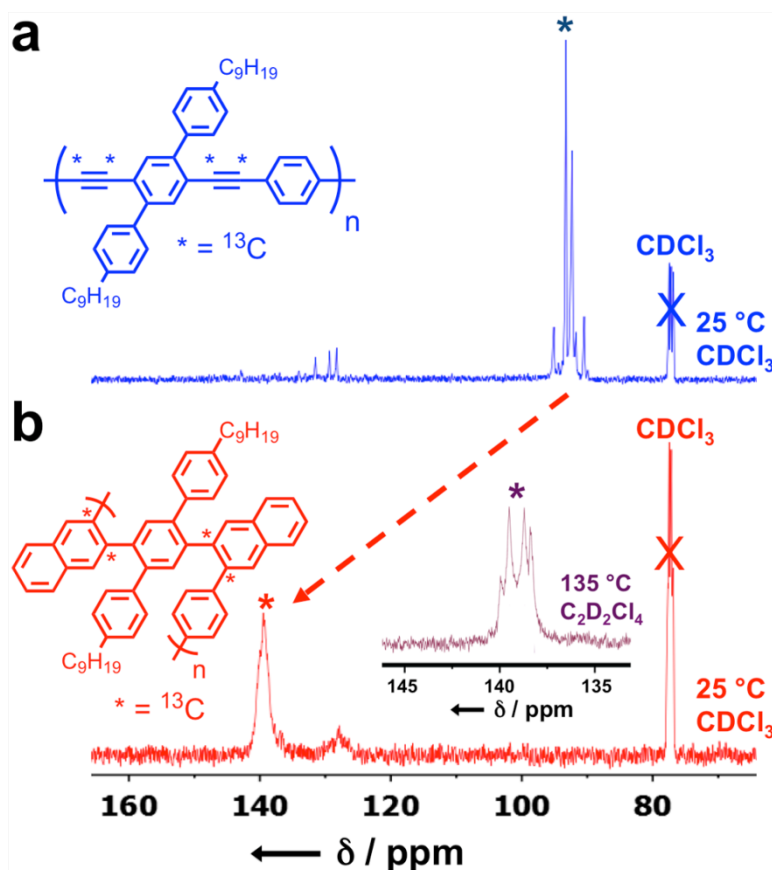


**Figure 2.5.** Partial  $^{13}\text{C}$  NMR spectra ( $\text{CDCl}_3$ , 100 MHz, rt) of a  $^{13}\text{C}$ -enriched sample of **1** (a, blue spectrum) that was benzannulated to provide  $^{13}\text{C}$ -enriched **3** (b, red spectrum). The resonances of the enriched carbons (\*) shift to the aromatic region of the spectrum, and no resonances corresponding to residual alkynes are observed. Inset: Partial  $^{13}\text{C}$  NMR spectrum of **3** ( $\text{C}_2\text{D}_2\text{Cl}_4$ , 125 MHz, 135 °C) obtained at increased temperature shows resolution and coupling of the two inequivalent  $^{13}\text{C}$ -enriched resonances.

## 2.5 Conclusions

In conclusion, we have demonstrated a new approach to prepare otherwise inaccessible polyphenylene architectures using a Yamamoto-type benzannulation reaction. This finding is also the first example of an efficient cycloaddition reaction performed along a conjugated polymer backbone. The high specificity and efficiency of the reaction for polymer modification were characterized using isotopic labeling and supported by absorption, photoemission, FT-IR spectroscopies as well as a model compound study. Notably, the benzannulation reaction

tolerates additional aromatic substituents adjacent to each alkyne, producing a highly crowded polyphenylene with limited conformational freedom, as determined by size exclusion chromatography and Molecular Dynamics simulations. We intend to apply this approach to synthesize a wide variety of congested architectures, such as contorted polycyclic aromatic hydrocarbons, polyarylene dendrimers, and graphene nanoribbons and quantum dots.

## **2.6    *Acknowledgments***

This research was supported by the National Science Foundation (CHE-1124754). We also made use of the Cornell Center for Materials Research (CCMR) facilities with support from the NSF Materials Research Science and Engineering Centers (MRSEC) program (DMR-0520404). D.N.B. acknowledges the award of a Graduate Research Fellowship from the NSF. We acknowledge Fernando J. Uribe-Romo for help in preparing the graphical abstract.

## REFERENCES

- (1) A. C. Grimsdale, K. Leok Chan, R. E. Martin, P. G. Jokisz, A. B. Holmes, *Chem. Rev.* **2009**, *109*, 897–1091.
- (2) C. Li, M. Liu, N. G. Pschirer, M. Baumgarten, K. Müllen, *Chem. Rev.* **2010**, *110*, 6817–6855.
- (3) D. Turp, T.-T.-T. Nguyen, M. Baumgarten, K. Müllen, *New J. Chem.* **2012**, *36*, 282–298.
- (4) (a) T. Qin, J. Ding, L. Wang, M. Baumgarten, G. Zhou, K. Müllen, *J. Am. Chem. Soc.* **2009**, *131*, 14329–14336; (b) S. Bernhardt, M. Kastler, V. Enkelmann, M. Baumgarten, K. Müllen, *Chem. Eur. J.* **2006**, *12*, 6117–6128.
- (5) (a) T. Weil, T. Vosch, J. Hofkens, K. Peneva, K. Müllen, *Angew. Chem.* **2010**, *122*, 9252–9278; *Angew. Chem. Int. Ed.* **2010**, *49*, 9068–9093; (b) S. Bhosale, A. L. Sisson, P. Talukdar, A. Fürstenberg, N. Banerji, E. Vauthey, G. Bollot, J. Mareda, C. Röger, F. Würthner, N. Sakai, S. Matile, *Science* **2006**, *313*, 84–86; (c) A. L. Sisson, N. Sakai, N. Banerji, A. Fürstenberg, E. Vauthey, S. Matile, *Angew. Chem.* **2008**, *120*, 3787–3789; *Angew. Chem. Int. Ed.* **2008**, *47*, 3727–3729.
- (6) (a) Z. Tomović, M. D. Watson, K. Müllen, *Angew. Chem.* **2004**, *116*, 773–777; *Angew. Chem. Int. Ed.* **2004**, *43*, 755–758; (b) M. Müller, C. Kübel, K. Müllen, *Chem. Eur. J.* **1998**, *4*, 2099–2109; (c) F. Morgenroth, E. Reuther, K. Müllen, *Angew. Chem.* **1997**, *109*, 647–649; *Angew. Chem. Int. Ed. Engl.* **1997**, *36*, 631–634.
- (7) (a) K. Okamoto, C. K. Luscombe, *Polym. Chem.* **2011**, *2*, 2424–2434; (b) E. L. Lanni, A. J. McNeil, *J. Am. Chem. Soc.* **2009**, *131*, 16573–16579; (c) R. Miyakoshi, K. Shimono, A. Yokoyama, T. Yokozawa, *J. Am. Chem. Soc.* **2006**, *128*, 16012–16013.

- (8) (a) J. He, J. L. Crase, S. H. Wadumethrige, K. Thakur, L. Dai, S. Zou, R. Rathore, C. S. Hartley, *J. Am. Chem. Soc.* **2010**, *132*, 13848–13857; (b) C. S. Hartley, J. He, *J. Org. Chem.* **2010**, *75*, 8627–8636; (c) S. M. Mathew, C. S. Hartley, *Macromolecules* **2011**, *44*, 8425–8432.
- (9) E. Ohta, H. Sato, S. Ando, A. Kosaka, T. Fukushima, D. Hashizume, M. Yamasaki, K. Hasegawa, A. Muraoka, H. Ushiyama, K. Yamashita, T. Aida, *Nature Chem.* **2011**, *3*, 68–73.
- (10) L. Dössel, L. Gherghel, X. Feng, K. Müllen, *Angew. Chem.* **2011**, *123*, 2588–2591; *Angew. Chem. Int. Ed.* **2011**, *50*, 2540–2543.
- (11) (a) A. R. Marshall, U. H. F. Bunz, *Macromolecules* **2001**, *34*, 4688–4690; (b) J. B. Beck, A. Kokil, D. Ray, S. J. Rowan, C. Weder, *Macromolecules* **2001**, *35*, 590–593.
- (12) R. M. Moslin, C. G. Espino, T. M. Swager, *Macromolecules* **2009**, *42*, 452–454.
- (13) The highly electron-rich alkynes of poly(thienyl ethynylenes) undergo additions to tetracyanoethylene or 7,7,8,8-tetracyanoquinodimethane. Conversions of ~25% of the alkynes are typical. See, for example: Y. Yuan, T. Michinobu, M. Ashizawa, T. Mori, *J. Polym. Sci., Part A: Polym. Chem.* **2011**, *49*, 1013–1020.
- (14) N. Asao, T. Nogami, S. Lee, Y. Yamamoto, *J. Am. Chem. Soc.* **2003**, *125*, 10921–10925.
- (15) (a) A. J. Blake, P. A. Cooke, K. J. Doyle, S. Gair, N. S. Simpkins, *Tetrahedron Lett.* **1998**, *39*, 9093–9096; (b) E. Ohta, H. Sato, S. Ando, A. Kosaka, T. Fukushima, D. Hashizume, M. Yamasaki, K. Hasegawa, A. Muraoka, H. Ushiyama, K. Yamashita, T. Aida, *Nature Chem.* **2011**, *3*, 68–73.
- (16) W. L. Jorgensen, D. S. Maxwell, J. Tirado-Rives, *J. Am. Chem. Soc.* **1996**, *118*, 11225–11236.
- (17) S. J. Plimpton, *Comp. Phys.* **1995**, *117*, 1–19.

(18) (a) C. E. Halkyard, M. E. Rampey, L. Kloppenburg, S. L. Studer-Martinez, U. H. F. Bunz, *Macromolecules* **1998**, *31*, 8655–8659; (b) V. E. Williams, T. M. Swager, *Macromolecules* **2000**, *33*, 4069–4073; (c) U. H. F. Bunz, *Chem. Rev.* **2000**, *100*, 1605–1644.

## APPENDIX ONE

## **Table of Contents**

<b>A. Materials and Instrumentation</b>	42
<b>B. Synthetic Procedures</b>	43
<b>C. NMR Spectroscopy</b>	53
<b>D. Fourier Transform Infrared Spectroscopy</b>	66
<b>E. Thermogravimetric Analysis</b>	68
<b>F. Polymer Molecular Weight Characterization</b>	69
<b>G. Polymer Simulations</b>	70
<b>H. References to Appendix</b>	73



**A. Materials.** All reagents were purchased from commercial sources and used without further purification. CH<sub>2</sub>Cl<sub>2</sub>, PhMe, and MeOH were purchased from commercial sources and purified using a custom-built alumina-column based solvent purification system. Other solvents were purchased from commercial sources and used without further purification

**Instrumentation.** Infrared spectra were recorded on a Thermo Nicolet iS10 with a diamond ATR attachment and are uncorrected. Ultraviolet/visible/near infrared absorbance spectra were recorded on a Cary 5000 spectrophotometer with a Hg lamp.

Photoemission and excitation spectra were recorded on a Horiba Jobin Yvon Fluorolog-3 fluorescence spectrophotometer equipped with a 450 W Xe lamp, double excitation and double emission monochromators, a digital photon-counting photomultiplier and a secondary InGaAs detector for the NIR range. Correction for variations in lamp intensity over time and wavelength was achieved with a solid-state silicon photodiode as the reference. The spectra were further corrected for variations in photomultiplier response over wavelength and for the path difference between the sample and the reference by multiplication with emission correction curves generated on the instrument.

Thermogravimetric analysis was carried out on a TA Instruments Q500 Thermogravimetric Analyzer in a N<sub>2</sub> atmosphere using a 10 °C/min ramp without equilibration delay.

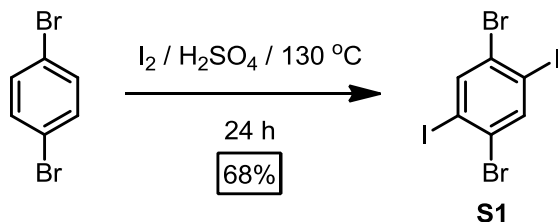
Mass spectra were obtained on a Waters MALDI micro MX MALDI-TOF mass spectrometer using positive ionization and a reflectron detector. MALDI samples were prepared by depositing the analyte dissolved in a saturated dithranol solution onto a stainless steel sample plate. The plate was dried in air before loading it into the instrument.

NMR spectra were recorded on a Varian 400 MHz, a Varian 500 MHz or a Bruker ARX 300 MHz spectrometer using a standard <sup>1</sup>H/X Z-PFG probe at ambient temperature with a 20 Hz sample spin rate.

Size exclusion chromatography (SEC) was performed on two 7.5-μm columns (PolyPore, Varian, Inc.) connected in series. Tetrahydrofuran was used as the mobile phase at 1.0 mL/min flow from a Shimadzu LC-20AD isocratic pump. The detector system consisted of a miniDawn three angle, light-scattering system, followed downstream by an Optilab Rex differential refractometer from Wyatt Technologies.

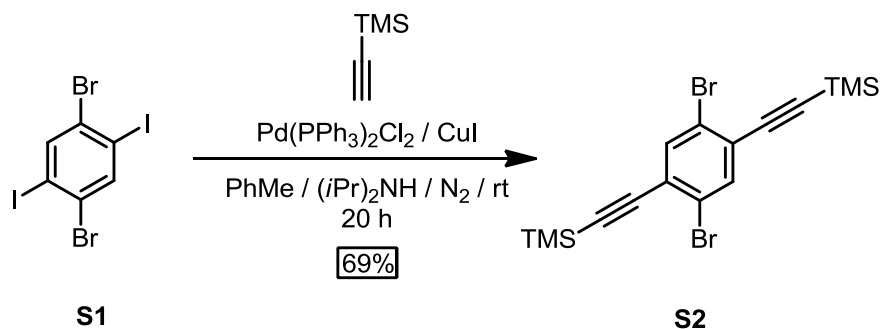
## B. Synthetic Procedures

### Scheme A1.1. Synthesis of S1.



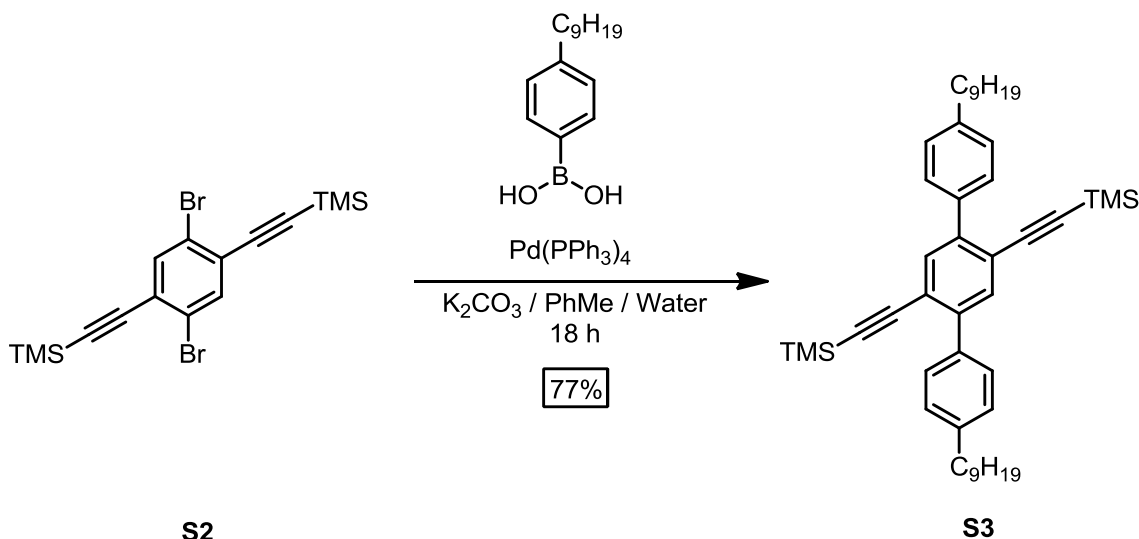
**1,4-dibromo-2,5-diiodobenzene S1:** **S1** was synthesized using the method of Hart *et al.*<sup>1</sup> Its  $^1\text{H}$  and  $^{13}\text{C}$  NMR spectra were consistent with previously reported data.

### Scheme A1.2. Synthesis of S2.



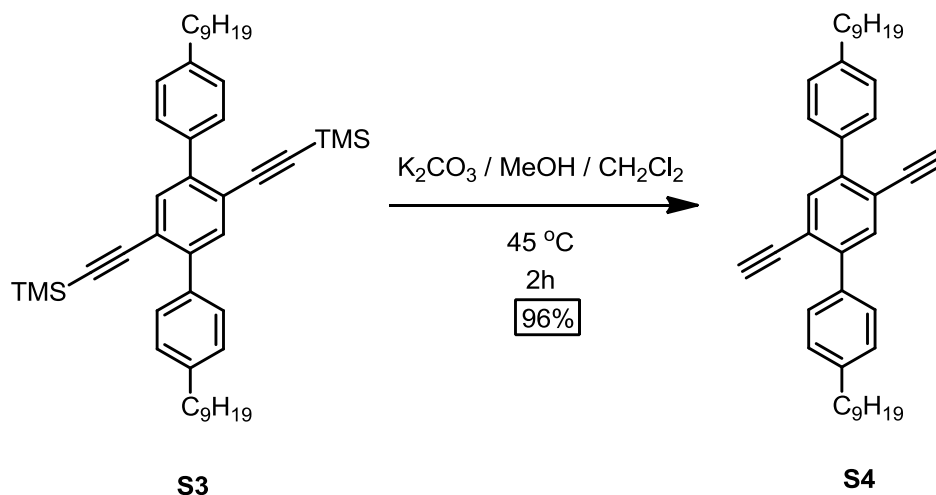
**Synthesis of S2:** Anhydrous PhMe (30 mL) and freshly distilled diisopropylamine (15 mL) were added to a 100 mL flask and sparged with  $\text{N}_2$  for 20 min. 1,4-dibromo-2,5-diiodobenzene (3.000 g, 6.15 mmol), TMS-acetylene (1.510 g, 15.38 mmol),  $\text{Pd(PPh}_3)_2\text{Cl}_2$  (216 mg, 0.308 mmol) and CuI (117 mg, 0.615 mmol) were added to the solution, in sequence. The mixture was stirred at rt for 20 h. The crude reaction mixture was filtered through celite and washed with additional  $\text{CH}_2\text{Cl}_2$  (400 mL). Evaporation of the solvent provided the crude product as a solid, which was purified by chromatography ( $\text{SiO}_2$ , hexanes) followed by recrystallization from DMSO to give **S2** (1.801 g, 69% yield) as white needles.  $^1\text{H}$  and  $^{13}\text{C}$  NMR spectroscopy were consistent with the report of Tovar *et al.*<sup>2</sup>

**Scheme A1.3.** Synthesis of **S3**.



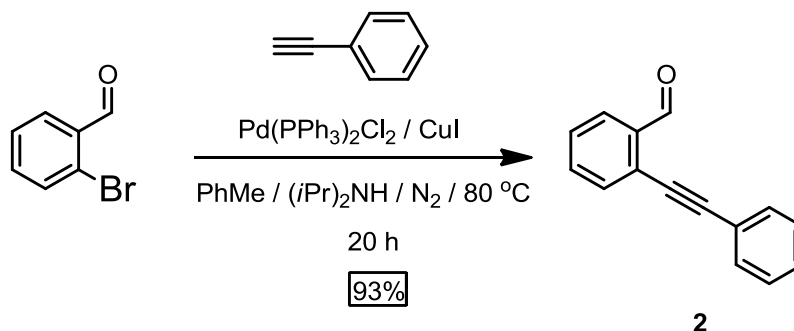
**Synthesis of S3:** **S2** (0.650 g, 1.518 mmol), 4-*n*-nonylphenylboronic acid (0.829 g, 3.339 mmol),  $\text{K}_2\text{CO}_3$  (0.629 g, 4.553 mmol),  $\text{Pd}(\text{PPh}_3)_4$  (0.175 g, 0.152 mmol) were dissolved in a mixture of PhMe (15 mL) and water (3 mL), subjected to three freeze-pump-thaw cycles and backfilled with a  $\text{N}_2$  atmosphere. The mixture was heated to 100 °C for 18 h. The solution was cooled to rt, filtered through celite, and washed with additional  $\text{CH}_2\text{Cl}_2$  (250 mL). The solvent was evaporated and the resulting oil was purified by chromatography ( $\text{SiO}_2$ , hexanes to 1% v/v EtOAc/hexanes) to give **S3** (0.786 g, 77% yield) as a yellow oil that solidified slowly. **S3**:  $^1\text{H}$  NMR (400 MHz,  $\text{CDCl}_3$ )  $\delta$  7.59 (s, 2H), 7.55 (d,  $J = 7.8$  Hz, 4H), 7.24 (d,  $J = 7.8$  Hz, 4H), 2.68 (t,  $J = 7.8$  Hz, 4H), 1.68 (m, 4H), 1.39-1.25 (m, 24H), 0.95-0.91 (m, 6H), 0.18 (s, 18H).  $^{13}\text{C}$  NMR (100 MHz,  $\text{CDCl}_3$ )  $\delta$  142.81, 142.73, 136.75, 134.49, 129.49, 128.27, 121.95, 104.98, 99.54, 36.12, 32.31, 31.94, 30.12, 30.00, 29.77, 29.67, 23.09, 14.53, 0.42. IR (solid, ATR) 2956, 2923, 2853, 2155, 1521, 1479, 1376, 1248, 1187, 1017, 906, 863, 839, 758, 722, 699  $\text{cm}^{-1}$ . HRMS (EI) calcd for  $[\text{C}_{46}\text{H}_{66}\text{Si}_2]^+$  674.4703, found 674.4706.

**Scheme A1.4.** Synthesis of **S4**.



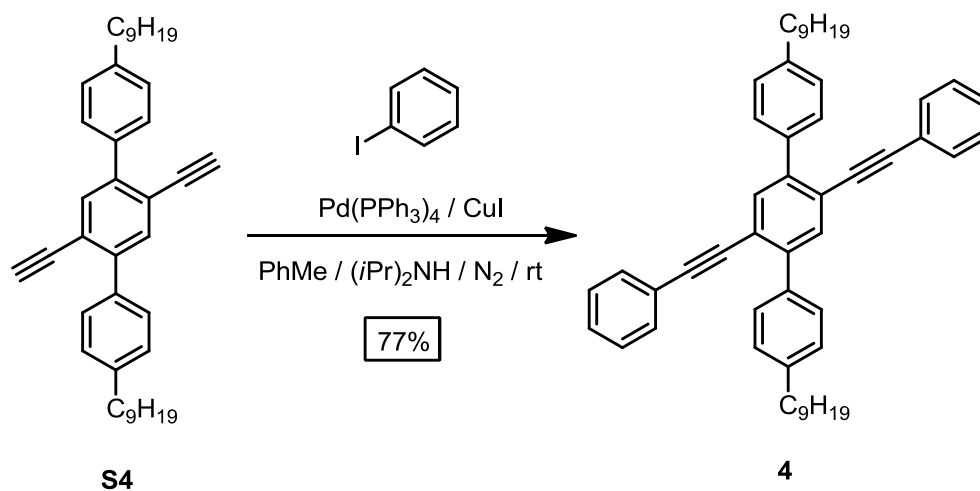
**Synthesis of S4:**  $\text{K}_2\text{CO}_3$  (2.87 g, 20.7 mmol) was suspended in MeOH (41 mL) and a solution of **S3** (1.400 g, 2.073 mmol) dissolved in  $\text{CH}_2\text{Cl}_2$  (10 mL) was added. The mixture was stirred at  $45^\circ\text{C}$  for 2 h, after which it was cooled to rt and poured into aqueous HCl (2M, 10 mL). The solution was washed with  $\text{Et}_2\text{O}$  (3x50 mL), and the combined organic layers were washed with brine (20 mL), dried ( $\text{MgSO}_4$ ) and filtered. The solvent was evaporated to give **S4** (1.060 g, 96% yield) as a white solid that was used without further purification. **S4:**  $^1\text{H}$  NMR (300 MHz,  $\text{CDCl}_3$ )  $\delta$  7.63 (s, 2H), 7.55 (d,  $J = 8.0$  Hz, 4H), 7.25 (d,  $J = 8.0$  Hz, 4H), 3.14 (s, 2H), 2.66 (t,  $J = 7.6$  Hz, 4H), 1.67 (m, 4H), 1.40-1.25 (m, 24H), 0.91-0.87 (m, 6H).  $^{13}\text{C}$  NMR (75 MHz,  $\text{CDCl}_3$ )  $\delta$  142.89, 142.71, 136.33, 135.11, 129.11, 128.30, 121.07, 82.91, 81.74, 35.92, 32.06, 31.54, 29.72, 29.69, 29.59, 29.50, 22.84, 14.28. IR (solid, ATR) 3287, 2953, 2918, 2851, 1522, 1480, 1468, 1414, 1376, 1265, 1139, 1018, 902, 841, 823, 721, 666  $\text{cm}^{-1}$ . HRMS (EI) calcd for  $[\text{C}_{40}\text{H}_{50}]^+$  530.3913, found 530.3896.

**Scheme A1.5.** Synthesis of **2**.



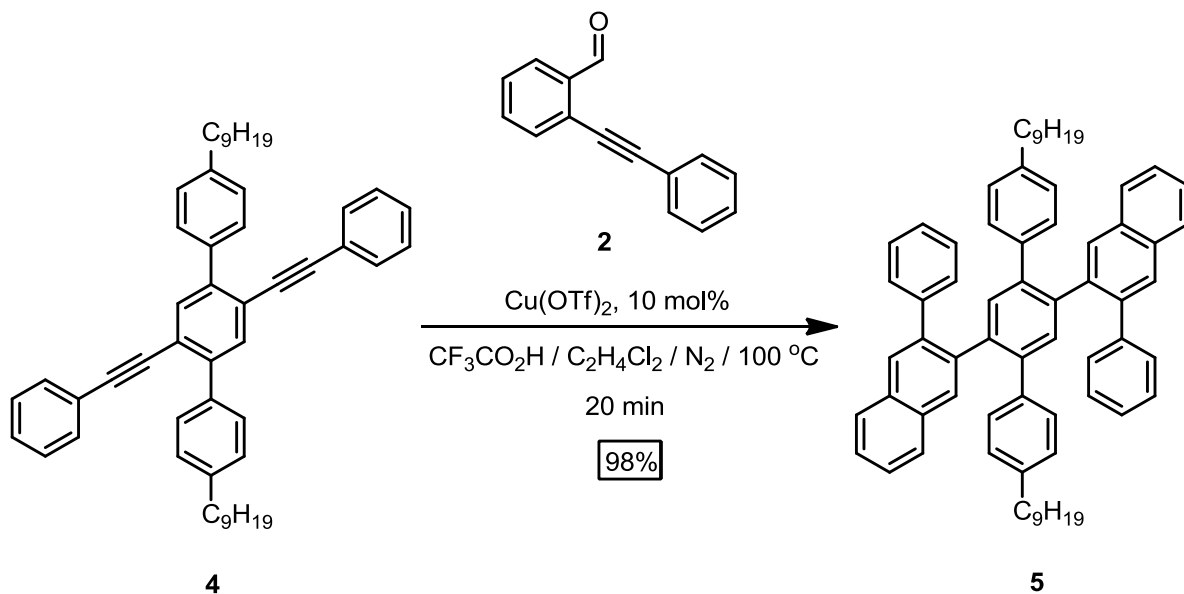
**Synthesis of 2-(phenylethynyl)benzaldehyde 2:** **2** was synthesized using the method of Fairfax *et al.*<sup>3</sup>

**Scheme A1.6.** Synthesis of **4**.



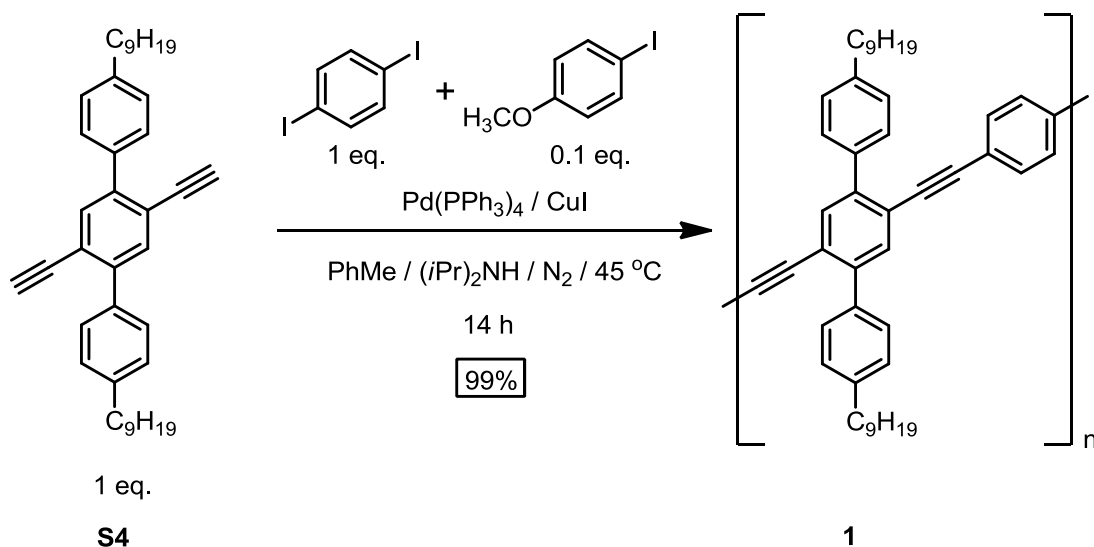
**Synthesis of 4:** **S4** (0.300 g, 0.565 mmol), iodobenzene (0.346 mg, 1.695 mmol) and freshly distilled diisopropylamine (9 mL) were dissolved in anhydrous PhMe (28 mL), subjected to three freeze-pump-thaw cycles, and backfilled with N<sub>2</sub>. Pd(PPh<sub>3</sub>)<sub>4</sub> (33 mg, 0.028 mmol) and CuI (11 mg, 0.057 mmol) were added, and another freeze-pump-thaw cycle was performed. After stirring for 2 h at rt, the reaction mixture was filtered through celite and washed with CH<sub>2</sub>Cl<sub>2</sub> (150 mL). The solvent was evaporated and the crude product was purified by chromatography (SiO<sub>2</sub>, 3% v/v EtOAc/hexanes) to give **4** (0.296 g, 77% yield) as a yellow solid. **4**: <sup>1</sup>H NMR (400 MHz, CDCl<sub>3</sub>) δ 7.72 (s, 2H), 7.67 (d, *J* = 8.1 Hz, 4H), 7.39-7.33 (m, 4H), 7.33-7.27 (m, 6H), 2.70 (t, *J* = 7.5 Hz, 4H), 1.69 (m, 4H), 1.44-1.23 (m, 24H), 0.93-0.86 (m, 6H). <sup>13</sup>C NMR (100 MHz, CDCl<sub>3</sub>) δ 142.69, 142.33, 136.89, 133.89, 131.56, 129.32, 128.41, 128.38, 128.19, 123.50, 121.73, 93.78, 89.63, 35.92, 32.07, 31.70, 29.77, 29.75, 29.53, 29.52, 22.85, 14.29. IR (solid, ATR) 3061, 2954, 2922, 2851, 1597, 1572, 1496, 1466, 1441, 1377, 1261, 1189, 1122, 1068, 1027, 1018, 903, 853, 834, 810, 752, 723, 687 cm<sup>-1</sup>. HRMS (EI) calcd for [C<sub>52</sub>H<sub>58</sub>]<sup>+</sup> 682.4539, found 682.4551.

**Scheme A1.7.** Synthesis of **5**.



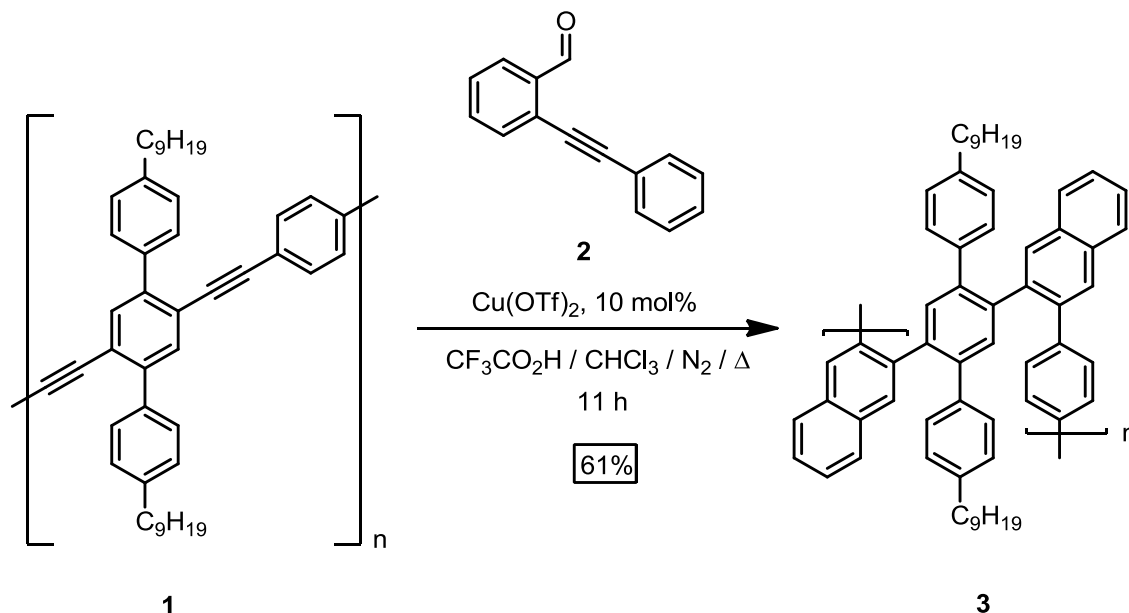
**Synthesis of 5:** Dialkyne **4** (0.273 g, 0.400 mmol) and benzaldehyde **2** (0.330 g, 1.600 mmol) were dissolved in 1,2-dichloroethane (16 mL) under  $\text{N}_2$ .  $\text{Cu(OTf)}_2$  (58 mg, 0.160 mmol) and  $\text{CF}_3\text{CO}_2\text{H}$  (0.135 mL, 1.760 mmol) were added in quick succession. The solution was heated to reflux for 20 min, after which it was cooled to rt and poured into a saturated aqueous  $\text{NaHCO}_3$  solution (50 mL). The aqueous layer was washed with extracted with  $\text{CH}_2\text{Cl}_2$  (3x50 mL), and the combined organic layers were dried ( $\text{MgSO}_4$ ) and filtered. The solvent was evaporated to provide the product as a crude solid, which was purified by chromatography ( $\text{SiO}_2$ , 2% v/v EtOAc/hexanes) to give **5** (0.348 g, 98% yield) as an off-white solid. **5**:  $^1\text{H}$  NMR (500 MHz,  $\text{CDCl}_3$ )  $\delta$  8.05 (s, 2H), 7.67 (d,  $J = 8.1$  Hz, 4H), 7.88-7.84 (m, 4H), 7.66 (s, 2H), 7.53-7.48 (m, 6H), 7.22-7.17 (m, 2H), 7.16-7.11 (m, 2H), 6.77 (d,  $J = 7.7$  Hz, 8H), 6.55 (d,  $J = 8.1$  Hz, 4H), 2.52 (td,  $J = 8.0$  Hz, 2.2 Hz, 4H), 1.60 (m, 4H), 1.39-1.25 (m, 24H), 0.94-0.89 (m, 6H).  $^{13}\text{C}$  NMR (125 MHz,  $\text{CDCl}_3$ )  $\delta$  141.1, 140.9, 140.0, 139.6, 139.2, 139.1, 137.8, 133.9, 133.1, 132.9, 130.6, 129.4, 129.0, 128.9, 127.9, 127.9, 127.8, 127.5, 126.2, 35.7, 32.1, 31.8, 29.8, 29.7, 29.5, 29.4, 22.9, 14.3. IR (solid, ATR) 3053, 2953, 2923, 2852, 1941, 1671, 1596, 1489, 1456, 1371, 1260, 1074, 1014, 914, 889, 796, 772, 759, 746, 695  $\text{cm}^{-1}$ . HRMS (EI) calcd for  $[\text{C}_{68}\text{H}_{70}]^+$  886.5478, found 886.5509.

**Scheme A1.8.** Synthesis of polymer **1**.



**Synthesis of polymer 1:** **S4** (0.200 g, 0.377 mmol), 1,4-diiodobenzene (0.125 g, 0.377 mmol) and 4-iodoanisole (0.009 g, 0.04 mmol) were dissolved in anhydrous  $\text{PhMe}$  (12 mL) and freshly distilled diisopropylamine (4 mL). The solution was subjected to three freeze-pump-thaw cycles and backfilled with  $\text{N}_2$ . While the solution was frozen,  $\text{Pd(PPh}_3)_4$  (22 mg, 0.019 mmol) and  $\text{CuI}$  (7 mg, 0.038 mmol) were added under positive  $\text{N}_2$  pressure. After another freeze-pump-thaw cycle, the flask was filled with  $\text{N}_2$  and heated to  $45\text{ }^\circ\text{C}$ . After 14 h at  $45\text{ }^\circ\text{C}$ , the solution was cooled to rt and poured into a saturated aqueous  $\text{NH}_4\text{Cl}$  solution (100 mL). The aqueous solution was washed with  $\text{CH}_2\text{Cl}_2$  (3x50 mL). The combined organic layers, including some undissolved polymer were concentrated to a total volume of 3 mL and were precipitated into vigorously stirred  $\text{MeOH}$  (500 mL). The precipitate was collected by filtration and dried under vacuum to give the polymer **1** (227 mg, 99% yield) as a yellow solid. **1**:  $^1\text{H}$  NMR (300 MHz,  $\text{CDCl}_3$ )  $\delta$  7.70 (s, 2H), 7.63 (d,  $J = 7.8\text{ Hz}$ , 4H), 7.28 (d,  $J = 7.8\text{ Hz}$ , 4H), 7.26 (s, 4H), 2.70 (t,  $J = 7.5\text{ Hz}$ , 4H), 1.70 (m, 4H), 1.44-1.22 (m, 24H), 0.91-0.84 (m, 6H).  $^{13}\text{C}$  NMR (100 MHz,  $\text{C}_2\text{D}_2\text{Cl}_4$ )  $\delta$  142.93, 142.11, 136.90, 133.98, 131.53, 129.35, 128.29, 121.92, 109.95, 36.18, 32.24, 31.96, 30.05, 30.02, 29.95, 29.80, 23.12, 14.56. IR (solid, ATR) 3046, 2952, 2922, 2852, 1511, 1467, 1379, 1261, 1185, 1099, 1017, 901, 830, 721,  $694\text{ cm}^{-1}$ .

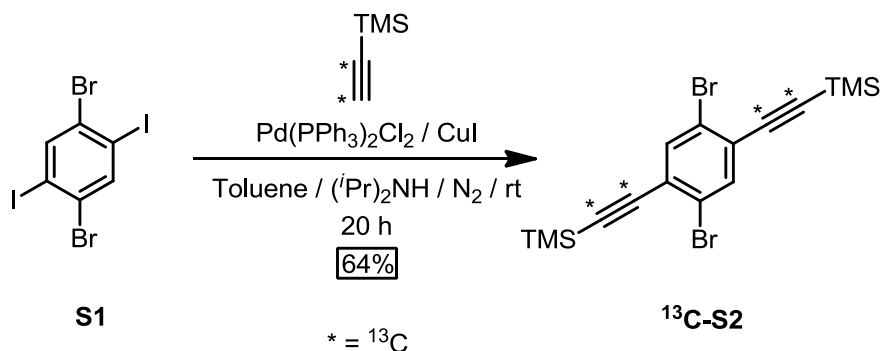
**Scheme A1.9.** Synthesis of polymer **3**.



**Synthesis of polymer 3:** Polymer **1** (0.180 g) was sonicated in  $\text{CHCl}_3$  (10 mL) until finely dispersed and was heated until the polymer dissolved. The solution was transferred into a 25 mL Schlenk tube and sparged with  $\text{N}_2$ .  $\text{Cu}(\text{OTf})_2$  (11 mg, 0.030 mmol), **2** (366 mg, 1.779 mmol), and  $\text{CF}_3\text{CO}_2\text{H}$  (0.14 mL, 1.779 mmol) were added under positive  $\text{N}_2$  pressure. The tube was sealed and heated to 100 °C for 11 h, after which it was cooled to rt. The mixture was poured into a saturated aqueous  $\text{NaHCO}_3$  solution (75 mL) and was extracted with  $\text{CH}_2\text{Cl}_2$  (3x50 mL). The combined organic layers were dried ( $\text{MgSO}_4$ ), filtered and the solvent was evaporated. The crude product was dissolved in minimum amount of  $\text{CH}_2\text{Cl}_2$  and precipitated into a large excess of vigorously stirring acetone (200 mL). The resulting precipitate was collected by centrifugation and subjected to Soxhlet extraction using acetone as the liquid phase for 24 h. The remaining insoluble powder **3** (147 mg, 61% yield) was recovered from the extraction as a brown solid. **3**:  $^1\text{H}$  NMR (400 MHz,  $\text{CDCl}_3$ )  $\delta$  8.20-5.05 (m, 26H), 2.33 (brs, 4H), 1.65-0.50 (m, 34H).  $^{13}\text{C}$  NMR (75 MHz,  $\text{CDCl}_3$ )  $\delta$  141.75-135.77 (br), 133.58 (brs), 131.56-127.05 (br), 124.41 (brs), 35.69, 32.04, 29.51 (brs), 22.82, 14.26. IR (solid, ATR) 3053, 3015, 2924, 2853, 1673, 1596, 1488, 1456, 1370, 1229, 1139, 1017, 950, 891, 833, 746  $\text{cm}^{-1}$ .

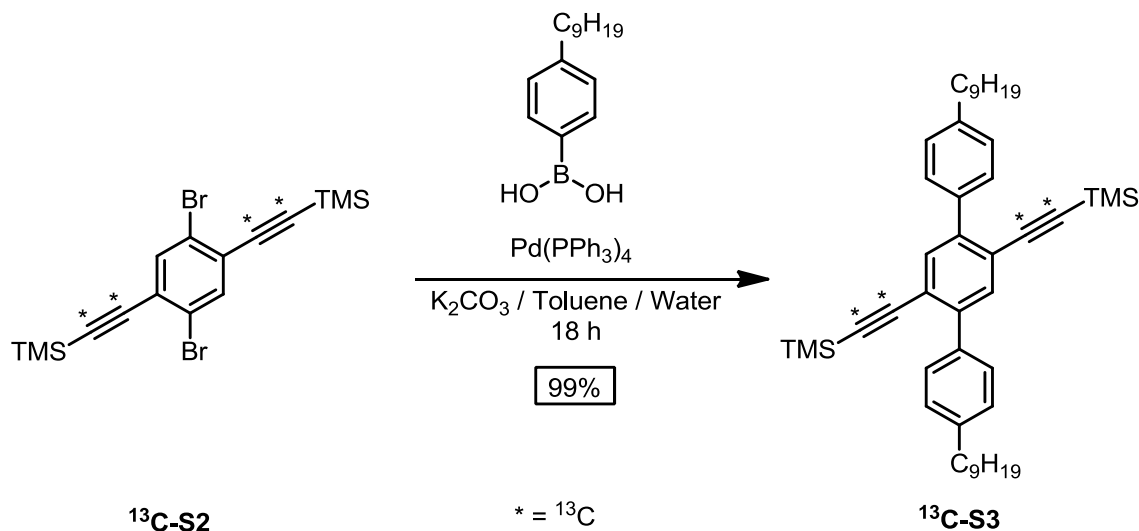


**Scheme A1.10.** Synthesis of  $^{13}\text{C}$ -**S2**.



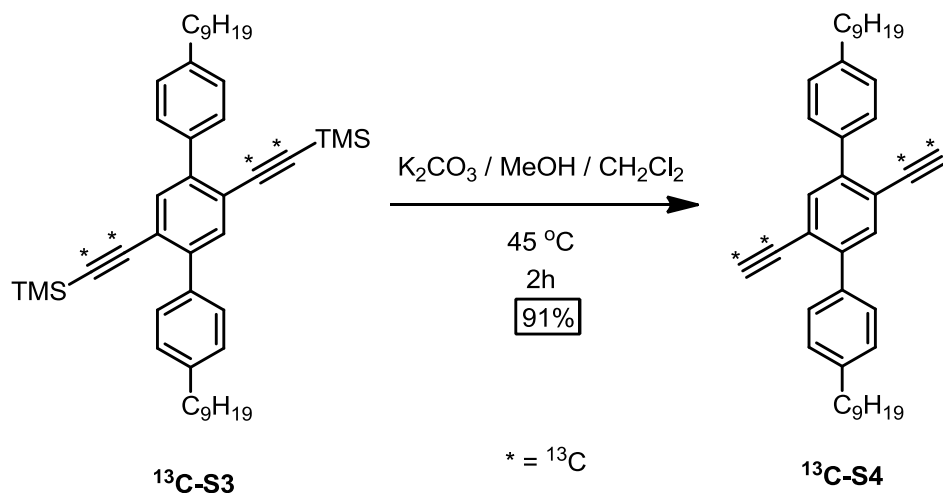
**Synthesis of  $^{13}\text{C}$ -S2:**  $^{13}\text{C}$ -S2 was synthesized under the same conditions as S2. Trimethylsilylacetylene- $^{13}\text{C}_2$  (0.113 g, 1.128 mmol) and S1 (0.230 g, 0.513 mmol) were used.  $^{13}\text{C}$ -S2 was obtained (0.129 g, 64% yield).  $^{13}\text{C}$ -S2:  $^1\text{H}$  NMR (300 MHz,  $\text{CDCl}_3$ )  $\delta$  7.65 (d,  $J_{\text{CH}} = 4.6$  Hz, 2H), 0.26 (d,  $J_{\text{CH}} = 2.5$  Hz, 18H).  $^{13}\text{C}$  NMR (75 MHz,  $\text{CDCl}_3$ )  $\delta$  103.4 (d,  $J_{\text{CC}} = 139.0$  Hz), 100.9 (d,  $J_{\text{CC}} = 139.0$  Hz).

**Scheme A1.11.** Synthesis of  $^{13}\text{C}$ -S3.



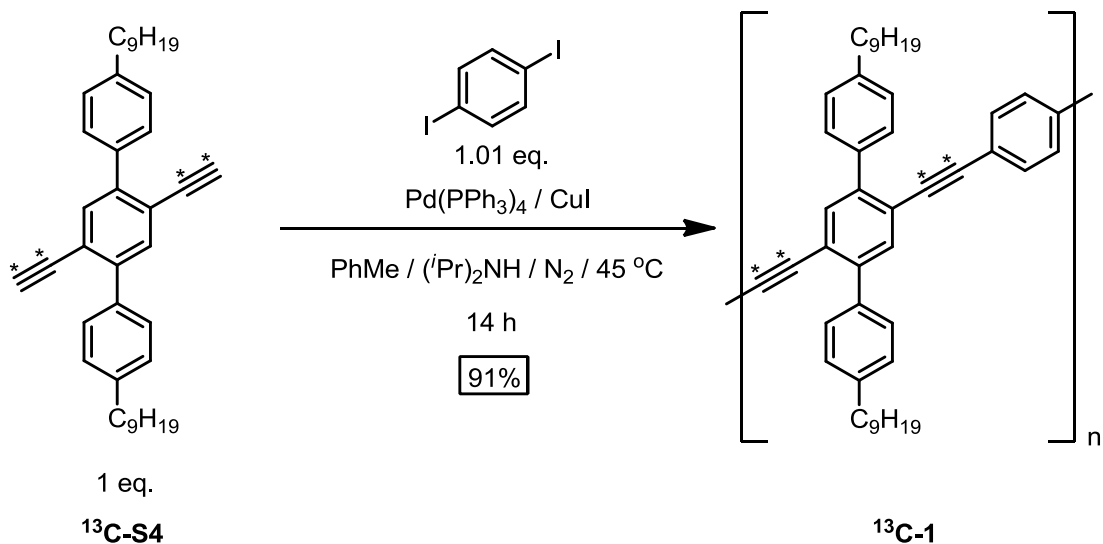
**Synthesis of  $^{13}\text{C}$ -S3:**  $^{13}\text{C}$ -S3 was synthesized under the same conditions as S3. Instead of S2,  $^{13}\text{C}$ -S2 (0.129 g, 0.298 mmol) was used.  $^{13}\text{C}$ -S3 was obtained (0.203g, 99% yield).  $^{13}\text{C}$ -S3:  $^1\text{H}$  NMR (300 MHz,  $\text{CDCl}_3$ )  $\delta$  7.60-7.55 (m, 4H), 7.31-7.13 (m, 6H), 2.70-2.56 (m, 4H), 1.71-1.57 (m, 4H), 1.40-1.16 (m, 24H), 0.94-0.86 (m, 6H), 0.15 (d,  $J_{\text{CH}} = 2.6$  Hz, 18H).  $^{13}\text{C}$  NMR (75 MHz,  $\text{CDCl}_3$ )  $\delta$  105.1 (d,  $J_{\text{CC}} = 136.7$  Hz), 99.4 (d,  $J_{\text{CC}} = 136.7$  Hz).

**Scheme A1.12.** Synthesis of  $^{13}\text{C}$ -S4.



**Synthesis of  $^{13}\text{C}$ -S4:**  $^{13}\text{C}$ -S4 was synthesized under the same conditions as S4. Instead of S3,  $^{13}\text{C}$ -S4 was used.  $^{13}\text{C}$ -S4 was obtained (0.146 g, 91% yield).  $^{13}\text{C}$ -S4:  $^1\text{H}$  NMR (300 MHz,  $\text{CDCl}_3$ )  $\delta$  7.65 (d,  $J_{\text{CH}} = 2.6$  Hz, 2H), 7.56 (d,  $J = 8.2$  Hz, 4H) 7.29-7.27 (m, 4H), 3.15 (dd,  $J_{\text{CH}} = 201.2, 99.3$  Hz, 2H) 2.68 (t,  $J = 7.5$  Hz, 4H), 1.73-1.63 (m, 4H), 1.45-1.22 (m, 24H), 0.93-0.86 (m, 6H).  $^{13}\text{C}$  NMR (75 MHz,  $\text{CDCl}_3$ )  $\delta$  82.9 (d,  $J_{\text{CC}} = 177.8$  Hz), 80.8 (d,  $J_{\text{CC}} = 177.8$  Hz).

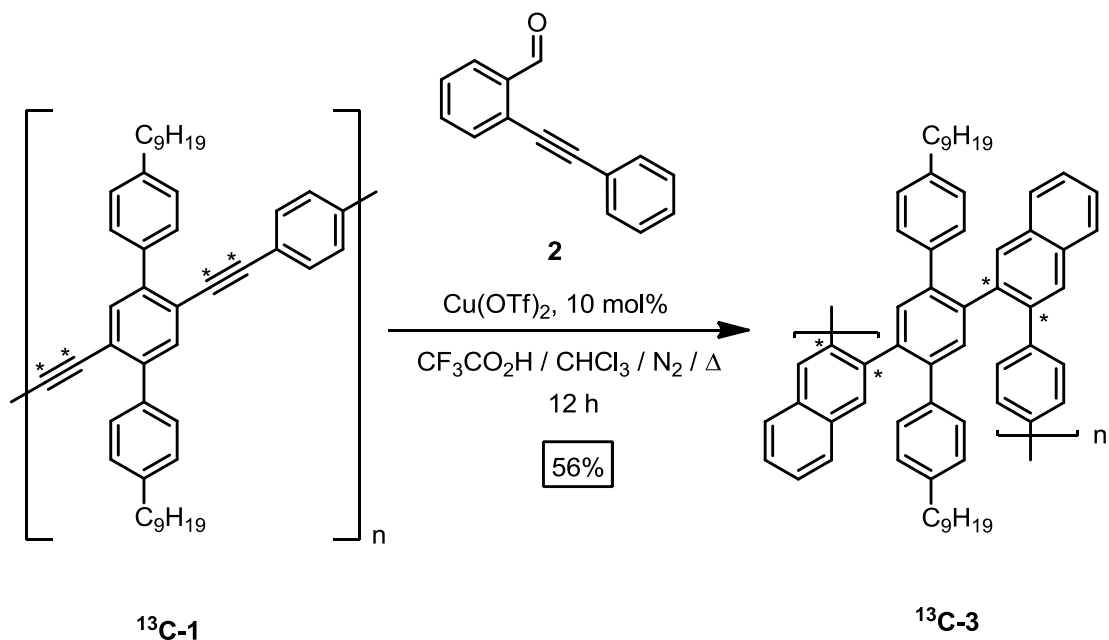
**Scheme A1.13.** Synthesis of  $^{13}\text{C}$ -1.



**Synthesis of  $^{13}\text{C}$ -1:**  $^{13}\text{C}$ -1 was synthesized under the similar conditions as PPE 1. Instead of S4, S4- $^{13}\text{C}_4$  (0.143 g, 0.267 mmol) and 1,4-diiodobenzene (0.089 g, 0.270 mmol) were used.  $^{13}\text{C}$ -1 was obtained (0.150 g, 91% yield).  $^{13}\text{C}$ -1:  $^1\text{H}$  NMR (400 MHz,  $\text{CDCl}_3$ )  $\delta$  7.69 (d,  $J_{\text{CH}} = 3.9$  Hz, 2H), 7.62 (d,  $J_{\text{HH}} = 7.8$  Hz, 4H), 7.29 (d,  $J_{\text{HH}} = 7.8$  Hz, 4H), 7.26 (s, 2H), 2.71 (t,  $J_{\text{HH}} = 7.3$  Hz, 4H), 1.71 (m, 4H), 1.45-1.21 (m, 24H), 0.94-0.84 (m, 6H).  $^{13}\text{C}$  NMR (100 MHz,  $\text{CDCl}_3$ )  $\delta$  131.5,

129.3, 128.3, 94.2 (d,  $J_{CC} = 184.2$  Hz), 91.4 (d,  $J_{CC} = 184.2$  Hz), 36.0, 32.1, 31.6, 29.6, 29.5, 22.8, 14.2.

**Scheme A1.14.** Synthesis of  $^{13}\text{C}$ -**3**.



**Synthesis of  $^{13}\text{C}$ -**3**:**  $^{13}\text{C}$ -**3** was synthesized under the similar conditions as polymer **3**. Instead of polymer **1**,  $^{13}\text{C}$ -**1** (0.020 g) was used.  $^{13}\text{C}$ -**3** was obtained (0.015 g, 56% yield).  $^{13}\text{C}$ -**3**:  $^1\text{H}$  NMR (400 MHz,  $\text{CDCl}_3$ )  $\delta$  8.21-5.59 (m, 26H), 2.40 (brs, 4H), 1.70-0.36 (m, 34H).  $^{13}\text{C}$  NMR (100 MHz,  $\text{CDCl}_3$ )  $\delta$  141.5-135.6 (br), 130.8-125.2 (br), 32.1, 29.7.

### C. NMR Spectra

**Figure A1.1.**  $^1\text{H}$  NMR of **S3** (300 MHz,  $\text{CDCl}_3$ , 298 K).

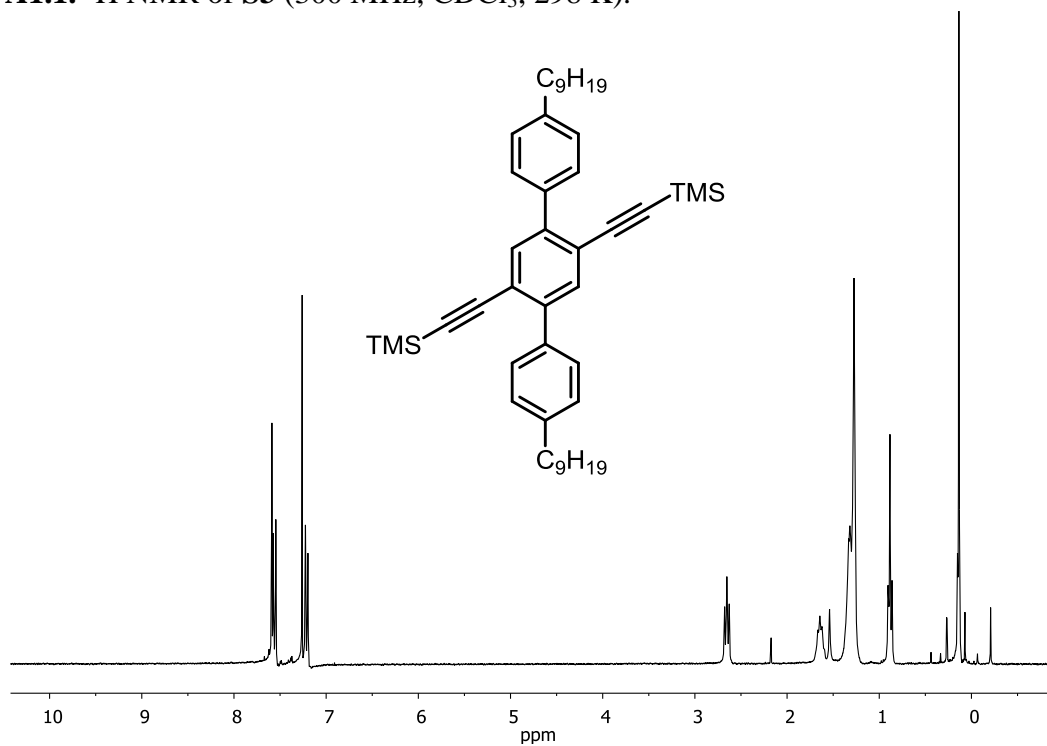


**Figure A1.2.**  $^{13}\text{C}$  NMR of **S3** (75 MHz,  $\text{CDCl}_3$ , 298 K).

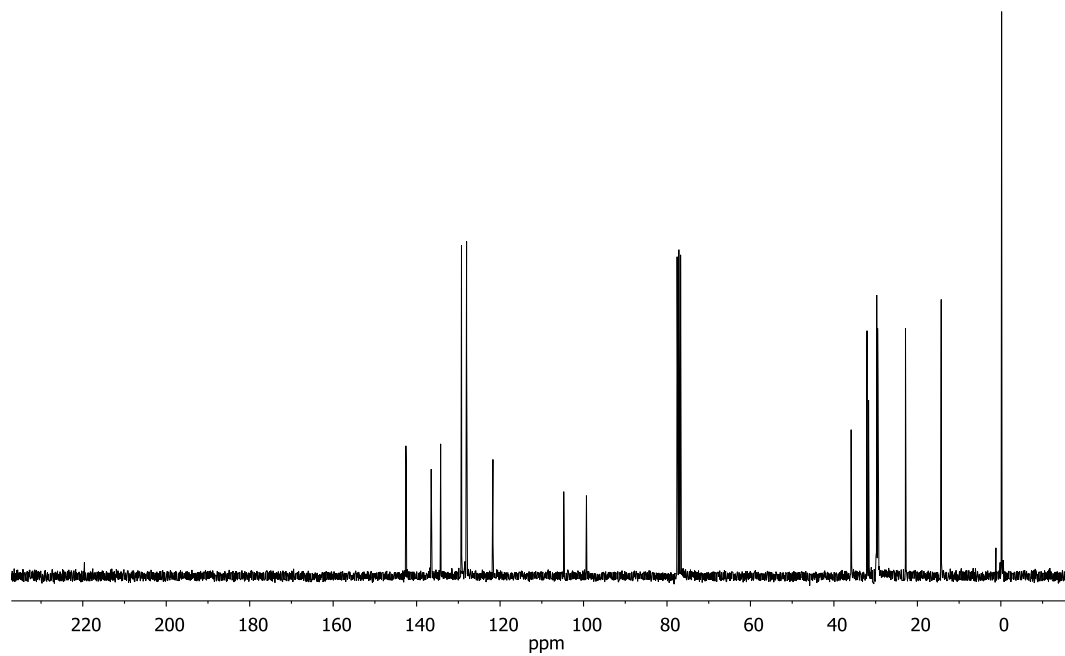


**Figure A1.3.**  $^1\text{H}$  NMR of **S4** (300 MHz,  $\text{CDCl}_3$ , 298 K).

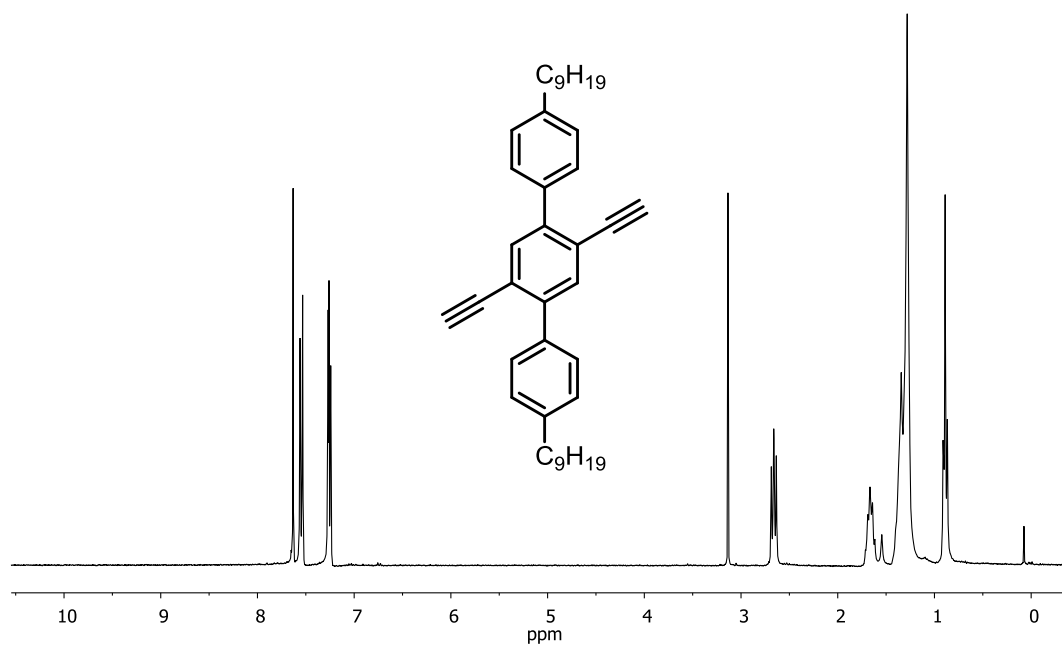


**Figure A1.4.**  $^{13}\text{C}$  NMR of **S4** (75 MHz,  $\text{CDCl}_3$ , 298 K).

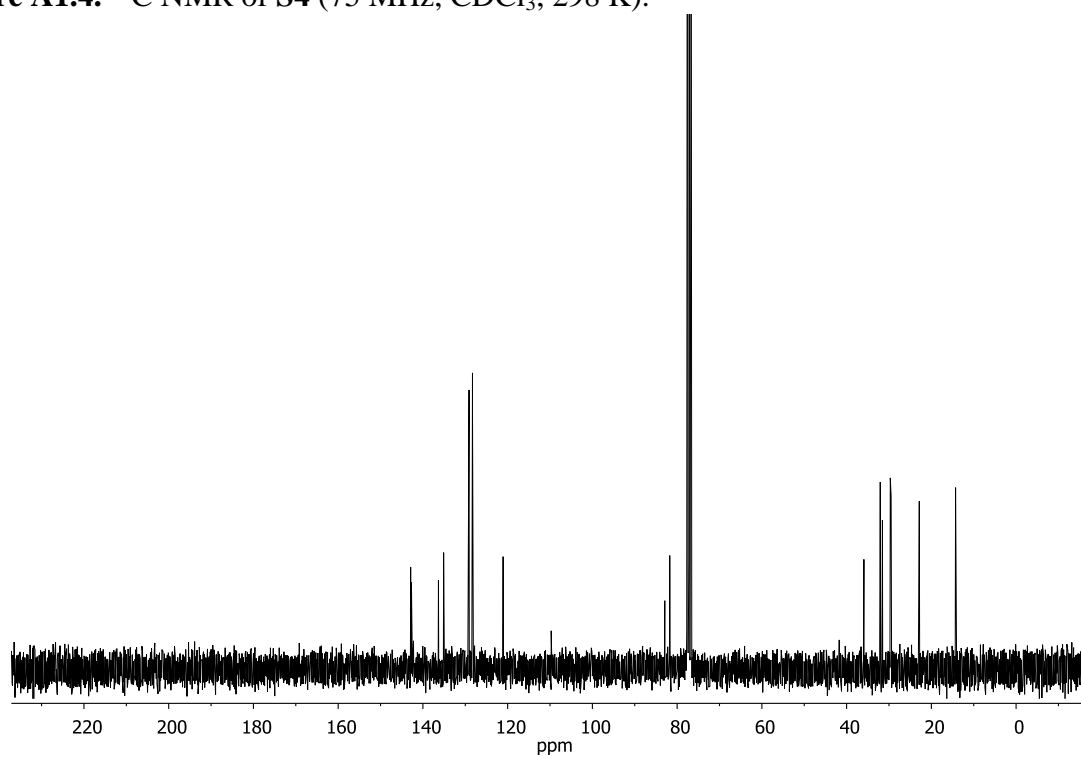


**Figure A1.5.**  $^1\text{H}$  NMR of **4** (400 MHz,  $\text{CDCl}_3$ , 298 K).

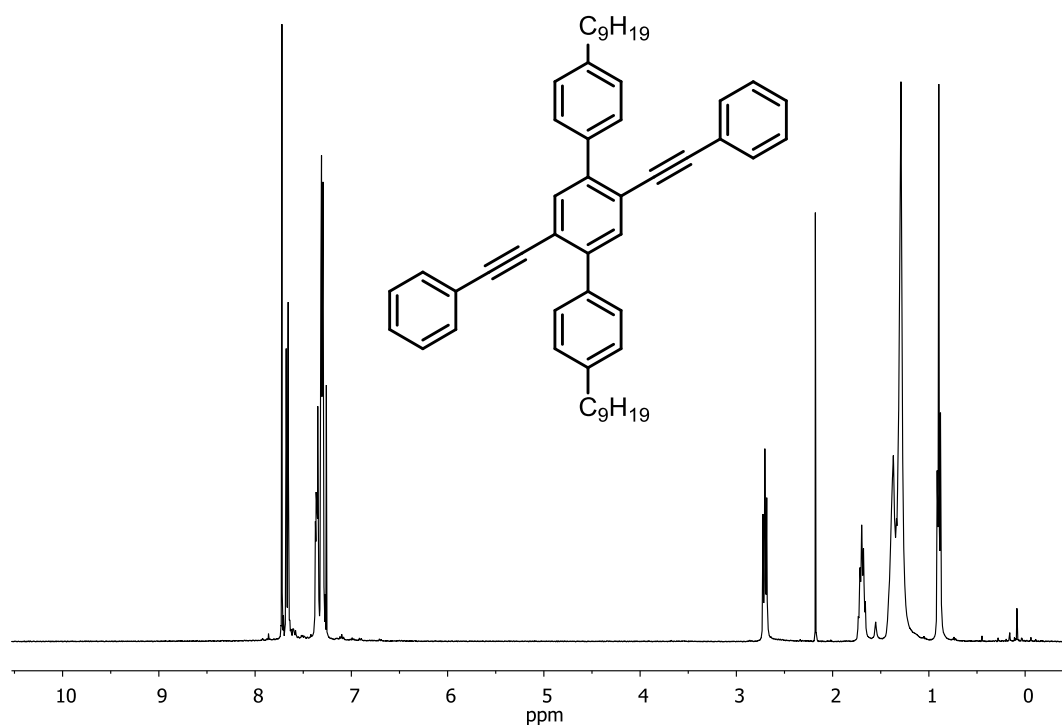


**Figure A1.6.**  $^{13}\text{C}$  NMR of **4** (100 MHz,  $\text{CDCl}_3$ , 298 K).

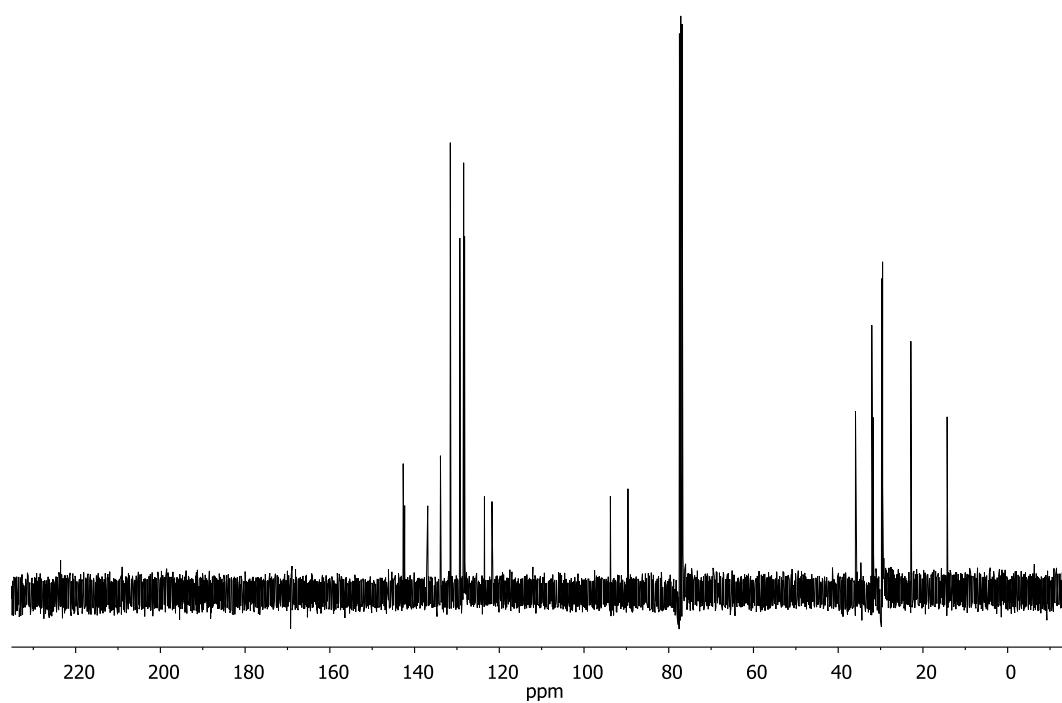


**Figure A1.7.**  $^1\text{H}$  NMR of **5** (500 MHz,  $\text{CDCl}_3$ , 298 K).

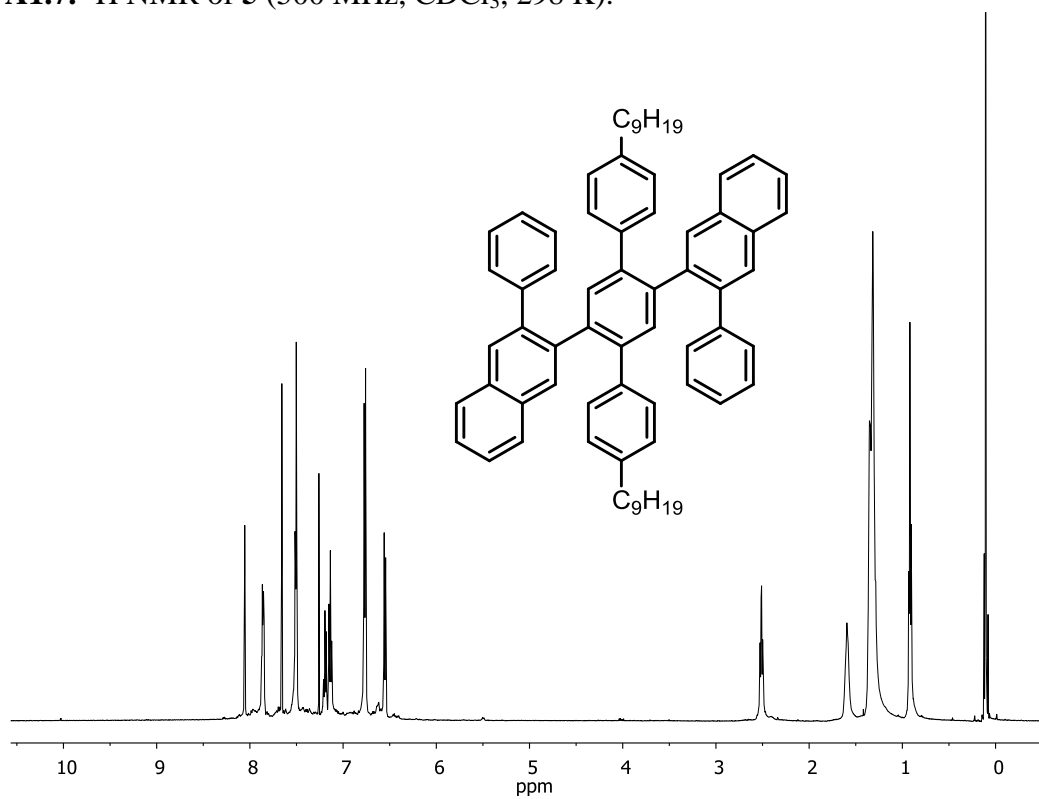


**Figure A1.8.**  $^{13}\text{C}$  NMR of **5** (125 MHz,  $\text{CDCl}_3$ , 298 K).

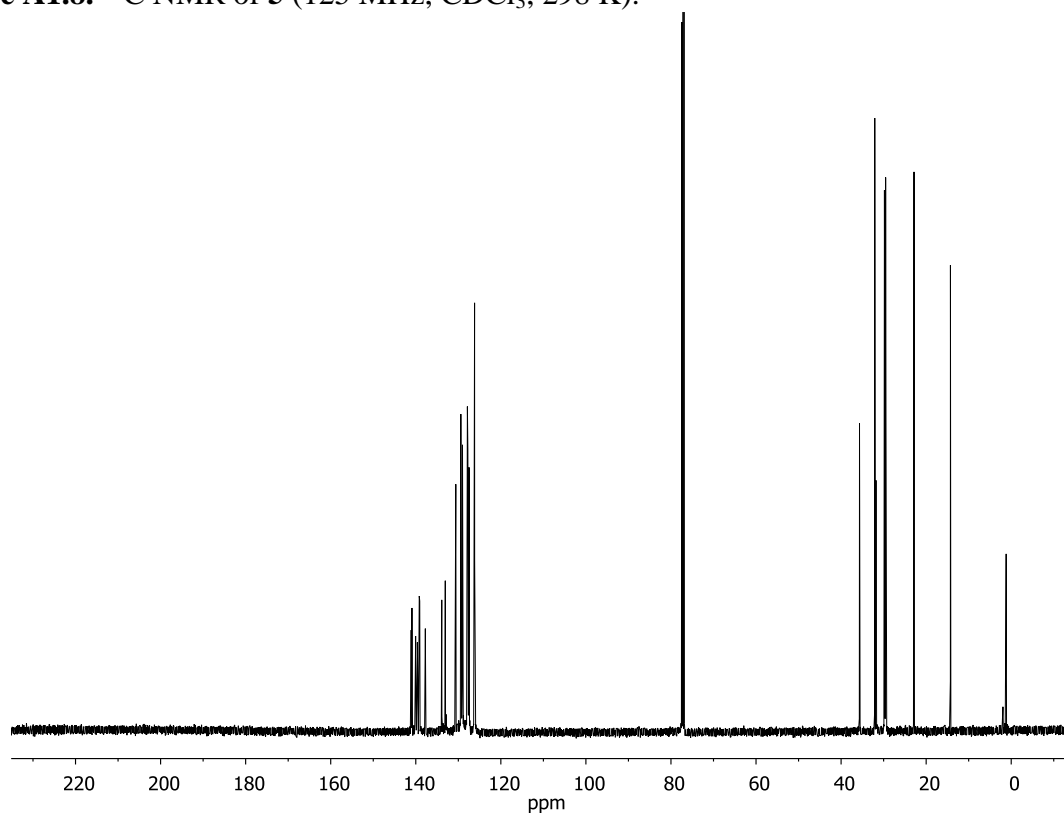


**Figure A1.9.**  $^1\text{H}$  NMR of polymer **1** (400 MHz,  $\text{CDCl}_3$ , 323 K).

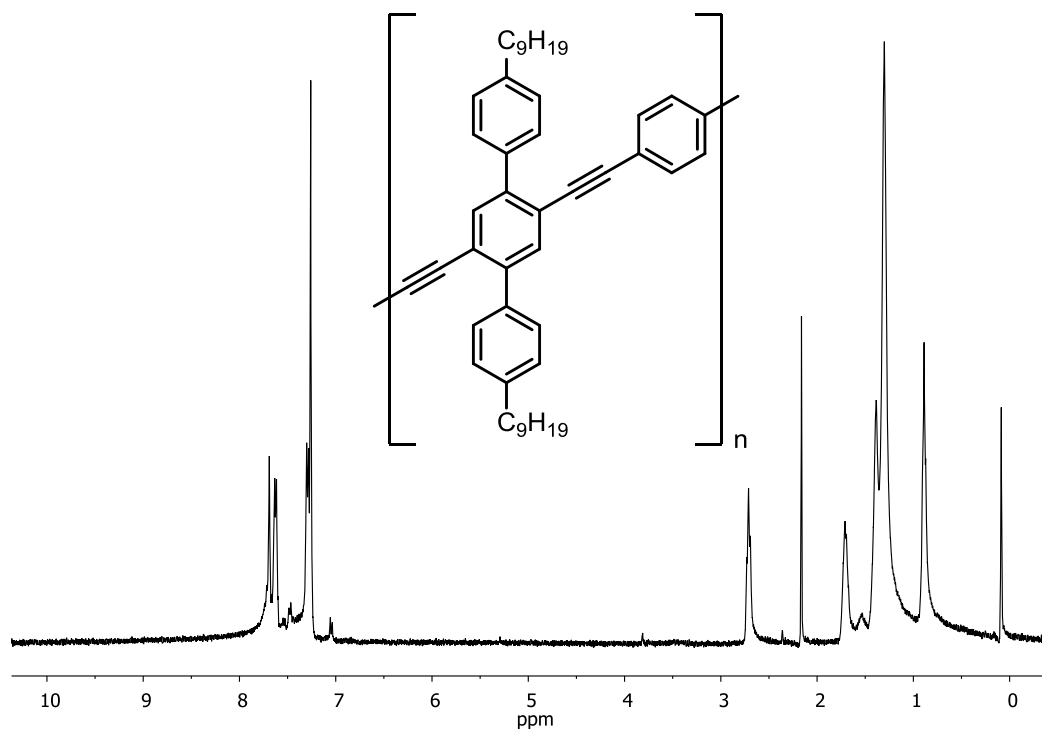


**Figure A1.10.**  $^{13}\text{C}$  NMR of polymer **1** (100 MHz,  $\text{C}_2\text{D}_2\text{Cl}_4$ , 393 K).

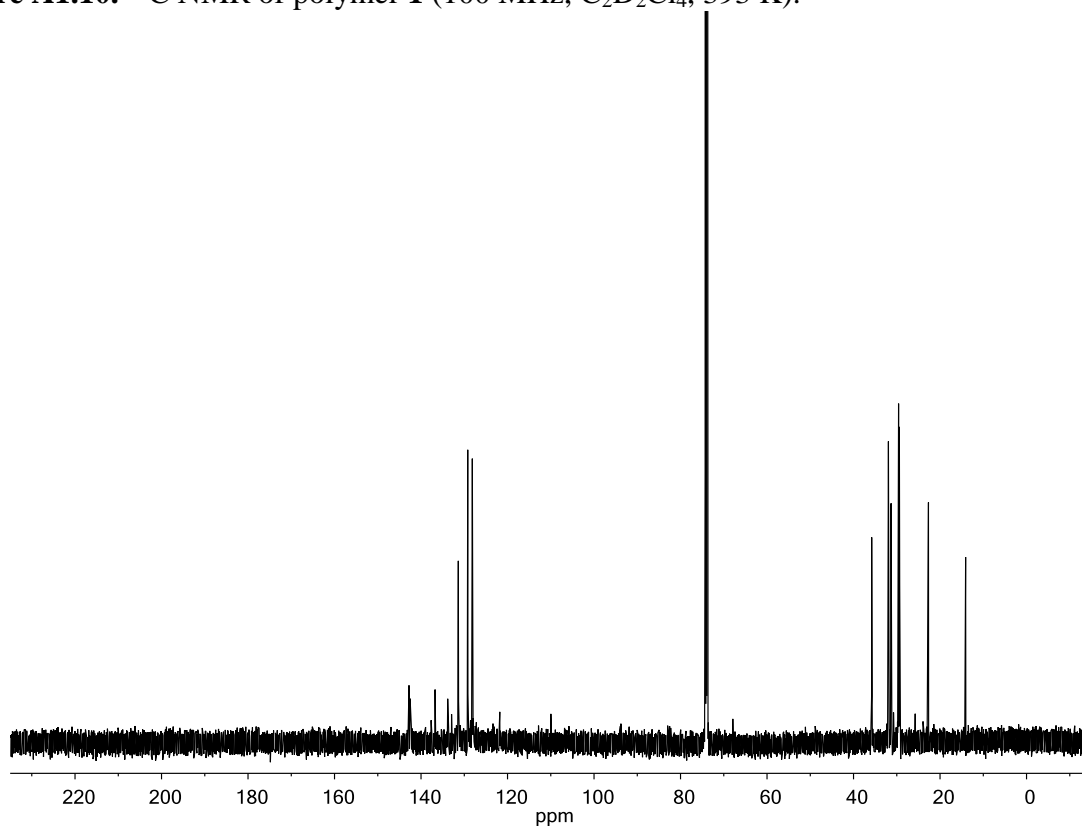




**Figure A1.11.**  $^1\text{H}$  NMR of polymer **3** (400 MHz,  $\text{CDCl}_3$ , 298 K).

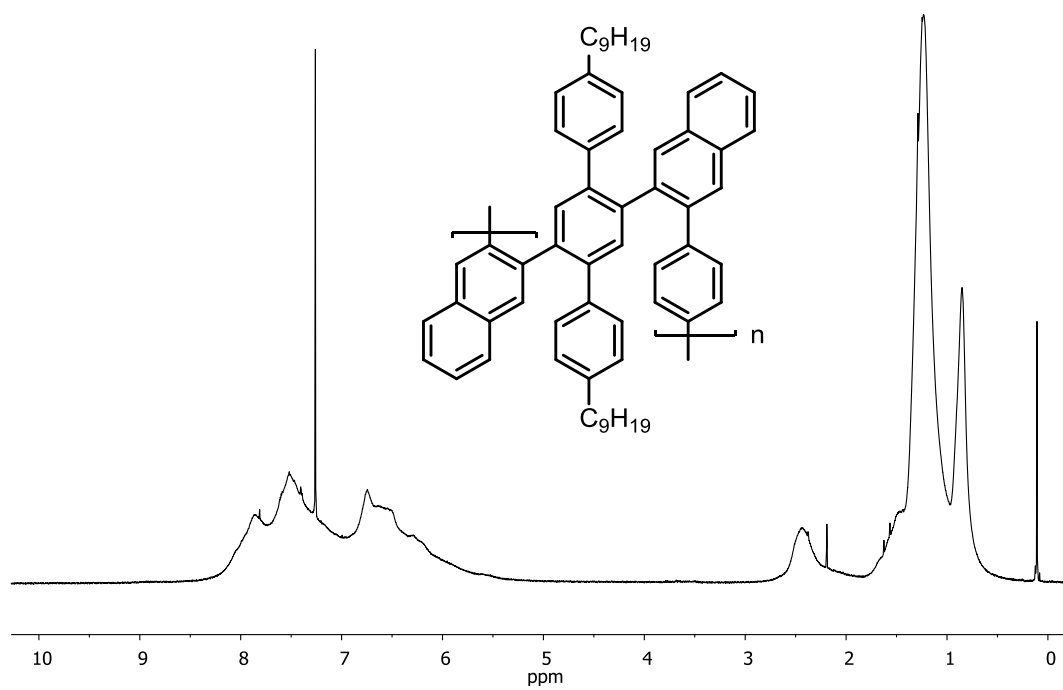


**Figure A1.12.**  $^{13}\text{C}$  NMR of polymer **3** (75 MHz,  $\text{CDCl}_3$ , 298 K).

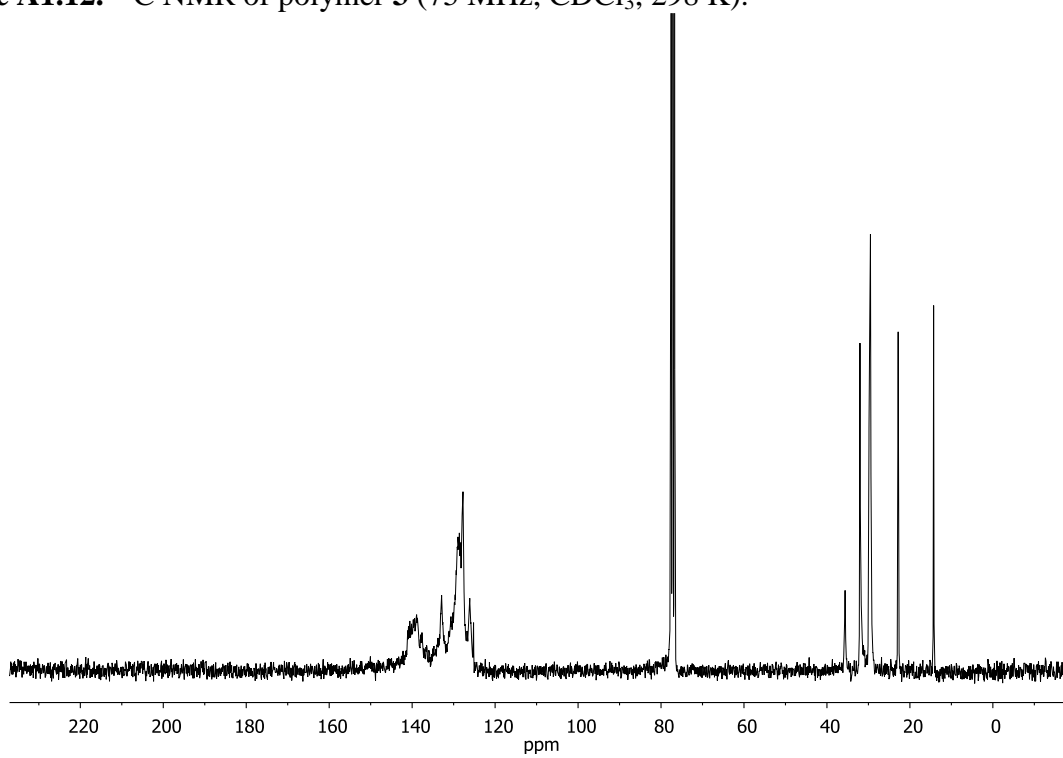


**Figure A1.13.**  $^1\text{H}$  NMR of  $^{13}\text{C}$ -S2 (300 MHz,  $\text{CDCl}_3$ , 298 K).

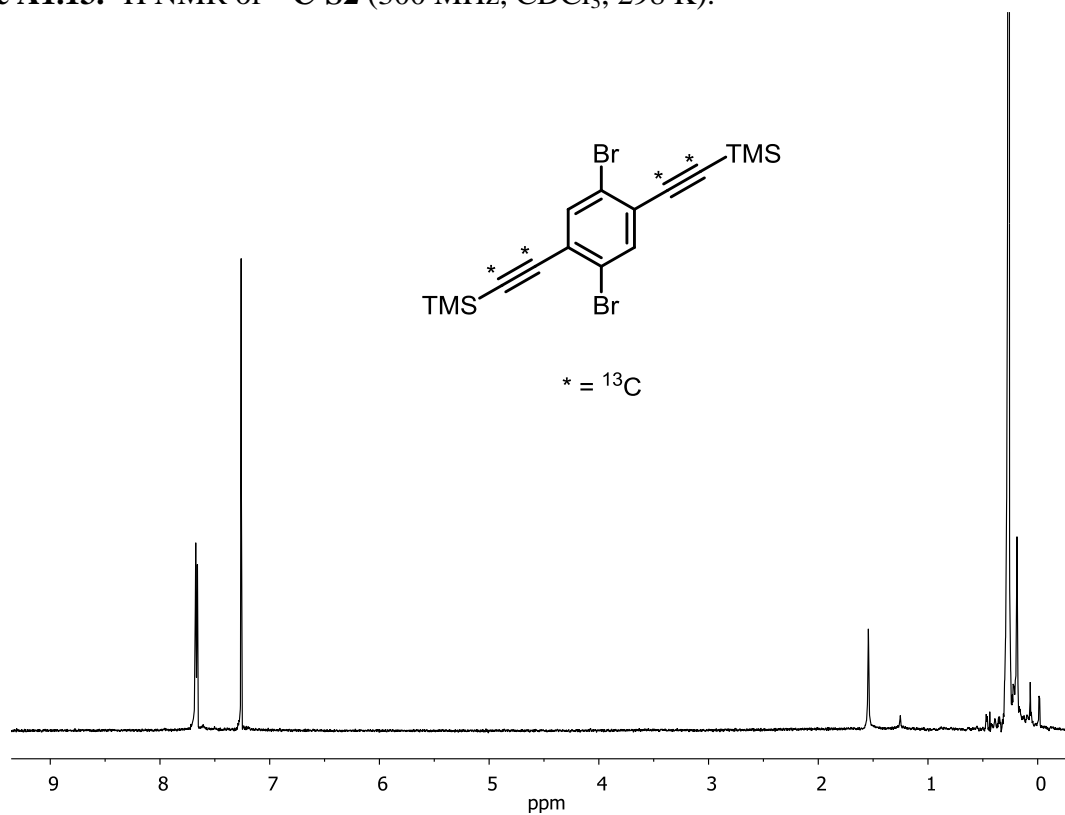


**Figure A1.14.**  $^{13}\text{C}$  NMR of  $^{13}\text{C}$ -S2 (75 MHz,  $\text{CDCl}_3$ , 298 K).

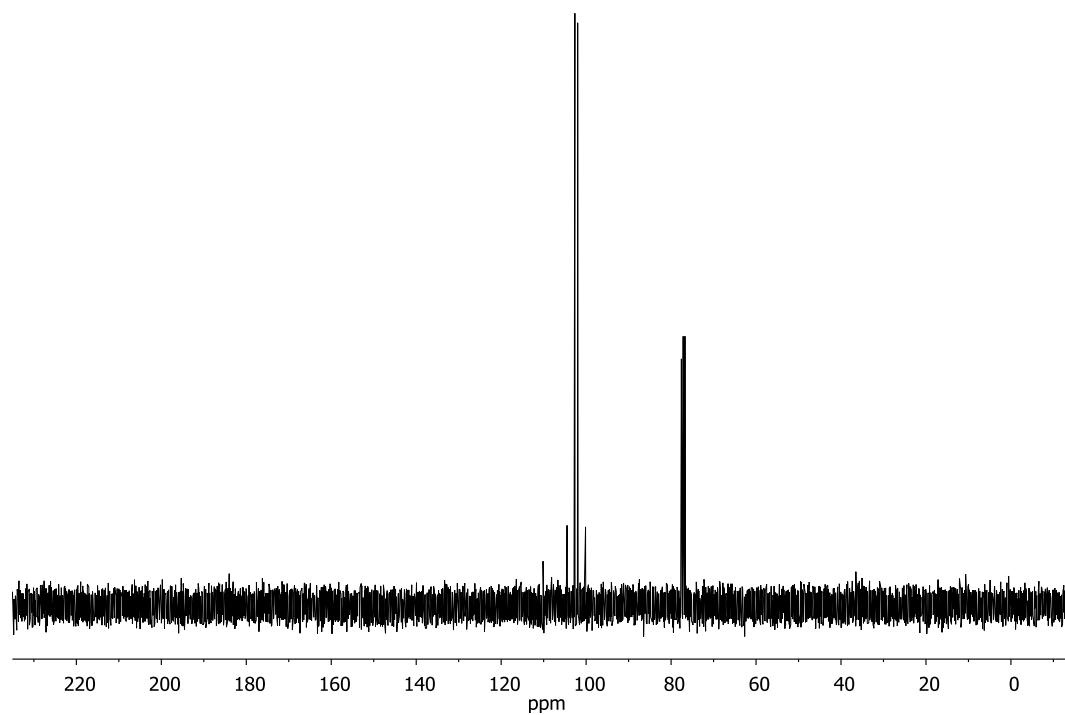


**Figure A1.15.**  $^1\text{H}$  NMR of  $^{13}\text{C}$ -S3 (300 MHz,  $\text{CDCl}_3$ , 298 K).

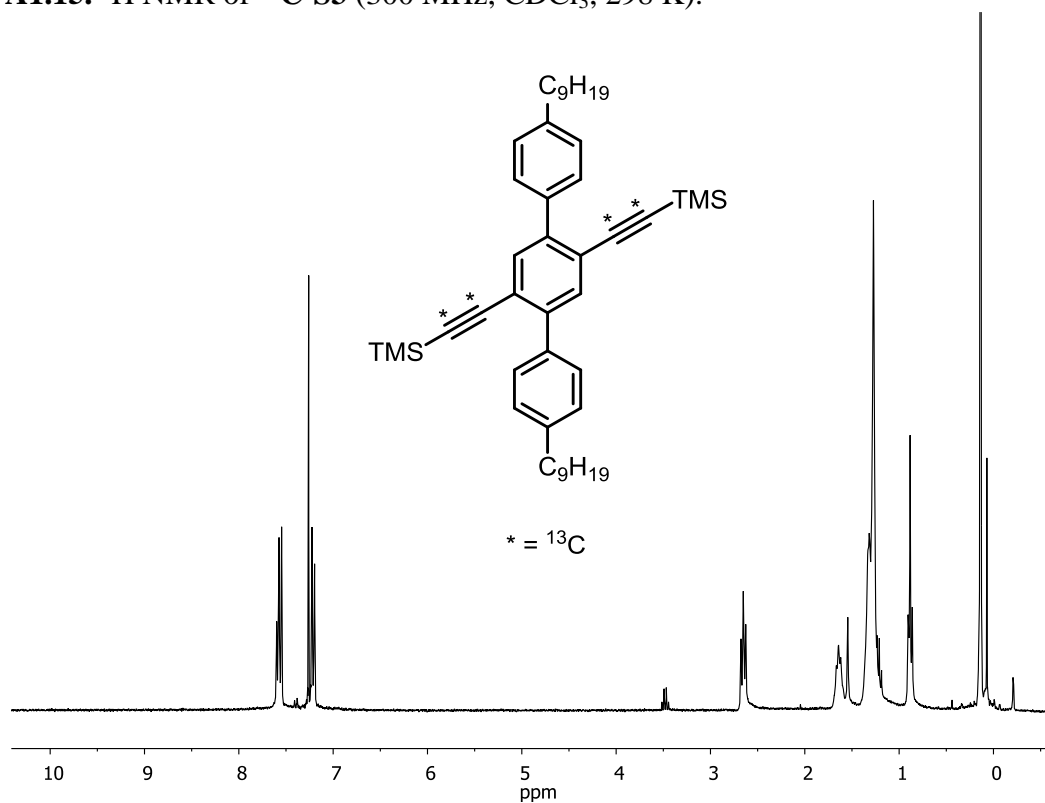


**Figure A1.16.**  $^{13}\text{C}$  NMR of  $^{13}\text{C}$ -S3 (100 MHz,  $\text{CDCl}_3$ , 298 K).

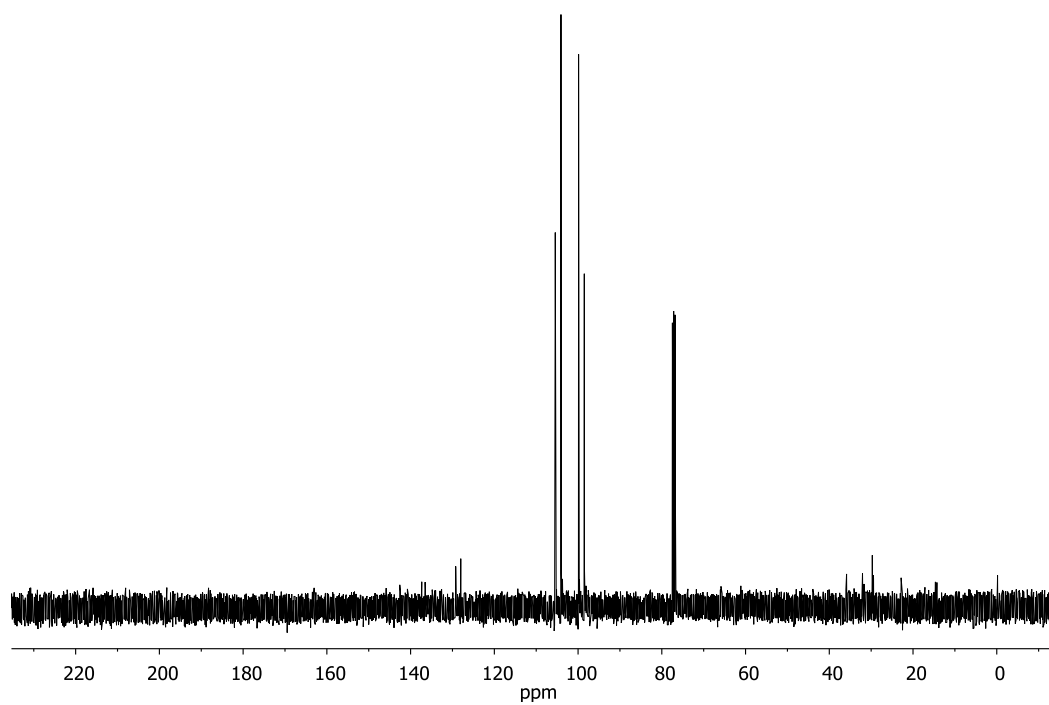


**Figure A1.17.**  $^1\text{H}$  NMR of  $^{13}\text{C}$ -S4 (400 MHz,  $\text{CDCl}_3$ , 298 K).

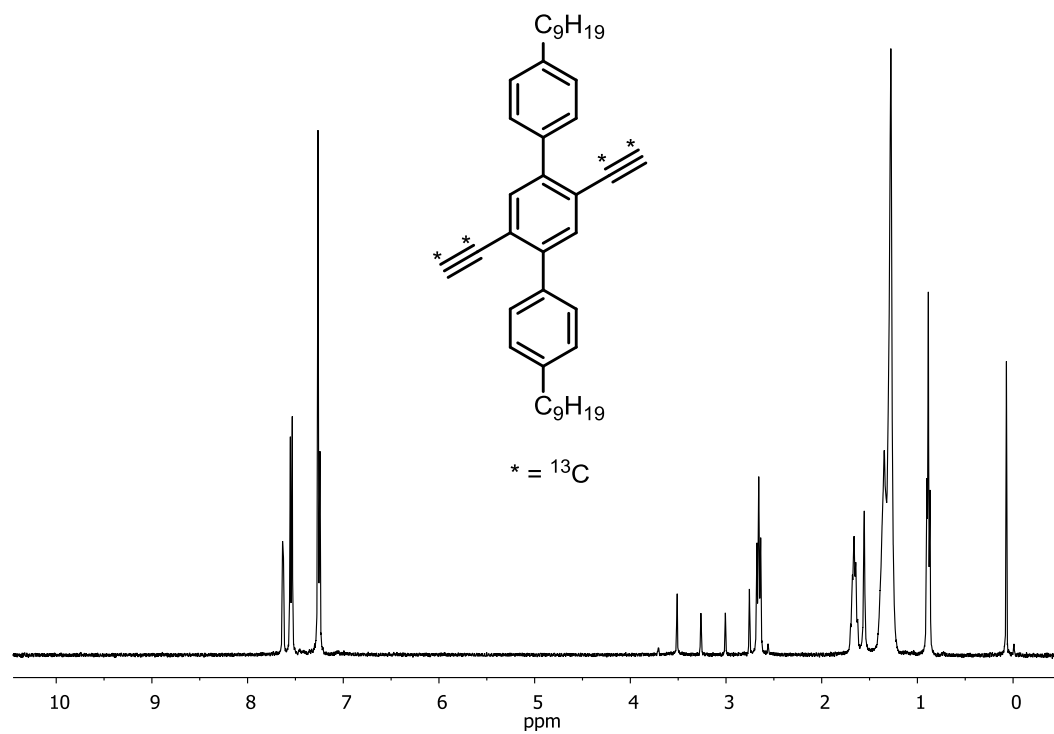


**Figure A1.18.**  $^{13}\text{C}$  NMR of  $^{13}\text{C}$ -S4 (100 MHz,  $\text{CDCl}_3$ , 298 K).

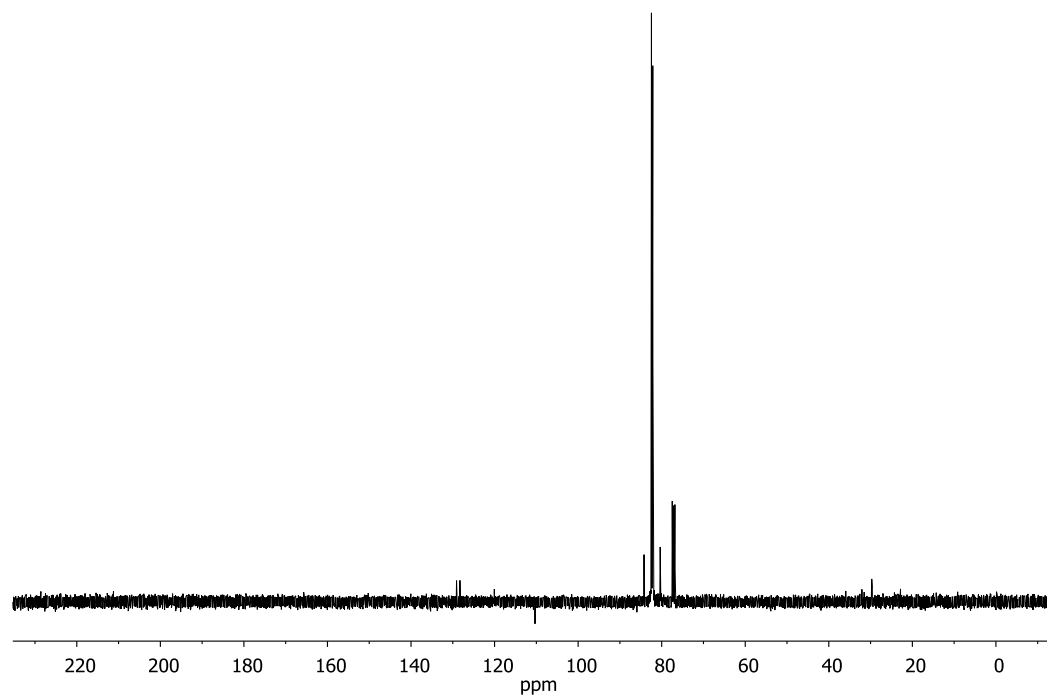


**Figure A1.19.**  $^1\text{H}$  NMR of  $^{13}\text{C}$ -1 (400 MHz,  $\text{CDCl}_3$ , 298 K).

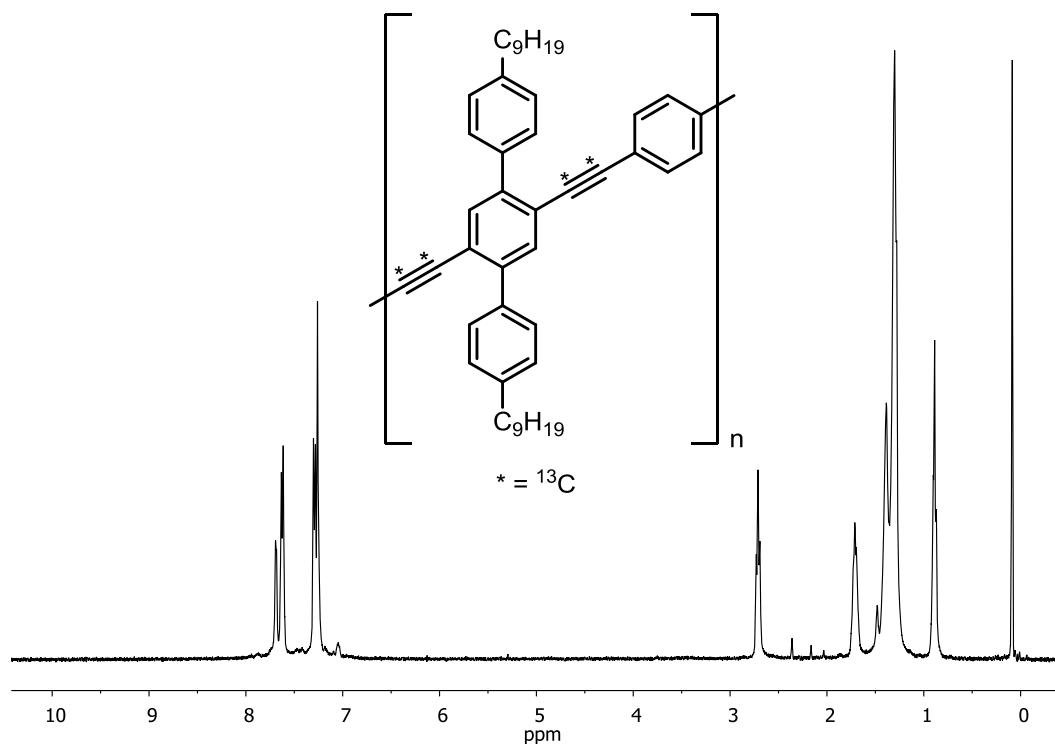


**Figure A1.20.**  $^{13}\text{C}$  NMR of  $^{13}\text{C}$ -1 (100 MHz,  $\text{CDCl}_3$ , 298 K).

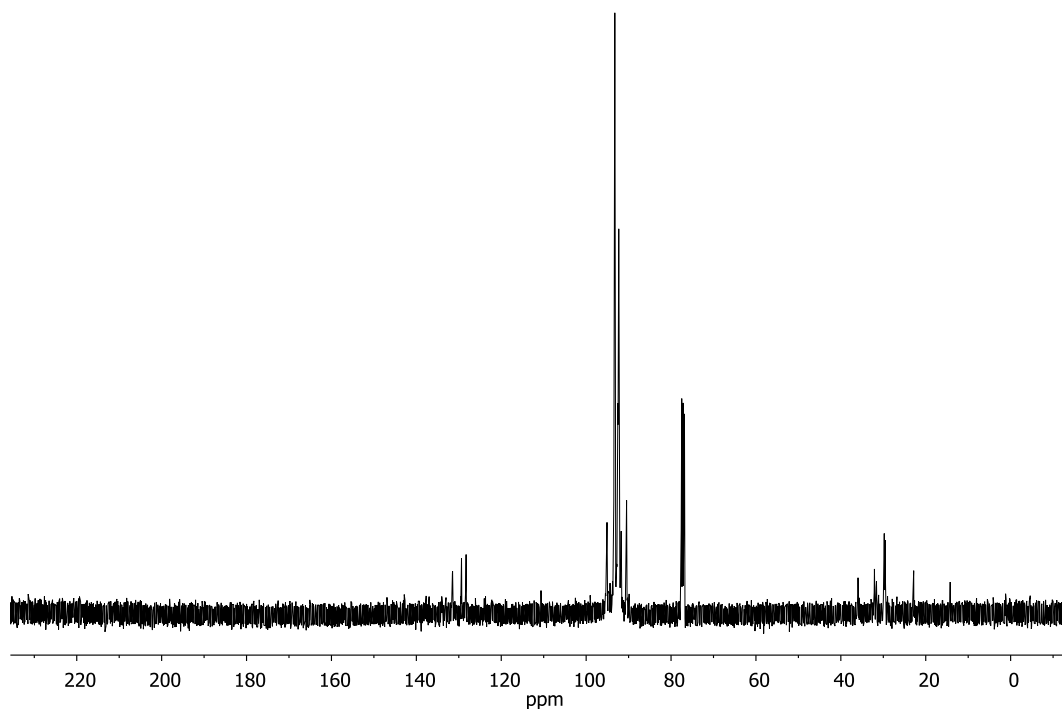


**Figure A1.21.**  $^1\text{H}$  NMR of  $^{13}\text{C}$ -3 (300 MHz,  $\text{CDCl}_3$ , 298 K).

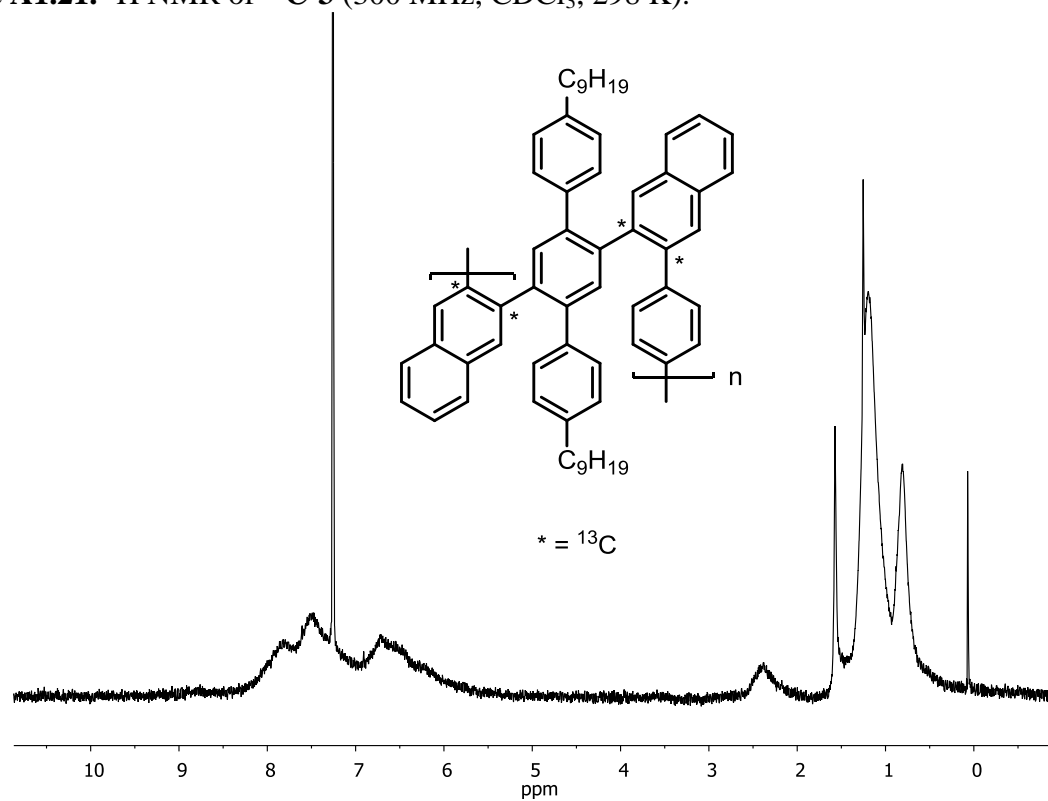


**Figure A1.22.**  $^{13}\text{C}$  NMR of  $^{13}\text{C}$ -3 (100 MHz,  $\text{CDCl}_3$ , 298 K).

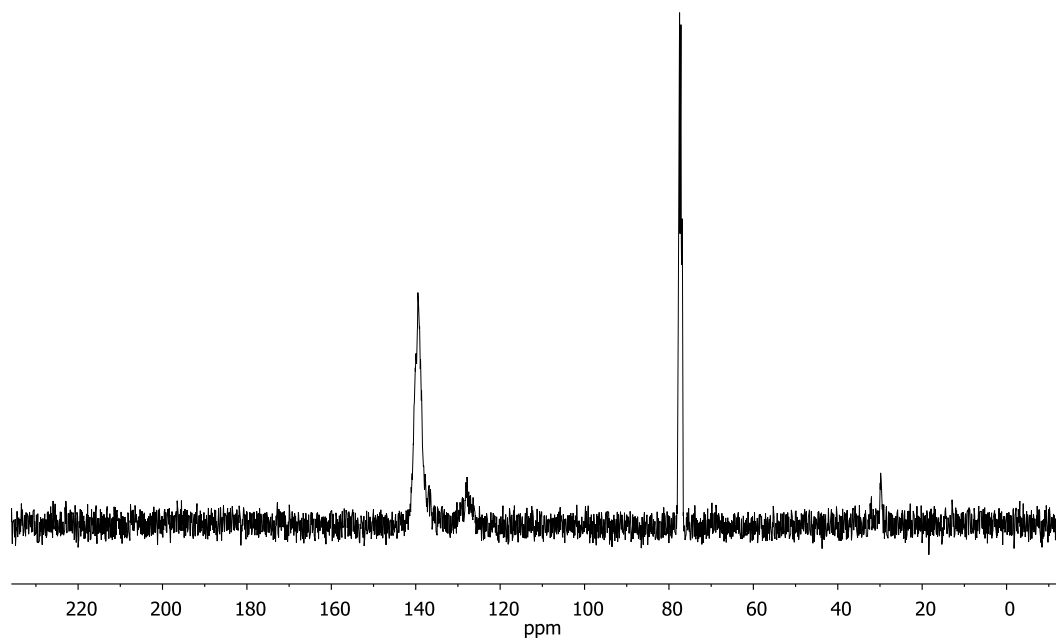


**Figure A1.23.** Comparison of the  $^{13}\text{C}$  NMR of  $^{13}\text{C}$ -**3** (100 MHz,  $\text{CDCl}_3$ , 298 K, blue trace) and **3** (75 MHz,  $\text{CDCl}_3$ , 298 K, red trace).

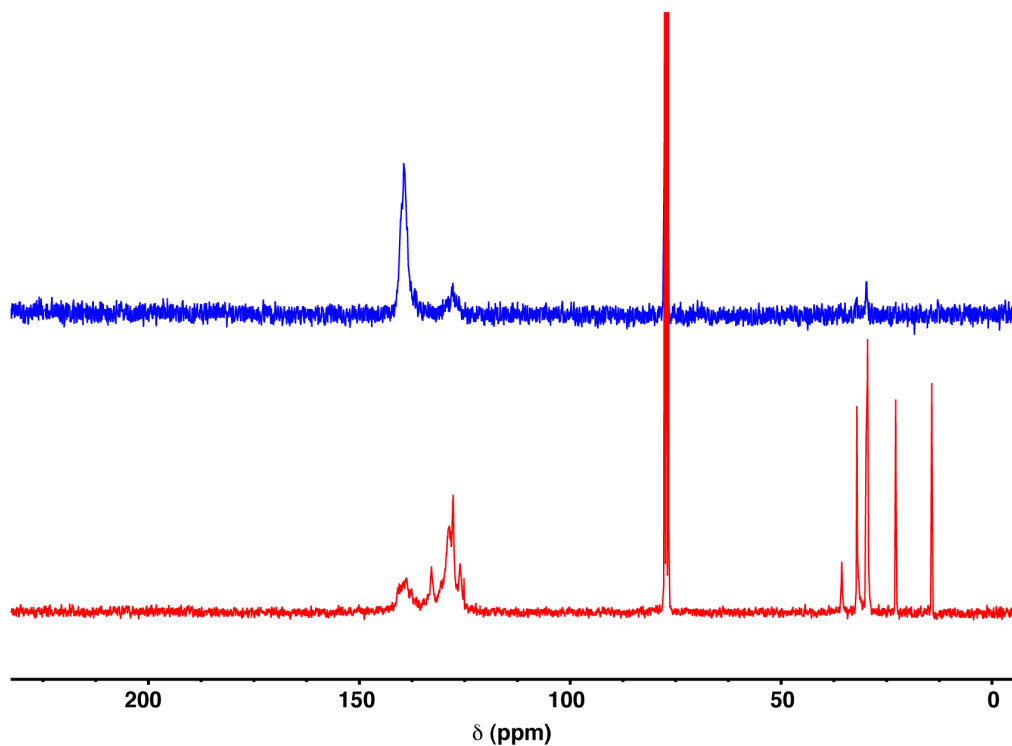


**Figure A1.24.** Partial  $^1\text{H}$  NMR of  $^{13}\text{C}$ -**3** (500 MHz,  $1,1,2,2\text{-C}_2\text{D}_2\text{Cl}_4$ ) at various temperatures.

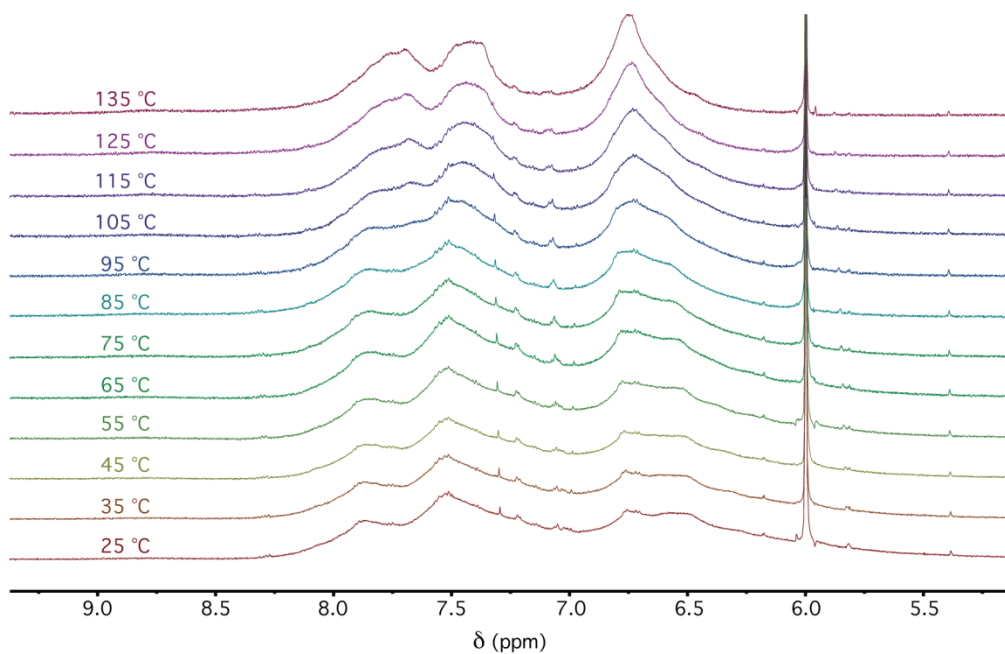


**Figure A1.25.** Partial  $^{13}\text{C}$  NMR of  $^{13}\text{C}$ -**3** (125 MHz, 1,1,2,2- $\text{C}_2\text{D}_2\text{Cl}_4$ ) at various temperatures.

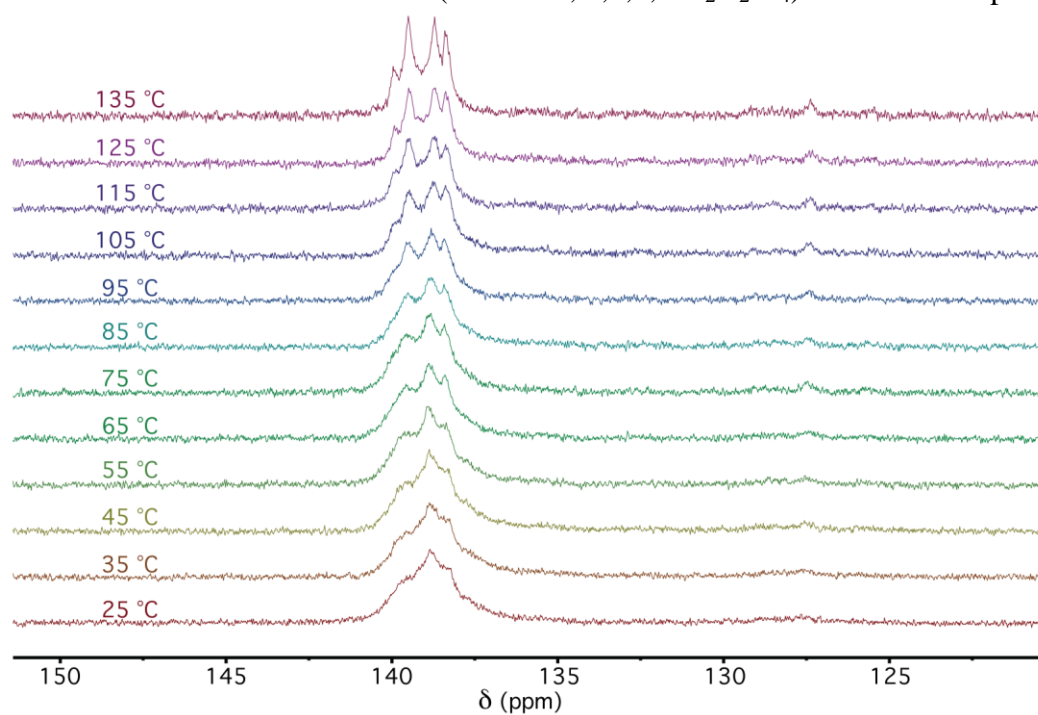
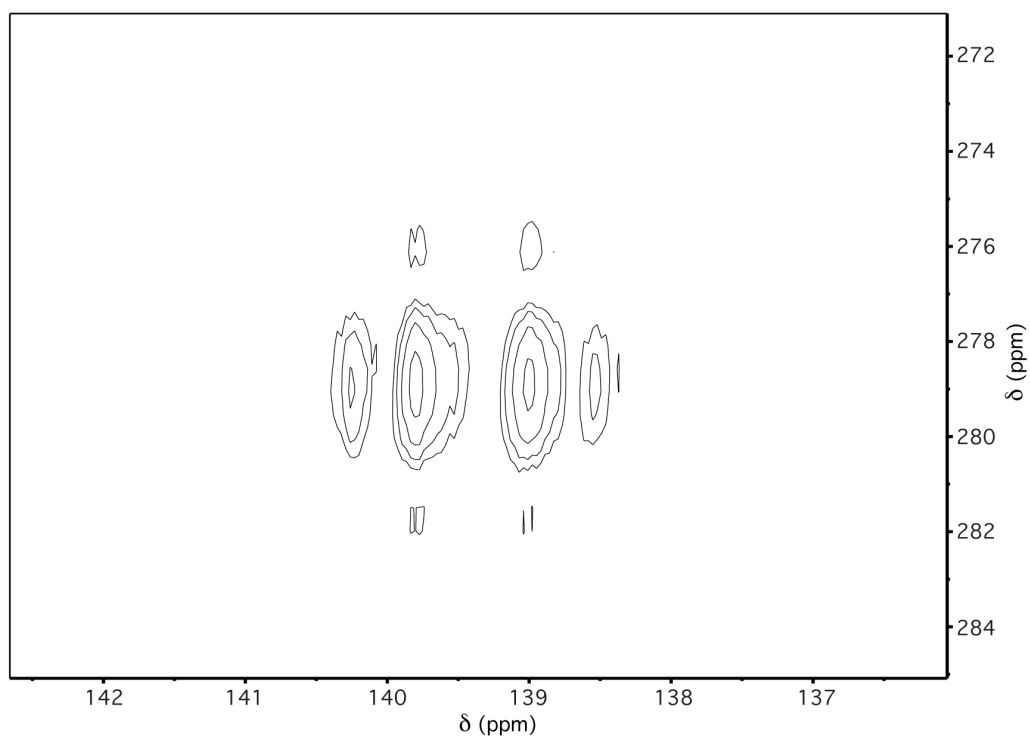


**Figure A1.26.** 2D-INADEQUATE spectrum of  $^{13}\text{C}$ -**3** (125 MHz, 1,1,2,2- $\text{C}_2\text{D}_2\text{Cl}_4$ , 408 K).





## D. IR Spectra

Figure A1.27. FTIR spectra of polymer 1 and polymer 3.

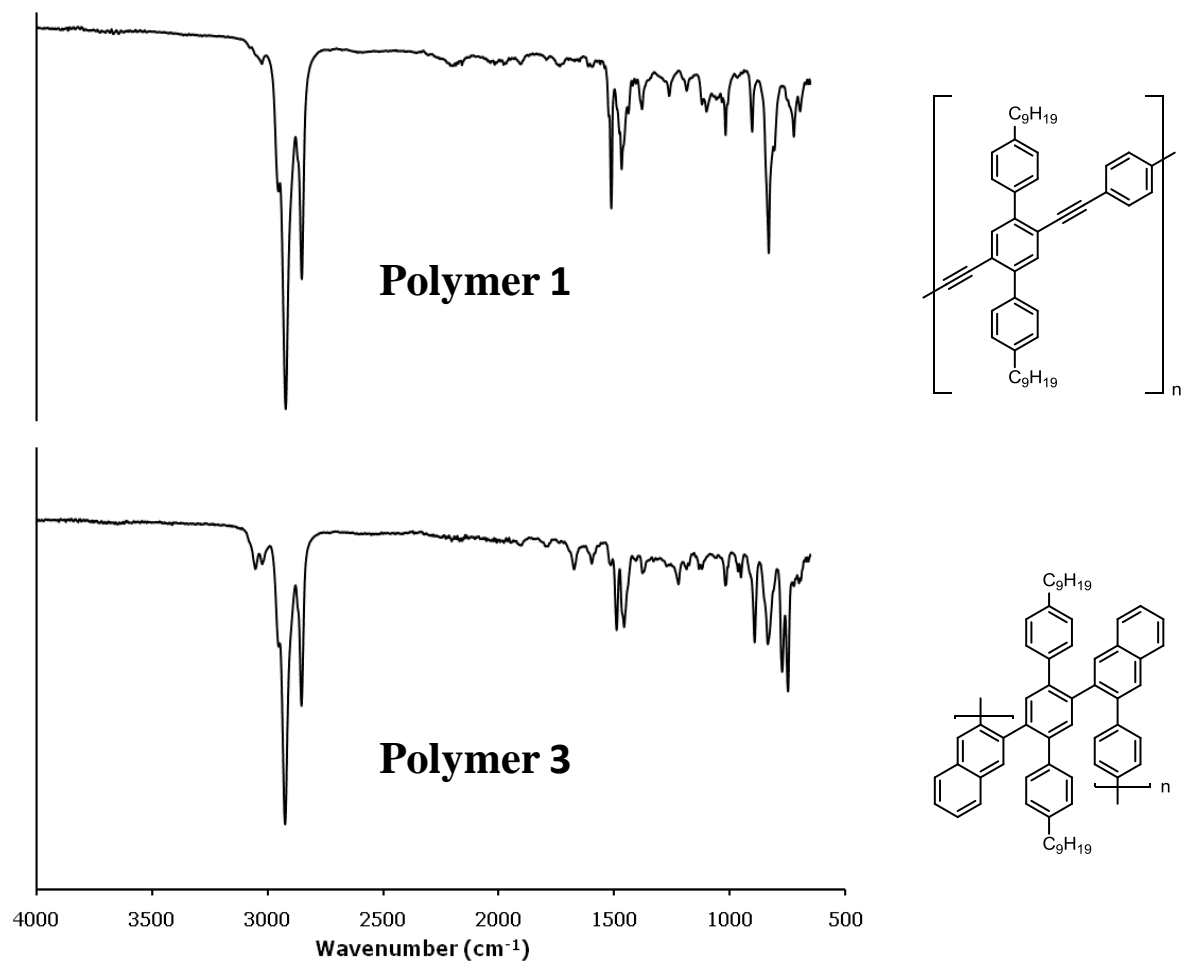
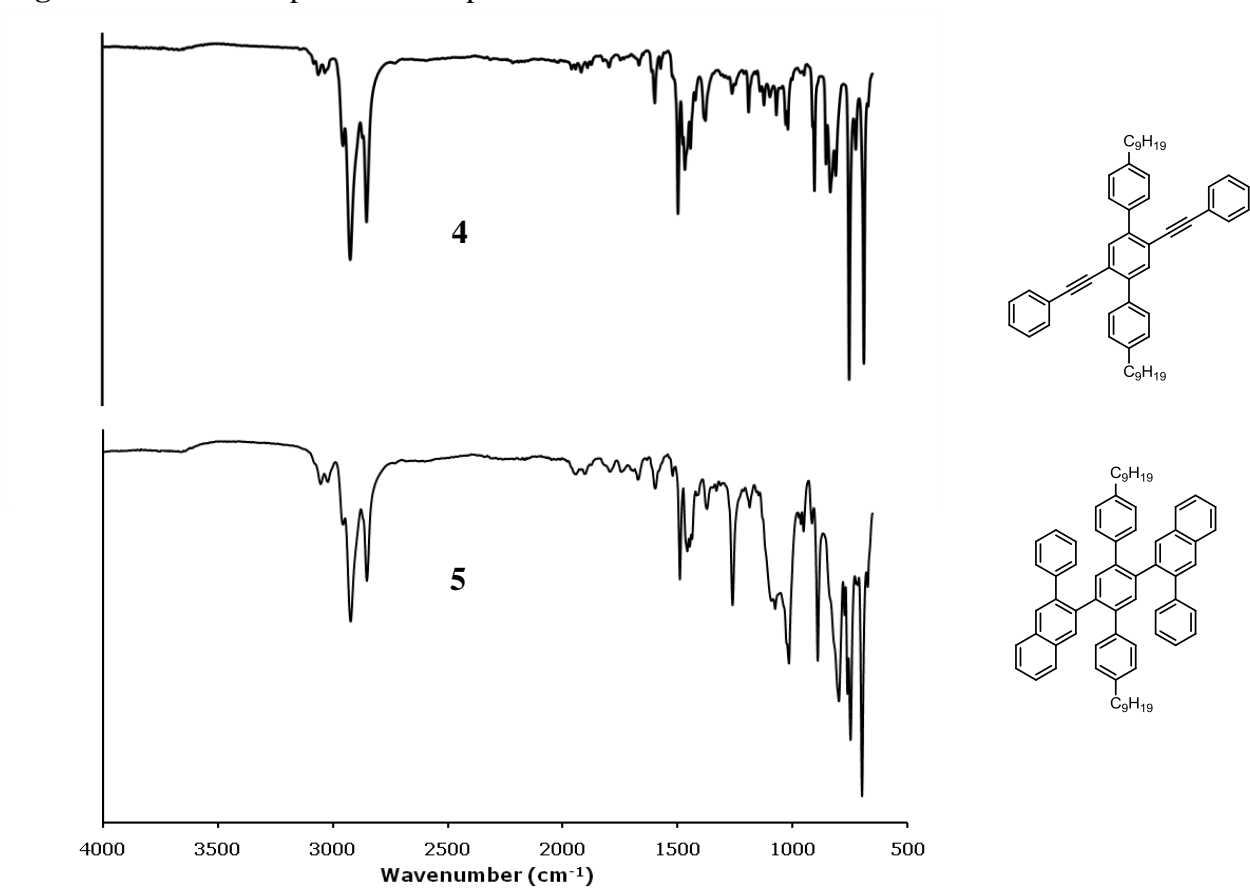


**Figure A1.28.** FTIR spectra of compounds **4** and **5**.



### E. Thermogravimetric Analysis

**Figure A1.29.** Thermogravimetric analysis of polymer 1.

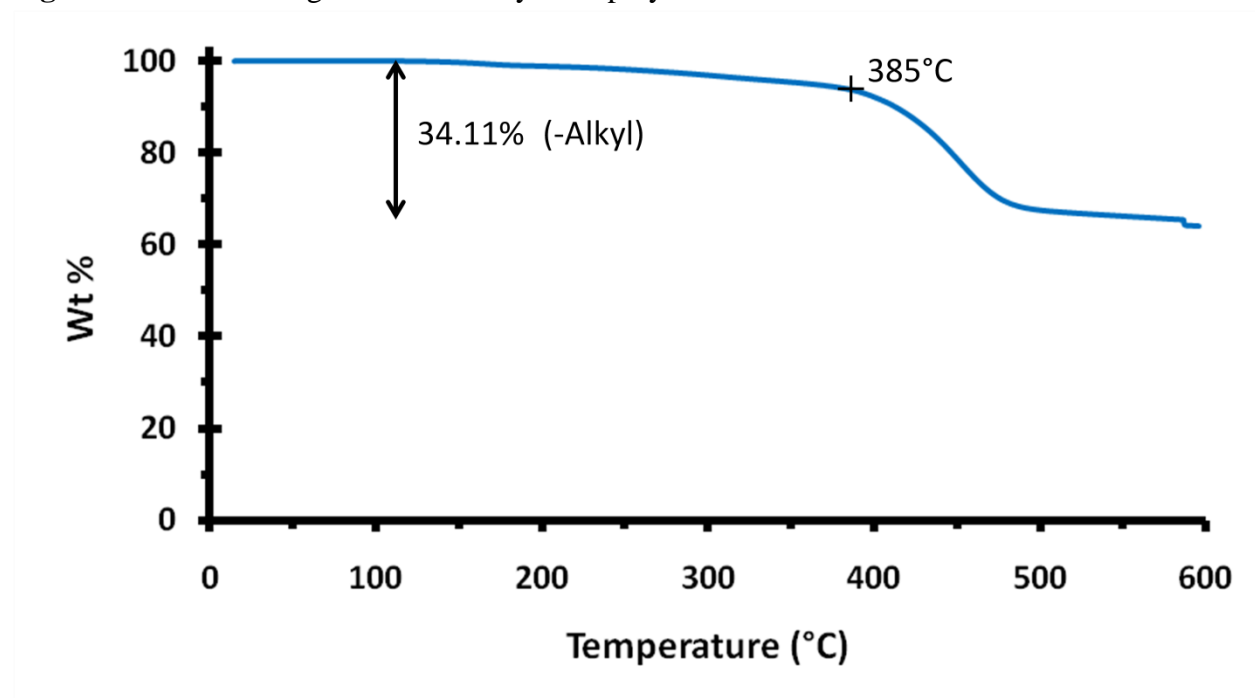
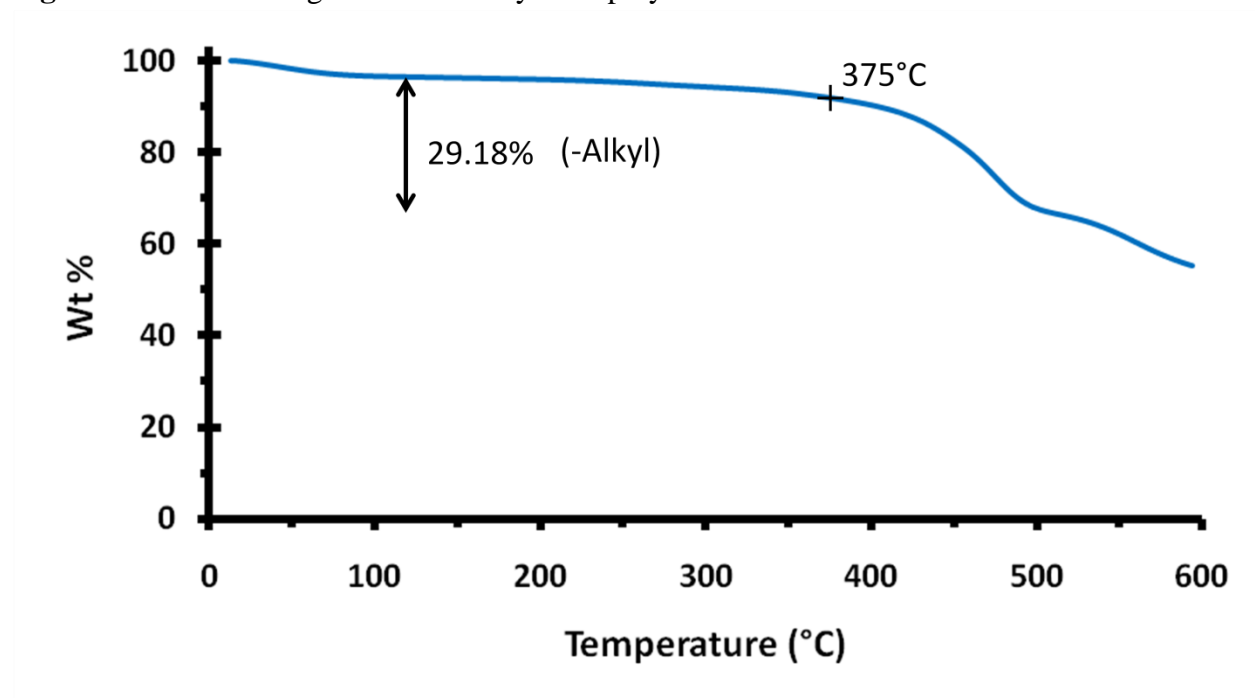


**Figure A1.30.** Thermogravimetric analysis of polymer 3.



## F. Polymer Molecular Weight Characterization

**Figure A1.31.** Size-exclusion chromatograms of polymer **1** (blue) and polymer **3** (red), as detected by their light-scattering intensity.

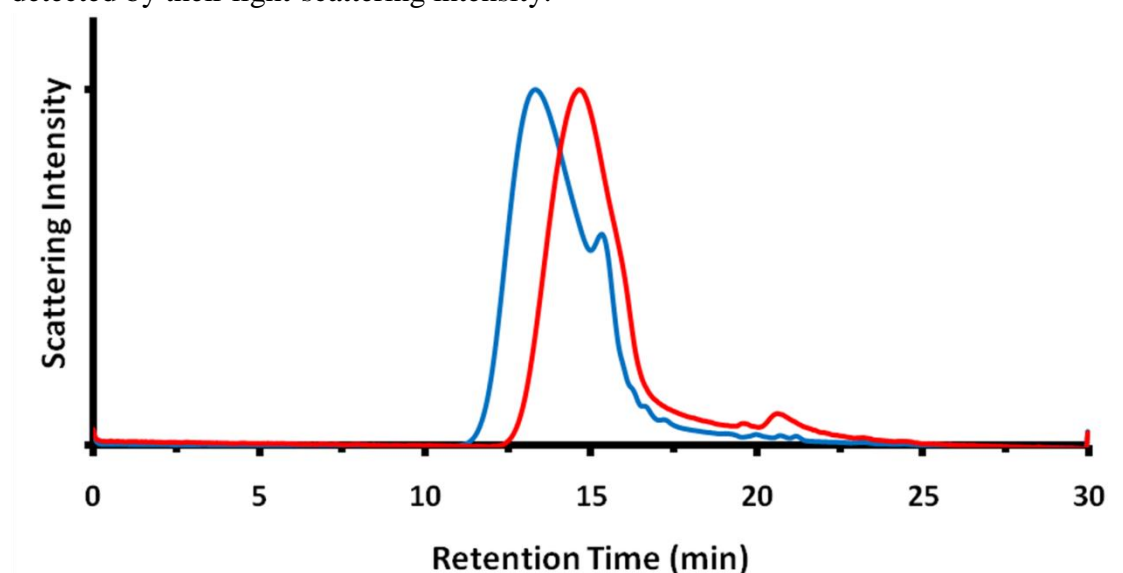


**Figure A1.32.** Size-exclusion chromatograms of polymer **1** (blue) and polymer **3** (red), as detected by changes in refractive index of the THF mobile phase.

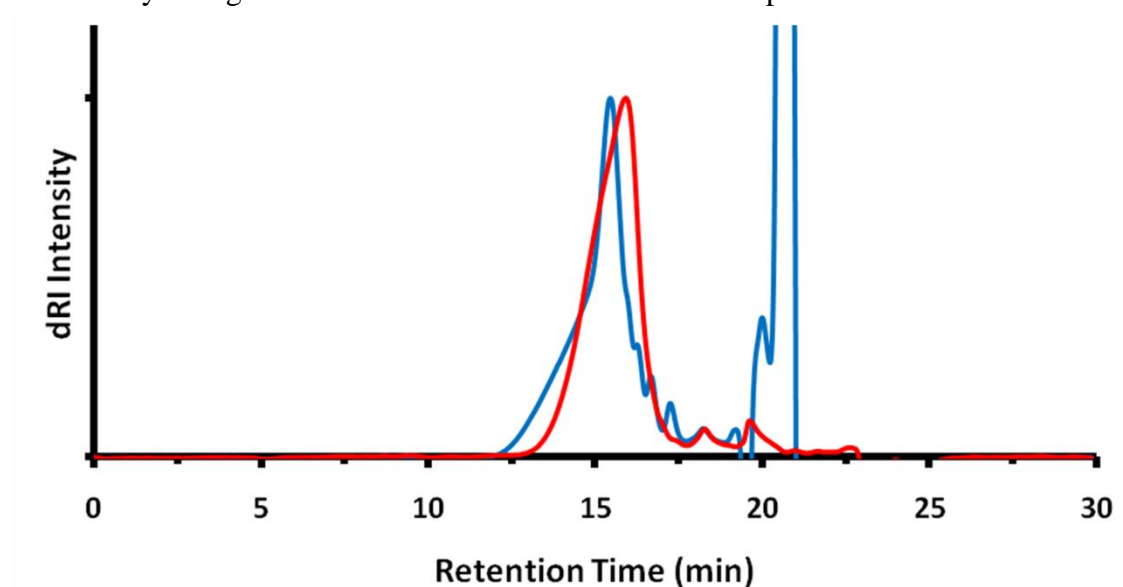


**Table A1.1.** Molecular Weight Determination of Polymers **1** and **3**.

	$M_n$ (kDa)	$M_w$ (kDa)	PDI	$dn/dc$ (mL/g)	$D_p$
Polymer <b>1</b>	7.85	27.7	3.53	0.265	12
Polymer <b>3</b>	39.6	65.3	1.65	0.130	49
$^{13}\text{C}$ -Polymer <b>1</b>	9.72	14.1	1.45	0.265	15

## G. Polyphenylene Simulations

The compact structure of **3** in an organic solvent was examined using a Molecular Dynamics (MD) simulation approach that provides an atomically explicit representation of the dynamics of the system under the influence of appropriately chosen inter- and intra- molecular forces. The LAMMPS software package was used for this purpose, with 10 Å non-bonded cutoffs and 1 fs time steps using a velocity-Verlet integrator.<sup>4</sup> The OPLS-AA forcefield was used for its simplicity and proven ability to depict the properties of organic liquids.<sup>5</sup> The pressure and temperature were set at 1 atm and 300 K, respectively, using Nosé-Hoover barostat and thermostat in an isobaric-isothermal (NPT) ensemble. The solvent “box” in the simulation contained 11,740 *ortho*-dichlorobenzene molecules (solvent) and one 24-unit **3** polymer. The box was equilibrated for 1 ns, sufficient to reach a steady-state volume of approximately 2230 nm<sup>3</sup>. Following equilibration, structural data for the polymer were collected every 0.2 ps for 3 ns.

The resulting structure of the polymer was highly contorted. We observed a large variety of individually different monomeric conformations, which, in total, led to a compact, albeit somewhat distorted, structure for the solvated polymer. We investigated eight different dihedral angles within the polymer that we determined to be primarily responsible for particular polymer conformations; these eight were examined to distinguish between different resultant conformers (Figure A1.33). Each dihedral angle was calculated and collected throughout the simulation. Preferred angles were found by locating peaks in histograms generated by the data; Gaussian distributions were fitted to each peak to estimate an average angle value as well as a standard deviation (Table A1.2). Default angles that generate the planar structure in Figure A1.33 are given as a point of reference. Most of the peaks deviated substantially from in-plane angles. There is also considerable spread, with some peaks overlapping (especially dihedrals 2 and 7). Each peak was identified with a letter to allow observations of overall monomer conformations. The more common monomer conformations were found by searching the structures for monomers identified by a distinctive 8-letter code signifying the eight angles in the neighborhood of specific peak angles. This analysis is complicated by overlap between peaks. As a consequence, a *range* of possible frequencies of occurrence are given. In Figure S34, the three most common conformations are shown as a 12-unit polyphenylene **3** with no side chains in order to make viewing easier. The relative compactness of each conformer can be compared by looking at their lengths; conformers 1, 2, and 3 have lengths of 7.0, 11.5, and 8.6 nm, respectively. It is apparent that the most common conformer 1 is far more compact than the relatively more planar conformer 2. Conformations such as those found in conformers 1 and 3 are probably responsible for **3**'s compact structure.

While the inherent limitations of MD effectively preclude a definitive sampling of the polymer's overall conformation, our simulations qualitatively demonstrate that steric congestion promotes the existence of highly compact, non-planar conformers. It also provides the locations of specific, favorable dihedral angles, with an estimated standard deviation. The large standard

deviations we observe suggest that there might be significant variability between two monomers of the same conformational type. In the future, more advanced simulation techniques, such as Replica Exchange could shed more quantitative evidence for the overall conformational behavior of the polyphenylene.<sup>6</sup>

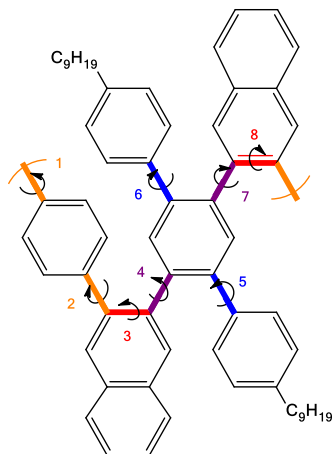


**Figure A1.33.** Numbered dihedrals were calculated to differentiate distinct conformers. Dihedrals of the same color would be expected to have the same angular preferences. The shown planar structure is the default starting position for the simulations.

**Table A1.2.** Common polyphenylene **3** Dihedral Monomers

Angle #	Default Angle	Mean Peak Angles $\pm$ Standard Deviation			
		A	B	C	D
1,2	0°	-157° $\pm$ 10°	-23° $\pm$ 12°	25° $\pm$ 10°	166° $\pm$ 11°
3,8	0°	-10° $\pm$ 9°	13° $\pm$ 9°		
4,7	180°	-127° $\pm$ 13°	-68° $\pm$ 20°	60° $\pm$ 9°	122° $\pm$ 13°
5,6	0° or 180°	-23° $\pm$ 9°	24° $\pm$ 9°		
		157° $\pm$ 9°	156° $\pm$ 9°		

\*Since rotations about the phenyl group associated with this dihedral are bilaterally symmetric, angles 180° away from each other are equivalent.

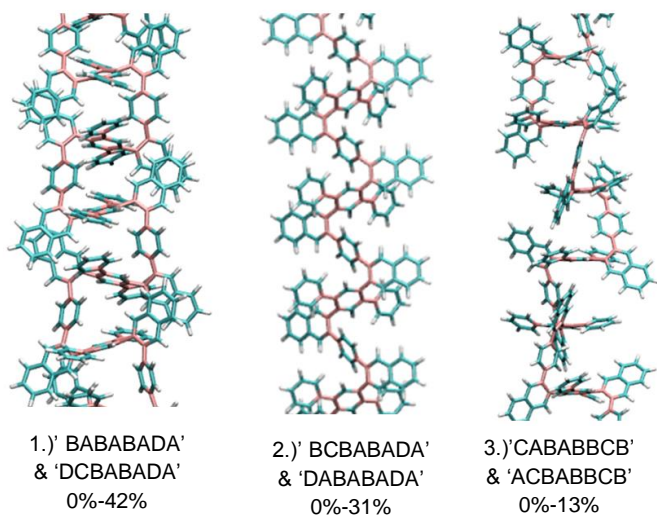


**Figure A1.34.** Illustration of the most common monomer conformations in the simulated polyphenylene **3**. Each conformer has two eight letter codes because each should give roughly equivalent structures due to symmetry. Carbons linking phenyl groups are shown in pink to assist viewing. The full 12 units of each polymer are not shown.

## H. References to Appendix

- (1) Hart, H.; Harada, K.; Du, C. J. F. *J. Org. Chem.* **1985**, *50*, 3104-3110.
- (2) Tovar, J. D.; Swager, T. M. *J. Organomet. Chem.* **2002**, *653*, 215-222.
- (3) Fairfax, D. J.; Austin, D. J.; Xu, S. L.; Padwa, A. *J. Chem. Soc., Perkin Trans. 1* **1992**, 2837-2844.
- (4) Plimpton, S. *J. Comp. Phys.* **1995**, *117*, 1-19.
- (5) Jorgensen, W. L.; Maxwell, D. S.; Tirado-Rives, J. *J. Am. Chem. Soc.* **1996**, *118*, 11225-11236.
- (6) Earl, D. J.; Deem, M. W. *PCCP* **2005**, *7*, 3910-3916.



## CHAPTER THREE

### ACCESSING EXTENDED AND PARTIALLY FUSED HEXABENZOCORONENES USING A BENZANNULATION / CYCLODEHYDROGENATION APPROACH

#### 3.1 *Abstract*

A rapid and efficient approach to prepare extended or partially fused hexabenzocoronene derivatives is described. The method is based on the sequential benzannulation and cyclodehydrogenation (Scholl oxidation) of simple diaryl alkynes. The benzannulation reaction proceeds efficiently on highly congested substrates and with complete regioselectivity. Scholl oxidation of the resulting oligo(arylene)s proceeds without rearrangements and provides either fully fused or specific partially fused polycyclic aromatic hydrocarbon products. The partially fused derivatives are a new class of contorted aromatic systems with high solubility, enhanced visible absorption, and reversible redox processes. The efficiency and specificity of the benzannulation and oxidation reactions are promising for accessing new classes of organic semiconductors and carbon nanostructures. The work in this chapter was previously published in *Chemical Science* ([Arslan, H.; Uribe-Romo, F. J.; Smith, B. J.; Dichtel, W. R. *Chemical Science* **2013**, 4, 3973.] - Reproduced by permission of The Royal Society of Chemistry)

#### 3.2 *Introduction*

Extended polycyclic aromatic hydrocarbons (PAHs),<sup>1-4</sup> such as the hexabenzocoronenes (HBCs), are functional  $\pi$ -electron systems whose desirable optical and electronic properties have attracted interest for organic thin film transistor (OTFT)<sup>5-7</sup> and organic photovoltaic (OPV) devices.<sup>8, 9</sup> The device properties of specific PAHs depend both on their electronic structure and packing behaviour. The nature of these assemblies is influenced by molecular shape, the position and

identity of solubilizing groups, molecule-substrate interactions, and processing methods used to form thin films. For example, Müllen and coworkers have made major contributions to both the synthesis of novel HBC derivatives and their solid-state organization.<sup>10-12</sup> Other instructive examples of the interplay between HBC structure and long-range order that produce emergent properties include nanotubes derived from amphiphilic HBCs studied by Aida<sup>13-15</sup> and contorted HBCs studied by Nuckolls<sup>16-25</sup> and Miao<sup>26</sup> for OTFTs and OPVs.

Efficient and convergent syntheses of HBCs with novel substitution patterns, extended conjugation, or nonplanar structures will allow their full potential to be realized. Less symmetric substitution patterns, such as those of interest for amphiphilic derivatives, can require laborious syntheses, while introducing additional fused rings confers lower HOMO-LUMO gaps and can induce curvature. Here we introduce a new strategy to access HBC derivatives by benzannulating readily accessible diarylalkynes. We recently demonstrated the high efficiency of this transformation to convert the alkyne functions of a poly(phenylene ethynylene) (PPE) into 2,3-diarylnaphthalene moieties.<sup>27</sup> The reaction tolerates aryl substituents adjacent to the alkynes, a promising feature for PAH synthesis provided that the resulting oligoarylenes can be cyclodehydrogenated efficiently and without rearrangements.

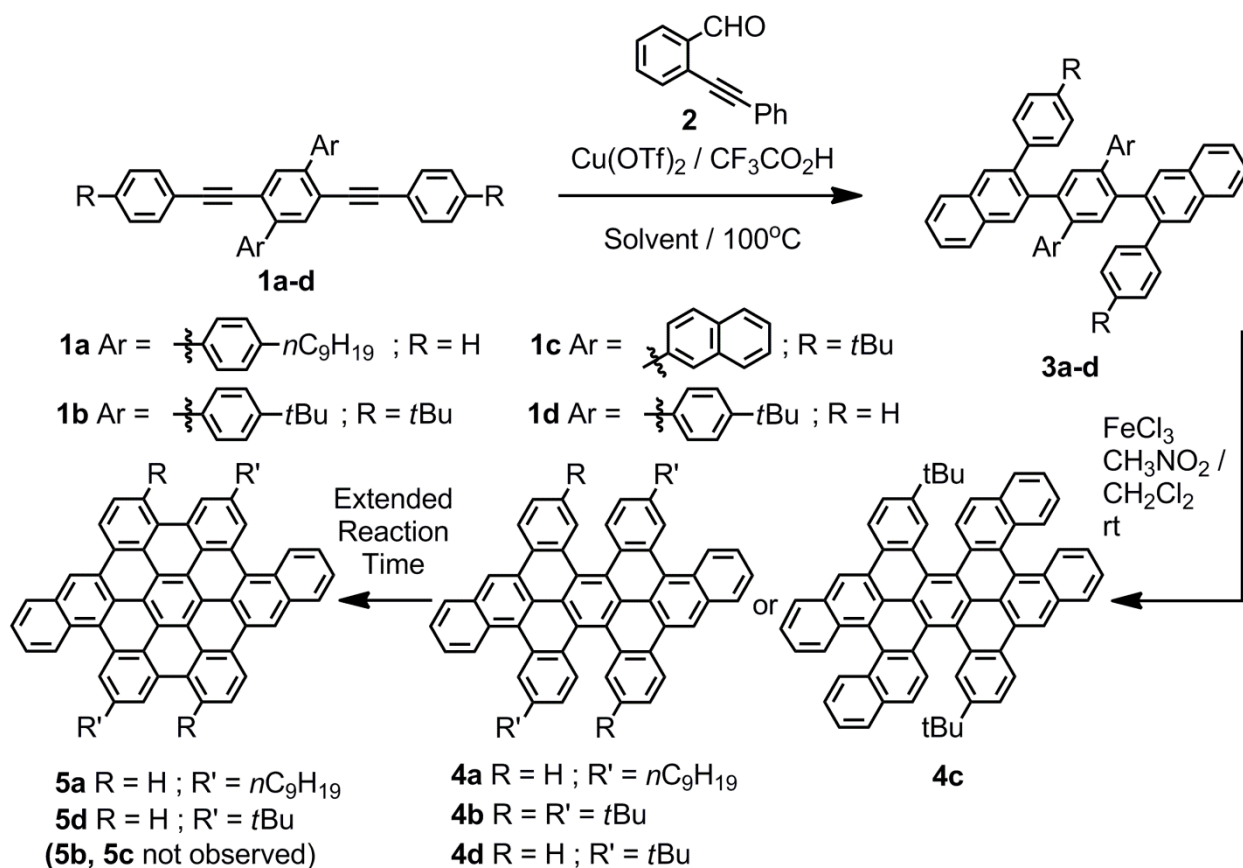


**Figure 3.1.** A series of dialkyne compounds **1a-d** provide partially fused HBC derivatives **4a-d** and fully fused products **5a** and **5d** using a two-step benzannulation/cyclodehydrogenation protocol.

### 3.3 Design and Synthesis of PAHs

Substituted diarylalkyne derivatives **1a-d** are ideal substrates to evaluate the benzannulation/cyclodehydrogenation approach for PAH synthesis (Figure 3.1). This strategy provides HBC derivatives with extended conjugation and complementary substitution patterns relative to existing methods. Here we show that the benzannulation reaction is efficient for several HBC precursors and that typical Scholl oxidation conditions do not induce rearrangements. In some cases, complete cyclodehydrogenation is achieved; however, shorter reaction times or strategically placed substituents provide partially fused products. When complete oxidation does not occur, the order of carbon-carbon bond formation is well defined,

providing specific, non-planar coronene derivatives **4a-c** that exhibit high solubility, strong visible absorption, and reversible redox processes. Collectively, these molecular compounds also represent important model systems for oxidizing benzannulated PPEs to produce structurally precise graphene nanoribbons, and their lack of rearrangements show great promise in this regard.

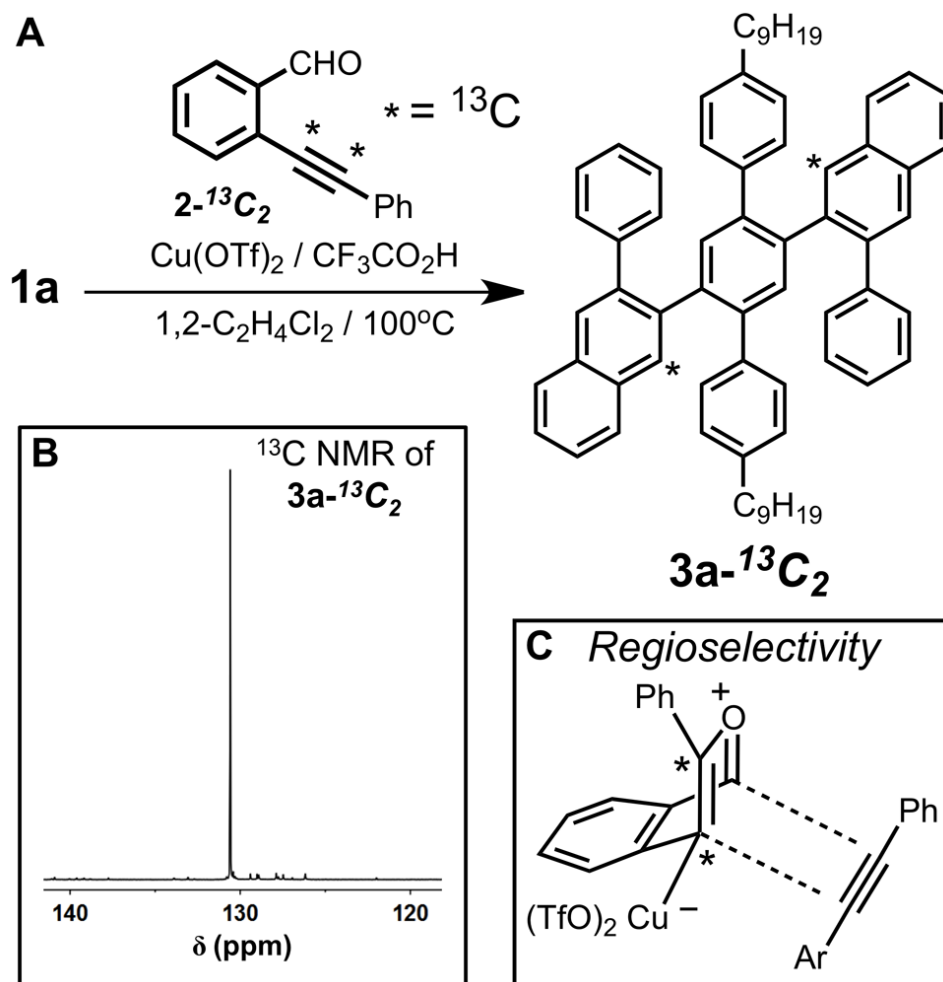


**Figure 3.2.** **A.** The benzannulation of **1a** with  $2\text{-}^{13}\text{C}_2$  provides the labelled derivative **3a- $^{13}\text{C}_2$** , indicating that the reaction is regioselective. **B.** Partial  $^{13}\text{C}$  NMR of **3a- $^{13}\text{C}_2$** . **C.** Regiochemistry of the benzannulation reaction consistent with this experiment.

We evaluated the generality and efficiency of the benzannulation reaction across several substituted di(arylethynyl)benzene derivatives. The di(*n*-nonyl)terphenyl compound **1a** is a molecular analogue of the repeat unit of our previously reported PPE system<sup>27</sup> that was

benzannulated in the presence of 2-(phenylethynyl)benzaldehyde, Cu(OTf)<sub>2</sub>, and CF<sub>3</sub>CO<sub>2</sub>H in DCE at 80 °C. These conditions provide the oligoarylene **3a** in 98% isolated yield. We also evaluated dialkynes **1b** and **1c**, which have four and two peripheral *t*-butyl substituents, respectively. The *t*Bu groups serve three primary functions: 1) they are effective solubilizing groups for PAHs; 2) they are convenient and sensitive NMR handles for rapidly diagnosing side reactions and rearrangements; and 3) oxidation of *t*Bu-substituted substrates often do not fuse completely because of steric hindrance.<sup>28</sup> Such partially oxidized products offer unique properties associated with their non-planar structures as well as insight into the sequence of C-C bond forming steps of fully fused systems. Finally, we evaluated compound **1d**, which has 2-naphthyl groups as central aryl substituents. This compound provides access to larger fused aromatic systems and serves as a model for a benzannulated polymer that might provide a graphene nanoribbon with an armchair edge structure. Dialkynes **1b-1d** were each benzannulated in similarly high efficiency based on analysis of their crude reaction mixtures.

We also benzannulated **1a** with isotopically labelled benzaldehyde **2-<sup>13</sup>C<sub>2</sub>** (Figure 3.2). The resulting benzannulated product **3a-<sup>13</sup>C<sub>2</sub>** contained one isotopic label per reactive site, as determined by mass spectroscopy, <sup>13</sup>C NMR spectroscopy (Figure 3.2b), and a full complement of 2D NMR spectroscopy experiments (Figure A2.26 and A2.46– A2.53 in the Appendix). The incorporation of a single isotopic label at these positions is consistent with Yamamoto's proposed mechanism<sup>29</sup> with the regioselectivity indicated in Figure 3.2c, while the other <sup>13</sup>C label is eliminated upon aromatization of the newly formed naphthalene. This regioselectivity might derive from the formal [4+2] cycloaddition occurring in a stepwise manner, in which the first new carbon-carbon σ bond is formed between the less hindered alkyne carbon and the oxonium carbon of the benzopyrilium intermediate. The regioselectivity of the benzannulation

reaction, combined with isotopic labelling, offer a powerful means to characterize Scholl oxidation products. These findings also suggest that non-symmetric derivatives of **2** will provide PAHs with specifically placed substituents.

### 3.4 *Cyclodehydrogenation Kinetics and Pathways of Scholl Reaction*

Dinonyl derivative **3a** was cyclodehydrogenated using FeCl<sub>3</sub>. MALDI-TOF mass spectrum of the reaction mixture after 1 h indicated a loss of 12 amu, corresponding to the formation of 6 C-C bonds and complete fusion of the coronene core. Although <sup>1</sup>H and <sup>13</sup>C NMR spectroscopy of **5a** were consistent with the expected structure, the low solubility and propensity of this compound to aggregate complicated its definitive structural characterization. Furthermore, King *et al.* noted rearrangements in a closely related system that had been misassigned in the literature for many years (Figure 3.3).<sup>30</sup> Therefore, we prepared several additional model compounds that would exhibit improved solubility to enable unambiguous characterization of the fused PAHs. These model systems incorporate 4'-*t*Buphenyl substituents, as well as variations of the central arylene group.

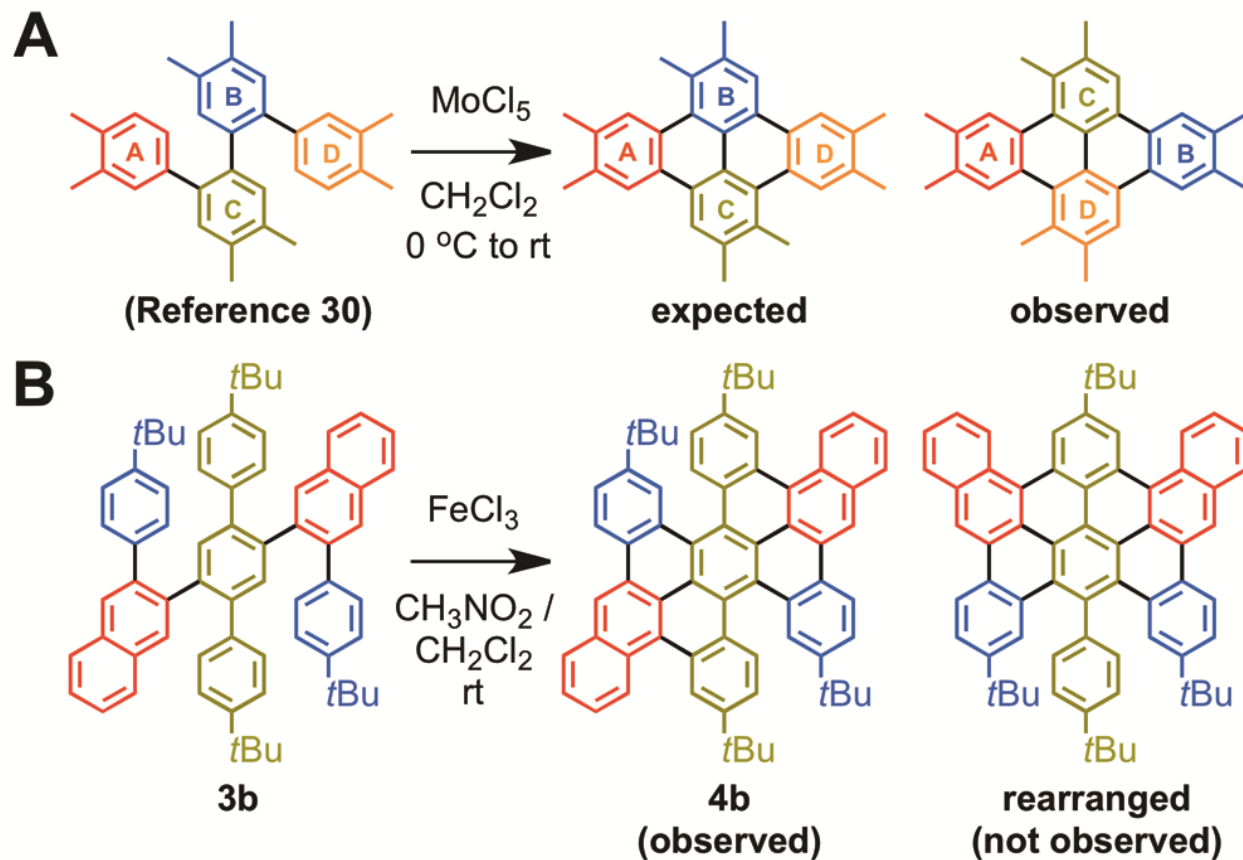


**Figure 3.3** A. Rearrangement during the Scholl oxidation observed by King *et al.*<sup>30</sup> B. The expected (observed) and possible rearranged (not observed) products for the oxidation of **3b**.

In order to investigate the possibility of rearrangements during the oxidation, we subjected **3b** to the same Scholl oxidations conditions. By incorporating the *t*Bu groups on the central terphenyl and external phenyl groups, **3b** does not fuse completely. MALDI-TOF MS indicated a reduction in mass of 8 amu, corresponding to the formation of four of the six expected C-C bonds. The  $^1\text{H}$  NMR spectrum of **4b** provides unambiguous evidence that 1,2-aryne rearrangements observed in other systems do not occur (Figure 3.4). For example, two singlets corresponding to *t*Bu resonances are observed at 1.46 and 1.25 ppm, respectively, which integrate to a 1:1 ratio. The analogous rearrangement to that reported by King and coworkers would instead provide a compound with three *t*Bu resonances in a 1:2:1 integration ratio (Figure 3.3b). The aromatic region of the  $^1\text{H}$  NMR spectrum of **4b** indicates the formation of the non-

rearranged but partially fused structure depicted in Figure 3.4. Eleven aromatic

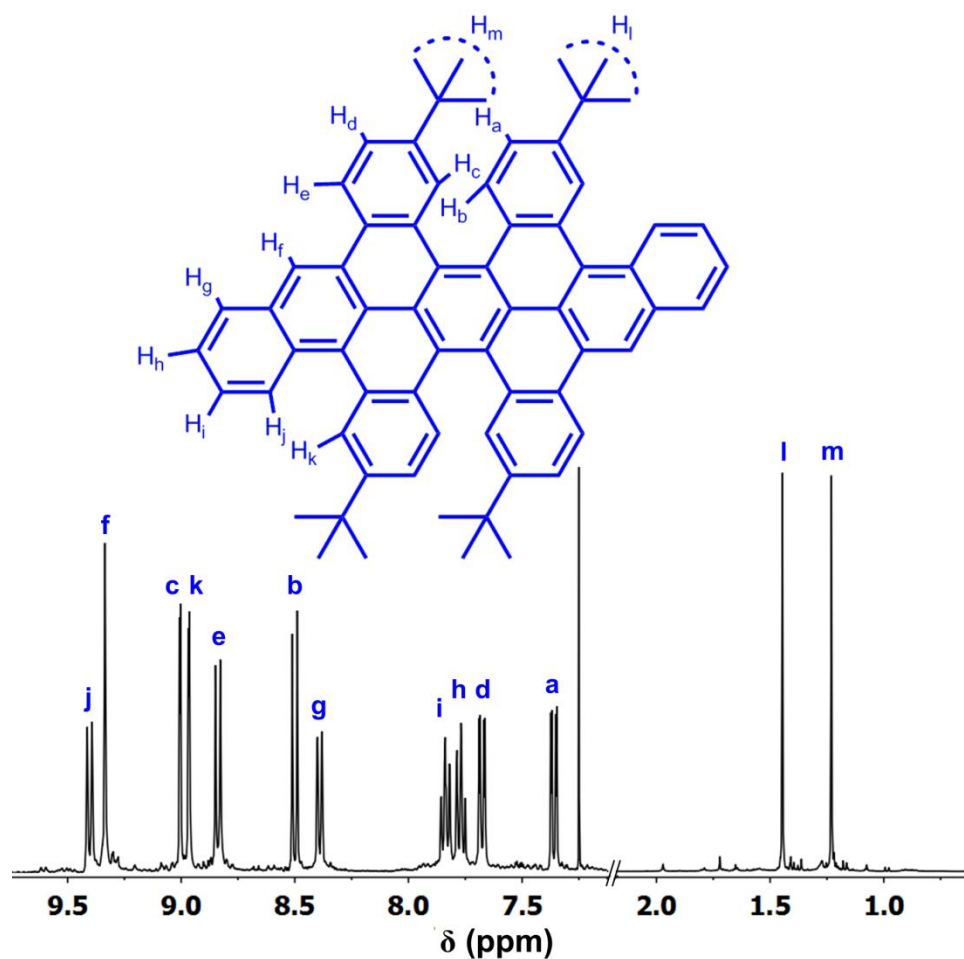


**Figure 3.4.** Partial  $^1\text{H}$  NMR spectrum of the aromatic and *t*Bu regions of **4b**.

resonances are observed, rather than nine expected for the fully fused compound. A complete assignment of the spectrum using complementary 2D NMR experiments (COSY, ROESY, HSQC and HMBC; see section D in the Appendix Two) indicates that C-C bonds between the *t*Bu functionalized aromatic rings do not form. We hypothesize that steric hindrance associated with these groups causes distortions from planarity that prevent these final two C-C bonds from forming. The ROESY spectrum of **4b** is consistent with this hypothesis, as clear cross peaks are observed between  $\text{H}_c$  and  $\text{H}_b$  (7 bonds apart) and  $\text{H}_j$  and  $\text{H}_k$  (6 bonds apart) in addition to those



between adjacent hydrogen atoms on the periphery. A derivative that contains central 2-naphthyl substituents (**3c**), also partially fuses under the oxidation conditions. MALDI-TOF MS indicated the formation of four C-C bonds. The regiochemistry of bond formation was unambiguously characterized by NMR spectroscopy. Interestingly, only one C-C bond was formed between each pair of adjacent naphthalene systems, which we also attribute to steric interactions associated with the *t*Bu groups.

We next analyzed the reaction mixtures of various Scholl oxidations as a function of reaction time and gained insight into the order and relative rates of C-C bond formation within these benzannulated compounds. We first characterized the oxidation of compound **3d**, which retains the two 4-*t*Bu phenyl substituents on the central aromatic ring but lacks the external *t*Bu groups of compound **3b**. Prior to FeCl<sub>3</sub> addition, **3d** exhibits an isotopically resolved MALDI-TOF mass spectrum corresponding to its expected mass (Figure 3.5, *t* = 0). A spectrum of the reaction mixture recorded 20 min after adding the oxidant exhibits its most intense peak eight mass units lower, corresponding to the formation of four new C-C bonds. No peaks are observed for species of intermediate mass between **3d** and this partially fused intermediate, and low intensity signals 1–4 amu lower than the main peak correspond to further fused products. At 60 min, these peaks increase in intensity, and the mass spectrum indicates essentially complete formation of **5d** at 240 min. By analogy to **4b**, in which the final two C-C bonds do not form even at extended reaction times, we hypothesized that the four C-C bonds formed rapidly in **4d** correspond to those present in **4b**. This hypothesis is further supported by a similar study of the oxidation of the di-*n*-nonyl functionalized compound **3a**. MALDI-TOF MS of the oxidation of **3a** at *t* = 5 min also indicated formation of an intermediate oxidation product

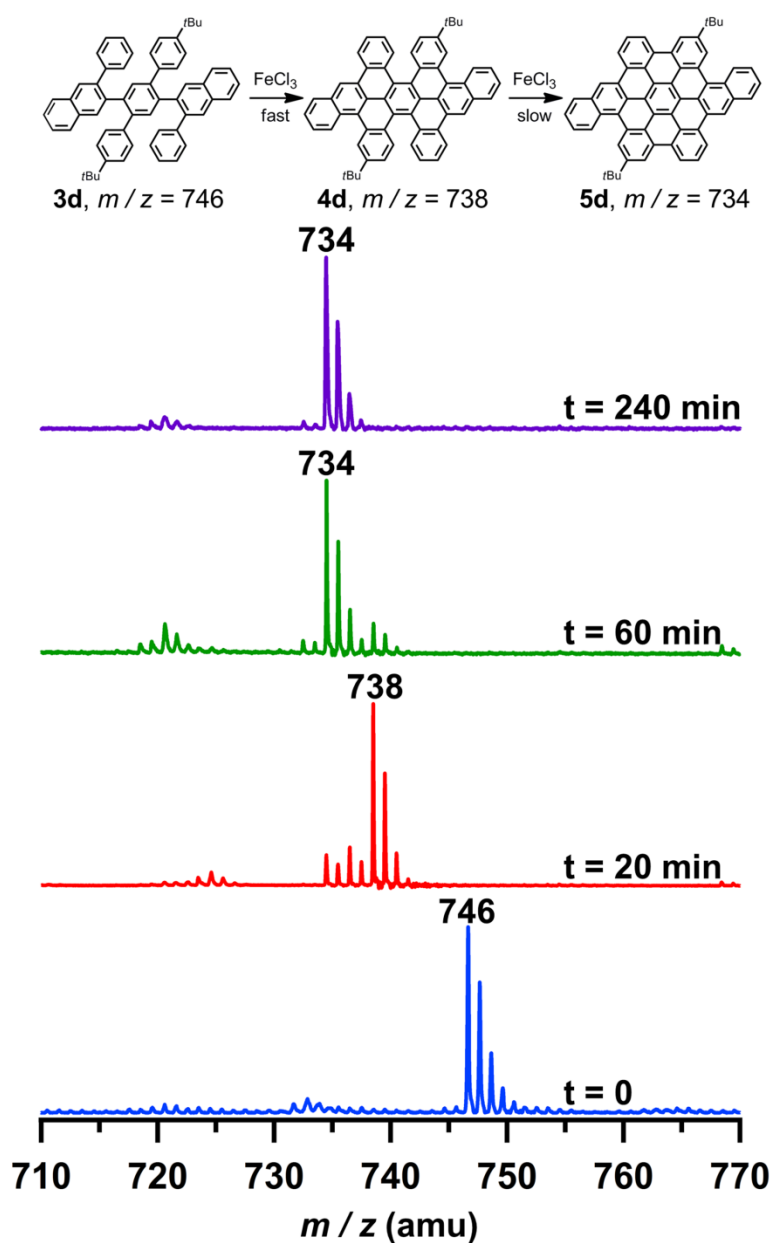


**Figure 3.5.** MALDI-TOF MS spectra taken of the oxidation of **3d** as a function of reaction time. Four carbon-carbon bonds are formed in fewer than 20 minutes, while full oxidation occurs after longer reaction times.

containing the first four C-C bonds, followed by complete oxidation at longer reaction times. We stopped a preparative scale oxidation of **3a** after 5 min and isolated the partially oxidized product, which was highly soluble in many organic solvents.  $^1\text{H}$  NMR analysis indicated twelve resolved aromatic resonances consistent with the structure **4a** (Sections C and D in the

Appendix). Interestingly, partial fusion of a related *o*-phenylene containing systems was observed by Müllen<sup>31</sup> and Moore.<sup>32</sup> However, a different regiochemistry (order of bond formation) was observed. A comparison of these results suggests that the course of the Scholl oxidation is highly sensitive to subtle changes in structure.

### 3.5 Conformational Analysis of PAHs

The partially fused systems are nonplanar PAHs, as indicated by calculating their structures using Density Functional Theory (DFT). We optimized the geometries of **4a-d** and **5a-d** (for **4a** and **5a**, the *n*-nonyl chains were truncated to methyl groups). Each of the partially fused structures **4a-d** show significant distortion from planarity, in which the dihedral torsion angle at the site of final cyclodehydrogenation is 56° (Figure 3.6 and Figure A2.88 in the Appendix). For compound **4a**, we considered two possible conformations, namely twisted (Figure 3.6) and anti (Figure A2.89 in the Appendix). The two structures are energetically similar, with the twisted conformation predicted to be 0.9 kcal/mol more stable in the gas phase, and both structures exhibit large deviations from planarity. Their barrier to interconversion is high (>20 kcal/mol), and only a single conformation of **4a** was observed by NMR spectroscopy. Although both structures are viable, we predict **that 4a** adopts the twisted form based on previous work with a similar contorted compound<sup>26</sup> and the limited conformational freedom of precursor **3a**. In contrast, fully fused compounds **5a** and **5d** are nearly planar (2–3° dihedral angle). For **5b** and **5c**, which were not observed experimentally, the internal arene torsion of the optimized structure is 10–11°, suggesting that the strain of forming the final carbon-carbon bonds precludes complete fusion of these compounds.

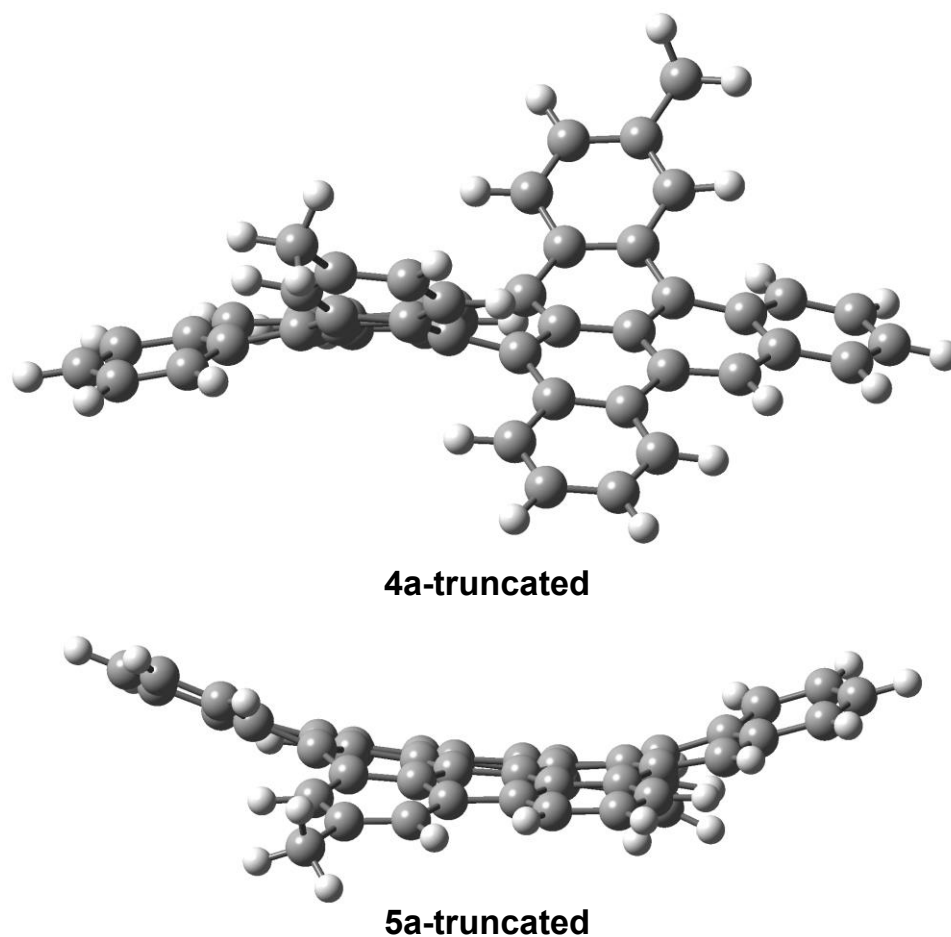


**Figure 3.6.** DFT-optimized structures of partially and fully fused compounds **4a** and **5a**, respectively. The  $n$ -C<sub>9</sub>H<sub>19</sub> chains were truncated to –CH<sub>3</sub> groups in the calculations.

### 3.6 Photophysical Characteristics of PAHs

Contorted HBCs have attracted interest for their shape complementarity to fullerenes and distinct optical and electronic properties. For example, HBCs are typically yellow compounds, whereas solutions of **4a** and **4b** are orange and those of **4c** are red. UV/vis spectroscopy indicated similar spectra for each compound, with significant absorption bands in the 450–550 nm range and molar absorptivity  $\geq 20,000 \text{ M}^{-1}\text{cm}^{-1}$  (Figure 3.7a). The absorption onsets of each compound, from which the optical HOMO–LUMO gaps are determined, are  $\sim 540 \text{ nm}$  for **4a** and **4b** and  $575 \text{ nm}$  for the more extended derivative **4c**. These onsets correspond to optical HOMO–LUMO gaps of  $2.32 \text{ eV}$  for both **4a** and **4b** and  $2.16 \text{ eV}$  for **4c** (These optical and electrochemical HOMO–

LUMO gaps are collected in Table A2.3 in the Appendix). For all structures analyzed computationally, both the HOMO and LUMO are delocalized across the molecule, consistent with a small Stokes shift (see Table A2.1 in the Appendix). The DFT calculated HOMO-LUMO gaps trend is consistent with the experimental values (2.72 eV, 2.76 eV, and 2.60 eV for **4a**, **4b**, and **4c**, respectively). The lowest energy optical transition of **4a** is influenced by its nonplanar structure, as evidenced by the spectrum of the corresponding fully fused derivative **5a**, which does not absorb strongly in this region (Figure A2.86 in the Appendix). A contorted PAH most similar in structure to the aromatic core of **4a-c** exhibits similar absorbance and fluorescence properties,<sup>33</sup> and these effects on the absorbance of nonplanar coronene derivatives were also noted by Nuckolls and coworkers.<sup>23</sup> Each compound is strongly fluorescent, and **4a** and **4b** have nearly identical photoemission spectra with  $\lambda_{\text{max}}$  at 505 nm (Figure 3.7b). The emission of **4c** has a very similar peak shape and  $\lambda_{\text{max}}$  of 540 nm. These maximum emission wavelengths correspond to low Stokes shifts (~25 nm) for each compound that are consistent with their expected rigid structures. The partially fused derivatives described here maintain reasonable fluorescence quantum yield, whereas nonplanarity induced by incorporating five-membered rings into similar systems was accompanied by dramatic reductions in their quantum yield.<sup>23</sup>

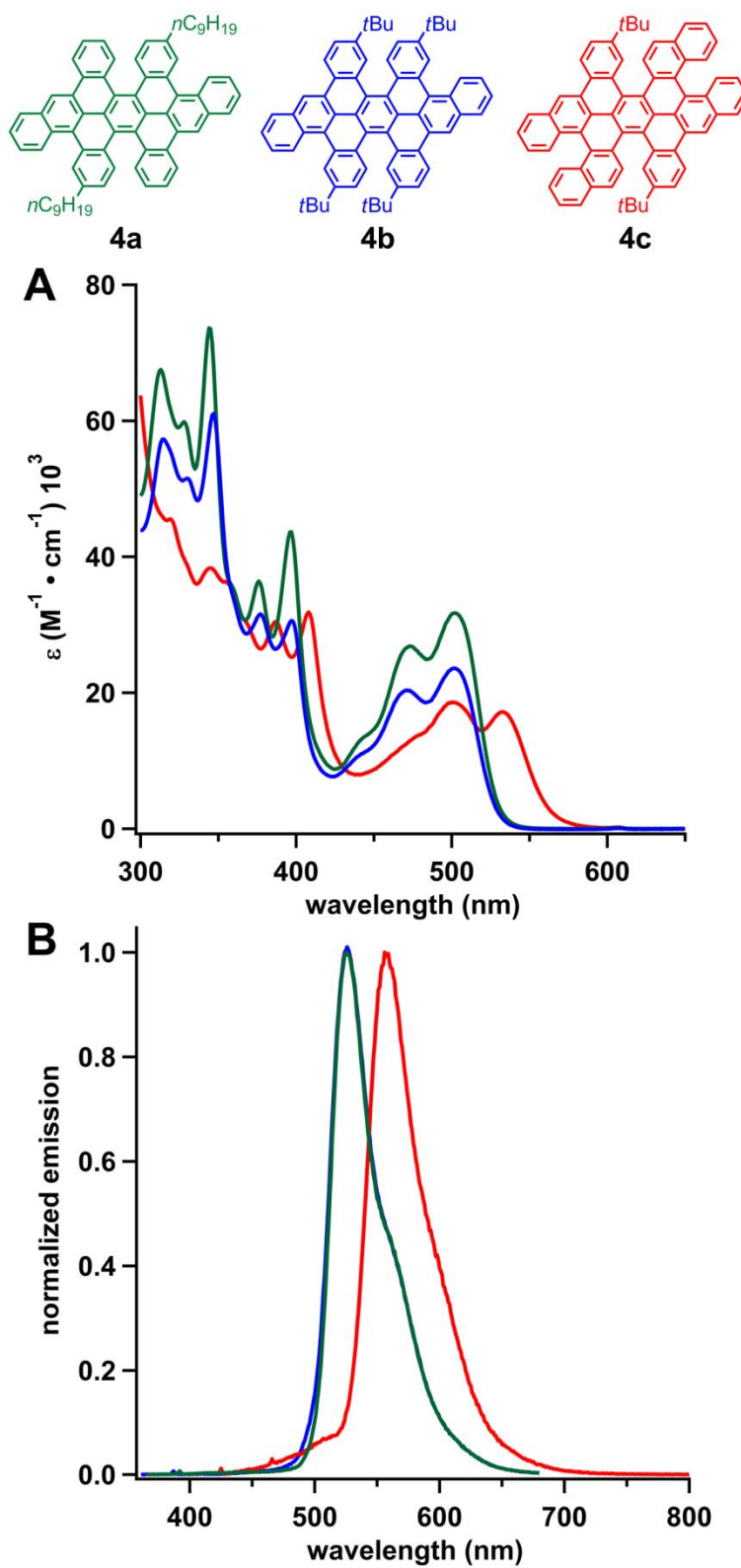


**Figure 3.7. A.** UV/vis and **(B)** fluorescence spectra of contorted compounds **4a-c**

### 3.7 *Electrochemical Properties of PAHs*

Electrochemical studies provided additional insight into the redox processes and energy levels of the partially fused compounds (Figure 3.8). Cyclic voltammetry of **4a-c** was performed in 0.1 M Bu<sub>4</sub>NPF<sub>6</sub> in CH<sub>2</sub>Cl<sub>2</sub> on a Pt button electrode, with potentials reported relative to the ferrocene/ferrocenium (Fc/Fc<sup>+</sup>) redox couple. **4a** and **4b** exhibit two electrochemically irreversible but chemically reversible oxidation processes, each with a first onset potential of 0.22 V. The corresponding oxidation processes are also observed for **4c** at similar onset potentials of 0.24 V. Differences in the reduction processes of these compounds are more pronounced. **4a** and **4b** are reduced at onset potentials of -1.79 and -1.80 V, respectively. The reduction of **4a** is chemically reversible, whereas the reduction of **4b** is chemically irreversible and may correspond to a multielectron reduction process. The reduction of **4c** occurs at a less negative potential of -1.57 V and is also chemically irreversible. These measurements give rise to electrochemical HOMO-LUMO gaps of 2.01, 2.02, and 1.81 eV for **4a-c**, respectively, which correspond reasonably well to those determined optically. In contrast, CV of a film of the fully fused derivative **5a**-<sup>13</sup>C<sub>2</sub> cast on a Pt button working electrode exhibited no reduction processes at potentials >-2.2 V. The oxidation onset of these films is at 0.40 V, 0.18 V more positive than **4a** and is chemically irreversible (Figure A2.89 in the Appendix). Overall, the similar oxidation potentials of each compound, along with the shift in the reduction potential of **4c** relative to **4a** and **4b** suggest that the extended conjugation of **4c** predominantly lowers its LUMO energy, making it a better electron acceptor.

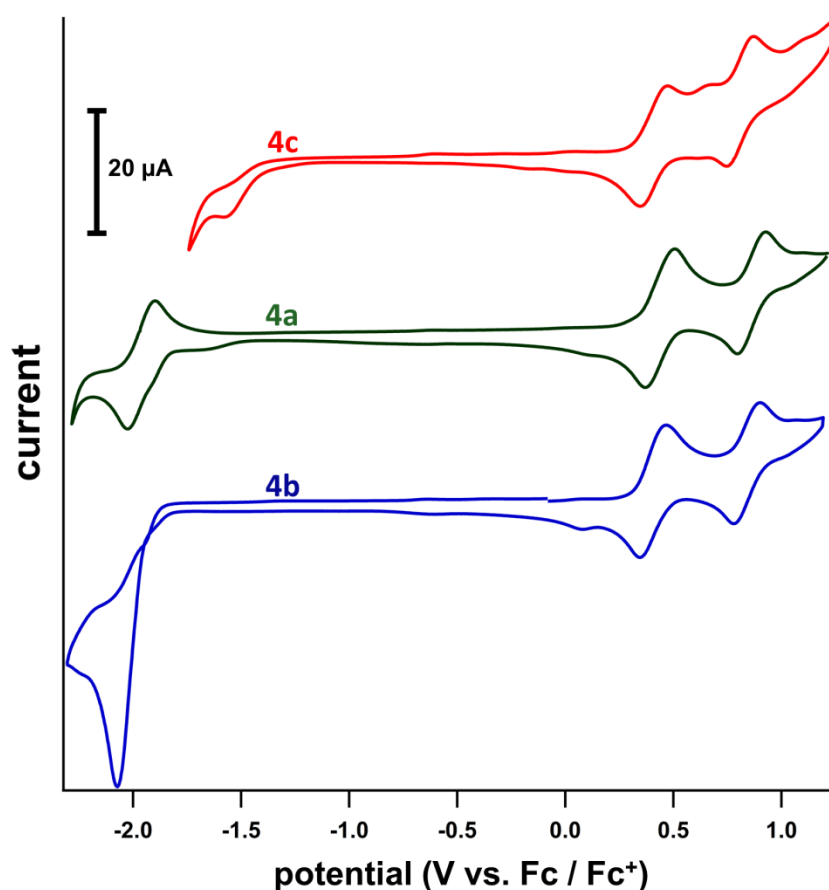


**Figure 3.8.** Cyclic voltammetry (0.1 M Bu<sub>4</sub>NPF<sub>6</sub> in CH<sub>2</sub>Cl<sub>2</sub>; Pt button electrode) of **4a-4c**.

### 3.8 Conclusions

We have demonstrated a sequential benzannulation-cyclodehydrogenation strategy to access new PAH architectures from easily prepared arylene ethynylenes. This approach provides efficient access to both fully fused and partially fused hexabenzocoronene derivatives with extended conjugation and differing substitution patterns than those available from existing methods. Rearranged products were not observed under these conditions. The partially fused derivatives are underexplored and feature high solubility, increased absorptivity in the visible spectrum, and reversible redox processes. The high efficiency of the benzannulation reaction shows great



promise for synthesizing other novel PAH systems. The benzannulated derivatives explored here are also important models for accessing graphene nanoribbons by applying the benzannulation-cyclodehydrogenation approach to appropriately substituted PPEs. This study confirms the promise of such an approach in that no rearrangements were observed in the Scholl oxidation step, although complete fusion in the polymer systems should be demonstrated carefully. We will next apply these methods to access new carbon nanostructures and other aromatic systems.

### **3.9    *Acknowledgments***

This work was supported by the Beckman Young Investigator Program of the Arnold and Mabel Beckman Foundation, the NSF (CHE-1124754), the Doctoral New Investigator Program of the ACS Petroleum Research Fund (52019-DNI7), the Cottrell Scholar Program of the Research Corporation for Science Advancement, and a Sloan Research Fellowship from the Alfred P. Sloan Foundation. We acknowledge Dr. Ivan Keresztes for assistance with NMR spectroscopy.

## REFERENCES

- (1) S. Pogodin and I. Agranat, *Org. Lett.*, 1999, **1**, 1387-1390.
- (2) L. T. Scott, *Pure Appl. Chem.*, 1996, **68**, 291-300.
- (3) A. C. Grimsdale and K. Müllen, *Angew. Chem. Int. Ed.*, 2005, **44**, 5592-5629.
- (4) B. Hajgató, M. S. Deleuze and K. Ohno, *Chemistry – A European Journal*, 2006, **12**, 5757-5769.
- (5) S. R. Forrest, *Nature*, 2004, **428**, 911-918.
- (6) C. D. Dimitrakopoulos and P. R. L. Malenfant, *Adv. Mater.*, 2002, **14**, 99-117.
- (7) X. Guo, M. Myers, S. Xiao, M. Lefenfeld, R. Steiner, G. S. Tulevski, J. Tang, J. Baumert, F. Leibfarth, J. T. Yardley, M. L. Steigerwald, P. Kim and C. Nuckolls, *Proceedings of the National Academy of Sciences*, 2006, **103**, 11452-11456.
- (8) C. Li, M. Liu, N. G. Pschirer, M. Baumgarten and K. Müllen, *Chem. Rev.*, 2010, **110**, 6817-6855.
- (9) L. Schmidt-Mende, A. Fechtenkötter, K. Müllen, E. Moons, R. H. Friend and J. D. MacKenzie, *Science*, 2001, **293**, 1119-1122.
- (10) T. M. Figueira-Duarte and K. Müllen, *Chem. Rev.*, 2011, **111**, 7260-7314.
- (11) W. Pisula, X. Feng and K. Müllen, *Chem. Mater.*, 2011, **23**, 554-567.
- (12) B. Schmaltz, T. Weil and K. Müllen, *Adv. Mater.*, 2009, **21**, 1067-1078.
- (13) J. P. Hill, W. S. Jin, A. Kosaka, T. Fukushima, H. Ichihara, T. Shimomura, K. Ito, T. Hashizume, N. Ishii and T. Aida, *Science*, 2004, **304**, 1481-1483.
- (14) W. Jin, T. Fukushima, M. Niki, A. Kosaka, N. Ishii and T. Aida, *Proc. Natl. Acad. Sci. U.S.A.*, 2005, **102**, 10801-10806.
- (15) Y. Yamamoto, T. Fukushima, Y. Suna, N. Ishii, A. Saeki, S. Seki, S. Tagawa, M.

Taniguchi, T. Kawai and T. Aida, *Science*, 2006, **314**, 1761-1764.

(16) C.-Y. Chiu, B. Kim, A. A. Gorodetsky, W. Sattler, S. Wei, A. Sattler, M. Steigerwald and C. Nuckolls, *Chem. Sci.*, 2011, **2**, 1480-1486.

(17) Y. S. Cohen, S. Xiao, M. L. Steigerwald, C. Nuckolls and C. R. Kagan, *Nano Lett.*, 2006, **6**, 2838-2841.

(18) A. M. Hiszpanski, S. S. Lee, H. Wang, A. R. Woll, C. Nuckolls and Y.-L. Loo, *ACS Nano*, 2013, **7**, 294-300.

(19) S. J. Kang, S. Ahn, J. B. Kim, C. Schenck, A. M. Hiszpanski, S. Oh, T. Schiros, Y.-L. Loo and C. Nuckolls, *J. Am. Chem. Soc.*, 2013, **135**, 2207-2212.

(20) S. J. Kang, J. B. Kim, C.-Y. Chiu, S. Ahn, T. Schiros, S. S. Lee, K. G. Yager, M. F. Toney, Y.-L. Loo and C. Nuckolls, *Angewandte Chemie-International Edition*, 2012, **51**, 8594-8597.

(21) Y.-L. Loo, A. M. Hiszpanski, B. Kim, S. Wei, C.-Y. Chiu, M. L. Steigerwald and C. Nuckolls, *Org. Lett.*, 2010, **12**, 4840-4843.

(22) K. N. Plunkett, K. Godula, C. Nuckolls, N. Tremblay, A. C. Whalley and S. Xiao, *Org. Lett.*, 2009, **11**, 2225-2228.

(23) A. C. Whalley, K. N. Plunkett, A. A. Gorodetsky, C. L. Schenck, C.-Y. Chiu, M. L. Steigerwald and C. Nuckolls, *Chem. Sci.*, 2011, **2**, 132-135.

(24) S. X. Xiao, M. Myers, Q. Miao, S. Sanaur, K. L. Pang, M. L. Steigerwald and C. Nuckolls, *Angew. Chem. Int. Ed.*, 2005, **44**, 7390-7394.

(25) S. Xiao, S. J. Kang, Y. Wu, S. Ahn, J. B. Kim, Y.-L. Loo, T. Siegrist, M. L. Steigerwald, H. Li and C. Nuckolls, *Chem. Sci.*, 2013, **4**, 2018-2023.

(26) J. Luo, X. Xu, R. Mao and Q. Miao, *J. Am. Chem. Soc.*, 2012, **134**, 13796-13803.

- (27) H. Arslan, J. D. Saathoff, D. N. Bunck, P. Clancy and W. R. Dichtel, *Angew. Chem. Int. Ed.*, 2012, **51**, 12051-12054.
- (28) A. Pradhan, P. Dechambenoit, H. Bock and F. Durola, *Angew. Chem. Int. Ed.*, 2011, **50**, 12582-12585.
- (29) N. Asao, T. Nogami, S. Lee and Y. Yamamoto, *J. Am. Chem. Soc.*, 2003, **125**, 10921-10925.
- (30) J. L. Ormsby, T. D. Black, C. L. Hilton, Bharat and B. T. King, *Tetrahedron*, 2008, **64**, 11370-11378.
- (31) X. Feng, J. Wu, V. Enkelmann and K. Müllen, *Org. Lett.*, 2006, **8**, 1145-1148.
- (32) Y. Lu and J. S. Moore, *Tetrahedron Lett.*, 2009, **50**, 4071-4077.
- (33) Y. Fujimaki, M. Takekawa, S. Fujisawa, S. Ohshima and Y. Sakamoto, *Polycyclic Aromat. Compd.*, 2004, **24**, 107-122.

## APPENDIX TWO

## Table of Contents

<b>A.</b>	Materials and Instrumentation	96
<b>B.</b>	Synthetic Procedures	97
<b>C.</b>	$^1\text{H}$ and $^{13}\text{C}$ NMR Spectroscopy	114
<b>D.</b>	2D NMR Spectra and Structural Assignments of Selected Compounds	137
<b>E.</b>	UV/Vis and Fluorescence Spectroscopy	173
<b>F.</b>	DFT Calculations	174
<b>G.</b>	Optical and Electrochemical Bandgaps	199
<b>H.</b>	References to Appendix	200

**A. Materials.** All reagents were purchased from commercial sources and used without further purification. CH<sub>2</sub>Cl<sub>2</sub>, PhMe, and MeOH were purchased from commercial sources and purified using a custom-built alumina-column based solvent purification system. Other solvents were purchased from commercial sources and used without further purification

**Instrumentation.** Infrared spectra were recorded on a Thermo Nicolet iS10 with a diamond ATR attachment and are uncorrected. Ultraviolet/visible/near infrared absorbance spectra were recorded on a Cary 5000 spectrophotometer with a Hg lamp.

Photoemission and excitation spectra were recorded on a Horiba Jobin Yvon Fluorolog-3 fluorescence spectrophotometer equipped with a 450 W Xe lamp, double excitation and double emission monochromators, a digital photon-counting photomultiplier and a secondary InGaAs detector for the NIR range. Correction for variations in lamp intensity over time and wavelength was achieved with a solid-state silicon photodiode as the reference. The spectra were further corrected for variations in photomultiplier response over wavelength and for the path difference between the sample and the reference by multiplication with emission correction curves generated on the instrument.

MALDI-TOF mass spectrometry was performed on a Waters MALDI micro MX MALDI-TOF mass spectrometer using positive ionization and a reflectron detector. MALDI samples were prepared by depositing the analyte dissolved in a saturated dithranol or tetracyanoquinodimethane solution onto a stainless steel sample plate. The plate was dried in air before loading it into the instrument. Calibration of the mass range was performed by addition of poly(ethylene-oxide) standards.

Gas chromatography/electron impact mass spectrometry was performed on an Agilent 6890N Network GC System with a JEOL JMS-GCmate II Mass Spectrometer (magnetic sector).

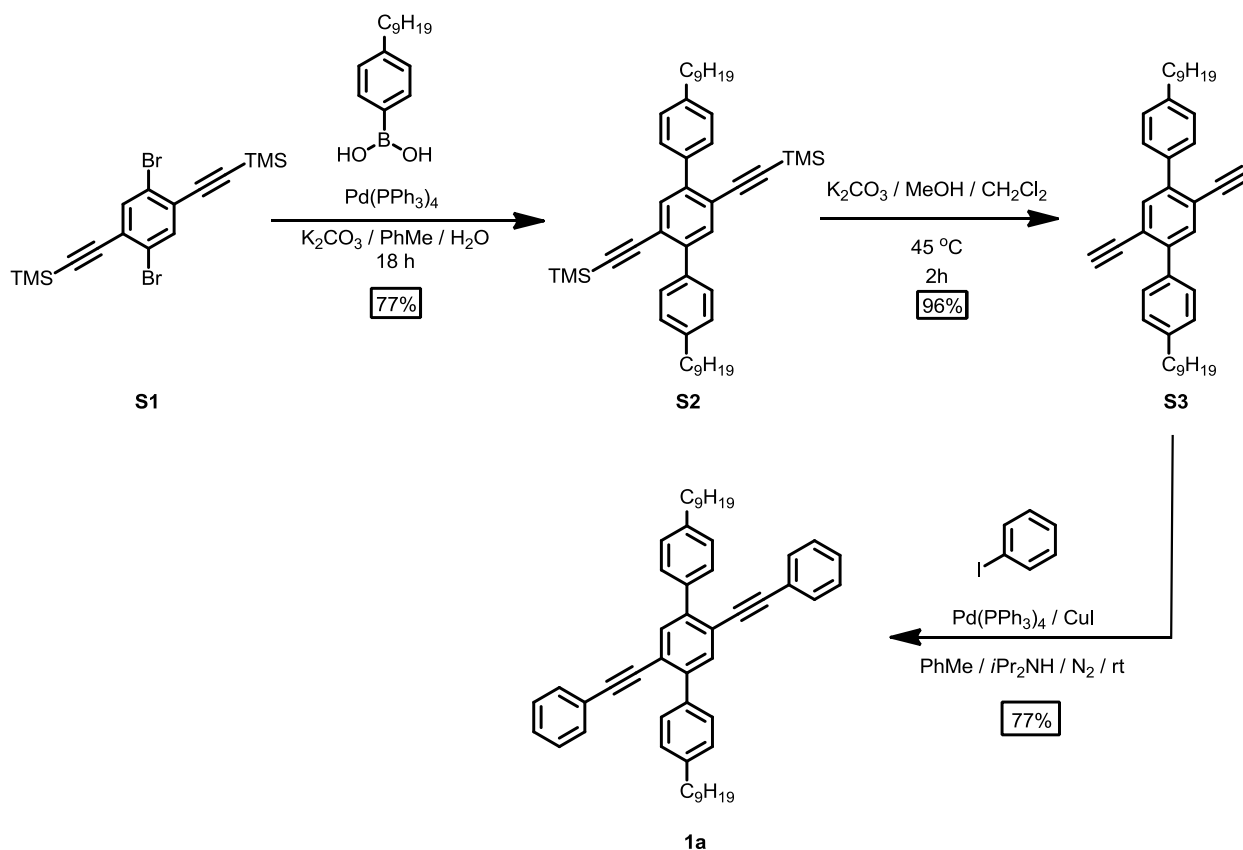
NMR spectra were recorded on a Varian 400 MHz, a Varian 500 MHz or a Bruker ARX 300 MHz spectrometer using a standard <sup>1</sup>H/X Z-PFG probe at ambient temperature with a 20 Hz sample spin rate.

Electrochemistry experiments were performed on a Princeton Applied Research VersaSTAT 3 potentiostat using a standard three electrode configuration with a Pt-button electrode as the working electrode, a coiled Pt wire as counter and a Pt wire as the quasi-reference electrode. Potentials were reported relative to Fc/Fc<sup>+</sup> redox couple.

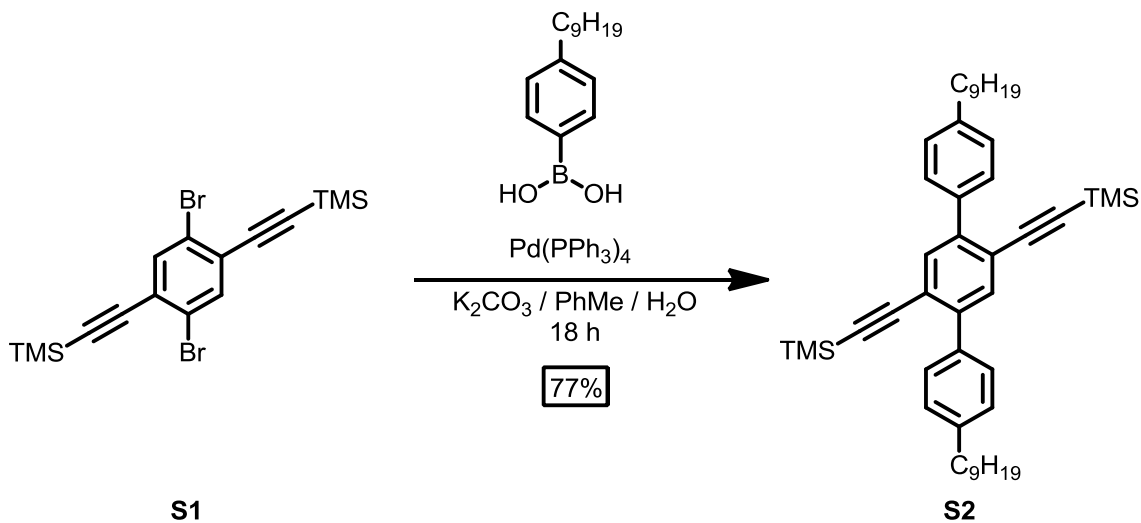
1,4-dibromo-2,5-diiodobenzene<sup>1</sup> and **S1**<sup>2</sup> were prepared from reported protocols.

## B. Synthetic Procedures

### Scheme A2.1. Overall synthesis of **1a**.



### Scheme A2.2. Synthesis of **S2**.

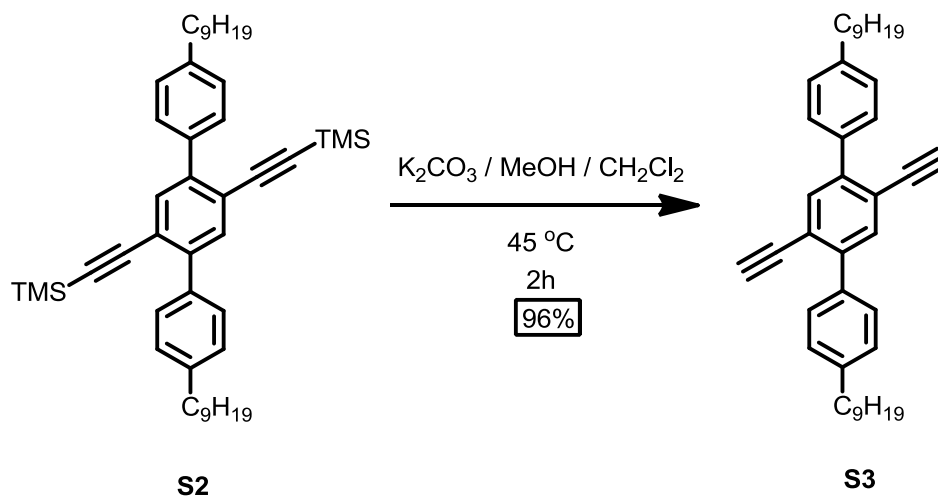


**Synthesis of S2:** **S1** (0.650 g, 1.518 mmol), 4-*n*-nonylphenylboronic acid (0.829 g, 3.339 mmol),  $\text{K}_2\text{CO}_3$  (0.629 g, 4.553 mmol),  $\text{Pd(PPh}_3)_4$  (0.175 g, 0.152 mmol) were dissolved in a



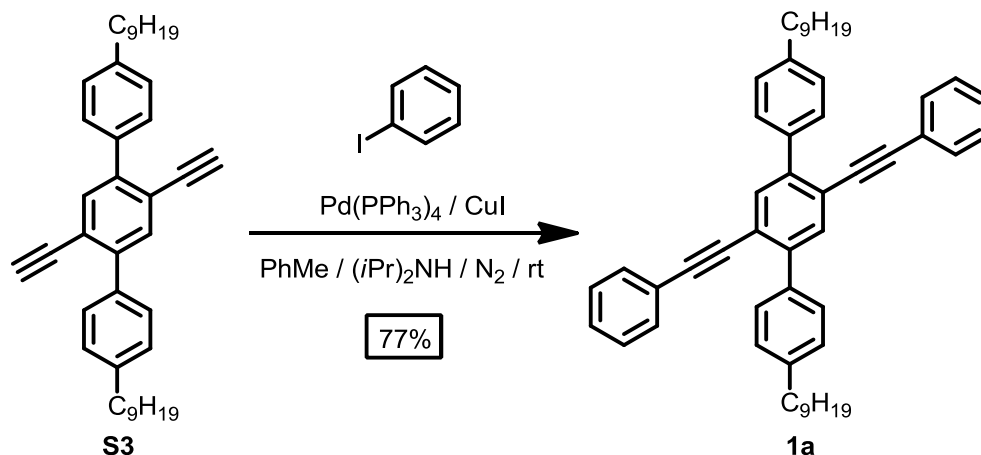
mixture of PhMe (15 mL) and water (3 mL), subjected to three freeze-pump-thaw cycles and backfilled with a N<sub>2</sub> atmosphere. The mixture was heated to 100 °C for 18 h. The solution was cooled to rt, filtered through celite, and washed with additional CH<sub>2</sub>Cl<sub>2</sub> (250 mL). The solvent was evaporated and the resulting oil was purified by chromatography (SiO<sub>2</sub>, hexanes to 1% v/v EtOAc/hexanes) to give **S2** (0.786 g, 77% yield) as a yellow oil that solidified slowly. **S2**: <sup>1</sup>H NMR (400 MHz, CDCl<sub>3</sub>) δ 7.59 (s, 2H), 7.55 (d, *J* = 7.8 Hz, 4H), 7.24 (d, *J* = 7.8 Hz, 4H), 2.68 (t, *J* = 7.8 Hz, 4H), 1.68 (m, 4H), 1.39-1.25 (m, 24H), 0.95-0.91 (m, 6H), 0.18 (s, 18H). <sup>13</sup>C NMR (100 MHz, CDCl<sub>3</sub>) δ 142.81, 142.73, 136.75, 134.49, 129.49, 128.27, 121.95, 104.98, 99.54, 36.12, 32.31, 31.94, 30.12, 30.00, 29.77, 29.67, 23.09, 14.53, 0.42. IR (solid, ATR) 2956, 2923, 2853, 2155, 1521, 1479, 1376, 1248, 1187, 1017, 906, 863, 839, 758, 722, 699 cm<sup>-1</sup>. HRMS (EI, *m/z*): calcd for [C<sub>46</sub>H<sub>66</sub>Si<sub>2</sub>]<sup>+</sup> 674.4703, found 674.4706.

**Scheme A2.3.** Synthesis of **S3**.



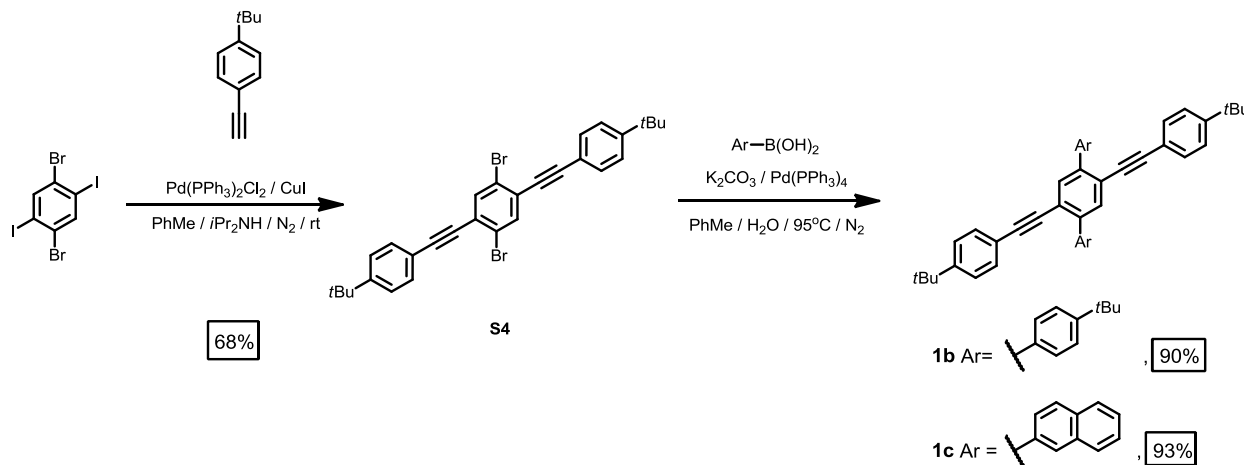
**Synthesis of S3:** K<sub>2</sub>CO<sub>3</sub> (2.87 g, 20.7 mmol) was suspended in MeOH (41 mL) and a solution of **S2** (1.400 g, 2.073 mmol) dissolved in CH<sub>2</sub>Cl<sub>2</sub> (10 mL) was added. The mixture was stirred at 45 °C for 2 h, after which it was cooled to rt and poured into aqueous HCl (2M, 10 mL). The solution was washed with Et<sub>2</sub>O (3x50 mL), and the combined organic layers were washed with brine (20 mL), dried (MgSO<sub>4</sub>) and filtered. The solvent was evaporated to give **S3** (1.060 g, 96% yield) as a white solid that was used without further purification. **S3**: <sup>1</sup>H NMR (300 MHz, CDCl<sub>3</sub>) δ 7.63 (s, 2H), 7.55 (d, *J* = 8.0 Hz, 4H), 7.25 (d, *J* = 8.0 Hz, 4H), 3.14 (s, 2H), 2.66 (t, *J* = 7.6 Hz, 4H), 1.67 (m, 4H), 1.40-1.25 (m, 24H), 0.91-0.87 (m, 6H). <sup>13</sup>C NMR (75 MHz, CDCl<sub>3</sub>) δ 142.89, 142.71, 136.33, 135.11, 129.11, 128.30, 121.07, 82.91, 81.74, 35.92, 32.06, 31.54, 29.72, 29.69, 29.59, 29.50, 22.84, 14.28. IR (solid, ATR) 3287, 2953, 2918, 2851, 1522, 1480, 1468, 1414, 1376, 1265, 1139, 1018, 902, 841, 823, 721, 666 cm<sup>-1</sup>. HRMS (EI, *m/z*): calcd for [C<sub>40</sub>H<sub>50</sub>]<sup>+</sup> 530.3913, found 530.3896.

**Scheme A2.4.** Synthesis of **1a**.

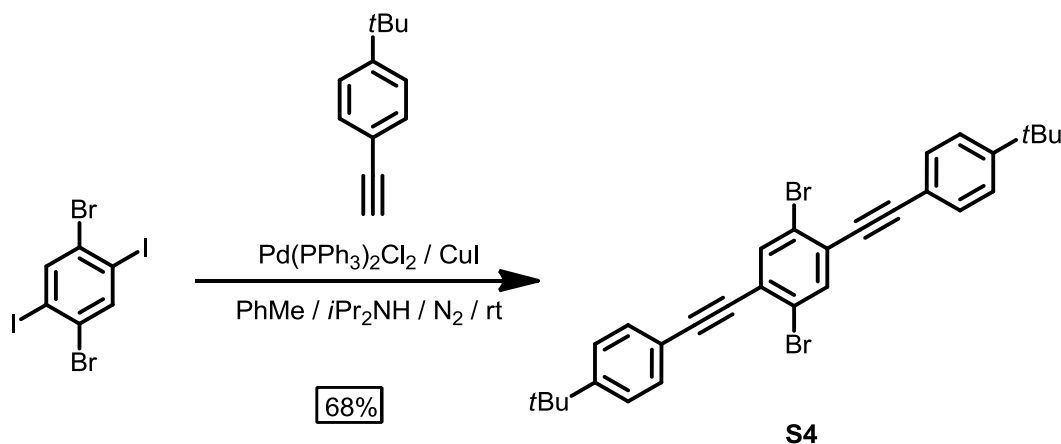


**Synthesis of 1a:** **S3** (0.300 g, 0.565 mmol), iodobenzene (0.346 mg, 1.695 mmol) and freshly distilled  $i\text{Pr}_2\text{NH}$  (9 mL) were dissolved in anhydrous PhMe (28 mL), subjected to three freeze-pump-thaw cycles, and backfilled with  $\text{N}_2$ .  $\text{Pd(PPh}_3)_4$  (33 mg, 0.028 mmol) and  $\text{CuI}$  (11 mg, 0.057 mmol) were added, and another freeze-pump-thaw cycle was performed. After stirring for 2 h at rt, the reaction mixture was filtered through celite and washed with  $\text{CH}_2\text{Cl}_2$  (150 mL). The solvent was evaporated and the crude product was purified by chromatography ( $\text{SiO}_2$ , 3% v/v EtOAc/hexanes) to give **1a** (0.296 g, 77% yield) as a yellow solid. **1a**:  $^1\text{H}$  NMR (400 MHz,  $\text{CDCl}_3$ )  $\delta$  7.72 (s, 2H), 7.67 (d,  $J = 8.1$  Hz, 4H), 7.39-7.33 (m, 4H), 7.33-7.27 (m, 6H), 2.70 (t,  $J = 7.5$  Hz, 4H), 1.69 (m, 4H), 1.44-1.23 (m, 24H), 0.93-0.86 (m, 6H).  $^{13}\text{C}$  NMR (100 MHz,  $\text{CDCl}_3$ )  $\delta$  142.69, 142.33, 136.89, 133.89, 131.56, 129.32, 128.41, 128.38, 128.19, 123.50, 121.73, 93.78, 89.63, 35.92, 32.07, 31.70, 29.77, 29.75, 29.53, 29.52, 22.85, 14.29. IR (solid, ATR) 3061, 2954, 2922, 2851, 1597, 1572, 1496, 1466, 1441, 1377, 1261, 1189, 1122, 1068, 1027, 1018, 903, 853, 834, 810, 752, 723, 687  $\text{cm}^{-1}$ . HRMS (EI,  $m/z$ ): calcd for  $[\text{C}_{52}\text{H}_{58}]^+$  682.4539, found 682.4551.

**Scheme A2.5.** Overall syntheses of the dialkynes **1b** and **1c**.

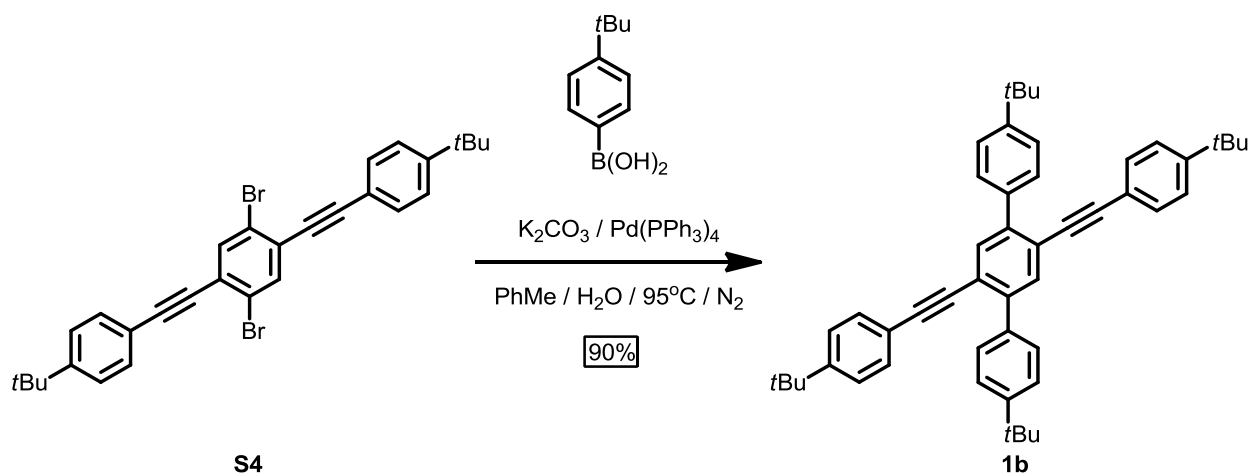


### Scheme A2.6. Synthesis of **S4**



**Synthesis of **S4**:** Anhydrous PhMe (31 mL) and freshly distilled  $i\text{Pr}_2\text{NH}$  (10 mL) were added to a 100 mL flask and sparged with  $\text{N}_2$  for 20 min. 1,4-dibromo-2,5-diiodobenzene (3.000 g, 6.15 mmol), 1-(*tert*-butyl)-4-ethynylbenzene (2.433 g, 15.38 mmol),  $\text{Pd(PPh}_3)_2\text{Cl}_2$  (216 mg, 0.308 mmol) and CuI (117 mg, 0.615 mmol) were added to the solution, in sequence. The mixture was stirred at rt for 14 h. The crude reaction mixture was filtered through a pad of  $\text{SiO}_2$  gel and washed with additional  $\text{CH}_2\text{Cl}_2$  (200 mL). Evaporation of the solvent provided the crude product as a solid, which was purified by chromatography ( $\text{SiO}_2$ , hexanes) to provide **S4** (2.310 g, 68% yield) as a white powder.  $^1\text{H}$  and  $^{13}\text{C}$  NMR spectroscopy were consistent with the report of Hseuh *et al.*<sup>3</sup> **S4**:  $^1\text{H}$  NMR (300 MHz,  $\text{CDCl}_3$ )  $\delta$  7.77 (s, 2H), 7.58 – 7.47 (m, 4H), 7.46 – 7.35 (m, 4H), 1.34 (s, 18H).  $^{13}\text{C}$  NMR (75 MHz,  $\text{CDCl}_3$ )  $\delta$  152.68, 136.05, 131.70, 126.58, 125.63, 123.81, 119.46, 97.03, 86.49, 77.58, 77.16, 76.74, 35.06, 31.30.

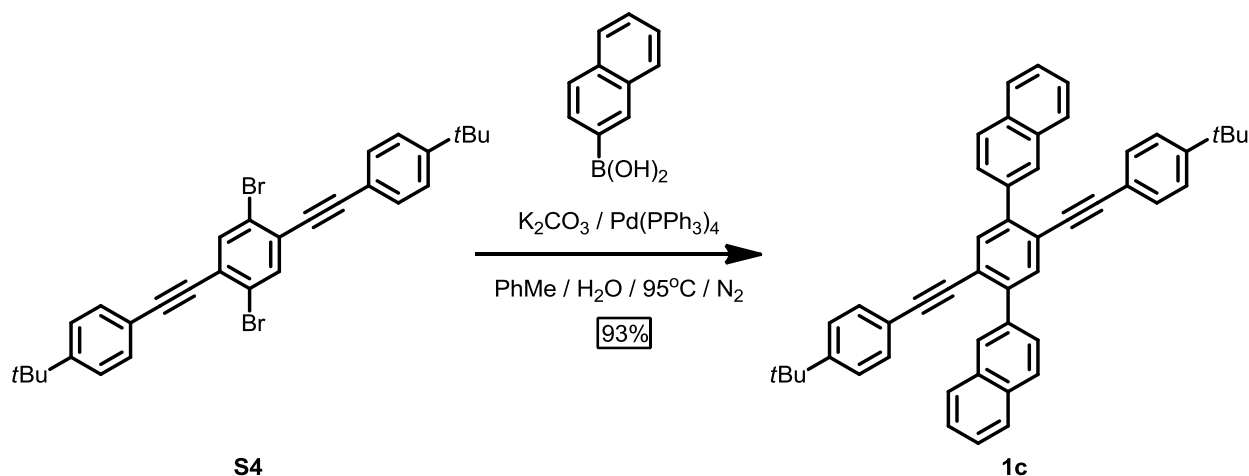
### Scheme A2.7. Synthesis of **1b**



**Synthesis of **1b**:** **S4** (0.400 g, 0.729 mmol), 4-(*tert*-benzeneboronic acid (0.286 g, 1.605 mmol), and  $\text{K}_2\text{CO}_3$  (0.465 g, 3.36 mmol) were added to a 50 mL flask equipped with a condenser. The

flask was evacuated under high vacuum and backfilled with N<sub>2</sub> three times. Degassed solvents, PhMe (7.3 mL) and DI H<sub>2</sub>O (2.4 mL) were added under positive N<sub>2</sub> pressure at 77 K. The mixture was subjected to three freeze-pump-thaw cycles and the catalyst, Pd(PPh<sub>3</sub>)<sub>4</sub> (0.042 g, 0.036 mmol) was quickly added under N<sub>2</sub> while still frozen. The flask was subjected to two more freeze-pump-thaw cycles to ensure air-free atmosphere. It was heated to 95°C, stirred for 12 hours and cooled down to rt. The mixture was transferred to a 250 mL beaker and the product crashed out upon addition of MeOH (70 mL). It was filtered through a coarse fritted funnel, and the ppt was washed with H<sub>2</sub>O (100 mL) and additional MeOH (125 mL) to give the product **1b** (0.428 g, 90% yield) as an off-white powder. <sup>1</sup>H NMR (300 MHz, CDCl<sub>3</sub>) δ 7.71 (s, 2H), 7.69 (d, *J* = 8.4 Hz, 4H), 7.51 (d, *J* = 8.4 Hz, 4H), 7.33 (d, *J* = 8.7 Hz, 4H), 7.28 (d, *J* = 8.7 Hz, 4H), 1.42 (s, 18H), 1.31 (s, 18H). <sup>13</sup>C NMR (75 MHz, CDCl<sub>3</sub>) δ 151.67, 150.70, 142.09, 136.79, 133.81, 131.30, 129.13, 125.42, 125.02, 121.79, 120.54, 93.96, 89.11, 34.94, 34.81, 31.58, 31.31. IR (solid, ATR) 3035, 2959, 2903, 2866, 1505, 1480, 1462, 1393, 1362, 1268, 1202, 1112, 1104, 1013, 905, 838 cm<sup>-1</sup>. HRMS (EI, *m/z*): calcd for [C<sub>50</sub>H<sub>54</sub>]<sup>+</sup> 654.4226, found 654.4234.

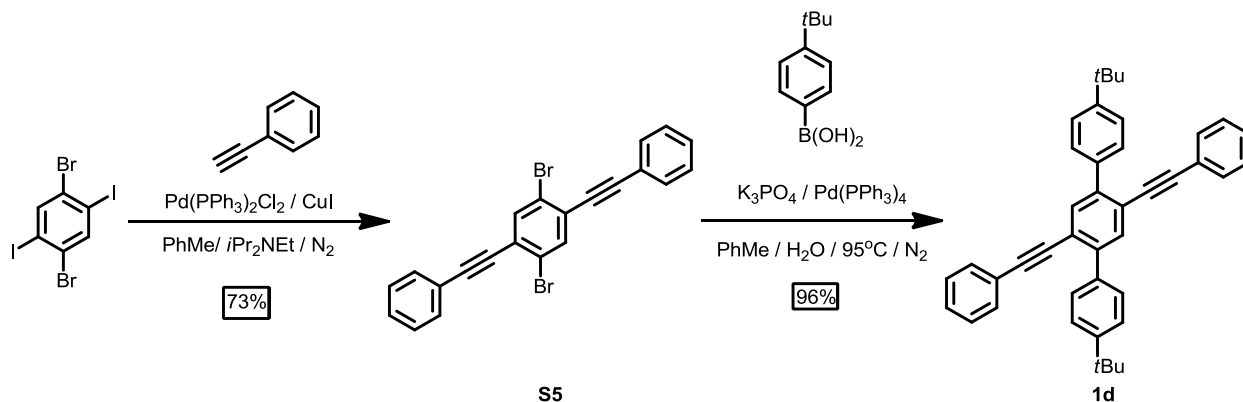
#### Scheme A2.8. Synthesis of **1c**



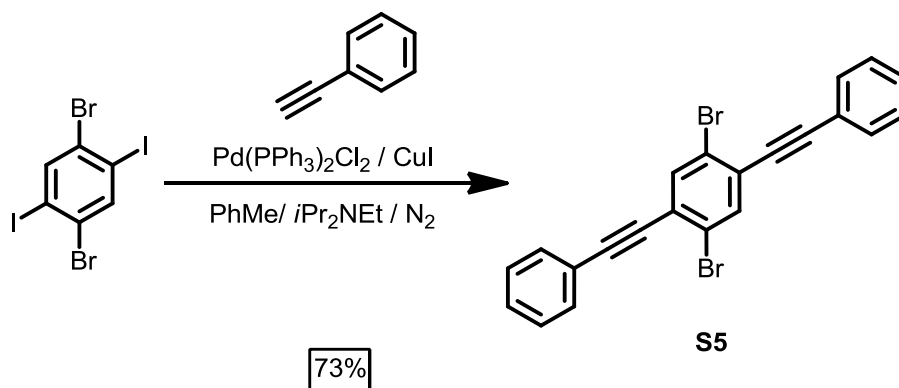
**Synthesis of **1c**:** **1c** was synthesized using a similar procedure as that used to prepare **1b**. **S4** (0.300 g, 0.547 mmol), 2-naphthaleneboronic acid (0.207 g, 1.204 mmol), K<sub>2</sub>CO<sub>3</sub> (0.348 g, 2.52 mmol), Pd(PPh<sub>3</sub>)<sub>4</sub> (0.032 g, 0.027 mmol), PhMe (5.5 mL) and H<sub>2</sub>O (1.8 mL) were used. MeOH (50 mL) was added and the resulting precipitate was recovered by filtration through a coarse fritted funnel. The crude solid was washed with H<sub>2</sub>O (50 mL) and additional MeOH (100 mL) to provide the product **1c** (0.325 g, 93% yield) as an off-white powder. <sup>1</sup>H NMR (500 MHz, CDCl<sub>3</sub>) δ 8.23 (s, 2H), 8.00 – 7.88 (m, 8H), 7.86 (s, 2H), 7.53 (dd, *J* = 6.3, 3.2 Hz, 4H), 7.32 – 7.18 (m, 8H), 1.28 (s, 18H). <sup>13</sup>C NMR (125 MHz, CDCl<sub>3</sub>) δ 151.94, 142.55, 137.41, 134.35, 133.60, 133.18, 131.41, 128.57, 128.51, 127.90, 127.76, 127.58, 126.32, 125.46, 122.38, 120.45, 94.63, 88.92, 34.98, 31.33. IR (solid, ATR) 3031, 2962, 2865, 2209, 1598, 1516, 1506, 1489, 1464, 1395, 1363, 1348, 1194, 1130, 1117, 1105, 1017, 982, 967, 955, 946, 911, 898, 868, 861, 847,

830, 823, 775, 771, 754, 736, 713, 695  $\text{cm}^{-1}$ . HRMS (EI,  $m/z$ ): calcd for  $[\text{C}_{50}\text{H}_{42}]^+$  642.3287, found 642.3278.

**Scheme A2.9.** Overall synthesis of **1d**

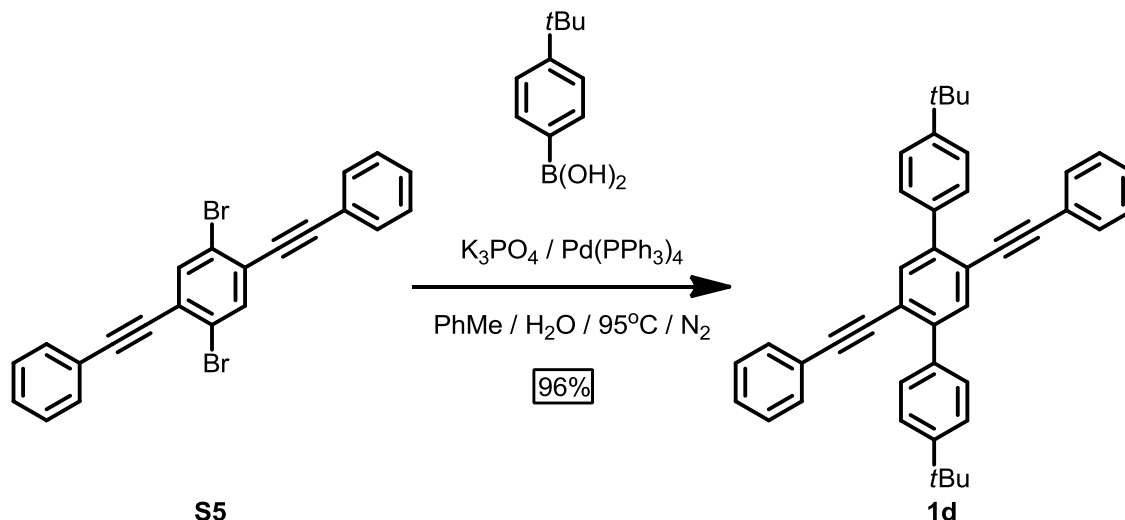


**Scheme A2.10.** Synthesis of **S5**



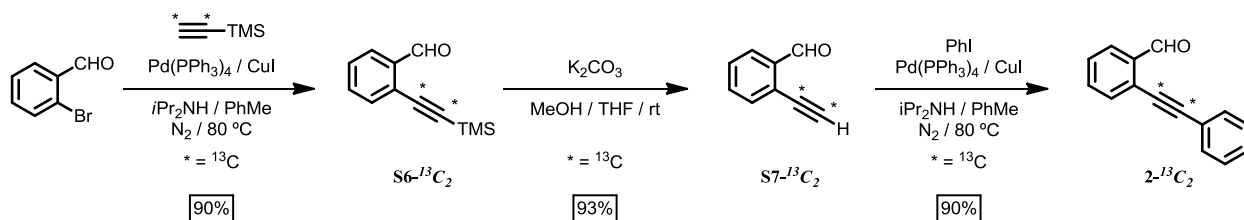
**Synthesis of S5:** Anhydrous PhMe (41 mL) and freshly distilled  $i\text{Pr}_2\text{NH}$  (10 mL) were added to a 100 mL flask and bubbled with  $\text{N}_2$  for 20 min. 1,4-dibromo-2,5-diiodobenzene (1.000 g, 2.05 mmol), ethynylbenzene (0.461 g, 4.51 mmol),  $\text{Pd(PPh}_3)_2\text{Cl}_2$  (72 mg, 0.103 mmol) and CuI (39 mg, 0.205 mmol) were added to the solution, in sequence. The mixture was stirred at rt for 20 min. The crude reaction mixture was poured into a 1 M HCl solution (50 mL) and extracted with  $\text{CH}_2\text{Cl}_2$  (3x50 mL). Combined organic layers were dried ( $\text{MgSO}_4$ ), filtered and the solvent was evaporated. The crude product was purified by flash column chromatography ( $\text{SiO}_2$ , 1% v/v EtOH/hexanes) to give **S5** (0.650 g, 73% yield) as a white powder.  $^1\text{H}$  and  $^{13}\text{C}$  NMR spectroscopy were consistent with the report of Liang *et al.*<sup>4</sup> **S5**:  $^1\text{H}$  NMR (400 MHz,  $\text{CDCl}_3$ )  $\delta$  7.79 (s, 2H), 7.61 – 7.54 (m, 4H), 7.42 – 7.34 (m, 6H).  $^{13}\text{C}$  NMR (101 MHz,  $\text{CDCl}_3$ )  $\delta$  136.15, 131.94, 129.27, 128.61, 126.54, 123.86, 122.44, 96.80, 86.96.

### Scheme A2.11. Synthesis of **1d**

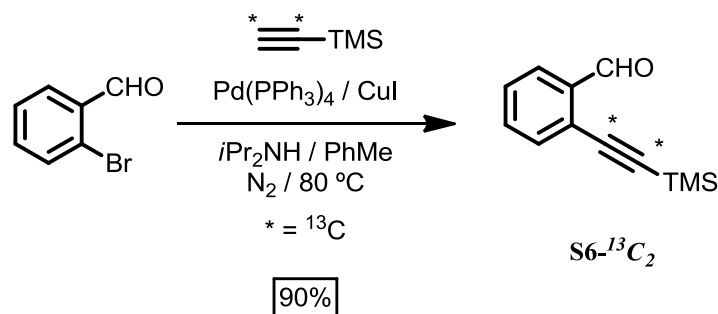


Synthesis of **1d**: **1d** was synthesized using a similar procedure as that used to prepare **1b**. **S5** (0.200 g, 0.459 mmol), 4-*tert*-benzeneboronic acid (0.204 g, 1.146 mmol),  $\text{K}_3\text{PO}_4$  (0.292 g, 1.376 mmol),  $\text{Pd(PPh}_3)_4$  (0.053 g, 0.046 mmol), PhMe (4.6 mL) and  $\text{H}_2\text{O}$  (1.5 mL) were used. After 13h the reaction mixture was cooled to rt and MeOH was added until precipitation was complete. The precipitate was collected using a coarse fritted funnel and washed with  $\text{H}_2\text{O}$  (50 mL) and MeOH (50mL), dried and **1d** (0.240g, 96% yield) was isolated as an off-white powder. **1d**:  $^1\text{H}$  NMR (400 MHz,  $\text{CDCl}_3$ )  $\delta$  7.72 (s, 2H), 7.69 (d,  $J = 8.5$  Hz, 4H), 7.52 (d,  $J = 8.5$  Hz, 4H), 7.37-7.32 (m, 4H), 7.32-7.27 (m, 6H), 1.41 (s, 18H).  $^{13}\text{C}$  NMR (100 MHz,  $\text{CDCl}_3$ )  $\delta$  150.81, 142.30, 136.71, 133.80, 131.56, 129.14, 128.40, 128.38, 125.06, 123.51, 121.79, 93.86, 89.69, 34.82, 31.56. IR (solid, ATR) 3033, 2961, 2867, 1595, 1572, 1498, 1477, 1443, 1385, 1362, 1266, 1200, 1175, 1160, 1110, 1068, 1014, 965, 912, 908, 898, 852, 837, 829, 752, 688  $\text{cm}^{-1}$ . HRMS (EI,  $m/z$ ): calcd for  $[\text{C}_{42}\text{H}_{38}]^+$  542.2974, found 542.2969.

### Scheme A2.12. Synthesis of **2- $^{13}\text{C}_2$**

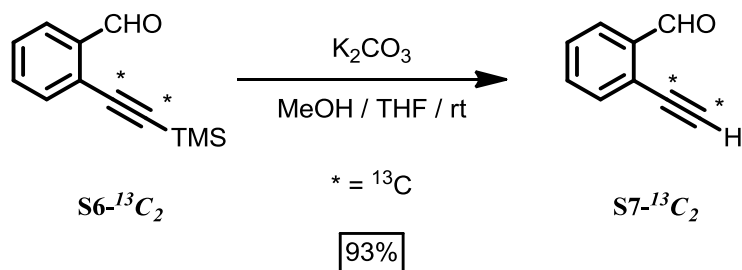


**Scheme A2.13.** Synthesis of **S6-<sup>13</sup>C<sub>2</sub>**



**Synthesis of S6-<sup>13</sup>C<sub>2</sub>.** 2-bromobenzaldehyde (0.526 g, 2.84 mmol), CuI (5 mg, 0.028 mmol), and Pd(PPh<sub>3</sub>)<sub>4</sub> (15 mg, 0.013 mmol) were loaded in a 25 mL Schlenk flask equipped with a magnetic stirrer. The flask was evacuated under dynamic vacuum to 150 mtorr and backfilled with N<sub>2</sub> three times. Anhydrous PhMe (3 mL) and anhydrous *i*Pr<sub>2</sub>NH (1 mL) were added via cannula under N<sub>2</sub>. The mixture was bubbled with N<sub>2</sub> for 20 min and trimethylsilylacetylene-<sup>13</sup>C<sub>2</sub> (99% atom <sup>13</sup>C, 0.435 mL, 300 mg, 2.994 mmol) was added dropwise with stirring. The mixture was heated to 80 °C and stirred for 12 h, after which it was quenched with saturated NH<sub>4</sub>Cl (*aq*), and extracted with CH<sub>2</sub>Cl<sub>2</sub> (3 x 10 mL). The combined organic extracts were rinsed with saturated NH<sub>4</sub>Cl (*aq*), water, and brine. The solution was dried over anhydrous MgSO<sub>4</sub>, filtered over celite, and concentrated to dryness. The obtained dark residue was purified by column chromatography (SiO<sub>2</sub>, 5% v/v THF/hexanes) to provide **S6-<sup>13</sup>C<sub>2</sub>** (0.554 g, 90% yield) as a yellow oil. <sup>1</sup>H NMR (400 MHz, CDCl<sub>3</sub>) δ 10.56 (d, *J*<sub>CH</sub> = 0.76 Hz, 1H), 7.91 (d, *J* = 7.95 Hz, 1H), 7.57 (m, *J* = 7.85, 1.71, 0.70 Hz, 1H), 7.54 (m, *J* = 7.75, 0.68 Hz, 1H), 7.43 (m, *J* = 7.75, 0.68 Hz, 1H), 0.28 (d, *J*<sub>CH</sub> = 2.48 Hz, 9H). <sup>13</sup>C NMR (100 MHz, CDCl<sub>3</sub>) δ 102.74 (d, *J*<sub>CC</sub> = 136.2 Hz), 100.02 (d, *J*<sub>CC</sub> = 136.3 Hz). EI-MS: calcd for [C<sub>10</sub><sup>13</sup>C<sub>2</sub>H<sub>14</sub>OSi]<sup>+</sup> 204.09, found 203.15.

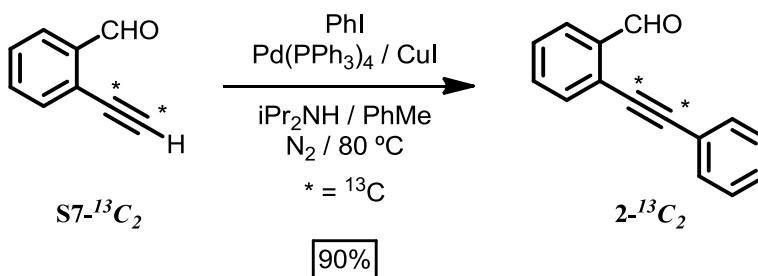
**Scheme A2.14.** Synthesis of **S7-<sup>13</sup>C<sub>2</sub>**



**Synthesis of S7-<sup>13</sup>C<sub>2</sub>.** **S6-<sup>13</sup>C<sub>2</sub>** (0.554 g, 2.71 mmol), and K<sub>2</sub>CO<sub>3</sub> (3.74 g, 27.11 mmol) were suspended in THF (6 mL) and MeOH (2 mL). The suspension was stirred at rt for 30 min. The mixture was added to 1 M HCl (3 mL), extracted with CH<sub>2</sub>Cl<sub>2</sub> (3 x 2 mL), after which the combined organic extracts were dried over anhydrous MgSO<sub>4</sub>, filtered over celite, and concentrated to dryness to afford **S7-<sup>13</sup>C<sub>2</sub>** (0.335 g, 93% yield) as a yellow solid. <sup>1</sup>H NMR (400

MHz, CDCl<sub>3</sub>)  $\delta$  10.54 (d,  $J_{\text{CH}} = 0.65$  Hz, 1H), 7.94 (m,  $J = 7.60, 1.29$  Hz, 1H), 7.60 (m,  $J = 7.06, 7.33, 7.06, 7.56$  Hz, 2H), 7.49 (m,  $J = 7.33, 1.02$  Hz, 1H), 3.46 (dd,  $J = 192.22, 55.95$  Hz, 9H). <sup>13</sup>C NMR (100 MHz, CDCl<sub>3</sub>)  $\delta$  82.73 (m,  $J = 535.66, 8.54, 2.33$  Hz), 81.01 (m,  $J = 534.92, 0.29$  Hz). HRMS (EI,  $m/z$ ): calcd for [C<sub>7</sub>H<sub>6</sub>O<sup>13</sup>C<sub>2</sub>]<sup>+</sup> 132.0486, found 132.0488

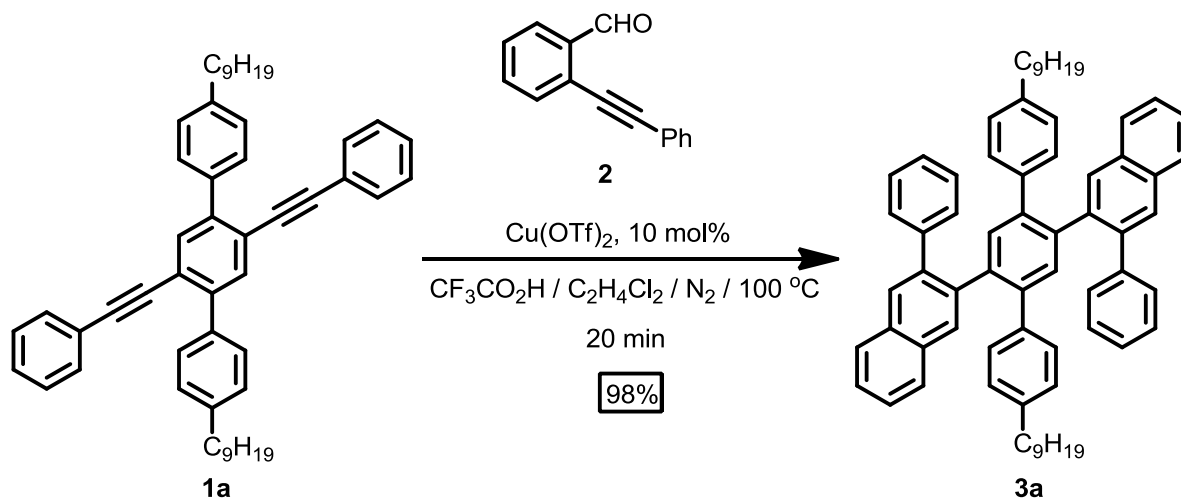
**Scheme A2.15.** Synthesis of 2-<sup>13</sup>C<sub>2</sub>



**Synthesis of 2-<sup>13</sup>C<sub>2</sub>.** S7-<sup>13</sup>C<sub>2</sub> (0.335 g, 2.53 mmol), CuI (5 mg, 0.027 mmol), and Pd(PPh<sub>3</sub>)<sub>4</sub> (16 mg, 0.014 mmol) were loaded in a 25 mL Schlenk flask equipped with a magnetic stirrer. The flask was evacuated under dynamic vacuum to 150 mtorr and backfilled with N<sub>2</sub> three times. A mixture containing anhydrous PhMe (5 mL), anhydrous *i*Pr<sub>2</sub>NH (2 mL), and PhI (0.608 g) were added via cannula under N<sub>2</sub>. The mixture was stirred at rt for 10 h, after which it was quenched with saturated NH<sub>4</sub>Cl (*aq*) and extracted with PhMe (3 x 10 mL). The combined organic extracts were rinsed with saturated NH<sub>4</sub>Cl (*aq*), water, and brine. The solution was dried over anhydrous MgSO<sub>4</sub>, filtered over celite and concentrated to dryness. The obtained dark residue was purified by column chromatography (SiO<sub>2</sub>, 5% *v/v* THF/hexanes) to provide 2-<sup>13</sup>C<sub>2</sub> (0.506 g, 90% yield) as a green oil. <sup>1</sup>H NMR (400 MHz, CDCl<sub>3</sub>)  $\delta$  10.66 (s, 1H), 7.97 (d,  $J = 7.27$  Hz, 1H), 7.65 (m,  $J = 5.45$ , Hz, 1H), 7.61-7.56 (m, 3H), 7.46 (m,  $J = 7.48$ , 1H), 7.39 (m,  $J = 2.51$ , 3H). <sup>13</sup>C NMR (100 MHz, CDCl<sub>3</sub>)  $\delta$  96.52 (d,  $J_{\text{CC}} = 184.82$  Hz), 84.97 (d,  $J_{\text{CC}} = 182.02$  Hz). HRMS (EI,  $m/z$ ): calcd for [C<sub>13</sub>H<sub>10</sub>O<sup>13</sup>C<sub>2</sub>]<sup>+</sup> 208.0799, found 208.0800.

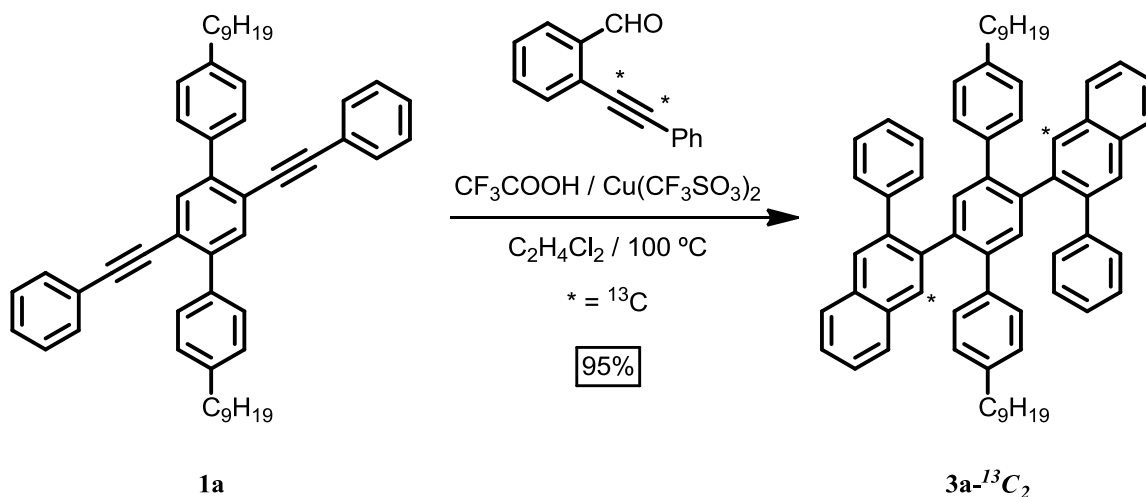


**Scheme A2.16.** Synthesis of **3a**.



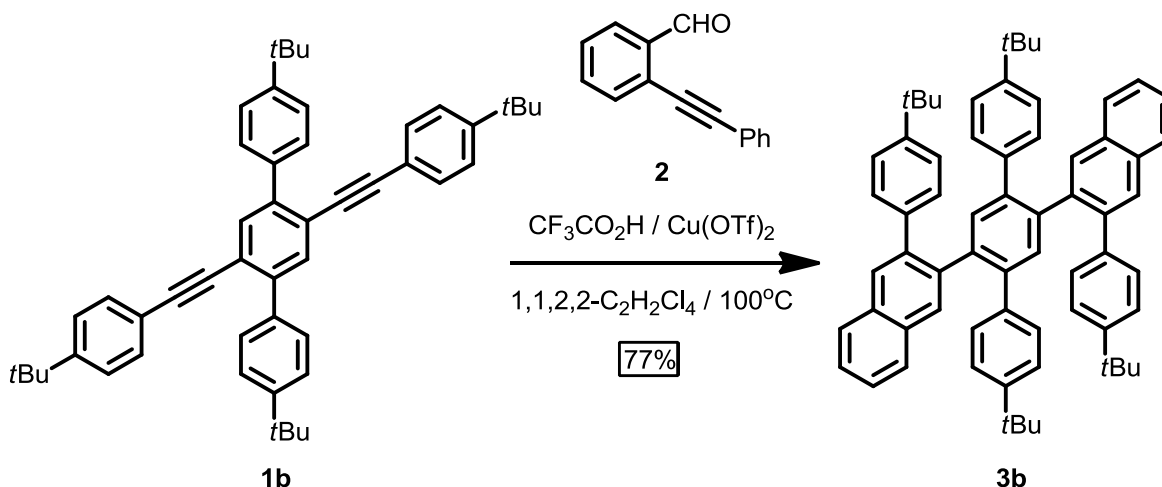
**Synthesis of 3a:** Dialkyne **1a** (0.273 g, 0.400 mmol) and benzaldehyde **2** (0.330 g, 1.600 mmol) were dissolved in 1,2-dichloroethane (16 mL) under  $\text{N}_2$ .  $\text{Cu}(\text{OTf})_2$  (58 mg, 0.160 mmol) and  $\text{CF}_3\text{CO}_2\text{H}$  (0.135 mL, 1.760 mmol) were added in quick succession. The solution was heated to reflux for 20 min, after which it was cooled to rt and poured into a saturated aqueous  $\text{NaHCO}_3$  solution (50 mL). The aqueous layer was washed with extracted with  $\text{CH}_2\text{Cl}_2$  (3x50 mL), and the combined organic layers were dried ( $\text{MgSO}_4$ ) and filtered. The solvent was evaporated to provide the product as a crude solid, which was purified by chromatography ( $\text{SiO}_2$ , 2% v/v EtOAc/hexanes) to give **2a** (0.348 g, 98% yield) as an off-white solid. **2a**:  $^1\text{H}$  NMR (500 MHz,  $\text{CDCl}_3$ )  $\delta$  8.05 (s, 2H), 7.67 (d,  $J = 8.1$  Hz, 4H), 7.88-7.84 (m, 4H), 7.66 (s, 2H), 7.53-7.48 (m, 6H), 7.22-7.17 (m, 2H), 7.16-7.11 (m, 2H), 6.77 (d,  $J = 7.7$  Hz, 8H), 6.55 (d,  $J = 8.1$  Hz, 4H), 2.52 (td,  $J = 8.0$  Hz, 2.2 Hz, 4H), 1.60 (m, 4H), 1.39-1.25 (m, 24H), 0.94-0.89 (m, 6H).  $^{13}\text{C}$  NMR (125 MHz,  $\text{CDCl}_3$ )  $\delta$  141.1, 140.9, 140.0, 139.6, 139.2, 139.1, 137.8, 133.9, 133.1, 132.9, 130.6, 129.4, 129.0, 128.9, 127.9, 127.9, 127.8, 127.5, 126.2, 35.7, 32.1, 31.8, 29.8, 29.7, 29.5, 29.4, 22.9, 14.3. IR (solid, ATR) 3053, 2953, 2923, 2852, 1941, 1671, 1596, 1489, 1456, 1371, 1260, 1074, 1014, 914, 889, 796, 772, 759, 746, 695  $\text{cm}^{-1}$ . HRMS (EI,  $m/z$ ): calcd for  $[\text{C}_{68}\text{H}_{70}]^+$  886.5478, found 886.5509.

**Scheme A2.17.** Synthesis of **3a-<sup>13</sup>C<sub>2</sub>**.



**Synthesis of 3a-<sup>13</sup>C<sub>2</sub>:** **3a-<sup>13</sup>C<sub>2</sub>** was synthesized using a similar procedure as that used to prepare **3a**. **1a** (0.050 g, 0.073 mmol), **2-<sup>13</sup>C<sub>2</sub>** (0.090 g, 439 mmol), Cu(OTf)<sub>2</sub> (0.009 g, 0.026 mmol), CF<sub>3</sub>COOH (0.028 mL, 0.042 g, 0.439 mmol), 1,2-dichloroethane (1.3 mL) were used. **3a-<sup>13</sup>C<sub>2</sub>** was isolated as a yellow solid (0.062 g, 95% yield). <sup>1</sup>H NMR (500 MHz, CDCl<sub>3</sub>) δ 8.07 (d, *J*<sub>CH</sub> = 159.17 Hz, 2H), 7.87 (m, 4H), 7.67 (s, 2H), 7.52 (m, *J* = 3.64 Hz, 6H), 7.20-7.13 (m, 4H), 6.78-6.77 (m, 8H), 6.57-6.55 (d, *J* = 8.35 Hz, 4H) 2.52 (t, *J* = 7.6 Hz, 4H), 1.61 (t, *J* = 7.2 Hz, 4H), 1.33 (m, br, 24H), 0.93 (t, *J* = 6.7 Hz, 6H). <sup>13</sup>C NMR (125 MHz, CDCl<sub>3</sub>) δ 130.58 (s). MS: (*m/z* MALDI-TOF, TCNQ) calcd for [C<sub>66</sub>H<sub>70</sub><sup>13</sup>C<sub>2</sub>]<sup>+</sup> 888.5477, found 888.5207.

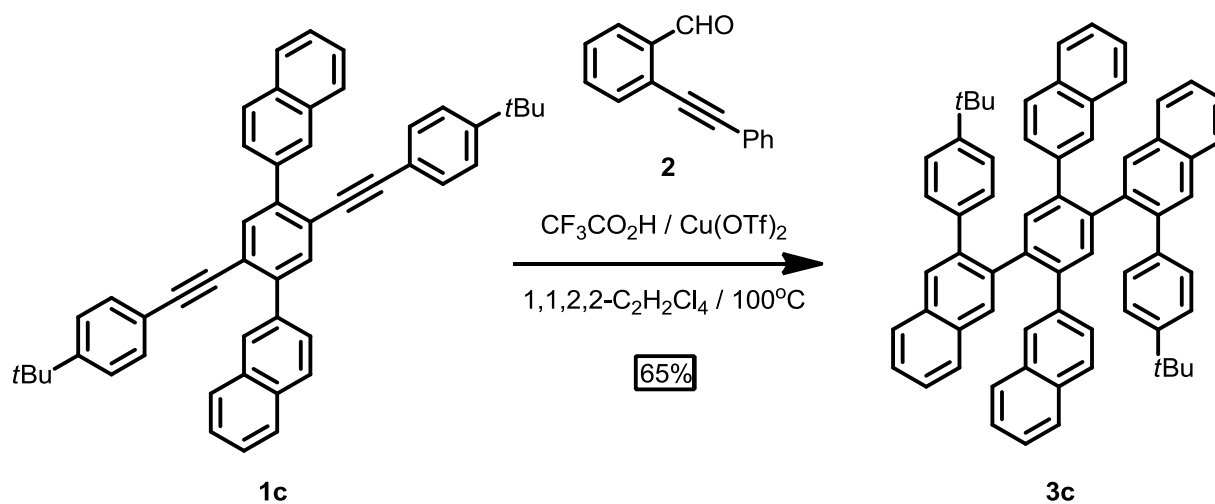
**Scheme A2.18.** Synthesis of **3b**.



**Synthesis of 3b:** **3b** was synthesized using a similar procedure that was used to prepare **3a**. **1b** (0.329 g, 0.502 mmol), benzaldehyde **2** (0.518 g, 2.51 mmol), Cu(OTf)<sub>2</sub> (18 mg, 0.050 mmol) and CF<sub>3</sub>CO<sub>2</sub>H (0.19 mL, 2.51 mmol) 1,1,2,2-tetrachloroethane (5 mL) were used. **3b** (0.330 g, 77% yield) was isolated as an off-white powder. **3b:** <sup>1</sup>H NMR (400 MHz, CDCl<sub>3</sub>) δ 8.12 (s, 2H),

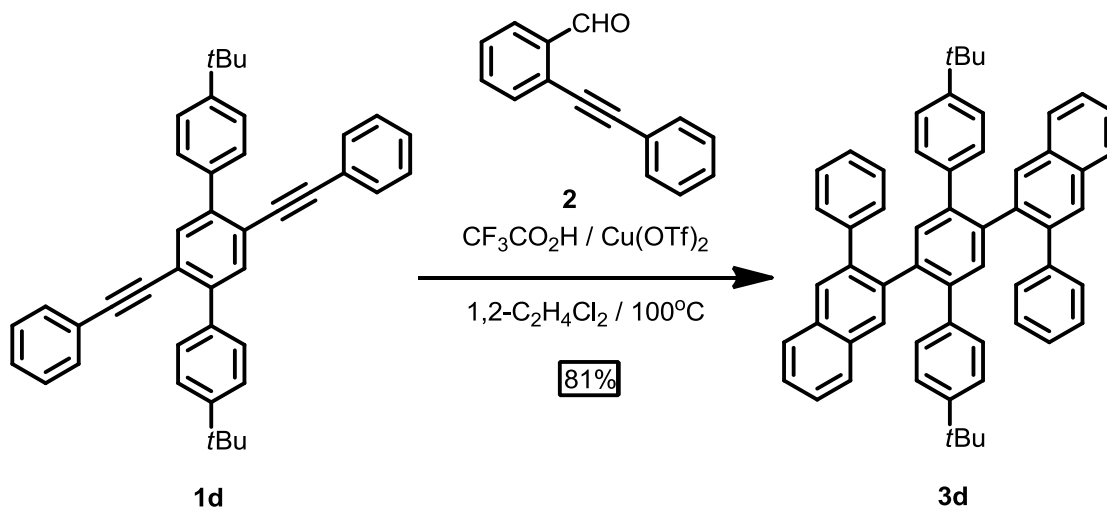
7.91-7.88 (m, 4H), 7.70 (s, 2H), 7.59 (s, 2H), 7.55-7.52 (m, 4H), 7.18 (d,  $J = 8.3$  Hz, 4H), 6.96 (d,  $J = 8.4$  Hz, 4H), 6.66 (d,  $J = 8.3$  Hz, 4H), 6.56 (d,  $J = 8.4$  Hz, 4H), 1.39 (s, 18H), 1.34 (s, 18H).  $^{13}\text{C}$  NMR (100MHz,  $\text{CDCl}_3$ )  $\delta$  148.9, 148.9, 140.0, 139.5, 139.4, 139.3, 138.0, 137.4, 133.8, 133.1, 133.0, 130.4, 128.8, 128.5, 128.5, 127.9, 127.7, 126.2, 126.1, 124.7, 124.2, 34.5, 34.5, 31.5, 31.5. IR (solid, ATR) 3052, 2960, 2865, 1516, 1489, 1473, 1458, 1393, 1362, 1269, 1214, 1199, 1132, 1111, 1022, 1011, 947, 919, 888, 852, 831, 748, 687, 668  $\text{cm}^{-1}$ . HRMS (MALDI-TOF,  $m/z$ ): calcd for  $[\text{C}_{66}\text{H}_{66}]^+$  858.5159, found 858.517

**Scheme A2.19.** Synthesis of **3c**.



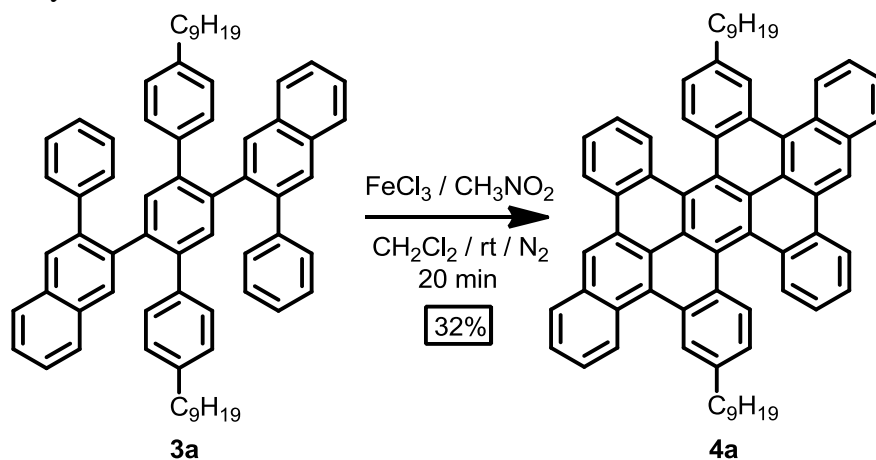
**Synthesis of 3c:** **3c** was synthesized using a similar procedure that was used to prepare **3a**. **1c** (0.305 g, 0.474 mmol), benzaldehyde **2** (0.490 g, 2.37 mmol),  $\text{Cu}(\text{OTf})_2$  (17 mg, 0.047 mmol),  $\text{CF}_3\text{CO}_2\text{H}$  (0.18 mL, 2.37 mmol) 1,1,2,2-tetrachloroethane (5.0 mL) were used. After purification by flash column chromatography ( $\text{SiO}_2$ , 3% v/v EtOAc/hexanes), **3c** was isolated as a white powder (0.260g, 65% yield). **3c**:  $^1\text{H}$  NMR (400 MHz,  $\text{CDCl}_3$ )  $\delta$  8.18 (s, 2H), 7.93 – 7.86 (m, 2H), 7.86 – 7.77 (m, 2H), 7.76 – 7.69 (m, 4H), 7.60 (s, 2H), 7.56 – 7.46 (m, 4H), 7.46 – 7.35 (m, 8H), 7.09 – 7.04 (m, 4H), 7.03 (d,  $J = 1.8$  Hz, 2H), 6.82 (dd,  $J = 8.5, 1.8$  Hz, 2H), 6.59 – 6.49 (m, 4H), 1.36 (s, 18H).  $^{13}\text{C}$  NMR (101 MHz,  $\text{CDCl}_3$ )  $\delta$  149.16, 140.52, 139.90, 139.44, 138.99, 138.21, 137.96, 134.16, 133.41, 133.21, 132.87, 132.00, 130.40, 128.96, 128.82, 128.40, 128.00, 127.92, 127.75, 127.47, 127.42, 126.76, 126.30, 126.24, 125.69, 125.54, 124.18, 53.09, 34.54, 31.75, 31.59, 22.82, 14.29, 0.16. IR (solid, ATR) 3054, 2959, 2865, 1788, 1596, 1507, 1489, 1452, 1394, 1361, 1260, 1215, 1177, 1088, 1215, 891, 856, 819, 742  $\text{cm}^{-1}$ . HRMS (MALDI-TOF,  $m/z$ ): calcd for  $[\text{C}_{66}\text{H}_{54}]^+$  846.4220, found 846.419.

**Scheme A2.20.** Synthesis of **3d**.



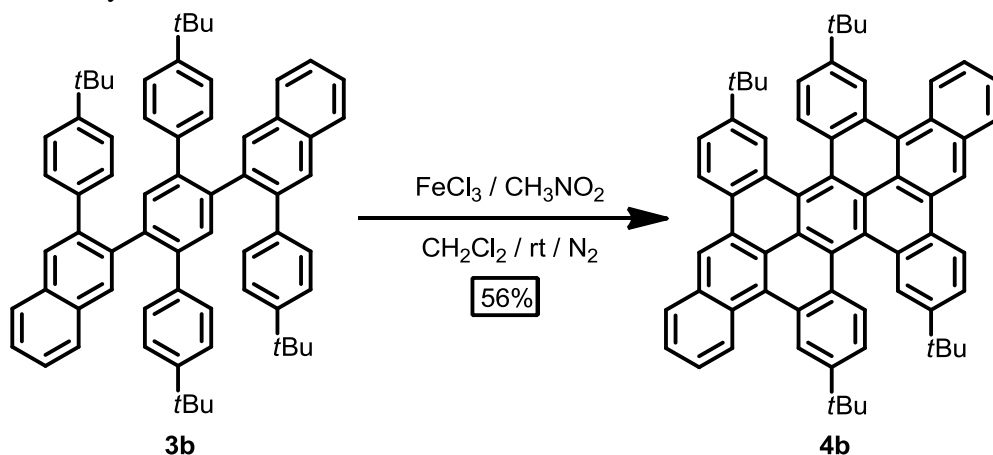
**Synthesis of 3d:** **3d** was synthesized using a similar procedure that was used to prepare **3a**. **1d** (0.180 g, 0.332 mmol), benzaldehyde **2** (0.205 g, 1.00 mmol),  $\text{Cu}(\text{OTf})_2$  (12 mg, 0.033 mmol),  $\text{CF}_3\text{CO}_2\text{H}$  (0.08 mL, 1.00 mmol) 1,2-dichloroethane (8.3 mL) were used. After purification by flash column chromatography ( $\text{SiO}_2$ , 2% v/v EtOAc/hexanes), **3d** was isolated as a white powder (0.201g, 81% yield). **3d**:  $^1\text{H}$  NMR (400 MHz,  $\text{CDCl}_3$ )  $\delta$  8.07 (s, 2H), 7.87 (dd,  $J = 6.1, 3.3$  Hz, 4H), 7.65 (s, 2H), 7.54 (s, 2H), 7.51 (dd,  $J = 6.1, 3.3$  Hz, 4H), 7.18 (t,  $J = 7.3$  Hz, 2H), 7.11 (t,  $J = 7.5$  Hz, 4H), 6.97 (d,  $J = 8.2$  Hz, 4H), 6.71 (d,  $J = 7.3$  Hz, 4H), 6.57 (d,  $J = 8.2$  Hz, 4H), 1.30 (s, 18H).  $^{13}\text{C}$  NMR (100 MHz,  $\text{CDCl}_3$ )  $\delta$  149.03, 141.01, 139.89, 139.55, 139.23, 139.08, 137.40, 133.81, 133.03, 132.93, 130.58, 129.21, 128.86, 128.69, 127.90, 127.75, 127.42, 126.19, 126.11, 124.70, 34.48, 31.48. IR (solid, ATR) 3056, 3029, 2900, 2864, 1490, 1477, 1459, 1437, 1372, 1363, 1270, 1027, 1113, 1011, 950, 915, 888, 835, 797, 772, 756, 745, 720, 696, 668  $\text{cm}^{-1}$ . HRMS (EI,  $m/z$ ): calcd for  $[\text{C}_{58}\text{H}_{50}]^+$  746.3913, found 746.3921.

**Scheme A2.21.** Synthesis of **4a**.



**Synthesis of 4a:** **3a** (0.100 g, 0.113 mmol) was dissolved in CH<sub>2</sub>Cl<sub>2</sub> (55.0 mL) under N<sub>2</sub> at rt. FeCl<sub>3</sub> (0.548 g, 3.381 mmol) dissolved in CH<sub>3</sub>NO<sub>2</sub> (5.0 mL) was added dropwise over 6 min, while the solution was bubbled with N<sub>2</sub>. Vigorous N<sub>2</sub> flow through the solution was maintained for 20 min, after which the reaction mixture was poured into a separatory funnel that contained H<sub>2</sub>O (100 mL). The organic phase was separated and the aqueous phase was washed with CH<sub>2</sub>Cl<sub>2</sub> (3 x 50 mL). The combined organic phases were dried (MgSO<sub>4</sub>), filtered, and the solvent was removed. Purification by chromatography (SiO<sub>2</sub>, 1:8 v/v CH<sub>2</sub>Cl<sub>2</sub>/hexanes) provided **4a** (0.032 g, 32% yield) as an orange solid. **4a**: <sup>1</sup>H NMR (500 MHz, CDCl<sub>3</sub>) δ 9.36 (s, 2H), 9.35 (d, *J* = 8.4 Hz, 2H), 8.96 (dd, *J* = 8.5, 1.2 Hz, 2H), 8.90 (dd, *J* = 8.2, 1.2 Hz, 2H), 8.68 (d, *J* = 1.8 Hz, 2H), 8.51 (d, *J* = 8.5 Hz, 2H), 8.40 (dd, *J* = 7.8, 1.6 Hz, 2H), 7.88 – 7.73 (m, 4H), 7.62 (ddd, *J* = 8.2, 6.8, 1.3 Hz, 2H), 7.38 (ddd, *J* = 8.1, 6.8, 1.2 Hz, 2H), 7.13 (dd, *J* = 8.5, 1.8 Hz, 2H), 2.78 (td, *J* = 7.3, 5.1 Hz, 4H), 1.69 (p, *J* = 7.6 Hz, 4H), 1.47 – 1.12 (m, 24H), 0.89 – 0.81 (m, 6H). <sup>13</sup>C NMR (125 MHz, CDCl<sub>3</sub>) δ 141.23, 133.01, 131.55, 131.27, 130.95, 130.74, 130.34, 129.10, 129.10, 128.87, 128.39, 128.28, 128.02, 127.67, 126.92, 126.56, 126.04, 125.91, 125.82, 124.68, 124.39, 124.13, 121.94, 121.36, 36.37, 32.03, 31.54, 29.72, 29.69, 29.54, 29.47, 22.80, 14.25. IR (solid, ATR) 3050, 2920, 2850, 1606, 1464, 1354, 1154, 904, 878, 834, 810, 785, 759, 744, 715 cm<sup>-1</sup>. HRMS (MALDI-TOF, *m/z*): calcd for [C<sub>68</sub>H<sub>62</sub>]<sup>+</sup> 878.4846, found 878.487.

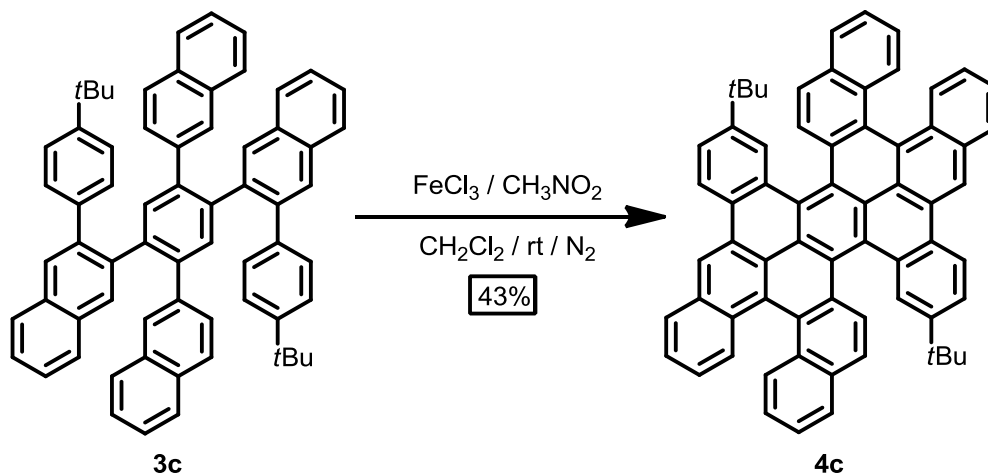
**Scheme A2.22. Synthesis of 4b.**



**Synthesis of 4b:** **4b** was synthesized using a similar procedure that was used to prepare **4a**. **3b** (0.076 g, 0.089 mmol), FeCl<sub>3</sub> (0.433 g, 2.671 mmol), CH<sub>2</sub>Cl<sub>2</sub> (45 mL) and CH<sub>3</sub>NO<sub>2</sub> (4.5 mL) were used. The reaction mixture was stirred for 20 min before workup. Purification of the crude product by chromatography (SiO<sub>2</sub>, 1:8 v/v CH<sub>2</sub>Cl<sub>2</sub>/hexanes) provided **4b** (0.043 g, 56% yield) as an orange solid. **4b**: <sup>1</sup>H NMR (400 MHz, CDCl<sub>3</sub>) δ 9.42 (d, *J* = 8.5 Hz, 2H), 9.35 (s, 2H), 9.00 (dd, *J* = 15.6, 1.9 Hz, 4H), 8.85 (d, *J* = 8.8 Hz, 2H), 8.51 (d, *J* = 8.7 Hz, 2H), 8.40 (d, *J* = 7.4 Hz, 2H), 7.85 (ddd, *J* = 8.4, 6.7, 1.3 Hz, 2H), 7.78 (ddd, *J* = 8.4, 6.7, 1.3 Hz, 2H), 7.69 (dd, *J* = 8.6, 2.0 Hz, 2H), 7.37 (dd, *J* = 8.7, 2.0 Hz, 2H), 1.46 (s, 18H), 1.25 (s, 18H). <sup>13</sup>C NMR (100 MHz, CDCl<sub>3</sub>) δ 149.19, 148.80, 133.09, 131.13, 130.94, 130.04, 129.07, 128.72, 128.62, 128.59,

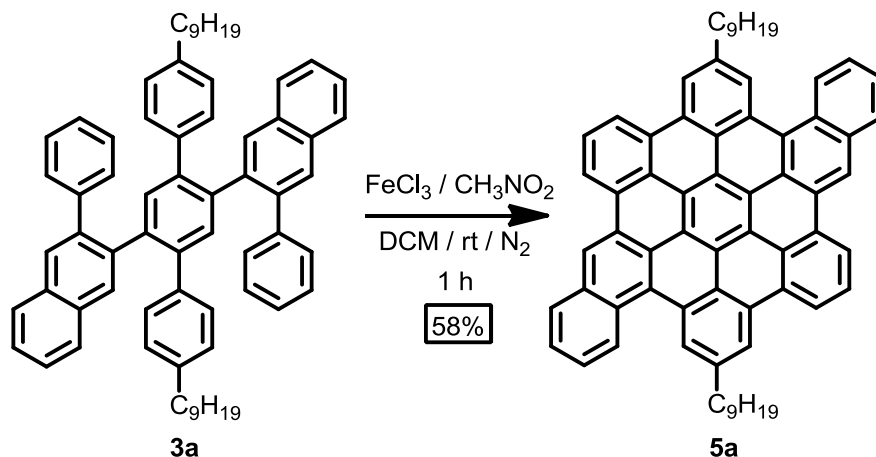
128.57, 128.27, 128.13, 128.04, 125.94, 125.89, 125.53, 125.45, 125.31, 124.92, 124.60, 123.78, 123.68, 121.64, 121.49, 35.26, 34.83, 31.44, 31.09. IR (solid, ATR) 3050, 2962, 2902, 2867, 1608, 1489, 1476, 1465, 1457, 1393, 1369, 1264, 902, 881, 824, 748  $\text{cm}^{-1}$ . HRMS (MALDI-TOF,  $m/z$ ): calcd for  $[\text{C}_{66}\text{H}_{58}]^+$  850.4533, found 850.447.

**Scheme A2.23.** Synthesis of **4c**.



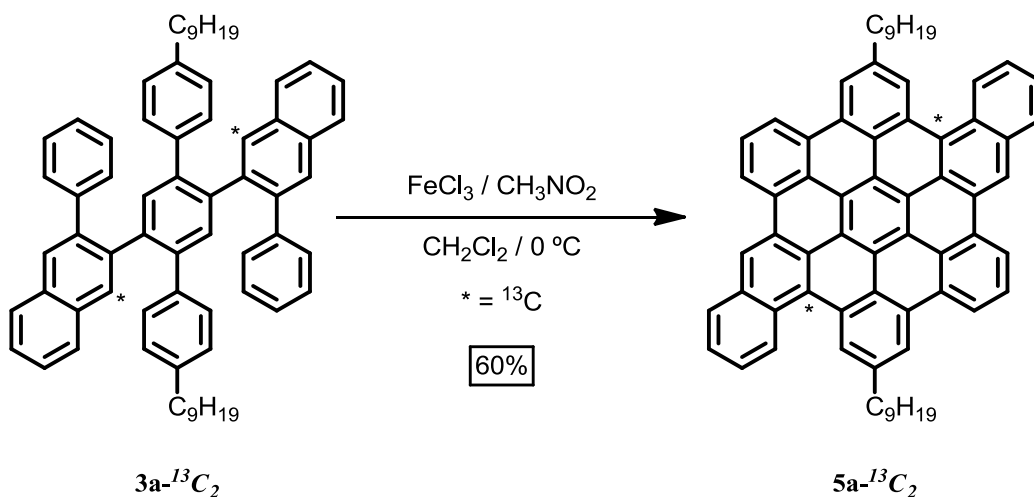
**Synthesis of 4c:** **4c** was synthesized using a similar procedure that was used to prepare **4a**. **3c** (0.180 g, 0.212 mmol),  $\text{FeCl}_3$  (0.620 g, 3.825 mmol),  $\text{CH}_2\text{Cl}_2$  (21 mL) and  $\text{CH}_3\text{NO}_2$  (4.0 mL) were used. The reaction mixture was stirred for 45 min before workup. Purification of the crude product by chromatography ( $\text{SiO}_2$ , 5% v/v EtOAc/hexanes) provided **4c** (0.076 g, 43% yield) as a red solid. **4c**:  $^1\text{H}$  NMR (500 MHz,  $\text{CDCl}_3$ )  $\delta$  9.42 (s, 2H), 9.18 (d,  $J = 2.0$  Hz, 2H), 8.96 (d,  $J = 8.6$  Hz, 2H), 8.69 (dd,  $J = 8.7, 3.5$  Hz, 4H), 8.38 (d,  $J = 8.1$  Hz, 2H), 8.15 (d,  $J = 8.6$  Hz, 2H), 7.85 – 7.79 (m, 2H), 7.77 (dd,  $J = 8.5, 2.1$  Hz, 2H), 7.72 (d,  $J = 8.7$  Hz, 4H), 7.52 (ddd,  $J = 8.3, 6.7, 1.4$  Hz, 2H), 7.47 – 7.38 (m, 2H), 7.22 (ddd,  $J = 8.5, 6.7, 1.4$  Hz, 2H), 1.28 (s, 18H).  $^{13}\text{C}$  NMR (126 MHz,  $\text{CDCl}_3$ )  $\delta$  149.29, 132.89, 132.16, 131.90, 130.91, 129.83, 129.65, 129.61, 129.58, 129.53, 128.65, 128.44, 128.41, 128.26, 128.23, 128.18, 128.04, 128.01, 127.69, 127.59, 127.54, 127.52, 127.21, 126.23, 126.21, 126.17, 126.16, 126.12, 125.82, 125.48, 125.07, 124.64, 124.29, 123.86, 123.68, 123.66, 122.81, 122.25, 77.41, 77.36, 77.16, 76.90, 35.07, 35.06, 31.35, 31.23, 31.22, 31.18, 31.16, 31.13, 30.80, 29.87, 0.17. IR (solid, ATR) 3064, 2959, 2925, 2859, 1735, 1507, 1455, 1361, 1261, 822, 753  $\text{cm}^{-1}$ . HRMS (MALDI-TOF,  $m/z$ ): calcd for  $[\text{C}_{66}\text{H}_{46}]^+$  838.3594, found 838.351.

**Scheme A2.24.** Synthesis of **5a**.



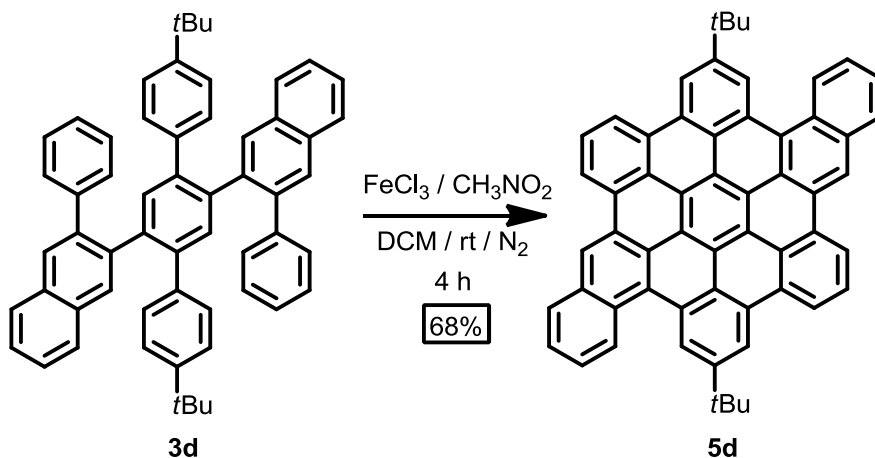
**Synthesis of 5a:** **3a** (0.100 g, 0.113 mmol) was dissolved in  $\text{CH}_2\text{Cl}_2$  (11.3 mL) under  $\text{N}_2$ .  $\text{FeCl}_3$  (0.329 g, 2.029 mmol) dissolved in  $\text{CH}_3\text{NO}_2$  (2 mL) was added dropwise over 5 min. The solution was stirred at rt, during which time product formation was monitored by MALDI-TOF mass spectrometry. After the reaction was complete (1 h), the reaction mixture was poured into MeOH (50 mL), forming a precipitate. The precipitate was recovered by filtration and washed with additional MeOH (100 mL) to give **5a** (0.057 g, 58% yield) as a yellow-brown powder. **5a:**  $^1\text{H}$  NMR (400 MHz,  $1,2\text{-CD}_2\text{Cl}_2$ )  $\delta$  9.22-8.68 (m, 10H), 8.16-8.07 (m, 2H), 7.92-7.80 (m, 2H), 7.63-7.47 (m, 6H), 3.05 (m, 4H), 1.89 (m, 4H), 1.45-0.46 (m, 30H).  $^{13}\text{C}$  NMR (75 MHz, 2:1  $\text{CS}_2:\text{CD}_2\text{Cl}_2$ )  $\delta$  130.3-118.3 (br) 32.9, 30.6, 30.4, 27.1, 23.8, 15.0. IR (solid, ATR) 3049, 2951, 2920, 2850, 1933, 1671, 1599, 1489, 1456, 1376, 1321, 1260, 1027, 908, 878, 847, 823, 746, 722, 699, 669, 653  $\text{cm}^{-1}$ . HRMS (EI,  $m/z$ ): calcd for  $[\text{C}_{68}\text{H}_{58}]^+$  874.4539, found 874.4519.

**Scheme A2.25.** Synthesis of **5a- $^{13}\text{C}_2$** .



**Synthesis of 5a-<sup>13</sup>C<sub>2</sub>:** 5a-<sup>13</sup>C<sub>2</sub> was synthesized using a similar procedure as that used to prepare 5a. 5a-<sup>13</sup>C<sub>2</sub> (0.025g 0.028 mmol), FeCl<sub>3</sub> (0.137 g, 0.843 mmol), CH<sub>3</sub>NO<sub>2</sub> (1 mL), 1,2-dichloroethane (14 mL). 5a-<sup>13</sup>C<sub>2</sub> was isolated as an orange solid (0.015 g, 60% yield). <sup>1</sup>H NMR (500 MHz, C<sub>2</sub>D<sub>2</sub>Cl<sub>4</sub>, 135 °C) δ (ppm) 9.21 (d, *J* = 7.4 Hz, 1H), 9.16 (s, 1H), 9.01 (s, 1H), 8.95 (d, *J* = 7.2 Hz, 1H), 8.87 (d, *J* = 7.7 Hz, 1H), 8.33 (d, *J* = 7.4 Hz, 1H), 7.98 (t, *J* = 7.7 Hz, 1H), 7.79 (m, 2H), 3.19 (t, *J* = 7.8 Hz, 2H), 2.10 (t, *J* = 7.5 Hz, 2H), 1.76 – 1.70 (m, 2H), 1.66 – 1.59 (m, 2H), 1.57 – 1.33 (m, 8H), 0.99 (t, *J* = 6.9 Hz, 3H). <sup>13</sup>C NMR (125 MHz, C<sub>2</sub>D<sub>2</sub>Cl<sub>4</sub>, 135 °C) δ (ppm) 126.47 (s). HRMS (MALDI-TOF, *m/z*): calcd for [C<sub>66</sub>H<sub>58</sub><sup>13</sup>C<sub>2</sub>]<sup>+</sup> 876.4539, found 876.461.

**Scheme A2.26.** Synthesis of 5d



**Synthesis of 5d:** The compound **5d** was synthesized using a similar procedure used to prepare 5a. **3d** (0.048 g, 0.064 mmol), FeCl<sub>3</sub> (0.188 g, 1.157 mmol), CH<sub>2</sub>Cl<sub>2</sub> (6.0 mL) and CH<sub>3</sub>NO<sub>2</sub> (1.0 mL) were used. The reaction mixture was stirred for 4 h before precipitation using MeOH. Upon filtration **5d** (0.032 g, 68% yield) was isolated as an orange solid. NMR characterization attempts were not successful due to low solubility of the compound. **5d**: IR (solid, ATR) 3054, 2952, 2865, 1598, 1583, 1475, 1464, 1391, 1361, 1279, 1252, 1199, 908, 876, 823, 748, 723, 696 cm<sup>-1</sup>. HRMS (MALDI-TOF, *m/z*): calcd for [C<sub>66</sub>H<sub>54</sub>]<sup>+</sup> 734.2968, found 734.302.



### C. NMR Spectra

**Figure A2.1.**  $^1\text{H}$  NMR of **S2** (300 MHz,  $\text{CDCl}_3$ , 300 K).

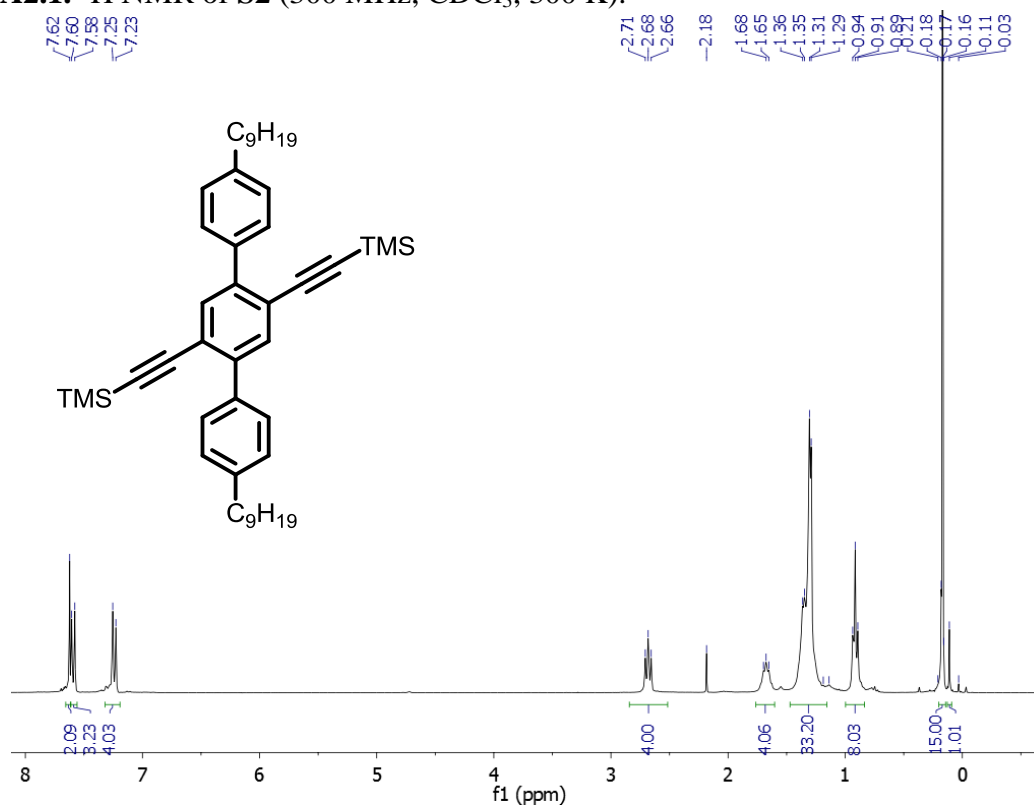


**Figure A2.2.**  $^{13}\text{C}$  NMR of **S2** (75 MHz,  $\text{CDCl}_3$ , 300 K).

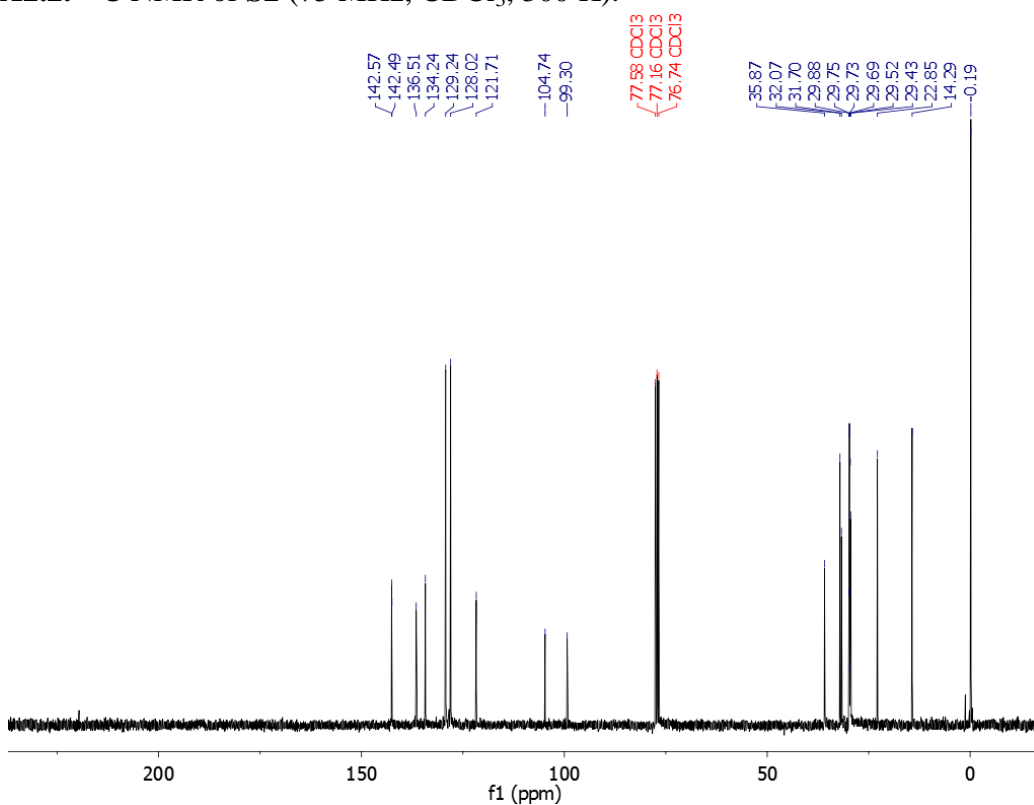


**Figure A2.3.**  $^1\text{H}$  NMR of **S3** (300 MHz,  $\text{CDCl}_3$ , 300 K).

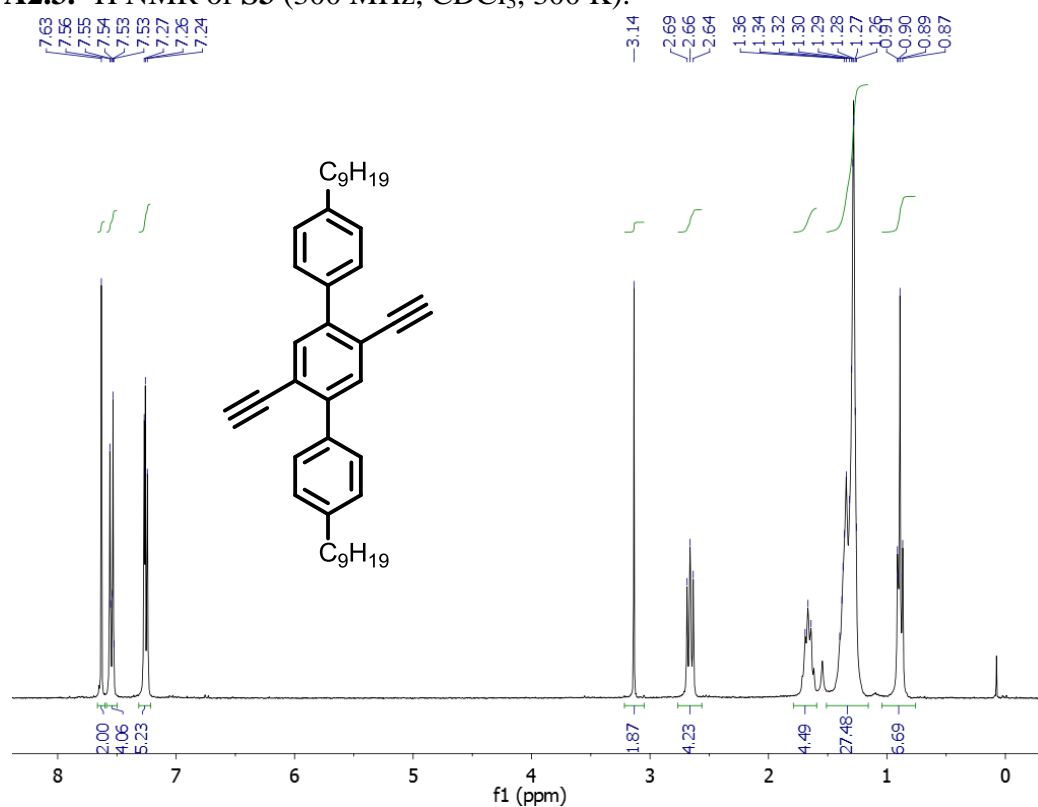


**Figure A2.4.**  $^{13}\text{C}$  NMR of **S3** (75 MHz,  $\text{CDCl}_3$ , 300 K).

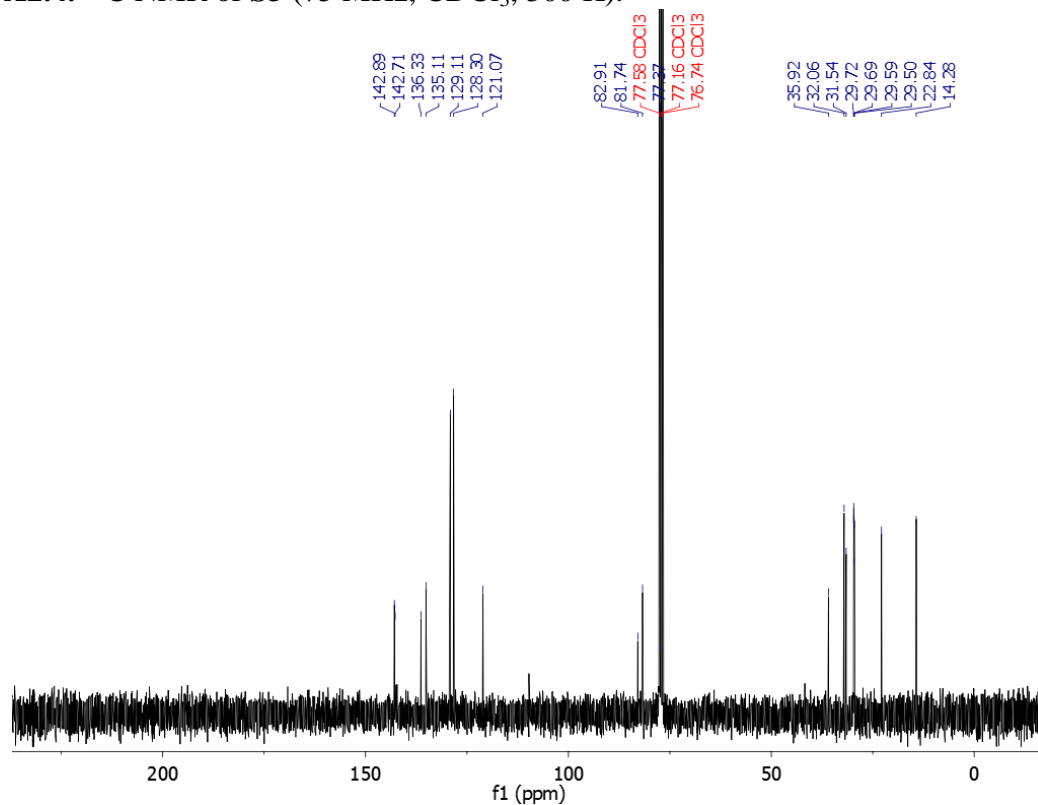


**Figure A2.5.**  $^1\text{H}$  NMR of **1a** (400 MHz,  $\text{CDCl}_3$ , 298 K).

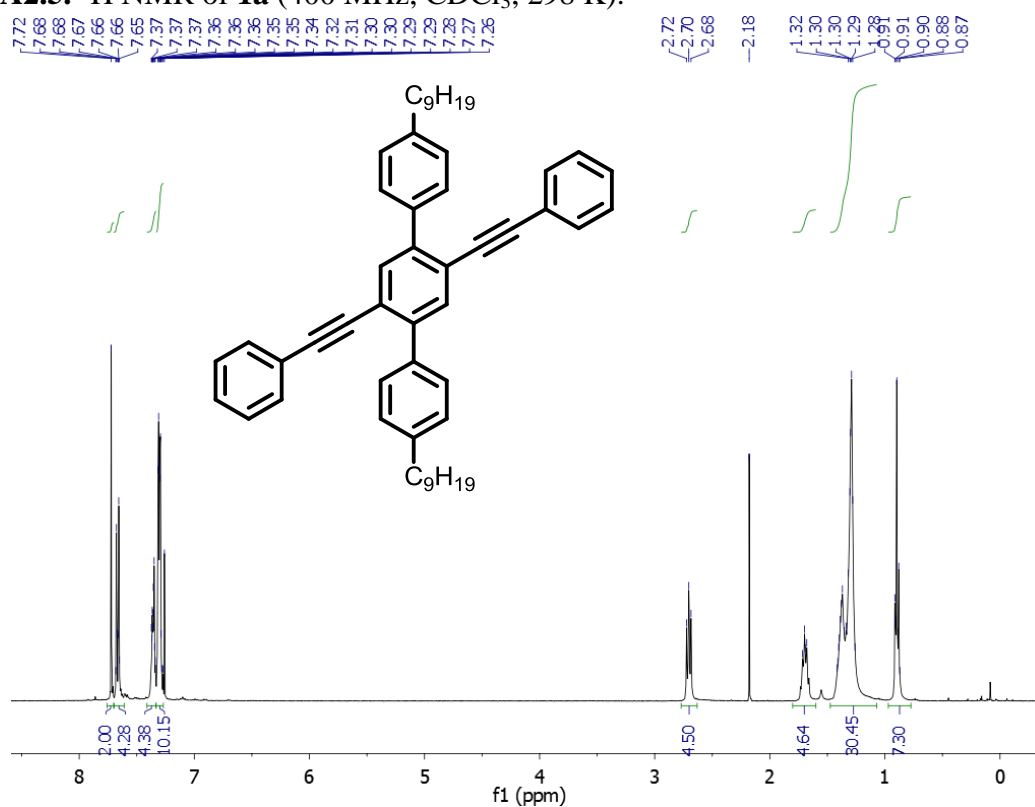


**Figure A2.6.**  $^{13}\text{C}$  NMR of **1a** (100 MHz,  $\text{CDCl}_3$ , 298 K).

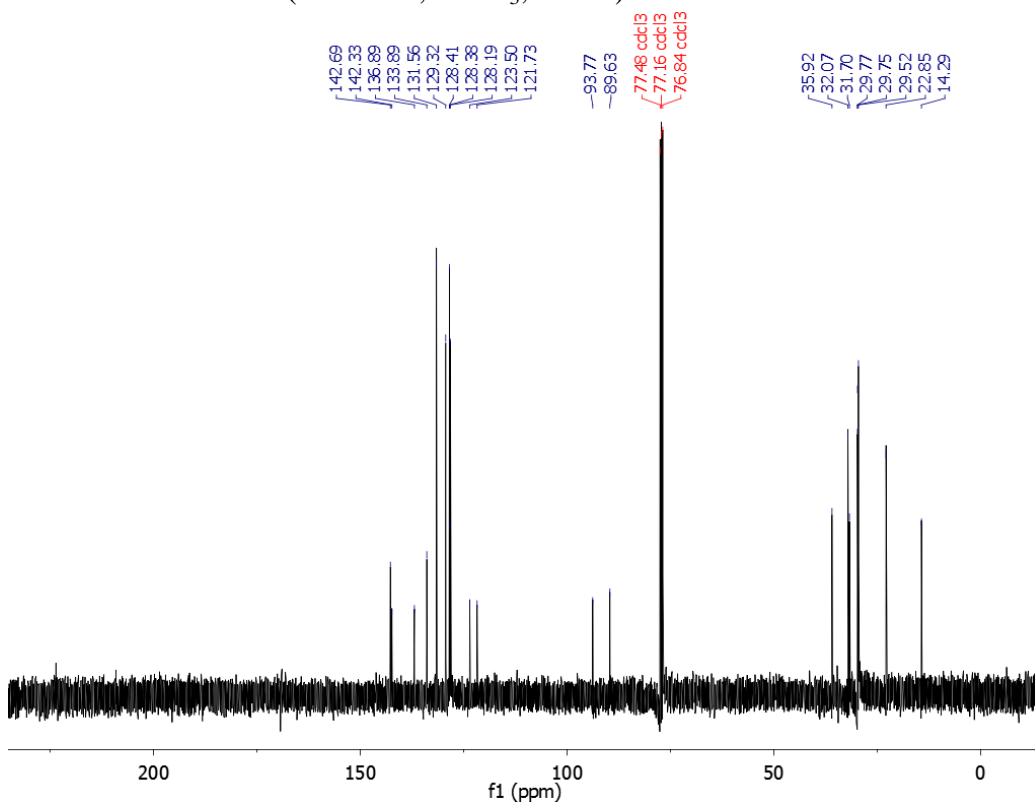


**Figure A2.7.**  $^1\text{H}$  NMR of **S4** (300 MHz,  $\text{CDCl}_3$ , 298 K).

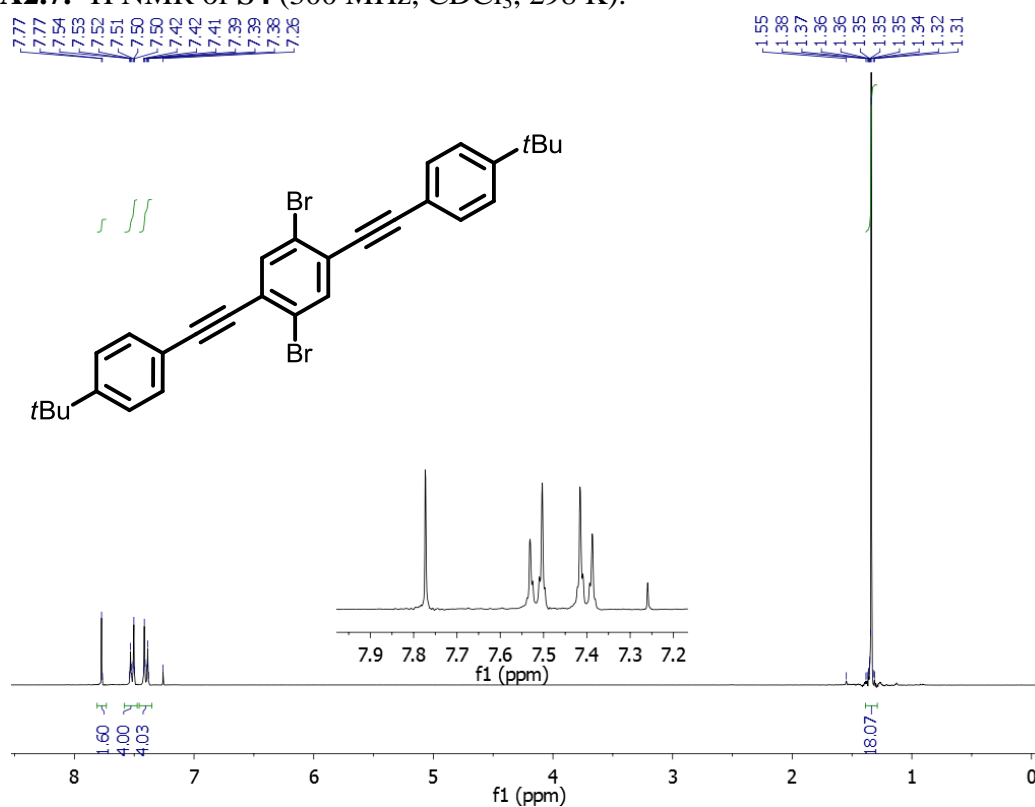


**Figure A2.8.**  $^{13}\text{C}$  NMR of **S4** (75 MHz,  $\text{CDCl}_3$ , 298 K).

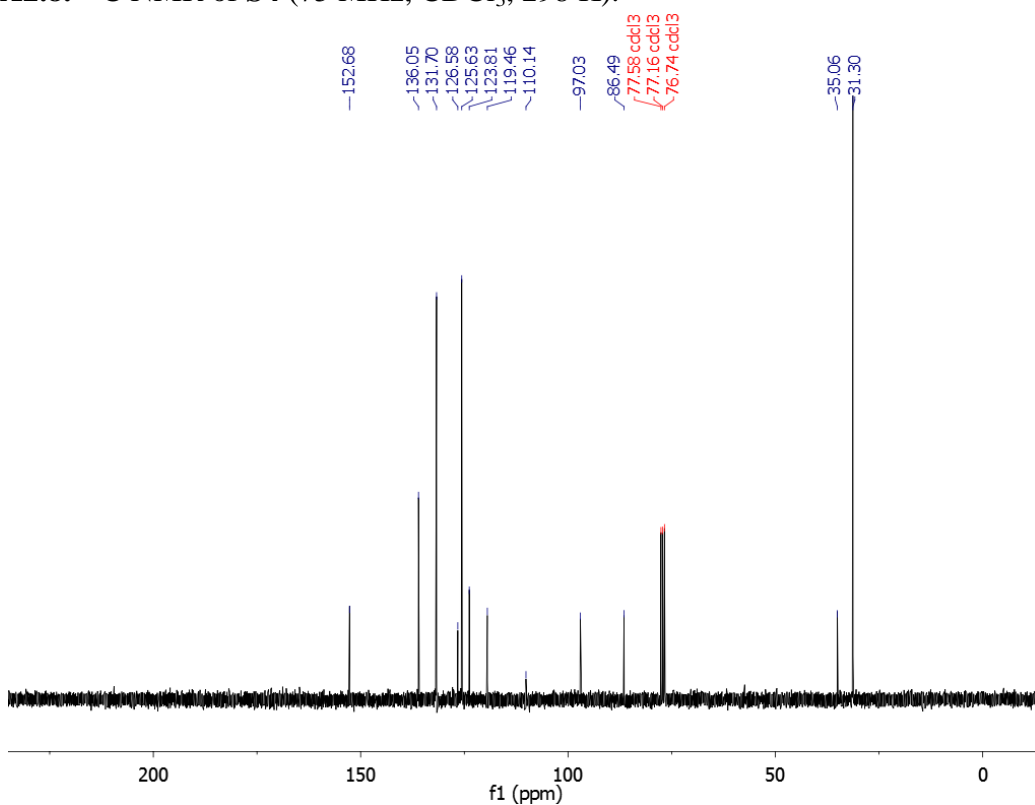


**Figure A2.9.**  $^1\text{H}$  NMR of **1b** (300 MHz,  $\text{CDCl}_3$ , 300 K).

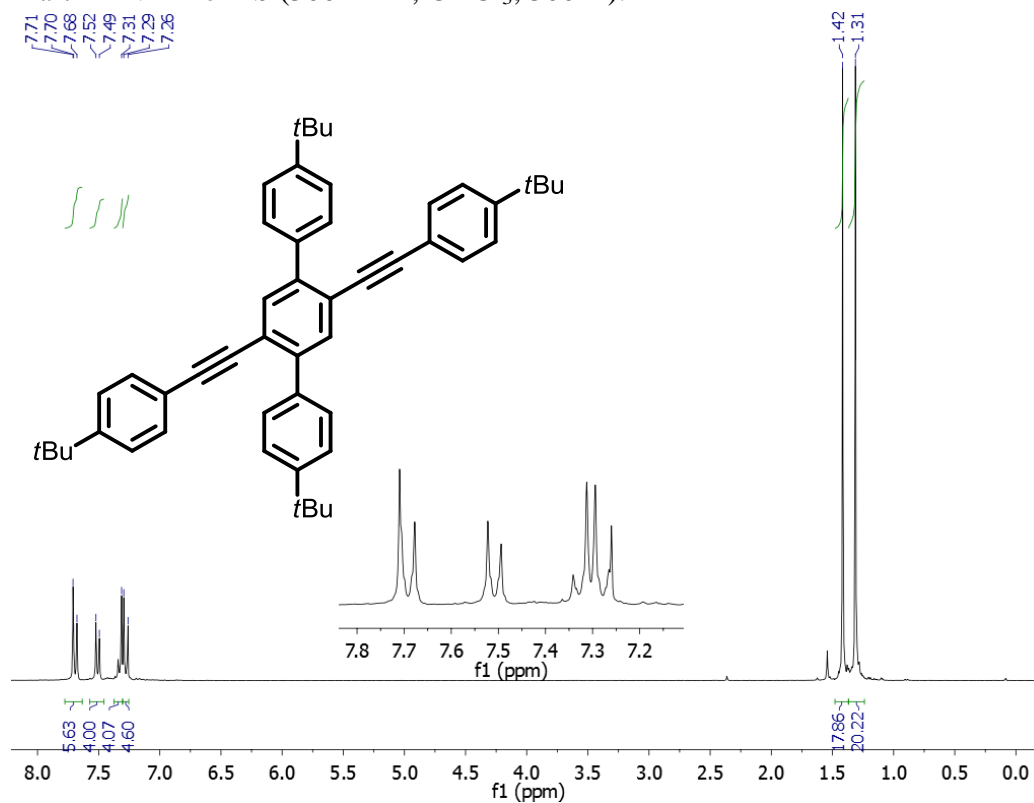


**Figure A2.10.**  $^{13}\text{C}$  NMR of **1b** (75 MHz,  $\text{CDCl}_3$ , 300 K).

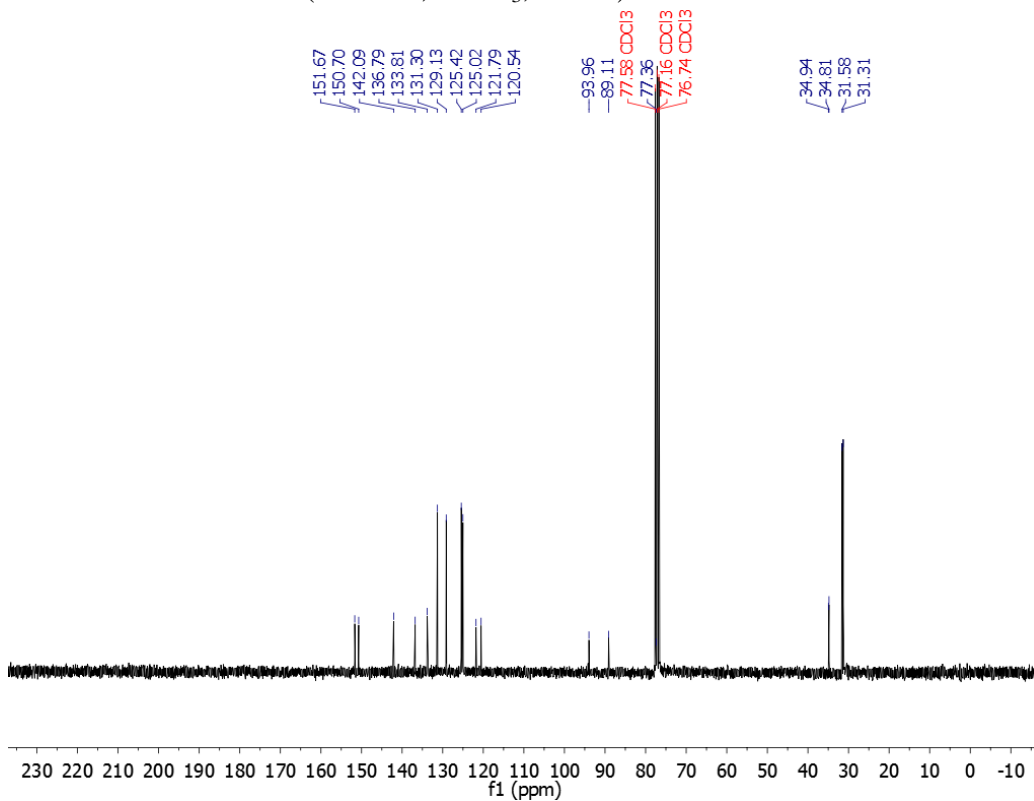


**Figure A2.11.**  $^1\text{H}$  NMR of **1c** (500 MHz,  $\text{CDCl}_3$ , 328 K).

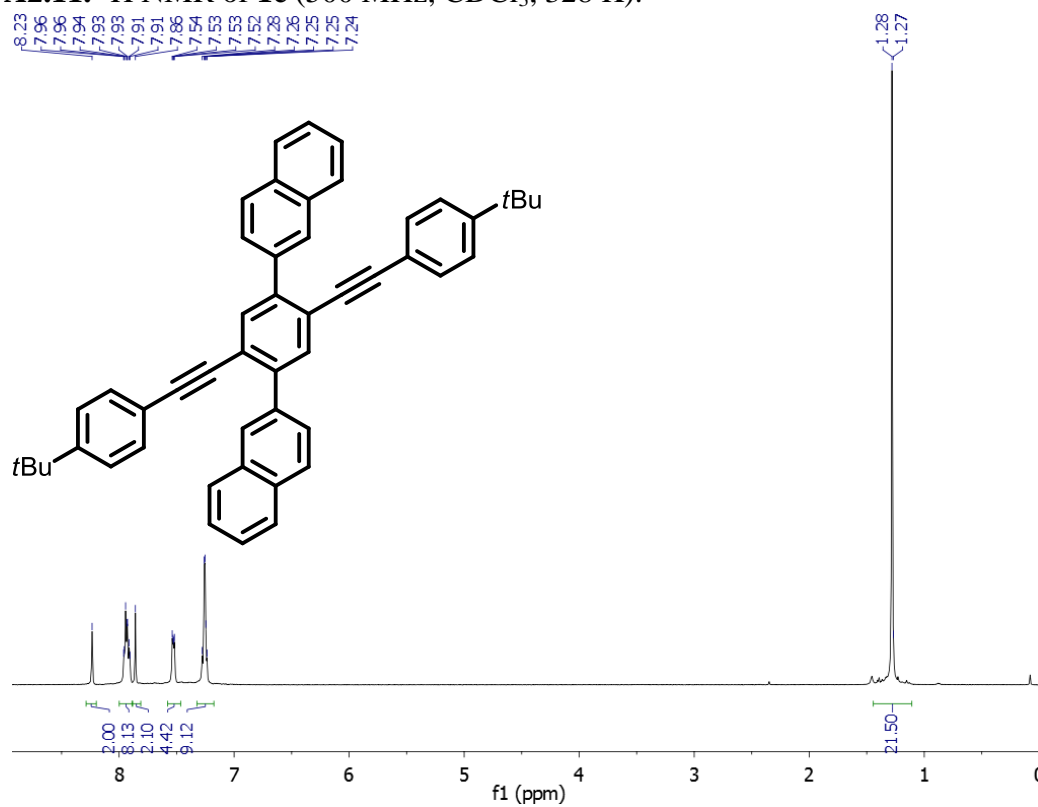


**Figure A2.12.**  $^{13}\text{C}$  NMR of **1c** (125 MHz,  $\text{CDCl}_3$ , 328 K).

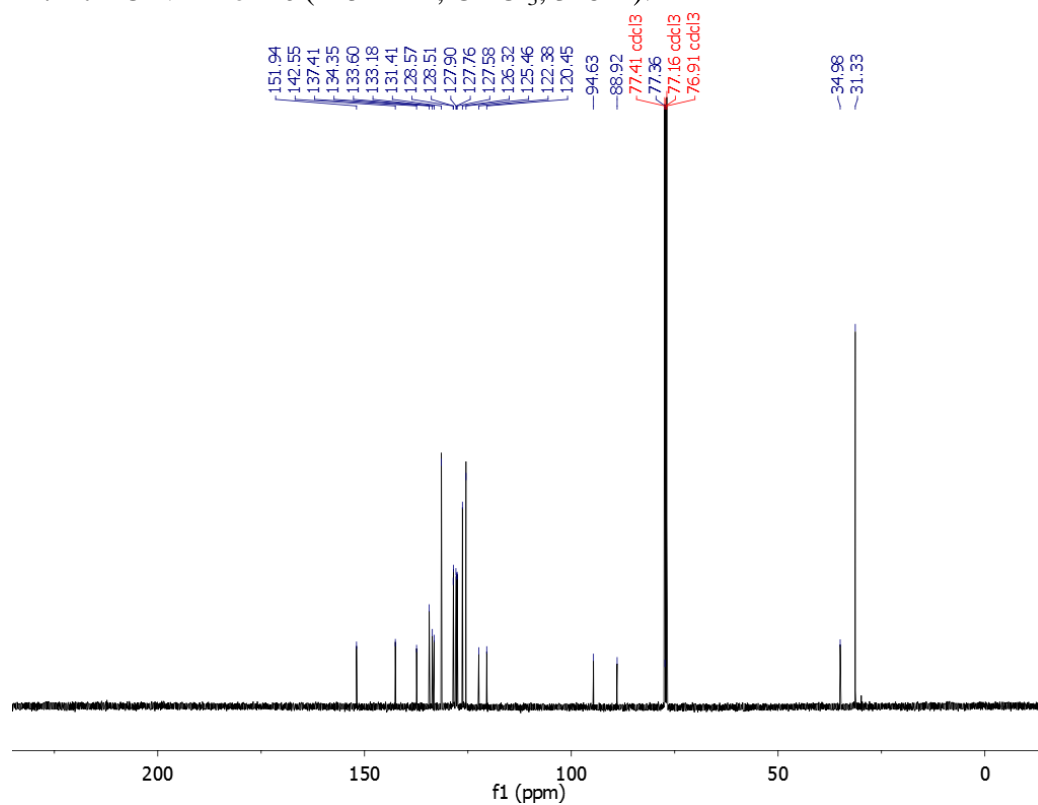


**Figure A2.13.**  $^1\text{H}$  NMR of **S5** (400 MHz,  $\text{CDCl}_3$ , 297 K).

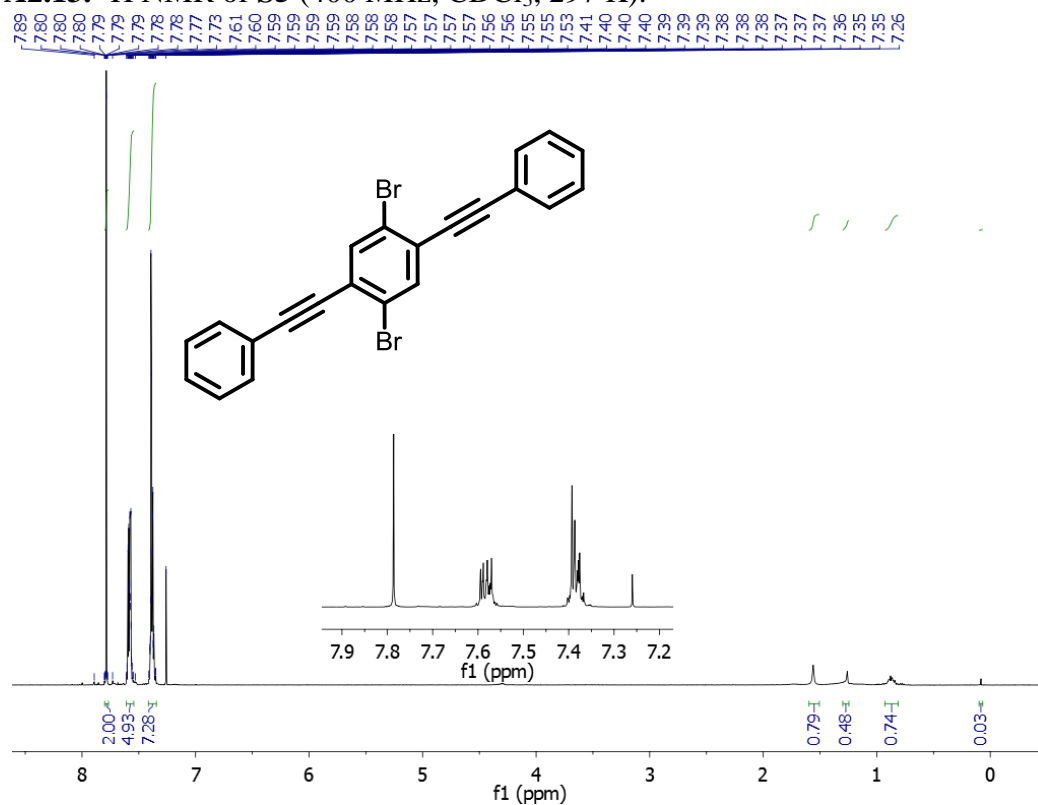


**Figure A2.14.**  $^{13}\text{C}$  NMR of **S5** (100 MHz,  $\text{CDCl}_3$ , 297 K).

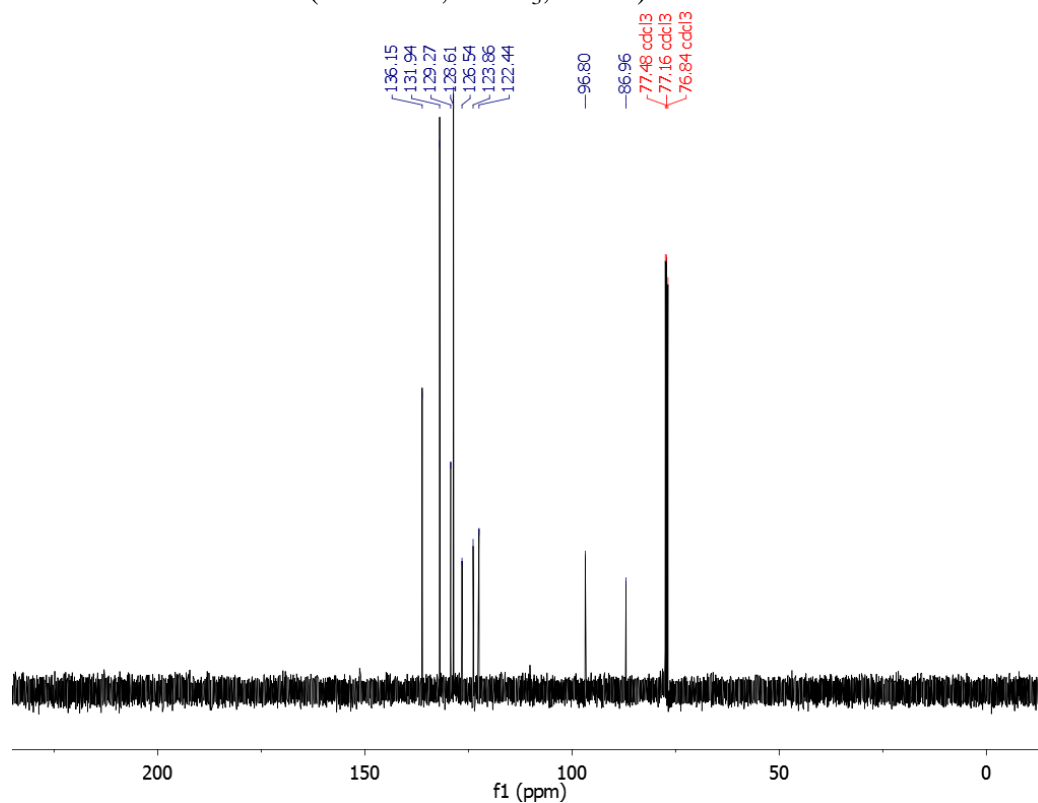


**Figure A2.15.**  $^1\text{H}$  NMR of **1d** (400 MHz,  $\text{CDCl}_3$ , 295 K).

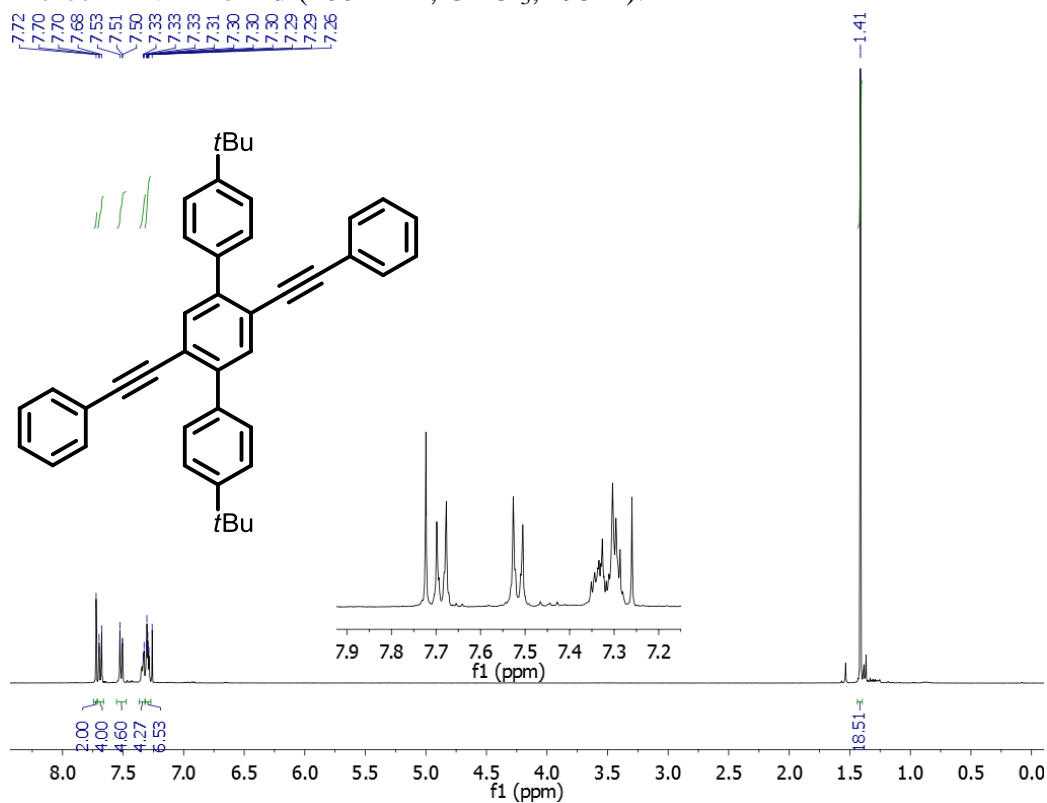
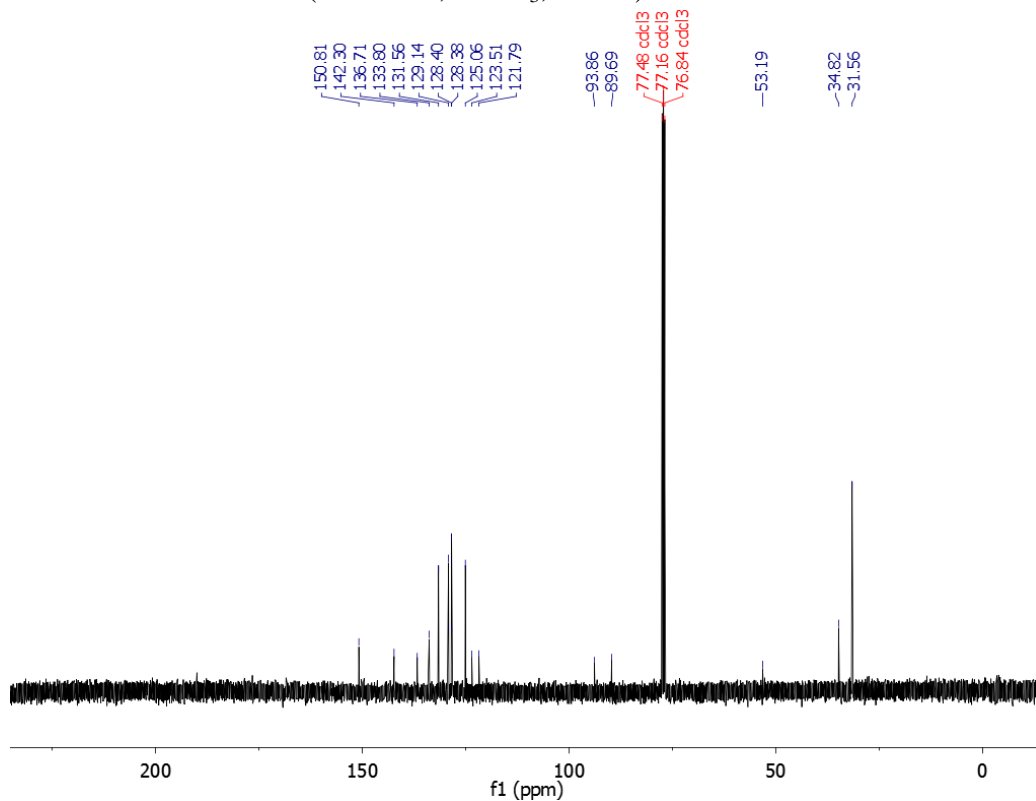


**Figure A2.16.**  $^{13}\text{C}$  NMR of **1d** (100 MHz,  $\text{CDCl}_3$ , 295 K).





Chemical structure: C[Si](C)(C)C#CC1=CC=CC=C1C=O

$^{13}\text{C}$  NMR spectrum (CDCl<sub>3</sub>) peaks (ppm):

- 10.56 (aldehyde)
- 7.92, 7.90, 7.89, 7.87, 7.86, 7.56, 7.55, 7.54, 7.52, 7.46, 7.45, 7.44, 7.44, 7.43, 7.26 (aromatic)
- 0.29 (TMS)
- 0.00 (CDCl<sub>3</sub>)

Integration values:

- 0.89 (aldehyde)
- 0.95, 2.02, 1.00 (aromatic)
- 8.81 (TMS)

Chemical structure of 2-(trimethylsilyl)ethynylbenzaldehyde (TMS-alkyne) is shown. The structure includes a benzene ring with a formyl group (CHO) and a trimethylsilyl (TMS) group. The TMS group is labeled with an asterisk (\*) indicating the  $^{13}\text{C}$  NMR signal. The chemical shift of the TMS group is indicated as  $\delta = 103.41$  ppm.

The  $^{13}\text{C}$  NMR spectrum shows a cluster of peaks between 90 and 110 ppm, corresponding to the alkyne carbons. The chemical shift of the alkyne carbons is indicated as  $\delta = 103.41$  ppm. The spectrum also shows a peak at  $\delta = 77.16$  ppm, which is the solvent peak (CDCl<sub>3</sub>).

Chemical shift values (ppm) are listed above the spectrum:

- 103.41
- 102.06
- 100.69
- 99.34
- 77.48 (odd)
- 77.16 (odd)
- 76.84 (odd)

The x-axis represents the chemical shift in ppm, ranging from -10 to 230.

**Figure A2.19.**  $^1\text{H}$  NMR spectrum of **S7**- $^{13}\text{C}_2$  (400 MHz,  $\text{CDCl}_3$ , 298 K).

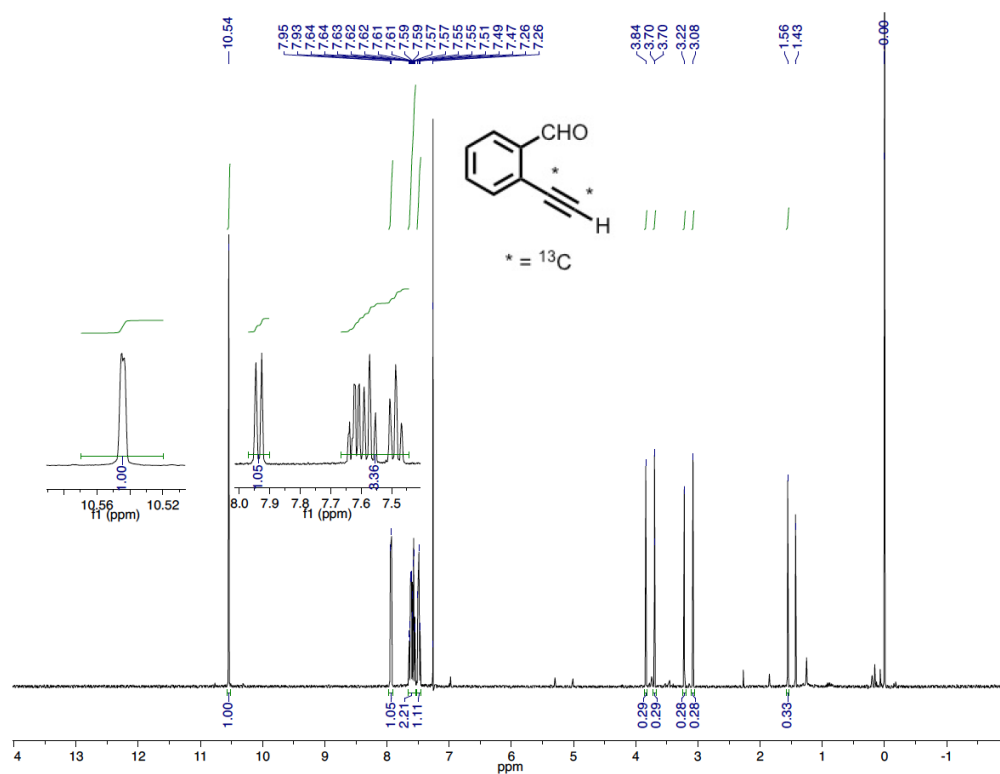


**Figure A2.20.**  $^{13}\text{C}$  NMR spectrum of **S7**- $^{13}\text{C}_2$  (100 MHz,  $\text{CDCl}_3$ , 298 K).

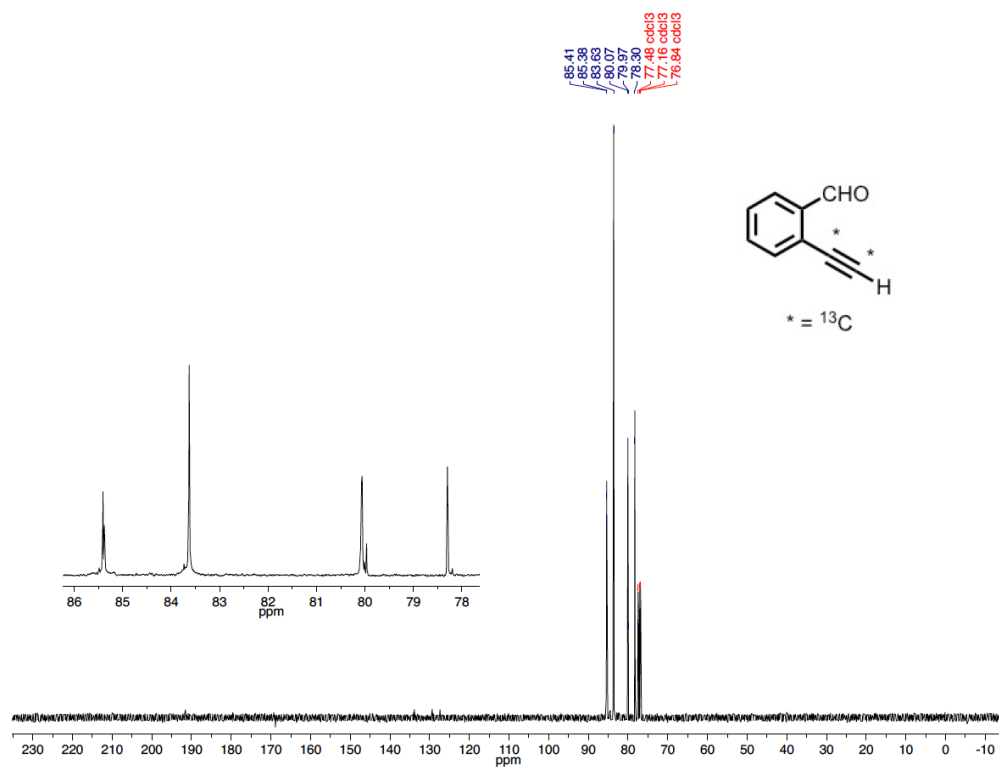


**Figure A2.21.**  $^1\text{H}$  NMR spectrum of **2- $^{13}\text{C}_2$**  (400 MHz,  $\text{CDCl}_3$ , 298 K).

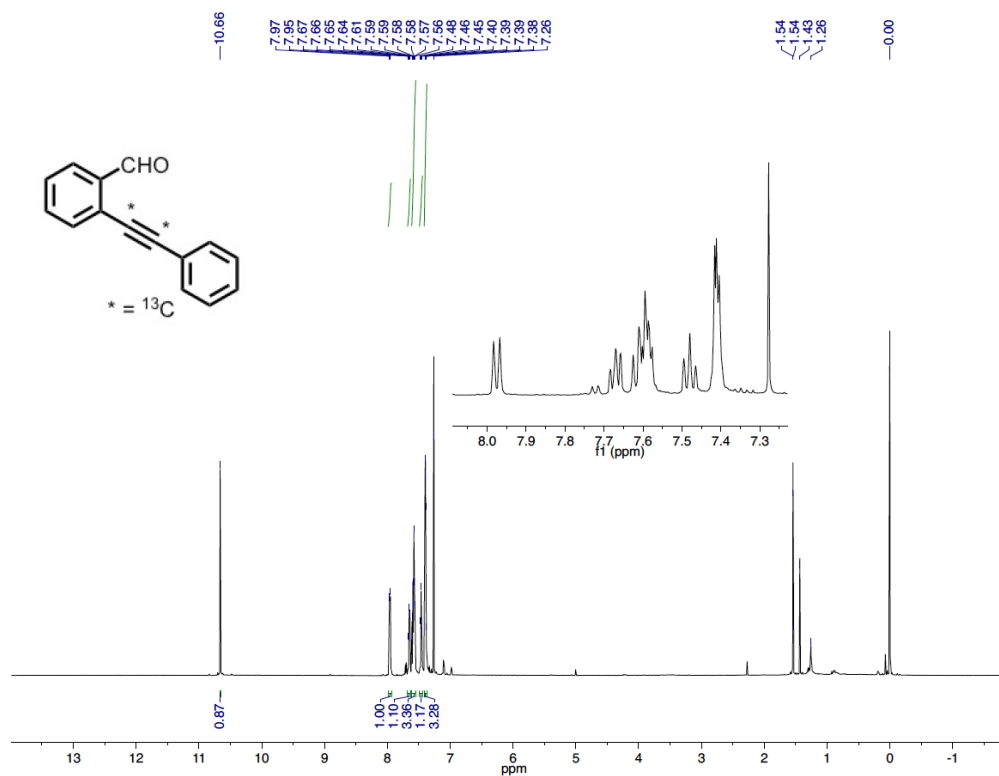


**Figure A2.22.**  $^{13}\text{C}$  NMR spectrum of **2- $^{13}\text{C}_2$**  (100 MHz,  $\text{CDCl}_3$ , 298 K).

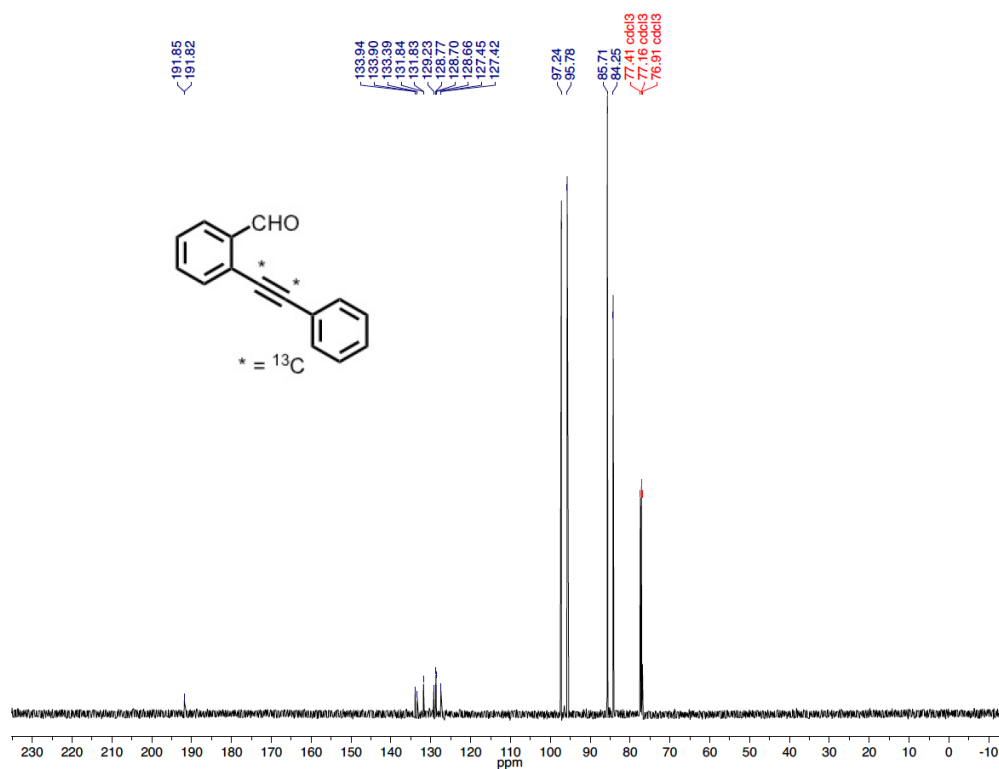


**Figure A2.23.**  $^1\text{H}$  NMR of **3a** (500 MHz,  $\text{CDCl}_3$ , 298 K).

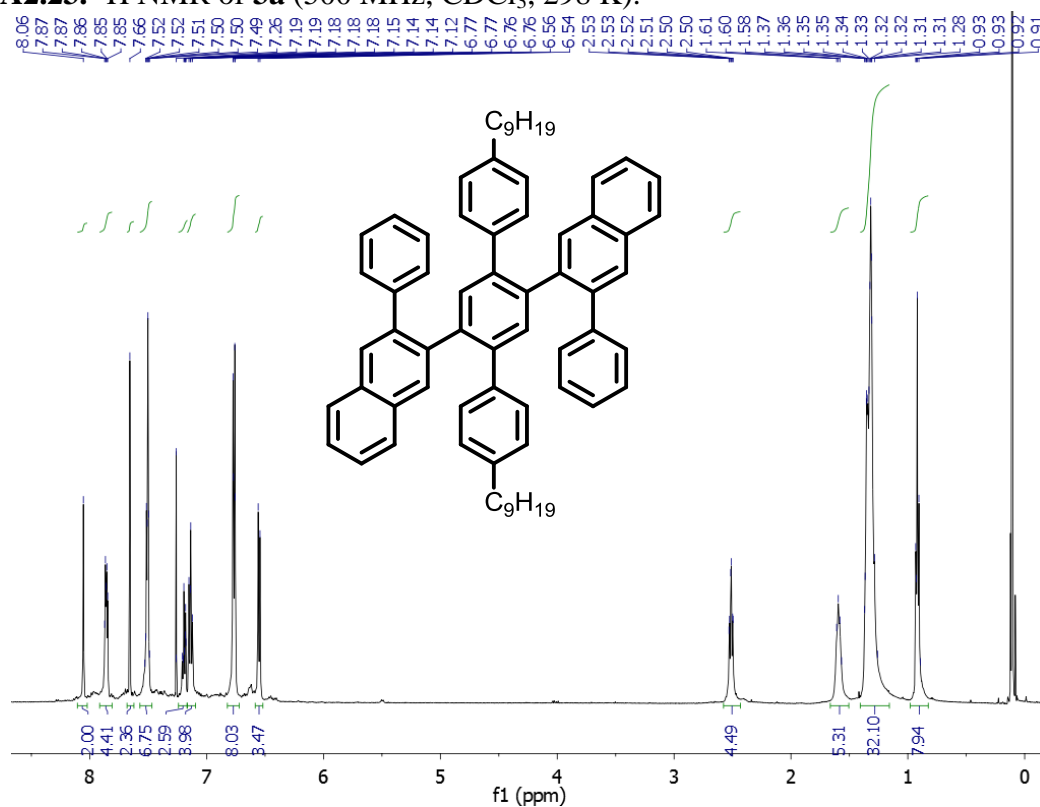


**Figure A2.24.**  $^{13}\text{C}$  NMR of **3a** (125 MHz,  $\text{CDCl}_3$ , 298 K).

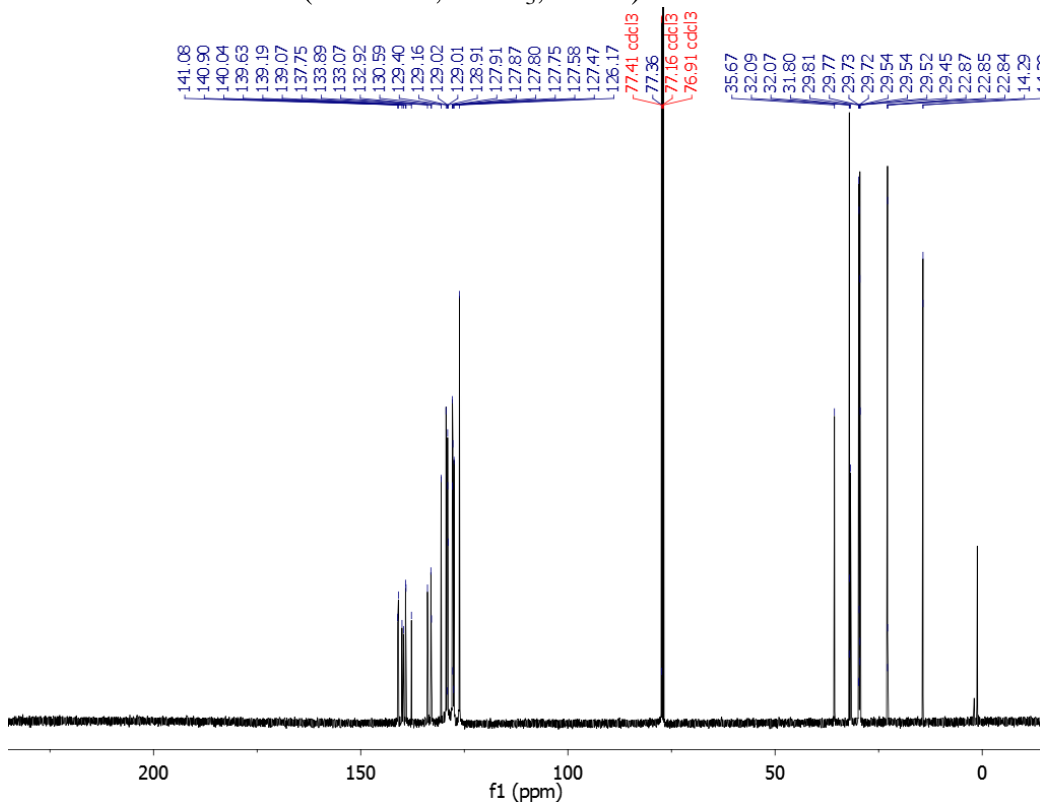


**Figure A2.25.**  $^1\text{H}$  NMR spectrum of **3a**- $^{13}\text{C}_2$  (500 MHz,  $\text{CDCl}_3$ , 298 K).

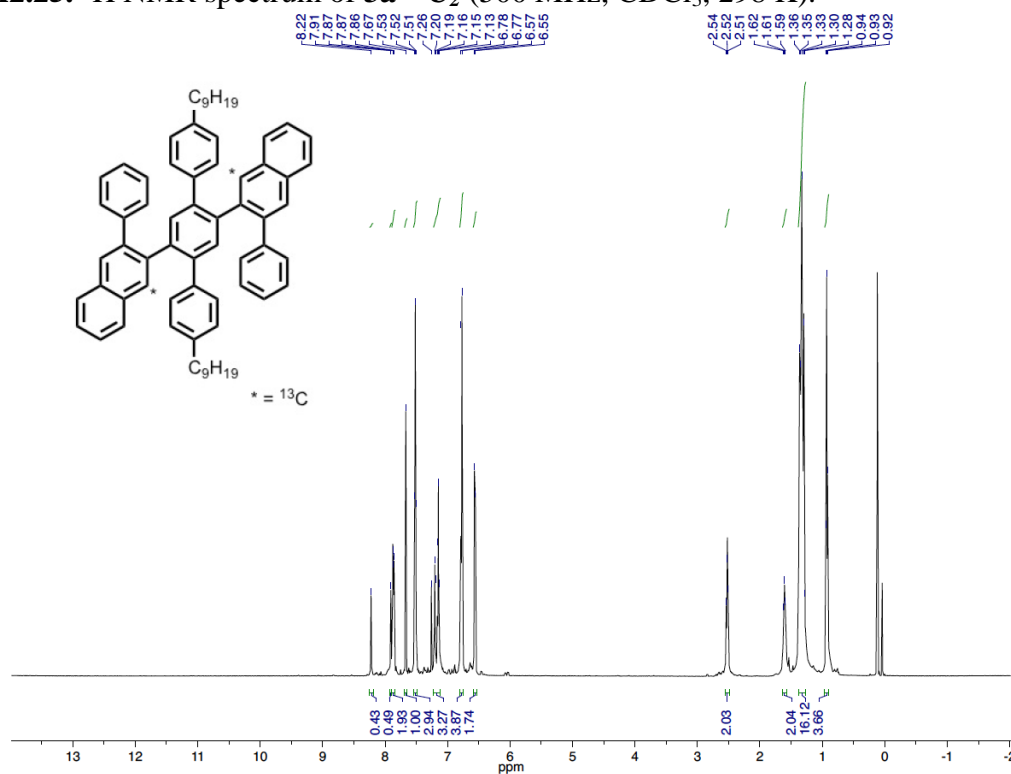


**Figure A2.26.** Partial  $^1\text{H}$  NMR spectra (500 MHz,  $\text{CDCl}_3$ , 298K) of **3a** and **3a**- $^{13}\text{C}_2$  that indicate  $^{13}\text{C}$ - $^1\text{H}$  coupling at the labeled position.

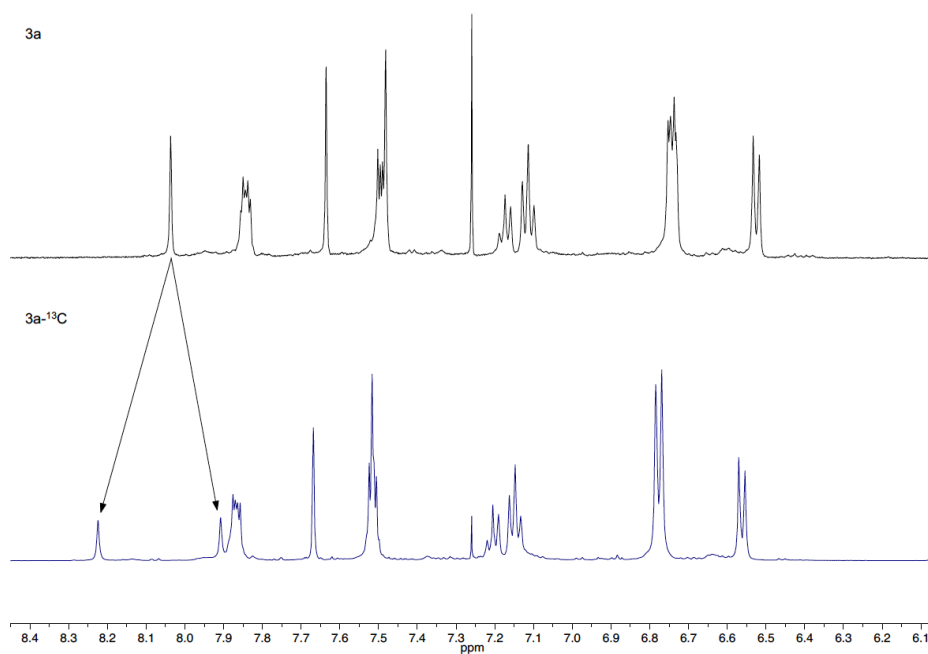


**Figure A2.27.**  $^{13}\text{C}$  NMR spectrum of **3a**- $^{13}\text{C}_2$  (125 MHz,  $\text{CDCl}_3$ , 298 K).

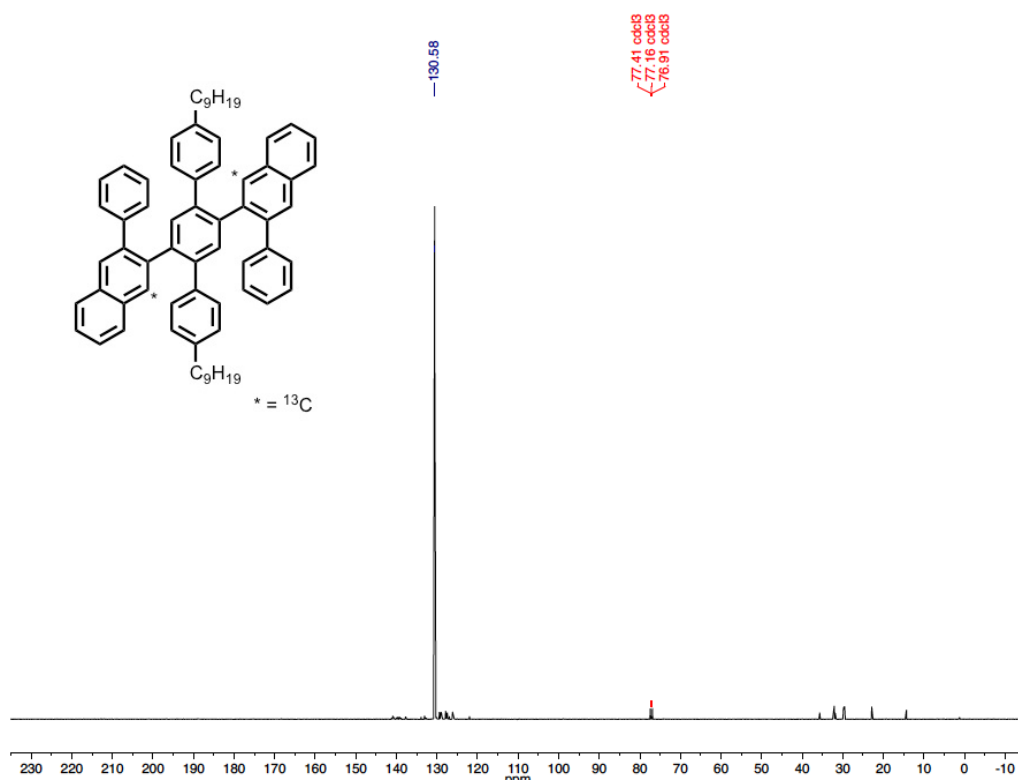


**Figure A2.28.**  $^1\text{H}$  NMR of **3b** (400 MHz,  $\text{CDCl}_3$ , 297 K).

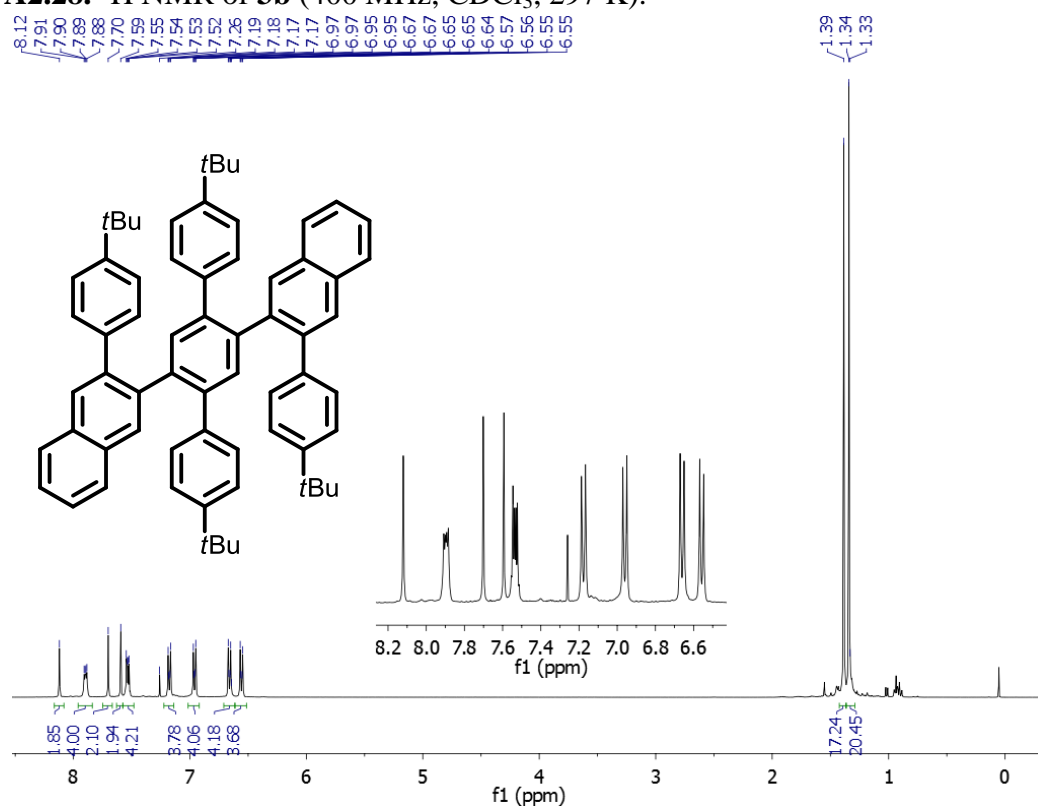


**Figure A2.29.**  $^{13}\text{C}$  NMR of **3b** (100 MHz,  $\text{CDCl}_3$ , 297 K).

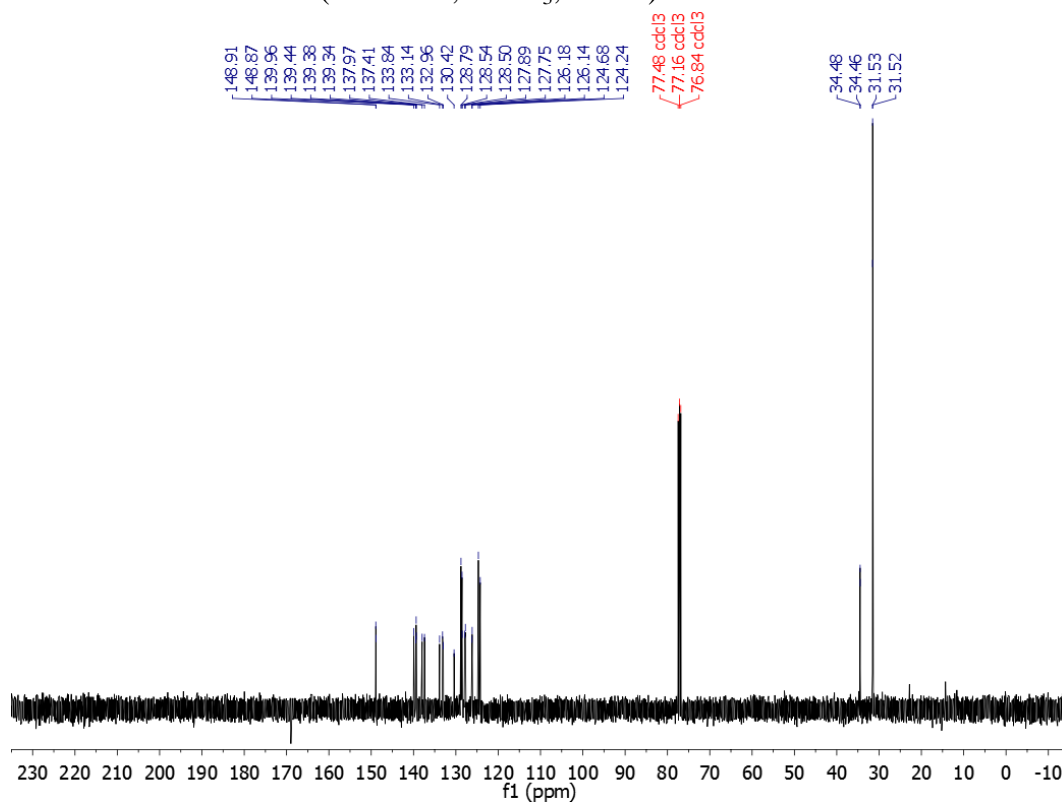


**Figure A2.30.**  $^1\text{H}$  NMR of **3c** (400 MHz,  $\text{CDCl}_3$ , 295 K).

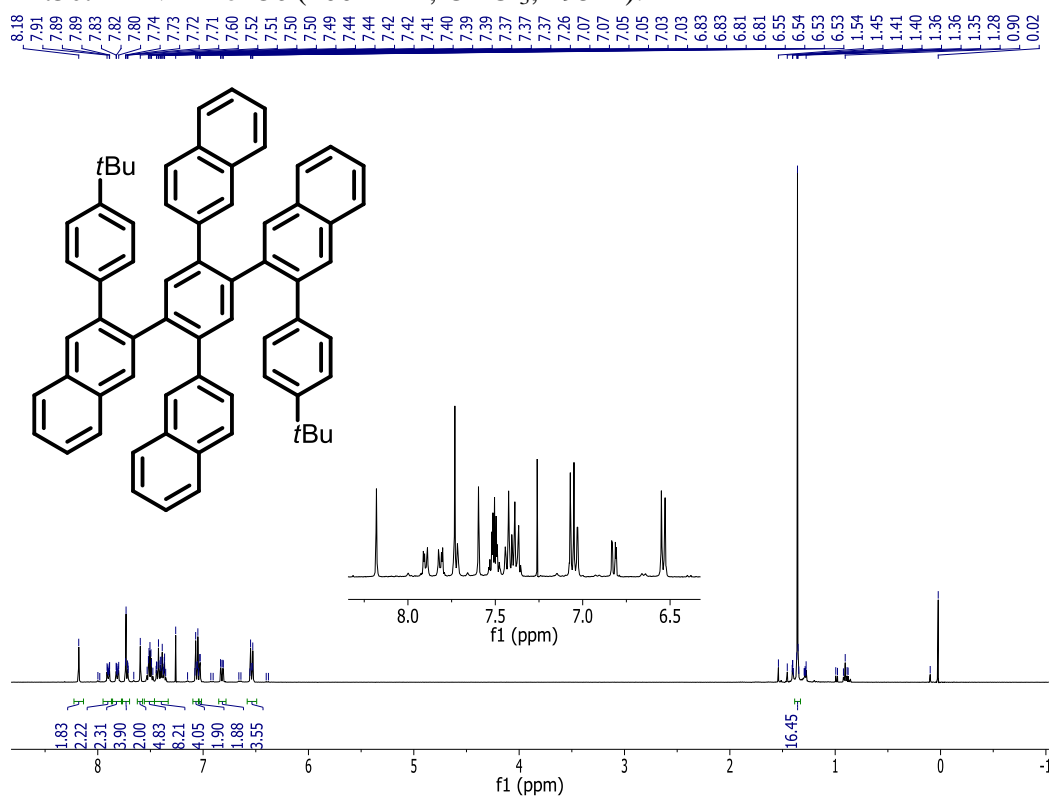


**Figure A2.31.**  $^{13}\text{C}$  NMR of **3c** (100MHz,  $\text{CDCl}_3$ , 295 K).

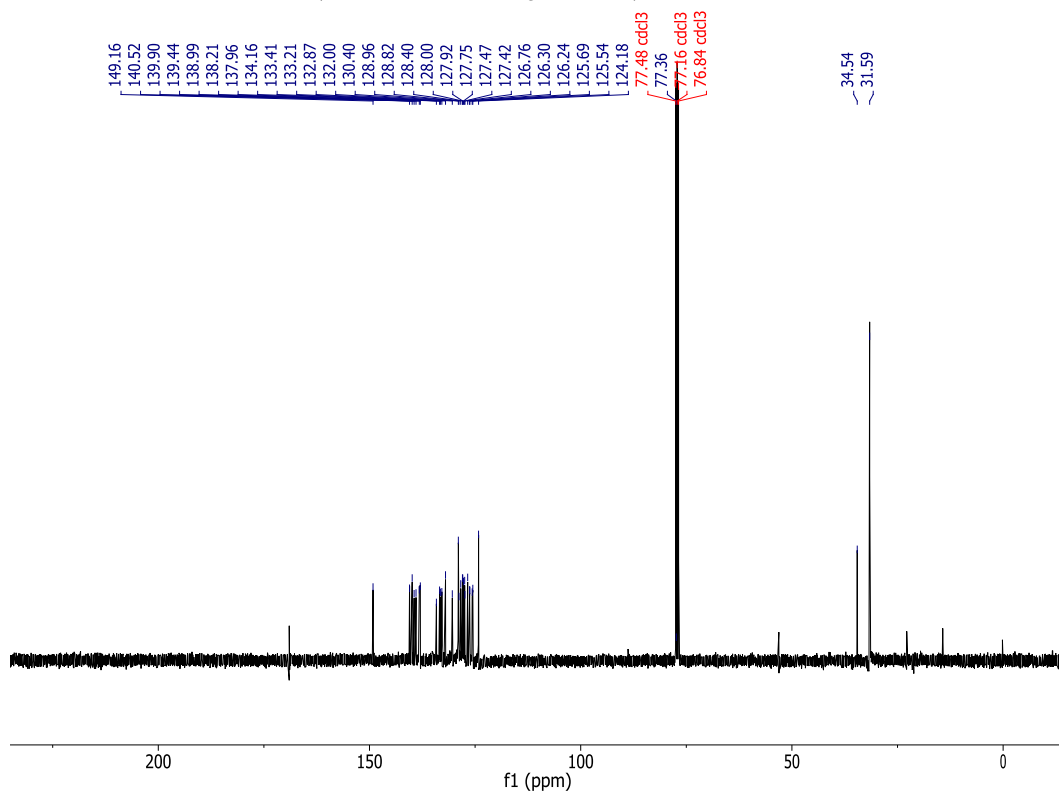




**Figure A2.32.**  $^1\text{H}$  NMR of **3d** (400 MHz,  $\text{CDCl}_3$ , 295 K).

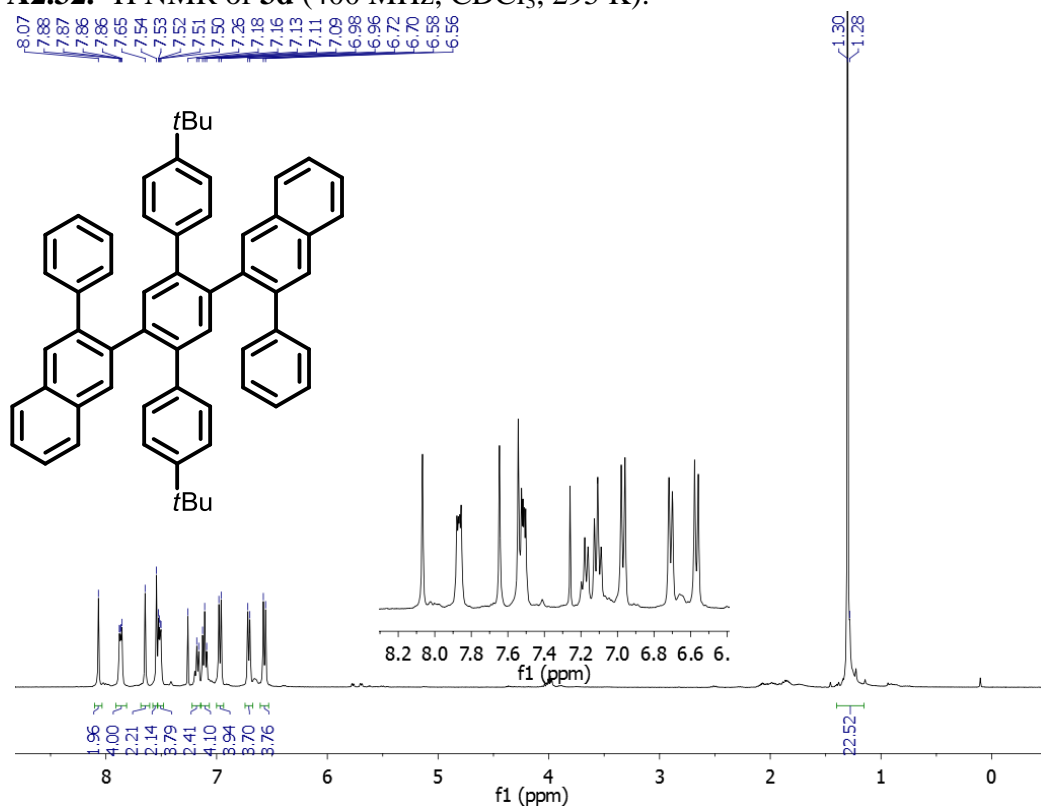


**Figure A2.33.**  $^{13}\text{C}$  NMR of **3d** (100MHz,  $\text{CDCl}_3$ , 295 K).

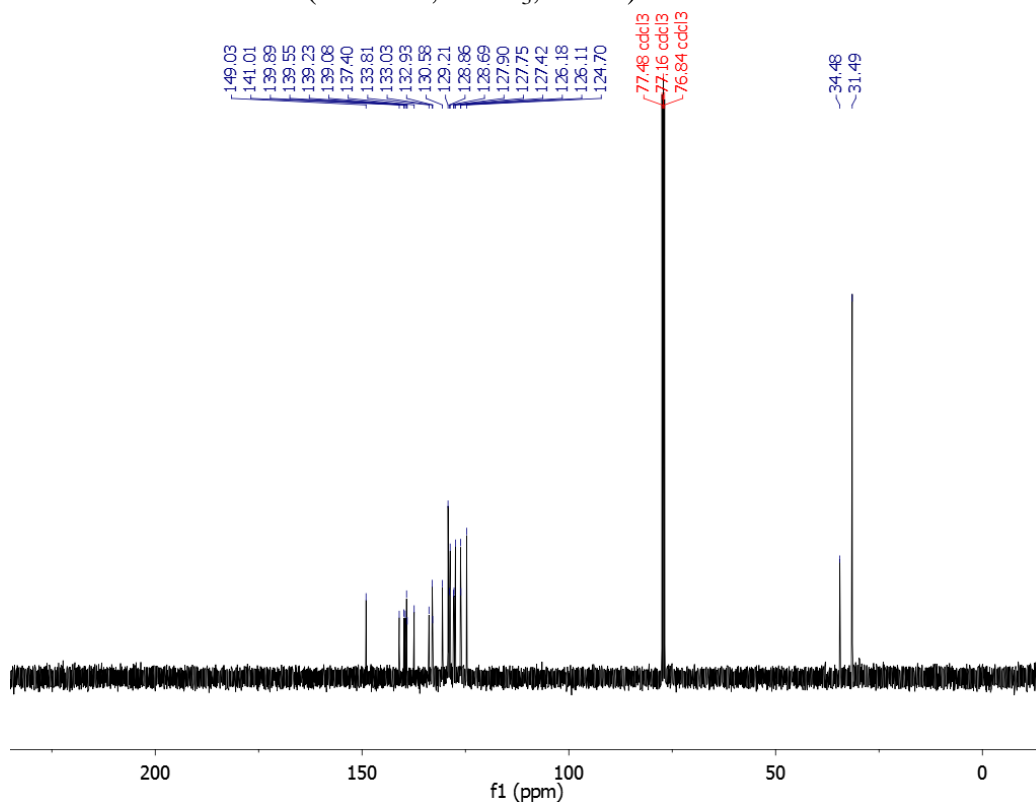


Figure A2.34.  $^1\text{H}$  NMR of **4a** (500 MHz,  $\text{CDCl}_3$ , 295 K).

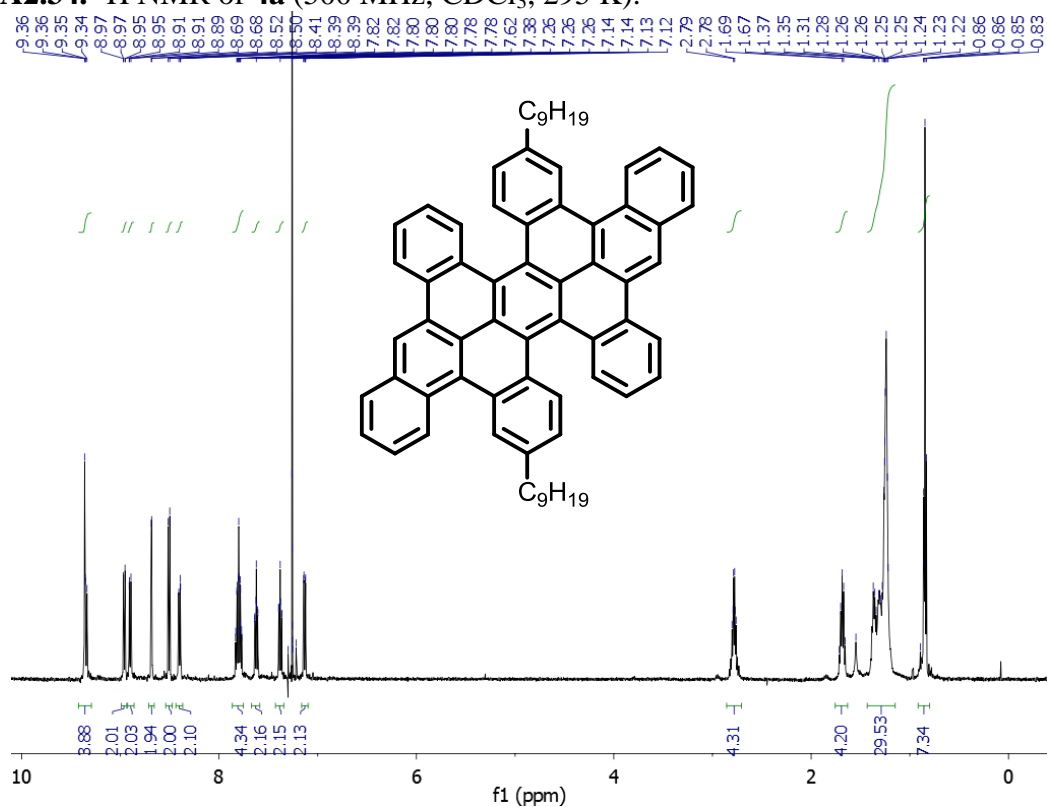
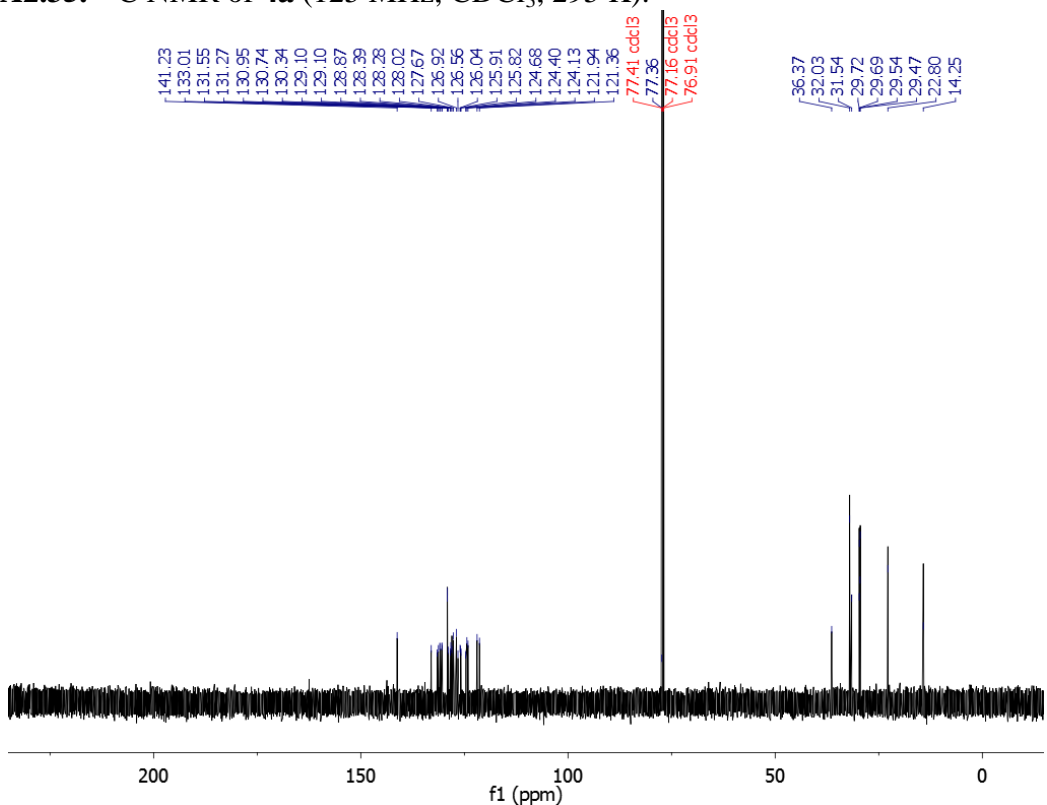
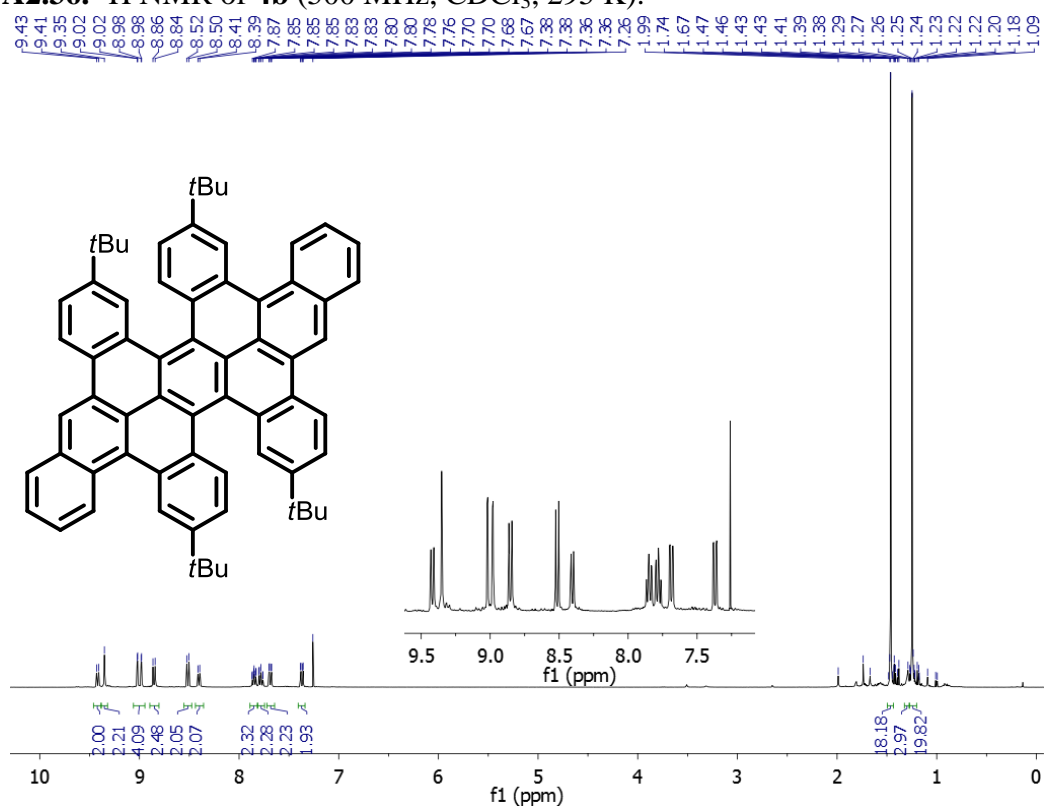


Figure A2.35.  $^{13}\text{C}$  NMR of **4a** (125 MHz,  $\text{CDCl}_3$ , 295 K).



**Figure A2.36.**  $^1\text{H}$  NMR of **4b** (500 MHz,  $\text{CDCl}_3$ , 295 K).



**Figure A2.37.**  $^{13}\text{C}$  NMR of **4b** (125 MHz,  $\text{CDCl}_3$ , 295 K).

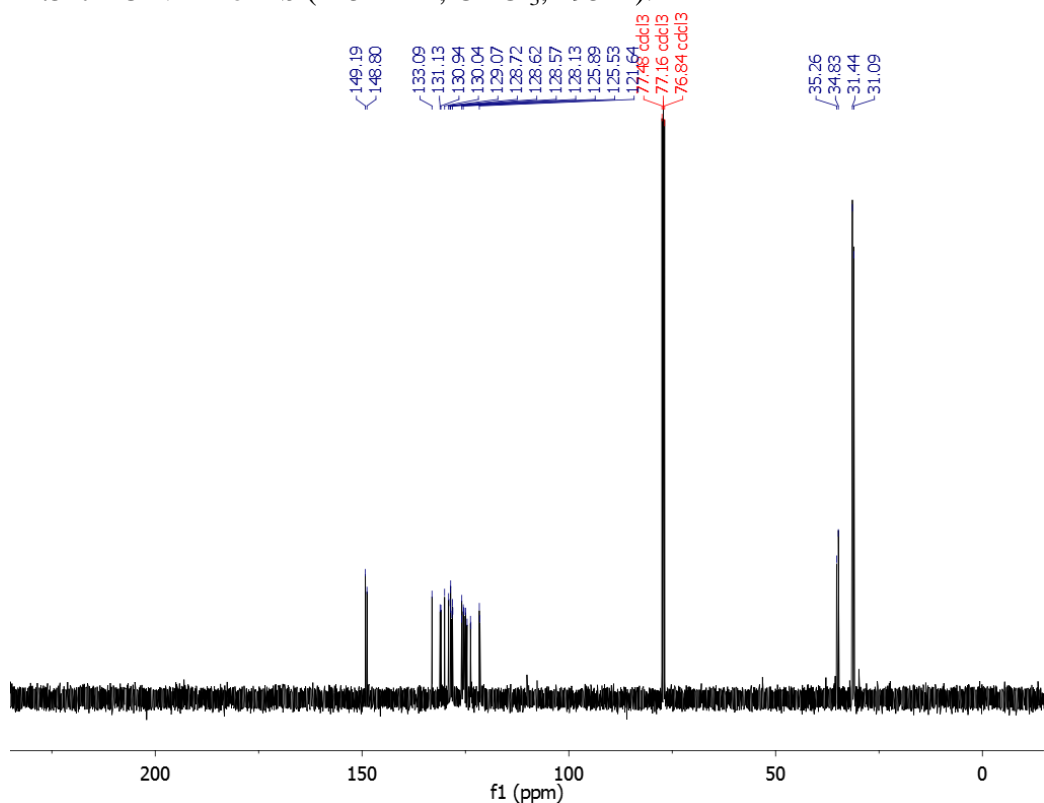


**Figure A2.38.**  $^1\text{H}$  NMR of **4c** (500 MHz,  $\text{CDCl}_3$ , 298 K).

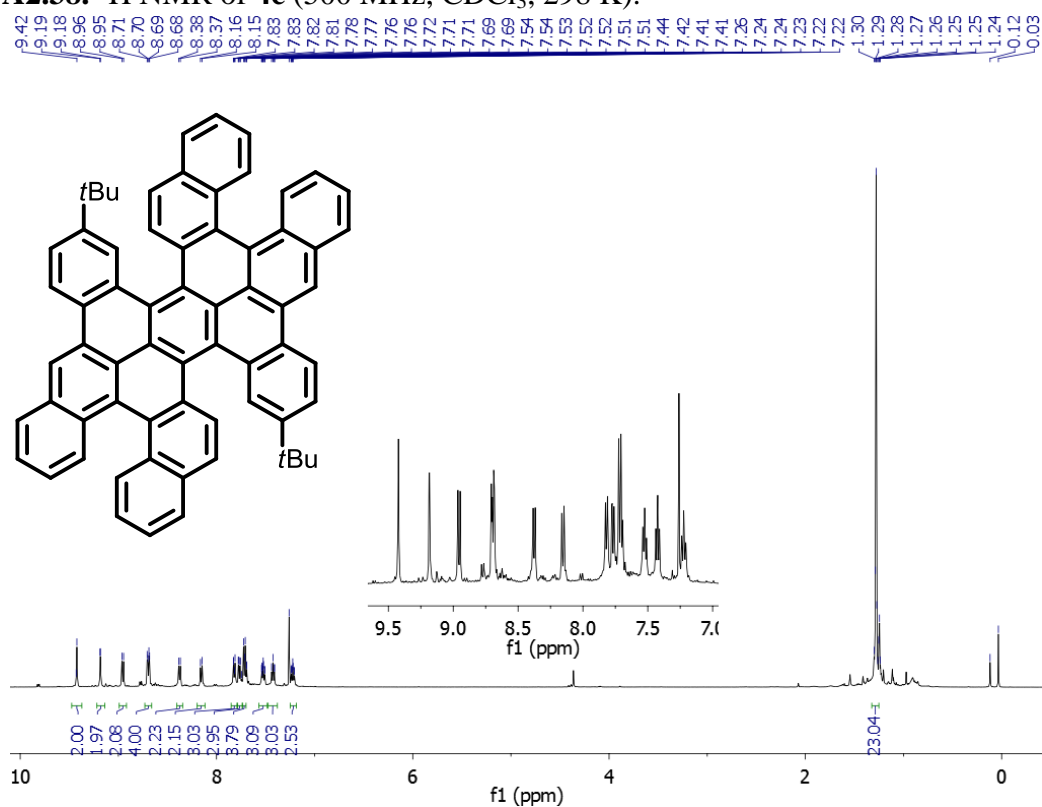


**Figure A2.39.**  $^{13}\text{C}$  NMR of **4c** (125 MHz,  $\text{CDCl}_3$ , 298 K).

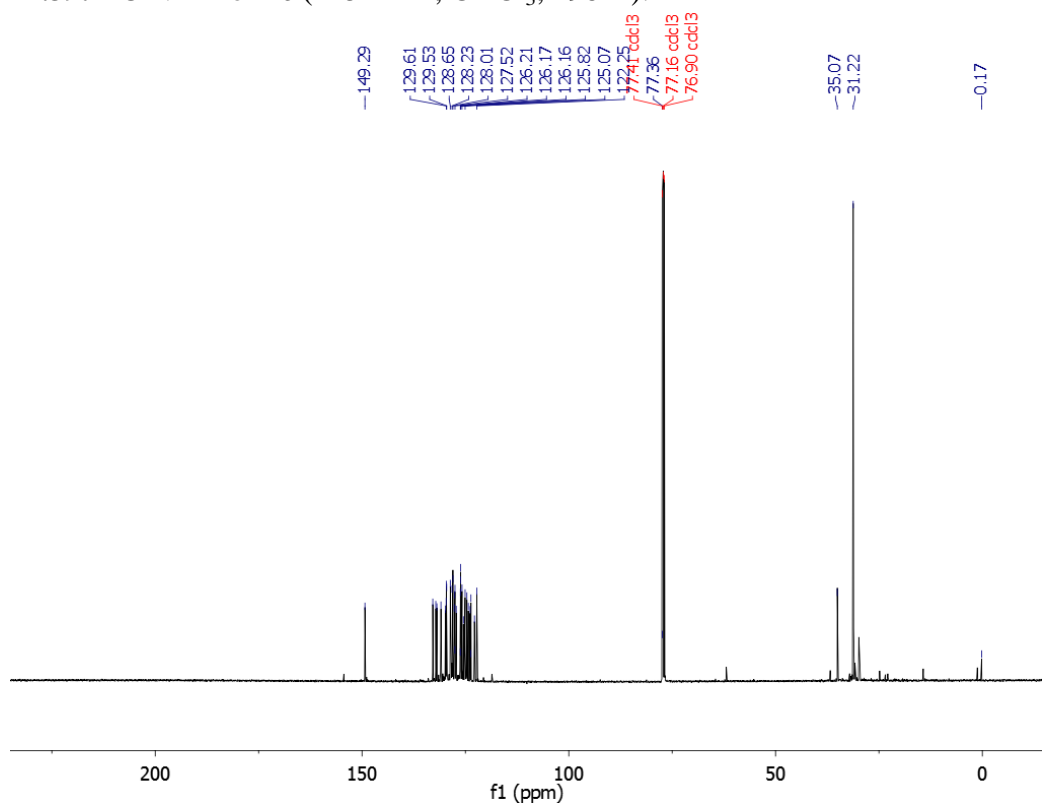


**Figure A2.40.**  $^1\text{H}$  NMR of **5a** (300 MHz,  $o\text{-C}_6\text{D}_4\text{Cl}_2$ , 353 K).

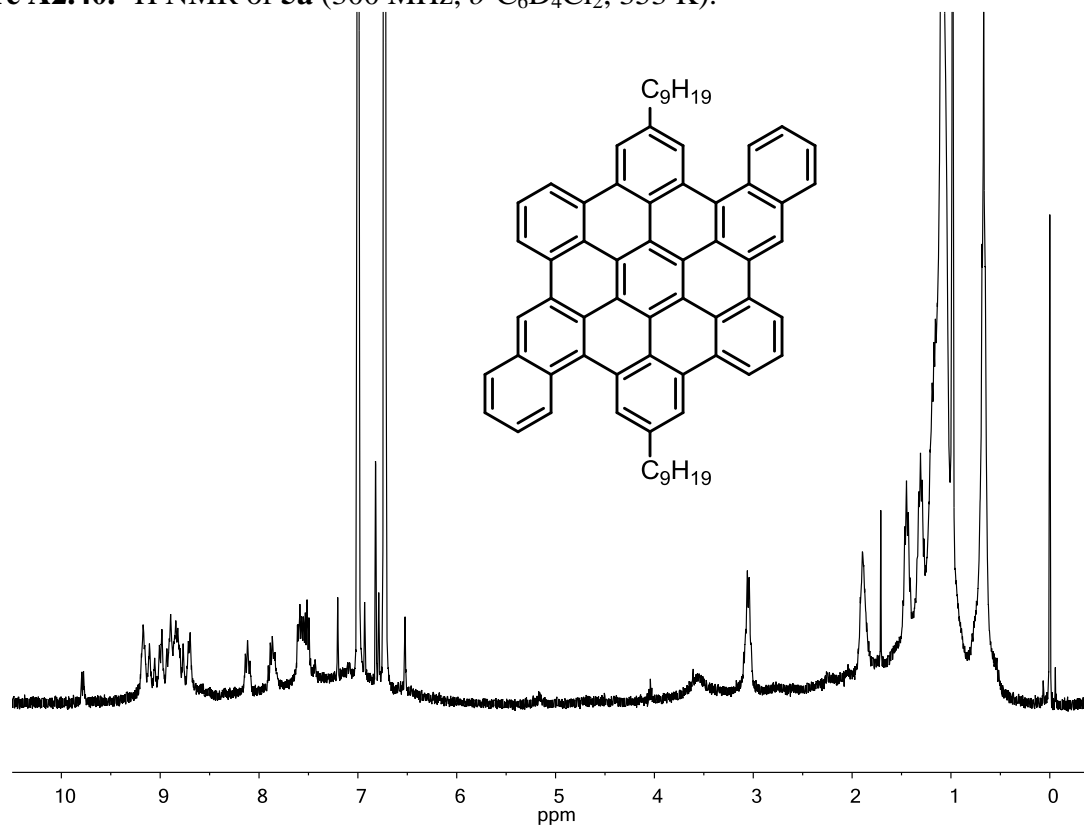


**Figure A2.41.**  $^1\text{H}$  NMR of **5a** (300 MHz,  $o\text{-C}_6\text{D}_4\text{Cl}_2$ , 353 K), aromatic region.

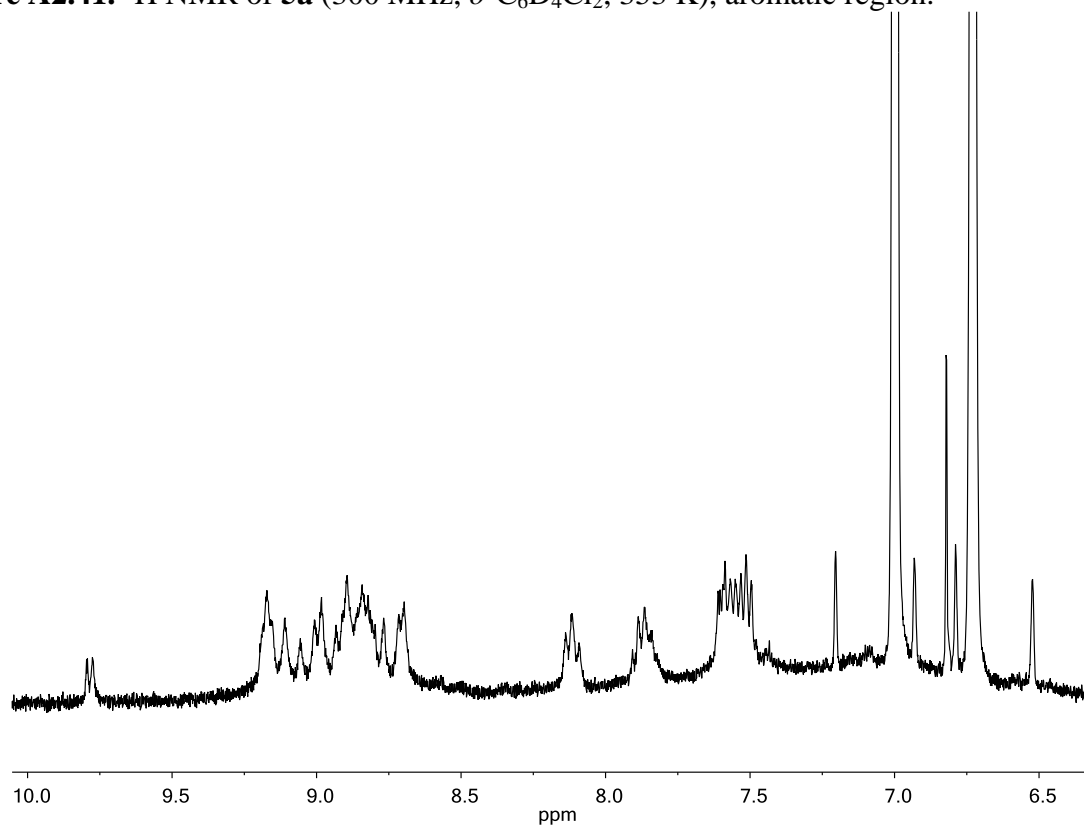


**Figure A2.42.**  $^{13}\text{C}$  NMR of **5a** (75 MHz, 2:1  $\text{CS}_2$ : $\text{CD}_2\text{Cl}_2$ , 298 K).

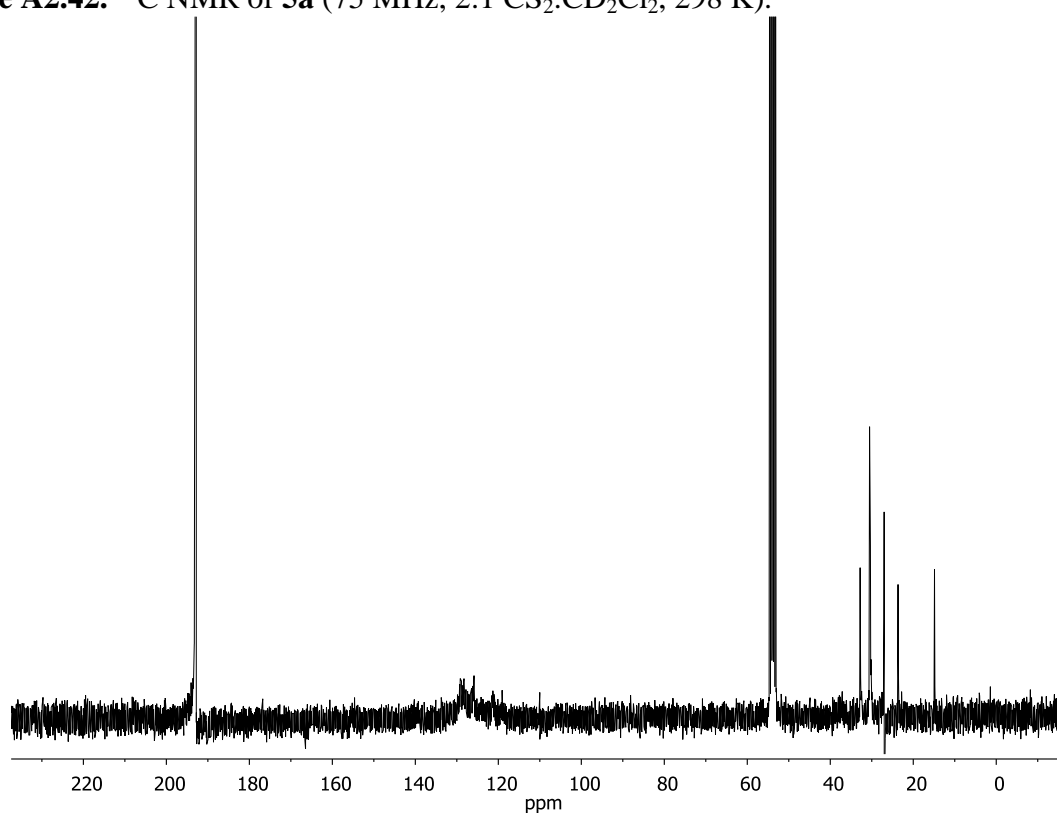


**Figure A2.43.**  $^1\text{H}$  NMR spectrum of **5a**- $^{13}\text{C}_2$  (500 MHz, 1,2- $\text{C}_2\text{H}_2\text{Cl}_4$ , 408 K).

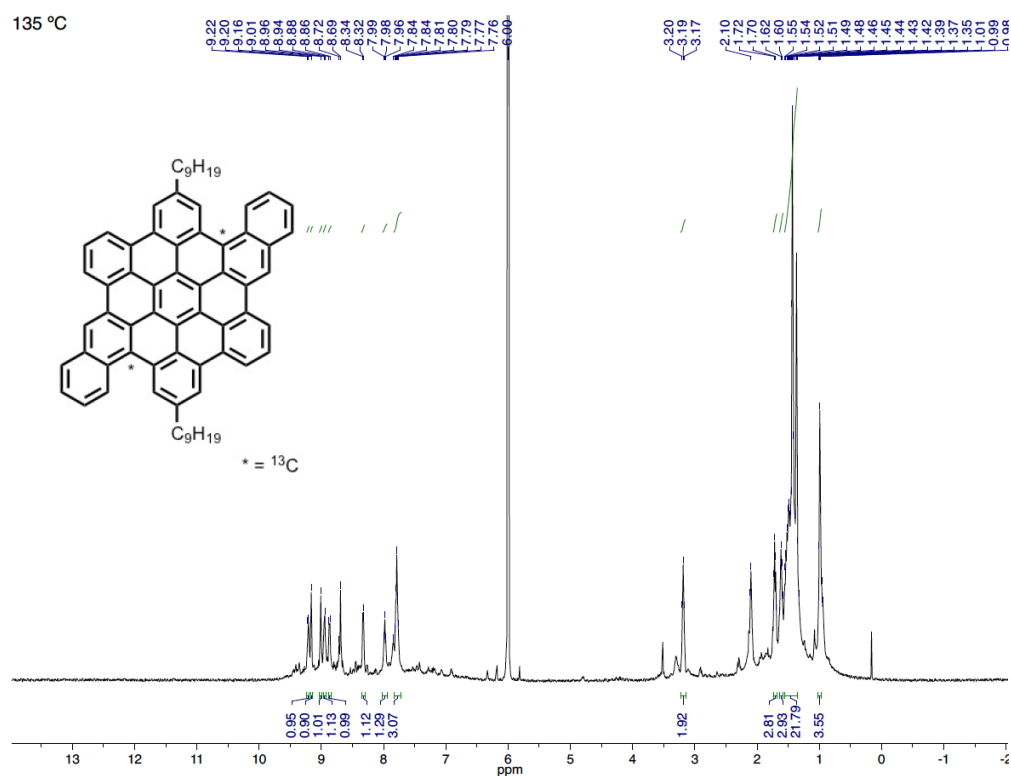


**Figure A2.44.**  $^1\text{H}$  NMR spectrum of **5a**- $^{13}\text{C}_2$  (500 MHz, 1,2- $\text{C}_2\text{H}_2\text{Cl}_4$ , 408 K).  $^1\text{H}$  signal assignment of aromatic region.

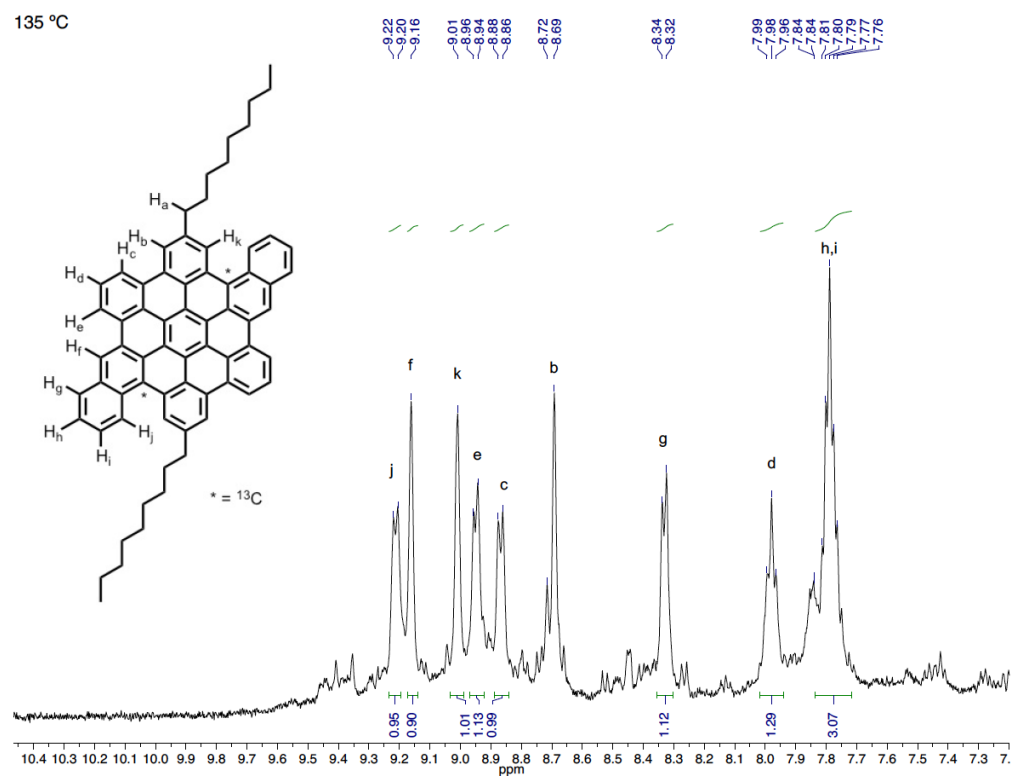
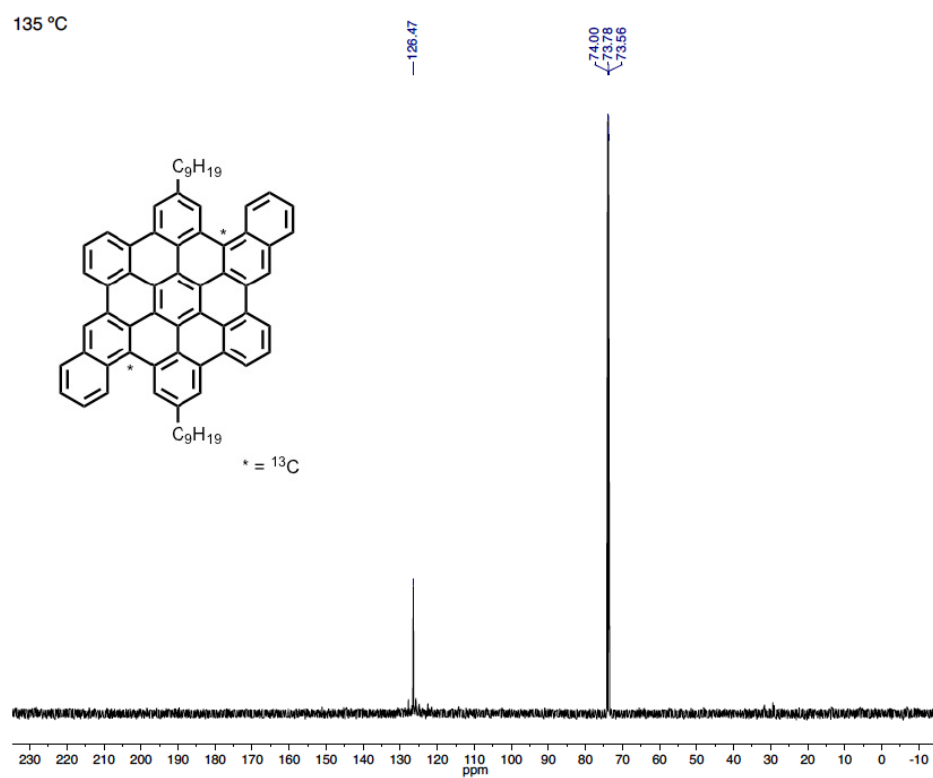


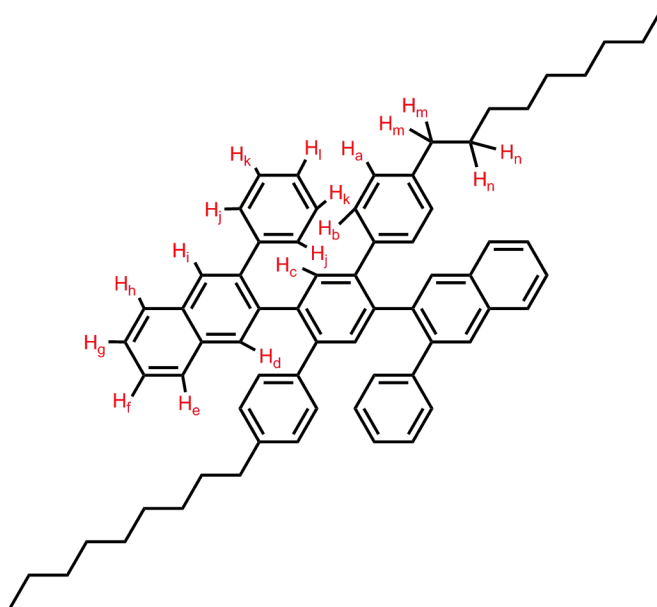
**Figure A2.45.**  $^{13}\text{C}$  NMR spectrum of **5a**- $^{13}\text{C}_2$ . (125 MHz, 1,2- $\text{C}_2\text{H}_2\text{Cl}_4$ , 408 K)





## D. 2D NMR Spectra and Structural Assignments of Selected Compounds

### Peak assignments for the compound 3a:



The peak corresponding to the proton  $H_d$  was assigned using the COESY and ROESY spectra (full assignments below). This is the proton signal that splits into two signals in the  $^{13}\text{C}$ -labeled benzannulated compound  $^{13}\text{C}_2$ -**3a** (Figure S24) due to the proton-carbon coupling.

**Figure A2.46.** Full COSY spectrum of **3a** (500 MHz, 500 MHz, CDCl<sub>3</sub>, 295 K).

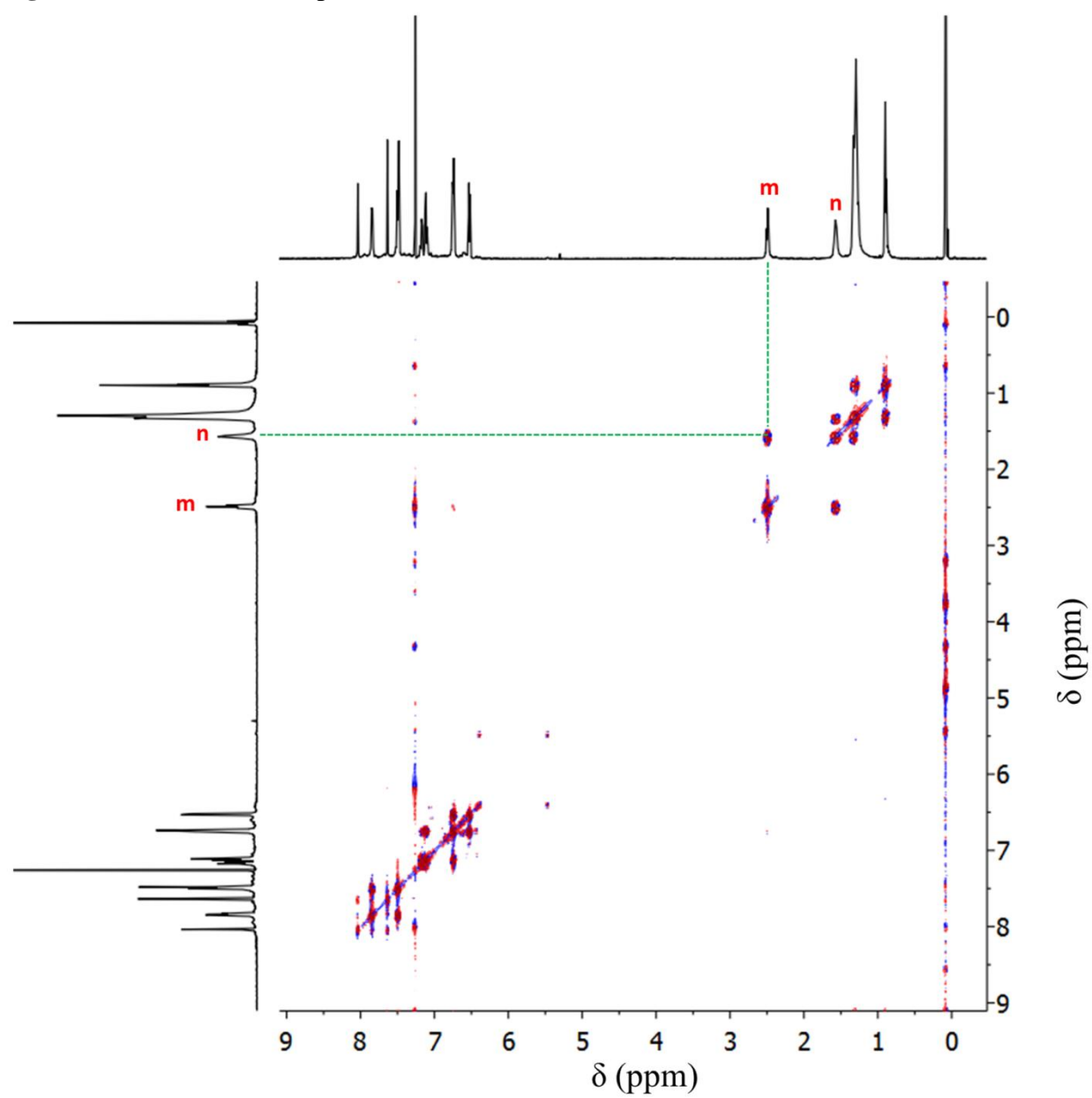


**Figure A2.47.** Partial COSY spectrum of **3a** showing the aromatic region (500 MHz, 500 MHz, CDCl<sub>3</sub>, 295 K).

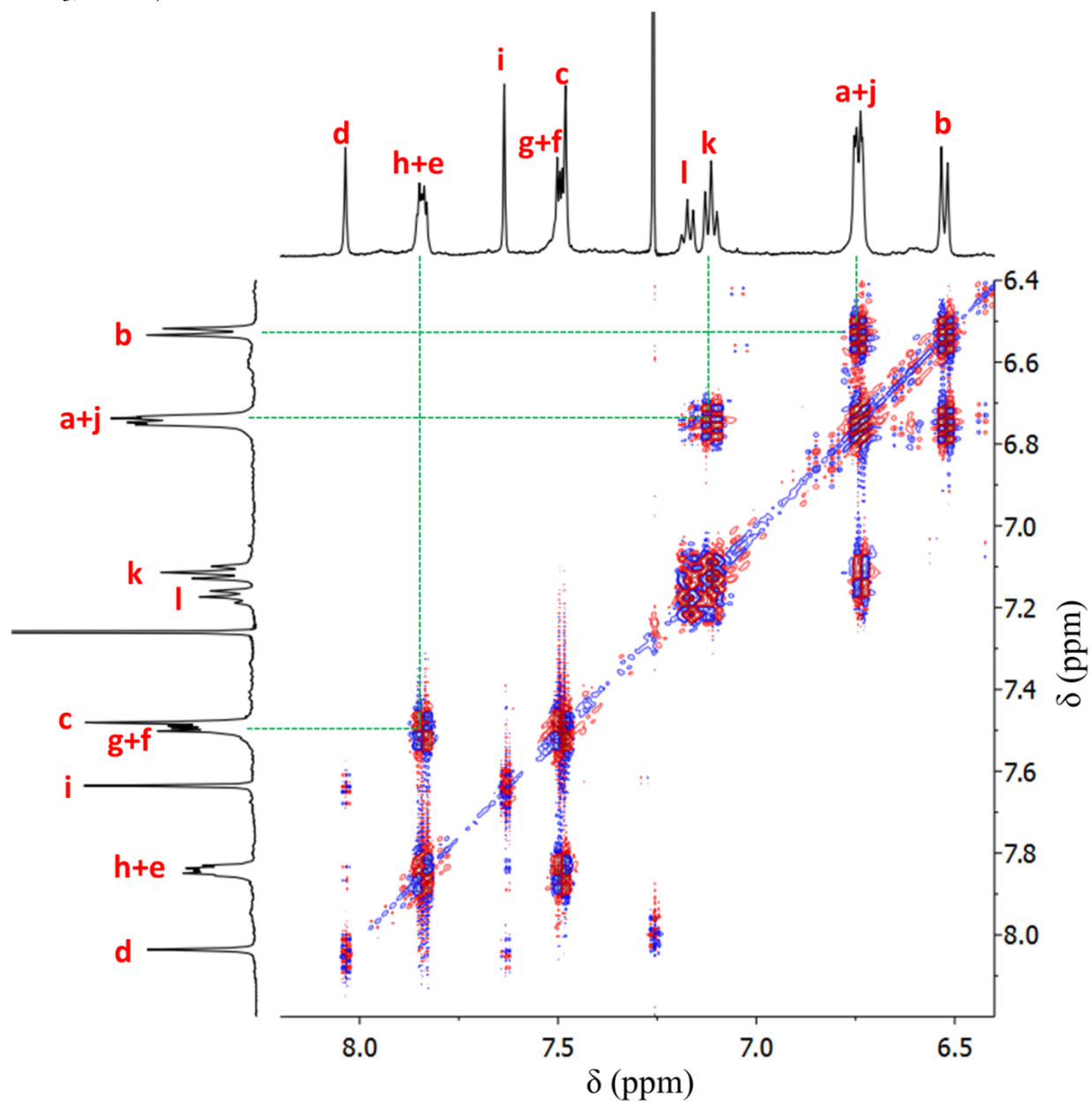


**Figure A2.48.** Full ROESY spectrum of **3a** (500 MHz, 500 MHz, CDCl<sub>3</sub>, 295 K).

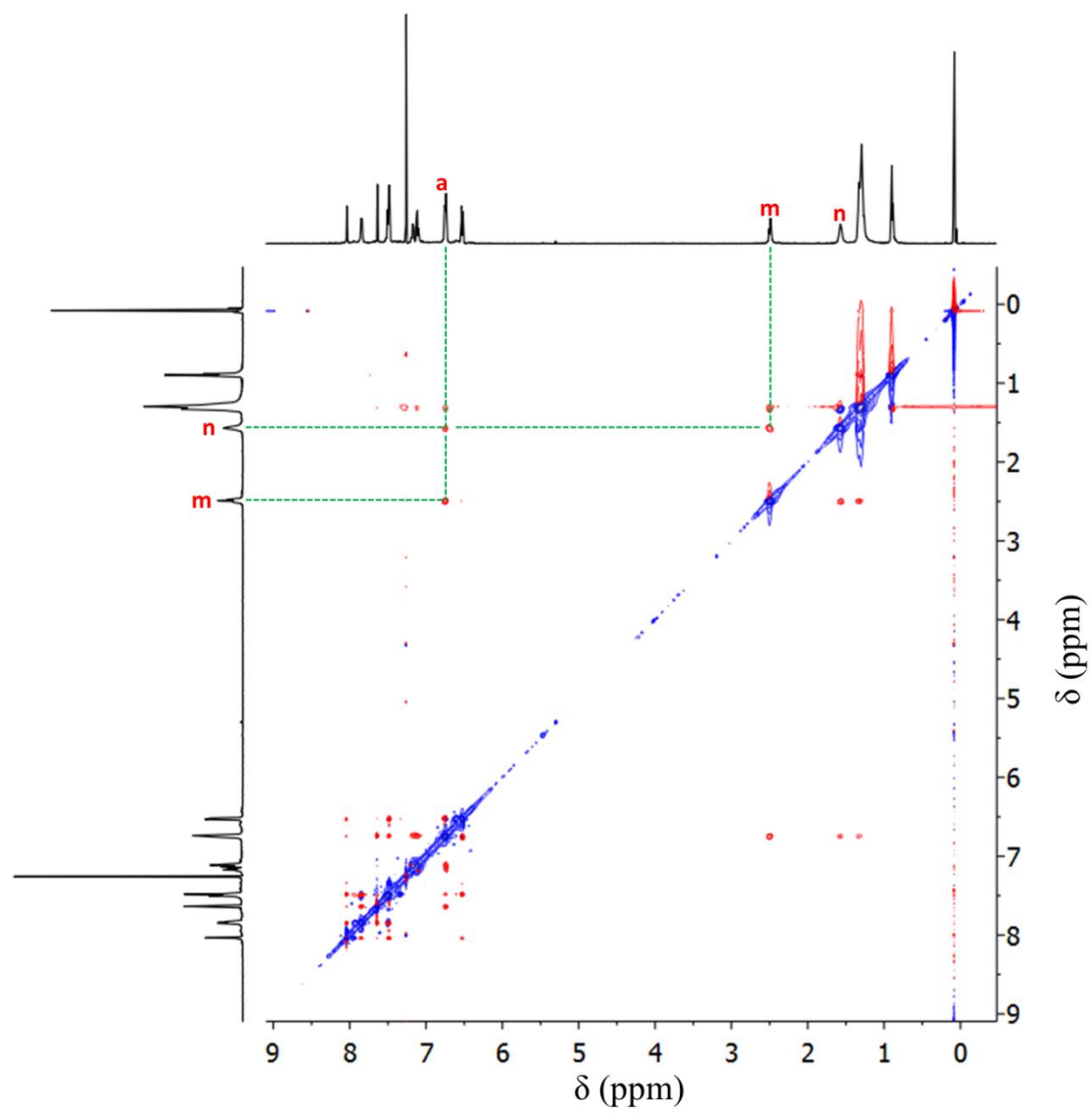


**Figure A2.49.** Partial ROESY spectrum of **3a** showing the aromatic region (500 MHz, 500 MHz, CDCl<sub>3</sub>, 295 K).

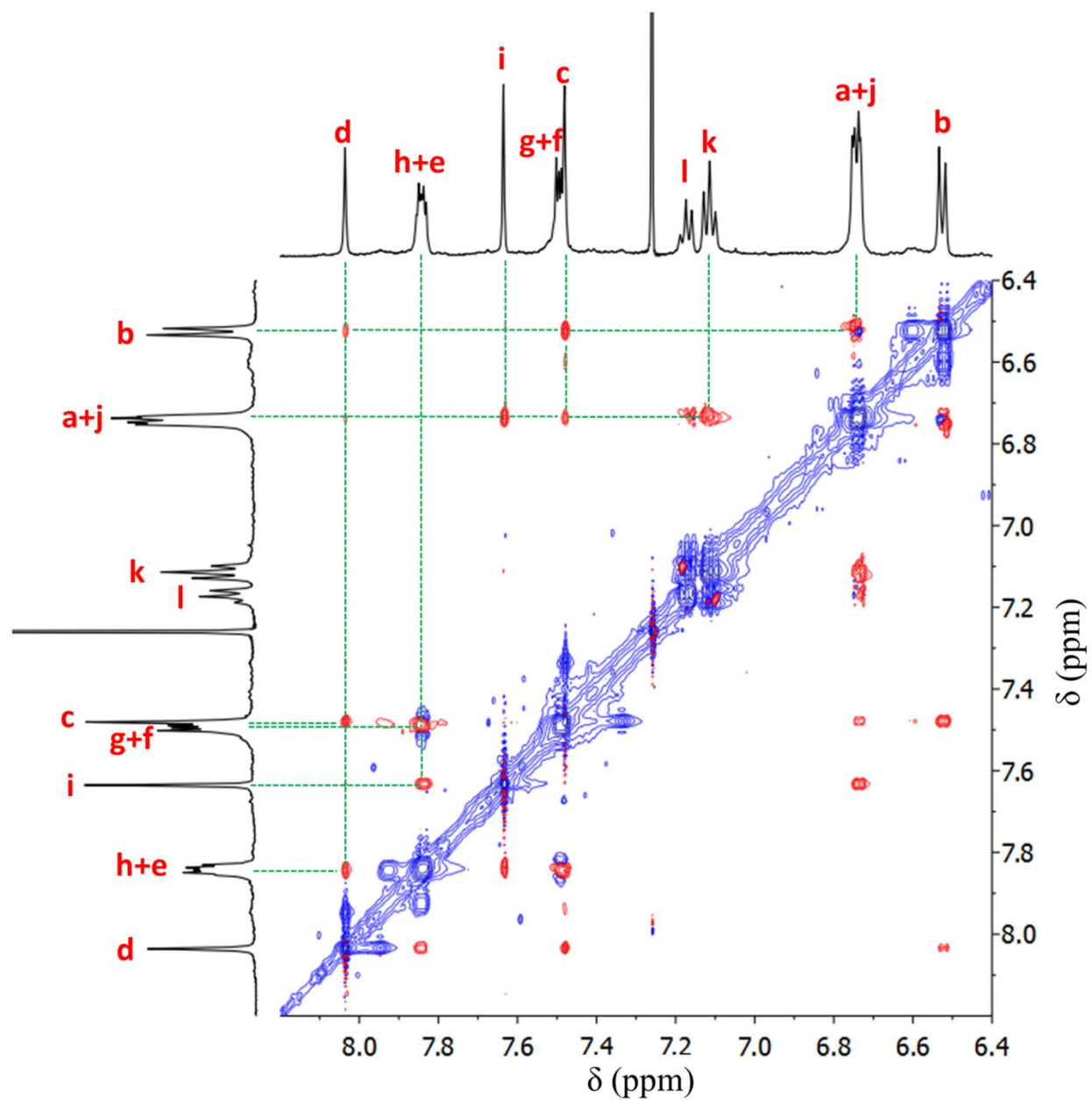


**Figure A2.50.** Full HSQC spectrum of **3a** (500 MHz, 125 MHz, CDCl<sub>3</sub>, 295 K).

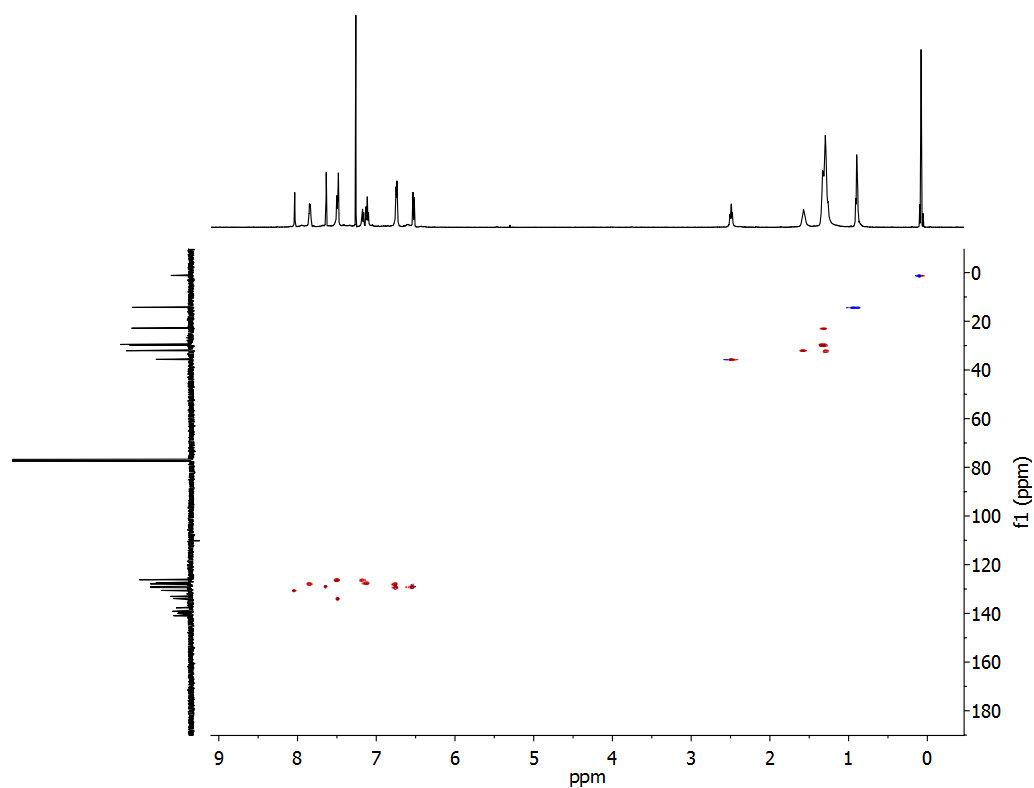


**Figure A2.51.** Partial HSQC spectrum of **3a** showing the aromatic region (500 MHz, 125 MHz, CDCl<sub>3</sub>, 295 K).

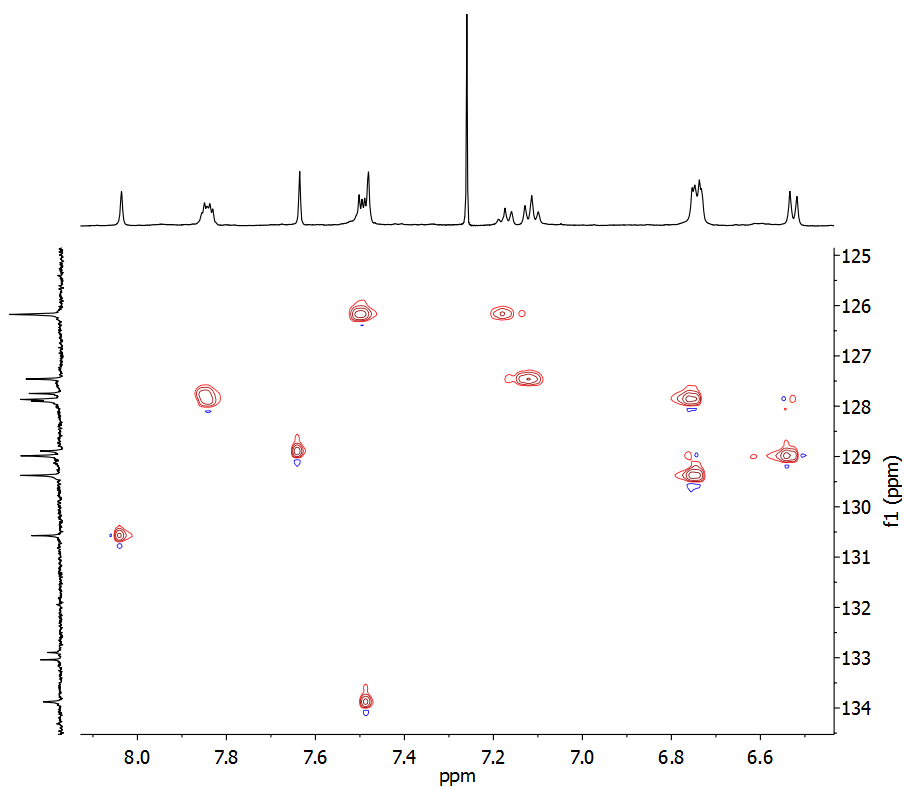


**Figure A2.52.** Full HMBC spectrum of **3a** (500 MHz, 125 MHz, CDCl<sub>3</sub>, 295 K).

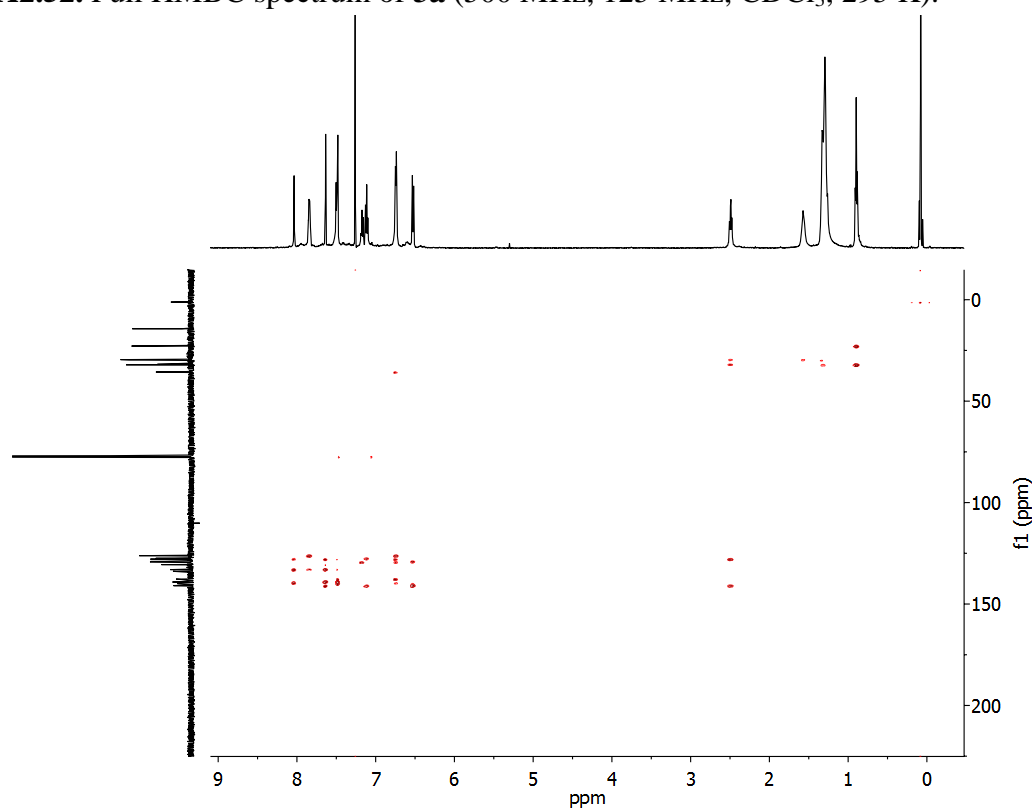
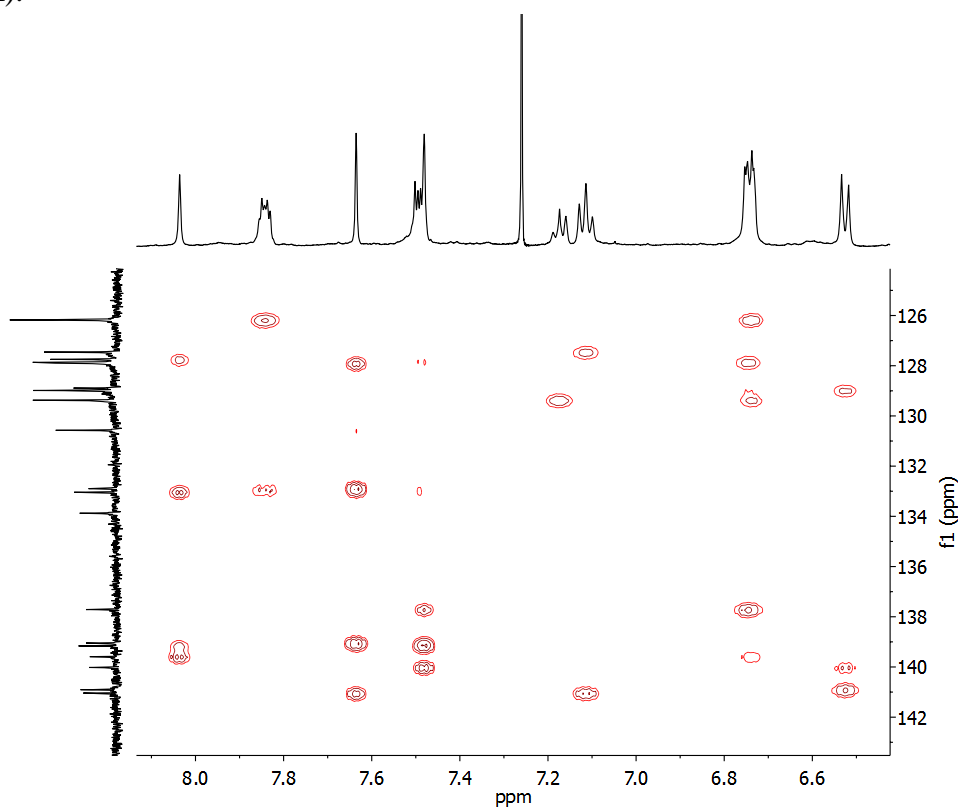
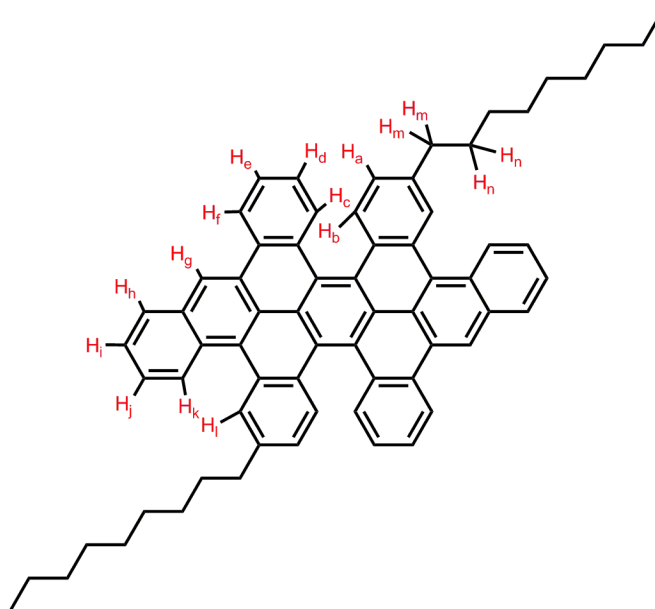


**Figure A2.53.** Partial HMBC spectrum of **3a** showing the aromatic region (500 MHz, 125 MHz, CDCl<sub>3</sub>, 295 K).



**Peak assignments for the compound 4a:**



COSY spectrum indicates a 1,2,4-trisubstituted aromatic spin system, which contains  $H_a$ ,  $H_b$  and  $H_l$ .  $H_a$  is coupled to both  $H_b$  and  $H_l$ , whereas  $H_b$  and  $H_k$  are only coupled to  $H_a$ . Therefore,  $H_a$  is in position 2 on the aromatic ring. Coupling constant between  $H_a$  and  $H_b$  is consistent with *o*-substitution pattern. Coupling constant between  $H_l$  and  $H_a$  is consistent with *m*-substitution pattern. As a result,  $H_b$  and  $H_l$  are at positions 1 and 4, respectively. As expected, this is the ring the nonyl chain is attached to, assigned using ROESY crosspeaks between  $H_a$  and  $H_m$  and  $H_l$  and  $H_m$ .

ROESY crosspeak between  $H_b$  and  $H_c$  indicates that a C-C bond didn't form between these two carbons. Note that after extended reaction time, this bond does form, forming the compound **5a**.

Rest of the protons on the periphery of the molecule can be assigned by using the ROESY and COSY crosspeaks as shown below.



**Figure A2.54.** Full COSY spectrum of **4a** (500 MHz, 500 MHz, CDCl<sub>3</sub>, 295 K).

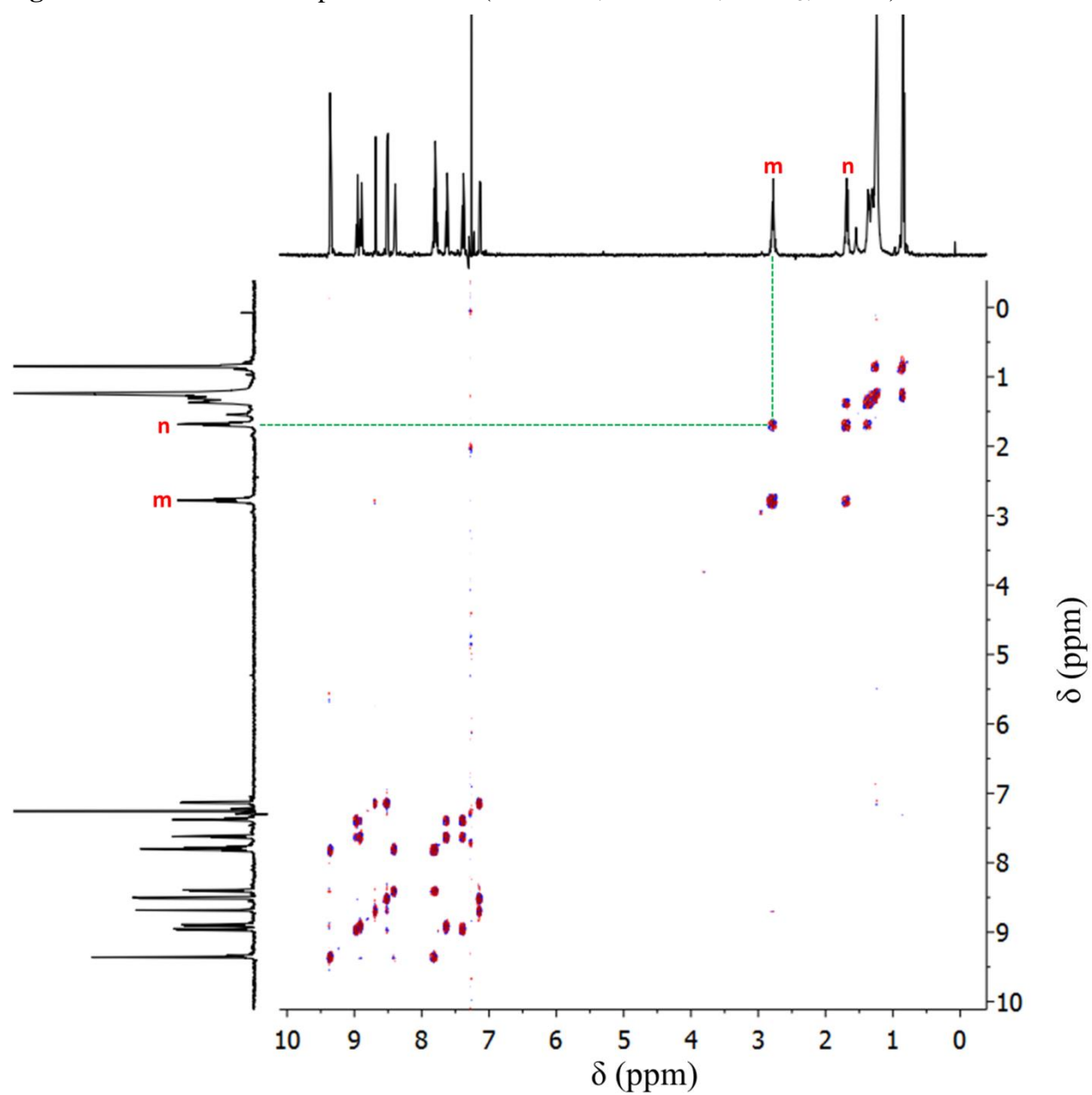


**Figure A2.55.** Partial COSY spectrum of **4a** showing the aromatic region (500 MHz, 500 MHz, CDCl<sub>3</sub>, 295 K).

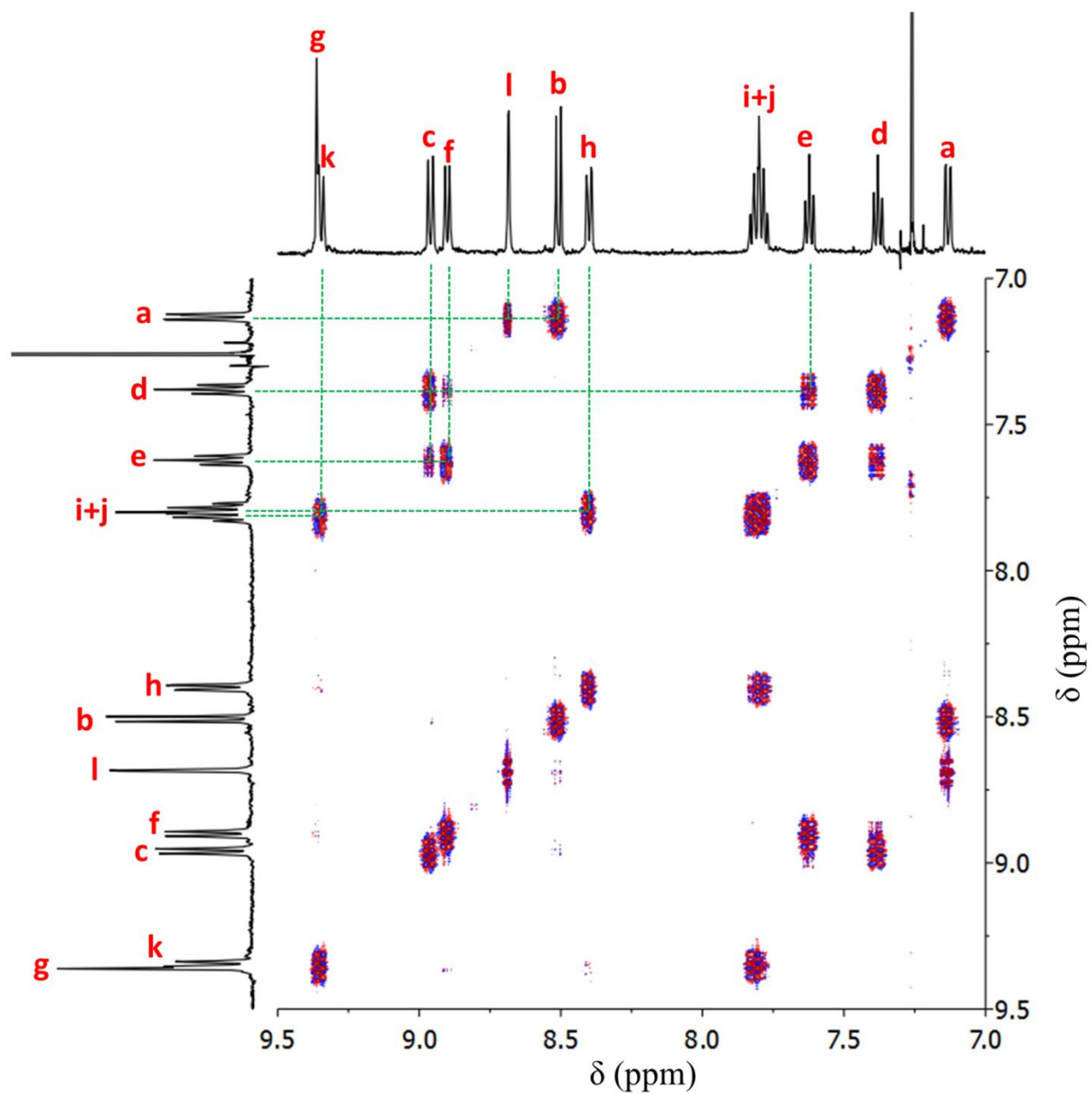


**Figure A2.56.** Full ROESY spectrum of **4a** (500 MHz, 500 MHz, CDCl<sub>3</sub>, 295 K).

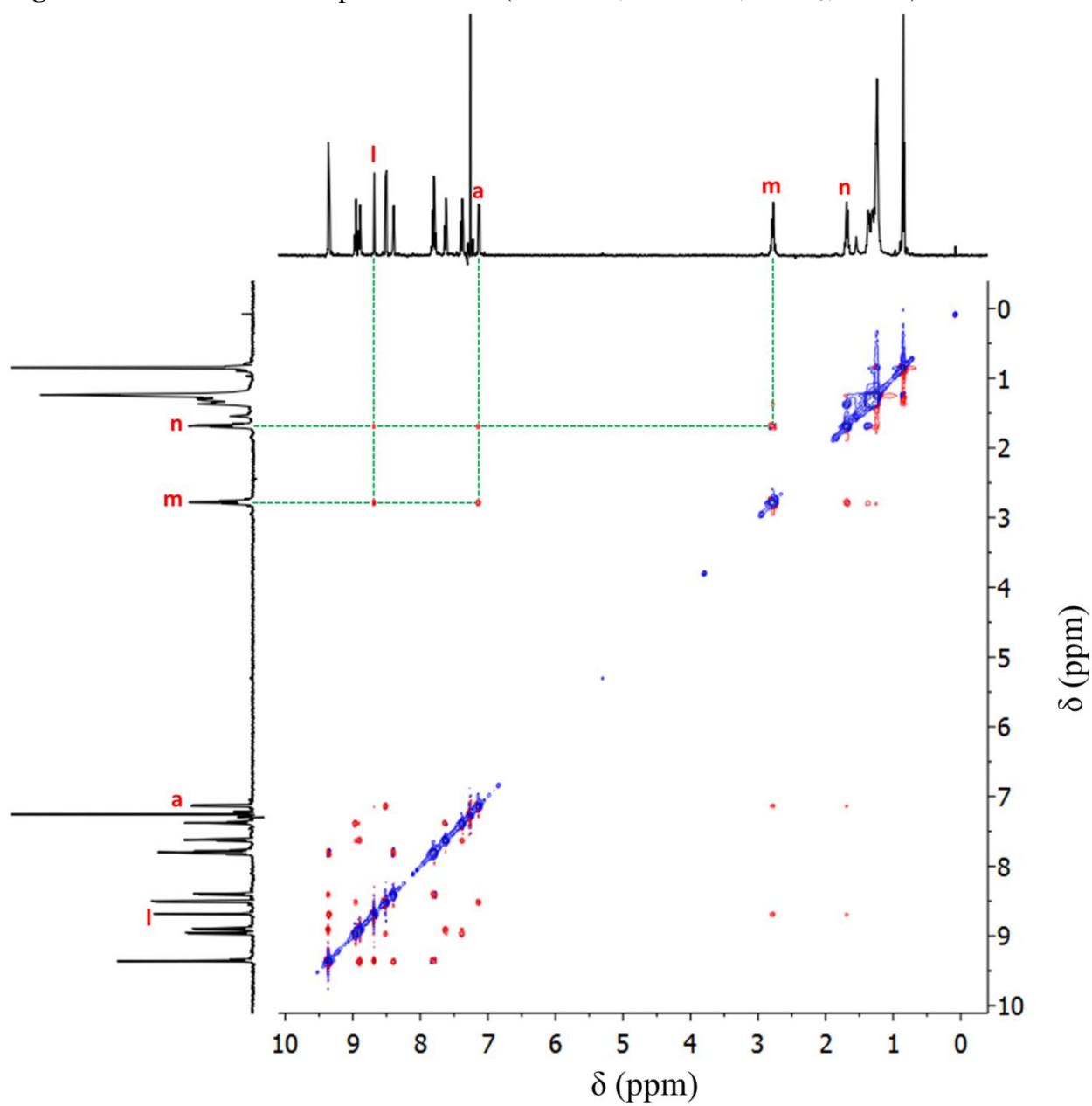


**Figure A2.57.** Partial ROESY spectrum of **4a** showing the aromatic region (500 MHz, 500 MHz, CDCl<sub>3</sub>, 295 K).

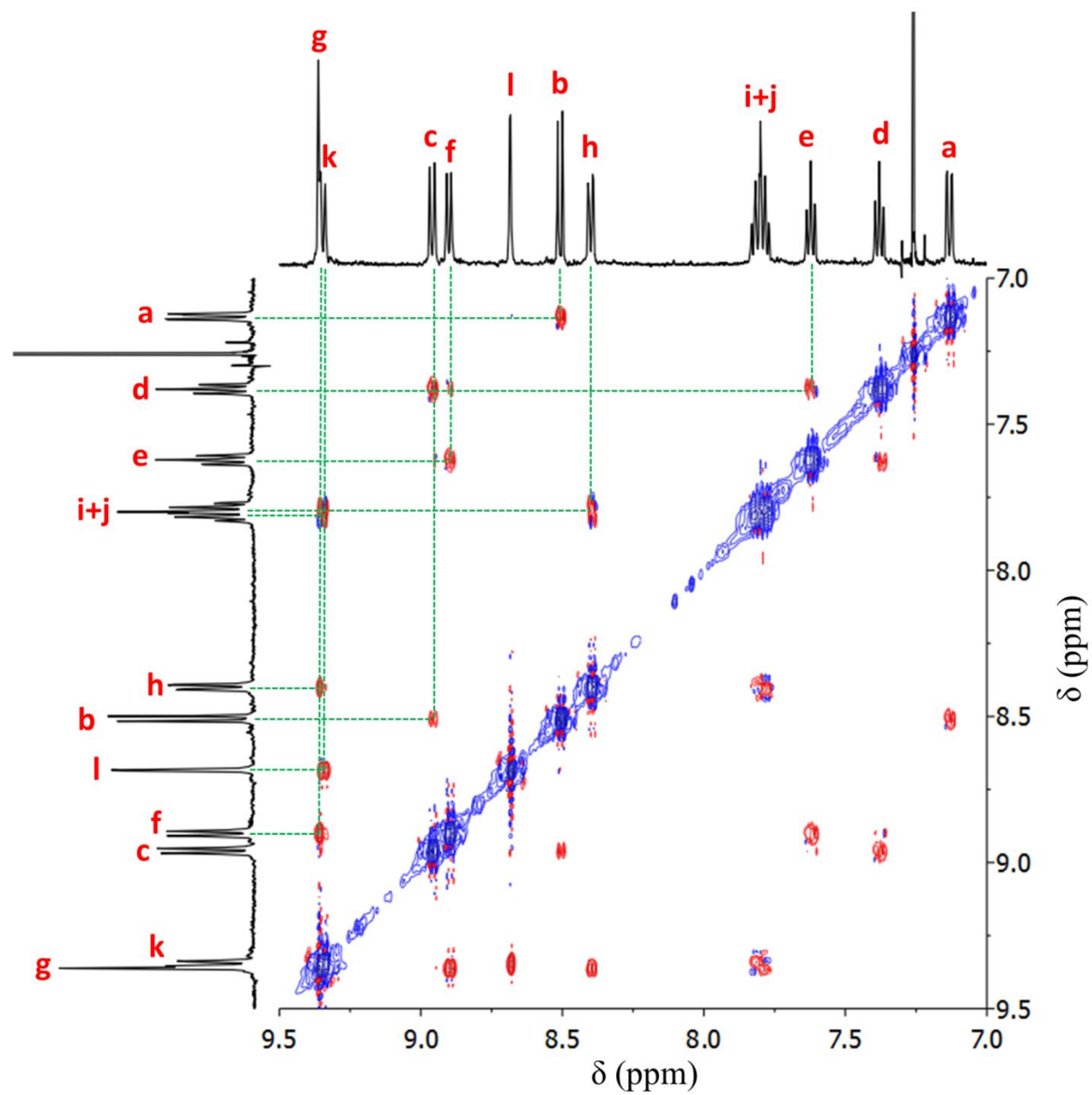


**Figure A2.58.** Full HSQC spectrum of **4a** (500 MHz, 125 MHz, CDCl<sub>3</sub>, 295 K).

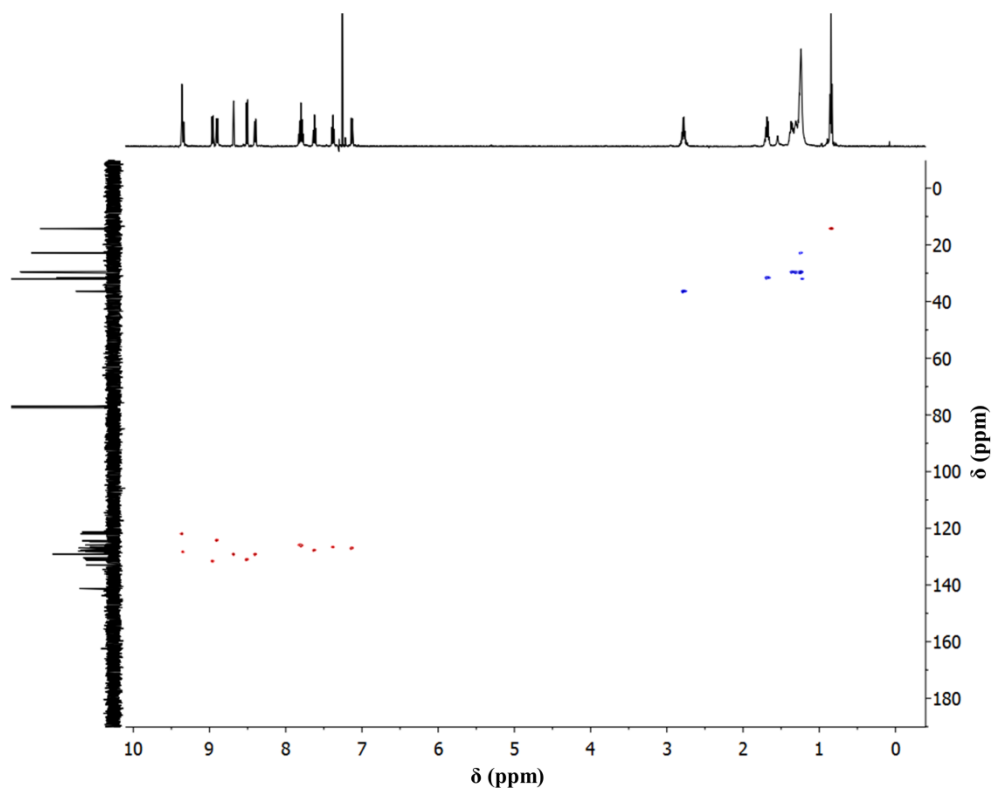


**Figure A2.59.** Partial HSQC spectrum of **4a** showing the aromatic region (500 MHz, 125 MHz, CDCl<sub>3</sub>, 295 K).

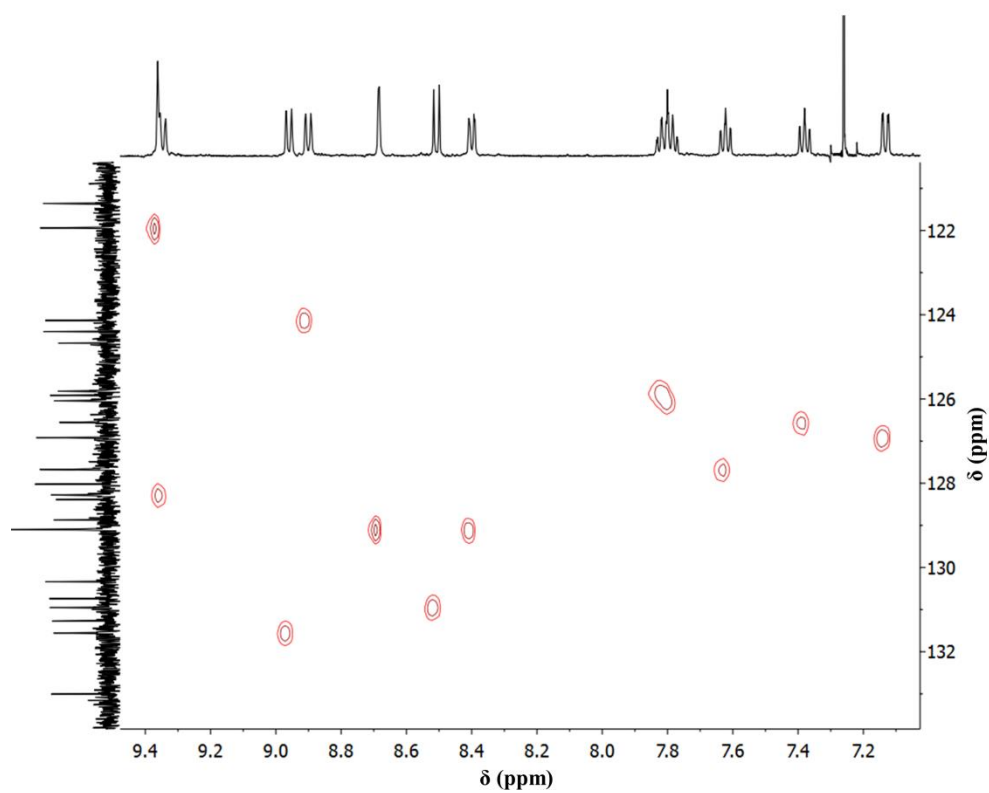


**Figure A2.60.** Full HMBC spectrum of **4a** (500 MHz, 125 MHz, CDCl<sub>3</sub>, 295 K).

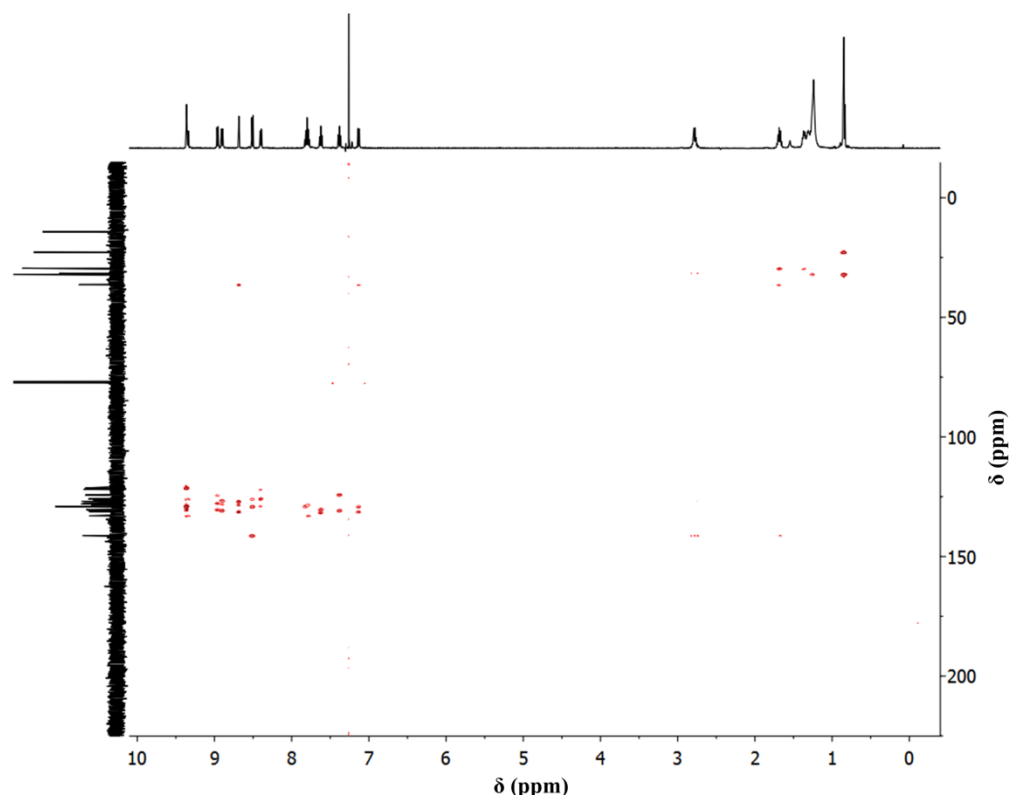
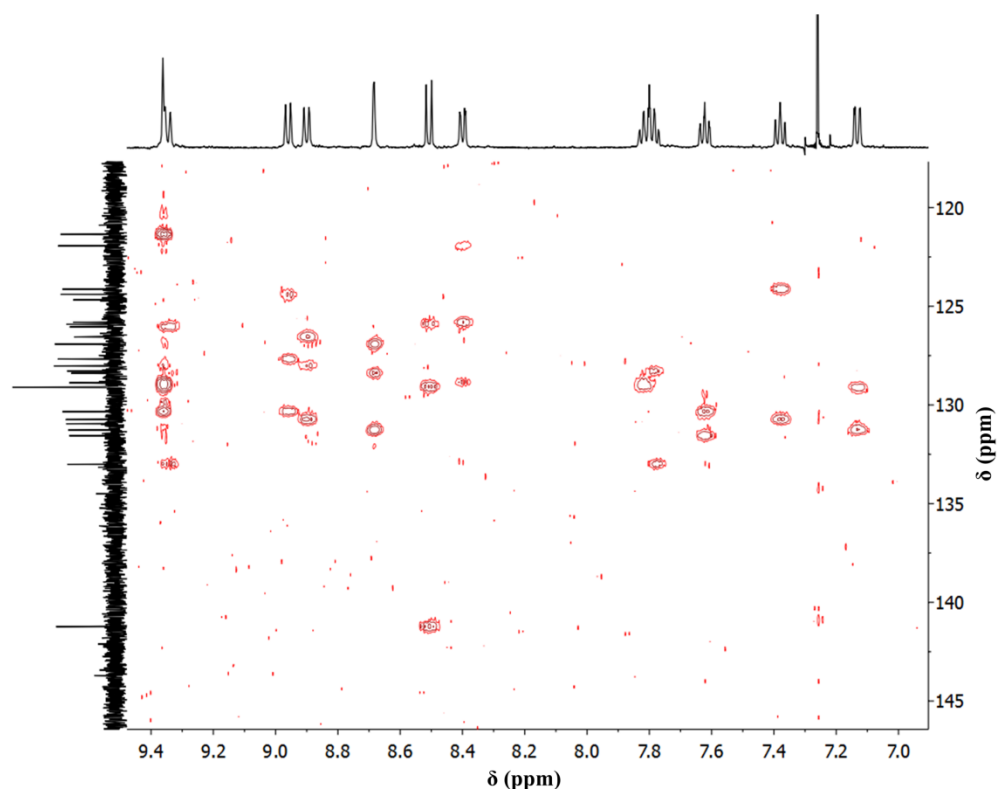
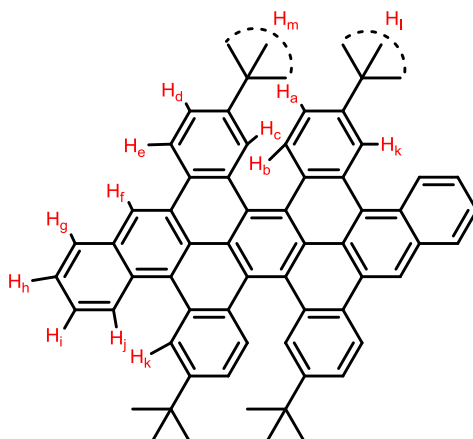


**Figure A2.61.** Partial HMBC spectrum of **4a** showing the aromatic region (500 MHz, 125 MHz, CDCl<sub>3</sub>, 295 K).



### Peak assignments for the compound 4b:



COSY spectrum indicates two 1,2,4-trisubstituted aromatic spin systems. First one contains  $H_a$ ,  $H_b$  and  $H_k$ .  $H_a$  is coupled to both  $H_b$  and  $H_k$ , whereas  $H_b$  and  $H_k$  are only coupled to  $H_a$ . Therefore,  $H_a$  is in position 2 on the aromatic ring. Coupling constant between  $H_a$  and  $H_b$  is consistent with *o*- substitution pattern. Coupling constant between  $H_k$  and  $H_a$  is consistent with *m*- substitution pattern. As a result,  $H_b$  and  $H_k$  are at positions 1 and 4, respectively. The second such spin system involves protons  $H_c$ ,  $H_d$  and  $H_e$ . By a similar analysis,  $H_c$ ,  $H_d$  and  $H_e$  are at positions 4,2, and 1, respectively. Location of these two spin systems can be assigned based on ROESY crosspeaks between  $H_e$  and  $H_f$ , and  $H_i$  and  $H_k$ .

ROESY crosspeak between  $H_b$  and  $H_c$  is a clear indication of an incomplete cyclodehydrogenation; because in the case of complete fusion, these two proton signals wouldn't be observed.

The two *t*-butyl groups can be assigned based on the ROESY spectrum.  $H_m$  has crosspeaks with  $H_c$  and  $H_d$ , and  $H_l$  has crosspeaks with  $H_a$  and  $H_k$ .

Rest of the protons on the periphery of the molecule can be assigned by using the ROESY and COSY crosspeaks as shown below.

**Figure A2.62.** Full COSY spectrum of **4b** (500 MHz, 500 MHz, CDCl<sub>3</sub>, 298 K).

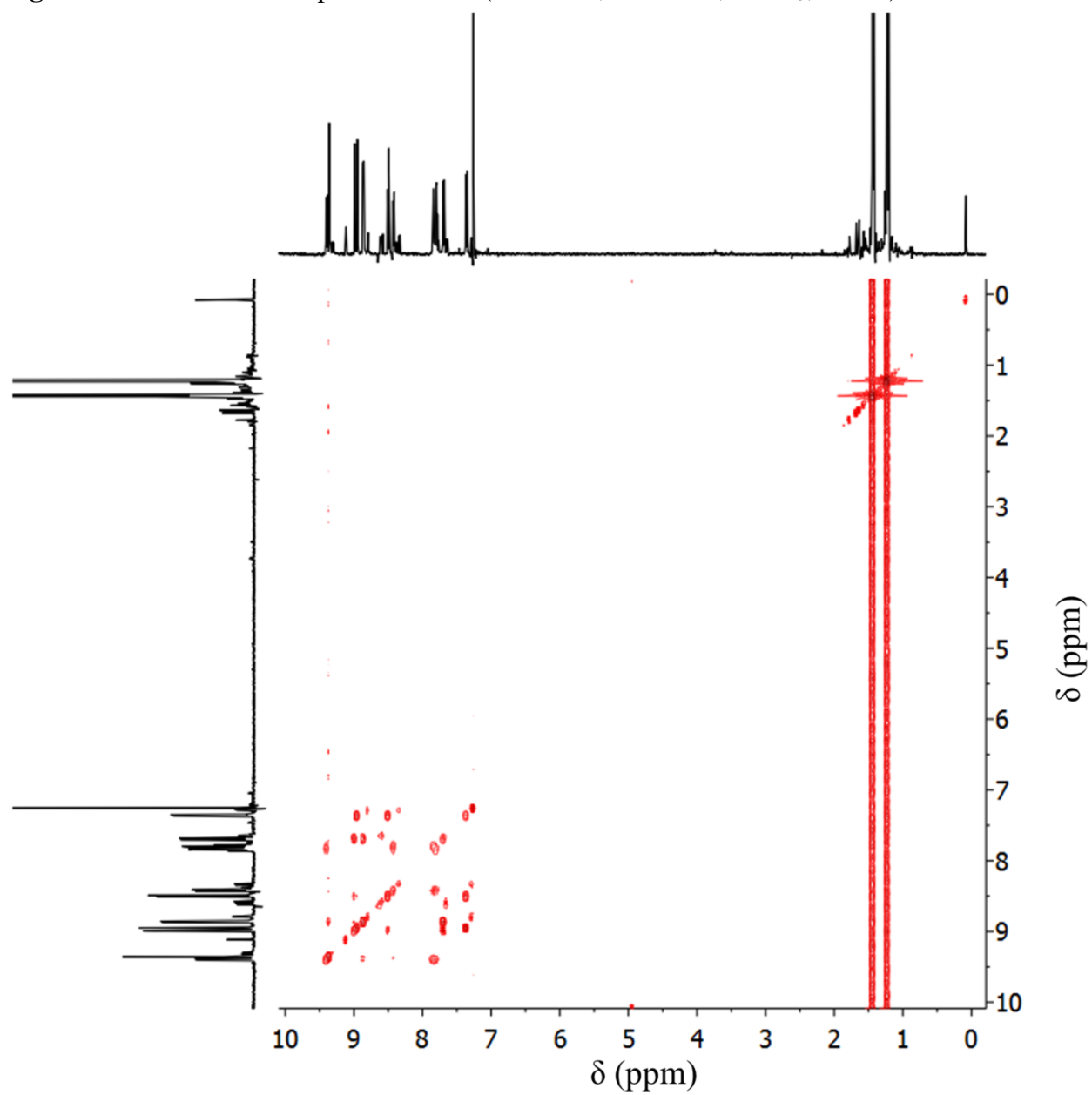




**Figure A2.63.** Partial COSY spectrum of **4b** showing the aromatic region (500 MHz, 500 MHz, CDCl<sub>3</sub>, 298 K).

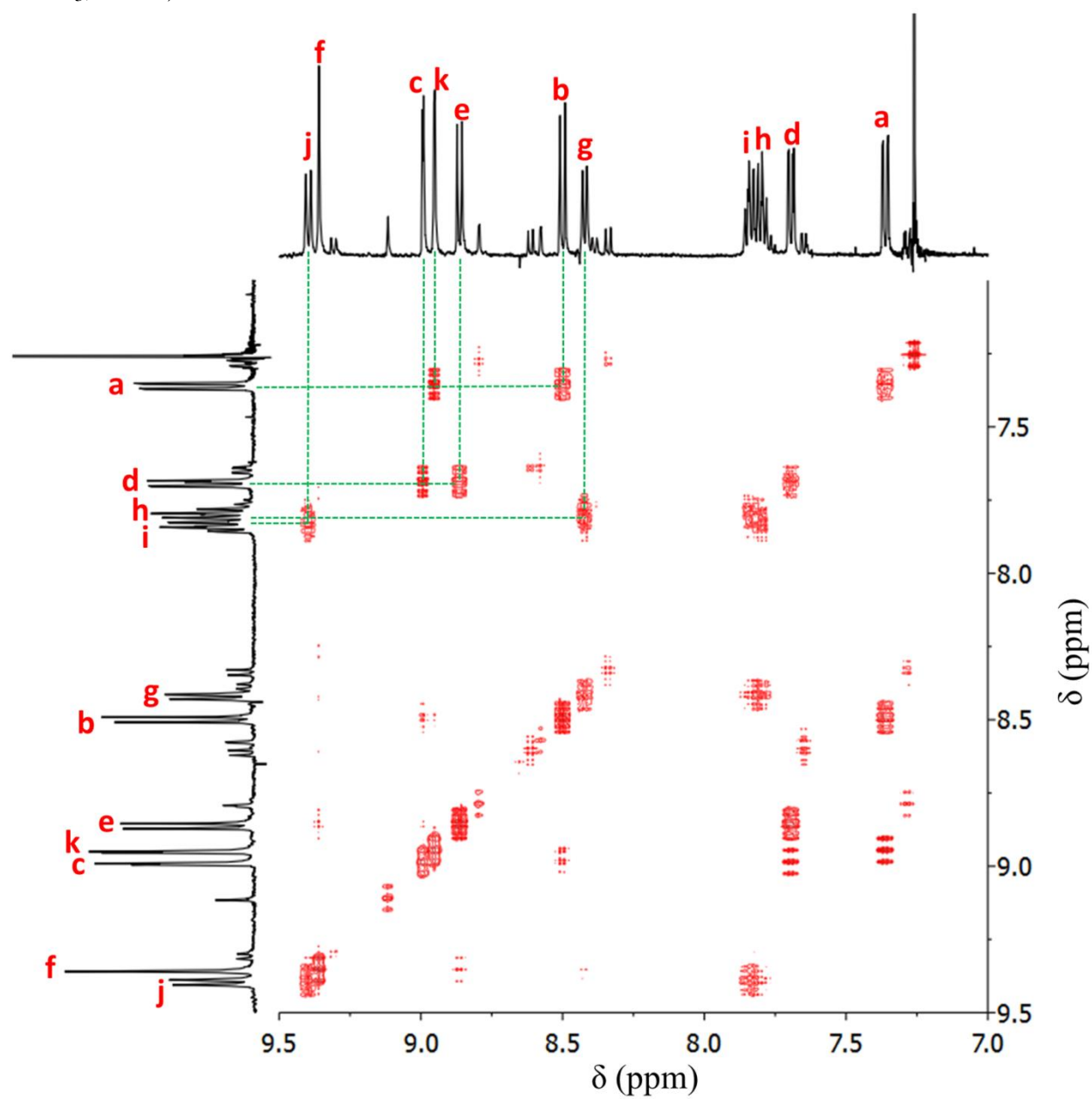


**Figure A2.64.** Full ROESY spectrum of **4b** (500 MHz, 500 MHz, CDCl<sub>3</sub>, 298 K).

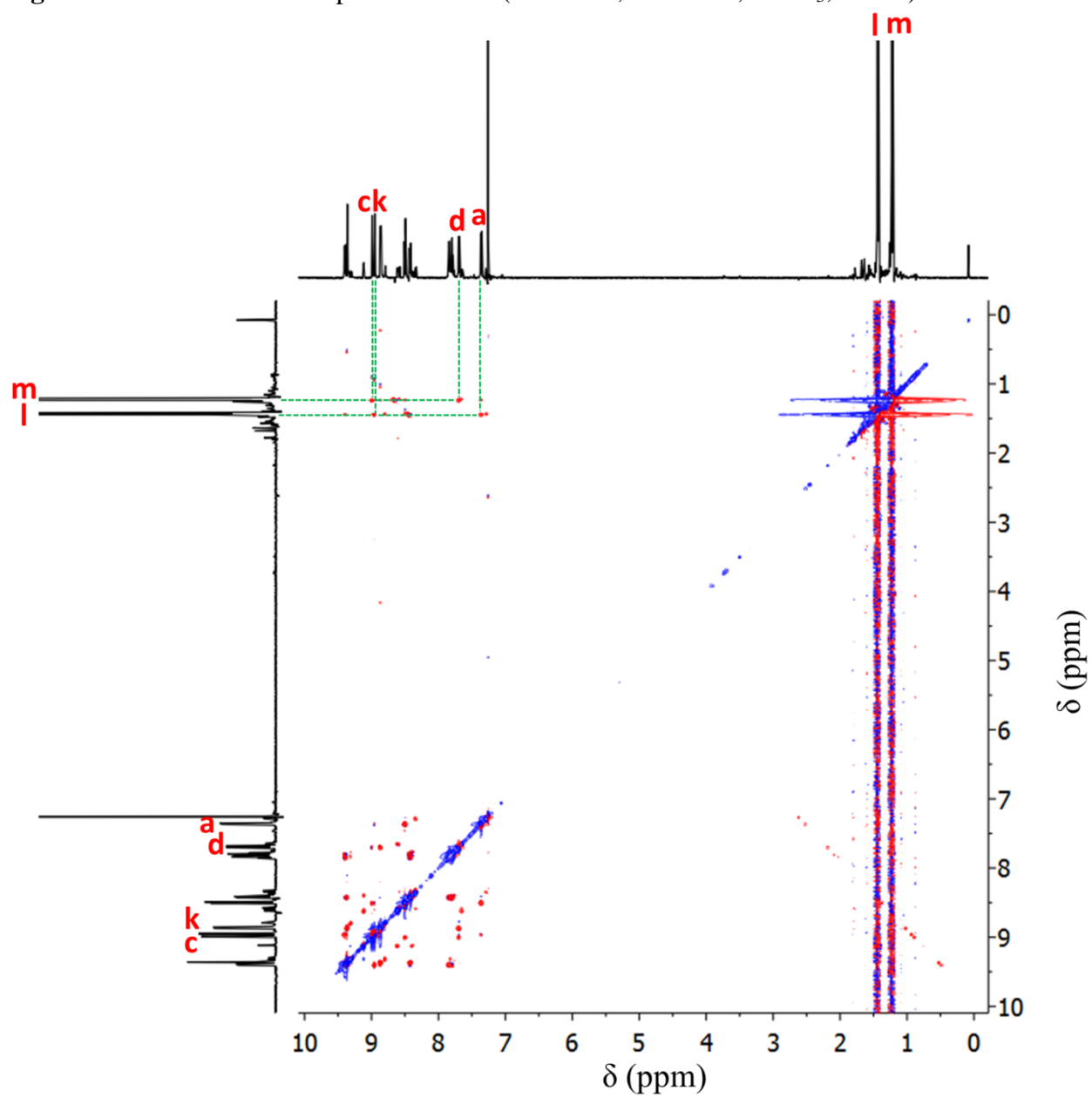


**Figure A2.65.** Partial ROESY spectrum of **4b** showing the aromatic region (500 MHz, 500 MHz, CDCl<sub>3</sub>, 298 K).

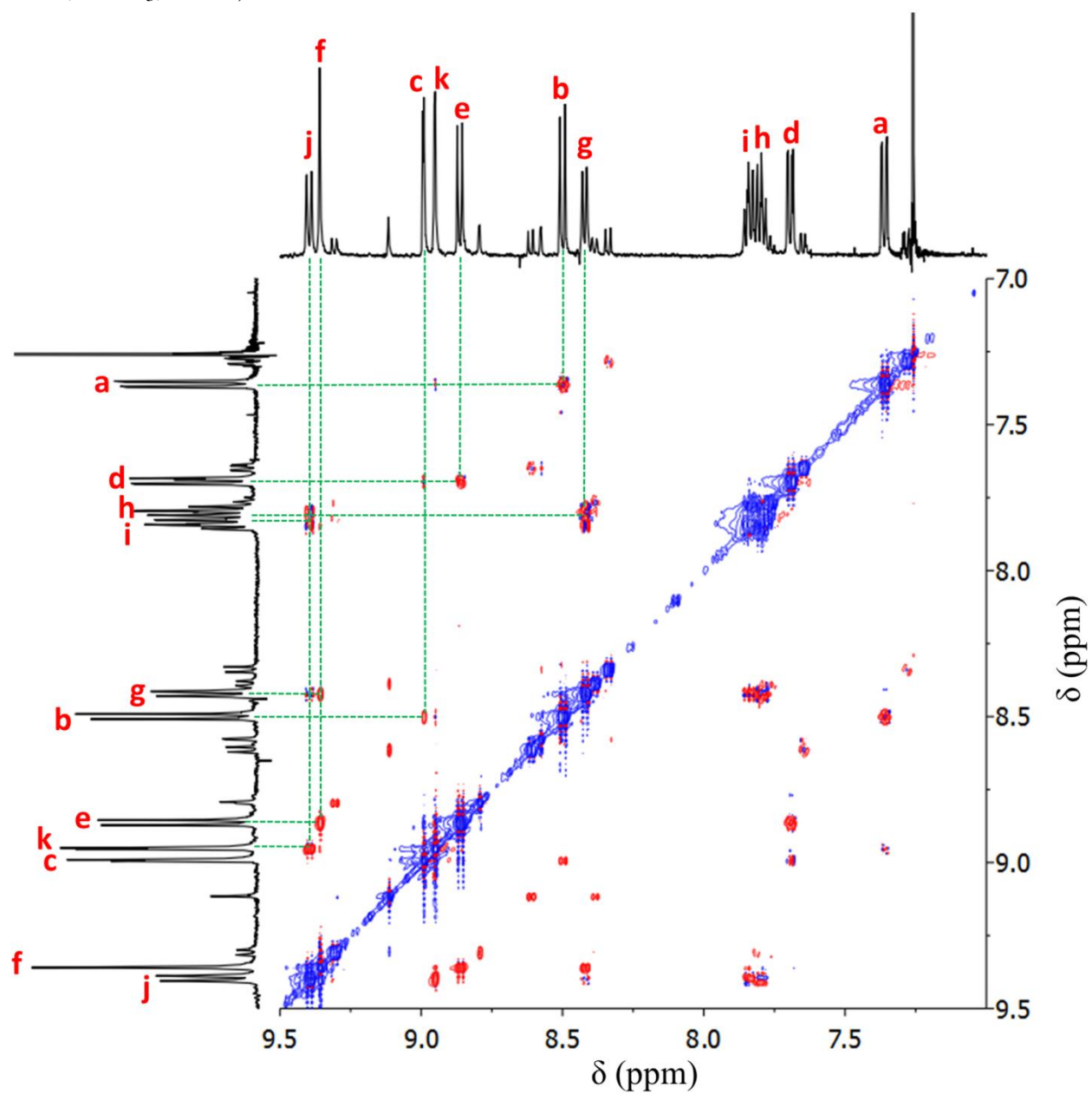


**Figure A2.66.** Full HSQC spectrum of **4b** (500 MHz, 125 MHz, CDCl<sub>3</sub>, 298 K).

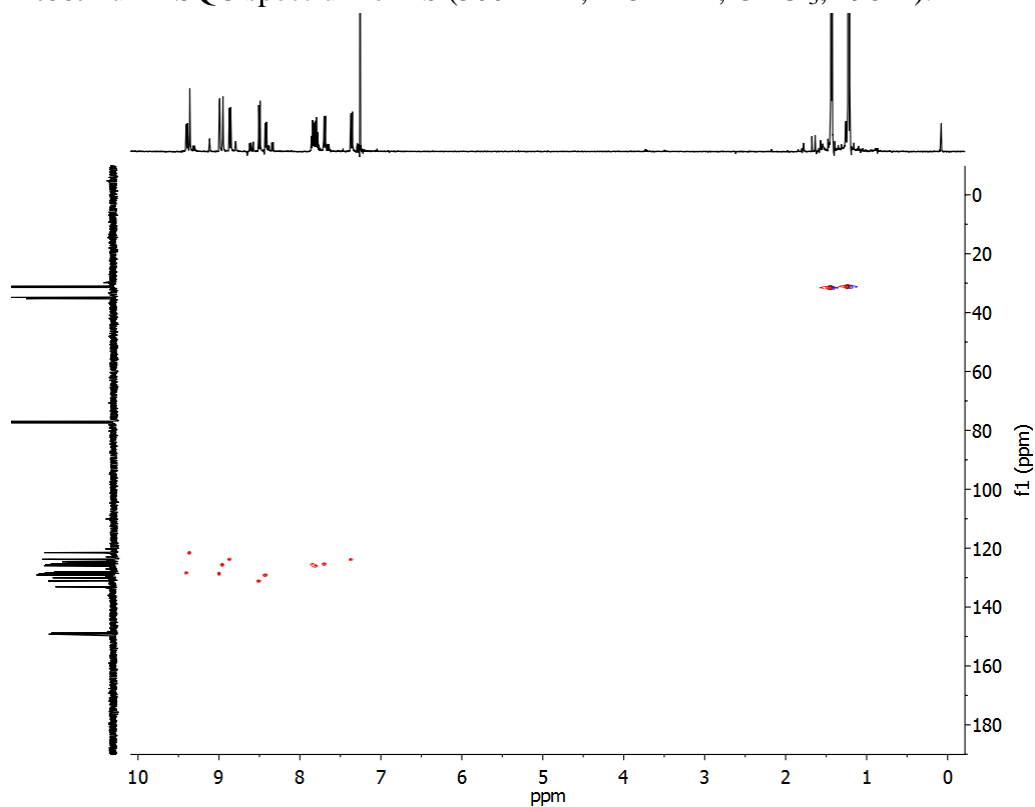


**Figure A2.67.** Partial HSQC spectrum of **4b** showing the aromatic region (500 MHz, 125 MHz, CDCl<sub>3</sub>, 298 K).

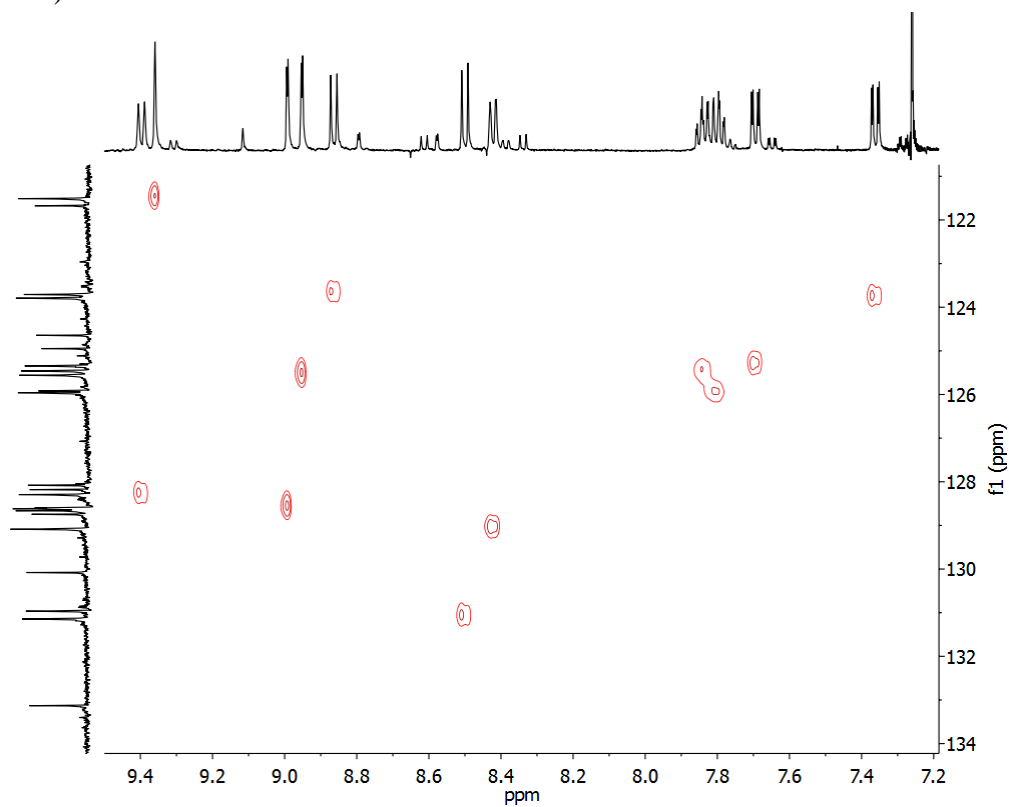


**Figure A2.68.** Full HMBC spectrum of **4b** (500 MHz, 125 MHz, CDCl<sub>3</sub>, 298 K).

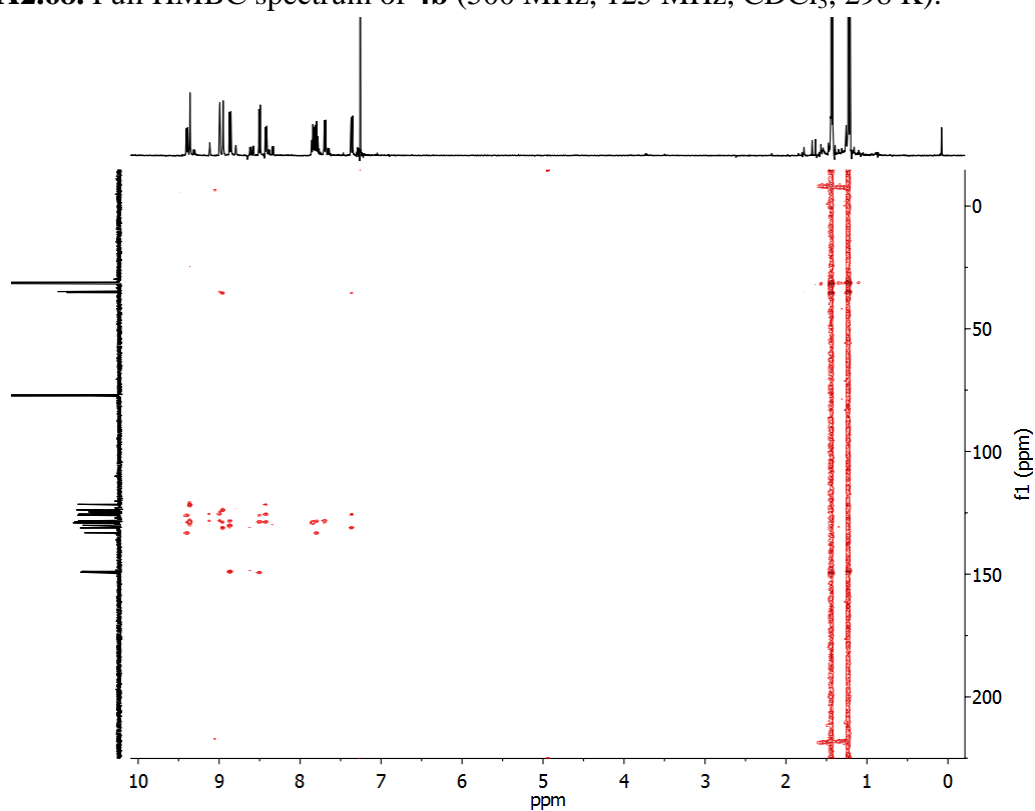
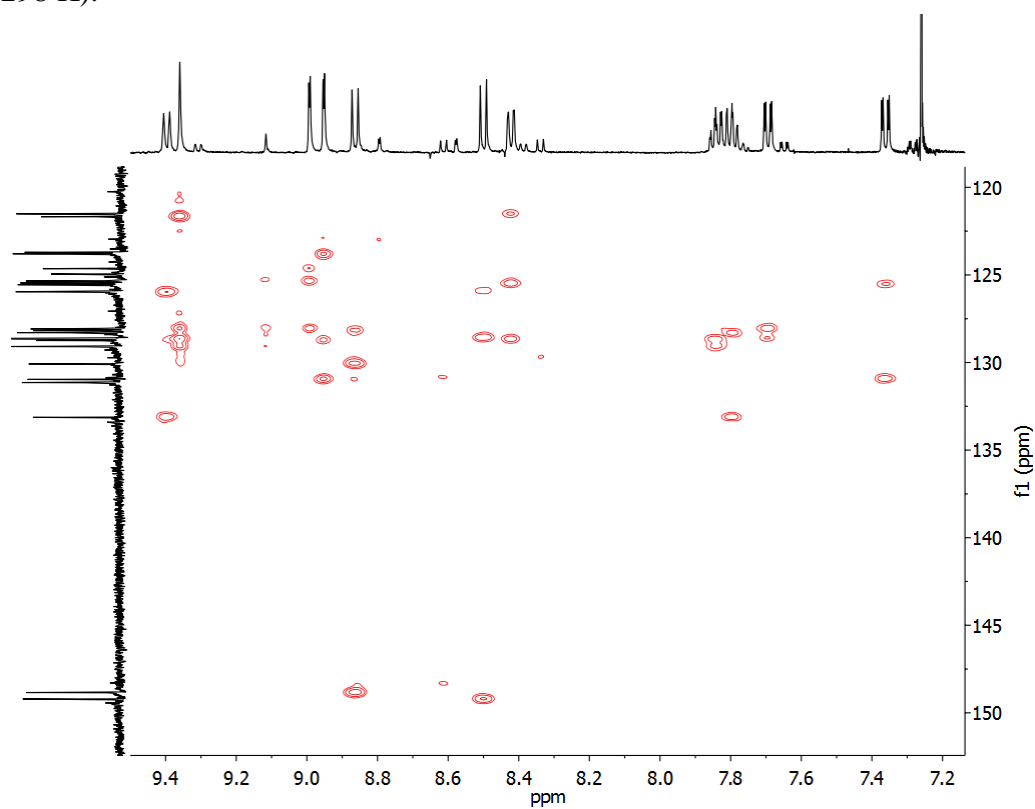
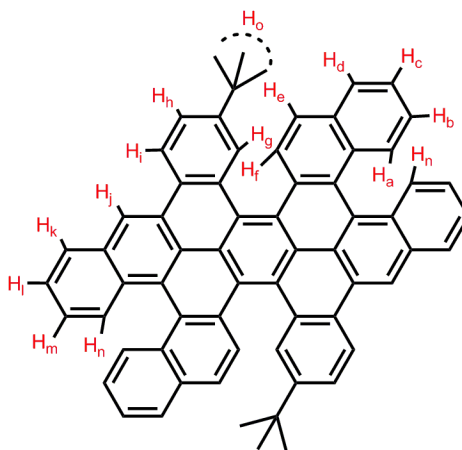


**Figure A2.69.** Partial HMBC spectrum of **4b** showing the aromatic region (500 MHz, 125 MHz, CDCl<sub>3</sub>, 298 K).



### Peak assignments for the compound **4c**:



COSY spectrum indicates a 1,2,4-trisubstituted aromatic spin system, which contains  $H_g$ ,  $H_h$  and  $H_i$ .  $H_h$  is coupled to both  $H_g$  and  $H_i$ , whereas  $H_g$  and  $H_i$  are only coupled to  $H_h$ . Therefore,  $H_h$  is in position 2 on the aromatic ring. Based on coupling constants,  $H_i$  and  $H_g$  are at positions 1 and 4, respectively. Furthermore, the *t*Bu group is attached to this ring based on ROESY crosspeaks between  $H_g$  and  $H_o$  and  $H_h$  and  $H_o$ .

Similar to the analyses for the compounds **4a** and **4b**, key ROESY crosspeaks allow us to determine which C-C bonds did not form in the molecule. The crosspeak between  $H_f$  and  $H_g$  indicates that a C-C bond didn't form at a similar position to **4a** and **4b**. This can be explained by the steric hindrance imposed by the *t*Bu group. Even after extended reaction times, this bond does not form. Another bond that does not form is the one between the carbons  $H_a$  and  $H_n$  are attached to, as supported by the ROESY crosspeak between two hydrogens. This is presumably due to the rigid and contorted structure of the molecule.

Rest of the protons on the periphery of the molecule can be assigned by using the ROESY and COSY crosspeaks as shown below.

**Figure A2.70.** Full COSY spectrum of **4c** (500 MHz, 500 MHz, CDCl<sub>3</sub>, 296 K).

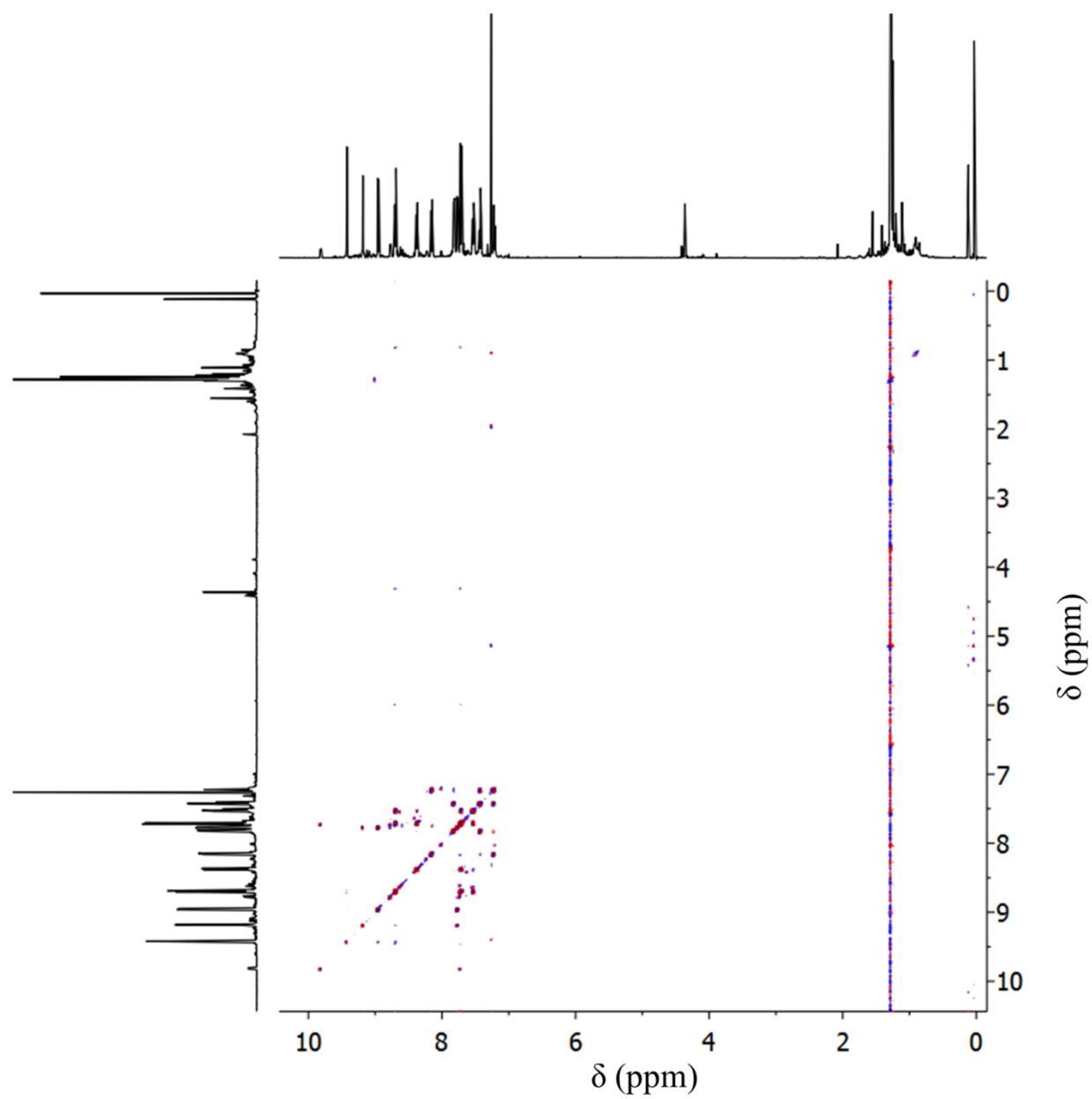


**Figure A2.71.** Partial COSY spectrum of **4c** showing the aromatic region (500 MHz, 500 MHz, CDCl<sub>3</sub>, 296 K).

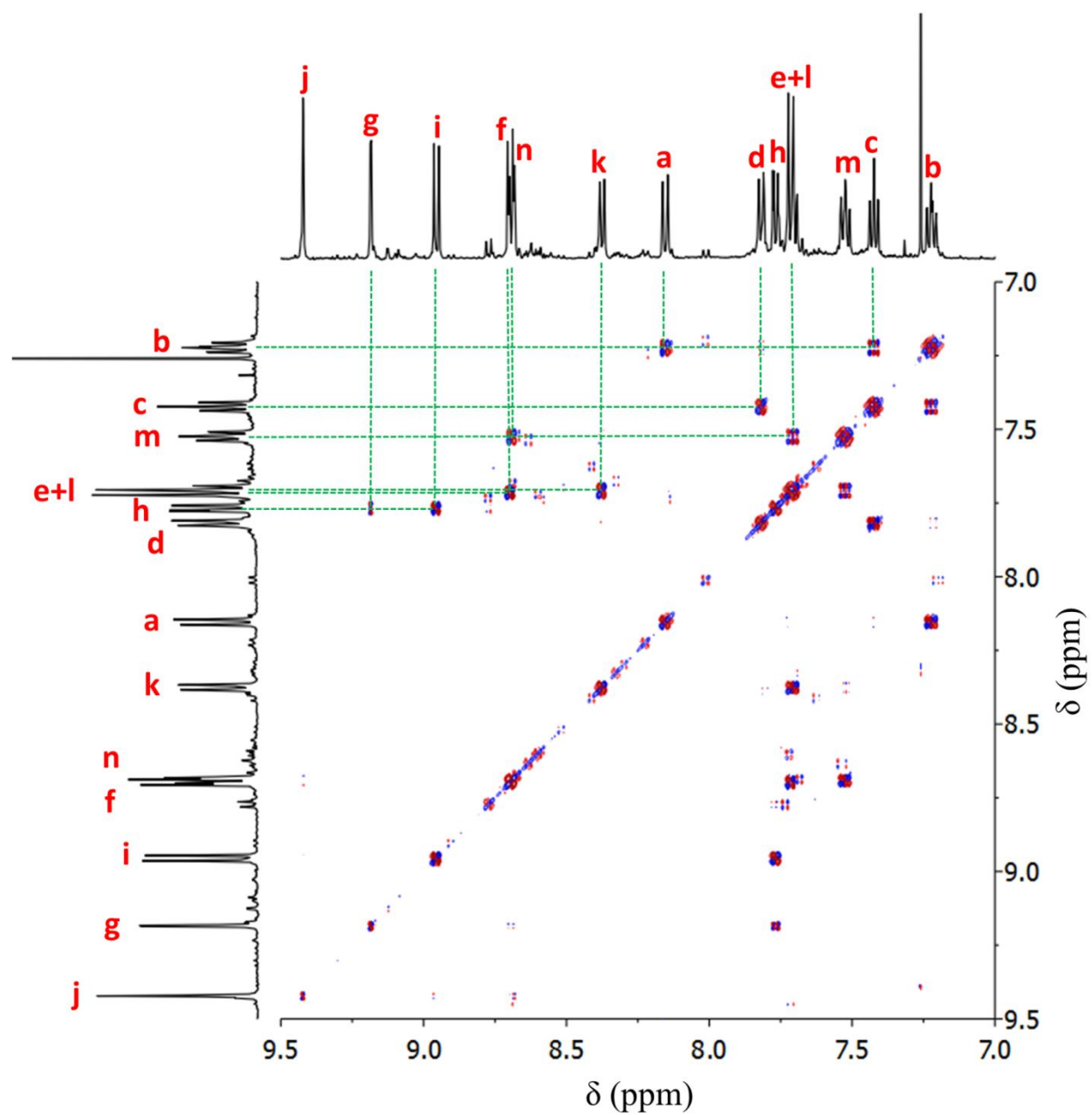




**Figure A2.72.** Full ROESY spectrum of **4c** (500 MHz, 500 MHz, CDCl<sub>3</sub>, 296 K).

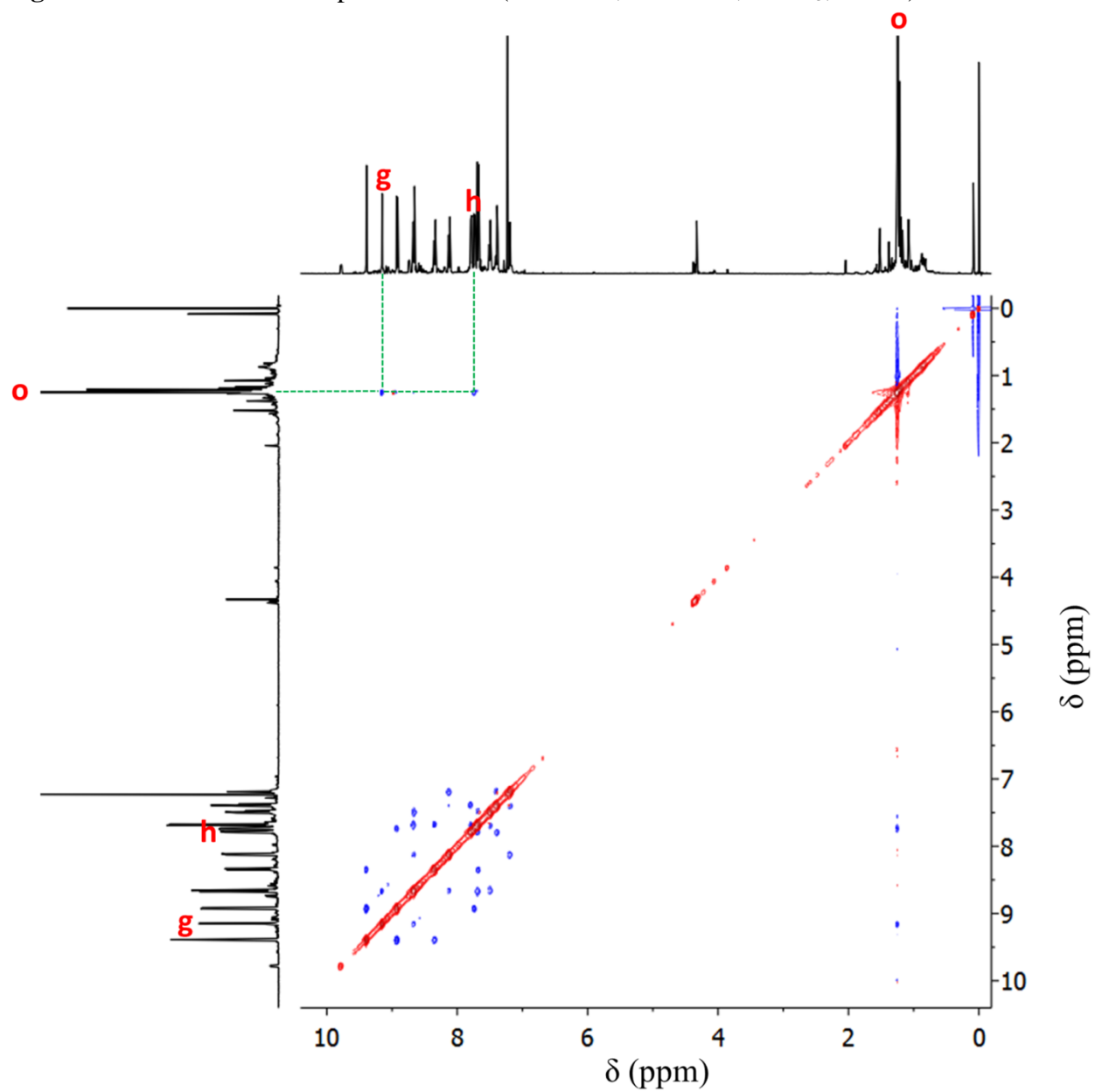


**Figure A2.73.** Partial ROESY spectrum of **4c** showing the aromatic region (500 MHz, 500 MHz, CDCl<sub>3</sub>, 296 K).

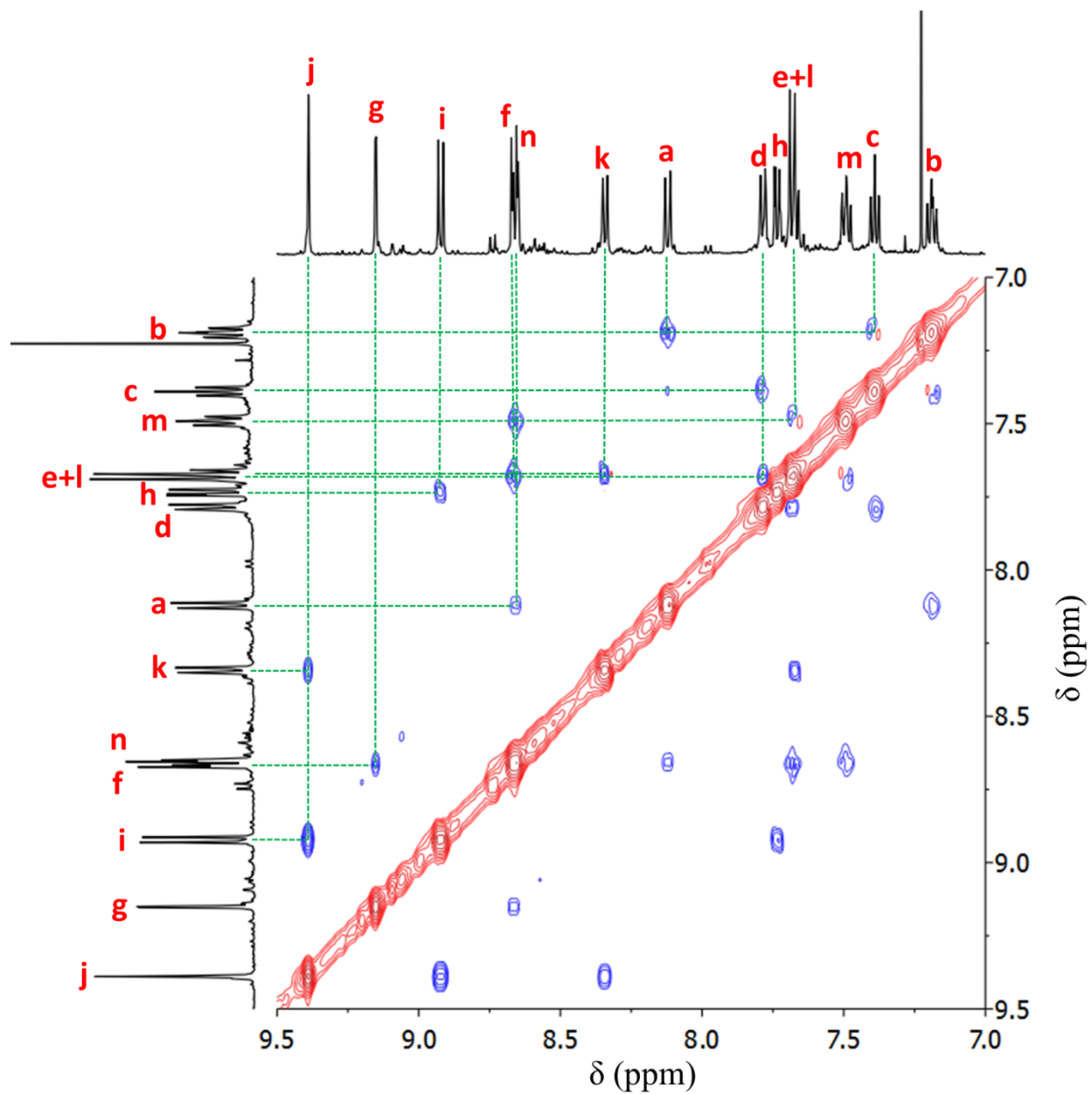


**Figure A2.74.** Full HSQC spectrum of **4c** (500 MHz, 125 MHz, CDCl<sub>3</sub>, 296 K).

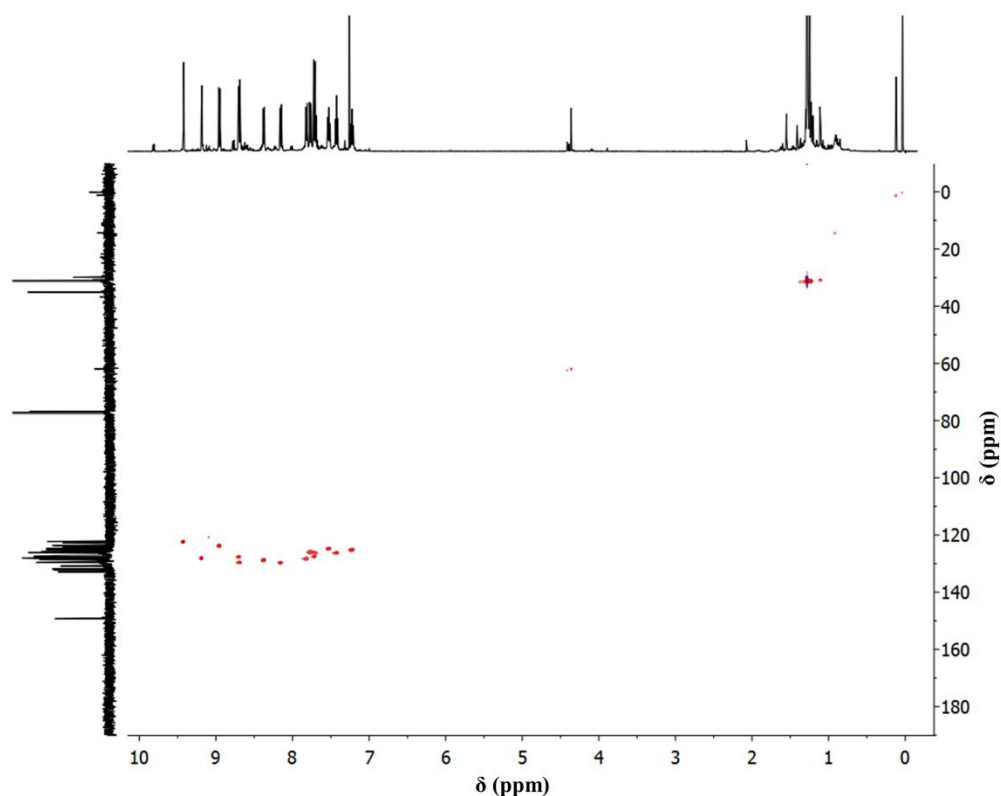


**Figure A2.75.** Partial HSQC spectrum of **4c** showing the aromatic region (500 MHz, 125 MHz, CDCl<sub>3</sub>, 298 K).

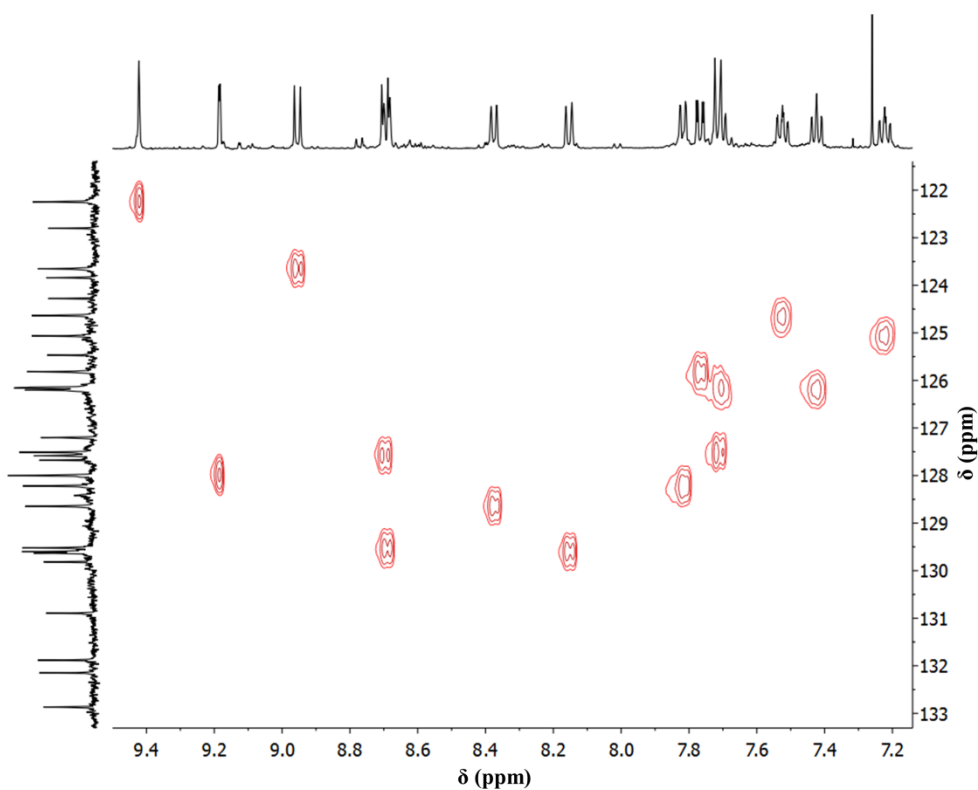


**Figure A2.76.** Full HMBC spectrum of **4c** (500 MHz, 125 MHz, CDCl<sub>3</sub>, 296 K).

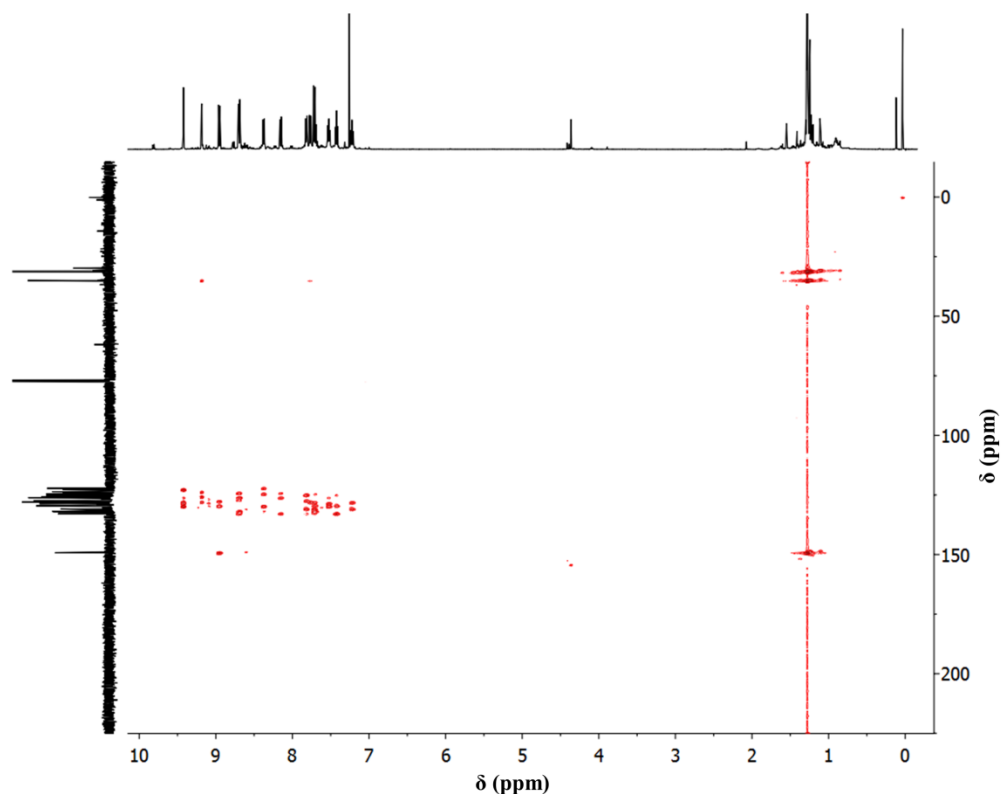
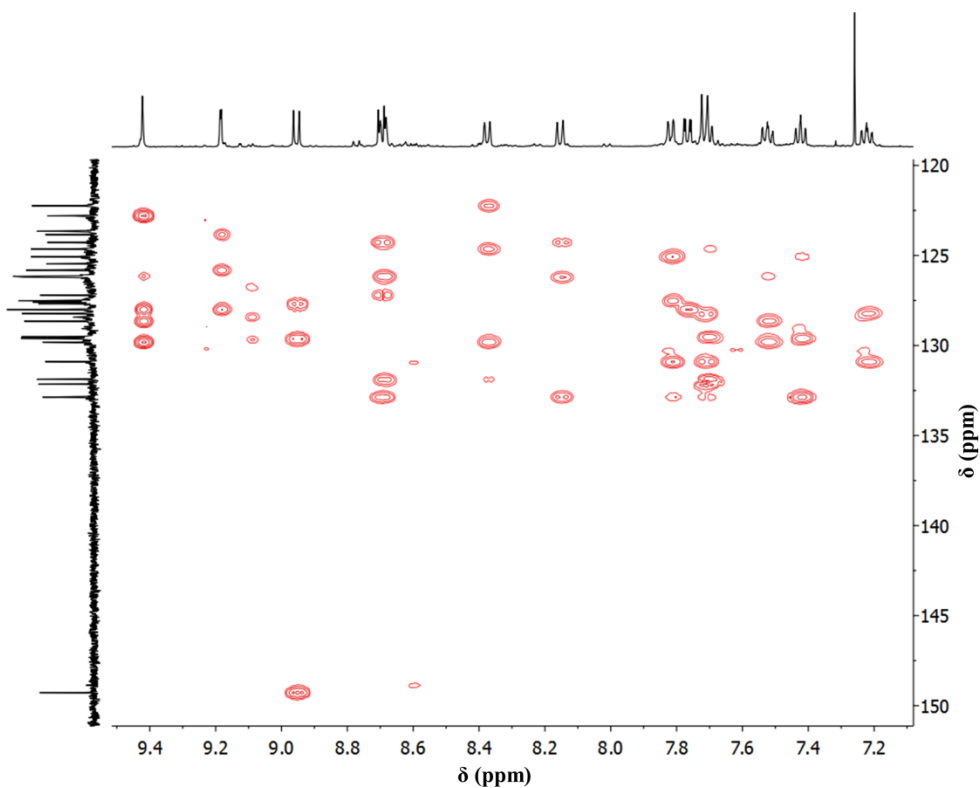


**Figure A2.77.** Partial HMBC spectrum of **4c** showing the aromatic region (500 MHz, 125 MHz, CDCl<sub>3</sub>, 296 K).



Peak assignments for the compound 5a- $^{13}\text{C}_2$ :

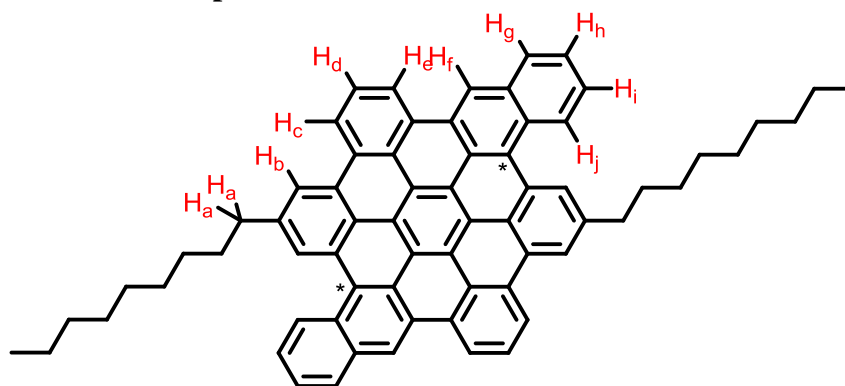


**Figure A2.78.** Full COSY spectrum of **5a**- $^{13}\text{C}_2$  (500 MHz, 500 MHz, 1,2- $\text{C}_2\text{H}_2\text{Cl}_4$ , 408 K).

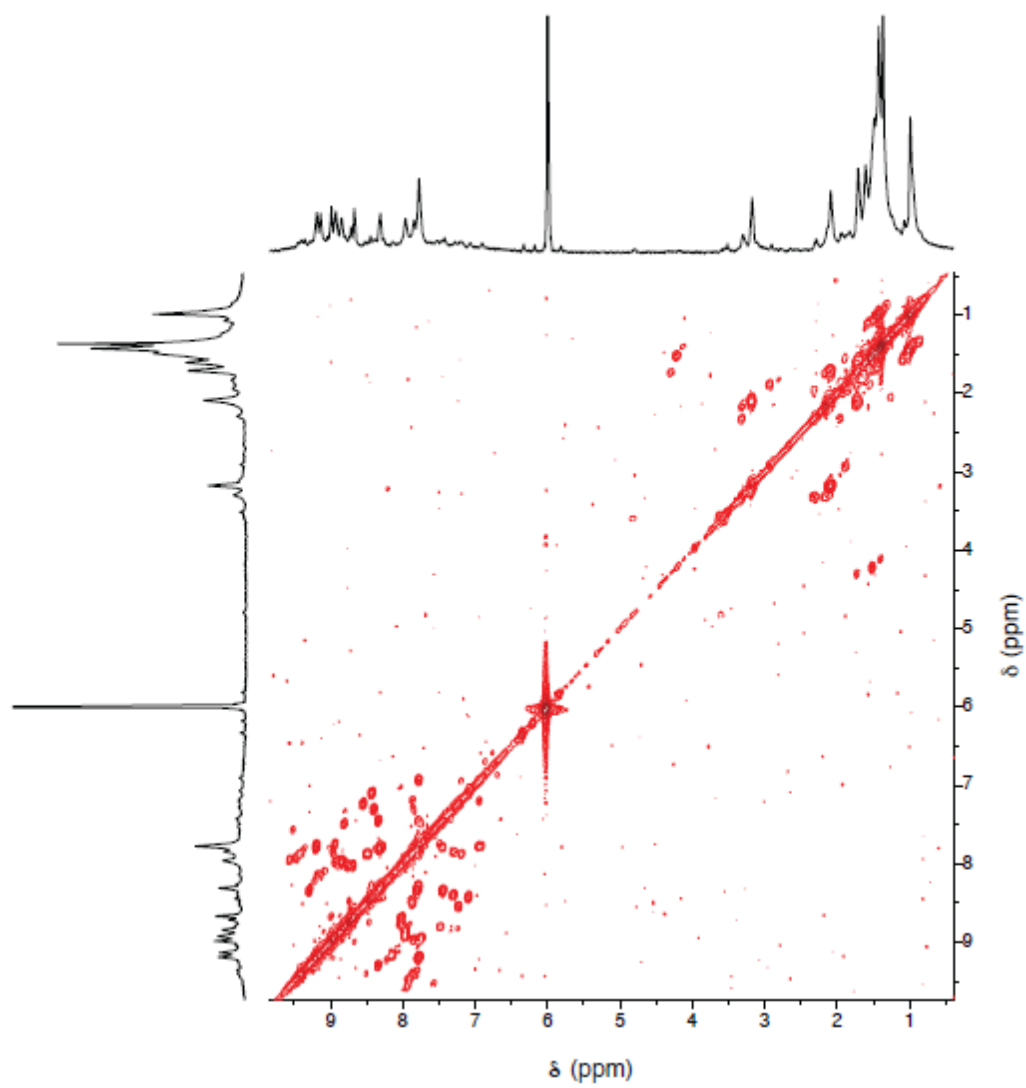


**Figure A2.79.** Partial COSY spectrum of **5a**- $^{13}\text{C}_2$  showing the aromatic region (500 MHz, 500 MHz, 1,2- $\text{C}_2\text{H}_2\text{Cl}_4$ , 408 K).

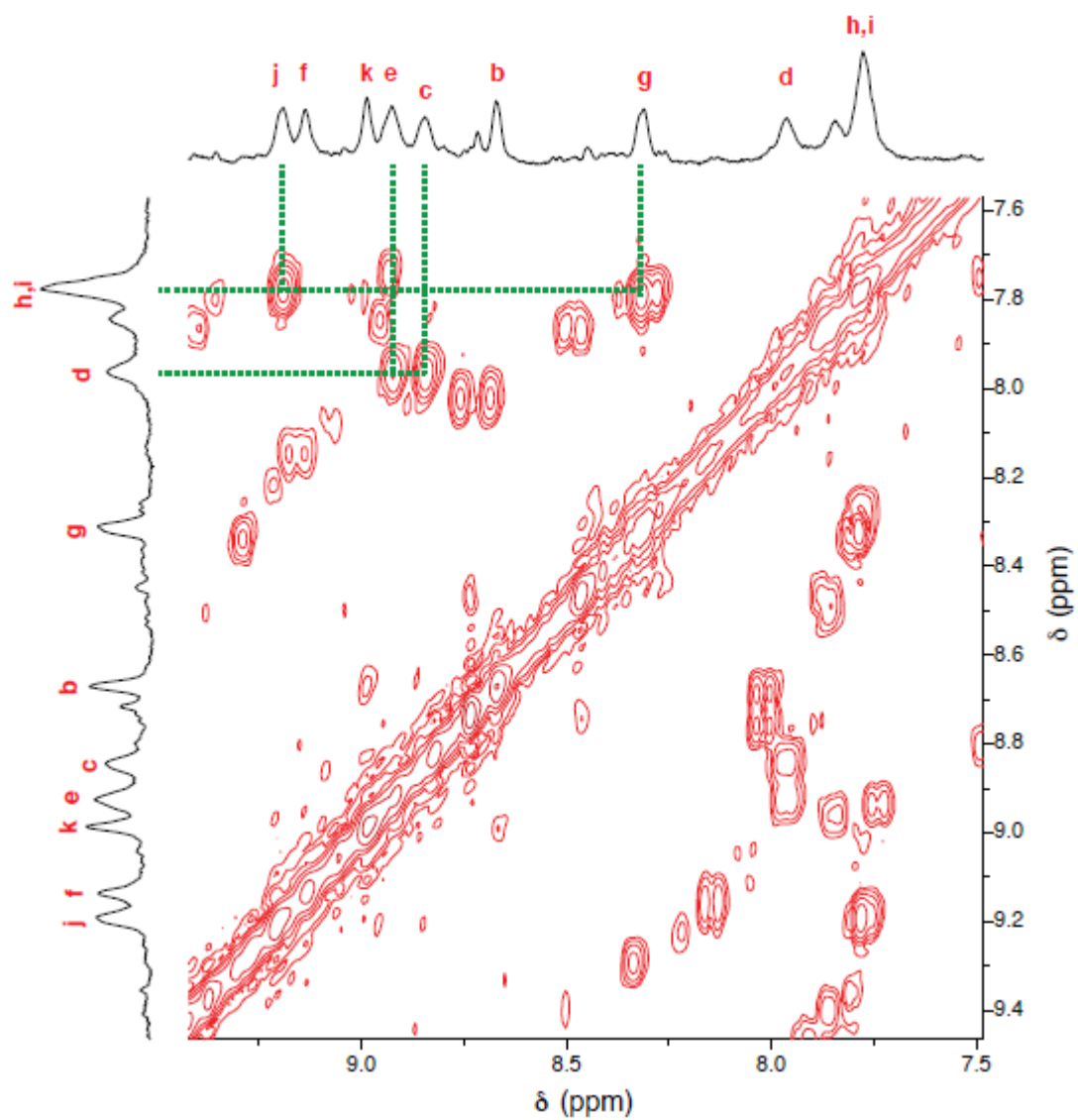


**Figure A2.80.** Full ROESY spectrum of **5a**- $^{13}\text{C}_2$  (500 MHz, 500 MHz, 1,2- $\text{C}_2\text{H}_2\text{Cl}_4$ , 408 K).

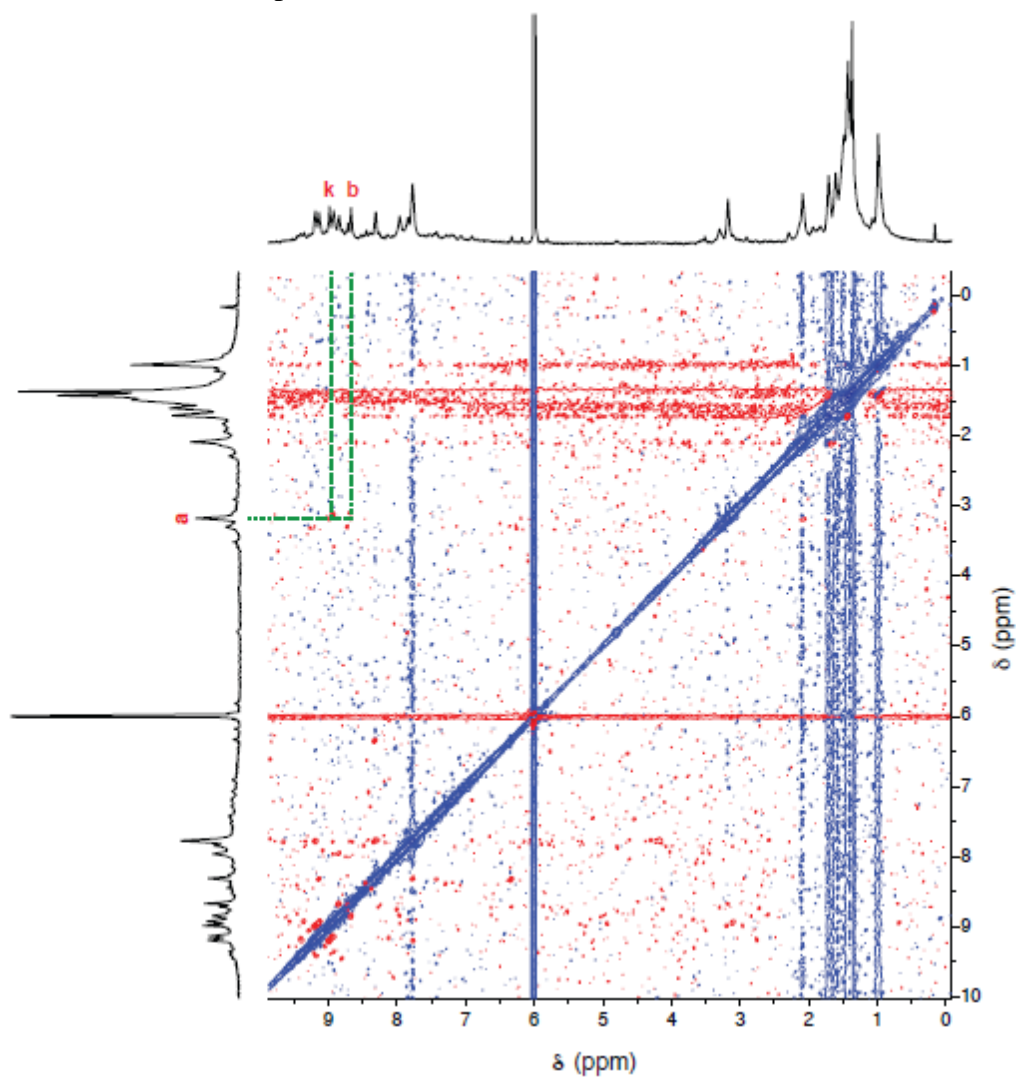




**Figure A2.81.** Partial ROESY spectrum of **5a**- $^{13}\text{C}_2$  showing the aromatic region (500 MHz, 500 MHz, 1,2- $\text{C}_2\text{H}_2\text{Cl}_4$ , 408 K).

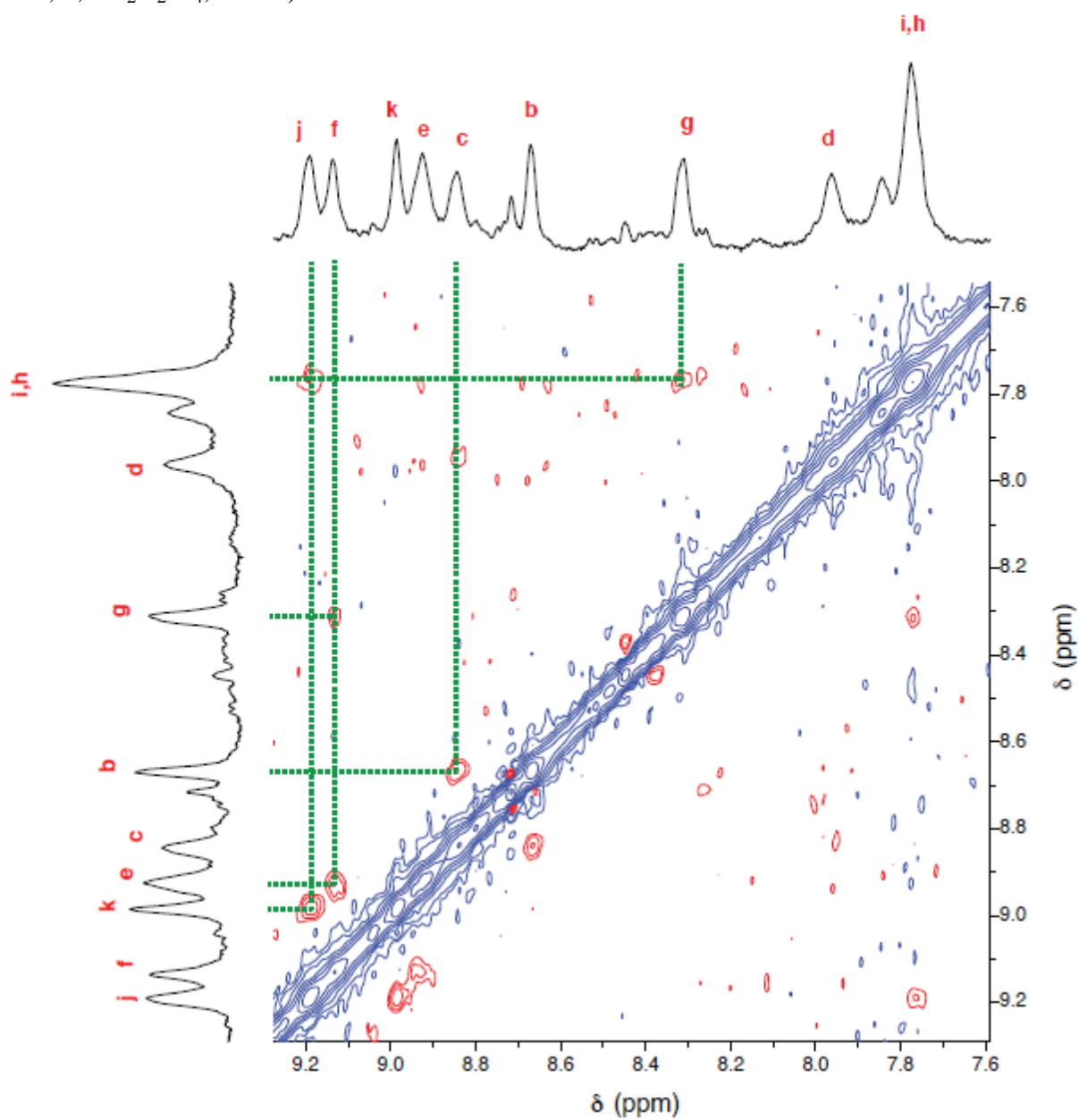


**Figure A2.82.** Full HSQC spectrum of **5a**- $^{13}\text{C}_2$  (500 MHz, 125 MHz, 1,2- $\text{C}_2\text{H}_2\text{Cl}_4$ , 408 K).

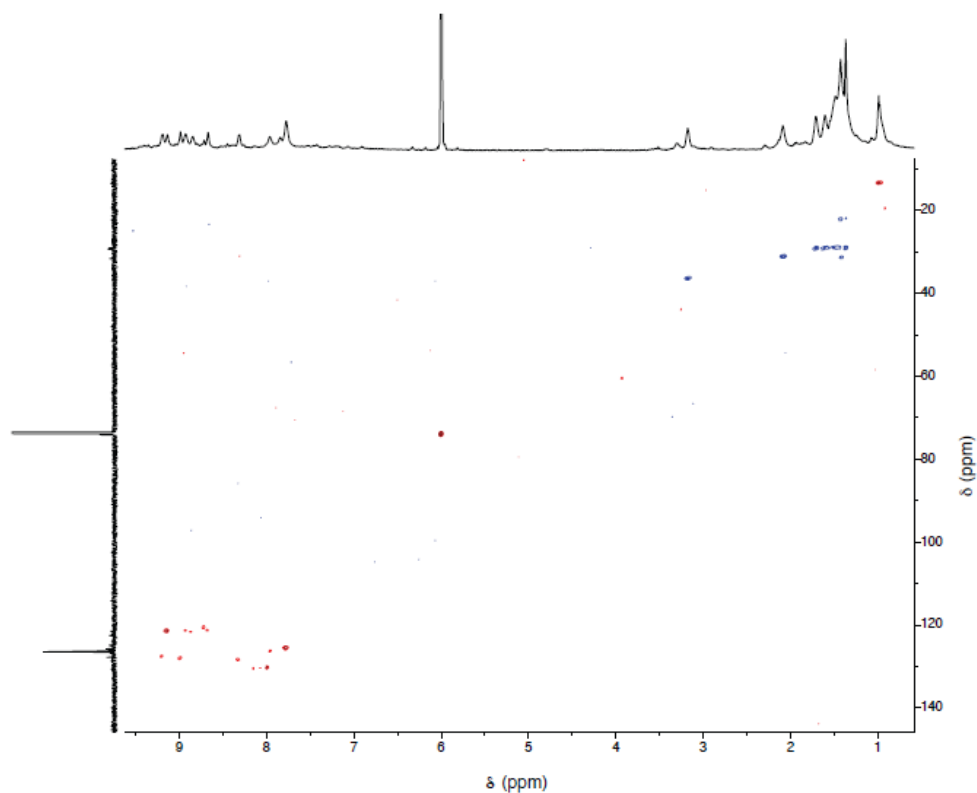


**Figure A2.83.** Partial HSQC spectrum of **5a**- $^{13}\text{C}_2$  showing the aromatic region (500 MHz, 125 MHz, 1,2- $\text{C}_2\text{H}_2\text{Cl}_4$ , 408 K).

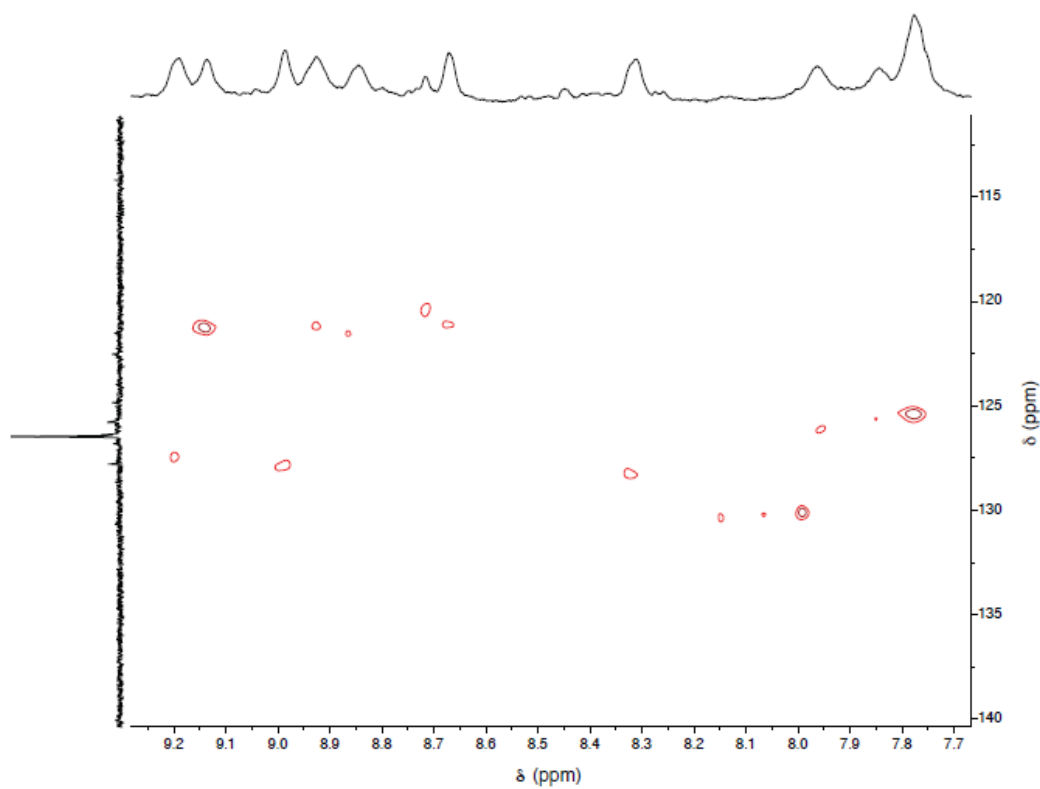


**Figure A2.84.** Full HMBC spectrum of **5a**- $^{13}\text{C}_2$  (500 MHz, 125 MHz, 1,2- $\text{C}_2\text{H}_2\text{Cl}_4$ , 408 K).

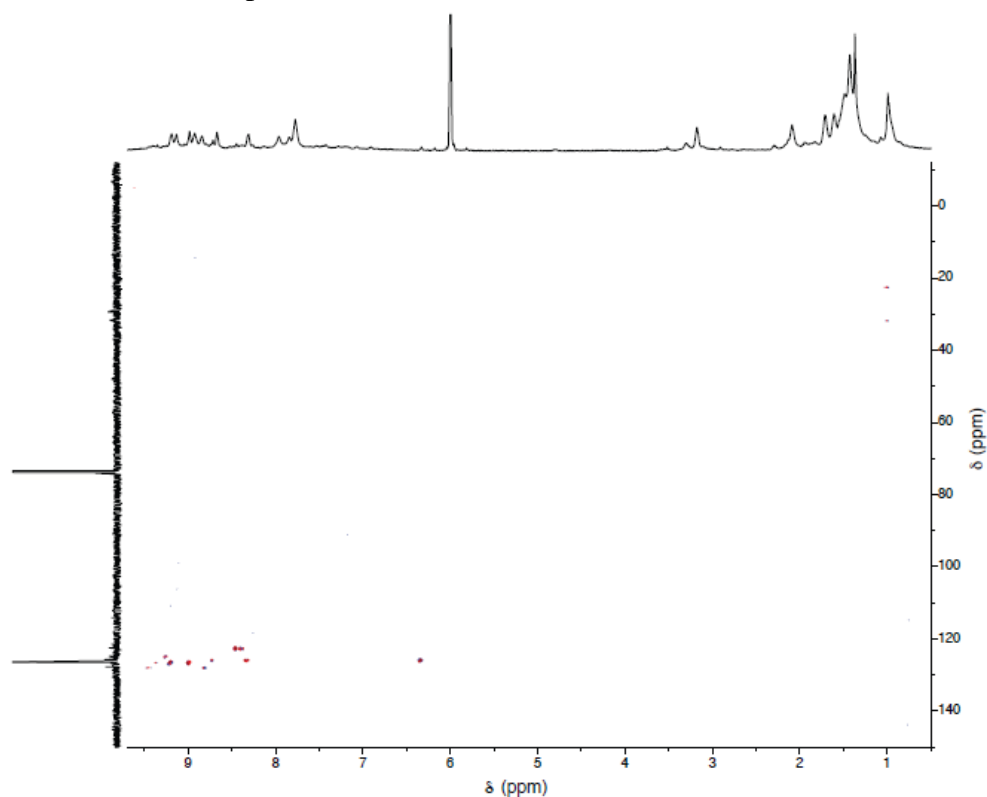
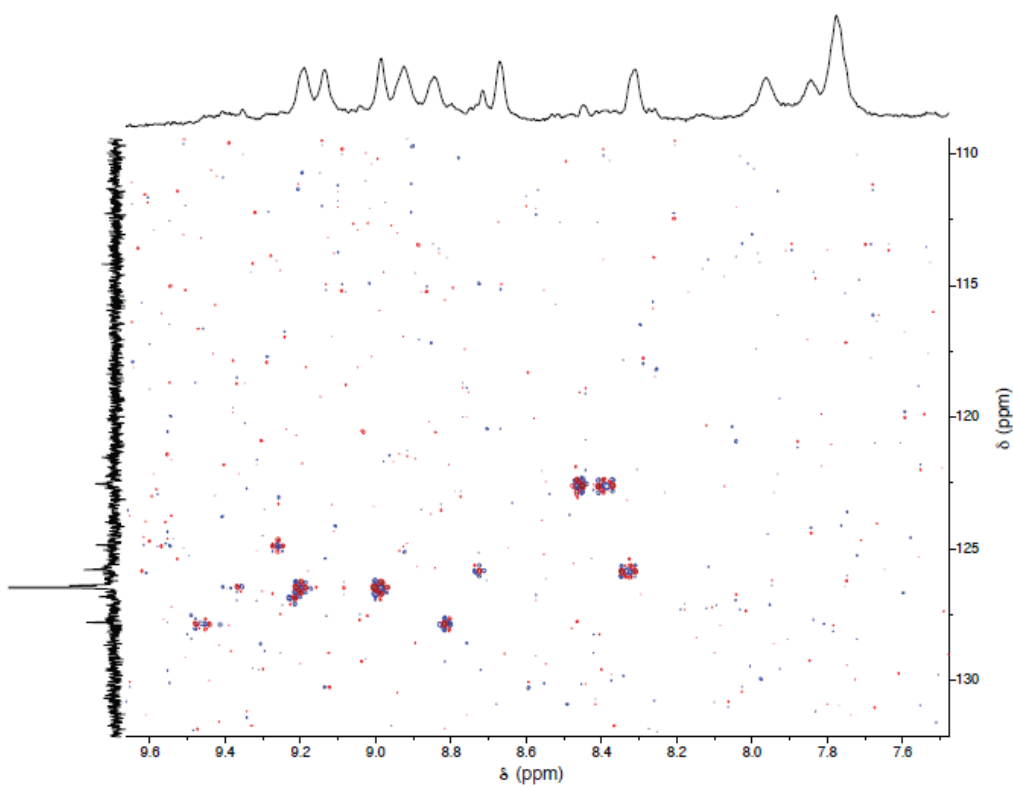


**Figure A2.85.** Partial HMBC spectrum of **5a**- $^{13}\text{C}_2$  showing the aromatic region (500 MHz, 125 MHz, 1,2- $\text{C}_2\text{H}_2\text{Cl}_4$ , 408 K).



### E. UV/Vis and Fluorescence Spectroscopy

**Figure A2.86.** UV/Vis absorption spectra of the compounds **4a** (green) and **5a-<sup>13</sup>C<sub>2</sub>** (pink).

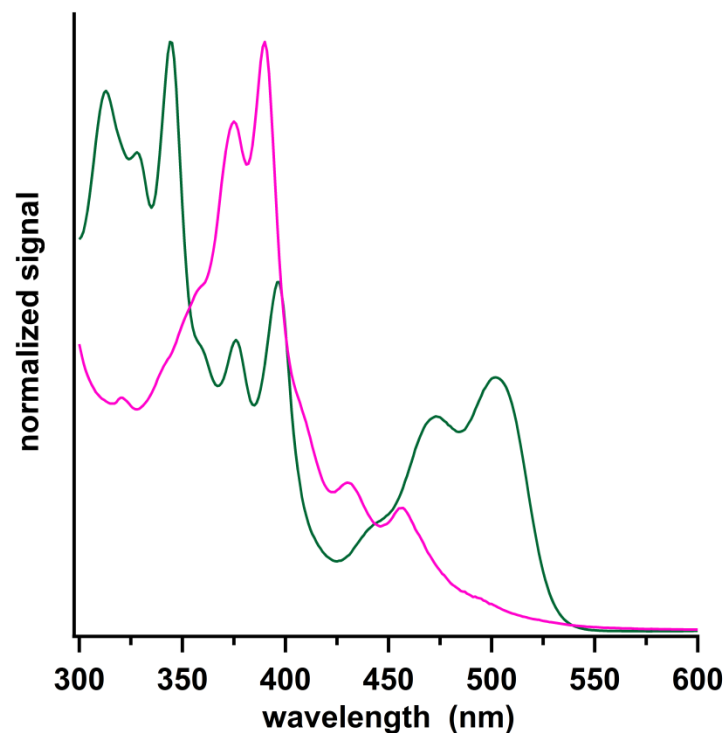
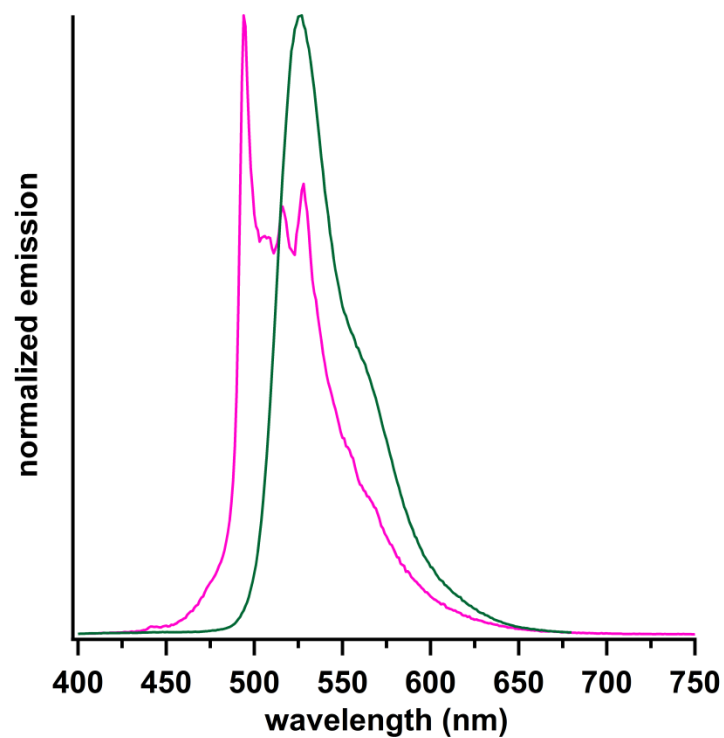


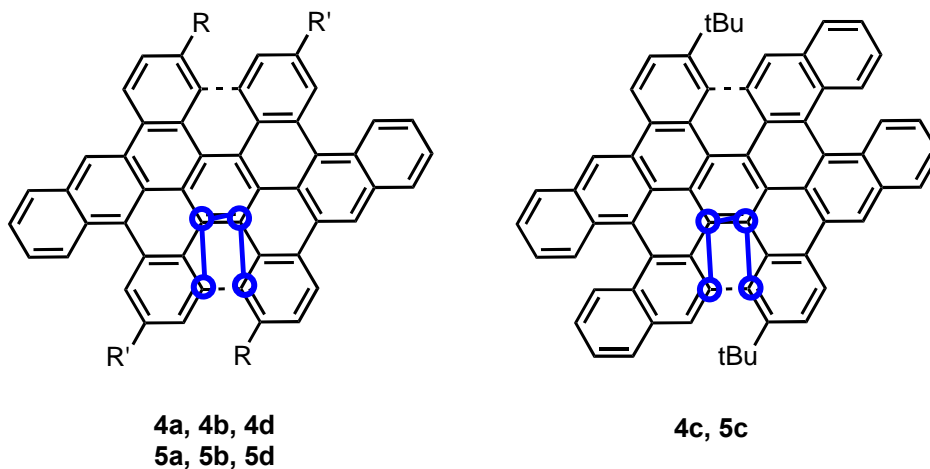
**Figure A2.87.** UV/Vis photoemission spectra of the compounds **4a** (green,  $\lambda_{\text{ex}} = 344$  nm) and **5a** (pink,  $\lambda_{\text{ex}} = 389$  nm).



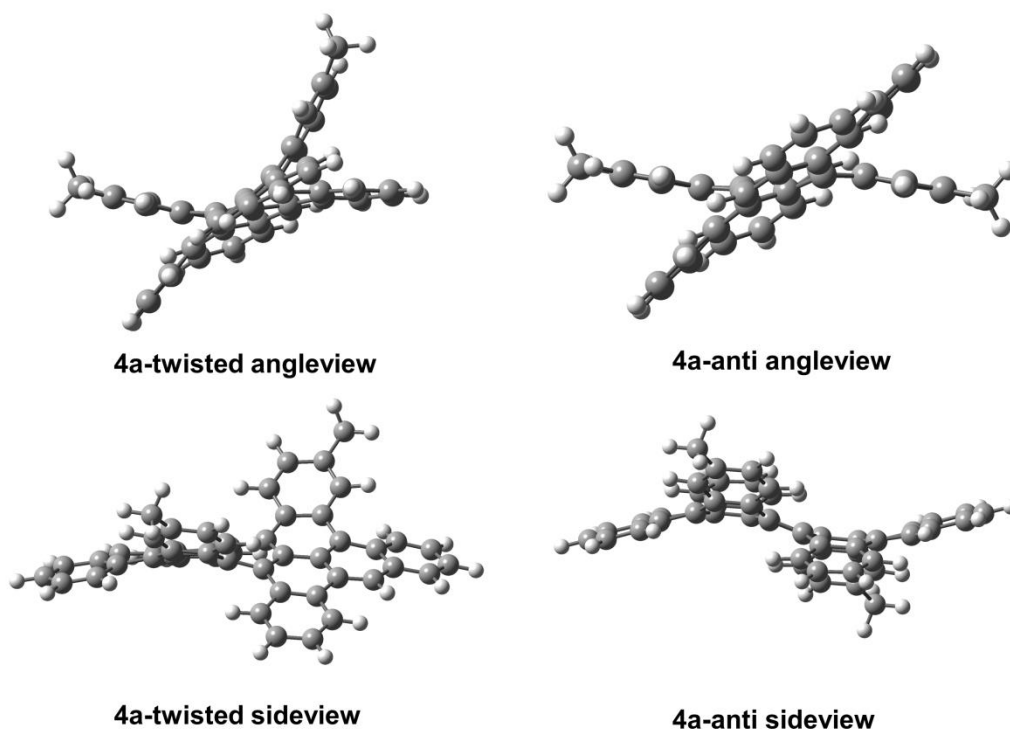
## F. DFT Calculations

DFT calculations were performed using the Gaussian 09 program, Revision A.02. [ENREF 5](#)<sup>5</sup> Geometries were optimized in the gas phase using the B3LYP functional and 6-31g(d) basis set on all atoms and confirmed as stationary states using frequency calculations. The torsional angles discussed the manuscript were measured from the dihedral angles illustrated in Figure SX.

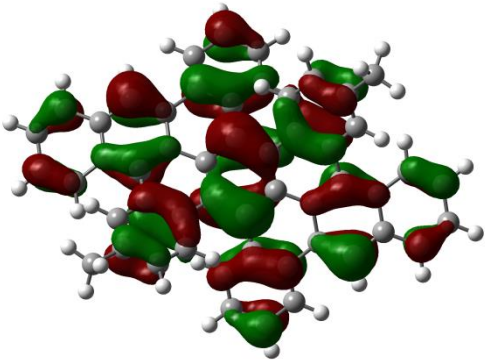
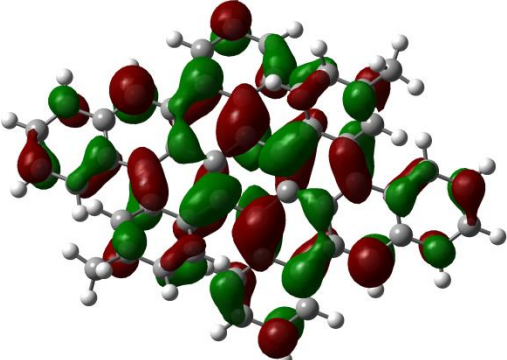
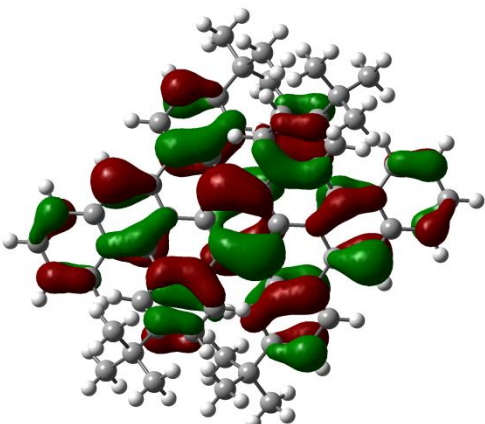
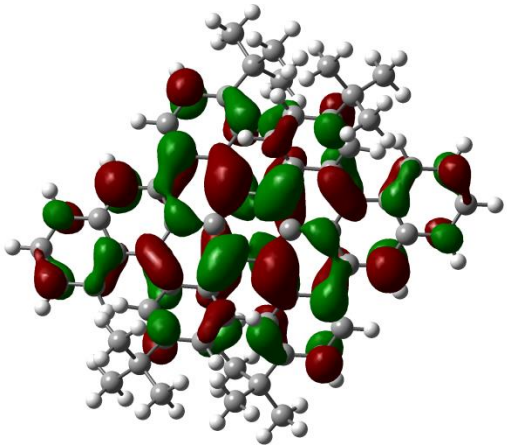
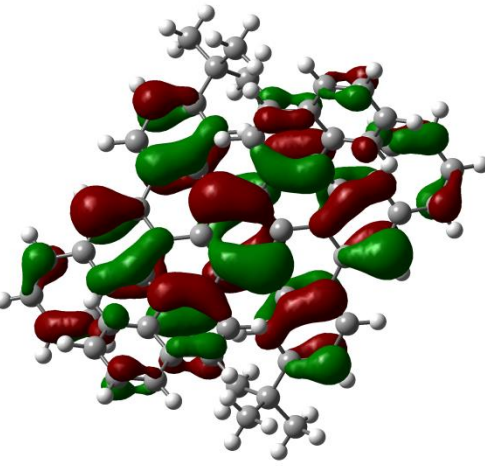
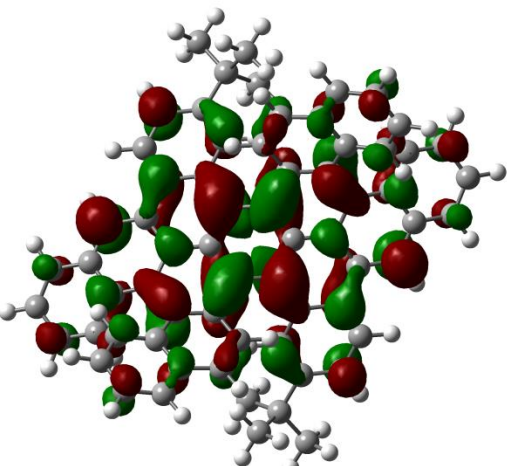
**Figure A2.88.** Illustration of the dihedral angles measured in the optimized structures to represent torsion

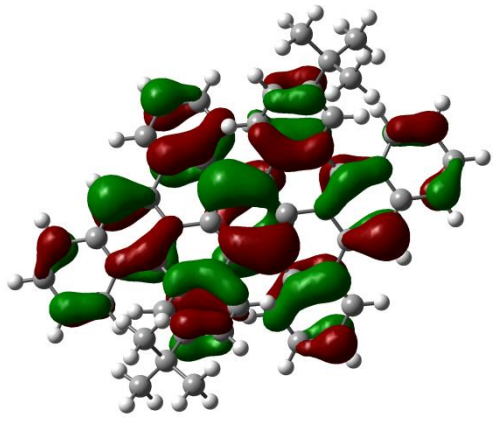
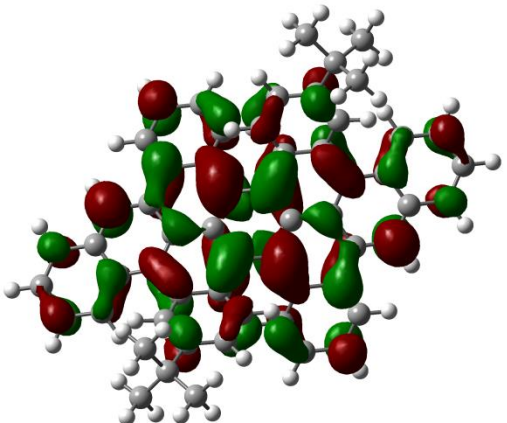
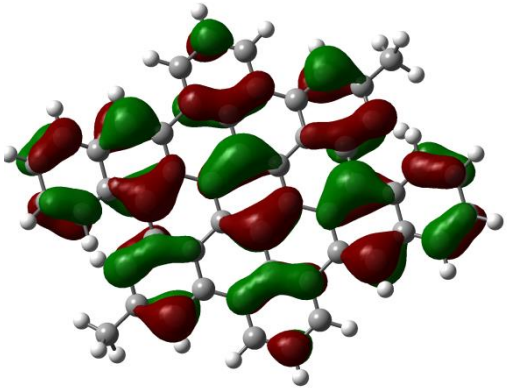
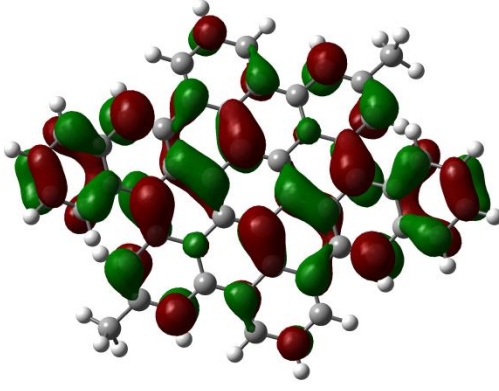
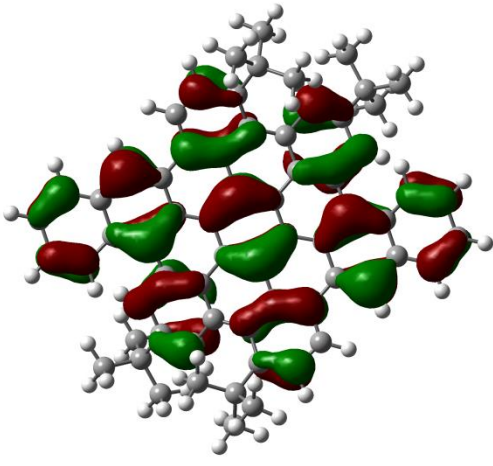
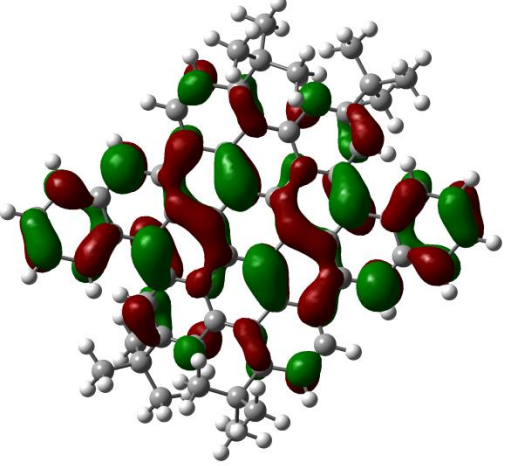


**Figure A2.89.** Two possible conformations of **4a**: twisted (left), and anti (right). The *n*-nonyl chains were truncated to methyl groups.

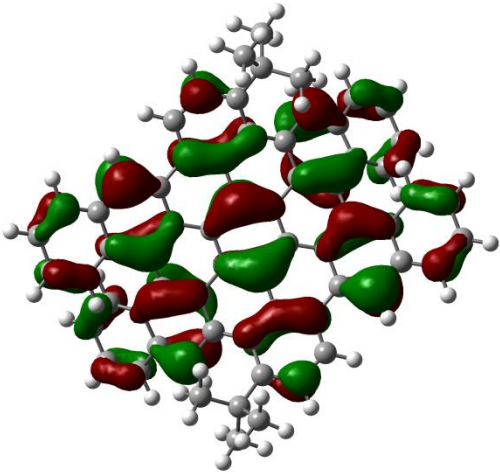
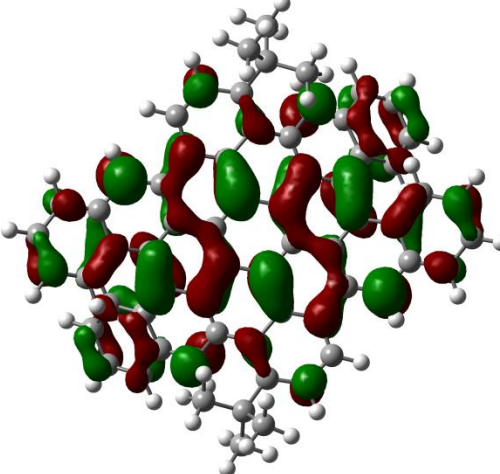
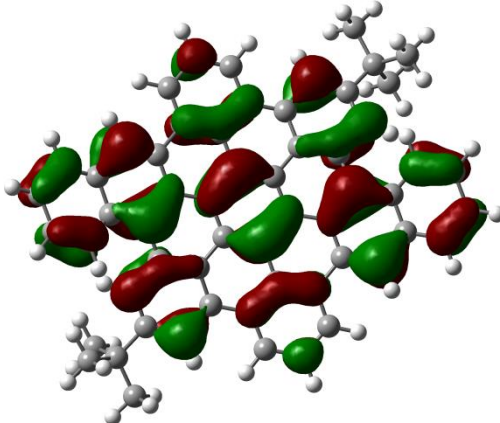
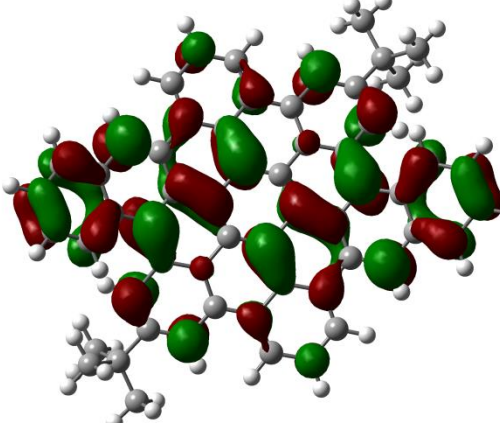


**Table A2.1.** Calculated HOMOs and LUMOs of compounds **4a-d** and **5a-d**

	HOMO	LUMO
<b>4a-truncated</b>		
<b>4b</b>		
<b>4c</b>		

	HOMO	LUMO
4d		
5a-truncated		
5b		



	HOMO	LUMO
5c		
5d		

**Table A2.2.** Cartesian coordinates of DFT computed geometries

**4a-truncated**

C	3.39268200	1.31642900	0.75578900
C	2.04837500	1.77231200	0.69533200
C	1.02926000	0.94419400	0.06252300
C	1.33427300	-0.43412100	-0.12692700



C	2.72069800	-0.85098500	-0.19797700
C	3.75681700	0.06912900	0.08522500
C	-0.28606200	1.38239100	-0.26403800
C	0.28601800	-1.38243000	-0.26409400
C	-1.02927000	-0.94423900	0.06264400
C	-1.33430400	0.43408000	-0.12675800
C	-2.04830100	-1.77234400	0.69559900
C	0.59605800	-2.71707900	-0.78363800
C	1.94718500	-3.13229700	-0.91288100
C	3.03330300	-2.20847700	-0.56342600
C	-0.59616200	2.71705900	-0.78349700
C	-1.94730300	3.13228000	-0.91257500
C	-3.03338000	2.20845700	-0.56300100
C	-2.72073200	0.85095600	-0.19761500
C	-3.39258900	-1.31644100	0.75625400
C	-3.75681600	-0.06915300	0.08572600
C	-0.13214800	-4.80490200	-1.82644700
C	2.21267200	-4.40797600	-1.45701000
C	1.19745100	-5.24314700	-1.88978300
C	-2.61868400	-3.61016500	2.19936600
C	-3.94724500	-3.15185800	2.30100700
C	-4.30005700	-2.01314500	1.59187700
H	-5.29539000	-1.61039900	1.73524600
C	-2.21285300	4.40797000	-1.45664600
C	-1.19768100	5.24315700	-1.88950400
H	-1.43798100	6.21729100	-2.30657700
C	0.13192700	4.80491700	-1.82631500
H	0.93571500	5.42707300	-2.21016800
C	4.30025600	2.01315300	1.59126700
C	3.94752900	3.15188000	2.30043700
C	2.61892800	3.61010700	2.19905800
H	2.30404500	4.48289300	2.76677900
C	4.36278400	-2.58675700	-0.62949000
C	5.41545600	-1.65467700	-0.51854100
C	5.11754000	-0.28521400	-0.22457800
C	6.76146900	-2.04911000	-0.75746200
C	7.77644600	-1.12305800	-0.78882700
H	8.79875200	-1.43317200	-0.98701300
C	7.47393800	0.24676700	-0.60803400
H	8.26092700	0.99001100	-0.70373600

C	6.18543200	0.65127700	-0.33225900
H	5.97398500	1.70990800	-0.24534800
C	-4.36286700	2.58674600	-0.62887200
C	-5.41552900	1.65466800	-0.51779300
C	-5.11758100	0.28520000	-0.22388900
C	-6.76157300	2.04911000	-0.75652600
C	-7.77655800	1.12306300	-0.78776600
H	-8.79888900	1.43318400	-0.98580900
C	-7.47403200	-0.24676600	-0.60703400
H	-8.26103800	-0.99000500	-0.70264200
C	-6.18549000	-0.65128500	-0.33144000
H	-5.97403400	-1.70991800	-0.24457600
H	-0.93597800	-5.42704200	-2.21023600
H	-2.30375600	-4.48301200	2.76697200
H	3.23706100	-4.74207100	-1.57288500
H	4.63424400	-3.61544700	-0.83881200
H	6.96563800	-3.10015100	-0.94828600
H	5.29561000	1.61041100	1.73451800
H	-3.23725700	4.74206200	-1.57240600
H	-4.63435000	3.61544200	-0.83813600
H	-6.96576300	3.10015500	-0.94730800
C	1.69511700	2.92499000	1.43708600
H	0.66268800	3.25306900	1.43892600
C	0.41843300	3.56149400	-1.29292600
H	1.44557100	3.22022900	-1.27731500
C	-0.41859300	-3.56149300	-1.29299000
H	-1.44572800	-3.22022400	-1.27726200
C	-1.69497100	-2.92506300	1.43727200
H	-0.66256400	-3.25320500	1.43890900
C	-4.93996400	-3.86309100	3.18887000
H	-5.88808900	-3.31937900	3.24662900
H	-5.15675000	-4.87241400	2.81499000
H	-4.55436400	-3.97735400	4.20948300
C	4.94050700	3.86334700	3.18782000
H	5.88759200	3.31806900	3.24789200
H	5.15960600	4.87139500	2.81181000
H	4.55394100	3.98072100	4.20769600
H	1.43770300	-6.21726900	-2.30690400

**4b**

C	-3.56480700	0.72526800	0.73605700
C	-2.67734600	-0.38339500	0.67791500
C	-1.37457200	-0.23950600	0.03789200
C	-0.88820900	1.08566400	-0.15303000
C	-1.83372800	2.18362700	-0.22785800
C	-3.20183200	1.96812900	0.05472300
C	-0.50629200	-1.31988700	-0.28870000
C	0.50633400	1.31987200	-0.28846000
C	1.37455300	0.23945900	0.03816700
C	0.88822700	-1.08569100	-0.15297300
C	2.67721100	0.38329700	0.67842500
C	0.96547700	2.61410900	-0.80615300
C	0.04609600	3.68586100	-0.94148300
C	-1.36722300	3.49385000	-0.59958300
C	-0.96532400	-2.61406000	-0.80666300
C	-0.04591600	-3.68580100	-0.94189700
C	1.36733200	-3.49382500	-0.59968700
C	1.83376400	-2.18364200	-0.22773500
C	3.56466000	-0.72537100	0.73664500
C	3.20182200	-1.96816600	0.05510400
C	2.73787300	3.97420300	-1.85924100
C	0.51988300	4.89323700	-1.48874500
C	1.82779300	5.04541800	-1.91818300
C	4.14728900	1.60211100	2.20508700
C	5.02176500	0.50336700	2.30925900
C	4.69519400	-0.63703800	1.57917600
H	5.30260900	-1.52344700	1.70661600
C	-0.51957900	-4.89311700	-1.48940000
C	-1.82738300	-5.04524100	-1.91917600
H	-2.12618300	-6.00087300	-2.33506700
C	-2.73746700	-3.97402100	-1.86035400
C	-4.69553400	0.63686200	1.57831600
C	-5.02225100	-0.50359700	2.30824700
C	-4.14773100	-1.60231900	2.20419900
H	-4.33362500	-2.50903400	2.76873300
C	-2.28430100	4.52733600	-0.67631400
C	-3.67325300	4.30856400	-0.56624600
C	-4.15835700	2.99582700	-0.26224800
C	-4.59696300	5.36244900	-0.81257000

C	-5.95063500	5.12676600	-0.84059400
H	-6.64615700	5.93639800	-1.04395300
C	-6.43211400	3.81040900	-0.64968300
H	-7.49533900	3.60612100	-0.74328800
C	-5.56256300	2.77894700	-0.36713900
H	-5.95231800	1.77254700	-0.27401800
C	2.28442800	-4.52729400	-0.67637900
C	3.67336000	-4.30852200	-0.56608400
C	4.15841000	-2.99581200	-0.26187700
C	4.59711000	-5.36236800	-0.81242200
C	5.95078100	-5.12666400	-0.84028300
H	6.64633500	-5.93626300	-1.04366400
C	6.43221700	-3.81031700	-0.64920600
H	7.49544500	-3.60599800	-0.74270700
C	5.56262100	-2.77889700	-0.36664300
H	5.95235200	-1.77249900	-0.27342300
H	4.33307300	2.50878600	2.76972300
H	-0.15550800	5.73195900	-1.61430000
H	-1.95782000	5.53850100	-0.89293800
H	-4.20461700	6.35715900	-1.01108900
H	-5.30300000	1.52325200	1.70565500
H	0.15583700	-5.73183000	-1.61488100
H	1.95799000	-5.53843400	-0.89319100
H	4.20479800	-6.35706000	-1.01109800
C	-3.00180500	-1.53154700	1.43139200
H	-2.31465500	-2.36926500	1.43616100
C	-2.27376100	-2.78205500	-1.30923600
H	-2.94172600	-1.93165600	-1.27290500
C	2.27404200	2.78217300	-1.30836300
H	2.94200800	1.93177900	-1.27193700
C	3.00153100	1.53140400	1.43202800
H	2.31438600	2.36912900	1.43670400
C	6.26539000	0.50556300	3.21797400
C	-6.26608200	-0.50588400	3.21667800
H	2.12669100	6.00109800	-2.33390000
C	6.10641700	-0.57609700	4.31297200
H	5.99580700	-1.57722300	3.88370500
H	6.98647200	-0.58838100	4.96792700
H	5.22414800	-0.37862900	4.93226900
C	7.52453500	0.19685200	2.37328700

H	8.41900500	0.19425700	3.00826700
H	7.45969000	-0.78283600	1.88807600
H	7.66640200	0.95076300	1.59024000
C	6.47788100	1.86451400	3.91275100
H	6.60518400	2.67783900	3.18907500
H	5.64213200	2.12139800	4.57337700
H	7.38314400	1.82534900	4.52910400
C	-6.47878100	-1.86494000	3.91118900
H	-6.60593600	-2.67814500	3.18735600
H	-5.64319500	-2.12195600	4.57197300
H	-7.38418900	-1.82584700	4.52733400
C	-7.52502400	-0.19698800	2.37175700
H	-8.41964200	-0.19450900	3.00653000
H	-7.46005400	0.78279600	1.88675600
H	-7.66671700	-0.95074100	1.58852700
C	-6.10731000	0.57559700	4.31188200
H	-5.22524000	0.37794500	4.93140600
H	-5.99647100	1.57677500	3.88279600
H	-6.98755200	0.58788000	4.96658500
C	4.18403700	4.07604000	-2.37940300
C	5.16633000	3.87622000	-1.20054000
C	4.43404700	2.98442300	-3.44655200
C	4.47675200	5.44576800	-3.02139100
H	5.03100900	4.65740400	-0.44328400
H	5.02219900	2.90926300	-0.70844500
H	6.20346400	3.92459100	-1.55563500
H	3.75152100	3.10283700	-4.29584000
H	5.46183100	3.05158600	-3.82385900
H	4.29448500	1.97633000	-3.04352700
H	5.51159800	5.47027900	-3.38092300
H	3.82342400	5.64242600	-3.87923500
H	4.35872300	6.26721100	-2.30547100
C	-4.18349200	-4.07575700	-2.38092700
C	-5.16611300	-3.87587900	-1.20234800
C	-4.43309800	-2.98408500	-3.44811200
C	-4.47614700	-5.44544400	-3.02303200
H	-5.03107100	-4.65708300	-0.44506300
H	-5.02205600	-2.90894000	-0.71019600
H	-6.20314600	-3.92416800	-1.55774600
H	-3.75035000	-3.10254300	-4.29721500

H	-5.46078600	-3.05112900	-3.82570300
H	-4.29353700	-1.97602100	-3.04501200
H	-5.51090900	-5.46987600	-3.38280900
H	-3.82263400	-5.64211800	-3.88073100
H	-4.35833900	-6.26691600	-2.30711000

#### 4c

C	3.58200200	-0.26334700	1.04151500
C	2.58688800	0.73031700	0.92355600
C	1.33039600	0.42681100	0.25146700
C	1.01992600	-0.95000700	0.04703500
C	2.11457700	-1.88389700	-0.08086300
C	3.43117700	-1.47572100	0.23789300
C	0.32527400	1.37772200	-0.09460600
C	-0.32524400	-1.37770400	-0.09467600
C	-1.33037300	-0.42680200	0.25139200
C	-1.01990500	0.95002200	0.04703800
C	-2.58688200	-0.73033800	0.92343400
C	-0.59360500	-2.71008900	-0.64451500
C	0.47943800	-3.61528800	-0.86268900
C	1.86094100	-3.20712300	-0.58380600
C	0.59365900	2.71011100	-0.64440800
C	-0.47936400	3.61534900	-0.86249300
C	-1.86087000	3.20719900	-0.58359400
C	-2.11456000	1.88391400	-0.08082200
C	-3.58209300	0.26324300	1.04131500
C	-3.43119300	1.47571200	0.23781600
C	-2.17520800	-4.30748000	-1.66970100
C	0.17410600	-4.87219700	-1.41745400
C	-1.11233700	-5.22025500	-1.79531900
C	-3.81007900	-2.19465200	2.44507300
C	-0.17401500	4.87227200	-1.41722100
C	1.11242100	5.22029900	-1.79513600
H	1.27781400	6.20385500	-2.22007100
C	2.17526400	4.30747500	-1.66963100
C	3.81033100	2.19458600	2.44504700
H	3.90520800	3.14140800	2.97110500
C	2.94282800	-4.02686500	-0.85822300
C	4.27259900	-3.56151400	-0.78035300
C	4.53402100	-2.25186800	-0.26546900

C	5.35225400	-4.35575500	-1.26096400
C	6.63135500	-3.85643800	-1.30803000
H	7.44512300	-4.46496100	-1.69292400
C	6.88016400	-2.52830300	-0.88426700
H	7.88076300	-2.11345500	-0.97044100
C	5.86323300	-1.75315300	-0.37387900
H	6.07146900	-0.73534400	-0.06701500
C	-2.94271300	4.02704400	-0.85786900
C	-4.27249900	3.56175300	-0.78006300
C	-4.53397400	2.25201700	-0.26543900
C	-5.35211900	4.35616900	-1.26047500
C	-6.63125500	3.85695400	-1.30758700
H	-7.44500200	4.46561000	-1.69231700
C	-6.88012600	2.52874500	-0.88409500
H	-7.88075100	2.11397100	-0.97032100
C	-5.86322600	1.75342800	-0.37390100
H	-6.07153000	0.73555600	-0.06730400
H	-3.90478400	-3.14142500	2.97125000
H	0.96253600	-5.59923000	-1.57570800
H	2.79258300	-5.03445300	-1.22967200
H	5.13581600	-5.35872700	-1.62148300
H	-0.96242500	5.59933700	-1.57542500
H	-2.79241800	5.03468800	-1.22914200
H	-5.13561800	5.35920100	-1.62079000
C	2.73446000	1.96077300	1.64026300
H	1.95923100	2.71127900	1.55485100
C	1.88122400	3.07227700	-1.09737300
H	2.67355700	2.34049800	-1.00769200
C	-1.88118200	-3.07229100	-1.09741300
H	-2.67353800	-2.34054600	-1.00766800
C	-2.73428500	-1.96076700	1.64021500
H	-1.95894500	-2.71116400	1.55484500
H	-1.27771900	-6.20380300	-2.22027600
C	-3.60778500	-4.62004000	-2.14134300
C	-4.56715700	-4.58625200	-0.92820000
C	-4.05463700	-3.56224300	-3.17836400
C	-3.71390600	-6.00863600	-2.80068500
H	-4.28921500	-5.34708700	-0.18942500
H	-4.55443700	-3.61465000	-0.42435000
H	-5.59646100	-4.78676100	-1.25048400

H	-3.39138900	-3.56290000	-4.05086700
H	-5.07291800	-3.77738300	-3.52486600
H	-4.05407000	-2.55110700	-2.75898300
H	-4.74522600	-6.18352900	-3.12727400
H	-3.06909100	-6.09227300	-3.68315800
H	-3.44902100	-6.81338100	-2.10528300
C	3.60782900	4.62001800	-2.14132400
C	4.56731100	4.58573100	-0.92828300
C	4.05446800	3.56251400	-3.17873700
C	3.71403600	6.00881600	-2.80022700
H	4.28955500	5.34639300	-0.18926100
H	4.55448200	3.61398200	-0.42471700
H	5.59661600	4.78617400	-1.25060400
H	3.39110200	3.56349200	-4.05114900
H	5.07271600	3.77769800	-3.52530900
H	4.05389700	2.55124500	-2.75968000
H	4.74529300	6.18360800	-3.12706900
H	3.06896600	6.09288400	-3.68247300
H	3.44953300	6.81338100	-2.10447200
C	4.76319700	1.16842800	2.70203900
C	4.61868300	-0.09626000	2.04777600
C	6.40413600	-0.95964900	3.48162200
H	7.00469900	-1.80026300	3.81863000
C	6.60594100	0.31815000	4.04439600
H	7.37887700	0.47034100	4.79277600
C	5.43929300	-1.15960700	2.51577200
H	5.29265300	-2.15709400	2.12383400
C	5.78491300	1.35734800	3.66637800
H	5.88559000	2.33748800	4.12680600
C	-4.76311700	-1.16862700	2.70193300
C	-4.61887000	0.09599700	2.04747200
C	-5.78479200	-1.35763600	3.66630000
H	-5.88521900	-2.33771200	4.12691100
C	-6.60616300	-0.31861900	4.04405100
H	-7.37904300	-0.47086200	4.79247600
C	-6.40481700	0.95908700	3.48090800
H	-7.00577700	1.79955500	3.81756900
C	-5.43993000	1.15914100	2.51512600
H	-5.29386300	2.15648100	2.12263000



**4d**

C	-3.61557100	-0.39493200	0.32054500
C	-2.43497700	-1.18429300	0.25505200
C	-1.23732200	-0.64746200	-0.38074600
C	-1.17741900	0.76274900	-0.56995300
C	-2.41028700	1.52309000	-0.64232000
C	-3.64768700	0.90224600	-0.35575300
C	-0.07941400	-1.40944500	-0.70771900
C	0.07940700	1.40947000	-0.70770600
C	1.23731500	0.64748300	-0.38074100
C	1.17741200	-0.76272600	-0.56996600
C	2.43497000	1.18430100	0.25507300
C	0.12323900	2.77840400	-1.22924900
C	-1.07603900	3.52533200	-1.36582600
C	-2.36339300	2.91345600	-1.01425300
C	-0.12325000	-2.77837900	-1.22925700
C	1.07602600	-3.52530600	-1.36585400
C	2.36338500	-2.91342700	-1.01430100
C	2.41028000	-1.52306600	-0.64235000
C	3.61556700	0.39494200	0.32053900
C	3.64768100	-0.90222400	-0.35578300
C	1.36530400	4.60456800	-2.27769700
C	-1.00457300	4.82249300	-1.91920500
C	0.19191900	5.36723700	-2.35180500
C	3.46896500	2.80421300	1.76569800
C	4.63202600	2.01906900	1.88071600
C	4.66480300	0.82590200	1.16269500
H	5.51049200	0.16488700	1.30002100
C	1.00454800	-4.82247200	-1.91922000
C	-0.19195300	-5.36722100	-2.35178800
H	-0.21011900	-6.36725500	-2.77633700
C	-1.36533800	-4.60455500	-2.27765500
H	-2.30322800	-4.99825200	-2.65957500
C	-4.66480200	-0.82591000	1.16270000
C	-4.63202400	-2.01910300	1.88067700
C	-3.46896900	-2.80424600	1.76563600
H	-3.37430100	-3.73171000	2.31899200
C	-3.55113400	3.62070400	-1.08302000
C	-4.80789200	2.99134600	-0.96743300
C	-4.87152300	1.59262400	-0.66694300

C	-6.00823700	3.71713200	-1.20668300
C	-7.22714800	3.08293100	-1.23167300
H	-8.13595500	3.64449300	-1.42980000
C	-7.28655000	1.68191700	-1.04491600
H	-8.23829400	1.16552900	-1.13688500
C	-6.14464200	0.96115700	-0.76881600
H	-6.21140400	-0.11624600	-0.67903000
C	3.55112800	-3.62067100	-1.08308800
C	4.80788500	-2.99131300	-0.96749600
C	4.87151600	-1.59259700	-0.66698000
C	6.00823000	-3.71709500	-1.20675800
C	7.22714200	-3.08289500	-1.23173100
H	8.13594900	-3.64445300	-1.42986600
C	7.28654500	-1.68188500	-1.04494100
H	8.23829000	-1.16549600	-1.13689000
C	6.14463700	-0.96112900	-0.76882900
H	6.21140100	0.11627100	-0.67901200
H	2.30318400	4.99825800	-2.65964600
H	3.37429100	3.73166000	2.31907600
H	-1.90923100	5.40625400	-2.04276800
H	-3.54905700	4.68369400	-1.29704500
H	-5.93615900	4.78443000	-1.40273800
H	-5.51048100	-0.16489100	1.30006200
H	1.90920400	-5.40623500	-2.04279300
H	3.54905200	-4.68365900	-1.29712700
H	5.93615200	-4.78438900	-1.40283300
C	-2.39855400	-2.38442800	0.99641000
H	-1.49155200	-2.97702700	0.99568700
C	-1.32205700	-3.33267300	-1.73637500
H	-2.22745000	-2.74014600	-1.71277900
C	1.32203300	3.33269000	-1.73640500
H	2.22742400	2.74015900	-1.71283500
C	2.39854600	2.38441100	0.99646800
H	1.49154200	2.97700700	0.99576800
C	5.81466600	2.40269500	2.79005100
C	-5.81463800	-2.40275900	2.79002400
H	0.21007700	6.36726500	-2.77636500
C	5.97638700	1.33850300	3.90185000
H	6.16924200	0.34327500	3.48793000
H	6.81722500	1.59684000	4.55741600

H	5.07204200	1.27508800	4.51753600
C	7.11360200	2.46745600	1.95199700
H	7.96501000	2.73912100	2.58801300
H	7.34451600	1.50531700	1.48257900
H	7.03085500	3.21777000	1.15717100
C	5.61189200	3.77380900	3.46324600
H	5.49528800	4.57696800	2.72655200
H	4.73458400	3.78166400	4.11989600
H	6.48530700	4.01432300	4.07983600
C	-5.61175500	-3.77384800	3.46323400
H	-5.49515200	-4.57701600	2.72654800
H	-4.73440400	-3.78164400	4.11982800
H	-6.48511900	-4.01439300	4.07988400
C	-7.11358600	-2.46761200	1.95199100
H	-7.96496900	-2.73931300	2.58802500
H	-7.34456900	-1.50550000	1.48255200
H	-7.03080600	-3.21794100	1.15718300
C	-5.97638300	-1.33855100	3.90180500
H	-5.07202100	-1.27507700	4.51746000
H	-6.16930000	-0.34334200	3.48786900
H	-6.81718500	-1.59692000	4.55740500

#### 5a-truncated

C	-3.54123600	-1.28547800	-0.22792500
C	-2.21064400	-1.79348900	-0.27671800
C	-1.09309400	-0.89660300	-0.15302700
C	-1.32967500	0.50379900	-0.10841500
C	-2.67703000	1.00453800	0.04058800
C	-3.76135800	0.10629900	0.15780000
C	0.23306400	-1.40139900	-0.16071100
C	-0.23305300	1.40140700	-0.16063000
C	1.09310500	0.89660900	-0.15293000
C	1.32968400	-0.50379400	-0.10840300
C	2.21066500	1.79349500	-0.27653000
C	1.99396200	3.17593000	-0.53498500
C	0.63524700	3.71398000	-0.44375800
C	-0.45969700	2.82698600	-0.23665700
C	-1.78103000	3.34327600	-0.12633400
C	-2.89838800	2.42397400	0.11905900
C	-1.99393000	-3.17591000	-0.53525300

C	-0.63520400	-3.71395300	-0.44411700
C	0.45971900	-2.82697000	-0.23686800
C	1.78105700	-3.34325400	-0.12657700
C	2.89838200	-2.42397500	0.11904400
C	2.67703400	-1.00453800	0.04062700
C	3.54125500	1.28548000	-0.22774000
C	3.76136000	-0.10631200	0.15794100
C	0.38200700	5.09131300	-0.53759100
C	-1.98135300	4.72429000	-0.25166900
C	-0.91103800	5.58831600	-0.45186400
H	-1.08751700	6.65692000	-0.53832400
C	3.08835200	3.97845900	-0.88198700
C	4.37973200	3.46041800	-0.98219700
C	4.58949600	2.12461400	-0.64412300
H	5.58527200	1.71395800	-0.75816200
C	1.98142800	-4.72423300	-0.25218500
C	0.91113700	-5.58824800	-0.45256900
H	1.08764500	-6.65682800	-0.53926200
C	-0.38192000	-5.09126200	-0.53820300
H	-1.19993200	-5.78983800	-0.66787000
C	-4.58947200	-2.12459900	-0.64435000
C	-4.37970600	-3.46039700	-0.98244400
C	-3.08832400	-3.97843500	-0.88225400
H	-2.93699300	-5.02303400	-1.13221000
C	-4.16945200	2.88325900	0.40945000
C	-5.23014600	2.00921000	0.72499000
C	-5.02738000	0.59308000	0.64716600
C	-6.48214800	2.52328800	1.16317500
C	-7.48517900	1.68433000	1.58505000
H	-8.43362600	2.08815000	1.92842600
C	-7.25505400	0.28951400	1.61566500
H	-8.01517900	-0.37389100	2.01937800
C	-6.06522600	-0.23747400	1.16160600
H	-5.89979700	-1.30348400	1.25009200
C	4.16939700	-2.88328600	0.40960300
C	5.23007400	-2.00925200	0.72524700
C	5.02734600	-0.59311700	0.64737600
C	6.48202400	-2.52335000	1.16355600
C	7.48504700	-1.68440600	1.58547900
H	8.43345500	-2.08824100	1.92894300

C	7.25496300	-0.28958200	1.61601700
H	8.01508200	0.37381600	2.01975300
C	6.06518300	0.23742400	1.16185500
H	5.89978300	1.30344200	1.25029100
H	1.20004900	5.78988500	-0.66709100
H	2.93701000	5.02305800	-1.13194200
H	-2.98150300	5.13863700	-0.20500000
H	-4.37091300	3.94681600	0.47330900
H	-6.61819200	3.60208900	1.18293200
H	-5.58524500	-1.71394100	-0.75839600
H	2.98160000	-5.13854300	-0.20562100
H	4.37081100	-3.94685000	0.47351800
H	6.61803600	-3.60215400	1.18335800
C	5.52881000	4.33515300	-1.42761000
H	5.91643400	4.93869200	-0.59584400
H	6.36091700	3.73610100	-1.81150200
H	5.22133000	5.03128400	-2.21575600
C	-5.52878300	-4.33513100	-1.42786400
H	-5.91636200	-4.93872400	-0.59611600
H	-6.36091600	-3.73607400	-1.81169000
H	-5.22131900	-5.03121100	-2.21606000

## 5b

C	-3.49875300	-1.23935500	0.30266100
C	-2.82529500	-0.01964400	0.01764100
C	-1.40513400	-0.01368600	-0.18924200
C	-0.69466900	-1.24317500	-0.17920100
C	-1.42250000	-2.49174300	-0.14815400
C	-2.83027200	-2.49995600	-0.01492900
C	-0.72247500	1.22976400	-0.21388600
C	0.72248700	-1.22975500	-0.21388800
C	1.40515000	0.01369600	-0.18925800
C	0.69468500	1.24318300	-0.17921300
C	2.82531300	0.01965700	0.01762000
C	3.53758000	-1.20318200	0.10356400
C	2.90221400	-2.44008200	-0.36359900
C	1.46985800	-2.46928500	-0.29133400
C	0.76863100	-3.70026900	-0.34659800
C	-0.69303800	-3.72799000	-0.24353100

C	-3.53756800	1.20319000	0.10358500
C	-2.90221400	2.44009700	-0.36358100
C	-1.46985200	2.46929100	-0.29134100
C	-0.76860700	3.70026700	-0.34665100
C	0.69306300	3.72799000	-0.24356700
C	1.42252300	2.49174600	-0.14817400
C	3.49877400	1.23935900	0.30265700
C	2.83029500	2.49995900	-0.01493400
C	3.60355900	-3.59816600	-0.80706600
C	1.52568400	-4.86781700	-0.50111200
C	2.88192700	-4.80266900	-0.76838900
H	3.39110200	-5.73338600	-0.99401000
C	4.76850900	-1.21352300	0.77612100
C	5.35895100	-0.04537400	1.26889700
C	4.73303300	1.16982500	0.96926400
H	5.17378600	2.08902200	1.33283200
C	-1.52564100	4.86781300	-0.50123100
C	-2.88188700	4.80266800	-0.76848900
H	-3.39103600	5.73337900	-0.99417100
C	-3.60355500	3.59818700	-0.80707700
C	-4.73301600	-1.16983700	0.96925700
C	-5.35895500	0.04535600	1.26887900
C	-4.76852100	1.21350700	0.77610600
H	-5.23142500	2.17221600	0.96333100
C	-1.39807900	-4.91816500	-0.22480100
C	-2.80672600	-4.95782000	-0.24489900
C	-3.55024500	-3.73387600	-0.20125700
C	-3.49288000	-6.19915300	-0.36162800
C	-4.85782600	-6.24404100	-0.51132700
H	-5.37012700	-7.19693800	-0.61207700
C	-5.58805100	-5.03482000	-0.58441200
H	-6.65669400	-5.06102300	-0.78004700
C	-4.95390300	-3.82052000	-0.43471100
H	-5.53111300	-2.91217400	-0.55067500
C	1.39810300	4.91816600	-0.22483000
C	2.80675000	4.95782100	-0.24490900
C	3.55026800	3.73387800	-0.20125200
C	3.49290800	6.19915300	-0.36163300
C	4.85785700	6.24403700	-0.51131000
H	5.37016100	7.19693300	-0.61205700

C	5.58808200	5.03481500	-0.58437300
H	6.65672900	5.06101500	-0.77998600
C	4.95393000	3.82051600	-0.43467700
H	5.53114000	2.91216800	-0.55062200
H	5.23140200	-2.17224000	0.96334700
H	1.05186500	-5.84238400	-0.49507000
H	-0.87784100	-5.86926300	-0.24495800
H	-2.90599200	-7.11479700	-0.35984500
H	-5.17375400	-2.08903900	1.33282700
H	-1.05180800	5.84237200	-0.49527200
H	0.87786700	5.86926600	-0.24498700
H	2.90602200	7.11479700	-0.35986500
C	6.64245900	-0.04896100	2.12077000
C	-6.64247400	0.04893500	2.12073500
C	6.33567800	0.56585500	3.50768700
H	7.24115400	0.58113500	4.12682700
H	5.97036200	1.59488700	3.42676900
H	5.57301600	-0.01861200	4.03467200
C	7.73622500	0.79138700	1.41984600
H	7.42657700	1.83253900	1.28118200
H	8.65525600	0.79628400	2.01866500
H	7.97692600	0.37839100	0.43330300
C	7.19978500	-1.46795300	2.34232500
H	6.48044500	-2.11358300	2.85873800
H	7.47997200	-1.95075300	1.39897500
H	8.10098100	-1.41643400	2.96364400
C	-7.19987600	1.46791400	2.34216600
H	-6.48059300	2.11361600	2.85856900
H	-7.48004000	1.95063100	1.39876600
H	-8.10109900	1.41639400	2.96344400
C	-7.73619300	-0.79152200	1.41986500
H	-7.42650400	-1.83267500	1.28130300
H	-8.65523400	-0.79640000	2.01866600
H	-7.97689000	-0.37862500	0.43327900
C	-6.33567300	-0.56575500	3.50770500
H	-5.97031300	-1.59477800	3.42687200
H	-5.57303900	0.01878600	4.03464900
H	-7.24115300	-0.58102500	4.12684000
C	5.00626000	-3.67212000	-1.49189800
C	5.58258200	-2.31735000	-1.96349800

C	6.03596300	-4.40164700	-0.59787300
C	4.84677400	-4.50178400	-2.80210200
H	4.83115700	-1.73224800	-2.50463900
H	5.96903900	-1.69636700	-1.15687900
H	6.41351600	-2.51000900	-2.65182600
H	5.68797200	-5.40416100	-0.32476400
H	6.98814100	-4.51301900	-1.13132800
H	6.23783000	-3.85904700	0.33076100
H	5.80419200	-4.52759600	-3.33483900
H	4.54990500	-5.53812500	-2.62417600
H	4.10206700	-4.04712500	-3.46451000
C	-5.00630900	3.67213700	-1.49181300
C	-5.58224000	2.31737200	-1.96388500
C	-6.03615100	4.40112900	-0.59750700
C	-4.84717000	4.50233100	-2.80172800
H	-4.83084900	1.73310400	-2.50599100
H	-5.96769600	1.69558200	-1.15741900
H	-6.41378500	2.51001700	-2.65147900
H	-5.68817500	5.40348300	-0.32379200
H	-6.98824300	4.51280900	-1.13105100
H	-6.23819200	3.85802900	0.33079200
H	-5.80451300	4.52761100	-3.33462100
H	-4.55113900	5.53884700	-2.62340900
H	-4.10201100	4.04845400	-3.46416000

### 5c

C	-3.61119900	-0.74297800	0.51205000
C	-2.79637700	0.37022300	0.21273600
C	-1.39478200	0.18496800	-0.04314200
C	-0.85626700	-1.12879700	-0.05654300
C	-1.75644200	-2.25152200	-0.09482600
C	-3.14984900	-2.05169600	0.05189500
C	-0.54624300	1.31768300	-0.09154800
C	0.54623700	-1.31768400	-0.09155100
C	1.39477600	-0.18497000	-0.04313200
C	0.85626100	1.12879500	-0.05652700
C	2.79637000	-0.37022500	0.21275400
C	3.31210500	-1.70633900	0.31968200
C	2.52590700	-2.82962500	-0.21220100
C	1.10432300	-2.65229400	-0.19573900



C	0.23084700	-3.75804700	-0.34148700
C	-1.22269900	-3.56753400	-0.32013800
C	-3.31211700	1.70633500	0.31965300
C	-2.52590700	2.82962700	-0.21219300
C	-1.10432600	2.65229500	-0.19571800
C	-0.23084600	3.75805500	-0.34141600
C	1.22269800	3.56753600	-0.32010300
C	1.75643400	2.25152100	-0.09480100
C	3.61119100	0.74297300	0.51207300
C	3.14984200	2.05169200	0.05191200
C	3.07273200	-4.06543300	-0.65487400
C	0.81549500	-5.02221400	-0.49657300
C	2.17882900	-5.15203100	-0.68854400
H	2.55978100	-6.14400900	-0.90557400
C	4.47565500	-1.89796800	1.03574800
C	-0.81549300	5.02223300	-0.49641700
C	-2.17882500	5.15205900	-0.68840100
H	-2.55978000	6.14405000	-0.90537300
C	-3.07272200	4.06545600	-0.65483000
C	-4.47568800	1.89796200	1.03569000
H	-4.82494000	2.90489300	1.23267400
C	-2.10460000	-4.61505400	-0.51714100
C	-3.49848800	-4.41241800	-0.59756100
C	-4.04289900	-3.11123200	-0.34888900
C	-4.36401000	-5.47749700	-0.97629000
C	-5.70513400	-5.26187600	-1.18105600
H	-6.35375000	-6.07899300	-1.48486600
C	-6.23245600	-3.95680900	-1.03101100
H	-7.28057500	-3.77011400	-1.24850500
C	-5.42632000	-2.91664100	-0.62592200
H	-5.84863800	-1.92370400	-0.53790100
C	2.10460100	4.61504900	-0.51714200
C	3.49848500	4.41240500	-0.59758800
C	4.04289200	3.11122000	-0.34889500
C	4.36401200	5.47746500	-0.97635800
C	5.70512900	5.26182300	-1.18114300
H	6.35374900	6.07892700	-1.48498000
C	6.23244700	3.95675700	-1.03107100
H	7.28056000	3.77005400	-1.24858200
C	5.42630800	2.91660700	-0.62594200

H	5.84861700	1.92366800	-0.53788600
H	4.82490100	-2.90489900	1.23274200
H	0.20356700	-5.91639600	-0.52894700
H	-1.73899400	-5.62144500	-0.68892500
H	-3.93199000	-6.46364700	-1.13001500
H	-0.20356200	5.91641600	-0.52869600
H	1.73899100	5.62143500	-0.68894500
H	3.93200300	6.46361700	-1.13010100
C	4.49020000	-4.33680700	-1.25461900
C	5.29072000	-3.07746100	-1.66139300
C	5.34251300	-5.21954800	-0.31309400
C	4.29382200	-5.11913800	-2.58875700
H	4.66463800	-2.36758600	-2.21261800
H	5.73671400	-2.54661900	-0.82148800
H	6.10980100	-3.38155900	-2.32306400
H	4.82831000	-6.15581900	-0.06907600
H	6.29461200	-5.47614300	-0.79379500
H	5.57425100	-4.71512800	0.63047600
H	5.26921200	-5.28610900	-3.05928300
H	3.83178400	-6.09957700	-2.45192300
H	3.67280600	-4.54895500	-3.28835800
C	-4.49016600	4.33684200	-1.25462700
C	-5.29065800	3.07750400	-1.66147500
C	-5.34253500	5.21955200	-0.31312600
C	-4.29373000	5.11921300	-2.58873700
H	-4.66454600	2.36766700	-2.21271800
H	-5.73666200	2.54661300	-0.82160600
H	-6.10972700	3.38161900	-2.32315200
H	-4.82833600	6.15580600	-0.06903000
H	-6.29459300	5.47618100	-0.79388900
H	-5.57435500	4.71510000	0.63040600
H	-5.26909500	5.28616700	-3.05932000
H	-3.83172800	6.09966100	-2.45184700
H	-3.67265300	4.54906800	-3.28831400
C	-5.18746700	0.81850500	1.61020400
C	-4.77277600	-0.52758600	1.34420500
C	-6.94280500	0.02347300	3.09906000
H	-7.78035000	0.22045400	3.76258700
C	-6.49098000	-1.30184300	2.90157600
H	-6.96638600	-2.11942000	3.43668100

C	5.18743200	-0.81851100	1.61026500
C	4.77275800	0.52758400	1.34424500
C	6.49098000	1.30182900	2.90160300
H	6.96639500	2.11941100	3.43669500
C	6.94279500	-0.02348800	3.09909700
H	7.78034800	-0.22046600	3.76261200
C	6.29322900	-1.05958200	2.47084800
H	6.60213600	-2.08873700	2.63877400
C	5.44068400	1.56778900	2.05038800
H	5.09757000	2.58837100	1.94037800
C	-6.29326700	1.05957200	2.47078800
H	-6.60219400	2.08872400	2.63869000
C	-5.44068900	-1.56779200	2.05035800
H	-5.09756100	-2.58837100	1.94034500

#### 5d

C	3.76592700	-0.04747100	0.01911400
C	2.67569800	-0.96424900	0.05563100
C	1.32644100	-0.48537700	-0.07396700
C	1.08919000	0.91442600	-0.11786300
C	2.19737700	1.83113200	-0.26154600
C	3.51772100	1.33998600	-0.36957700
C	0.24174200	-1.40011700	-0.06854600
C	-0.24174100	1.40012100	-0.06839800
C	-1.32643900	0.48538200	-0.07399700
C	-1.08918600	-0.91441600	-0.11804000
C	-2.67570500	0.96423800	0.05556800
C	-2.92943000	2.33734600	0.30940900
C	-1.82737800	3.29581800	0.20540100
C	-0.49956100	2.82030200	0.00241000
C	0.57766200	3.74362900	-0.11019900
C	1.93820600	3.24406000	-0.34368000
C	2.92940700	-2.33738700	0.30932300
C	1.82736300	-3.29584600	0.20513000
C	0.49955800	-2.82030600	0.00211200
C	-0.57765700	-3.74362000	-0.11067200
C	-1.93818600	-3.24402400	-0.34418400
C	-2.19736300	-1.83110600	-0.26190200
C	-3.76593200	0.04746400	0.01887500
C	-3.51770000	-1.33994800	-0.36996300

C	-2.04437000	4.68034500	0.28599000
C	0.30849100	5.11394200	0.00188500
C	-0.98848200	5.57632600	0.19327800
H	-1.17604300	6.64395400	0.26797600
C	-4.22666800	2.73532100	0.66929400
C	-5.27745900	1.82611300	0.79340000
C	-5.02512900	0.49365600	0.44790700
H	-5.81710000	-0.23447800	0.56271400
C	-0.30849300	-5.11394600	0.00126900
C	0.98846800	-5.57635300	0.19268700
H	1.17602500	-6.64399000	0.26727100
C	2.04435000	-4.68038200	0.28556800
H	3.04768900	-5.07061800	0.40840200
C	5.02509700	-0.49371200	0.44817300
C	5.27740300	-1.82620800	0.79353600
C	4.22662300	-2.73540400	0.66924300
H	4.40485300	-3.77414500	0.90853800
C	2.98987800	4.09643100	-0.62482700
C	4.28136900	3.62019800	-0.93099900
C	4.55514000	2.21603400	-0.85270600
C	5.29834400	4.51745900	-1.36100500
C	6.52387800	4.05489900	-1.77581200
H	7.28936800	4.74825800	-2.11314300
C	6.76438300	2.66169100	-1.80826500
H	7.70192700	2.28532200	-2.20860700
C	5.81098300	1.77268200	-1.36092700
H	6.00316300	0.71138800	-1.45274900
C	-2.98983800	-4.09636300	-0.62549900
C	-4.28130800	-3.62009400	-0.93170500
C	-4.55508400	-2.21594000	-0.85326800
C	-5.29825200	-4.51730500	-1.36188700
C	-6.52375700	-4.05469800	-1.77673000
H	-7.28922300	-4.74801700	-2.11419600
C	-6.76425700	-2.66148600	-1.80904200
H	-7.70177100	-2.28507000	-2.20941300
C	-5.81088900	-1.77252900	-1.36153200
H	-6.00306000	-0.71122500	-1.45325500
H	-3.04771500	5.07056700	0.40880900
H	-4.40490900	3.77403100	0.90872100
H	1.11430900	5.83658900	-0.04945800

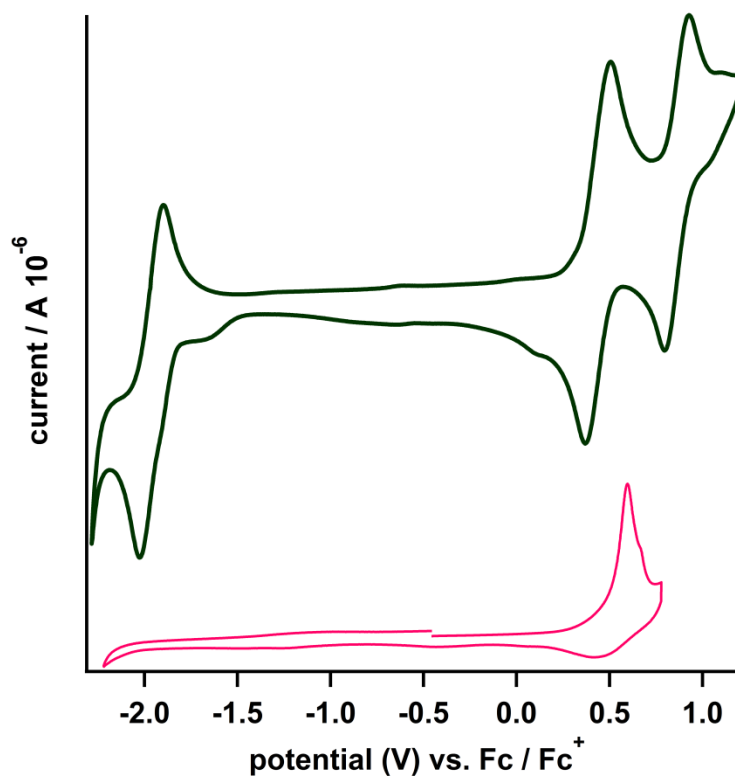
H	2.83112000	5.16719800	-0.68851800
H	5.07271100	5.58113800	-1.38097200
H	5.81706500	0.23440600	0.56310300
H	-1.11430800	-5.83658600	-0.05020600
H	-2.83107600	-5.16712300	-0.68930600
H	-5.07261900	-5.58098200	-1.38196000
C	-6.67459500	2.23075800	1.30154400
C	6.67451100	-2.23089900	1.30172300
C	-6.98517800	1.45813700	2.60603200
H	-7.98059600	1.72739400	2.98013700
H	-6.96879900	0.37418500	2.45227200
H	-6.25268300	1.69628200	3.38554100
C	-7.73922600	1.88180900	0.23451700
H	-7.75958700	0.80981800	0.01176000
H	-8.73860600	2.16520700	0.58676500
H	-7.54599200	2.41642700	-0.70274500
C	-6.77735700	3.73816200	1.60225900
H	-6.07437000	4.04810100	2.38380600
H	-6.58980200	4.34692700	0.71015900
H	-7.78725500	3.97434100	1.95568300
C	6.77733700	-3.73836400	1.60212000
H	6.07432400	-4.04851000	2.38356100
H	6.58986500	-4.34694700	0.70987800
H	7.78722700	-3.97456600	1.95555100
C	7.73922300	-1.88165300	0.23487800
H	7.75952500	-0.80961400	0.01234500
H	8.73858800	-2.16504800	0.58716900
H	7.54612600	-2.41609300	-0.70251500
C	6.98492500	-1.45854100	2.60640700
H	6.96849200	-0.37455800	2.45287700
H	6.25237100	-1.69690000	3.38579500
H	7.98032500	-1.72781700	2.98054500

## G. Optical and Electrochemical Bandgaps

**Table A2.3.** Optical and electrochemical bandgaps of the compounds **4a-4c** and **5a**

	cyclic voltammetry			B3LYP calculations	optical	
	$E_{\text{ox},1}$ (V)	$E_{\text{red},1}$ (V)	$\Delta(E_{\text{ox},1} - E_{\text{red},1})$ (V)		$\lambda_{\text{max}}$ (nm) (log $\epsilon$ )	$\lambda_{\text{end}}$ (nm) [E (eV)]
<b>4a</b>	0.22	-1.79	2.01	2.32	344 (4.87)	535 (2.32)
<b>4b</b>	0.22	-1.80	2.02	2.32	347 (4.79)	535 (2.32)
<b>4c</b>	0.24	-1.57	1.81	2.16	319 (4.65)	575 (2.16)
<b>5a</b>	0.40	—		3.00		490 (2.53)

**Figure A2.90.** Cyclic voltammograms of **4a** (green) and **5a** (pink)



## H. References to Appendix

- (1) H. Hart, K. Harada and C. J. F. Du, *J. Org. Chem.*, 1985, **50**, 3104-3110.
- (2) J. D. Tovar and T. M. Swager, *J. Organomet. Chem.*, 2002, **653**, 215-222.
- (3) H.-H. Hseuh, M.-Y. Hsu, T.-L. Wu and R.-S. Liu, *J. Org. Chem.*, 2009, **74**, 8448-8451.
- (4) B. Liang, M. Dai, J. Chen and Z. Yang, *J. Org. Chem.*, 2005, **70**, 391-393.
- (5) Gaussian 09, Revision A.02, G. W. T. M. J. Frisch, H. B. Schlegel, G. E. Scuseria, M. A. Robb, J. R. Cheeseman, G. Scalmani, V. Barone, B. Mennucci, G. A. Petersson, H. Nakatsuji, M. Caricato, X. Li, H. P. Hratchian, A. F. Izmaylov, J. Bloino, G. Zheng, J. L. Sonnenberg, M. Hada, M. Ehara, K. Toyota, R. Fukuda, J. Hasegawa, M. Ishida, T. Nakajima, Y. Honda, O. Kitao, H. Nakai, T. Vreven, J. A. Montgomery, Jr., J. E. Peralta, F. Ogliaro, M. Bearpark, J. J. Heyd, E. Brothers, K. N. Kudin, V. N. Staroverov, R. Kobayashi, J. Normand, K. Raghavachari, A. Rendell, J. C. Burant, S. S. Iyengar, J. Tomasi, M. Cossi, N. Rega, J. M. Millam, M. Klene, J. E. Knox, J. B. Cross, V. Bakken, C. Adamo, J. Jaramillo, R. Gomperts, R. E. Stratmann, O. Yazyev, A. J. Austin, R. Cammi, C. Pomelli, J. W. Ochterski, R. L. Martin, K. Morokuma, V. G. Zakrzewski, G. A. Voth, P. Salvador, J. J. Dannenberg, S. Dapprich, A. D. Daniels, O. Farkas, J. B. Foresman, J. V. Ortiz, J. Cioslowski, and D. J. Fox, Gaussian, Inc., Wallingford CT, 2009.

## CHAPTER FOUR

### ORIGINS OF THE REGIOSELECTIVITY IN THE ASAO-YAMAMOTO BENZANNULATION OF DIARYL ACETYLENES

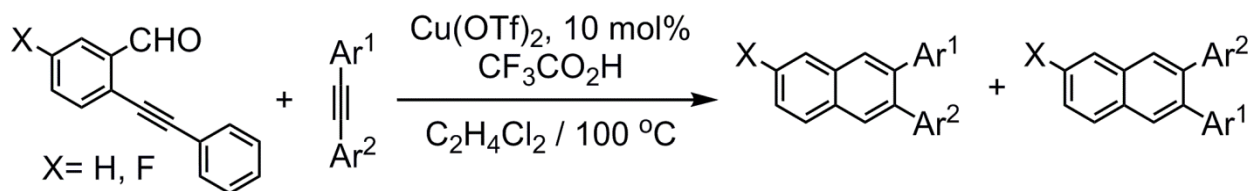
#### **4.1    *Abstract***

The Yamamoto benzannulation, which provides 2,3-disubstituted naphthalene products via a formal [4+2] cycloaddition between a 2-phenylethynylbenzaldehyde and an alkyne, is highly efficient and tolerant of congested substrates. These features enable its use to modify alkynes along poly(phenylene ethynylene) backbones, transforming these readily available conjugated polymers into densely substituted poly(arylene)s. In a recent application of this reaction to synthesize contorted polycyclic aromatic hydrocarbons (PAHs), an isotopic labeling study indicated complete regioselectivity for alkynes bearing one terphenyl and one phenyl substituent. In general, this finding suggests that functionalized benzaldehyde cycloaddition partners might provide PAHs with otherwise unavailable substitution patterns as single regioisomers. Here we probe the regioselectivity of the benzannulation reaction using both isotopically labeled and fluorine-substituted benzaldehydes. These experiments indicate that single regioisomers are obtained when one alkyne carbon preferentially stabilizes developing positive charge, and that the product distribution is insensitive to steric effects. Furthermore, alkynes substituted with electron withdrawing groups are poor substrates under  $\text{Cu}(\text{OTf})_2$ -catalyzed conditions. These studies provide a straightforward model to predict the regiochemical outcome of benzannulation reactions, which will inform the synthesis of inaccessible PAHs and carbon nanostructures.

#### **4.2    *Introduction***

Sterically congested aromatic systems, such as hexaarylbenzenes<sup>1-4</sup>, *o*-arylene polymers and





**Scheme 4.1.** The Asao-Yamamoto benzannulation of diarylalkynes with 2-phenylethynylbenzaldehydes provides two possible regioisomers when  $X \neq \text{H}$  and  $\text{Ar}^1 \neq \text{Ar}^2$ .

oligomers<sup>5-14</sup>, and polyphenylene dendrimers<sup>15-17</sup>, exhibit desirable optoelectronic properties, often exhibit rigid structures or specific conformations, and are precursors of fused polycyclic aromatic hydrocarbons (PAHs)<sup>18,19</sup> and graphene nanoribbons (GNRs)<sup>20-22</sup>. These motifs are most commonly accessed using transition metal-catalyzed cross-couplings<sup>21,22</sup>, cycloadditions between tetra(aryl)cyclopentadienones and alkynes<sup>2,20</sup>, or alkyne cyclotrimerizations<sup>1,3,4</sup>. Although these approaches are general and powerful, many structural motifs and substitution patterns remain outside their scope.

Complementary methods to prepare congested aromatic systems are needed to realize the full potential of these architectures. For example, we recently demonstrated that a benzannulation reaction first reported by Asao and Yamamoto<sup>23</sup> (Scheme 4.1) transforms the deactivated alkynes along a poly(phenylene ethynylene) (PPE) backbone into 2,3-diaryl naphthalene moieties.<sup>24</sup> This process transforms easily prepared PPEs into otherwise inaccessible, densely substituted poly(arylene)s. Alkynes bearing *o*-substituted aryl substituents are readily tolerated in both polymer and small molecule substrates, which we leveraged to prepare novel non-planar systems known as contorted hexabenzocoronenes<sup>25</sup> upon cyclodehydrogenation. During this study, an isotopic labeling experiment revealed that the cycloaddition is completely regioselective, indicating that the *o*-phenylethynylbenzaldehyde-derived cycloaddition partner discriminates between the alkyne carbons based on their terphenyl and phenyl substituents. This finding warrants further study because, if general, functionalized benzaldehyde cycloaddition partners

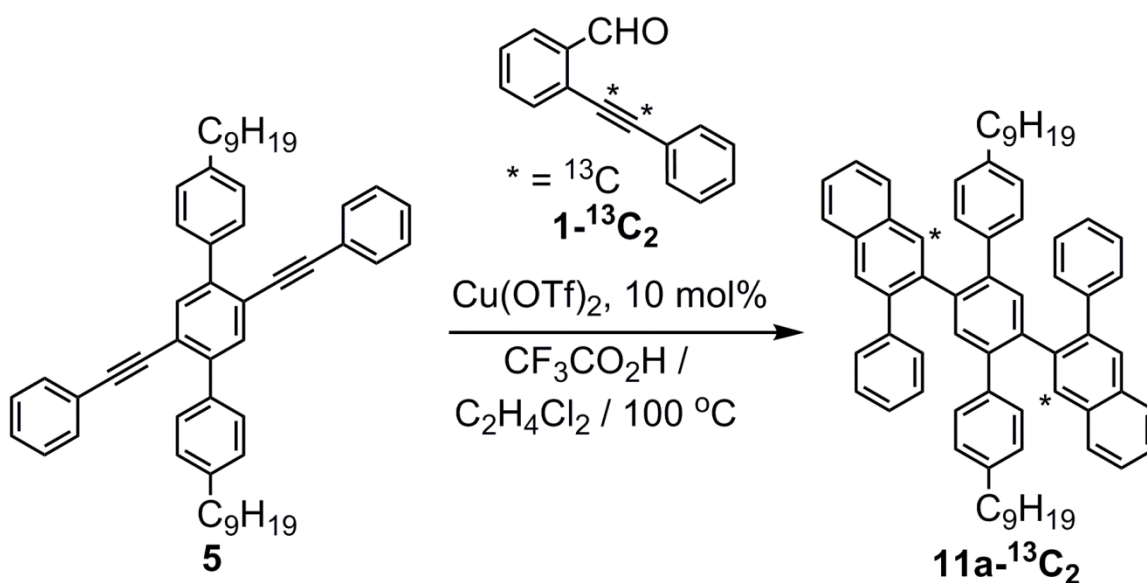
will provide access to large aromatic systems with new substitution patterns as single regioisomers.

Here we evaluate the regioselectivity of the benzannulation reaction using both  $^{13}\text{C}$ -labeled and fluorine-substituted *o*-phenylethynylbenzaldehydes across several diarylacetylene substrates (Scheme 4.1). Single regioisomers are obtained in most cases, even when polyfunctional alkynes are employed. Combinations of substituents on the diarylalkynes were chosen to elucidate the relative importance of steric and electronic factors that influence the regioselectivity. We found that electronic effects direct the regioselectivity of the benzannulation of alkynes bearing two different aryl substituents. Aryl substituents capable of stabilizing a developing positive charge on their pendant alkyne carbon direct the regiochemical outcome, while diarylalkynes bearing electron-withdrawing groups provide both poor regioselectivity and low yields. Sterically hindered aryl substituents, including 2,6-dimethylphenyl, neither interfere with the reaction nor influence its regioselectivity. These findings provide a simple model to employ the benzannulation reaction to access substituted naphthalene derivatives and large functional  $\pi$ -electron systems.

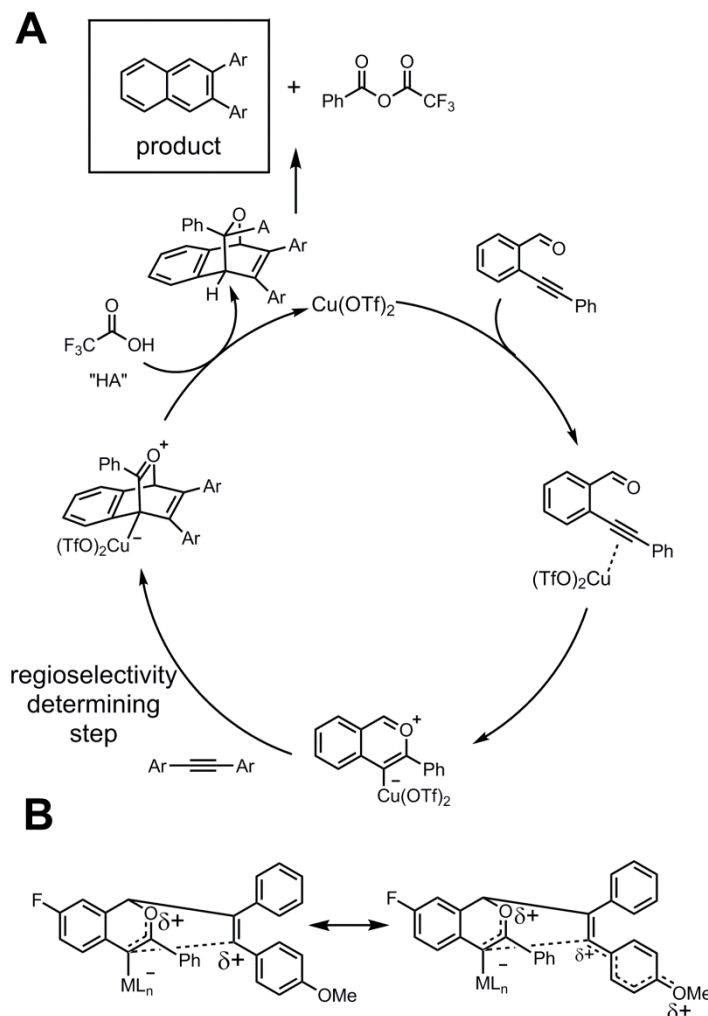
We previously found that the double benzannulation of dialkyne **5** provided the corresponding oligo(arylene) **11a**- $^{13}\text{C}_2$  as a single isotopomer out of three possible products, with one  $^{13}\text{C}$  atom incorporated per cycloaddition at the positions indicated in Scheme 4.2. These observations indicate that the benzannulation occurs regioselectively, such that the reactive intermediate derived from benzaldehyde **1**- $^{13}\text{C}_2$  perfectly differentiates between the terphenyl- and phenyl-substituted alkyne carbons. Although the symmetry of the naphthalene rings derived from **1** make the regiochemistry trivial in the absence of the isotopic label, this finding suggests that substituted benzaldehyde cycloaddition partners, such as **1-F**, will provide substituted

naphthalenes as single regioisomers. We set out to generalize this finding to other alkynes and develop a predictive model to allow rational synthetic planning. The regioselectivity observed in the benzannulation of **5** might be influenced by differences in steric demands or  $\pi$ -electron donation between the terphenyl and phenyl substituents. Previously, the regioselectivity of a related  $\text{AuCl}_3$ -catalyzed benzannulation, which provides naphthyl ketones, was attributed to electronic effects.<sup>26</sup> This question has not been addressed previously in the  $\text{Cu}(\text{OTf})_2$ -catalyzed formation of naphthalenes, nor have substituted *o*-phenylethynylbenzaldehydes been employed prior to this study.

The  $\text{Cu}(\text{OTf})_2$ -catalyzed benzannulation was proposed to proceed through a Cu-bound pyrylium ion intermediate (Scheme 4.3A).<sup>23</sup> This species reacts with an alkyne through a formal [4+2] cycloaddition. The observed regioselectivity in the reaction of **5** with **1-<sup>13</sup>C<sub>2</sub>**, and other substrates described in this work, is presumably set during this process. Based on the experiments described below, we propose that the cycloaddition proceeds either asynchronously



**Scheme 4.2.** The benzannulation of diyne **5** by <sup>13</sup>C-labeled benzaldehyde **1-<sup>13</sup>C<sub>2</sub>** provides the oligo(arylene) product as a single isotopomer.<sup>25</sup>



**Scheme 4.3.** **A.** Proposed mechanism of the Yamamoto benzannulation.<sup>23</sup> **B.** The observed regioselectivity is consistent with asynchronous bond formation with developing positive charge on one of the two alkyne carbons.

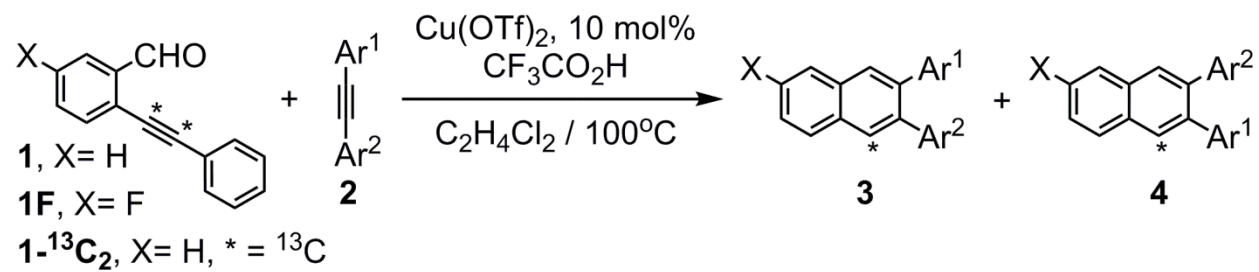
or through a cationic intermediate, both of which involve positive charge developing on one of the alkyne carbons. The aryl substituent that stabilizes this positive charge more effectively preferentially bonds to the Cu-bound carbon atom, thus determining the naphthalene regioisomer that will be formed (Scheme 4.3 B). Complete regioselectivity is expected from diaryl alkyne substrates that preferentially stabilize positive charge on one alkyne carbon relative to the other. However, it is also unclear whether bulky aryl groups, such as those with *ortho*-substituents, also influence the regiochemical outcome.

### 4.3 *Electronic Contributions to Regioselectivity*

We selected several model substrates to evaluate the relevance of steric and electronic effects to the regioselectivity of the benzannulation reaction with benzaldehyde **1** (Table 4.1), as well as its isotopically labeled analogue **1-<sup>13</sup>C<sub>2</sub>** and fluorine-substituted **1-F** (Table 4.2). Each of the four compounds is benzannulated efficiently under identical reaction conditions, and the products were isolated in good yields after purification by flash chromatography. The products were characterized using a full complement of 1D and 2D NMR techniques, in addition to high-resolution mass spectrometry and infrared spectroscopy, which allowed their structure to be determined unambiguously.

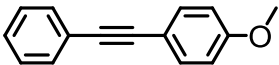
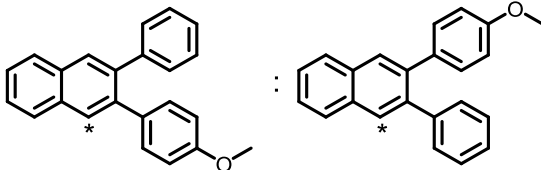
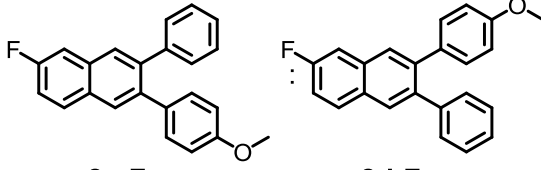
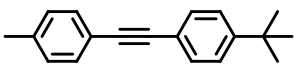
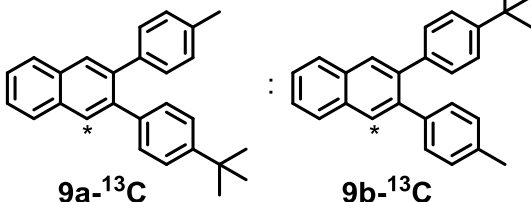
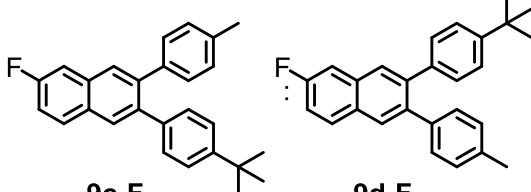
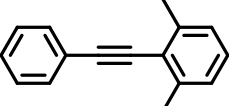
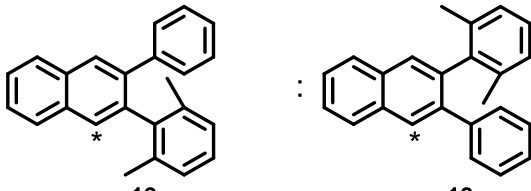
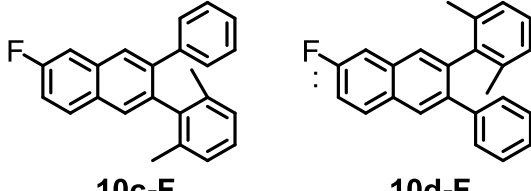
As discussed above, the experiments described in Tables 4.1 and 4.2 confirm that the benzannulation reaction is highly regioselective when one alkyne carbon preferentially stabilizes a developing positive charge. For example, 1-methoxy-4-(phenylethynyl)benzene **2** forms a single naphthalene product upon benzannulation with **1-<sup>13</sup>C<sub>2</sub>** and **1-F**. The complete regioselectivity of the reaction is easily diagnosed by comparing the <sup>1</sup>H NMR spectra of naphthalene **8** with its <sup>13</sup>C-enriched counterpart **8a-<sup>13</sup>C**. In the spectrum of **8** (Figure 4.1, top) the hydrogens adjacent to each phenyl substituent, Ha and Hd, respectively, both resonate with overlapping signals centered near 7.9 ppm. Only one of these resonances is split into a doublet in the spectrum of **8a-<sup>13</sup>C**, whose identity was unambiguously assigned as Hd by analyzing its <sup>1</sup>H, <sup>13</sup>C, ROESY, and COSY NMR spectra (Figures A3.35–A3.42). Benzannulation of **2** with **1-F** also produced a single fluoronaphthalene product **8c-F**, which corresponds to the same regiochemical outcome as the isotopic labeling experiment. In contrast, compound **3**, which bears electronically similar methyl and *t*-butyl substituents in the para positions of each phenyl ring, provides a nearly equal mixture of regioisomers. A similar comparison of <sup>1</sup>H NMR spectra

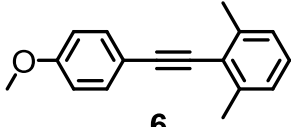
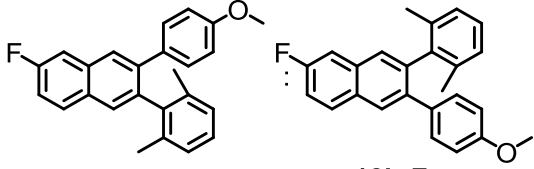
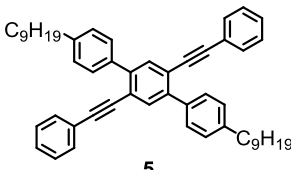
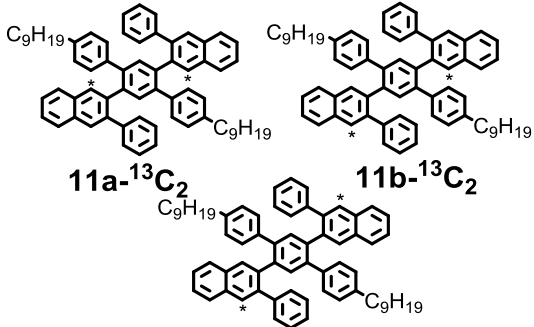
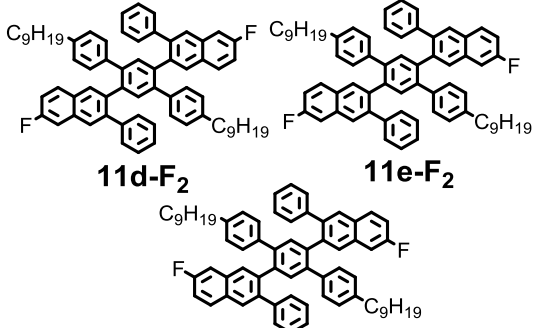
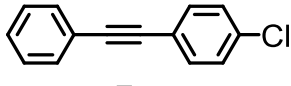
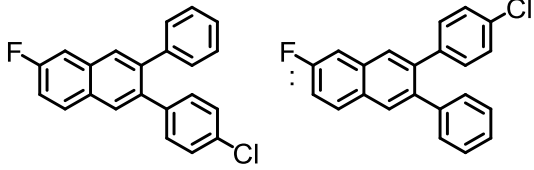
**Table 4.1.** Benzannulation of diaryl alkynes with **1**.



Diarylacetylene	Aldehyde	conversion (%)	Isolated yield (%)	Product(s)
 2	<b>1</b>	>99	85	 8
 3	<b>1</b>	>99	85	 9
 4	<b>1</b>	>99	>99	 10
 5	<b>1</b>	>99	98	 11

**Table 4.2.** Benzannulation of diarylacetylenes with  $1\text{-}^{13}\text{C}_2$  and  $1\text{-F}$ .

Diarylacetylene	Aldehyde	conversion (%)	Isolated yield (%)	Product(s)
 <b>2</b>	$1\text{-}^{13}\text{C}_2$	>99	78	 <b>8a-<math>^{13}\text{C}</math></b> : <b>8b-<math>^{13}\text{C}</math></b> >99:1
	$1\text{-F}$	>99	63	 <b>8c-F</b> : <b>8d-F</b> >99:1
 <b>3</b>	$1\text{-}^{13}\text{C}_2$	>99	95	 <b>9a-<math>^{13}\text{C}</math></b> : <b>9b-<math>^{13}\text{C}</math></b> 49:51
	$1\text{-F}$	>99	82	 <b>9c-F</b> : <b>9d-F</b> 49:51
 <b>4</b>	$1\text{-}^{13}\text{C}_2$	>99	>99	 <b>10a-<math>^{13}\text{C}</math></b> : <b>10b-<math>^{13}\text{C}</math></b> >99:1
	$1\text{-F}$	>99	97	 <b>10c-F</b> : <b>10d-F</b> >99:1

 <p><b>6</b></p>	<b>1-F</b>	>99	>99	 <p><b>12a-F</b>      <b>12b-F</b></p> <p>32:68</p>
 <p><b>5</b></p>	<b>1-<sup>13</sup>C<sub>2</sub></b>	>99	95	 <p><b>11a-<sup>13</sup>C<sub>2</sub></b>      <b>11b-<sup>13</sup>C<sub>2</sub></b></p> <p><b>11c-<sup>13</sup>C<sub>2</sub></b></p> <p>&gt;99:1:1</p>
	<b>1-F</b>	>99	90	 <p><b>11d-F<sub>2</sub></b>      <b>11e-F<sub>2</sub></b></p> <p><b>11f-F<sub>2</sub></b></p> <p>&gt;99:1:1</p>
 <p><b>7</b></p>	<b>1-F</b>	63	60	 <p><b>13a-F</b>      <b>13b-F</b></p> <p>55:45</p>



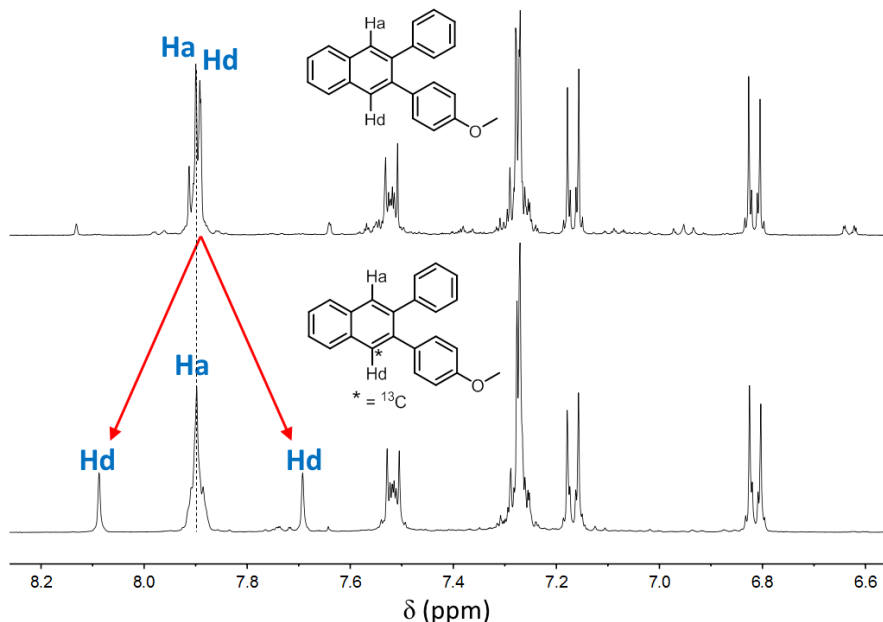


**Figure 4.1.** Partial  $^1\text{H}$  NMR spectra (400 MHz,  $\text{CDCl}_3$ , 298 K) of **8** (top) and the single regioisomer (400 MHz,  $\text{CDCl}_3$ , 298 K) of **8**- $^{13}\text{C}$  derived from the benzannulation of **2** with **1**- $^{13}\text{C}_2$  (bottom). The single isotopomer exhibits strong  $^1\text{H}$ - $^{13}\text{C}$  coupling only at the labeled position, which was unambiguously assigned as Hd based on multidimensional NMR experiments.

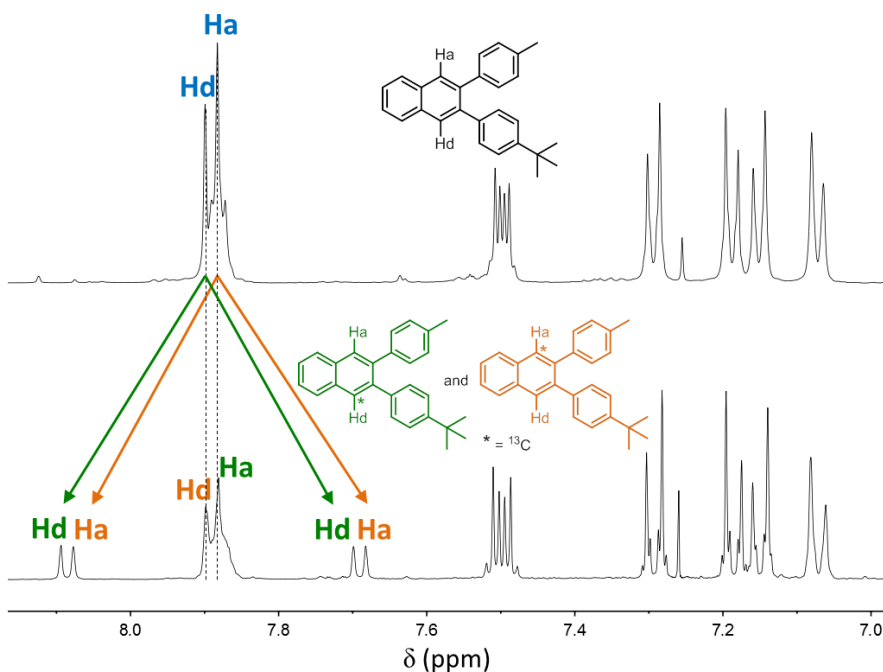


**Figure 4.2** Partial  $^1\text{H}$  NMR spectra (400 MHz,  $\text{CDCl}_3$ , 298 K) of **9** (top) and the two regioisomers (500 MHz,  $\text{CDCl}_3$ , 298 K) of **9**- $^{13}\text{C}$  derived from the benzannulation of **3** with **1**- $^{13}\text{C}_2$  (bottom). The mixture of two isotopomers gives rise to  $^1\text{H}$ - $^{13}\text{C}$  coupling to both Ha and Hd with nearly equal integration ratios.

of the corresponding naphthalene **9** and **9-<sup>13</sup>C** (Figure 4.2) indicates that both Ha and Hd peaks are coupled to a <sup>13</sup>C nucleus. Benzannulation of **3** with **1-F** also provided nearly equal amounts of the fluoronaphthalenes **9c-F** and **9d-F**. Finally, the dialkyne **5** preferentially forms a single regioisomer when reacted with both **1-<sup>13</sup>C<sub>2</sub>** (as noted previously) and **1-F**, which suggests that the terphenyl substituent serves as a better  $\pi$ -electron donor than the unsubstituted phenyl ring. The selective formation of the difluorinated oligoarylene structure **11d-F<sub>2</sub>** is promising for accessing larger polycyclic aromatic hydrocarbons with specific substitution patterns. Collectively, these results suggest that the regioselectivity of the benzannulation reaction is strongly influenced by  $\pi$ -electron donating substituents on the diarylacetylene substrate.

#### 4.4 *Electronic versus Steric Contributions*

We prepared compound **4**, which contains a 2,6-dimethylphenyl substituent, to evaluate the effect of steric hindrance on the benzannulation's efficiency and regioselectivity. Our previous studies have demonstrated the remarkable tolerance of the benzannulation reaction to phenylacetylenes bearing one ortho substituent (such as **5**), but 2,6-disubstituted phenyl moieties are undemonstrated. Nevertheless, **4** was benzannulated efficiently with **1**, **1-<sup>13</sup>C<sub>2</sub>**, and **1-F** and provided single regioisomers for the latter two cycloaddition partners, **10a-<sup>13</sup>C** and **10c-F**, respectively. These products correspond to the same regiochemical outcome as the methoxy-functionalized substrate **2**, which is consistent with the interpretation that the electron-donating nature of the two methyl groups, rather than their steric demands, direct the cycloaddition.

DFT calculations [B3LYP/6-31g(d), see Appendix 3] lend further support to this interpretation. A comparison of the relative energies of the vinyl carbocations derived from both **2** and **4** indicate a strong preference (6.7-9.2 kcal/mol) for localizing positive charge at the alkyne carbon adjacent to the substituted aromatic ring, which is consistent with the formation of

the observed regioisomers. In contrast, the two vinyl carbocations derived from diaryl acetylene **6**, which contains both 4-methoxyphenyl and 2,6-dimethylphenyl groups, are much closer in energy (1.3 kcal/mol in favor of the 4-MeOPh substituent). The benzannulation of **6** with **1-F** mirrors this trend: both regioisomers **12a-F** and **12b-F** are formed in a 32:68 ratio. Finally, these calculations also predict a small energy difference between the two vinyl carbocations derived from *p*-chlorodiphenylacetylene **7** (1.1 kcal/mol), and this substrate also forms a nearly equal mixture (55:45) of fluoronaphthalene regioisomers upon benzannulation with **1-F**. These calculations further show that the regiochemical outcome may be predicted from the inherent electronic properties of the alkyne substrate without considering the energies of specific intermediates or transition states of the net [4+2] cycloaddition associated with the benzannulation mechanism, whose energies might be influenced by steric factors associated with each substrate.

It should also be noted that the benzannulation of **7** proceeded to only 60% conversion, and unreacted **7** was observed by GC/MS and recovered upon purification. The reaction efficiency drops further when more powerful electron withdrawing substituents are present, such as a *p*-acetyl group (5% conversion). These findings demonstrate one remaining weakness of the benzannulation reaction: sufficiently electron-rich alkynes must be used, although electron withdrawing groups are tolerated on the benzaldehyde. The collective observations of the regiochemical outcome and efficiency associated with each alkyne substrate form the basis of an intuitive model for predicting the products of benzannulation reactions and designing syntheses that are likely to provide naphthalene-containing systems as single regioisomers.

#### 4.5 *Conclusions*

In conclusion, the series of compounds tested in this work indicate that diaryl acetylenes that preferentially stabilize developing positive charge at one of the two alkyne carbons is likely to be highly regioselective. These studies further confirm that the benzannulation reaction is remarkably tolerant of sterically demanding substituents but works poorly for alkyne substrates with electron withdrawing groups. Relative energies of the carbocations calculated by DFT corroborate well with the experimental distributions of the regioisomers. This regioselectivity provides rapid access to precursors of novel polycyclic aromatic hydrocarbons with predetermined substitution patterns and eliminates need for symmetric substrates in planning complex syntheses. In contrast, the reaction outcome can be predicted without considering steric factors, suggesting that they play little role in determining regioselectivity. Overall, the remarkable efficiency, tolerance of bulky substituents, and regioselectivity of the benzannulation reaction make it a very attractive method for preparing elaborate aromatic architectures and carbon-based nanostructures.

## REFERENCES

- (1) Pisula, W.; Kastler, M.; Wasserfallen, D.; Pakula, T.; Müllen, K. *J. Am. Chem. Soc.* **2004**, *126*, 8074.
- (2) Gagnon, E.; Halperin, S. D.; Métivaud, V.; Maly, K. E.; Wuest, J. D. *J. Org. Chem.* **2009**, *75*, 399.
- (3) Fechtenkötter, A.; Tchegotareva, N.; Watson, M.; Müllen, K. *Tetrahedron* **2001**, *57*, 3769.
- (4) Herwig, P.; Kayser, C. W.; Müllen, K.; Spiess, H. W. *Adv. Mater.* **1996**, *8*, 510.
- (5) Hartley, C. S. *J. Org. Chem.* **2011**, *76*, 9188.
- (6) Hartley, C. S.; He, J. *J. Org. Chem.* **2010**, *75*, 8627.
- (7) He, J.; Crase, J. L.; Wadumethrige, S. H.; Thakur, K.; Dai, L.; Zou, S.; Rathore, R.; Hartley, C. S. *J. Am. Chem. Soc.* **2010**, *132*, 13848.
- (8) He, J.; Mathew, S. M.; Cornett, S. D.; Grundy, S. C.; Hartley, C. S. *Org. Biomol. Chem.* **2012**, *10*, 3398.
- (9) Mathew, S. M.; Engle, J. T.; Ziegler, C. J.; Hartley, C. S. *J. Am. Chem. Soc.* **2013**, *135*, 6714.
- (10) Mathew, S. M.; Hartley, C. S. *Macromolecules* **2011**, *44*, 8425.
- (11) Ando, S.; Ohta, E.; Kosaka, A.; Hashizume, D.; Koshino, H.; Fukushima, T.; Aida, T. *J. Am. Chem. Soc.* **2012**, *134*, 11084.

- (12) Kajitani, T.; Suna, Y.; Kosaka, A.; Osawa, T.; Fujikawa, S.; Takata, M.; Fukushima, T.; Aida, T. *J. Am. Chem. Soc.* **2013**, *135*, 14564.
- (13) Ohta, E.; Sato, H.; Ando, S.; Kosaka, A.; Fukushima, T.; Hashizume, D.; Yamasaki, M.; Hasegawa, K.; Muraoka, A.; Ushiyama, H.; Yamashita, K.; Aida, T. *Nature Chem.* **2011**, *3*, 68.
- (14) Ito, S.; Takahashi, K.; Nozaki, K. *J. Am. Chem. Soc.* **2014**, *136*, 7547.
- (15) Nguyen, T. T.; Turp, D.; Wang, D.; Nolscher, B.; Laquai, F.; Mullen, K. *J. Am. Chem. Soc.* **2011**, *133*, 11194.
- (16) Nguyen, T. T.; Baumgarten, M.; Rouhanipour, A.; Rader, H. J.; Lieberwirth, I.; Mullen, K. *J. Am. Chem. Soc.* **2013**, *135*, 4183.
- (17) Weil, T.; Reuther, E.; Müllen, K. *Angew. Chem. Int. Ed.* **2002**, *41*, 1900.
- (18) Pradhan, A.; Dechambenoit, P.; Bock, H.; Durola, F. *Angew. Chem. Int. Ed.* **2011**, *50*, 12582.
- (19) Pradhan, A.; Dechambenoit, P.; Bock, H.; Durola, F. *J. Org. Chem.* **2013**, *78*, 2266.
- (20) Narita, A.; Feng, X.; Hernandez, Y.; Jensen, S. A.; Bonn, M.; Yang, H.; Verzhbitskiy, I. A.; Casiraghi, C.; Hansen, M. R.; Koch, A. H. R.; Fytas, G.; Ivasenko, O.; Li, B.; Mali, K. S.; Balandina, T.; Mahesh, S.; De Feyter, S.; Müllen, K. *Nature Chem.* **2014**, *6*, 126.
- (21) Yang, X.; Dou, X.; Rouhanipour, A.; Zhi, L.; Räder, H. J.; Müllen, K. *J. Am. Chem. Soc.* **2008**, *130*, 4216.
- (22) Dössel, L.; Gherghel, L.; Feng, X.; Müllen, K. *Angew. Chem. Int. Ed.* **2011**, *50*, 2540.

- (23) Asao, N.; Nogami, T.; Lee, S.; Yamamoto, Y. *J. Am. Chem. Soc.* **2003**, *125*, 10921.
- (24) Arslan, H.; Saathoff, J. D.; Bunck, D. N.; Clancy, P.; Dichtel, W. R. *Angew. Chem. Int. Ed.* **2012**, *51*, 12051.
- (25) Arslan, H.; Uribe-Romo, F. J.; Smith, B. J.; Dichtel, W. R. *Chemical Science* **2013**, *4*, 3973.
- (26) Asao, N.; Takahashi, K.; Lee, S.; Kasahara, T.; Yamamoto, Y. *J. Am. Chem. Soc.* **2002**, *124*, 12650.

## APPENDIX THREE



## Table of Contents

<b>A.</b>	Materials and Instrumentation	219
<b>B.</b>	Synthetic Procedures	220
<b>C.</b>	$^1\text{H}$ and $^{13}\text{C}$ NMR Spectroscopy	231
<b>D.</b>	2D NMR Spectra Assignments	248
<b>E.</b>	DFT Calculations	323
<b>F.</b>	References to Appendix	335

**A. Materials.** All reagents were purchased from commercial sources and used without further purification. CH<sub>2</sub>Cl<sub>2</sub>, and PhMe were purchased from commercial sources and purified using a custom-built alumina-column based solvent purification system. Other solvents were purchased from commercial sources and used without further purification. Compounds **1**, **1**-<sup>13</sup>C<sub>2</sub>, **5**, **11**,<sup>1</sup> and **11**-<sup>13</sup>C<sub>2</sub><sup>2</sup> were synthesized according to previously described procedures.

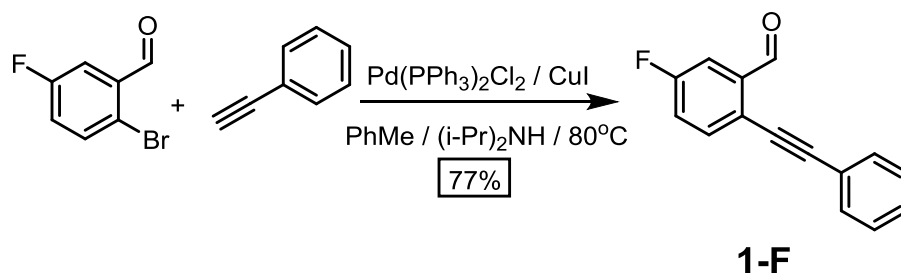
**Instrumentation.** Infrared spectra were recorded on a Thermo Nicolet iS10 with a diamond ATR attachment and are uncorrected.

Gas chromatography/electron impact mass spectrometry was performed on an Agilent 6890N Network GC System with a JEOL JMS-GCmate II Mass Spectrometer (magnetic sector).

NMR spectra were recorded on a Varian 400 MHz, a Varian 500 MHz or a Bruker ARX 300 MHz spectrometer using a standard <sup>1</sup>H/X Z-PFG probe at ambient temperature with a 20 Hz sample spin rate.

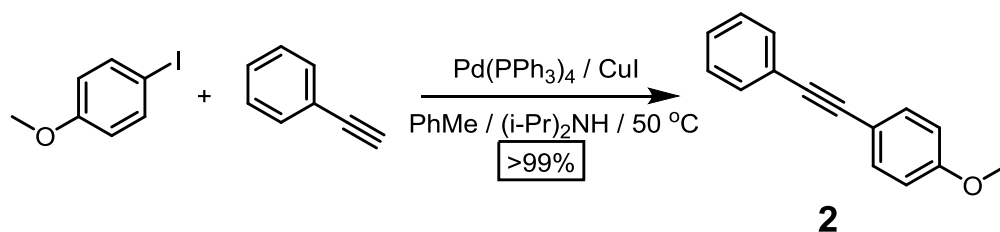
## B. Synthetic Procedures

### Scheme A3.1. Synthesis of **1-F**.



**Synthesis of 1-F:** 2-Bromo-5-fluorobenzaldehyde (1.000 g, 4.926 mmol),  $\text{Pd(PPh}_3)_2\text{Cl}_2$  (0.069 g, 0.099 mmol) and  $\text{CuI}$  (0.038 g, 0.197 mmol) were added to a 3-neck round bottomed flask equipped with a condenser. The flask was evacuated and backfilled with  $\text{N}_2$ .  $\text{N}_2$  was bubbled through a solution of phenylacetylene in DIPA. This solution (12 mL) and dry  $\text{PhMe}$  (25 mL) were added and the reaction was heated to  $80^\circ\text{C}$ . After stirring for 3h under  $\text{N}_2$  atmosphere, the mixture was cooled to rt. The reaction mixture was passed through a pad of celite and solvent was removed. Purification of the crude mixture by flash chromatography ( $\text{SiO}_2$ , 1% v/v  $\text{EtOAc}$ /hexanes to 4% v/v  $\text{EtOAc}$ /hexanes) to give **1-F** (0.849 g, 77% yield) as an off-white solid. **1-F:**  $^1\text{H}$  NMR (400 MHz,  $\text{CDCl}_3$ ) 10.60 (d,  $J = 3.2$  Hz, 1H), 7.69 – 7.60 (m, 2H), 7.59 – 7.52 (m, 2H), 7.44 – 7.35 (m, 3H), 7.30 (ddd,  $J = 8.5, 7.8, 2.8$  Hz, 1H).  $^{13}\text{C}$  NMR (100 MHz,  $\text{CDCl}_3$ )  $\delta$  190.65, 163.78, 161.27, 137.93, 137.87, 135.43, 135.36, 131.78, 129.32, 128.71, 123.18, 123.14, 122.25, 121.66, 121.43, 113.98, 113.75, 96.17, 96.15, 83.95. IR (solid, ATR) 3079, 2845, 2750, 2213, 1720, 1688, 1603, 1594, 1576, 1494, 1479, 1444, 1418, 1392, 1312, 1290, 1266, 1207, 1146, 1207, 1137, 1070, 1024, 997, 964, 917, 875, 829, 751, 685  $\text{cm}^{-1}$ . HRMS (EI,  $m/z$ ): calcd for  $[\text{C}_{15}\text{H}_{19}\text{FO}+\text{H}]^+$  225.07157, found 225.07086.

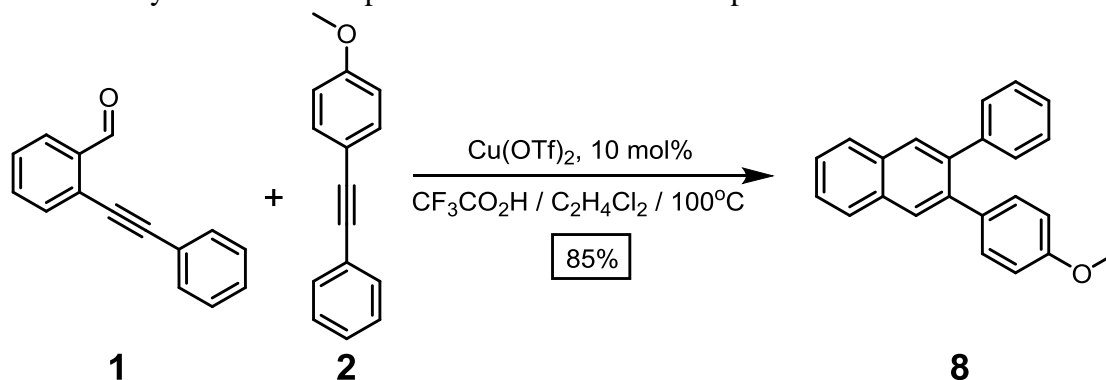
### Scheme A3.2. Synthesis of **2**.



**Synthesis of 2:** A solution of phenylacetylene (218 mg, 2.136 mmol) and 4-iodoanisole (250 mg, 1.068 mmol) in DIPA (5 mL) was bubbled with nitrogen for 20 min. The above solution was cannulated to a flask containing  $\text{Pd(PPh}_3)_4$  (37 mg, 0.032 mmol) and  $\text{CuI}$  (20 mg, 0.107 mmol) suspended in  $\text{PhMe}$  (4 mL) under  $\text{N}_2$  atmosphere. The mixture was heated to  $50^\circ\text{C}$  and stirred for 1 h. It was cooled to rt and added to a separatory funnel containing 50 mL  $\text{Et}_2\text{O}$ . It was extracted with aqueous 1 M  $\text{HCl}$  (50 mL), and brine (2 x 50 mL). The organic phase was dried ( $\text{MgSO}_4$ ), filtered and the solvent was removed. The crude product was purified by flash

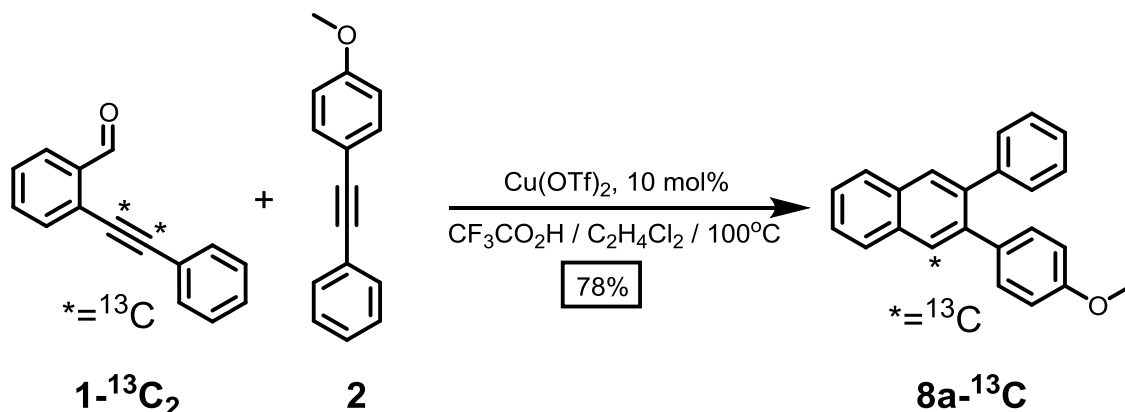
chromatography (SiO<sub>2</sub>, 1:4 v/v CHCl<sub>3</sub>:hexanes) to give **2** (0.2314g, >99% yield) as a white powder. **2**: <sup>1</sup>H NMR (500 MHz, CDCl<sub>3</sub>) δ 7.56 – 7.51 (m, 2H), 7.48 (d, *J* = 8.5 Hz, 2H), 7.38 – 7.29 (m, 3H), 6.93 – 6.84 (d, *J* = 8.5 Hz, 2H), 3.83 (s, 3H). <sup>13</sup>C NMR (126 MHz, CDCl<sub>3</sub>) δ 159.76, 133.19, 131.58, 128.44, 128.06, 123.74, 115.53, 114.14, 89.51, 88.21, 77.41, 77.16, 76.91, 55.44. IR (solid, ATR) 3053, 2936, 2837, 2535, 2214, 1604, 1593, 1567, 1507, 1456, 1439, 1315, 1287, 1246, 1174, 1137, 1107, 1069, 1025, 835, 779, 752, 689 cm<sup>-1</sup>. HRMS (EI, *m/z*): calcd for [C<sub>15</sub>H<sub>13</sub>O+H]<sup>+</sup> 209.09609, found 209.09552.

**Scheme A3.3.** Synthesis of **8**. Representative benzannulation procedure.



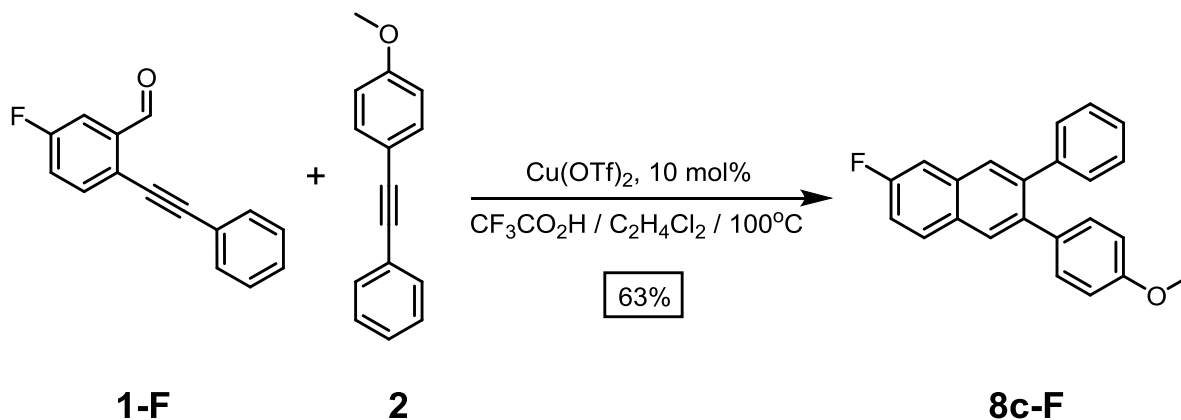
**Synthesis of 8:** Alkyne **2** (18 mg, 0.087 mmol) and benzaldehyde **1** (30 mg, 0.145 mmol) were dissolved in 1,2-dichloroethane (1.5 mL) under N<sub>2</sub>. Cu(OTf)<sub>2</sub> (5 mg, 0.015 mmol) and CF<sub>3</sub>CO<sub>2</sub>H (12 μL, 0.160 mmol) were added in quick succession. The solution was heated to 100 °C for 15 min, after which it was cooled to rt and poured into a saturated aqueous NaHCO<sub>3</sub> solution (25 mL). The aqueous layer was extracted with CH<sub>2</sub>Cl<sub>2</sub> (3x25 mL), and the combined organic layers were dried (MgSO<sub>4</sub>) and filtered. The solvent was evaporated to provide the crude mixture, which was purified by chromatography (SiO<sub>2</sub>, 4% v/v EtOAc/hexanes) to give **8** (23 mg, 85% yield) as a colourless goo. **8**: <sup>1</sup>H NMR (500 MHz, CDCl<sub>3</sub>) δ 7.89 – 7.83 (m, 2H), 7.87 (s, 1H), 7.86 (s, 1H), 7.53 – 7.45 (m, 2H), 7.24 (m, 5H), 7.13 (d, *J* = 8.7 Hz, 2H), 6.78 (d, *J* = 8.7 Hz, 2H), 3.79 (s, 3H). <sup>13</sup>C NMR (126 MHz, CDCl<sub>3</sub>) δ 158.38, 141.61, 139.16, 138.68, 133.81, 132.77, 132.54, 132.50, 131.05, 130.77, 129.99, 129.46, 129.22, 129.18, 128.77, 128.45, 127.90, 127.69, 127.65, 127.61, 127.45, 126.48, 126.24, 126.14, 126.11, 113.33, 55.20. IR (solid, ATR) 3054, 2922, 2850, 1711, 1609, 1515, 1489, 1457, 1436, 1360, 1288, 1245, 1220, 1177, 1032, 1023, 960, 892, 832, 763, 735, 700 cm<sup>-1</sup>. HRMS (EI, *m/z*): calcd for [C<sub>23</sub>H<sub>18</sub>O]<sup>+</sup> 310.13631, found 310.13460.

**Scheme A3.4.** Synthesis of **8a-<sup>13</sup>C**.



**Synthesis of 8a-<sup>13</sup>C:** **8a-<sup>13</sup>C** was synthesized using a similar procedure to that used to prepare **8**. Alkyne **2** (18 mg, 0.087 mmol), benzaldehyde **1-<sup>13</sup>C<sub>2</sub>** (30 mg, 0.145 mmol), 1,2-dichloroethane (1.5 mL), Cu(OTf)<sub>2</sub> (5 mg, 0.015 mmol) and CF<sub>3</sub>CO<sub>2</sub>H (12 μL, 0.160 mmol) were used. Chromatography (SiO<sub>2</sub>, 1:4 v/v CHCl<sub>3</sub>:hexanes) gave **8a-<sup>13</sup>C** (21 mg, 78% yield) as a colourless goo. **8a-<sup>13</sup>C**: <sup>1</sup>H NMR (400 MHz, CDCl<sub>3</sub>) δ 7.89 – 7.83 (m, 2H), 7.87 (s, 1H), 7.86 (d, *J*<sub>CH</sub> = 158 Hz, 1H), 7.53 – 7.45 (m, 2H), 7.24 (m, 5H), 7.13 (d, *J* = 8.7 Hz, 2H), 6.78 (d, *J* = 8.7 Hz, 2H), 3.79 (s, 3H). <sup>13</sup>C NMR (75 MHz, CDCl<sub>3</sub>) δ 129.30 (one <sup>13</sup>C-enriched carbon signal). IR (solid, ATR) 3052, 2925, 2833, 1608, 1513, 1488, 1454, 1434, 1331, 1287, 1244, 1176, 1074, 1032, 1023, 957, 887, 830, 802, 781, 772, 762, 747, 735, 714, 700 cm<sup>-1</sup>. HRMS (EI, *m/z*): calcd for [C<sub>22</sub><sup>13</sup>CH<sub>18</sub>O]<sup>+</sup> 311.13857, found 311.13758.

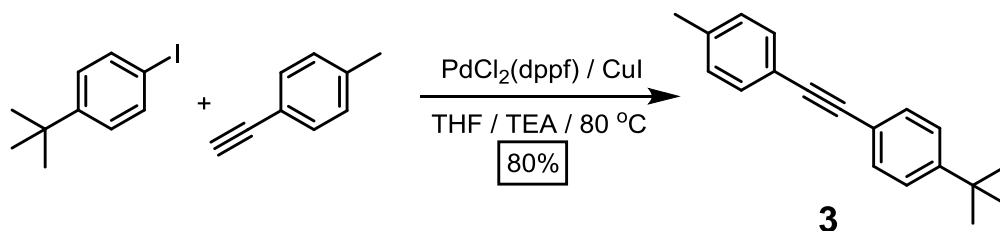
**Scheme A3.5.** Synthesis of **8c-F**.



**Synthesis of 8c-F:** **8c-F** was synthesized using a similar procedure to that used to prepare **8**. Alkyne **2** (22 mg, 0.107 mmol), benzaldehyde **1-F** (30 mg, 0.134 mmol), 1,2-dichloroethane (1.5 mL), Cu(OTf)<sub>2</sub> (5 mg, 0.013 mmol) and CF<sub>3</sub>CO<sub>2</sub>H (11 μL, 0.147 mmol) were used. Chromatography (SiO<sub>2</sub>, 1:2 v/v CHCl<sub>3</sub>:hexanes) gave **8c-F** (22 mg, 63% yield) as a colourless goo. **8c-F**: <sup>1</sup>H NMR (500 MHz, CDCl<sub>3</sub>) δ 7.86 – 7.82 (m, 1H), 7.84 (s, 1H), 7.80 (s, 1H), 7.47 (dd, *J* = 9.8, 2.5 Hz, 1H), 7.31 – 7.18 (m, 6H), 7.11 (d, *J* = 8.4 Hz, 2H), 6.78 (d, *J* = 8.4 Hz, 2H), 3.79 (s, 3H). <sup>13</sup>C NMR (126 MHz, CDCl<sub>3</sub>) δ 161.94, 159.98, 158.56, 141.39, 140.37, 138.20,

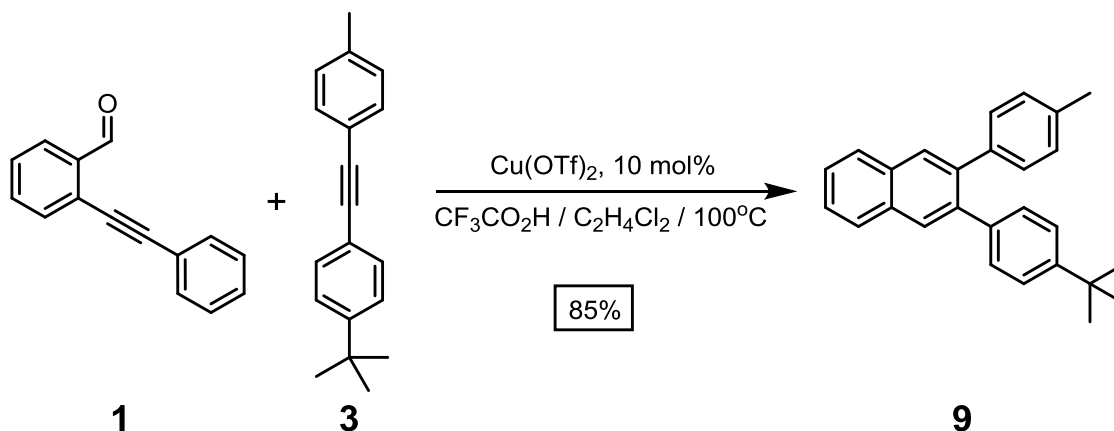
138.18, 133.64, 133.37, 133.29, 131.13, 130.22, 130.14, 130.05, 129.93, 129.31, 129.25, 128.92, 128.88, 128.09, 126.83, 116.87, 116.67, 113.51, 110.87, 110.71, 55.34. IR (solid, ATR) 3056, 2930, 2835, 1636, 1607, 1570, 1514, 1490, 1461, 1440, 1408, 1386, 1347, 1283, 1244, 1218, 1190, 1175, 1143, 1119, 1074, 1046, 1033, 1022, 973, 947, 897, 835, 807, 787, 777, 760, 736, 715, 700,  $\text{cm}^{-1}$ . HRMS (EI,  $m/z$ ): calcd for  $[\text{C}_{23}\text{H}_{17}\text{FO}]^+$  328.12579, found 328.12487.

**Scheme A3.6.** Synthesis of **3**.



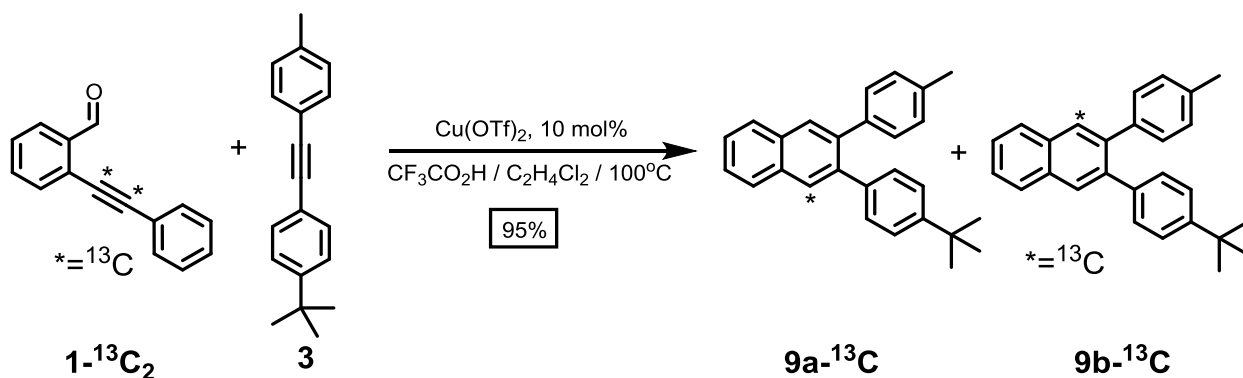
**Synthesis of 3:**  $\text{PdCl}_2(\text{dppf})$  (0.108 g, 0.154 mmol) and  $\text{CuI}$  (0.073 g, 0.0384 mmol) were added to a Schlenk flask. 1-*tert*-Bu-4-iodobenzene (2.000 g, 7.689 mmol) and 4-ethynyltoluene (0.893 g, 7.689 mmol) and THF (12.0 mL) were added under  $\text{N}_2$  atmosphere. TEA (6.0 mL) was added and the mixture was subjected to 3 freeze-pump-thaw cycles. The reaction was heated to  $80\text{ }^\circ\text{C}$ . After stirring for 20 h under  $\text{N}_2$  atmosphere, the mixture was cooled to rt. It was passed through a pad of celite and solvent was removed. The crude product was washed with MeOH (100 mL) to give **3** (1.522 g, 80% yield) as a white powder. **3:**  $^1\text{H}$  NMR (400 MHz,  $\text{CDCl}_3$ )  $\delta$  7.46 (d,  $J = 8.5$  Hz, 2H), 7.42 (d,  $J = 7.8$  Hz, 2H), 7.36 (d,  $J = 8.5$  Hz, 2H), 7.14 (d,  $J = 7.8$  Hz, 2H), 2.36 (s, 3H), 1.32 (s, 9H).  $^{13}\text{C}$  NMR (101 MHz,  $\text{CDCl}_3$ )  $\delta$  151.28, 138.13, 131.42, 131.21, 129.04, 125.28, 120.36, 109.99, 88.83, 88.80, 34.75, 31.17, 21.51. IR (solid, ATR) 2962, 2865, 2163, 1979, 1913, 1515, 1462, 1405, 1393, 1362, 1307, 1267, 1183, 1114, 1103, 1015, 832, 819, 737,  $703\text{ cm}^{-1}$ . HRMS (EI,  $m/z$ ): calcd for  $[\text{C}_{19}\text{H}_{20}+\text{H}]^+$  248.16487, found 248.16311.

**Scheme A3.7.** Synthesis of **9**.



**Synthesis of **9**:** **9** was synthesized using a similar procedure to that used to prepare **8**. Alkyne **3** (19 mg, 0.076 mmol), benzaldehyde **1** (26 mg, 0.126 mmol), 1,2-dichloroethane (1.5 mL),  $\text{Cu}(\text{OTf})_2$  (5 mg, 0.013 mmol) and  $\text{CF}_3\text{CO}_2\text{H}$  (11  $\mu\text{L}$ , 0.139 mmol) were used. Chromatography ( $\text{SiO}_2$ , 1:9 v/v  $\text{CHCl}_3$ :hexanes) gave **9** (24 mg, 85% yield) as a colourless goo. **9**:  $^1\text{H}$  NMR (500 MHz,  $\text{CDCl}_3$ )  $\delta$  7.90 (s, 1H), 7.91 – 7.85 (m, 2H), 7.88 (s, 1H), 7.52 – 7.48 (m, 2H), 7.29 (d,  $J$  = 8.3 Hz, 2H), 7.19 (d,  $J$  = 8.3 Hz, 2H), 7.15 (d,  $J$  = 8.0 Hz, 2H), 7.07 (d,  $J$  = 8.0 Hz, 2H), 2.36 (s, 3H), 1.34 (s, 9H).  $^{13}\text{C}$  NMR (126 MHz,  $\text{CDCl}_3$ )  $\delta$  149.51, 139.23, 139.16, 138.74, 138.65, 136.20, 132.79, 132.78, 129.99, 129.70, 129.60, 129.52, 128.70, 127.78, 126.22, 124.91, 77.41, 77.16, 76.91, 34.60, 31.53, 21.33. IR (solid, ATR) 3050, 2960, 2865, 1739, 1514, 1488, 1457, 1403, 1362, 1267, 1203, 1132, 1110, 1018, 851, 894, 886, 835, 820, 745, 706  $\text{cm}^{-1}$ . HRMS (EI,  $m/z$ ): calcd for  $[\text{C}_{27}\text{H}_{26}+\text{H}]^+$  351.21182, found 351.20945.

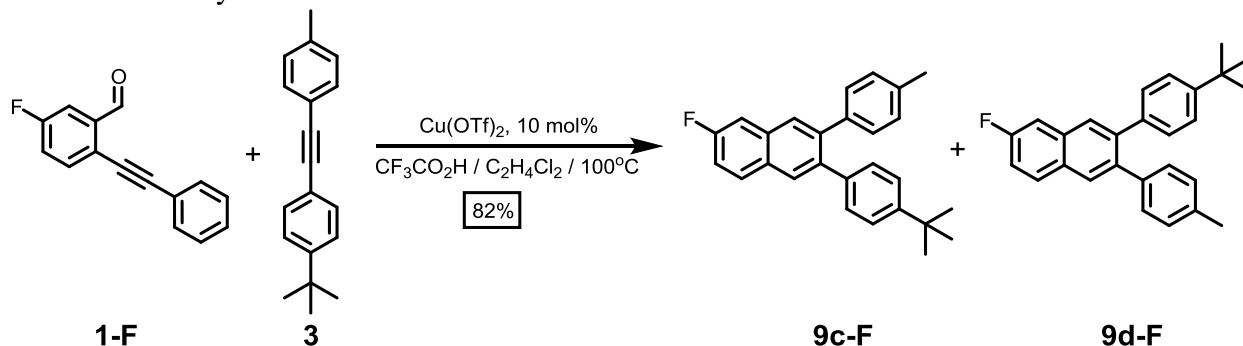
**Scheme A3.8.** Synthesis of **9a- $^{13}\text{C}$**  and **9b- $^{13}\text{C}$** .



**Synthesis of **9a- $^{13}\text{C}$**  and **9b- $^{13}\text{C}$** :** **9a- $^{13}\text{C}$**  and **9b- $^{13}\text{C}$**  were synthesized using a similar procedure to that used to prepare **8**. Alkyne **3** (21 mg, 0.084 mmol), benzaldehyde **1- $^{13}\text{C}_2$**  (25 mg, 0.120 mmol), 1,2-dichloroethane (1.5 mL),  $\text{Cu}(\text{OTf})_2$  (4 mg, 0.012 mmol) and  $\text{CF}_3\text{CO}_2\text{H}$  (10  $\mu\text{L}$ , 0.132 mmol) were used. Chromatography ( $\text{SiO}_2$ , 1:9 v/v  $\text{CHCl}_3$ :hexanes) gave **9a- $^{13}\text{C}$**  and **9b- $^{13}\text{C}$**  (29 mg, 95% yield) as a colourless goo, which was an inseparable mixture. **9a- $^{13}\text{C}$**  and **9b- $^{13}\text{C}$** :  $^1\text{H}$  NMR (400 MHz,  $\text{CDCl}_3$ ) **9a- $^{13}\text{C}$** : 7.90 (d,  $J_{\text{CH}}$  = 158.0 Hz, 1H), 7.91 – 7.85 (m, 2H), 7.88 (s, 1H), 7.52 – 7.48 (m, 2H), 7.29 (d,  $J$  = 8.3 Hz, 2H), 7.19 (d,  $J$  = 8.3 Hz, 2H), 7.15 (d,  $J$  = 8.0 Hz,

2H), 7.07 (d,  $J = 8.0$  Hz, 2H), 2.36 (s, 3H), 1.34 (s, 9H). **9b-<sup>13</sup>C**: 7.90 (s, 1H), 7.91 – 7.85 (m, 2H), 7.88 (d,  $J_{CH} = 158.0$  Hz, 1H), 7.52 – 7.48 (m, 2H), 7.29 (d,  $J = 8.3$  Hz, 2H), 7.19 (d,  $J = 8.3$  Hz, 2H), 7.15 (d,  $J = 8.0$  Hz, 2H), 7.07 (d,  $J = 8.0$  Hz, 2H), 2.36 (s, 3H), 1.34 (s, 9H). <sup>13</sup>C NMR (75 MHz, CDCl<sub>3</sub>)  $\delta$  129.60, 129.52 (two <sup>13</sup>C-enriched carbon signals) IR (solid, ATR) 3050, 2960, 2865, 1904, 1587, 1513, 1487, 1450, 1402, 1362, 1265, 1109, 1018, 950, 883, 834, 819, 738, 704 cm<sup>-1</sup>. HRMS (EI,  $m/z$ ): calcd for [C<sub>26</sub><sup>13</sup>CH<sub>26</sub>+H]<sup>+</sup> 352.21518, found 352.21293.

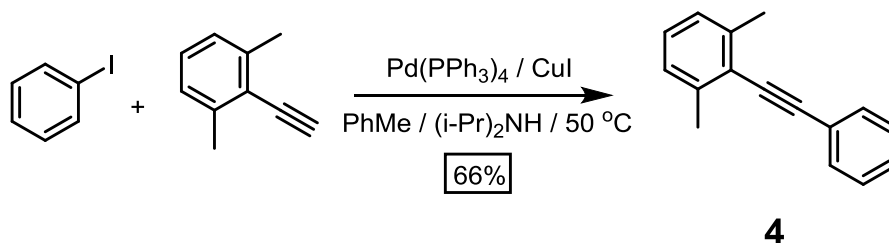
**Scheme A3.9.** Synthesis of **9c-F** and **9d-F**.



**Synthesis of 9c-F and 9d-F:** **9c-F** and **9d-F** were synthesized using a similar procedure to that used to prepare **8**. Alkyne **3** (89 mg, 0.357 mmol), benzaldehyde **1-F** (100 mg, 0.446 mmol), 1,2-dichloroethane (5.0 mL), Cu(OTf)<sub>2</sub> (16 mg, 0.045 mmol) and CF<sub>3</sub>CO<sub>2</sub>H (38  $\mu$ L, 0.491 mmol) were used. Chromatography (SiO<sub>2</sub>, 2.5% v/v EtOAc/hexanes) gave **9c-F** and **9d-F** (107 mg, 82% yield) as a colourless goo, which was an inseparable mixture. **9c-F** and **9d-F**: <sup>1</sup>H NMR (500 MHz, CDCl<sub>3</sub>) **9c-F**:  $\delta$  7.85 (s, 1H), 7.84 – 7.80 (m, 1H), 7.78 (s, 1H), 7.45 (dt,  $J = 10.0, 1.9$  Hz, 1H), 7.31 – 7.20 (m, 3H), 7.14 (d,  $J = 8.3$  Hz, 2H), 7.11 (d,  $J = 8.3$  Hz, 2H), 7.04 (d,  $J = 8.4$  Hz, 2H), 2.33 (s, 3H), 1.31 (s, 9H). **9d-F**:  $\delta$  7.84 – 7.80 (m, 1H), 7.83 (s, 1H), 7.80 (s, 1H), 7.45 (dt,  $J = 10.0, 1.9$  Hz, 1H), 7.31 – 7.20 (m, 3H), 7.14 (d,  $J = 8.3$  Hz, 2H), 7.11 (d,  $J = 8.3$  Hz, 2H), 7.04 (d,  $J = 8.4$  Hz, 2H), 2.33 (s, 3H), 1.31 (s, 9H). <sup>13</sup>C NMR (126 MHz, CDCl<sub>3</sub>)  $\delta$  161.96, 160.00, 159.99, 149.76, 149.74, 149.61, 149.60, 140.31, 140.24, 138.57, 138.51, 138.45, 138.44, 138.38, 138.37, 138.35, 138.30, 138.28, 136.45, 136.44, 136.30, 136.28, 133.48, 133.42, 133.41, 130.24, 130.23, 130.17, 130.16, 129.93, 129.80, 129.65, 129.53, 129.45, 128.93, 128.89, 128.85, 128.84, 128.81, 128.80, 128.76, 128.74, 124.96, 116.70, 116.69, 116.50, 116.49, 110.81, 110.80, 110.65, 110.64, 34.62, 34.60, 31.51, 31.50, 21.32, 21.31. IR (solid, ATR) 2962, 2867, 1905, 1635, 1599, 1512, 1492, 1459, 1422, 1399, 1362, 1346, 1265, 1219, 1190, 1144, 1119, 1110, 1046, 1015, 973, 948, 898, 836, 820, 762, 736, 703 cm<sup>-1</sup>. HRMS (EI,  $m/z$ ): calcd for [C<sub>27</sub>H<sub>25</sub>F]<sup>+</sup> 368.19348, found 368.19249.

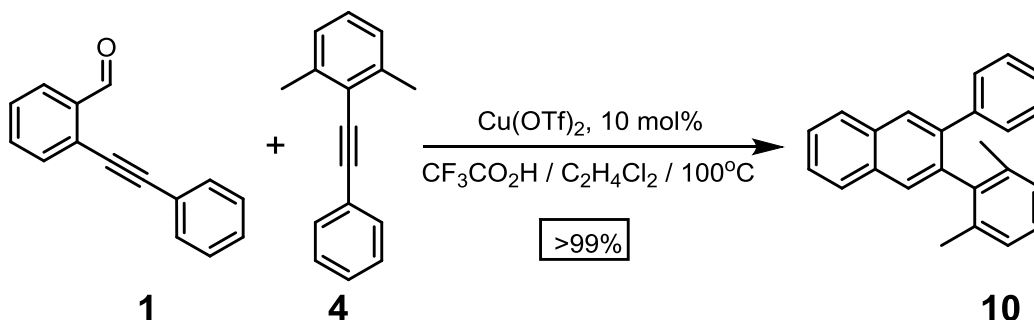


**Scheme A3.10.** Synthesis of **4**.



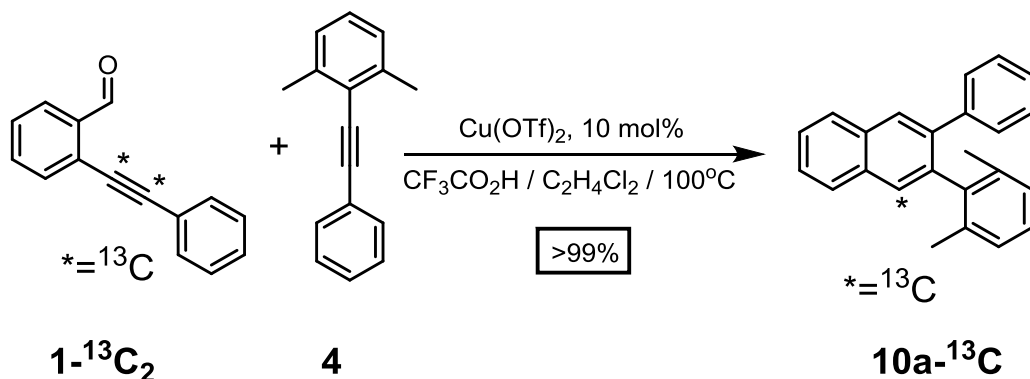
**Synthesis of 4:** A solution of 2-ethynyl-1,3-dimethylbenzene (100 mg, 0.768 mmol) and iodobenzene (313 mg, 1.536 mmol) in DIPA (2 mL) was bubbled with nitrogen for 20 min. The above solution was cannulated to a flask containing Pd(PPh<sub>3</sub>)<sub>4</sub> (44 mg, 0.038 mmol) and CuI (15 mg, 0.077 mmol) suspended in PhMe (4 mL) under N<sub>2</sub> atmosphere. The mixture was heated to 50 °C and stirred for 1 h. It was cooled to rt and added to a separatory funnel containing 50 mL Et<sub>2</sub>O. It was extracted with aqueous 1 M HCl (50 mL), and brine (2 x 50 mL). The organic phase was dried (MgSO<sub>4</sub>), filtered and the solvent was removed. The crude product was purified by flash chromatography (SiO<sub>2</sub>, hexanes) to give **4** (0.105g, 66% yield) as a clear oil. **4**: <sup>1</sup>H NMR (500 MHz, CDCl<sub>3</sub>) δ 7.55 (d, *J* = 7.1 Hz, 2H), 7.36 (m, 3H), 7.13 (t, *J* = 7.5 Hz, 1H), 7.08 (d, *J* = 7.5 Hz, 2H), 2.52 (s, 6H). <sup>13</sup>C NMR (75 MHz, CDCl<sub>3</sub>) δ 140.40, 131.53, 128.50, 128.23, 128.20, 127.91, 126.83, 123.97, 123.10, 97.97, 87.26, 21.28. IR (solid, ATR) 3061, 2916, 1596, 1570, 1489, 1466, 1441, 1376, 1300, 1164, 1085, 1068, 1026, 911, 768, 753, 731, 688 cm<sup>-1</sup>. HRMS (EI, *m/z*): calcd for [C<sub>16</sub>H<sub>14</sub>+H]<sup>+</sup> 207.11792, found 207.11644.

**Scheme A3.11.** Synthesis of **10**.



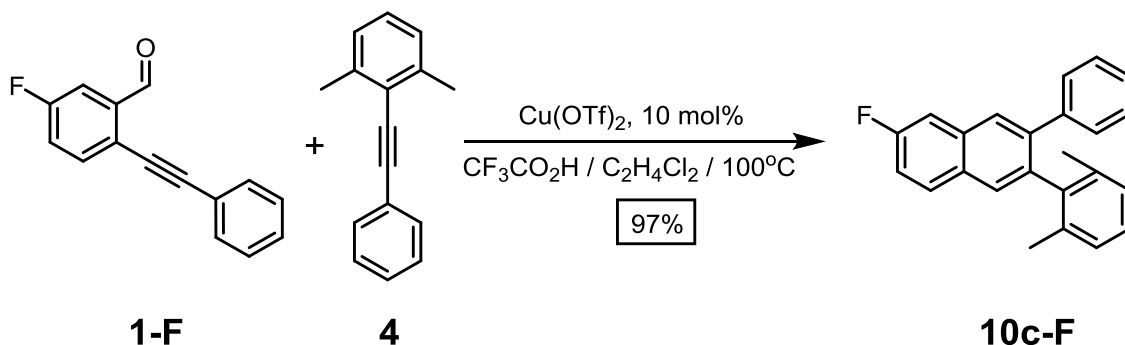
**Synthesis of 10:** **10** was synthesized using a similar procedure to that used to prepare **8**. Alkyne **4** (18 mg, 0.087 mmol), benzaldehyde **1** (30 mg, 0.145 mmol), 1,2-dichloroethane (1.5 mL), Cu(OTf)<sub>2</sub> (5 mg, 0.015 mmol) and CF<sub>3</sub>CO<sub>2</sub>H (12 μL, 0.160 mmol) were used. Chromatography (SiO<sub>2</sub>, 1:9 v/v CHCl<sub>3</sub>:hexanes) gave **10** (28 mg, >99% yield) as a colourless goo. **10**: <sup>1</sup>H NMR (500 MHz, CDCl<sub>3</sub>) δ 7.99 (s, 1H), 7.98 – 7.93 (m, 1H), 7.91 – 7.85 (m, 1H), 7.70 (s, 1H), 7.59 – 7.51 (m, 2H), 7.22 (s, 5H), 7.13 (t, *J* = 8.1, 1H), 7.03 (d, *J* = 8.1 Hz, 2H), 2.00 (s, 6H). <sup>13</sup>C NMR (126 MHz, CDCl<sub>3</sub>) δ 141.22, 140.77, 139.73, 137.72, 136.43, 132.99, 132.83, 129.22, 129.18, 127.98, 127.78, 127.76, 127.68, 127.29, 127.19, 126.83, 126.21, 126.20, 21.11. IR (solid, ATR) 3053, 2919, 1599, 1488, 1462, 1442, 1376, 1327, 1264, 1164, 1131, 1099, 1075, 1022, 958, 915, 890, 765, 746, 717, 697, 668 cm<sup>-1</sup>. HRMS (EI, *m/z*): calcd for [C<sub>24</sub>H<sub>20</sub>]<sup>+</sup> 308.15595, found 308.15514.

**Scheme A3.12.** Synthesis of **10a-<sup>13</sup>C**.



**Synthesis of 10a-<sup>13</sup>C:** **10a-<sup>13</sup>C** was synthesized using a similar procedure to that used to prepare **8**. Alkyne **4** (21 mg, 0.102 mmol), benzaldehyde **1-<sup>13</sup>C<sub>2</sub>** (30 mg, 0.145 mmol), 1,2-dichloroethane (1.5 mL), Cu(OTf)<sub>2</sub> (5 mg, 0.015 mmol) and CF<sub>3</sub>CO<sub>2</sub>H (12 μL, 0.160 mmol) were used. Chromatography (SiO<sub>2</sub>, 1:9 v/v CHCl<sub>3</sub>:hexanes) gave **10a-<sup>13</sup>C** (35 mg, >99% yield) as a colourless goo. **10a-<sup>13</sup>C**: <sup>1</sup>H NMR (400 MHz, CDCl<sub>3</sub>) δ 7.99 (s, 1H), 7.98 – 7.93 (m, 1H), 7.91 – 7.85 (m, 1H), 7.70 (d, *J*<sub>CH</sub> = 158.0 Hz, 1H), 7.59 – 7.51 (m, 2H), 7.22 (s, 5H), 7.13 (t, *J* = 8.1, 1H), 7.03 (d, *J* = 8.1 Hz, 2H), 2.00 (s, 6H). <sup>13</sup>C NMR (126 MHz, CDCl<sub>3</sub>) δ 129.22 (one <sup>13</sup>C-enriched carbon signal). IR (solid, ATR) 3052, 2920, 1580, 1488, 1463, 1441, 1376, 1272, 1191, 1163, 1131, 1075, 1022, 955, 914, 887, 796, 764, 746, 717, 698 cm<sup>-1</sup>. HRMS (EI, *m/z*): calcd for [C<sub>23</sub><sup>13</sup>CH<sub>20</sub>]<sup>+</sup> 309.16040, found 309.15851.

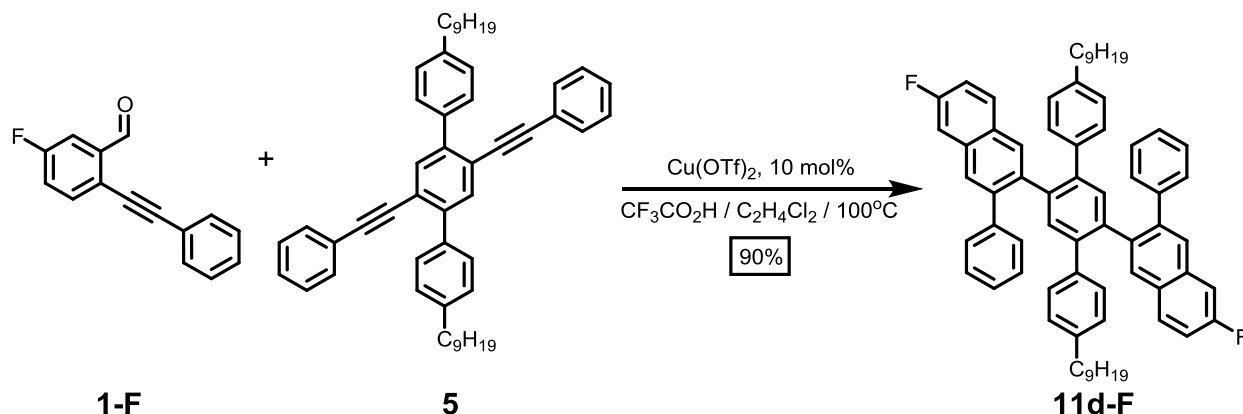
**Scheme A3.13.** Synthesis of **10c-F**.



**Synthesis of 10c-F:** **10c-F** was synthesized using a similar procedure to that used to prepare **8**. Alkyne **4** (21 mg, 0.103 mmol), benzaldehyde **1-F** (29 mg, 0.129 mmol), 1,2-dichloroethane (1.5 mL), Cu(OTf)<sub>2</sub> (5 mg, 0.013 mmol) and CF<sub>3</sub>CO<sub>2</sub>H (11 μL, 0.142 mmol) were used. Chromatography (SiO<sub>2</sub>, 1:9 v/v CHCl<sub>3</sub>:hexanes) gave **10c-F** (33 mg, 97% yield) as a colourless goo. **10c-F**: <sup>1</sup>H NMR (500 MHz, CDCl<sub>3</sub>) δ 7.91 (s, 1H), 7.85 (dd, *J* = 9.0, 5.6 Hz, 1H), 7.68 (s, 1H), 7.55 (dd, *J* = 9.8, 2.6 Hz, 1H), 7.31 (td, *J* = 8.7, 2.6 Hz, 1H), 7.21 (m, 5H), 7.12 (t, *J* = 7.6 Hz, 1H), 7.02 (d, *J* = 7.6 Hz, 2H), 1.98 (s, 6H). <sup>13</sup>C NMR (126 MHz, CDCl<sub>3</sub>) δ 161.95, 160.00, 140.87, 140.79, 140.47, 137.03, 137.01, 136.45, 136.43, 133.69, 133.61, 130.14, 130.06, 129.84, 129.20, 129.13, 128.70, 128.52, 128.48, 128.44, 127.82, 127.34, 127.28, 127.04, 116.73, 116.53, 110.97, 110.81, 21.09. IR (solid, ATR) 3057, 2918, 1636, 1602, 1571, 1489, 1462, 1442, 1377,

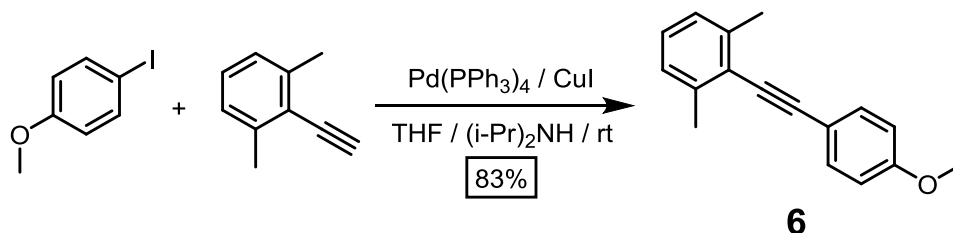
1347, 1265, 1218, 1185, 1144, 1120, 1074, 1020, 972, 945, 896, 849, 806, 763, 748, 740, 713, 697  $\text{cm}^{-1}$ . HRMS (EI,  $m/z$ ): calcd for  $[\text{C}_{24}\text{H}_{19}\text{F}]^+$  326.14653, found 326.14555.

**Scheme A3.14.** Synthesis of **11d-F**.



**Synthesis of 11d-F:** **11d-F** was synthesized using a similar procedure to that used to prepare **8**. Dialkyne **5** (30 mg, 0.045 mmol), benzaldehyde **1-F** (33 mg, 0.147 mmol), 1,2-dichloroethane (1.5 mL),  $\text{Cu(OTf)}_2$  (4 mg, 0.011 mmol) and  $\text{CF}_3\text{CO}_2\text{H}$  (9  $\mu\text{L}$ , 0.123 mmol) were used. Chromatography ( $\text{SiO}_2$ , 2%  $v/v$  EtOAc:hexanes) gave **11d-F** (37 mg, 90% yield) as a colourless goo. **11d-F**:  $^1\text{H}$  NMR (500 MHz,  $\text{CDCl}_3$ )  $\delta$  8.01 (s, 2H), 7.82 (dd,  $J = 9.0, 5.6$  Hz, 2H), 7.57 (s, 2H), 7.47 – 7.41 (m, 4H), 7.30 – 7.23 (m, 2H), 7.19 (t,  $J = 7.3$  Hz, 2H), 7.12 (t,  $J = 7.6$  Hz, 4H), 6.76 (d,  $J = 7.8$  Hz, 4H), 6.72 (d,  $J = 7.3$  Hz, 4H), 6.51 (d,  $J = 7.8$  Hz, 4H), 2.50 (td,  $J = 7.3, 2.5$  Hz, 4H), 1.66 – 1.50 (m, 4H), 1.43 – 1.17 (m, 24H), 0.90 (t,  $J = 6.7$  Hz, 6H).  $^{13}\text{C}$  NMR (126 MHz,  $\text{CDCl}_3$ )  $\delta$  161.96, 160.00, 141.02, 140.69, 140.61, 140.05, 138.96, 138.29, 138.27, 137.60, 133.82, 133.74, 133.67, 130.51, 130.17, 130.10, 129.88, 129.32, 128.95, 128.23, 128.19, 127.90, 127.61, 127.52, 126.39, 116.70, 116.50, 110.95, 110.79, 35.65, 32.07, 31.82, 29.86, 29.81, 29.72, 29.53, 29.45, 22.86, 14.30. IR (solid, ATR) 2924, 2853, 1635, 1602, 1491, 1464, 1443, 1417, 1349, 1262, 1215, 1186, 1144, 1119, 1015, 949, 895, 805, 750, 697, 668  $\text{cm}^{-1}$ . HRMS (EI,  $m/z$ ): calcd for  $[\text{C}_{68}\text{H}_{68}\text{F}_2+\text{H}]^+$  923.53619, found 923.53201.

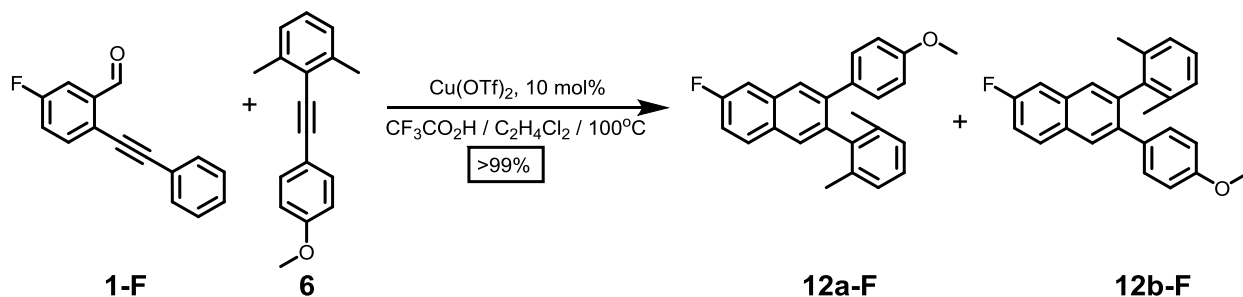
**Scheme A3.15.** Synthesis of **6**.



**Synthesis of 6:** A solution of 2-ethynyl-1,3-dimethylbenzene (50 mg, 0.768 mmol) and 4-iodoanisole (180 mg, 1.536 mmol) in DIPA (2 mL) was bubbled with nitrogen for 20 min. The above solution was cannulated to a flask containing  $\text{Pd(PPh}_3)_4$  (44 mg, 0.038 mmol) and  $\text{CuI}$  (15 mg, 0.077 mmol) suspended in THF (4 mL) under  $\text{N}_2$  atmosphere. The mixture was heated to 50  $^\circ\text{C}$  and stirred for 2 h. It was cooled to rt and added to a separatory funnel containing 50 mL

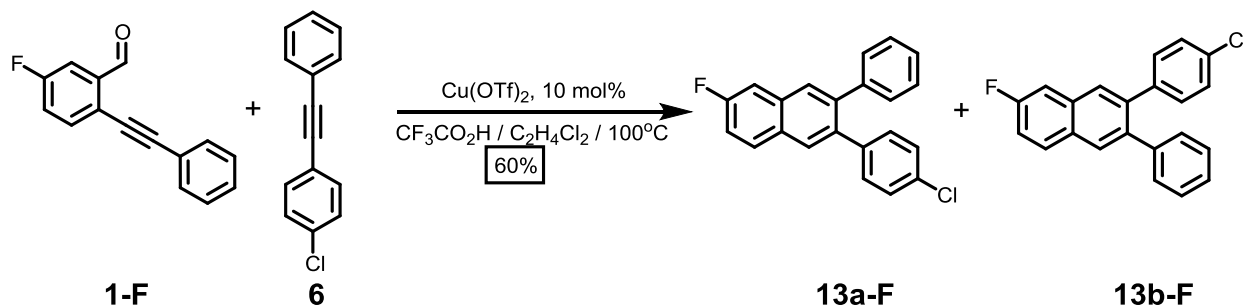
Et<sub>2</sub>O. It was extracted with aqueous 1 M HCl (50 mL), and brine (2 x 50 mL). The organic phase was dried (MgSO<sub>4</sub>), filtered and the solvent was removed. The crude product was purified by flash chromatography (SiO<sub>2</sub>, hexanes) to give **6** (76 mg, 83% yield) as colourless needles. **6**: <sup>1</sup>H NMR (599 MHz, CDCl<sub>3</sub>) δ 7.48 (d, *J* = 8.9 Hz, 2H), 7.11 (dd, *J* = 8.5, 6.3 Hz, 1H), 7.06 (d, *J* = 7.4 Hz, 2H), 6.89 (d, *J* = 8.9 Hz, 2H), 3.84 (s, 3H), 2.50 (s, 6H). <sup>13</sup>C NMR (126 MHz, CDCl<sub>3</sub>) δ 159.66, 140.16, 132.95, 127.56, 126.78, 123.42, 116.15, 114.15, 97.96, 85.94, 55.48, 21.29. IR (solid, ATR) 3068, 3003, 2967, 2914, 2838, 2733, 2533, 2208, 2035, 1930, 1891, 1602, 1568, 1508, 1465, 1441, 1377, 1301, 1285, 1244, 1181, 1172, 1142, 1105, 1087, 1025, 988, 918, 832, 808, 790, 768, 731, 713 cm<sup>-1</sup>. HRMS (EI, *m/z*): calcd for [C<sub>17</sub>H<sub>16</sub>O+H]<sup>+</sup> 237.12739, found 237.12670.

**Scheme A3.16. Synthesis of 12a-F and 12b-F.**



**Synthesis of 12a-F and 12b-F:** **12a-F** and **12b-F** were synthesized using a similar procedure to that used to prepare **8**. Alkyne **6** (24 mg, 0.100 mmol), benzaldehyde **1-F** (30 mg, 0.134 mmol), 1,2-dichloroethane (1.5 mL), Cu(OTf)<sub>2</sub> (5 mg, 0.013 mmol) and CF<sub>3</sub>CO<sub>2</sub>H (11 μL, 0.147 mmol) were used. Chromatography (SiO<sub>2</sub>, 4% v/v EtOAc/hexanes) gave **12a-F** and **12b-F** (39 mg, >99% yield) as a colorless goo, which was an inseparable mixture. **12a-F** and **12b-F**: <sup>1</sup>H NMR (599 MHz, CDCl<sub>3</sub>) **12b-F**: δ 7.93 – 7.88 (m, 1H), 7.91 (s, 1H), 7.59 (s, 1H), 7.45 (dd, *J* = 9.8, 2.6 Hz, 1H), 7.33 – 7.27 (m, 1H), 7.16 – 7.07 (m, 3H), 7.02 (d, *J* = 7.6 Hz, 2H), 6.74 (d, *J* = 8.5 Hz, 2H) 3.76 (s, 3H), 1.97 (s, 6H). **12a-F**: 7.86 (s, 1H) 7.82 (dd, *J* = 8.9, 5.6 Hz, 1H), 7.64 (s, 1H), 7.52 (dd, *J* = 9.9, 2.5 Hz, 1H), 7.33 – 7.27 (m, 1H), 7.16 – 7.07 (m, 3H), 7.02 (d, *J* = 7.6 Hz, 2H), 6.74 (d, *J* = 8.5 Hz, 2H) 3.76 (s, 3H), 1.97 (s, 6H). <sup>13</sup>C NMR (151 MHz, CDCl<sub>3</sub>) δ 161.78, 161.70, 160.16, 160.07, 158.73, 158.62, 140.67, 140.63, 140.39, 138.98, 138.68, 138.66, 137.10, 137.09, 136.43, 136.29, 133.76, 133.70, 133.38, 133.31, 133.26, 130.31, 130.25, 130.23, 130.20, 130.10, 130.03, 129.90, 129.66, 129.18, 128.78, 128.69, 128.55, 128.51, 128.15, 128.11, 127.39, 127.27, 127.23, 116.65, 116.49, 116.31, 113.33, 113.32, 110.84, 110.70, 110.69, 110.55, 55.24, 21.06, 21.03, 0.15. IR (solid, ATR) 2919, 2835, 1635, 1608, 1515, 1494, 1462, 1441, 1377, 1343, 1283, 1246, 1215, 1177, 1143, 1119, 1041, 1026, 972, 946, 898, 833, 807, 771, 736, 710, 668 cm<sup>-1</sup>. HRMS (EI, *m/z*): calcd for [C<sub>25</sub>H<sub>21</sub>FO]<sup>+</sup> 356.15595, found 356.15631.

**Scheme A3.17. Synthesis of 13a-F and 13b-F.**



**Synthesis of 13a-F and 13b-F:** **13a-F** and **13b-F** were synthesized using a similar procedure to that used to prepare **8**. 1-Chloro-4-(phenylethynyl)benzene (19 mg, 0.089 mmol), benzaldehyde **1-F** (25 mg, 0.111 mmol), 1,2-dichloroethane (1.5 mL), Cu(OTf)<sub>2</sub> (4 mg, 0.011 mmol) and CF<sub>3</sub>CO<sub>2</sub>H (9 μL, 0.123 mmol) were used. Chromatography (SiO<sub>2</sub>, hexanes) gave **13a-F** and **13b-F** (18 mg, 60% yield) as a colorless goo, which was an inseparable mixture. 37% of 1-Chloro-4-(phenylethynyl)benzene was recovered unreacted. **13a-F** and **13b-F**: <sup>1</sup>H NMR (599 MHz, CDCl<sub>3</sub>) **13a-F**: δ 7.88 – 7.84 (m, 1H), 7.84 (s, 1H), 7.81 (s, 1H), 7.48 (dd, *J* = 9.8, 2.5 Hz, 1H), 7.32 – 7.23 (m, 4H), 7.23 – 7.16 (m, 4H), 7.15 – 7.10 (m, 2H). **13b-F**: δ 7.88 – 7.84 (m, 1H), 7.87 (s, 1H), 7.78 (s, 1H), 7.48 (dd, *J* = 9.8, 2.5 Hz, 1H), 7.32 – 7.23 (m, 4H), 7.23 – 7.16 (m, 4H), 7.15 – 7.10 (m, 2H). <sup>13</sup>C NMR (126 MHz, CDCl<sub>3</sub>) δ 162.18, 162.13, 160.22, 160.17, 140.96, 140.90, 140.11, 139.76, 139.70, 139.03, 138.41, 138.39, 137.33, 137.31, 133.71, 133.64, 133.54, 133.46, 133.05, 132.91, 131.33, 130.38, 130.36, 130.31, 130.29, 130.06, 130.04, 129.97, 129.82, 129.69, 129.47, 129.09, 129.04, 128.85, 128.81, 128.29, 128.28, 128.23, 127.08, 126.95, 117.19, 117.13, 116.99, 116.92, 110.97, 110.94, 110.80, 110.78, 77.41, 77.37, 77.16, 76.90, 29.86. IR (solid, ATR) 3059, 2920, 2849, 1637, 1601, 1491, 1443, 1418, 1396, 1348, 1220, 1190, 1144, 1120, 1093, 1013, 973, 947, 899, 834, 768, 735, 707, 699 cm<sup>-1</sup>. HRMS (EI, *m/z*): calcd for [C<sub>22</sub>H<sub>14</sub>ClF]<sup>+</sup> 332.07626, found 332.07520.

### C. NMR Spectra

Figure A3.1.  $^1\text{H}$  NMR of **1-F** (400 MHz,  $\text{CDCl}_3$ , 298 K).

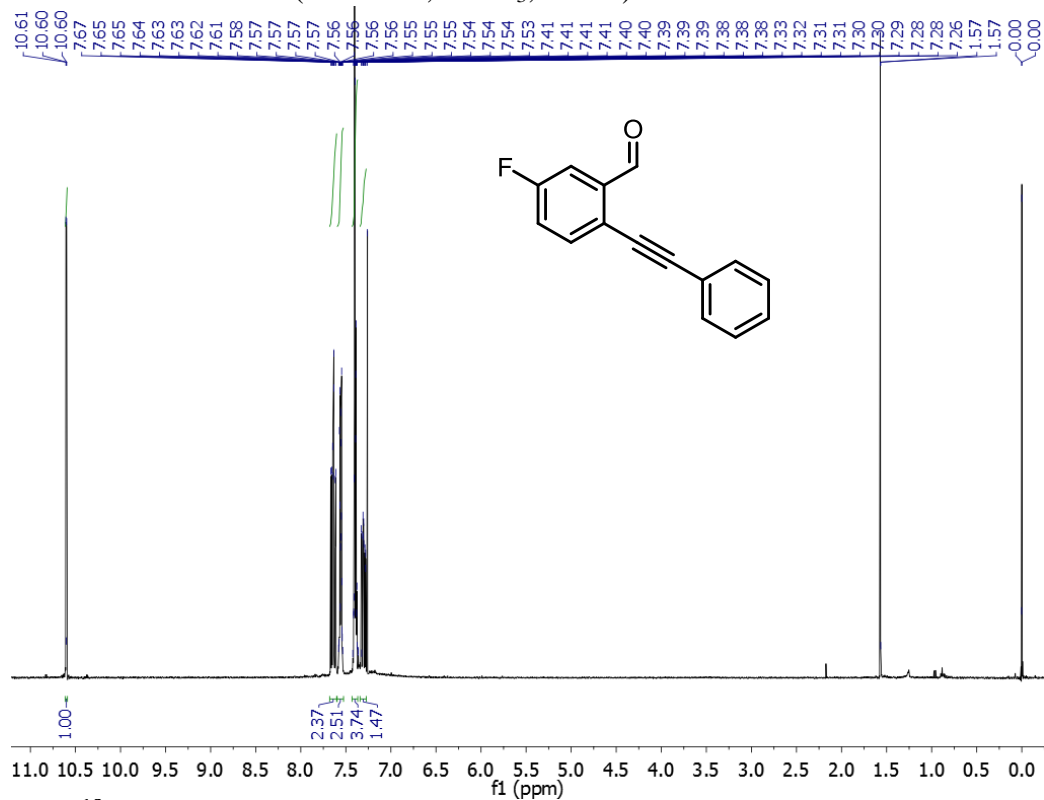


Figure A3.2.  $^{13}\text{C}$  NMR of **1-F** (100 MHz,  $\text{CDCl}_3$ , 298 K).

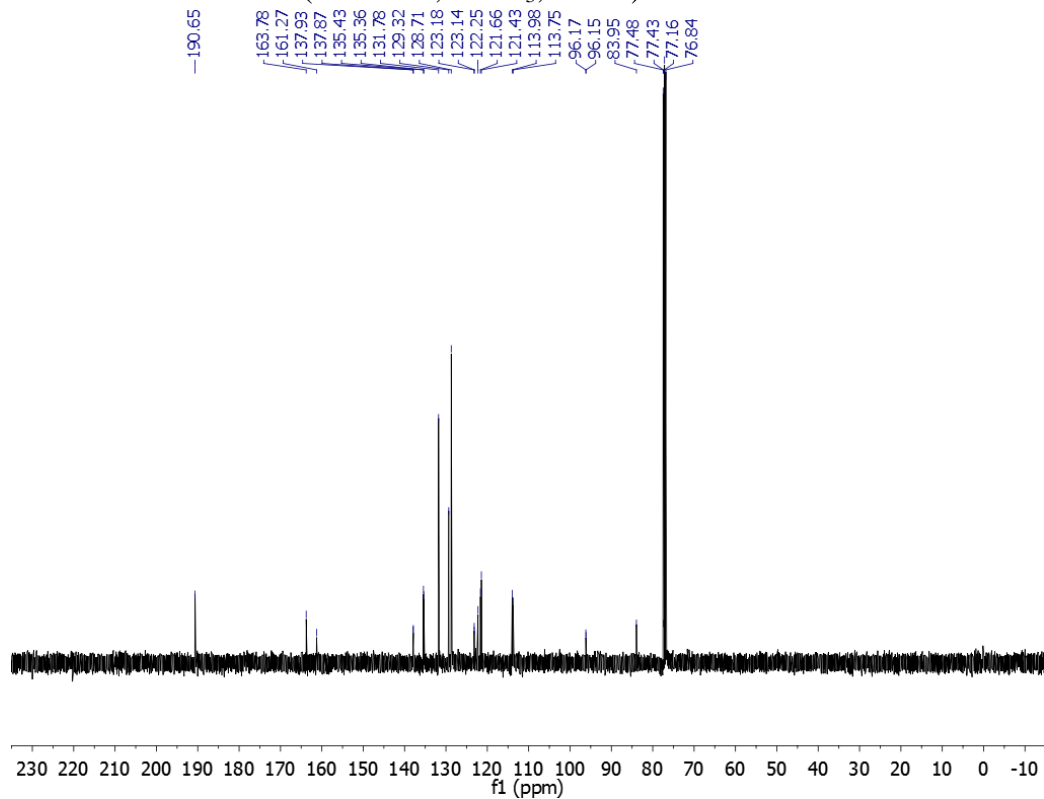


Figure A3.3.  $^1\text{H}$  NMR of **2** (500 MHz,  $\text{CDCl}_3$ , 298 K).

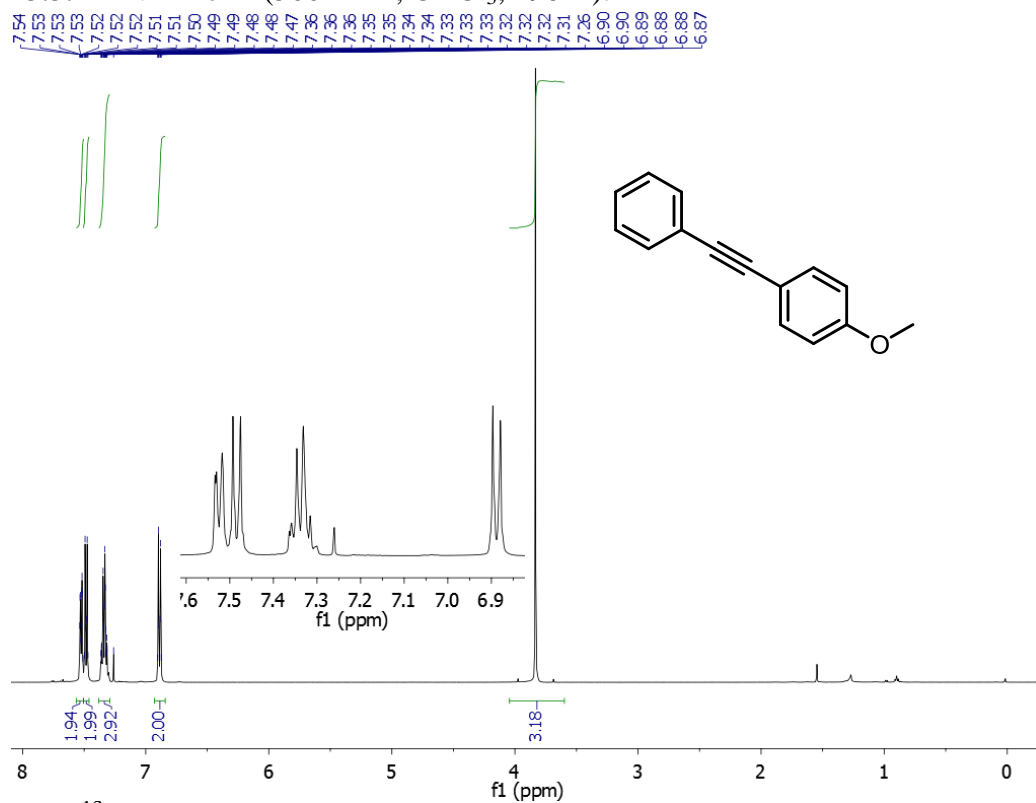


Figure A3.4.  $^{13}\text{C}$  NMR of **2** (125 MHz,  $\text{CDCl}_3$ , 298 K).

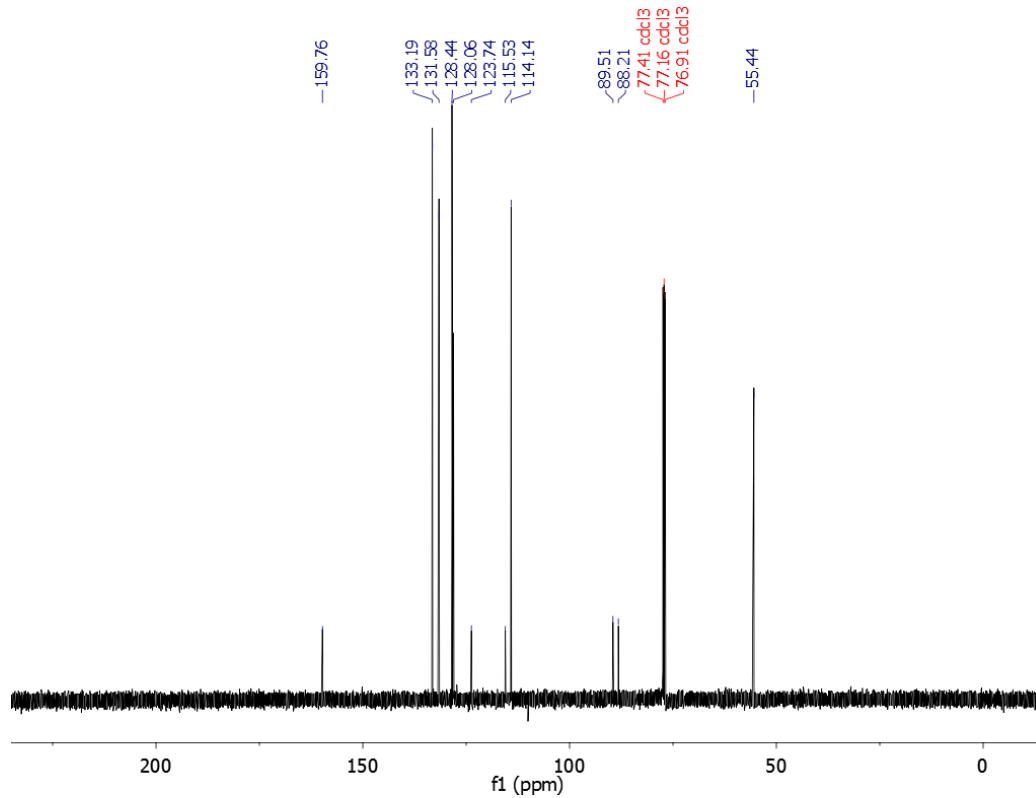


Figure A3.5.  $^1\text{H}$  NMR of **8** (500 MHz,  $\text{CDCl}_3$ , 298 K).

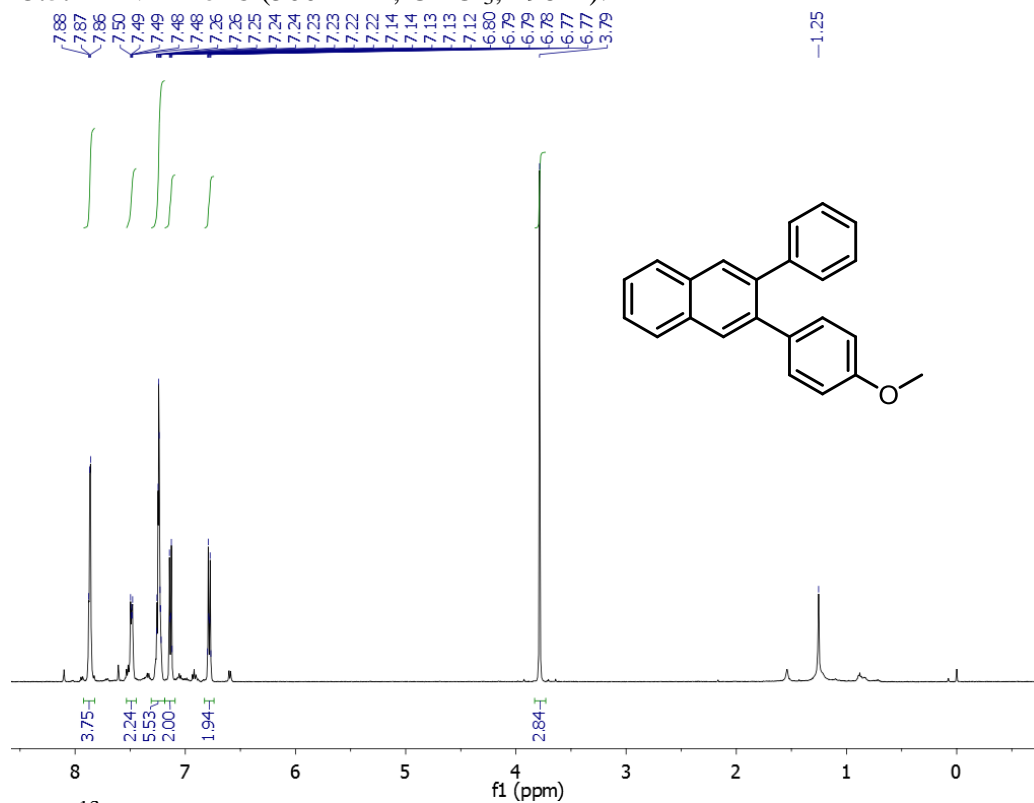


Figure A3.6.  $^{13}\text{C}$  NMR of **8** (125 MHz,  $\text{CDCl}_3$ , 298 K).

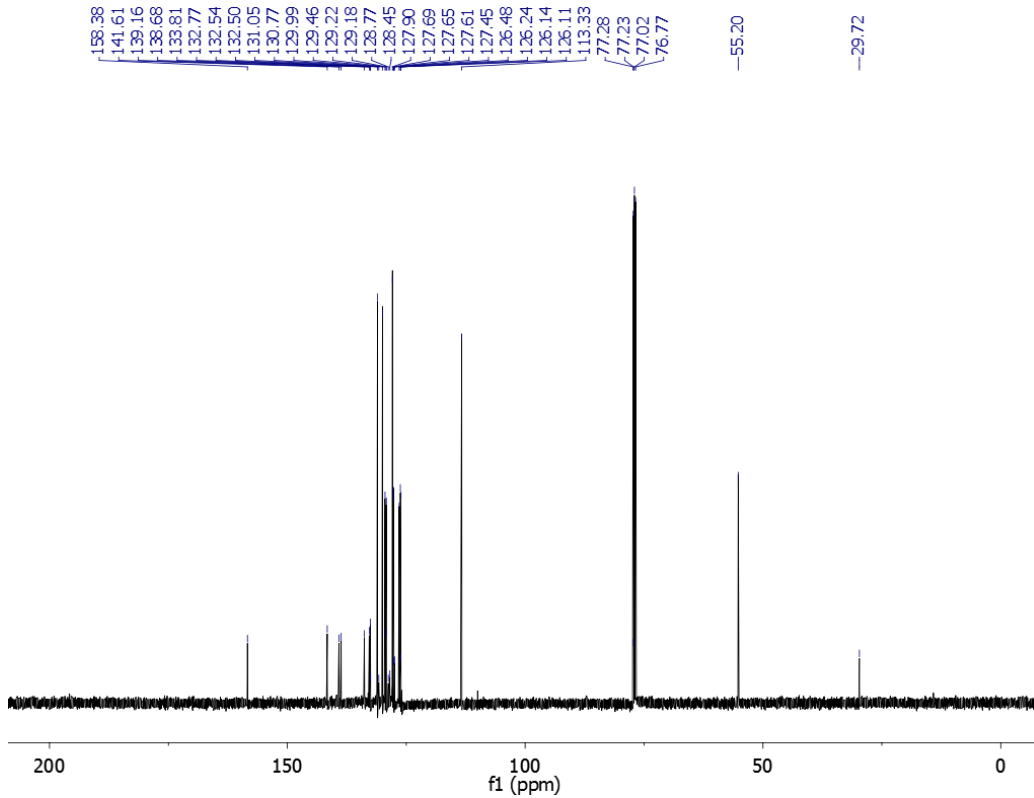




Figure A3.7.  $^1\text{H}$  NMR of **8a**- $^{13}\text{C}$  (400 MHz,  $\text{CDCl}_3$ , 298 K).

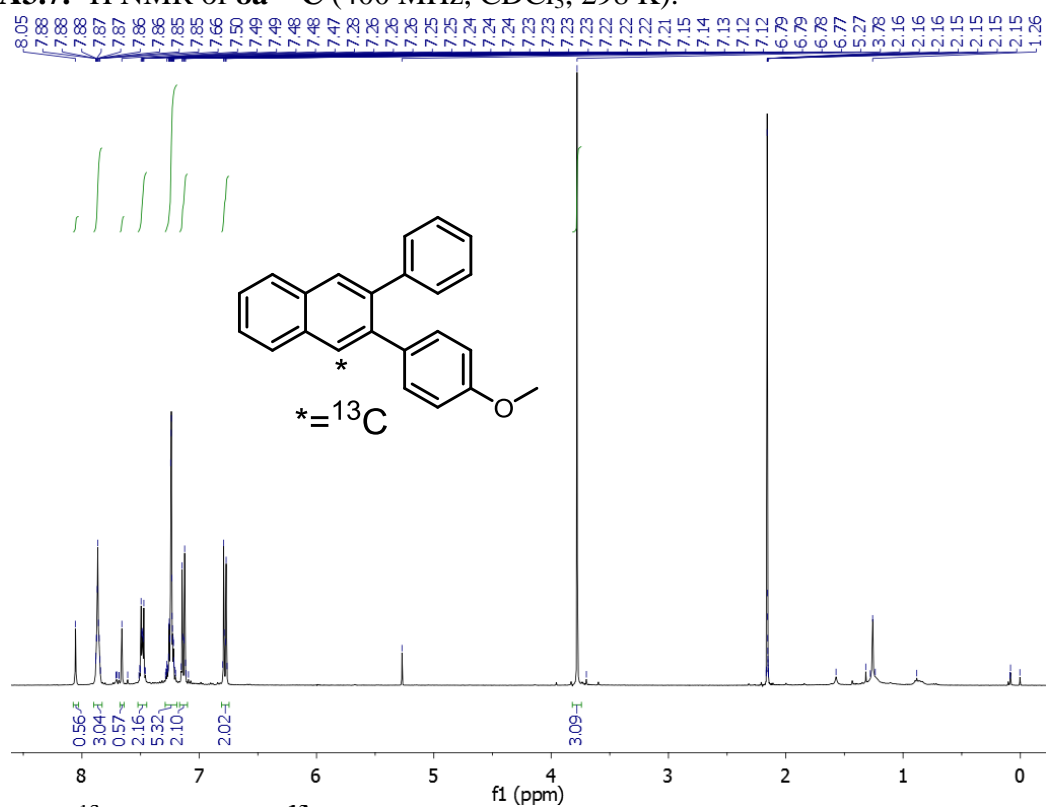
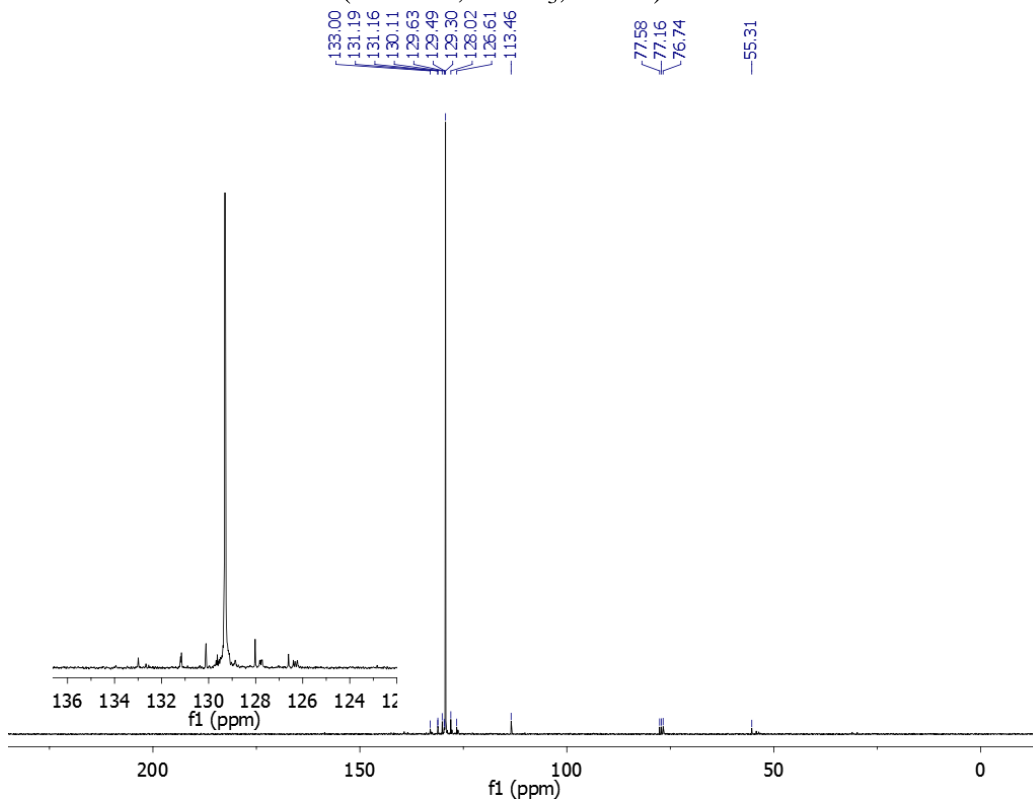
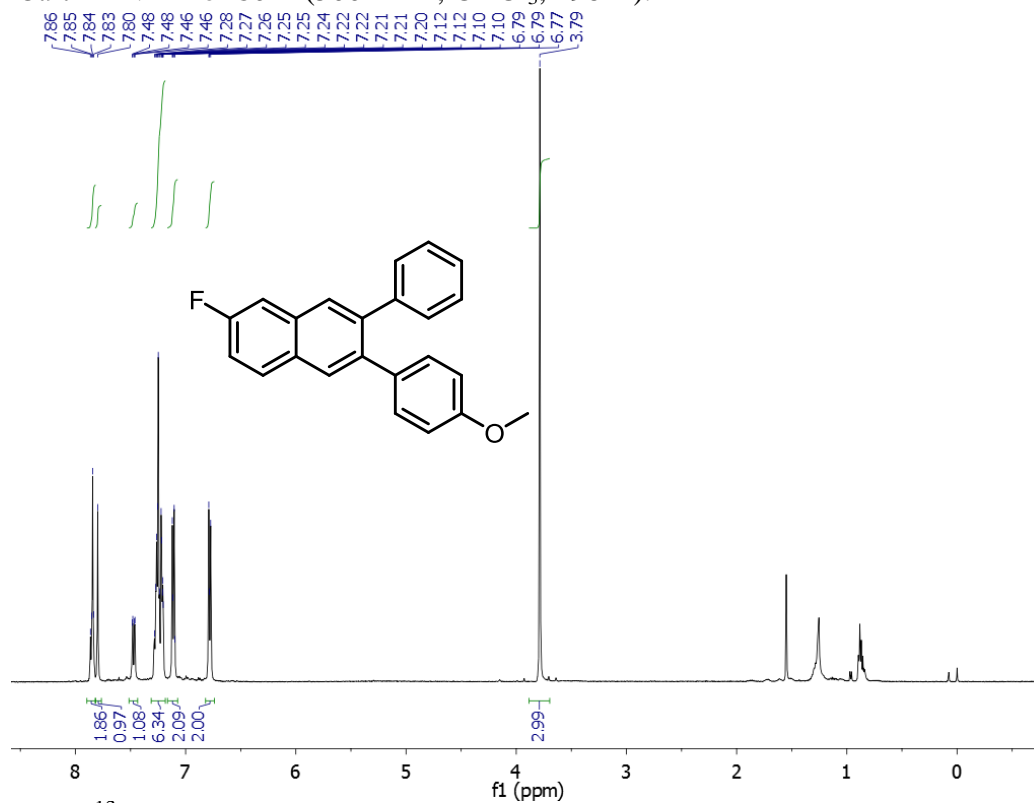


Figure A3.8.  $^{13}\text{C}$  NMR of **8a**- $^{13}\text{C}$  (75 MHz,  $\text{CDCl}_3$ , 298 K).



**Figure A3.9.**  $^1\text{H}$  NMR of **8c-F** (500 MHz,  $\text{CDCl}_3$ , 298 K).



**Figure A3.10.**  $^{13}\text{C}$  NMR of **8c-F** (125 MHz,  $\text{CDCl}_3$ , 298 K).

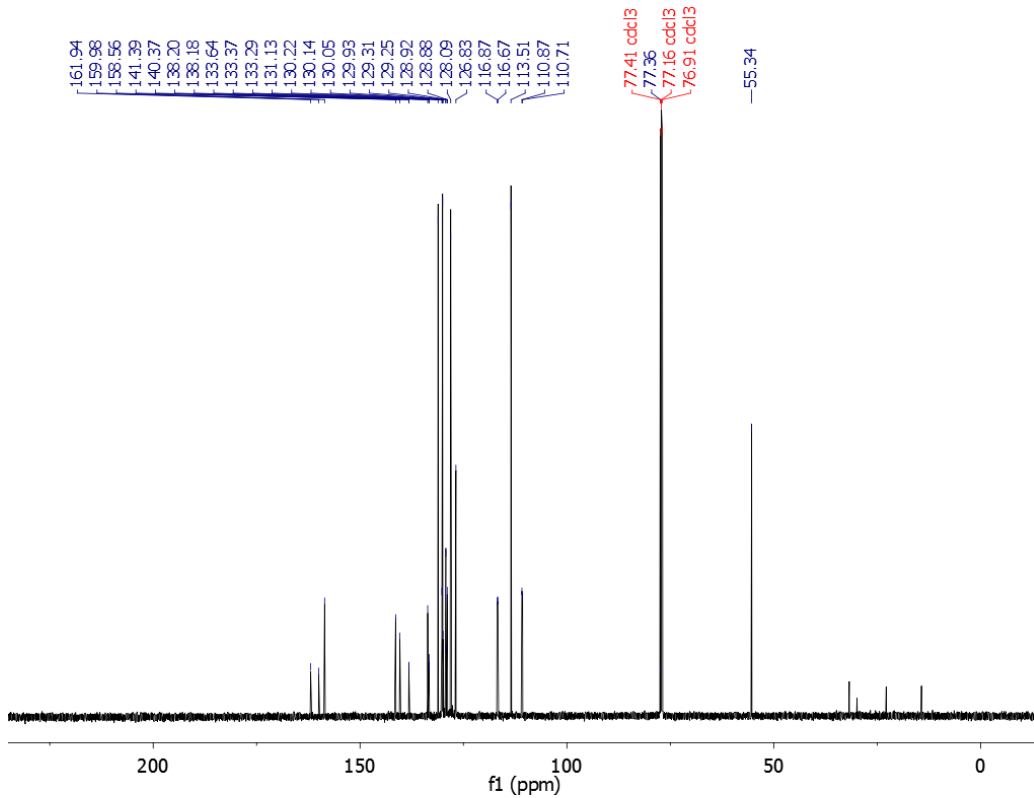


**Figure A3.11.**  $^1\text{H}$  NMR of **3** (400 MHz,  $\text{CDCl}_3$ , 298 K).

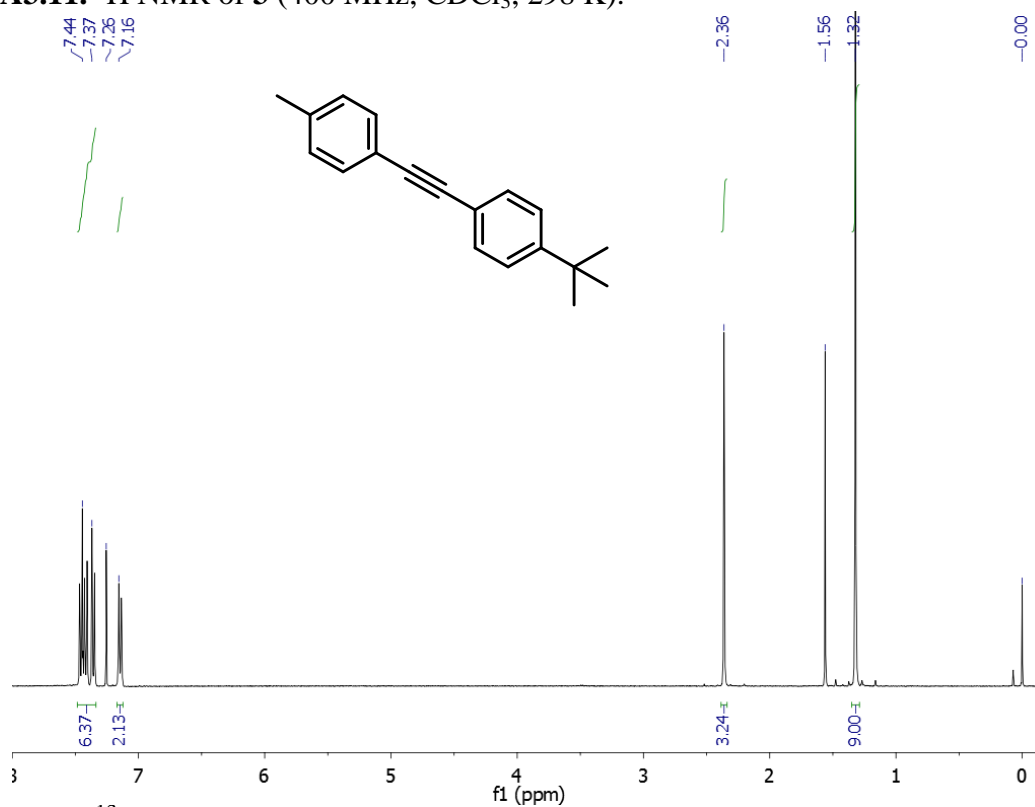


**Figure A3.12.**  $^{13}\text{C}$  NMR of **3** (100 MHz,  $\text{CDCl}_3$ , 298 K).

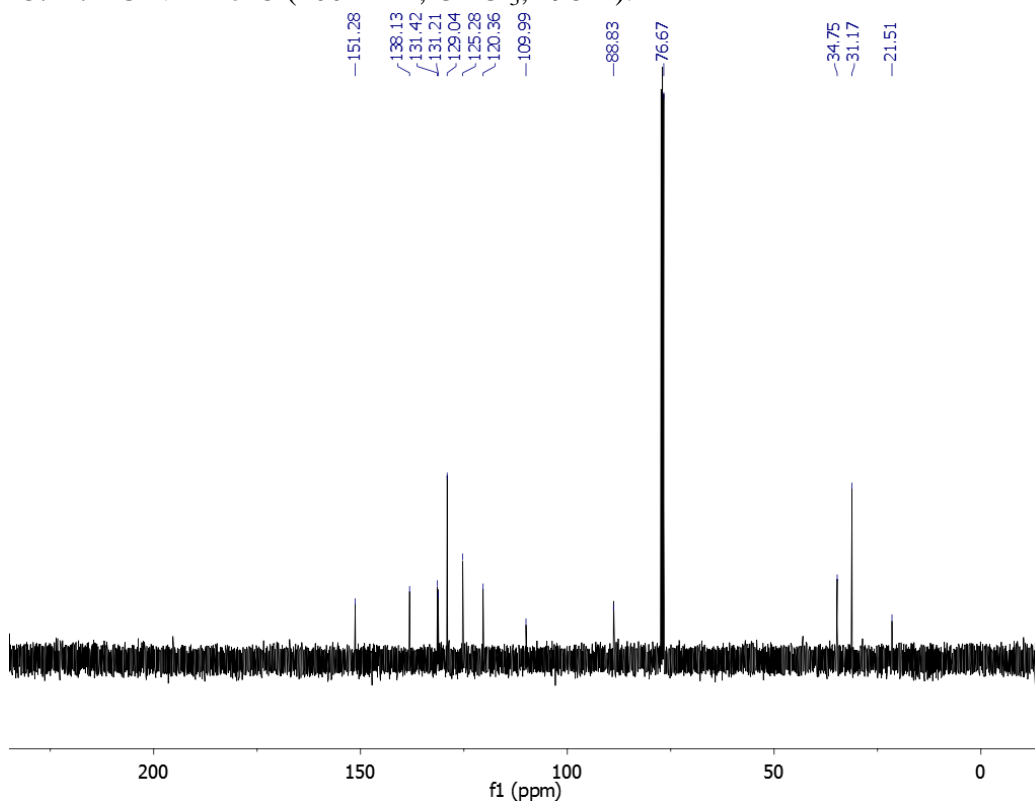


**Figure A3.13.**  $^1\text{H}$  NMR of **9** (500 MHz,  $\text{CDCl}_3$ , 298 K).

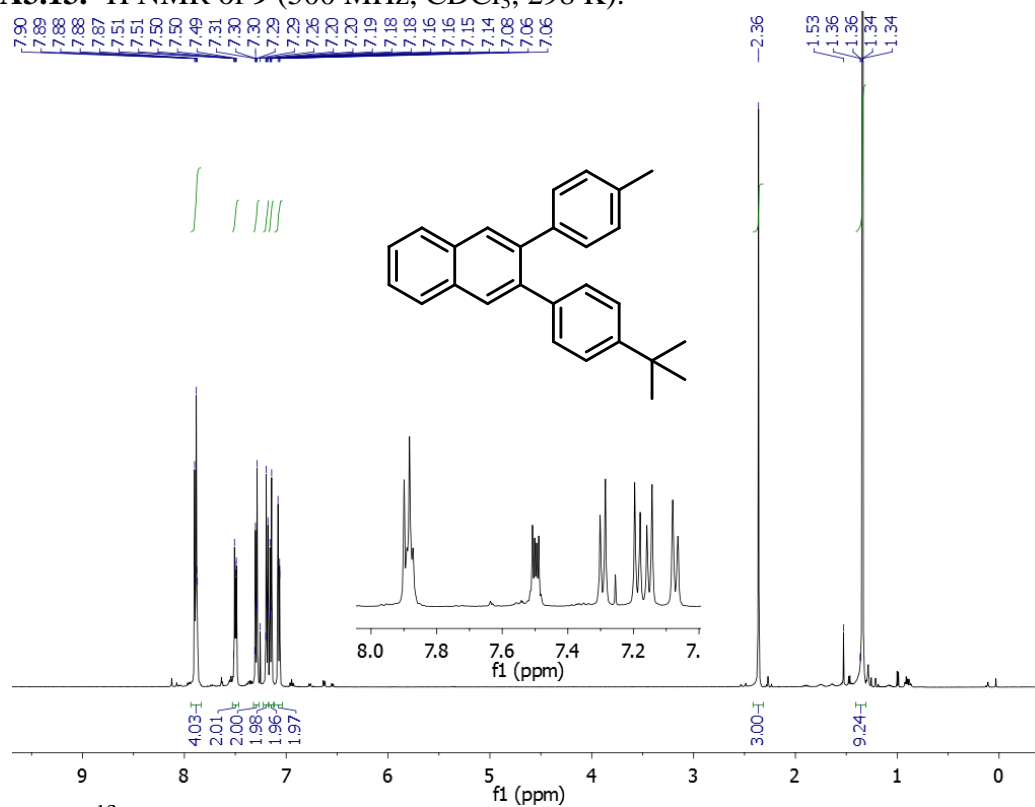


**Figure A3.14.**  $^{13}\text{C}$  NMR of **9** (125 MHz,  $\text{CDCl}_3$ , 298 K).

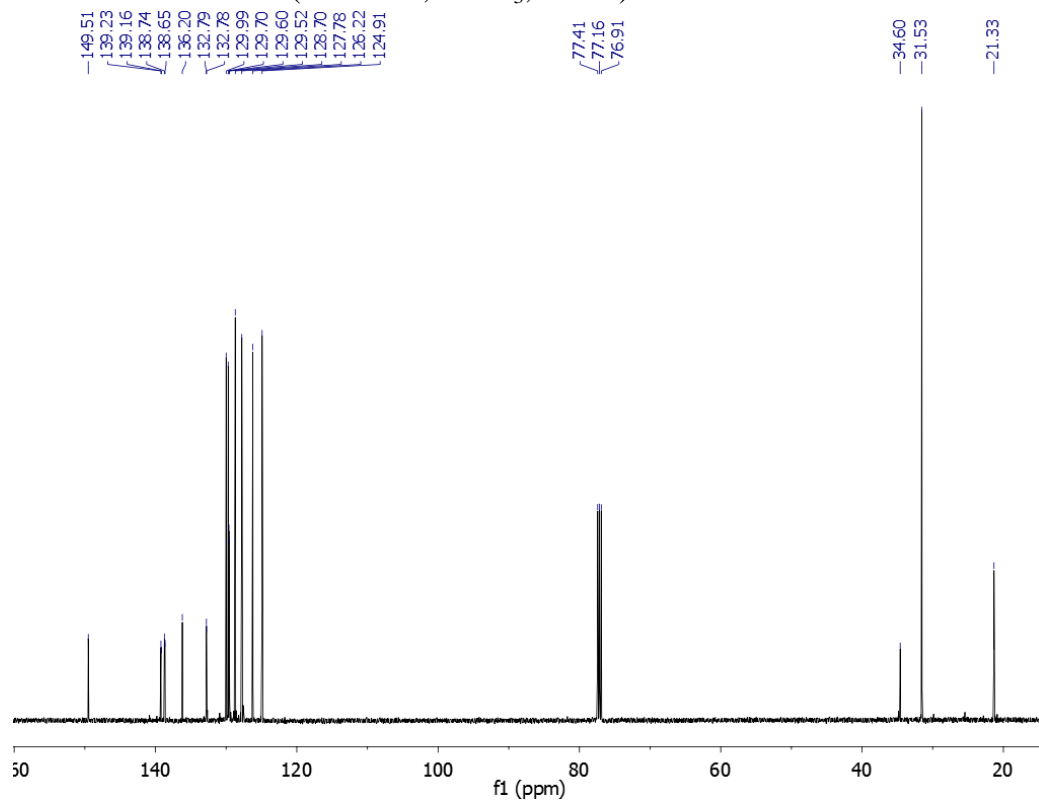
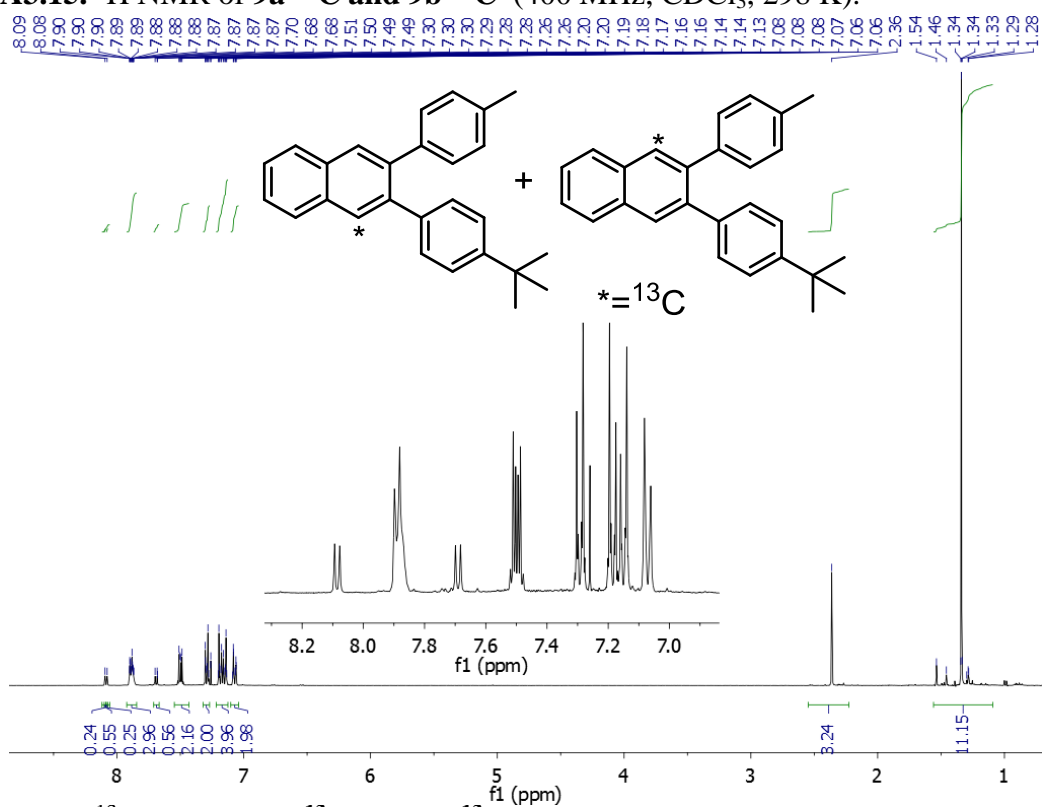
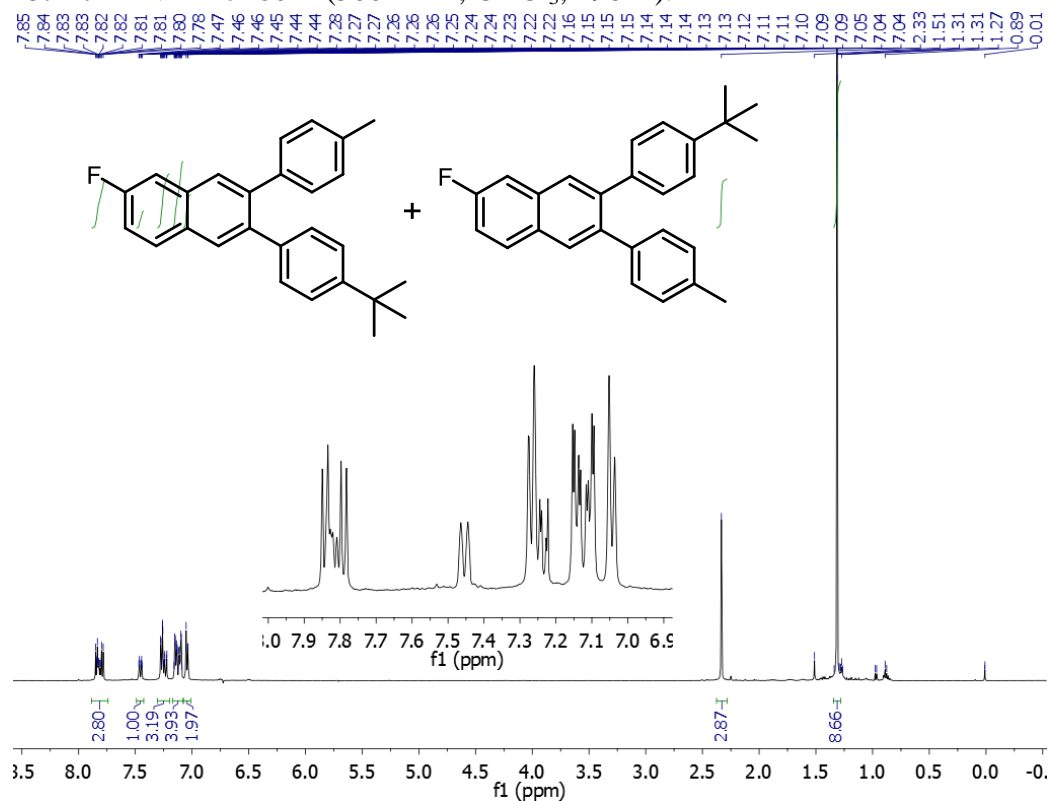


Figure A3.15.  $^1\text{H}$  NMR of **9a**- $^{13}\text{C}$  and **9b**- $^{13}\text{C}$  (400 MHz,  $\text{CDCl}_3$ , 298 K).



**Figure A3.17.**  $^1\text{H}$  NMR of **8c-F** (500 MHz,  $\text{CDCl}_3$ , 298 K).



**Figure A3.18.**  $^{13}\text{C}$  NMR of **8c-F** (125 MHz,  $\text{CDCl}_3$ , 298 K).

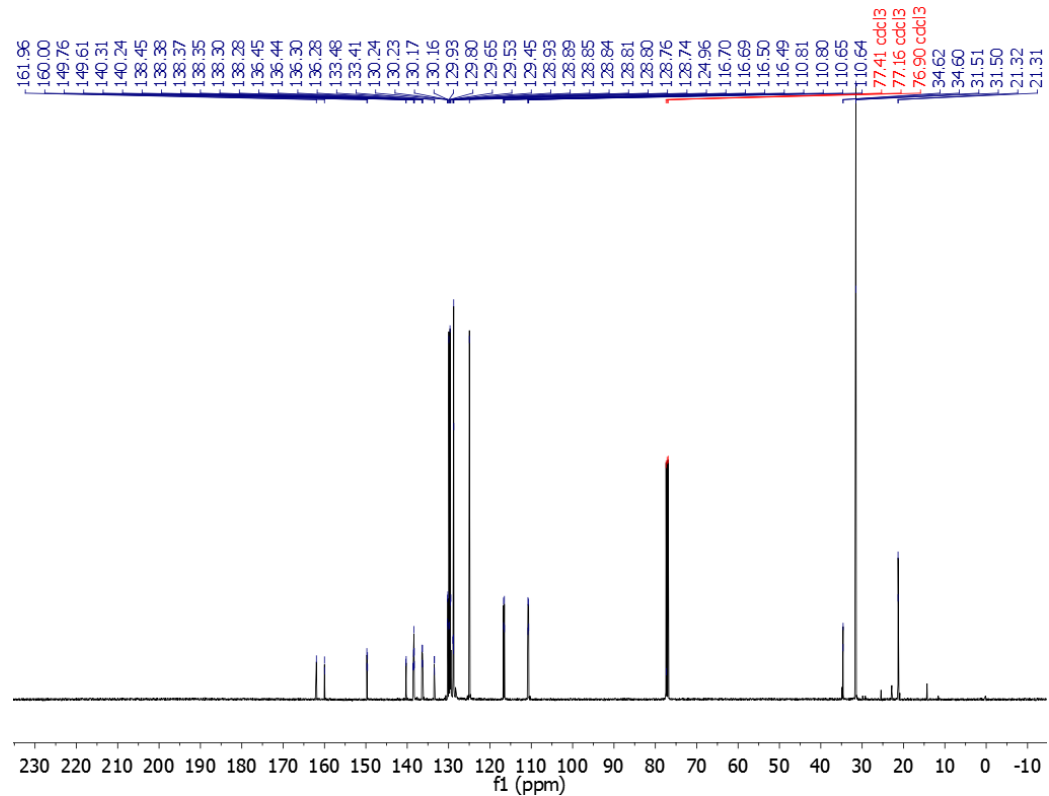


**Figure A3.19.**  $^1\text{H}$  NMR of **4** (500 MHz,  $\text{CDCl}_3$ , 298 K).

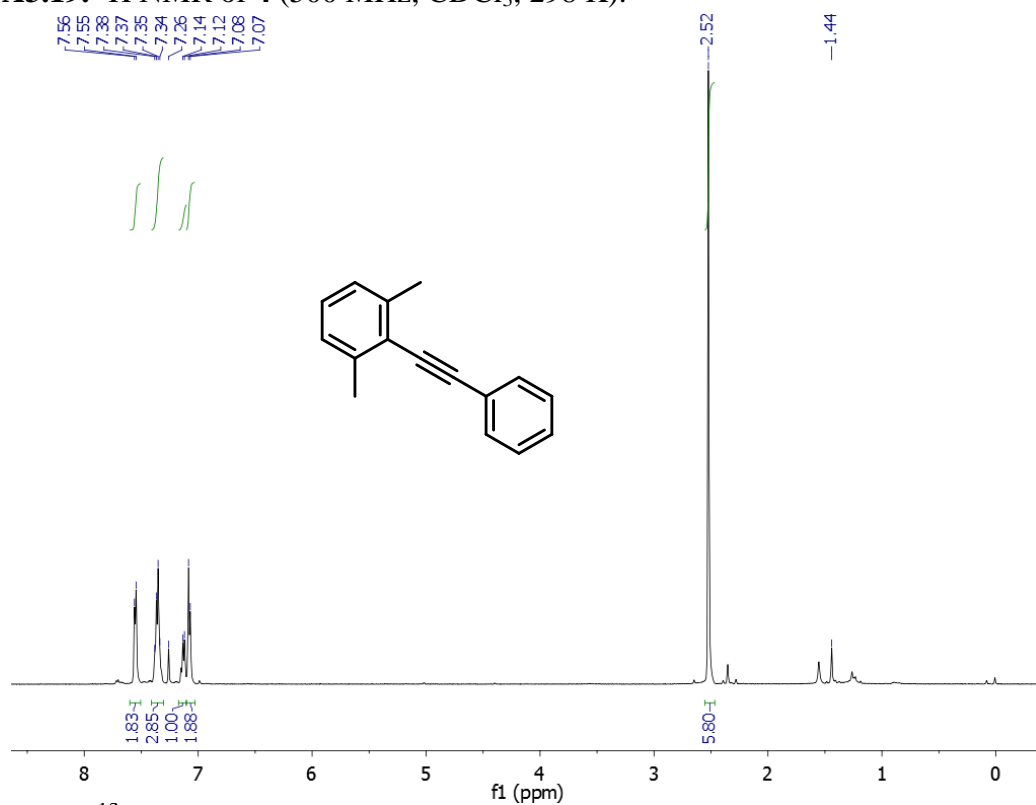


**Figure A3.20.**  $^{13}\text{C}$  NMR of **4** (125 MHz,  $\text{CDCl}_3$ , 298 K).

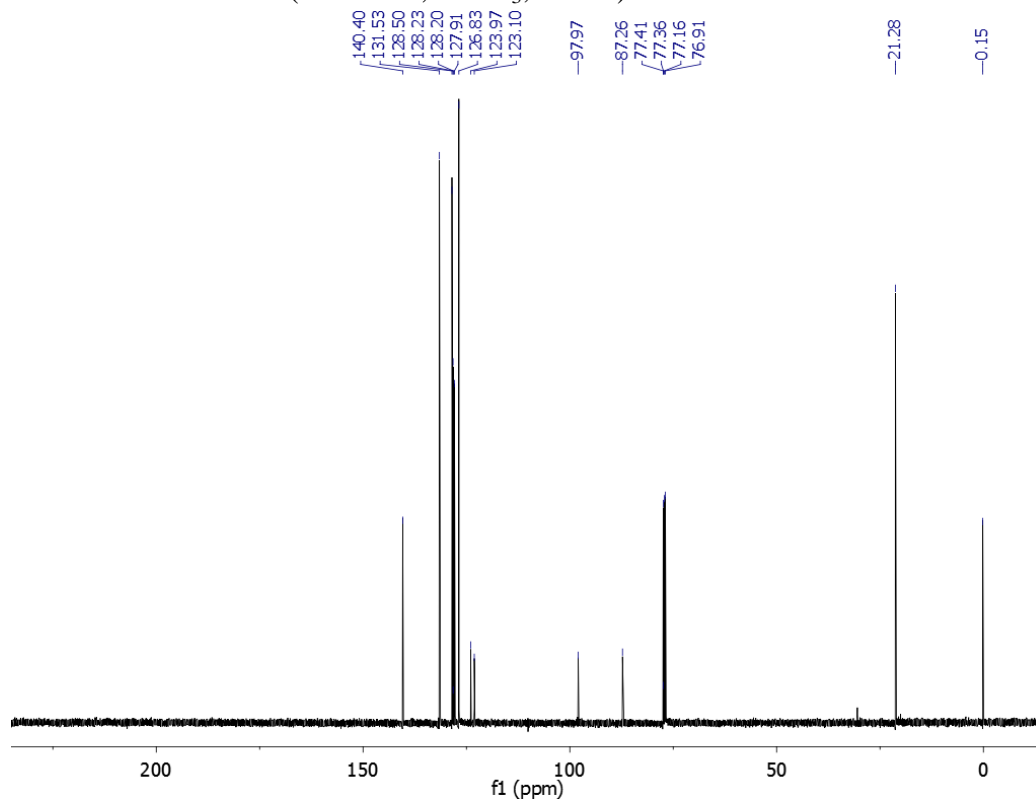


**Figure A3.21.**  $^1\text{H}$  NMR of **10** (500 MHz,  $\text{CDCl}_3$ , 298 K).

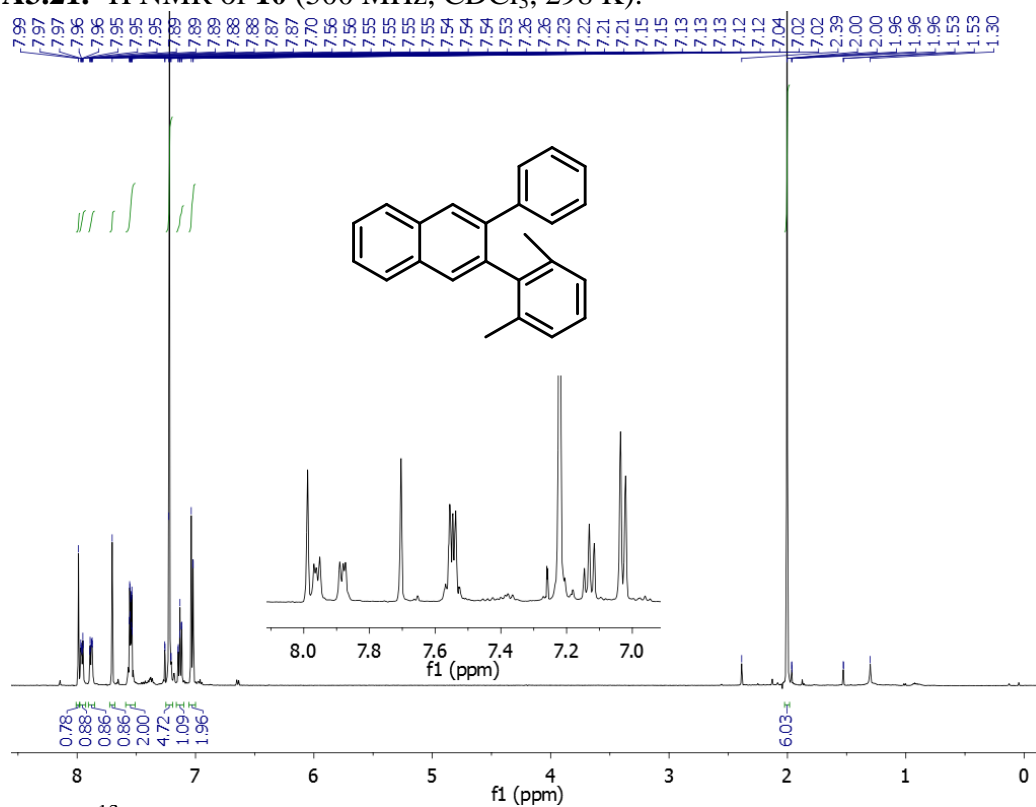


**Figure A3.22.**  $^{13}\text{C}$  NMR of **10** (125 MHz,  $\text{CDCl}_3$ , 298 K).

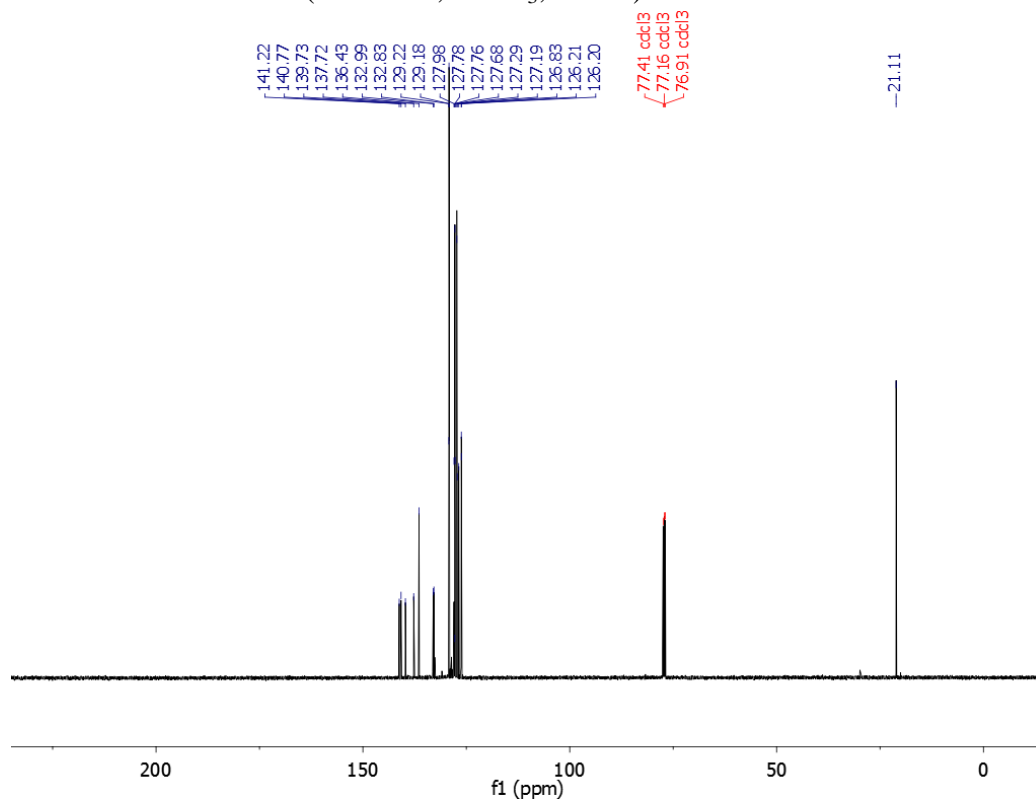




Figure A3.23.  $^1\text{H}$  NMR of **10a**- $^{13}\text{C}$  (400 MHz,  $\text{CDCl}_3$ , 298 K).

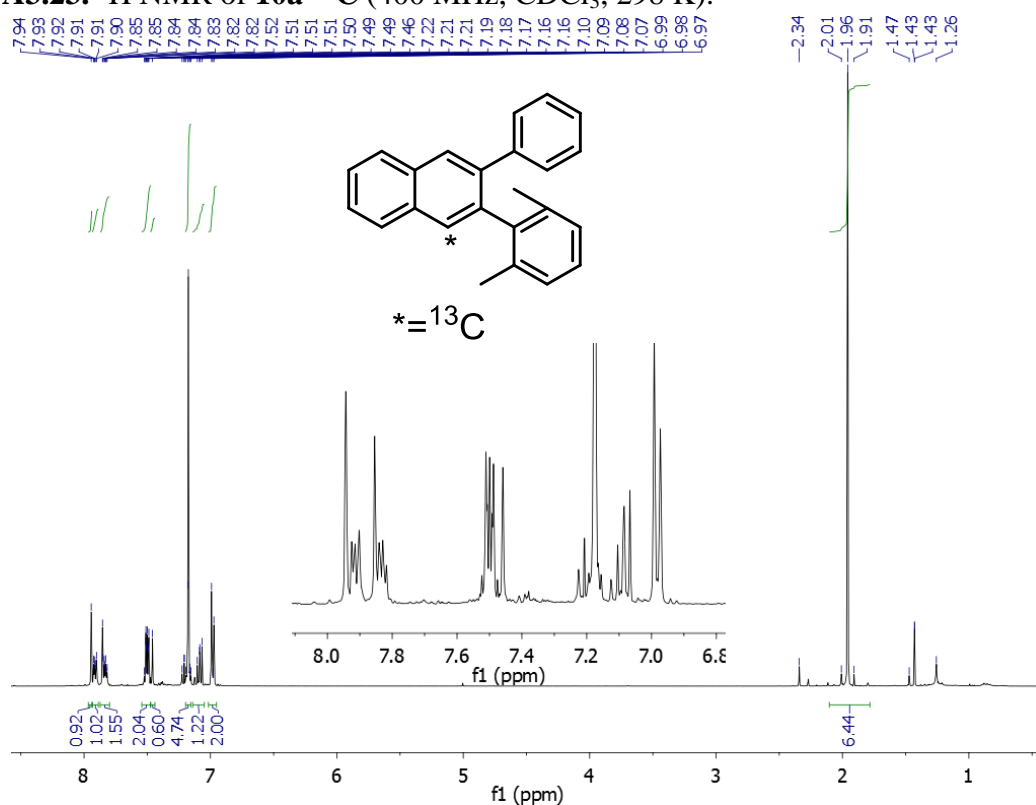
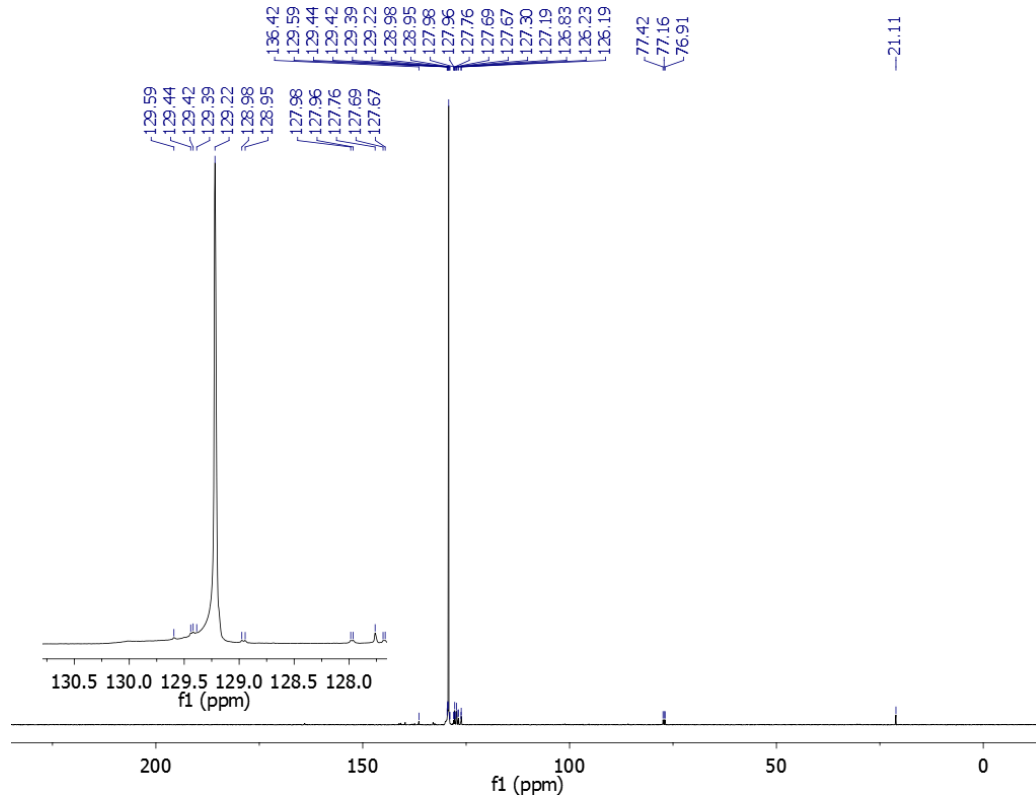
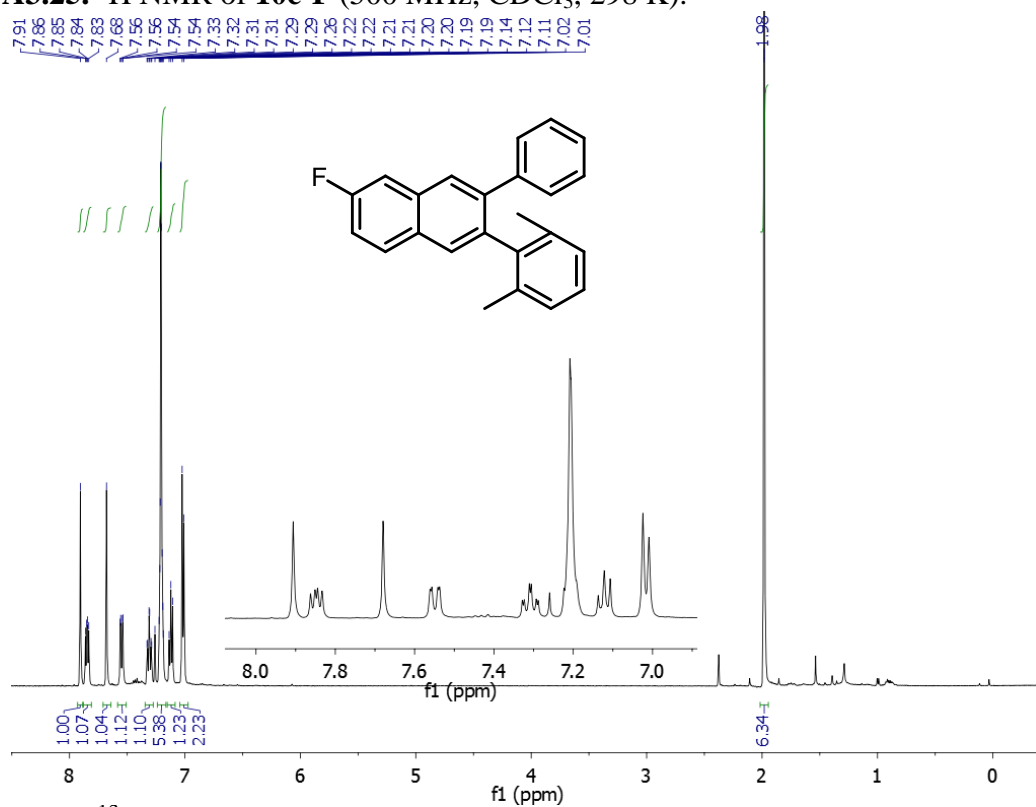


Figure A3.24.  $^{13}\text{C}$  NMR of **10a**- $^{13}\text{C}$  (125 MHz,  $\text{CDCl}_3$ , 298 K).



**Figure A3.25.**  $^1\text{H}$  NMR of **10c-F** (500 MHz,  $\text{CDCl}_3$ , 298 K).



**Figure A3.26.**  $^{13}\text{C}$  NMR of **10c-F** (125 MHz,  $\text{CDCl}_3$ , 298 K).

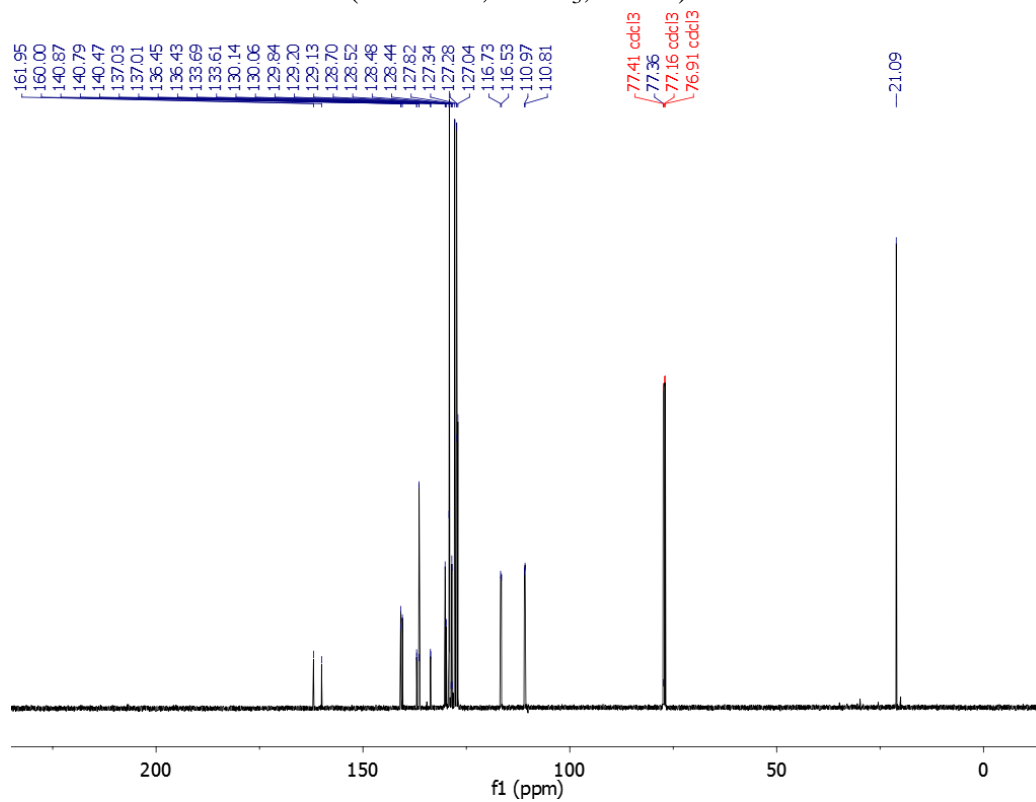


Figure A3.27.  $^1\text{H}$  NMR of **11d-F** (500 MHz,  $\text{CDCl}_3$ , 298 K).

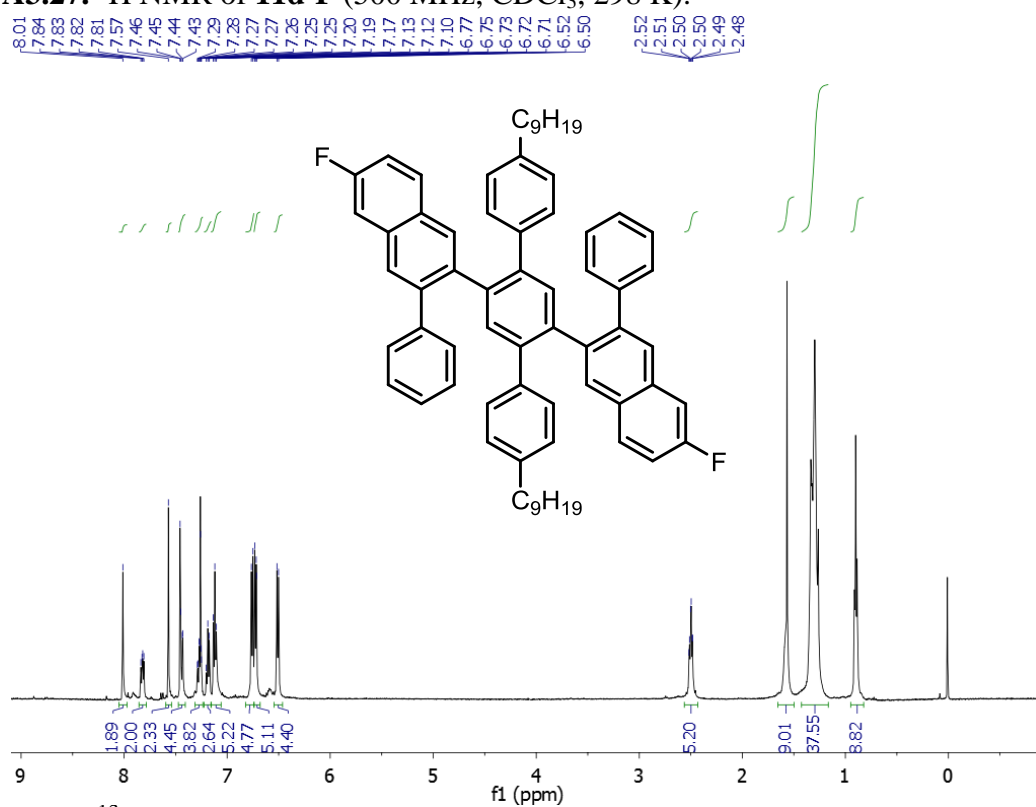
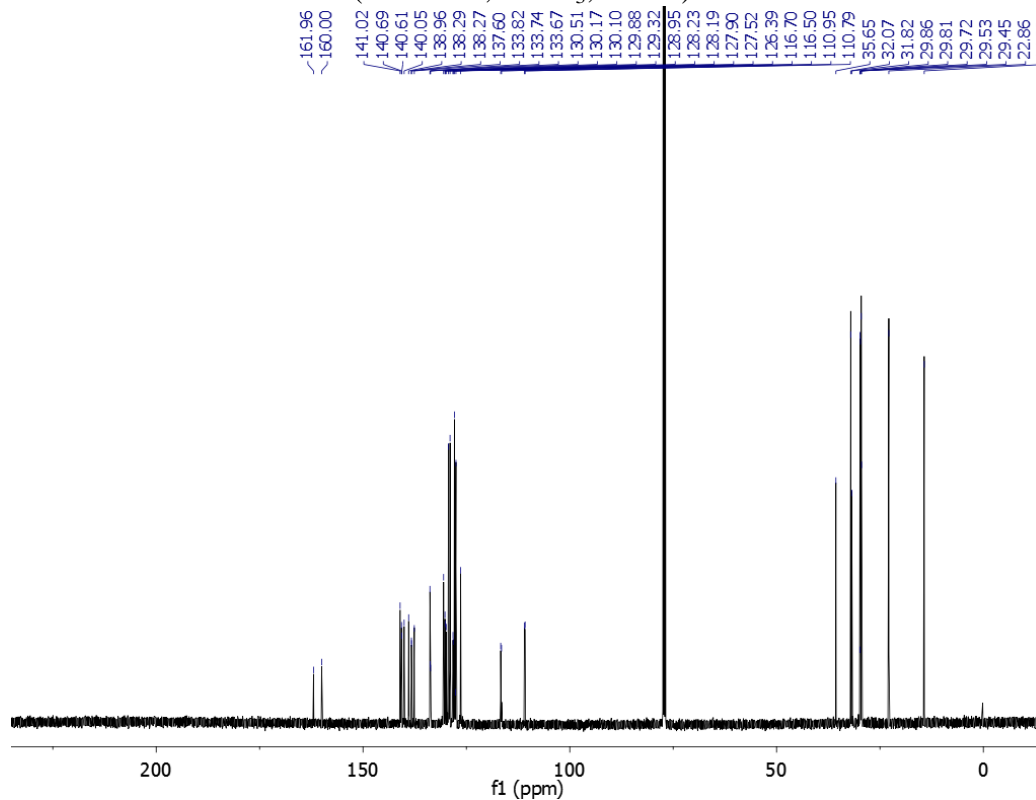
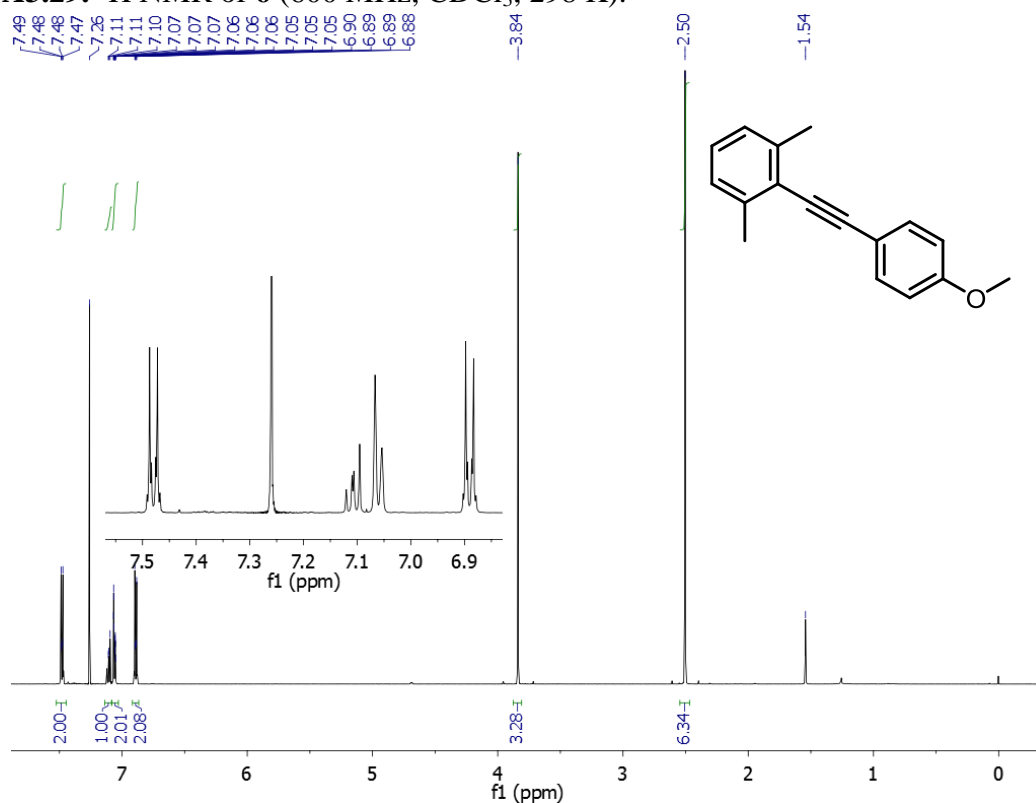


Figure A3.28.  $^{13}\text{C}$  NMR of **11d-F** (125 MHz,  $\text{CDCl}_3$ , 298 K).



**Figure A3.29.**  $^1\text{H}$  NMR of **6** (600 MHz,  $\text{CDCl}_3$ , 298 K).



**Figure A3.30.**  $^{13}\text{C}$  NMR of **6** (125 MHz,  $\text{CDCl}_3$ , 298 K).

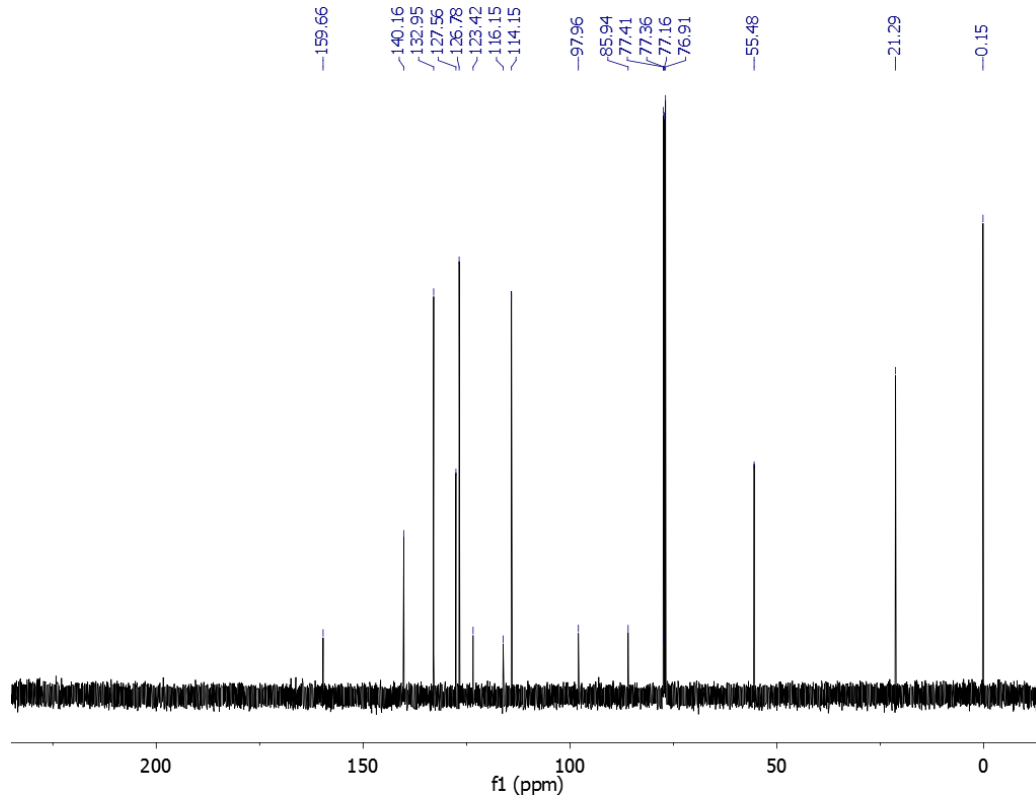


**Figure A3.31.**  $^1\text{H}$  NMR of **12a-F** and **12b-F** (600 MHz,  $\text{CDCl}_3$ , 298 K).

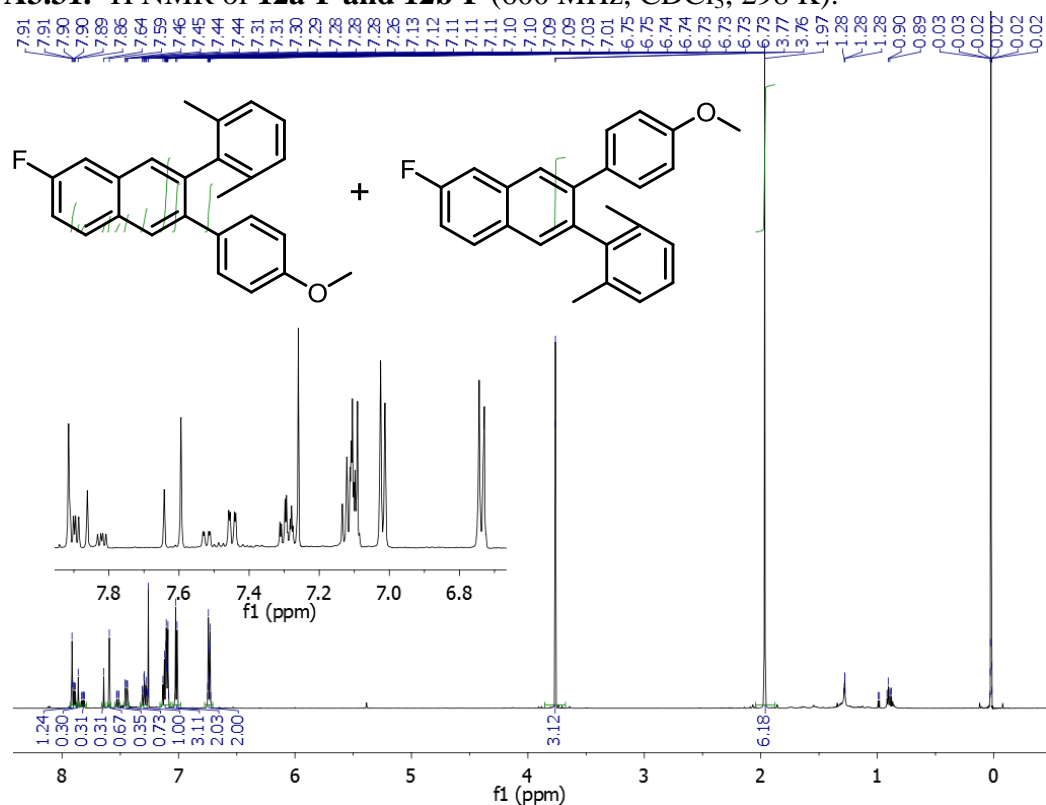


**Figure A3.32.**  $^{13}\text{C}$  NMR of **12a-F** and **12b-F** (150 MHz,  $\text{CDCl}_3$ , 298 K).

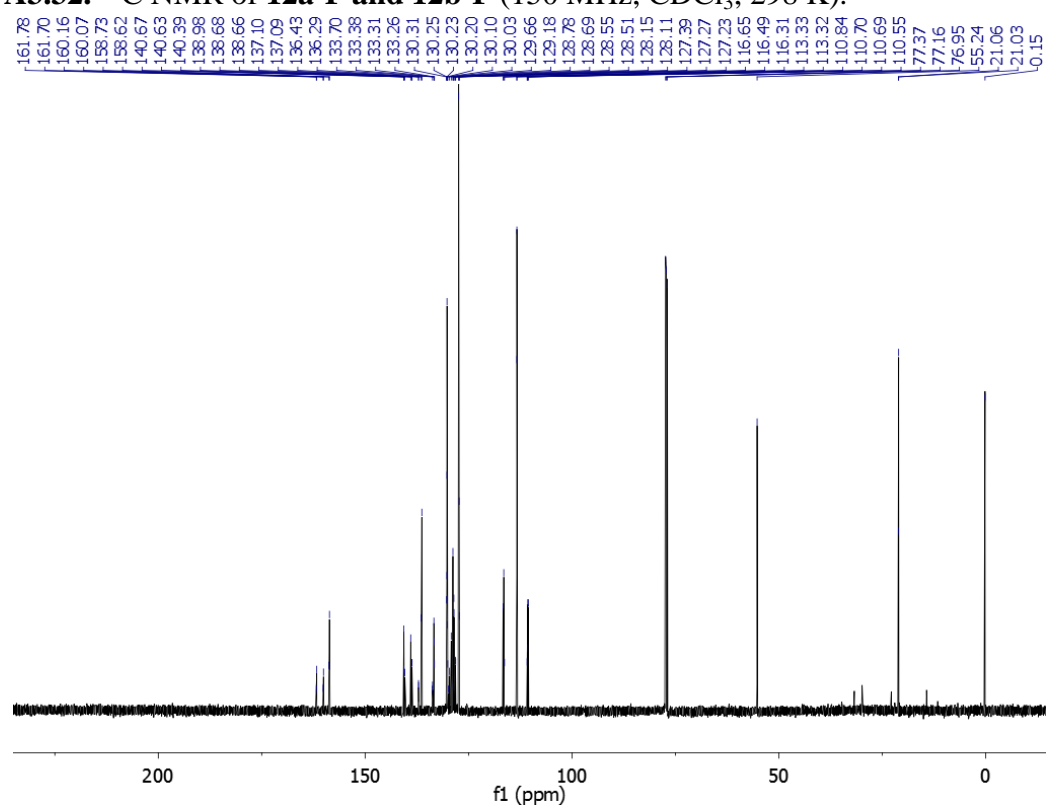


**Figure A3.33.**  $^1\text{H}$  NMR of **13a-F** and **13b-F** (600 MHz,  $\text{CDCl}_3$ , 298 K).

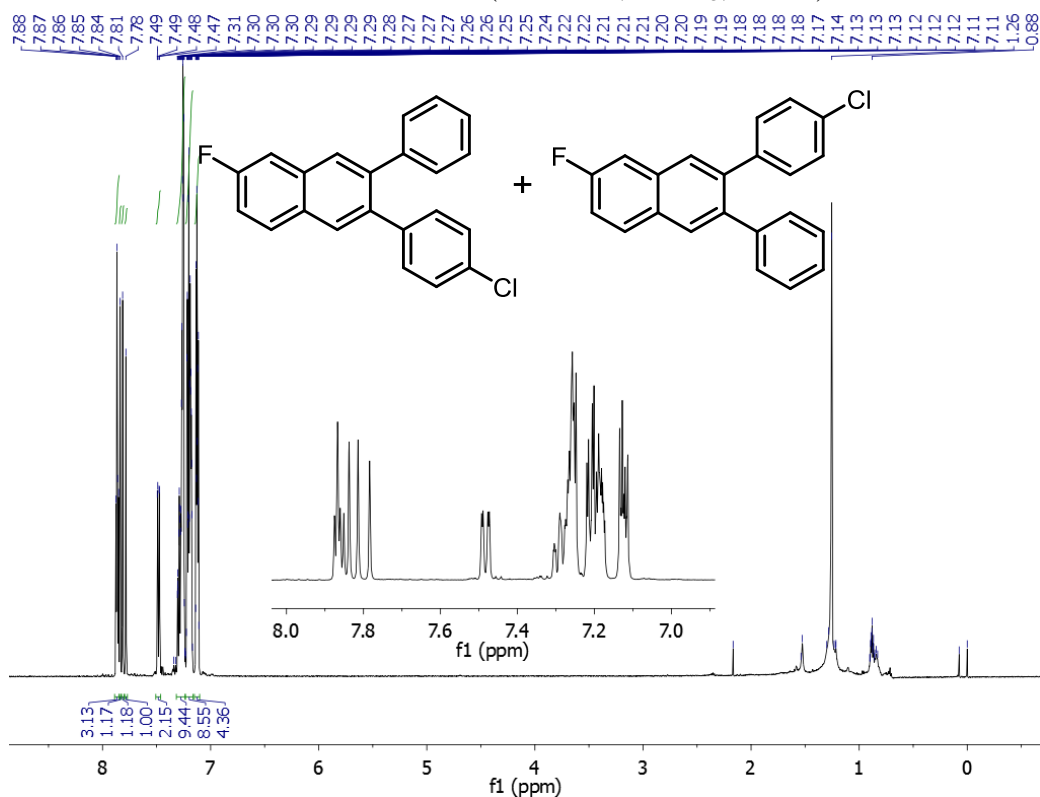
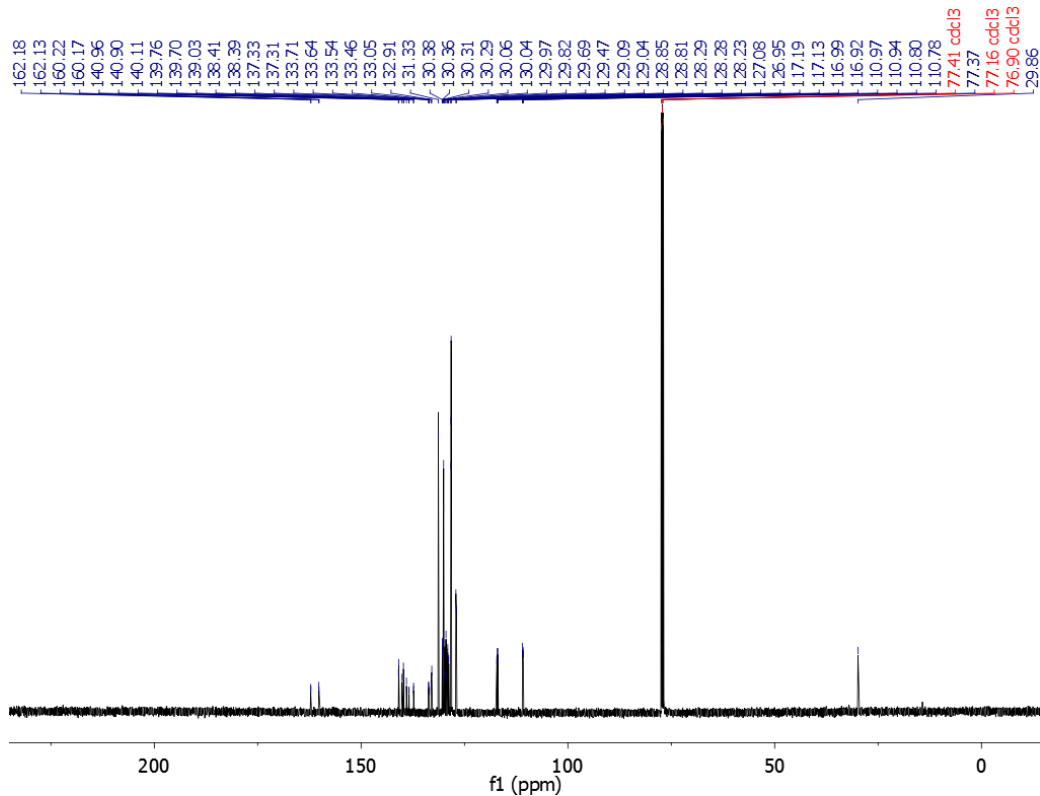


**Figure A3.34.**  $^{13}\text{C}$  NMR of **13a-F** and **13b-F** (125 MHz,  $\text{CDCl}_3$ , 298 K).



**D. 2D NMR Spectra Assignments**  
**Peak assignments for the compound 8:**

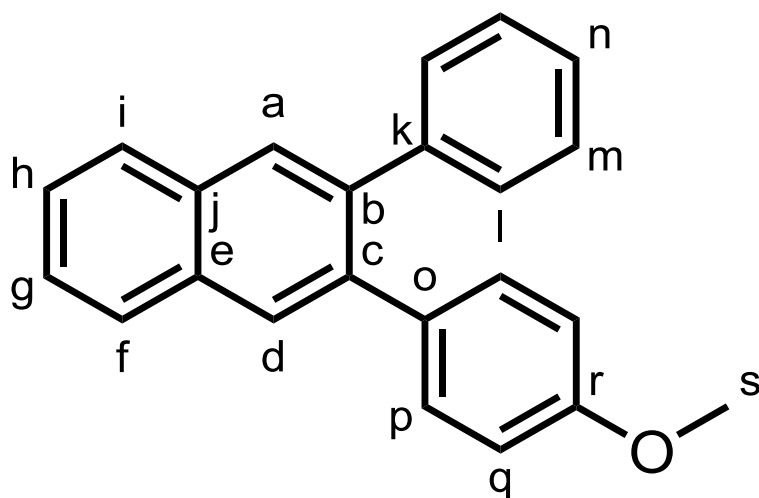


**Figure A3.35.** Full COSY spectrum of **8** (500 MHz, 500 MHz, CDCl<sub>3</sub>, 298 K).

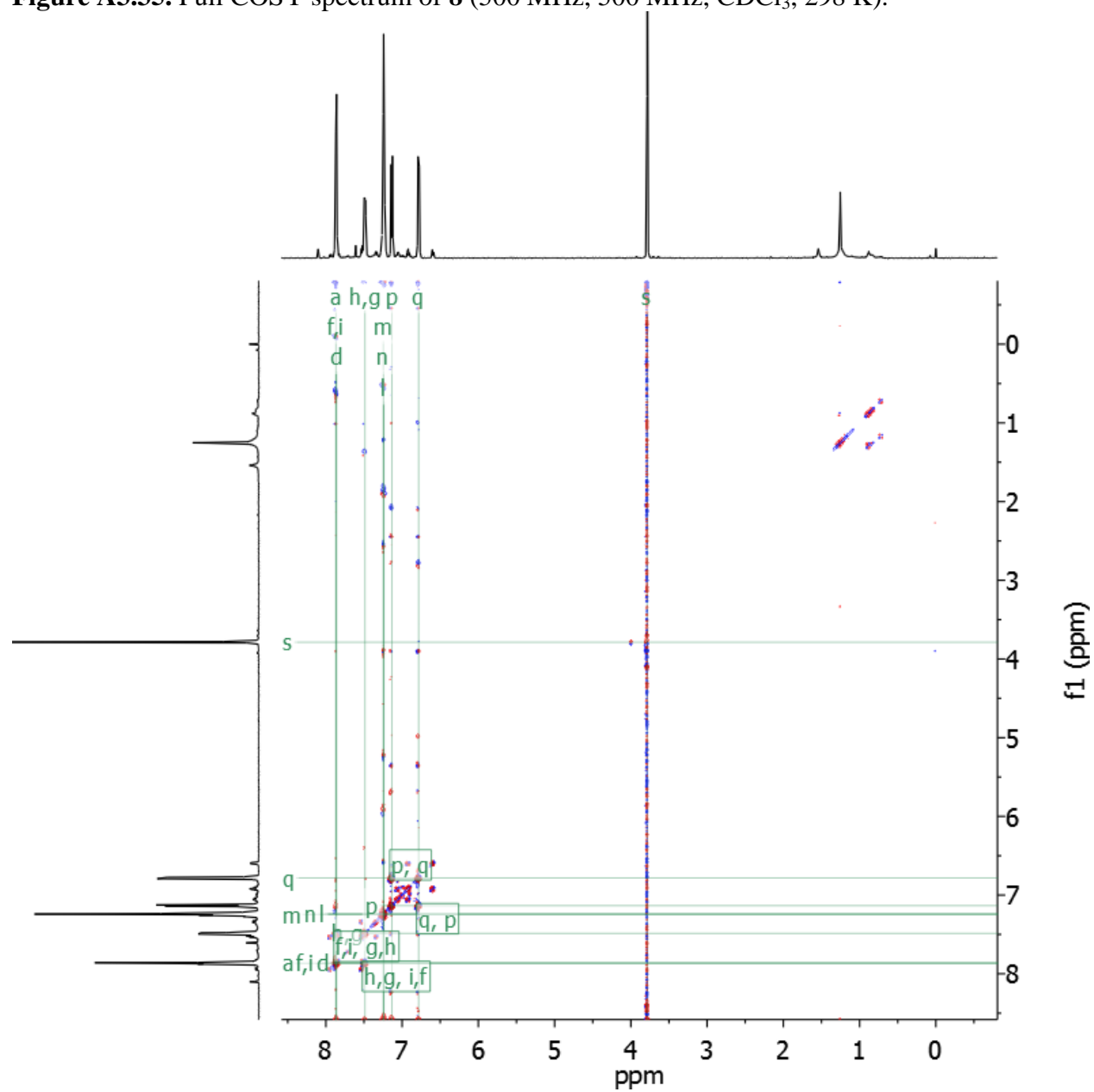




**Figure A3.36.** Partial COSY spectrum of **8** showing the aromatic region (500 MHz, 500 MHz, CDCl<sub>3</sub>, 298 K).

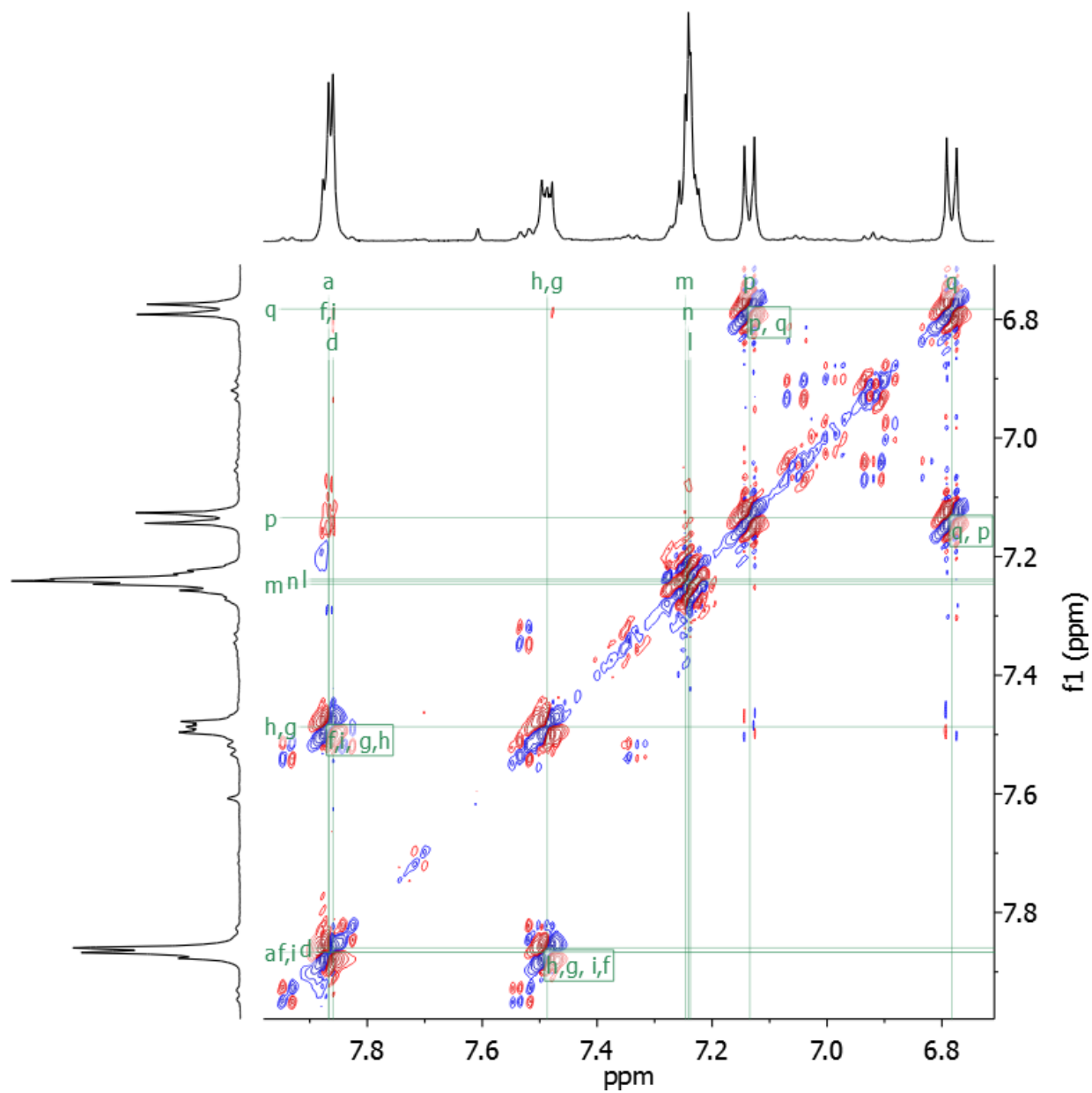


**Figure A3.37.** Full NOESY spectrum of **8** (500 MHz, 500 MHz, CDCl<sub>3</sub>, 298 K).

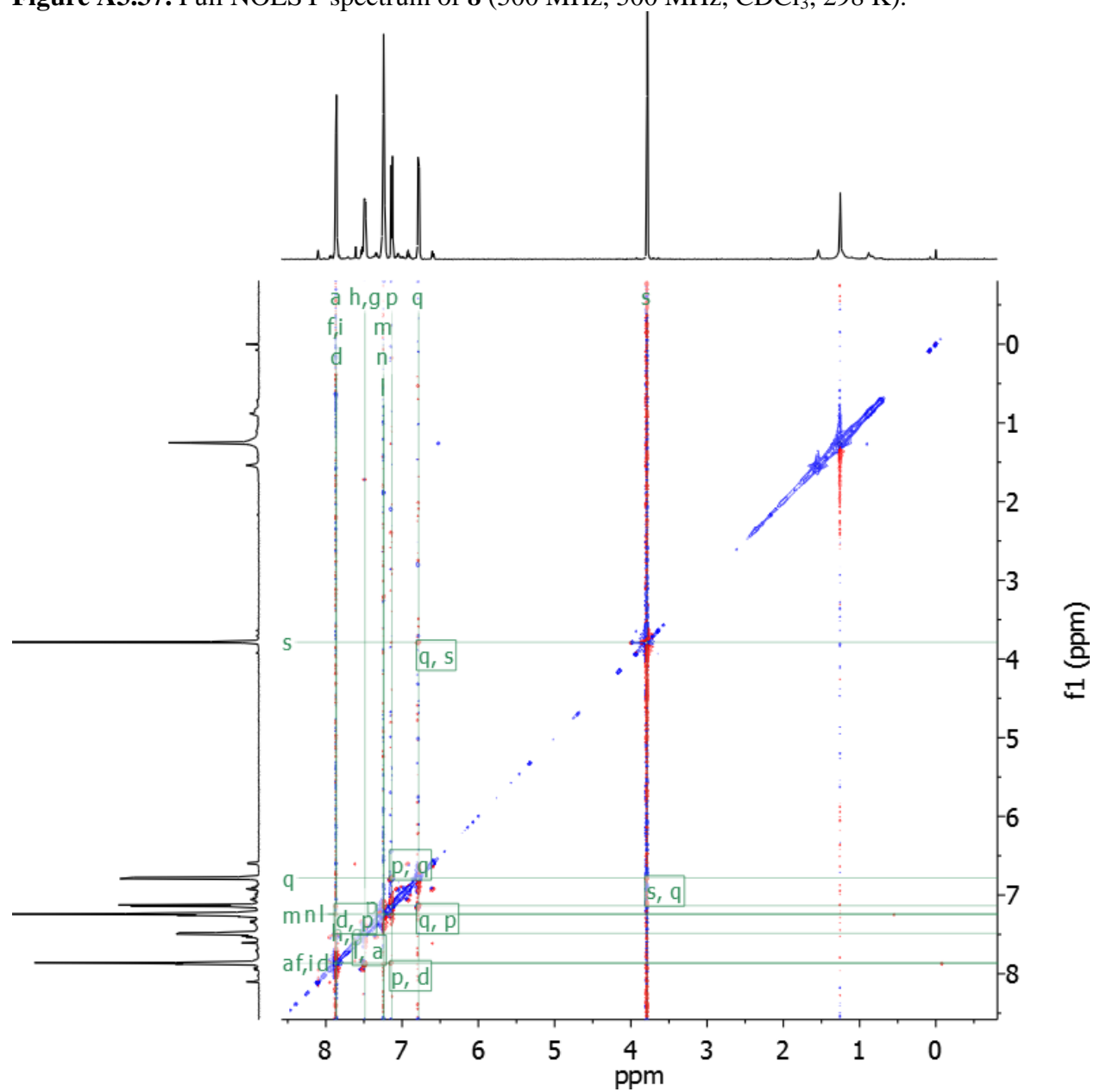


**Figure A3.38.** Partial NOESY spectrum of **8** showing the aromatic region (500 MHz, 500 MHz, CDCl<sub>3</sub>, 298 K).

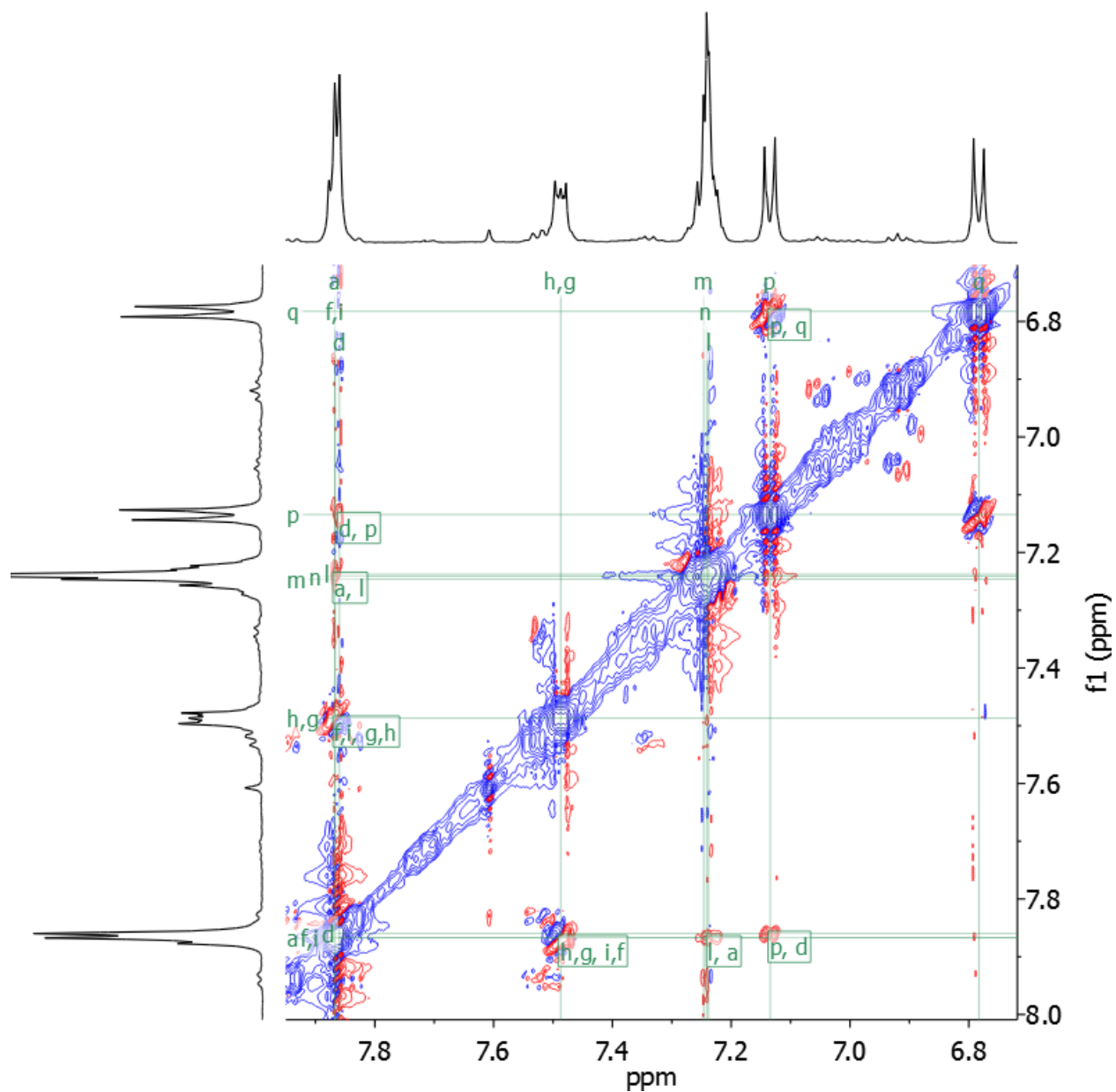




**Figure A3.40.** Partial HSQC spectrum of **8** showing the aromatic region (500 MHz, 125 MHz, CDCl<sub>3</sub>, 298 K).

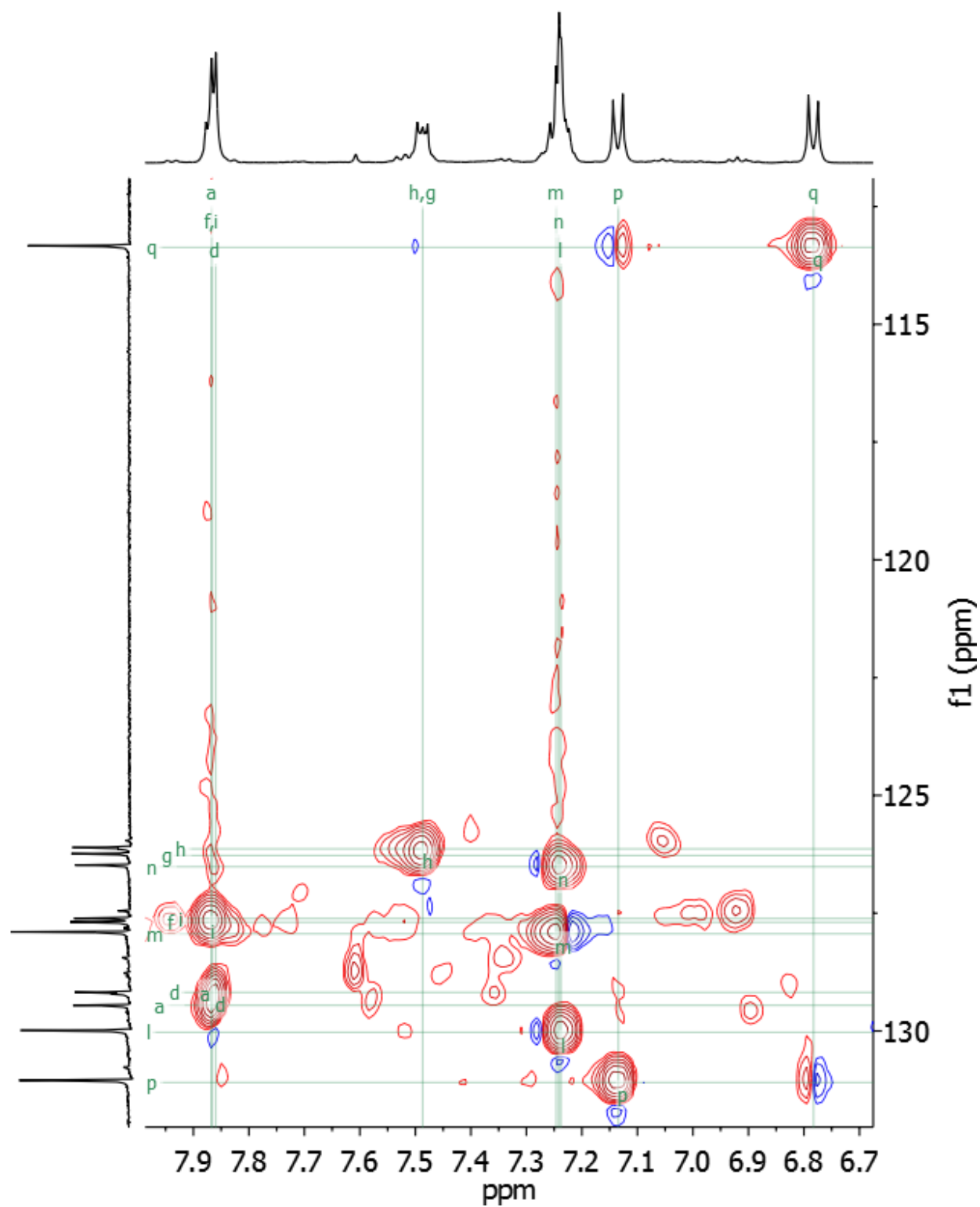


**Figure A3.41.** Full HMBC spectrum of **8** (500 MHz, 125 MHz, CDCl<sub>3</sub>, 298 K).

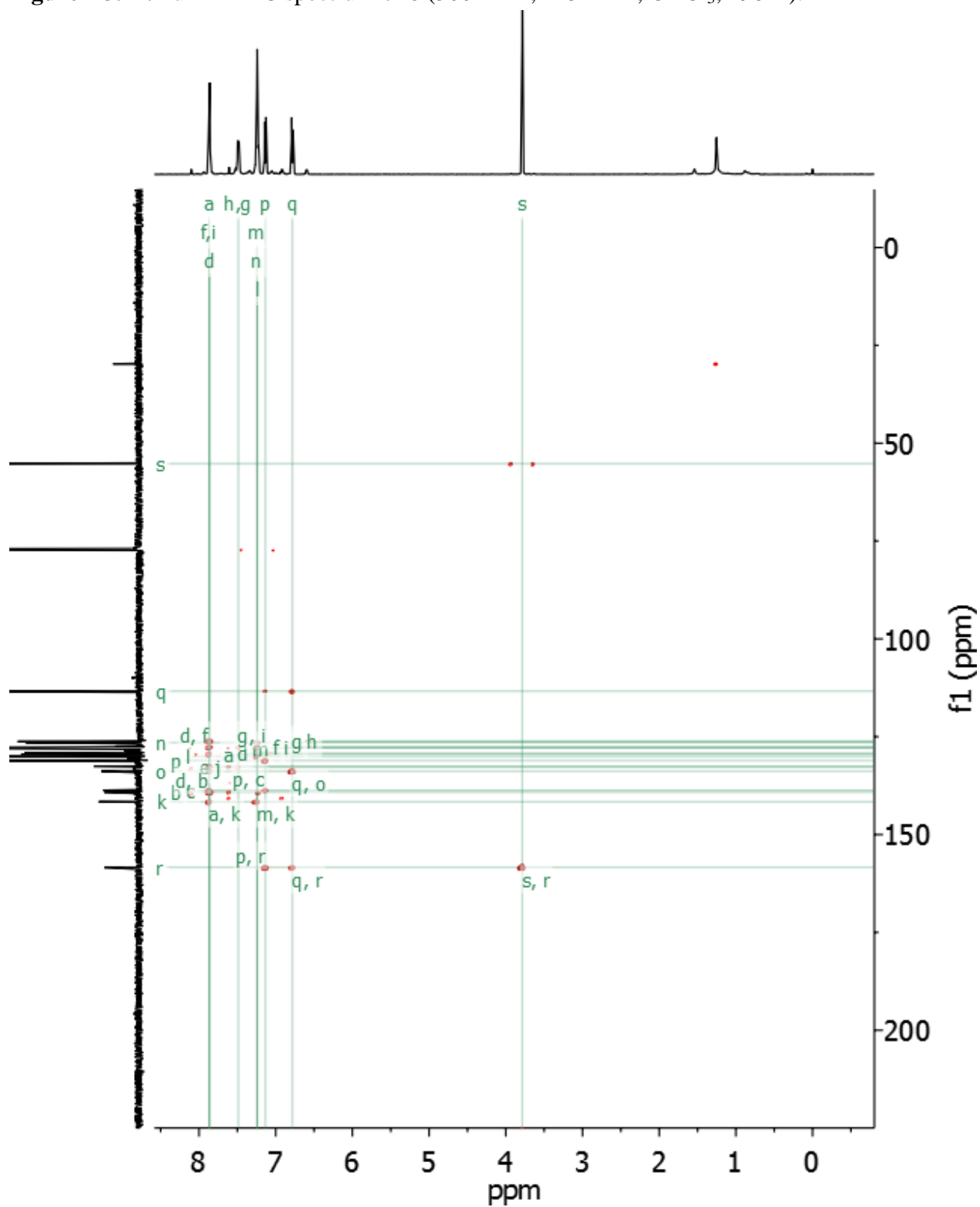
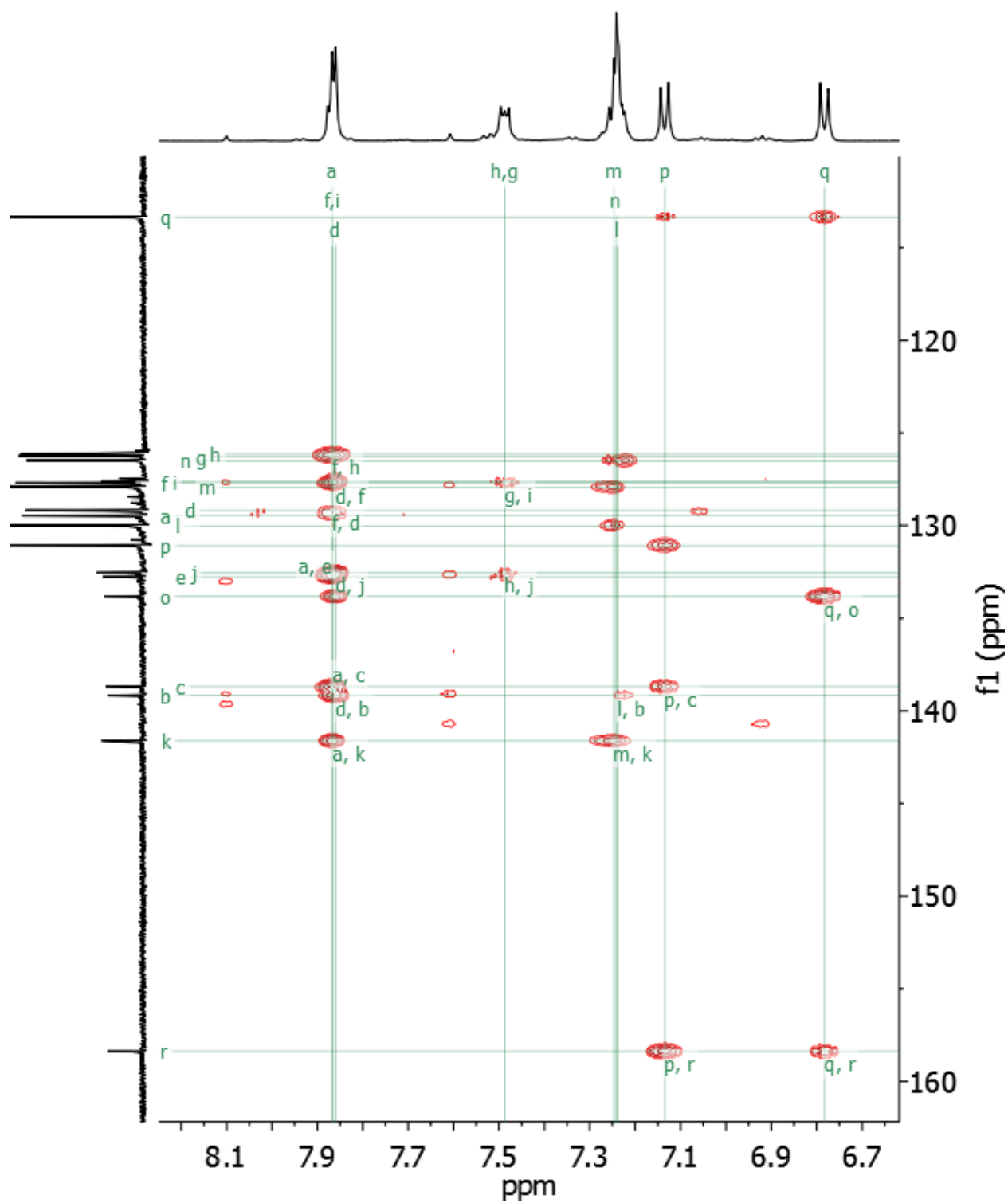


**Figure A3.42.** Partial HMBC spectrum of **8** showing the aromatic region (500 MHz, 125 MHz, CDCl<sub>3</sub>, 298 K).



Peak assignments for the compound 8c-F:

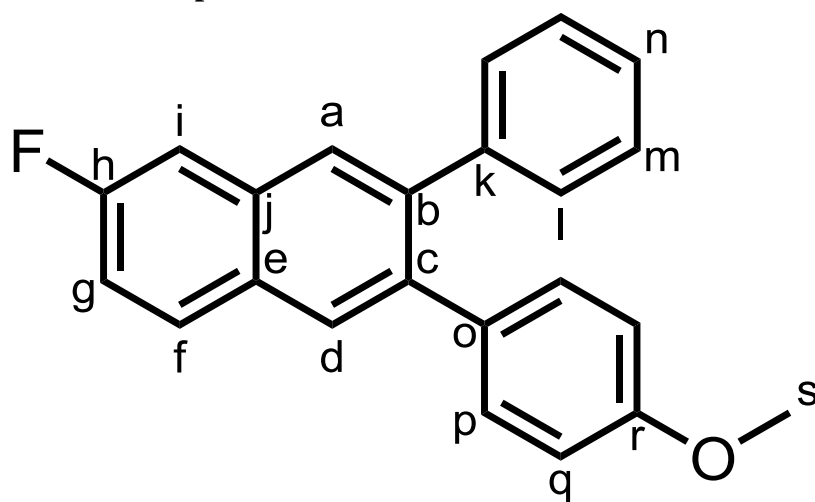




**Figure A3.43.** Full COSY spectrum of **8c-F** (500 MHz, 500 MHz, CDCl<sub>3</sub>, 298 K).

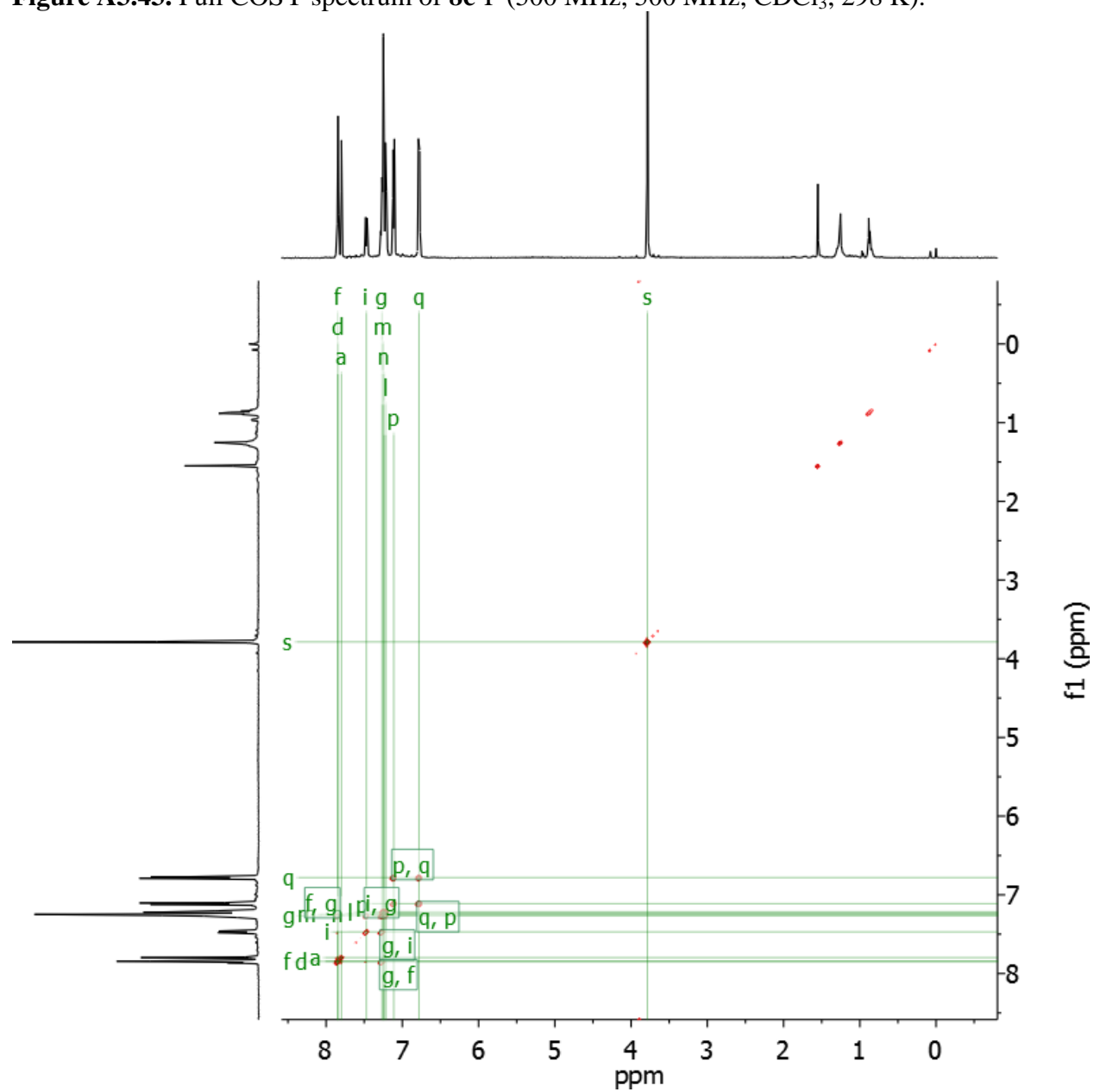


**Figure A3.44.** Partial COSY spectrum of **8c-F** showing the aromatic region (500 MHz, 500 MHz, CDCl<sub>3</sub>, 298 K).

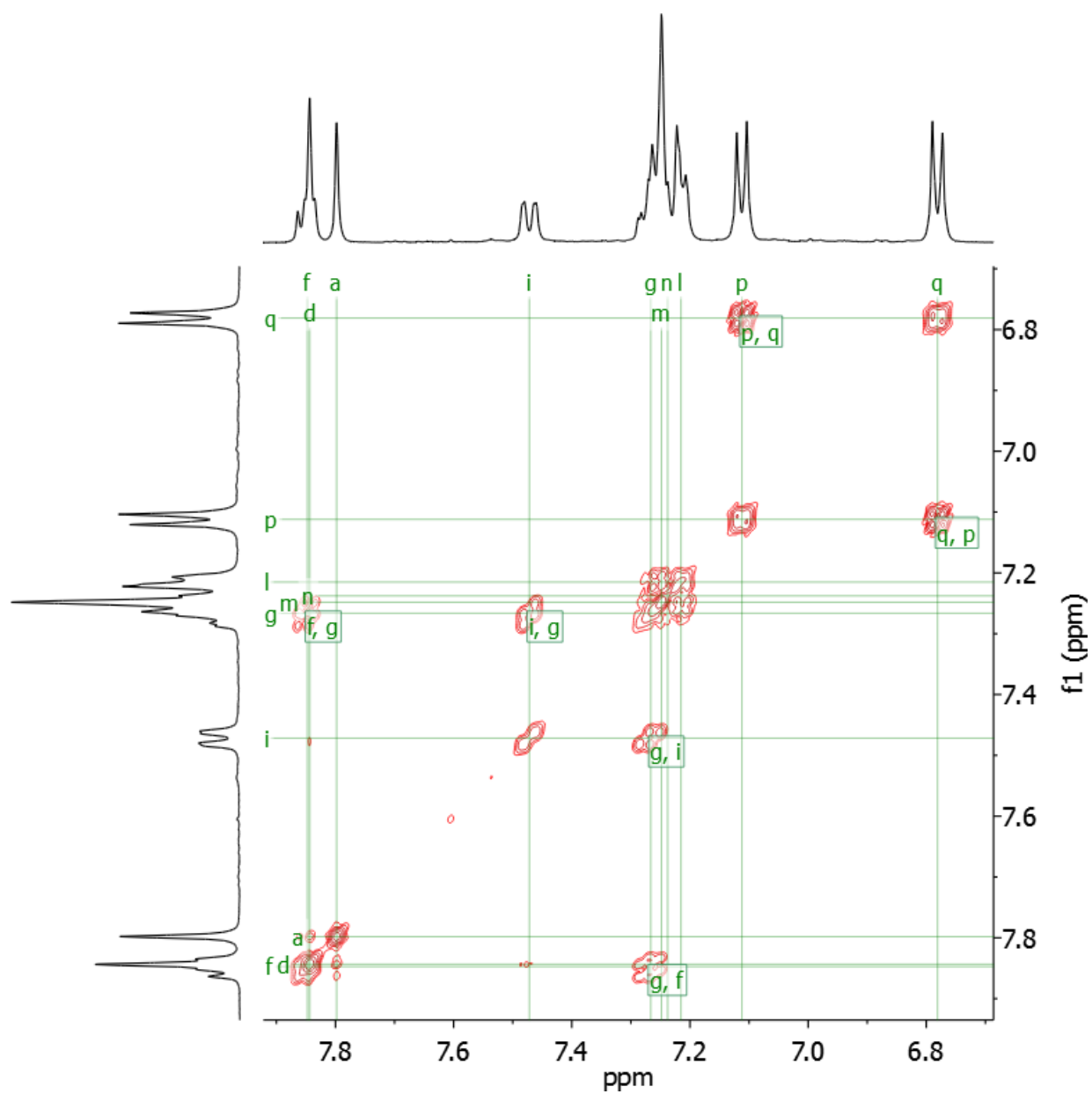


**Figure A3.45.** Full NOESY spectrum of **8c-F** (500 MHz, 500 MHz, CDCl<sub>3</sub>, 298 K).

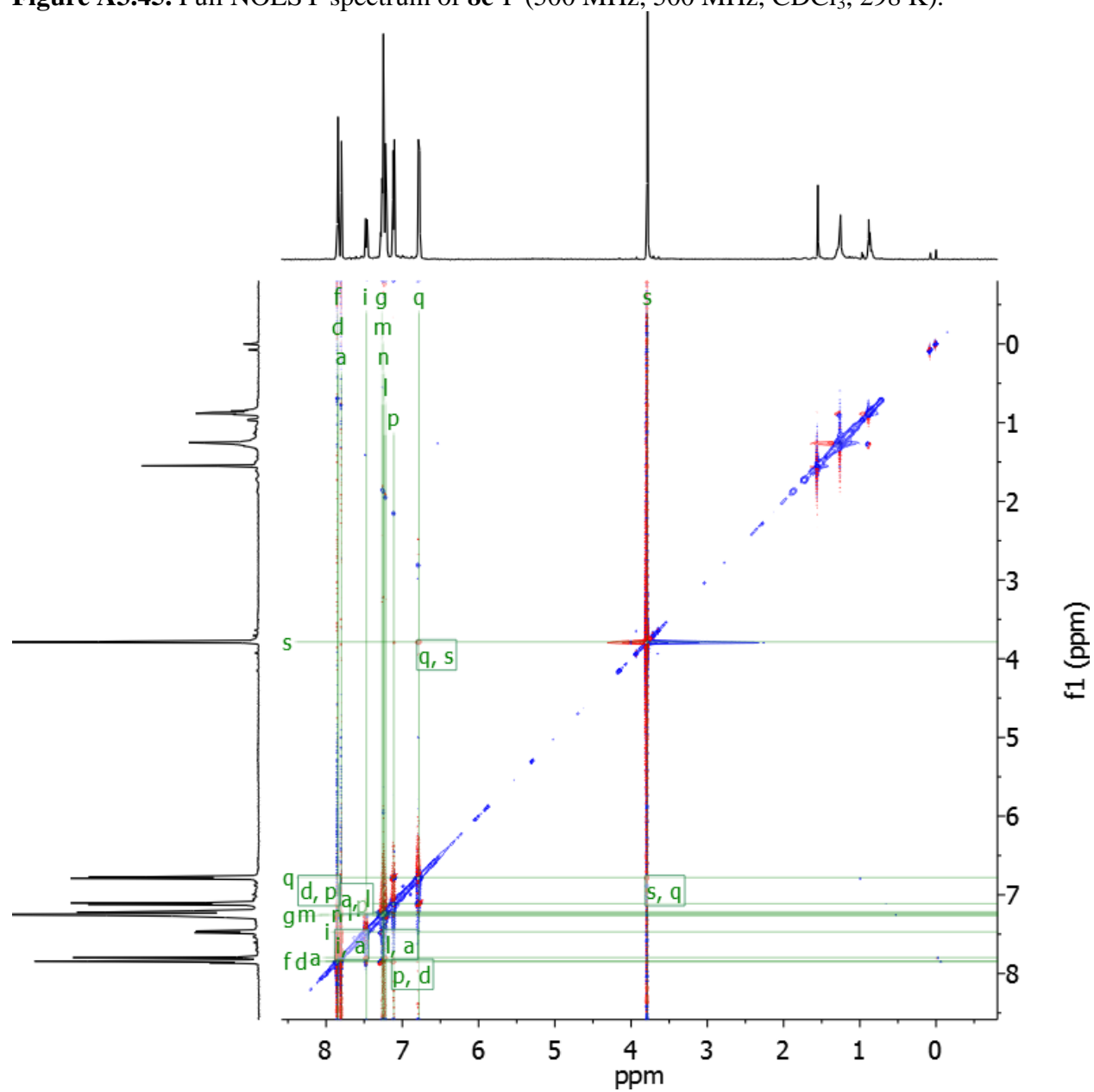


**Figure A3.46.** Partial NOESY spectrum of **8c-F** showing the aromatic region (500 MHz, 500 MHz, CDCl<sub>3</sub>, 298 K).

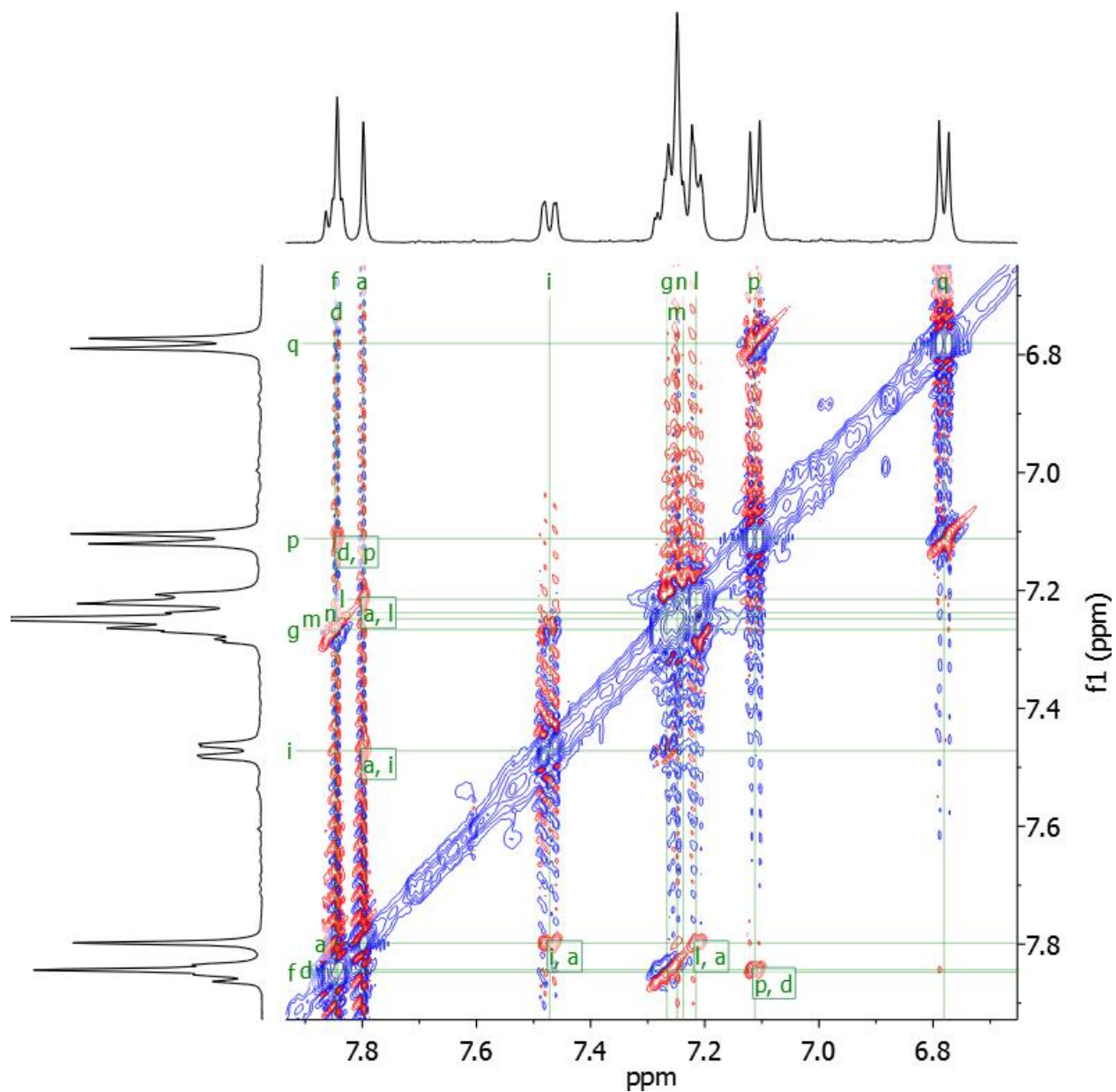


**Figure A3.47.** Full HSQC spectrum of **8c-F** (500 MHz, 125 MHz, CDCl<sub>3</sub>, 298 K).

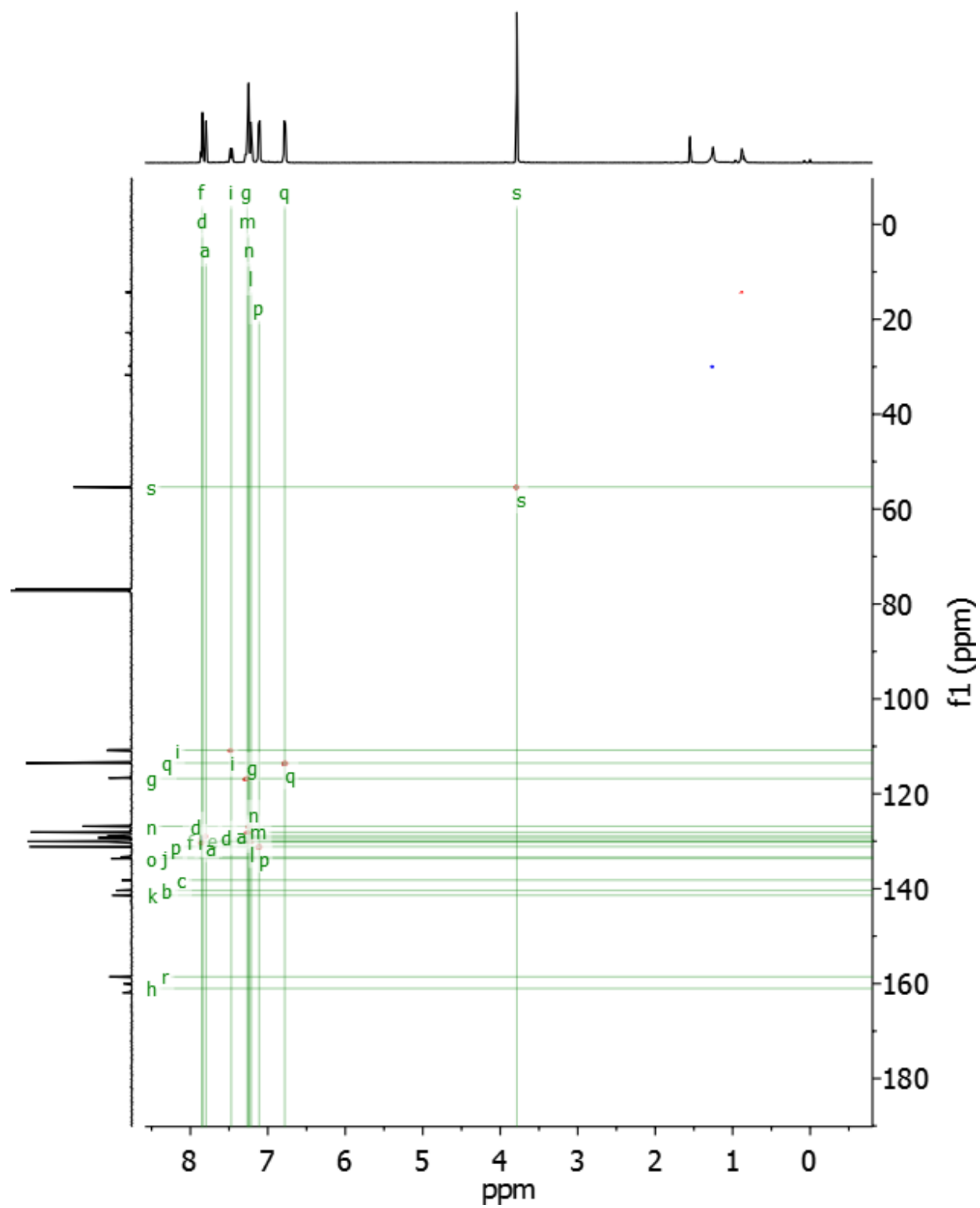


**Figure A3.48.** Partial HSQC spectrum of **8c-F** showing the aromatic region (500 MHz, 125 MHz, CDCl<sub>3</sub>, 298 K).

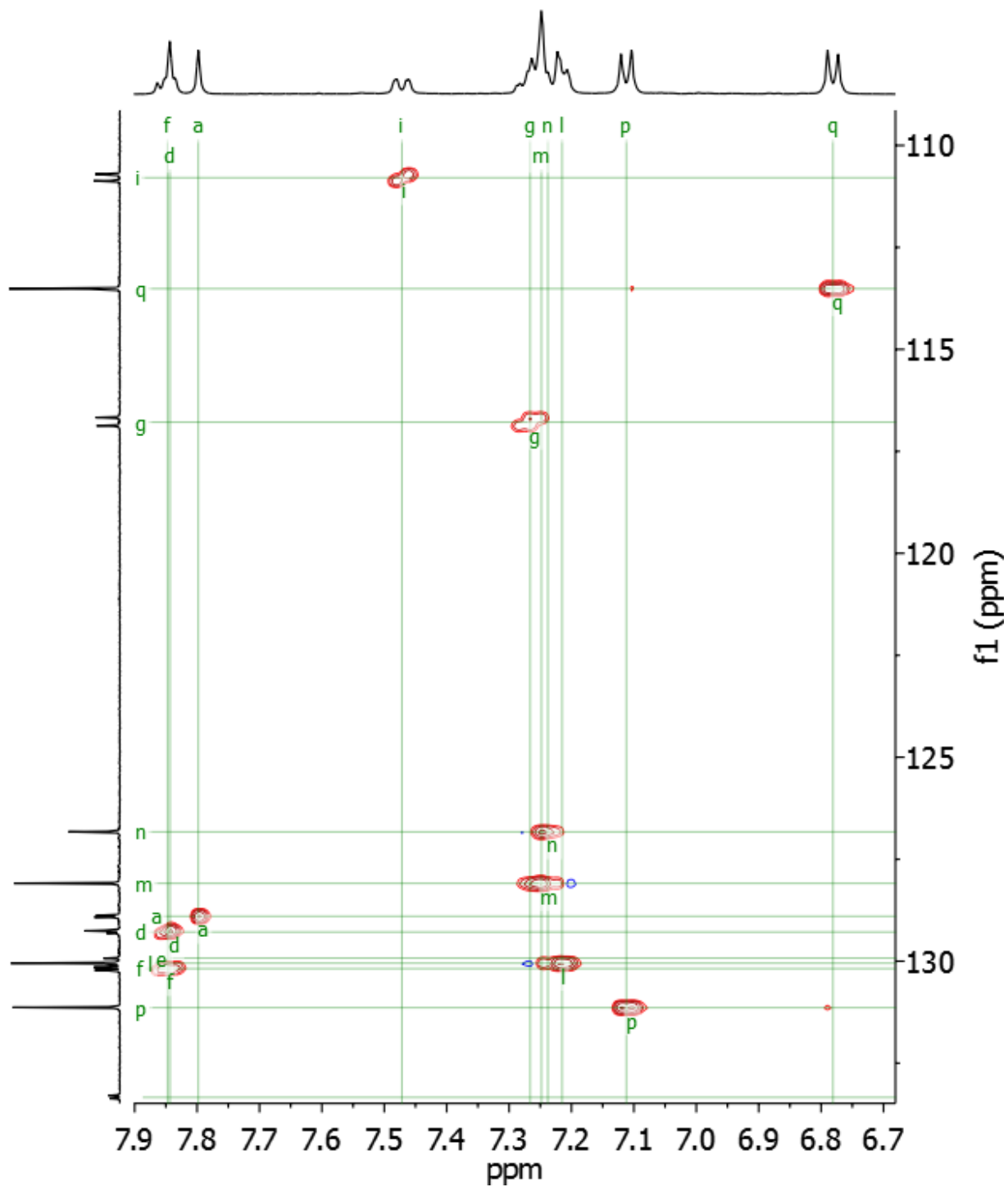


**Figure A3.49.** Full HMBC spectrum of **8c-F** (500 MHz, 125 MHz, CDCl<sub>3</sub>, 298 K).

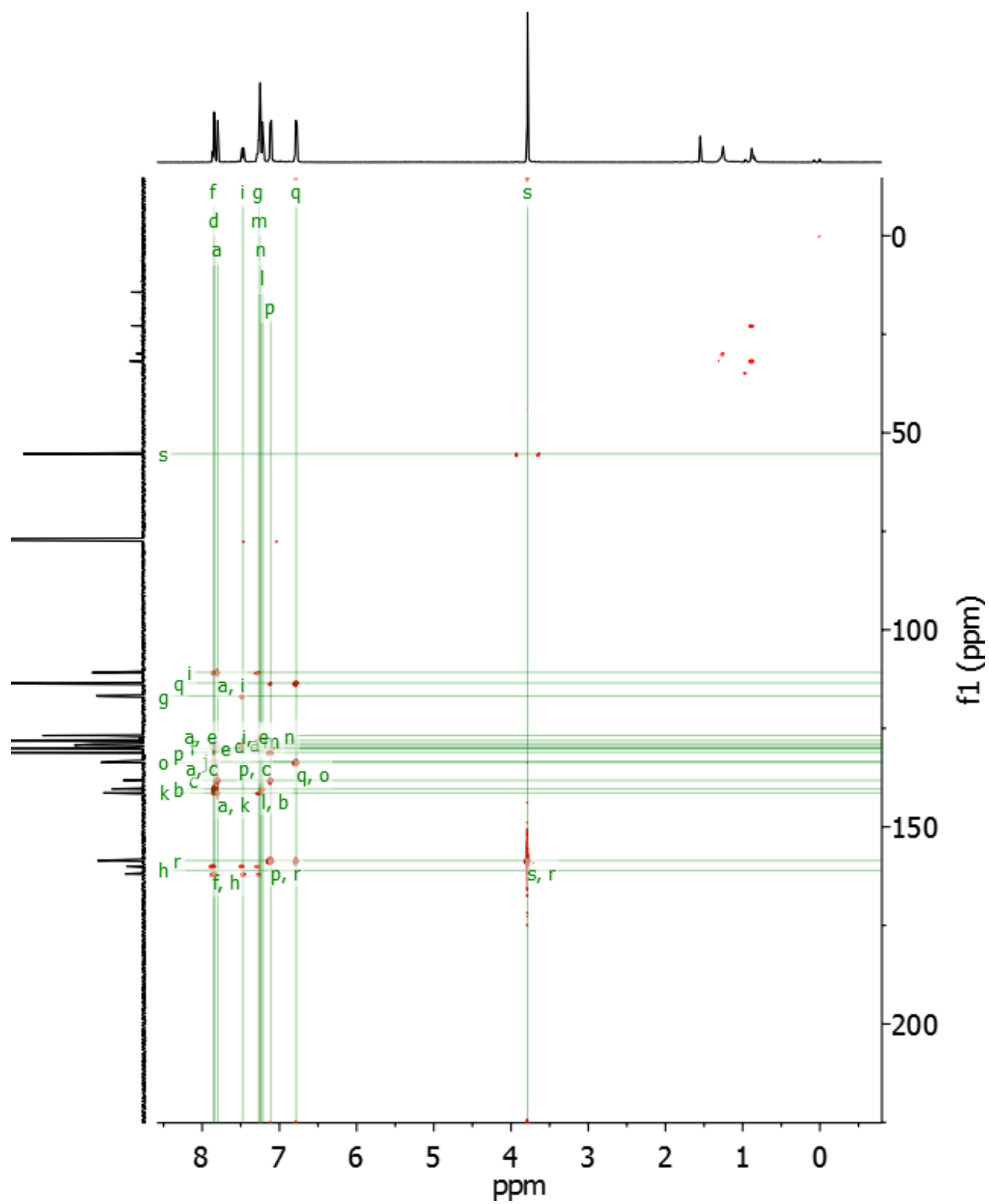
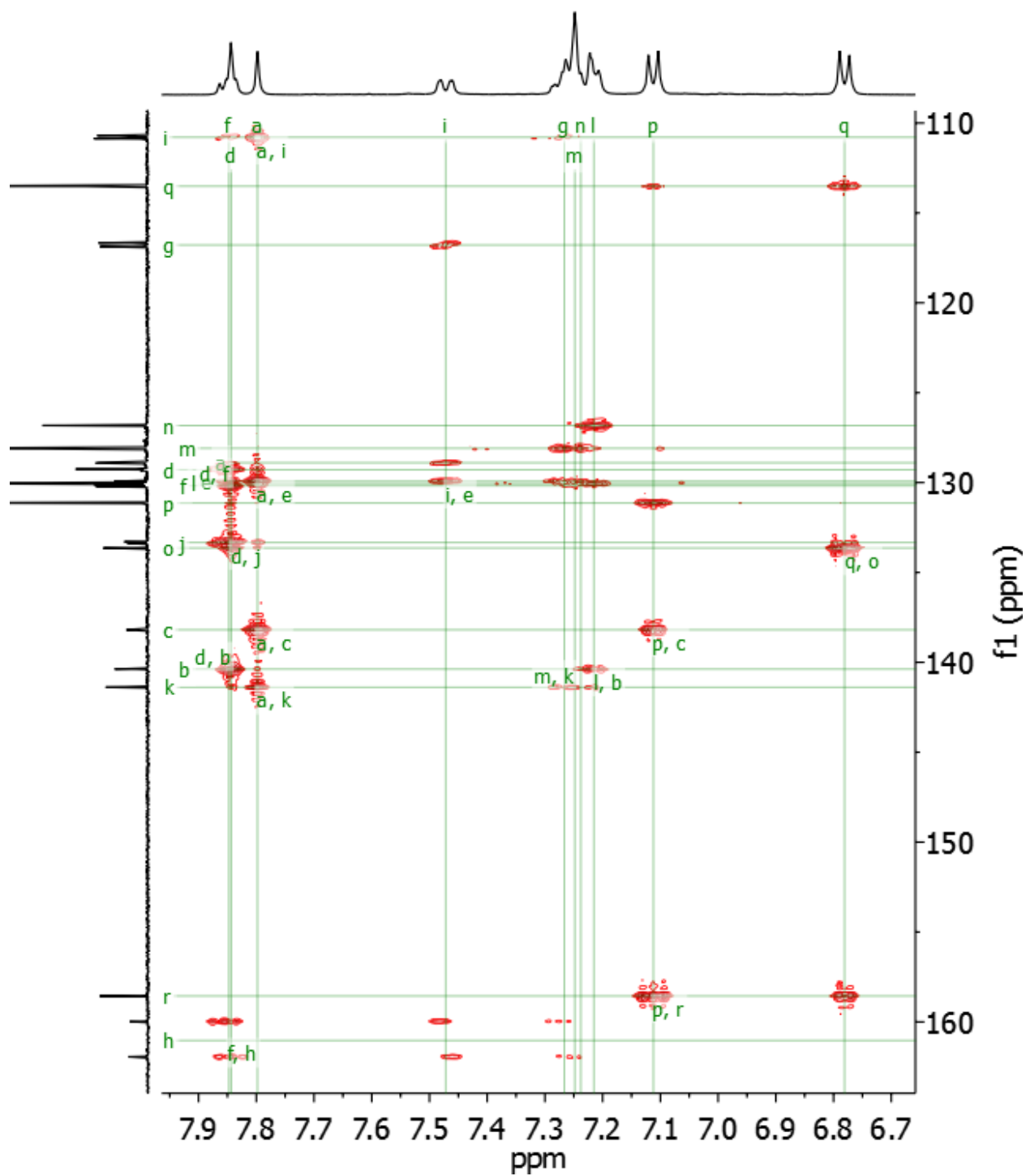


**Figure A3.50.** Partial HMBC spectrum of **8c-F** showing the aromatic region (500 MHz, 125 MHz, CDCl<sub>3</sub>, 298 K).





Peak assignments for the compound 9:

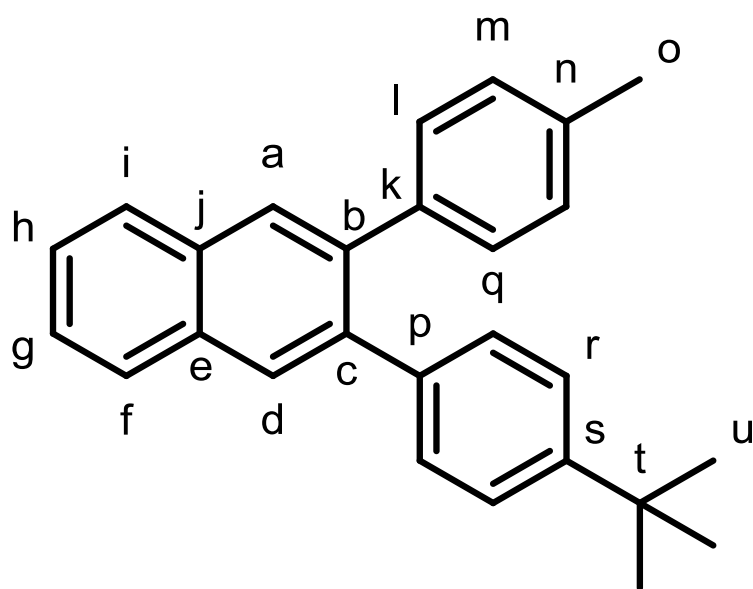


**Figure A3.51.** Full COSY spectrum of **9** (500 MHz, 500 MHz, CDCl<sub>3</sub>, 298 K).

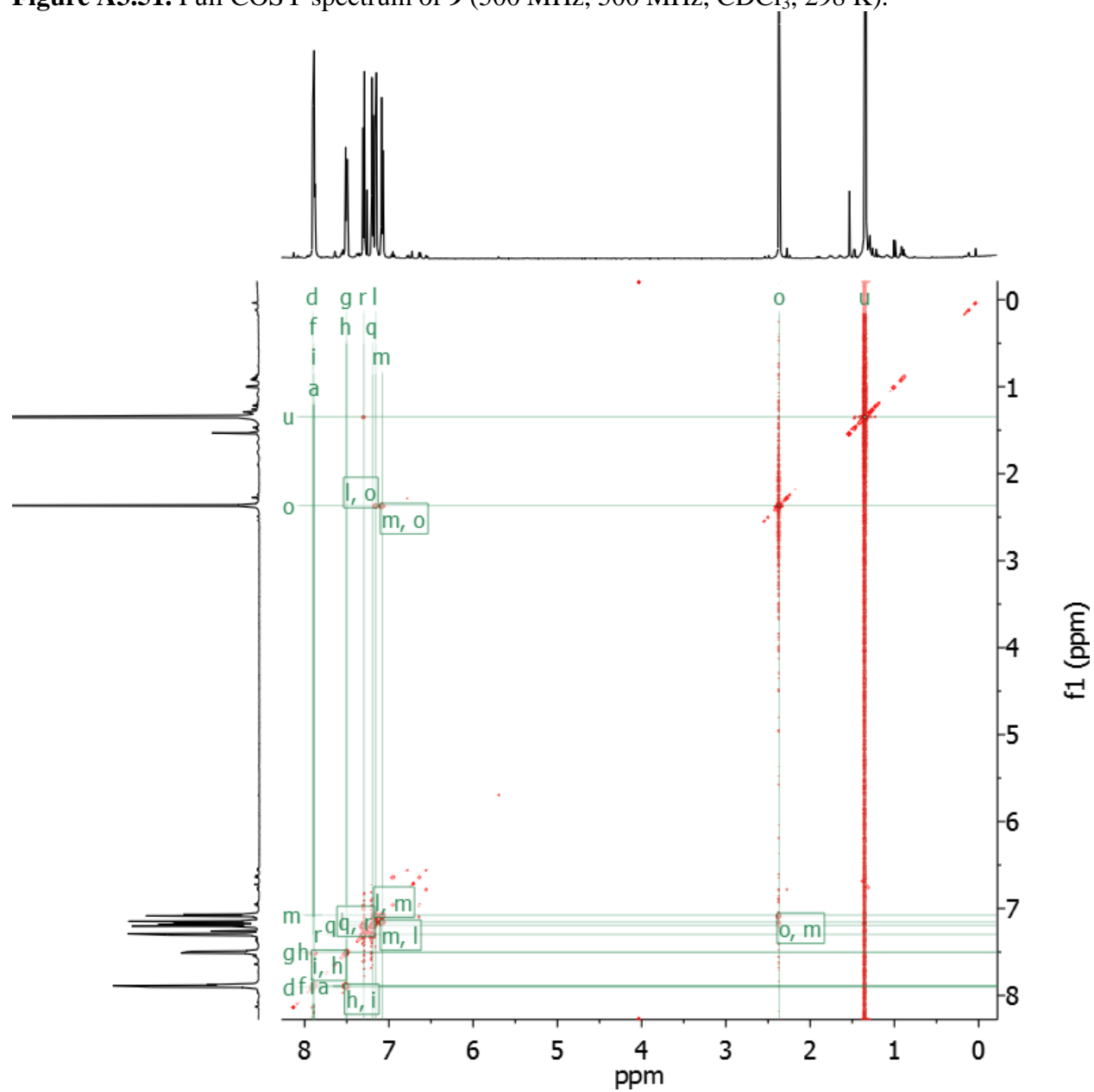


**Figure A3.52.** Partial COSY spectrum of **9** showing the aromatic region (500 MHz, 500 MHz, CDCl<sub>3</sub>, 298 K).

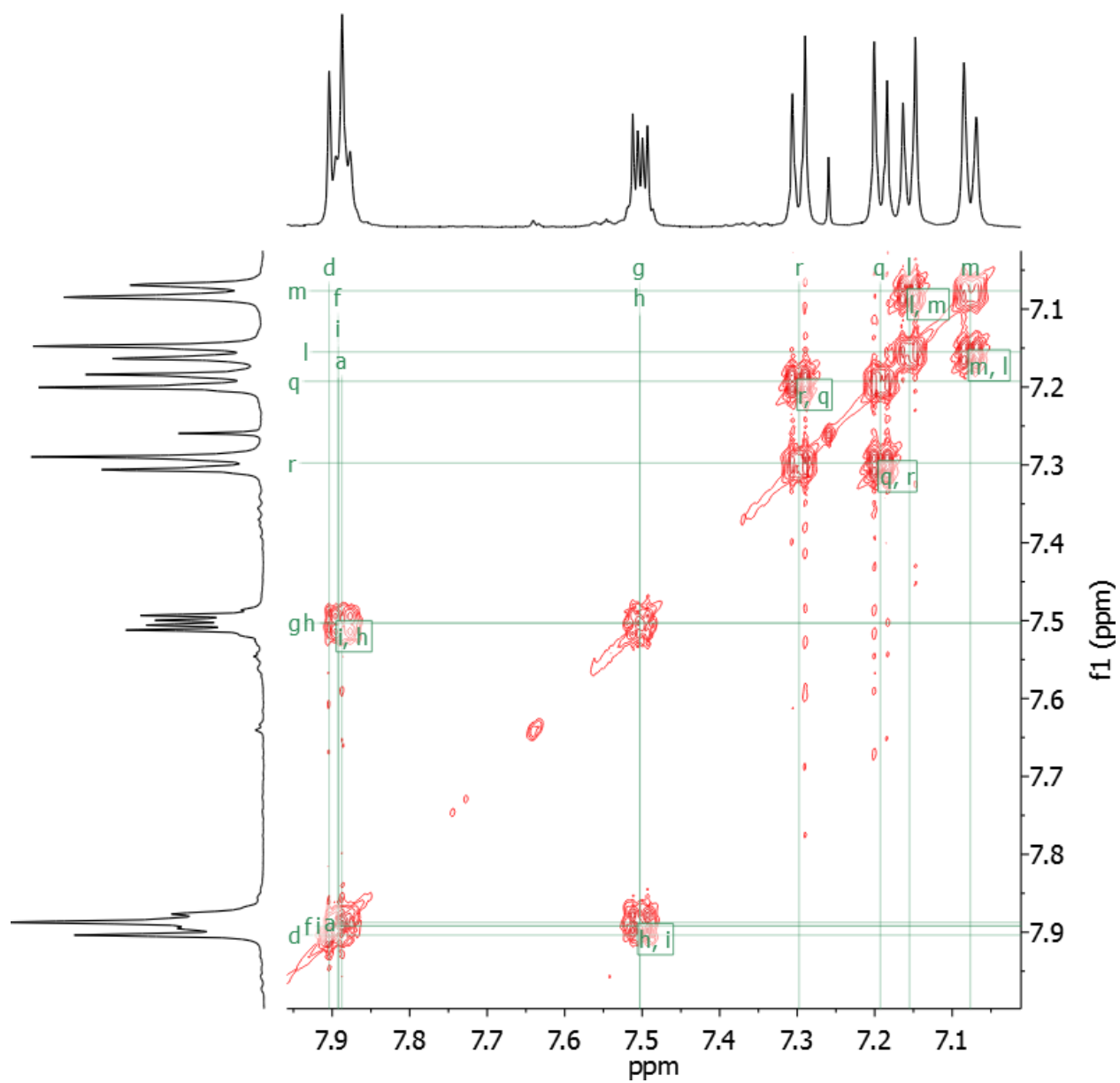


**Figure A3.53.** Full NOESY spectrum of **9** (500 MHz, 500 MHz, CDCl<sub>3</sub>, 298 K).

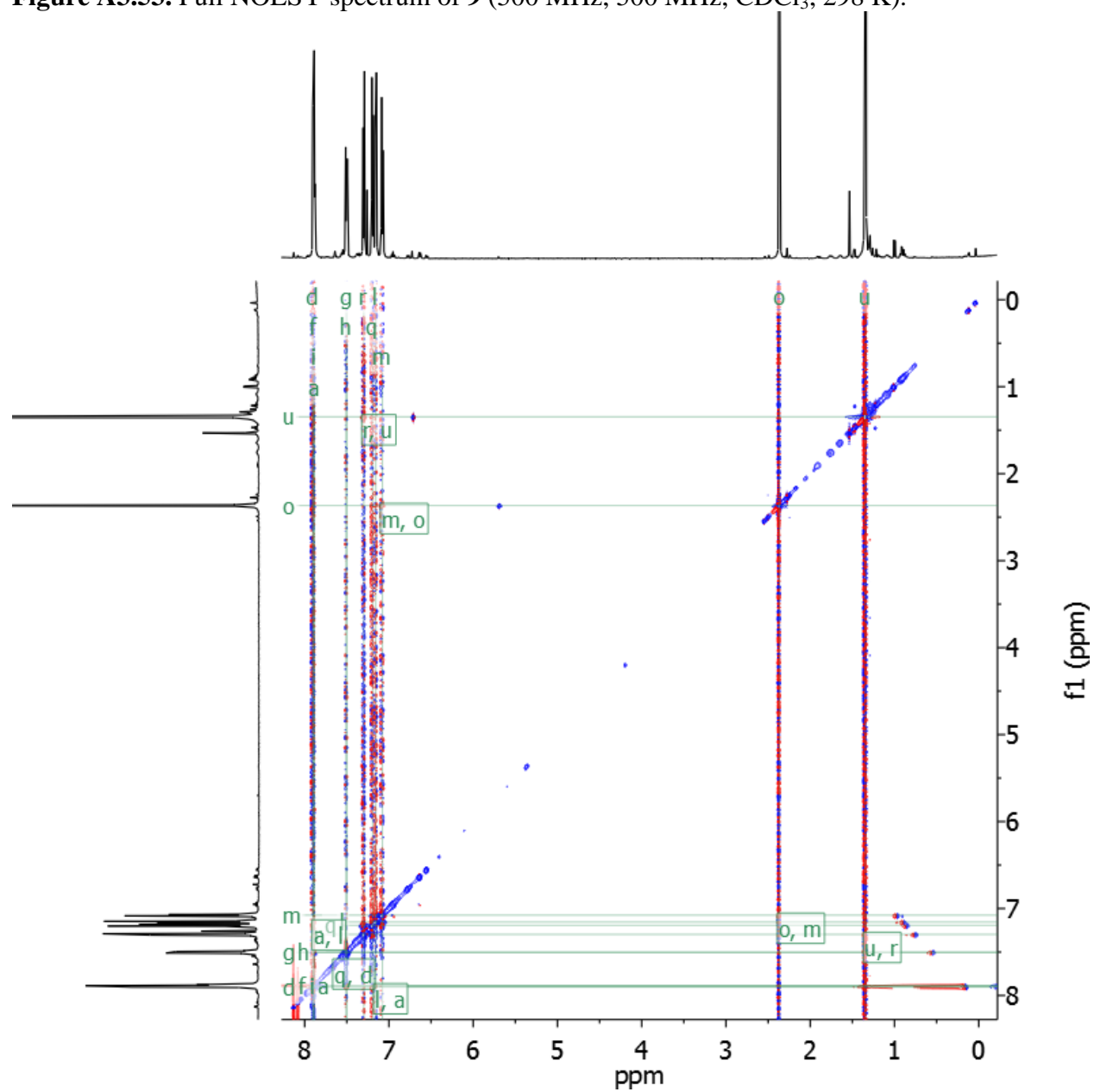


**Figure A3.54.** Partial NOESY spectrum of **9** showing the aromatic region (500 MHz, 500 MHz, CDCl<sub>3</sub>, 298 K).

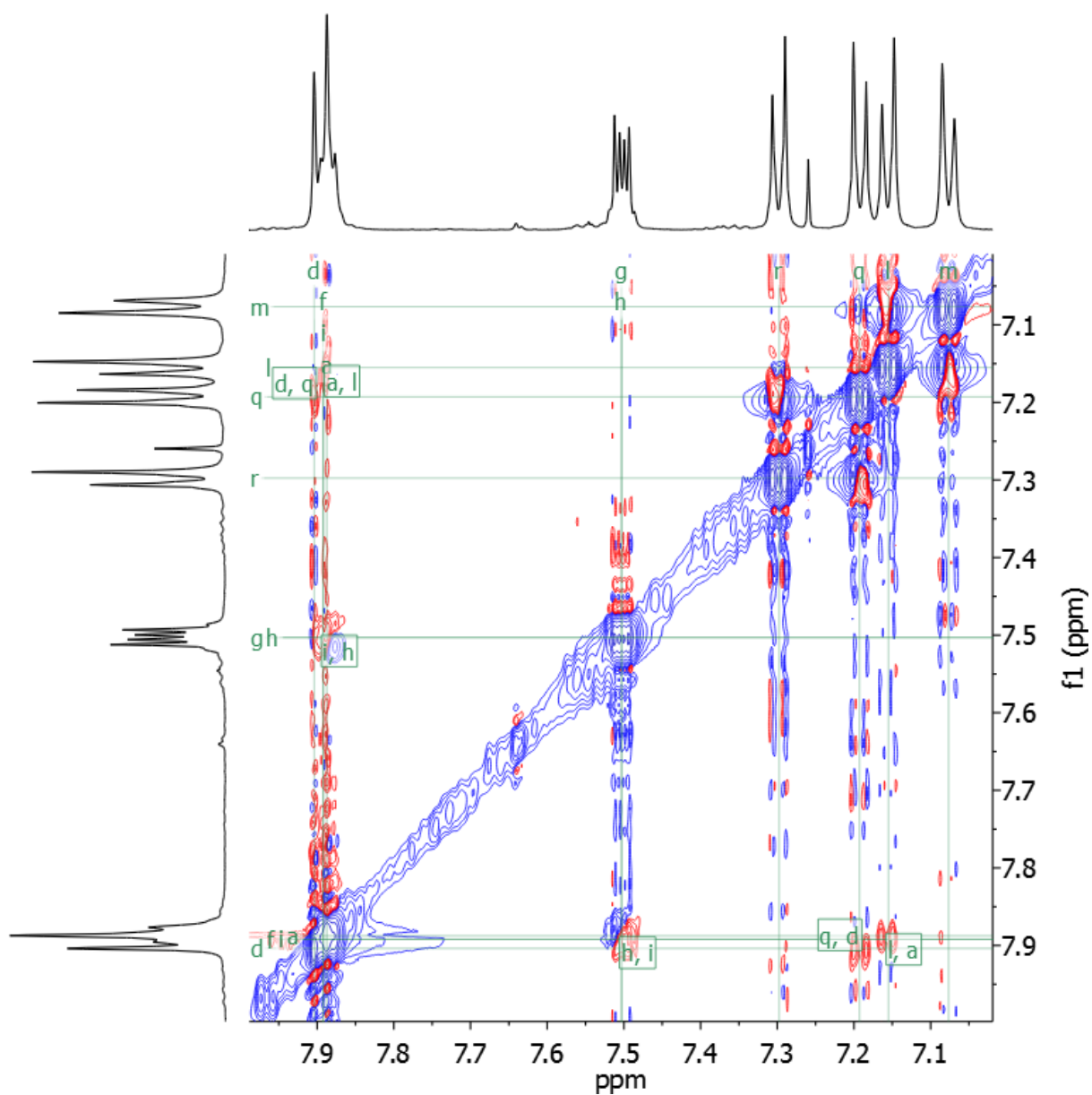


**Figure A3.55.** Full HSQC spectrum of **9** (500 MHz, 125 MHz, CDCl<sub>3</sub>, 298 K).

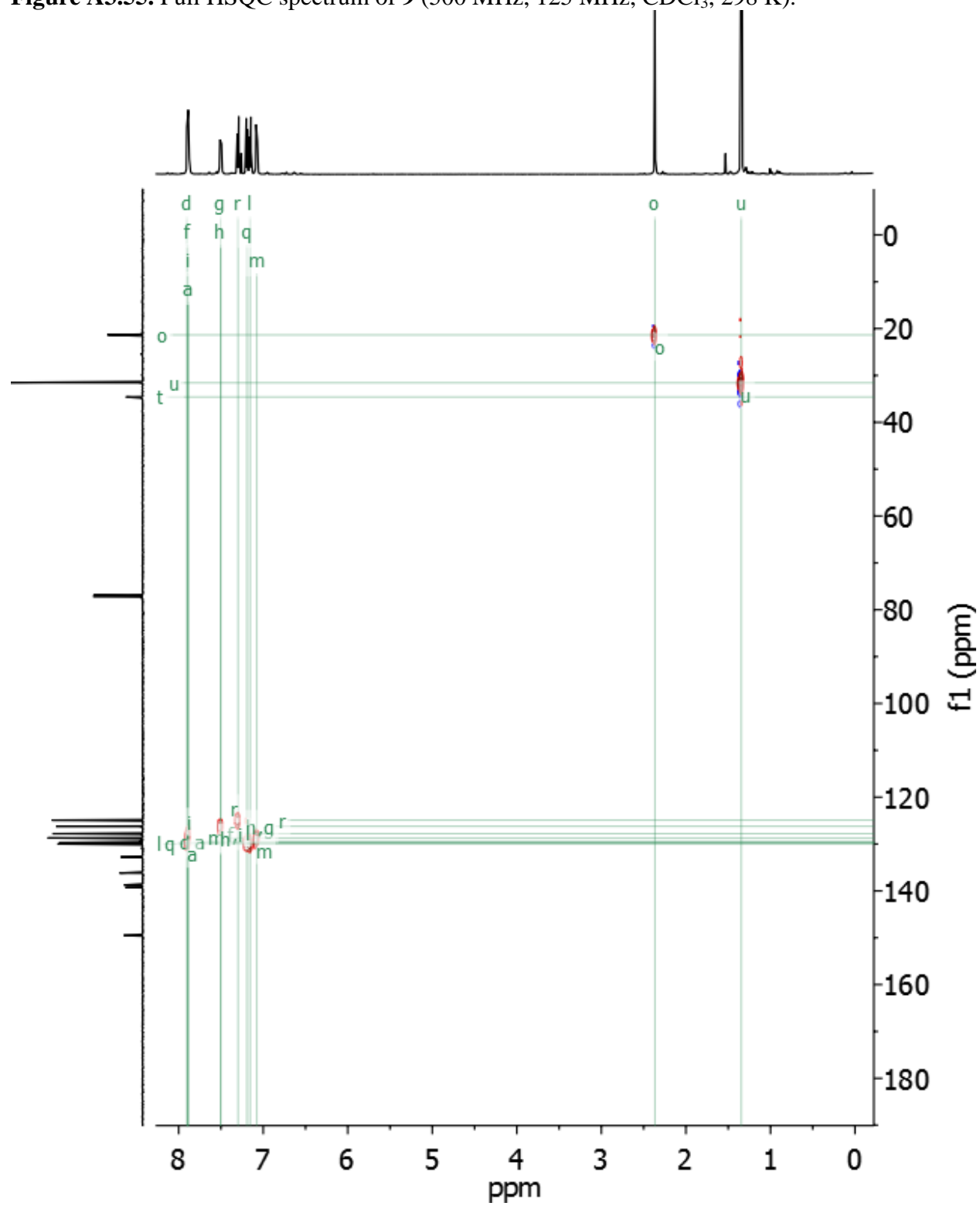
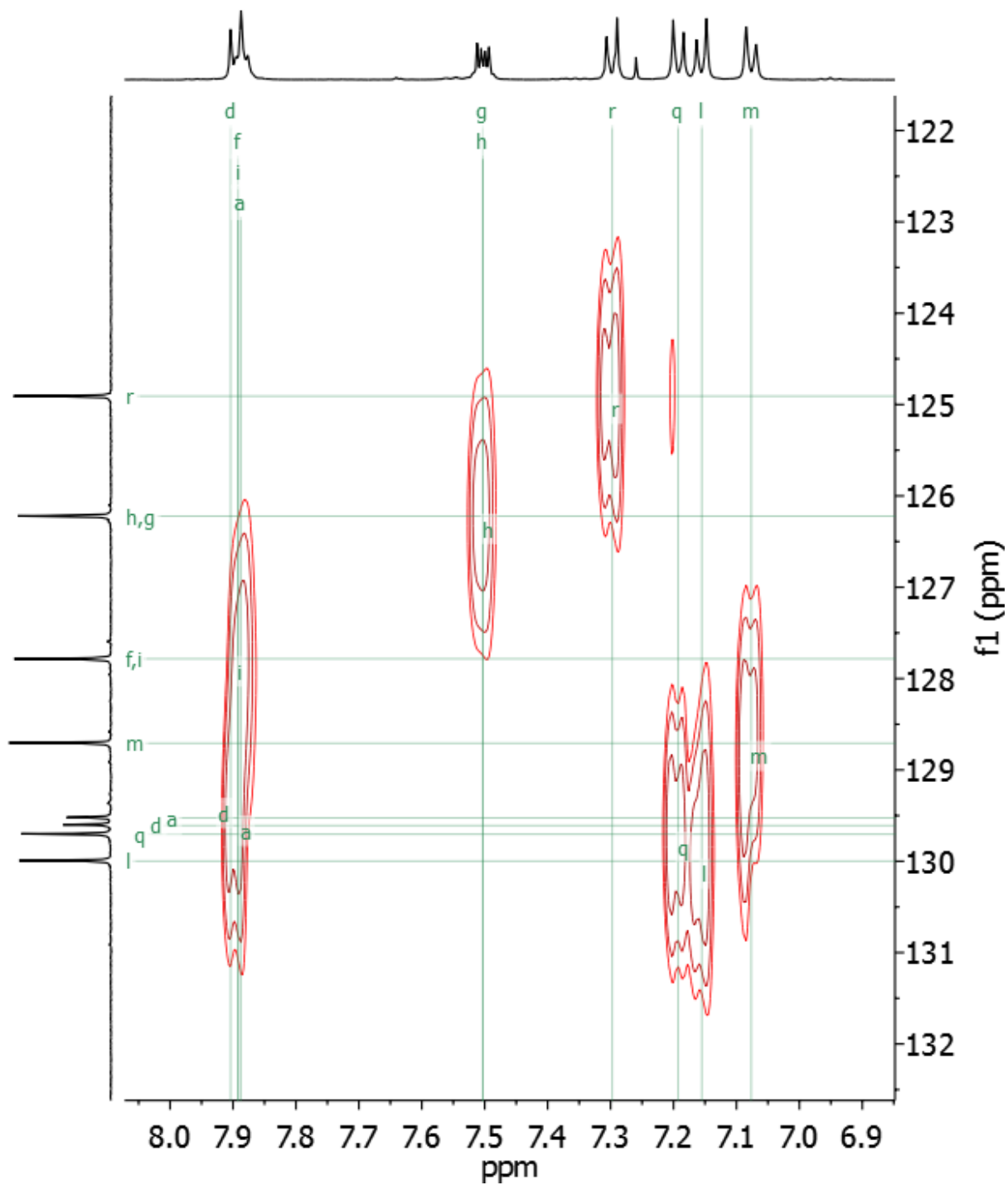


**Figure A3.56.** Partial HSQC spectrum of **9** showing the aromatic region (500 MHz, 125 MHz, CDCl<sub>3</sub>, 298 K).



Peak assignments for the compound 9c-F (blue) and 9d-F (green):

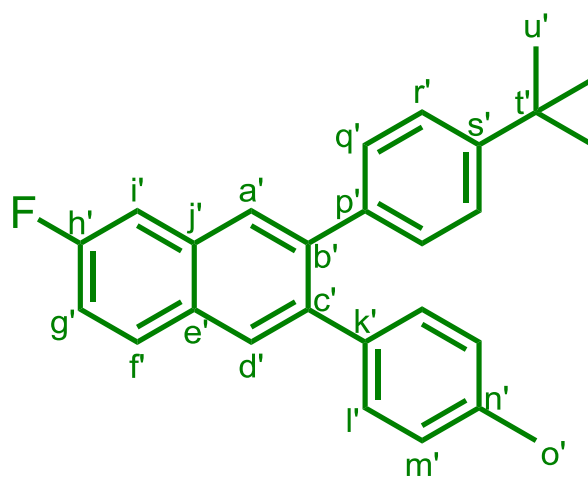
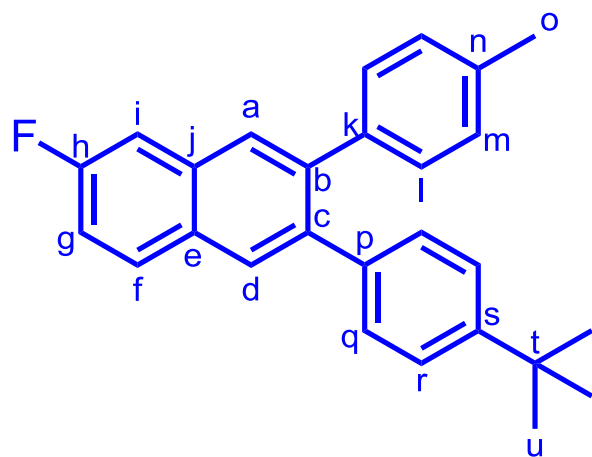




**Figure A3.57.** Full COSY spectrum of **9c-F** (blue) and **9d-F** (green) (500 MHz, 500 MHz, CDCl<sub>3</sub>, 298 K).

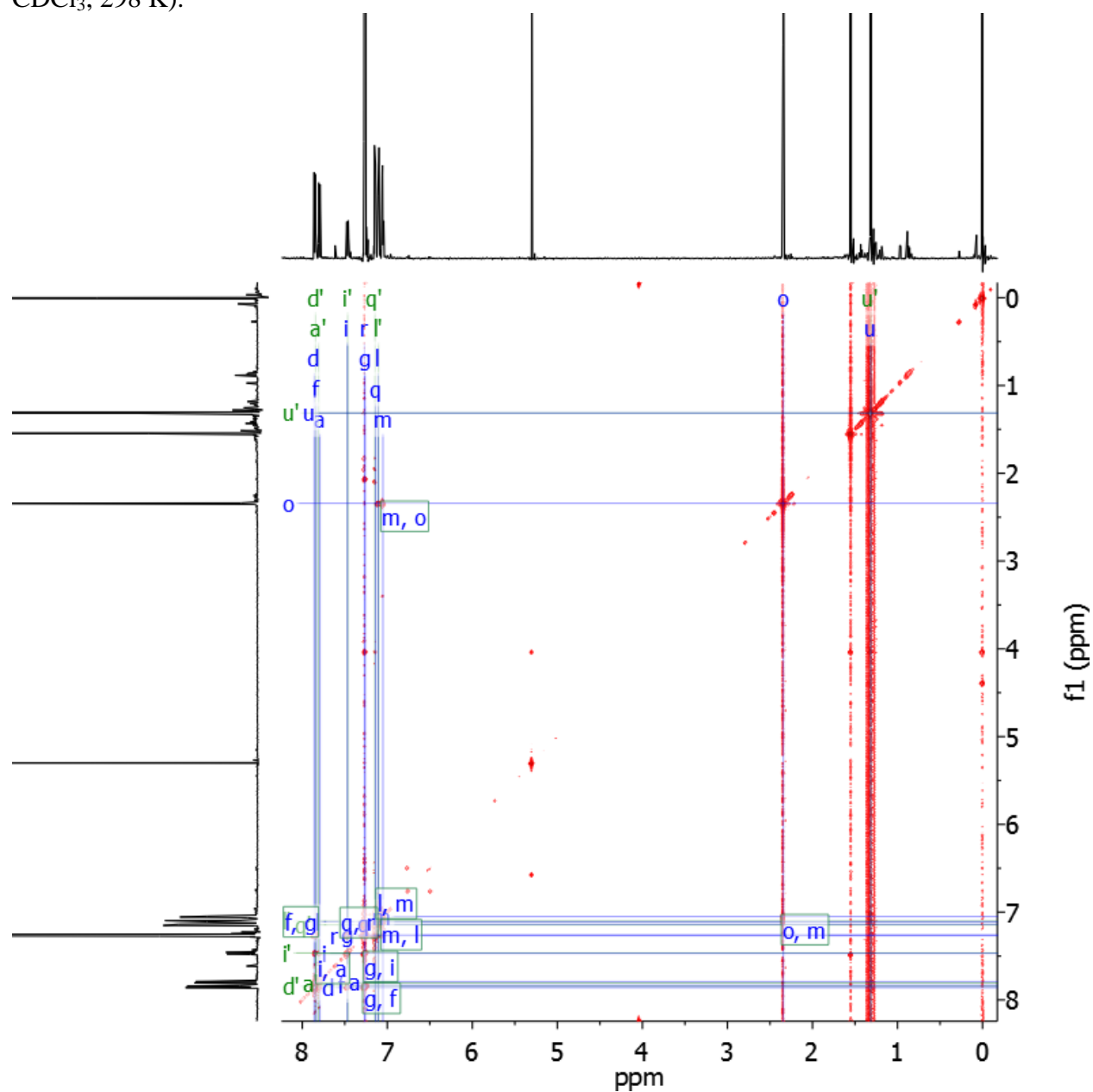


**Figure A3.58.** Partial COSY spectrum of **9c-F** (blue) and **9d-F** (green) showing the aromatic region (600 MHz, 600 MHz, CDCl<sub>3</sub>, 298 K).

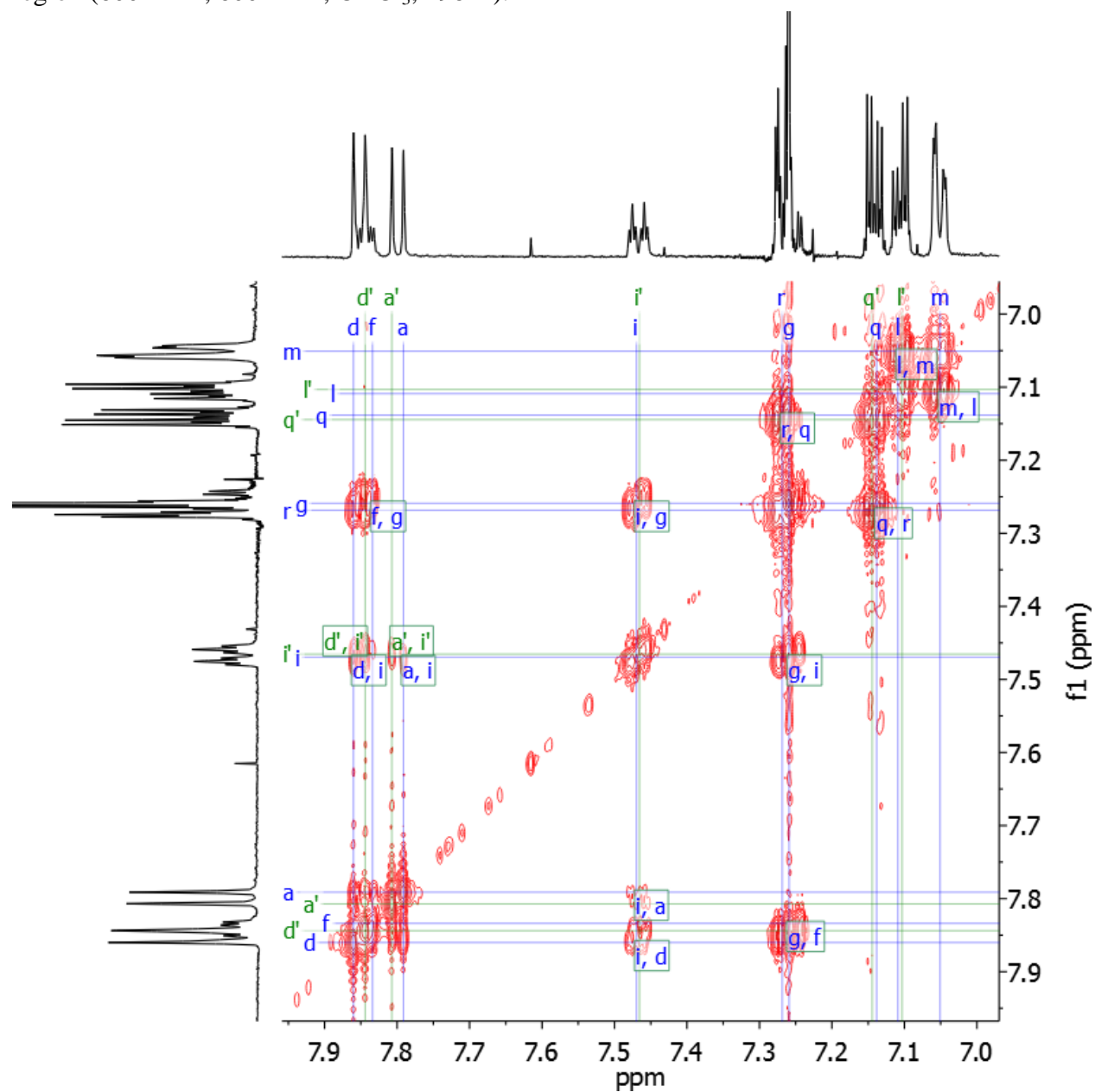


**Figure A3.59.** Full NOESY spectrum of **9c-F** (blue) and **9d-F** (green) (600 MHz, 600 MHz, CDCl<sub>3</sub>, 298 K).

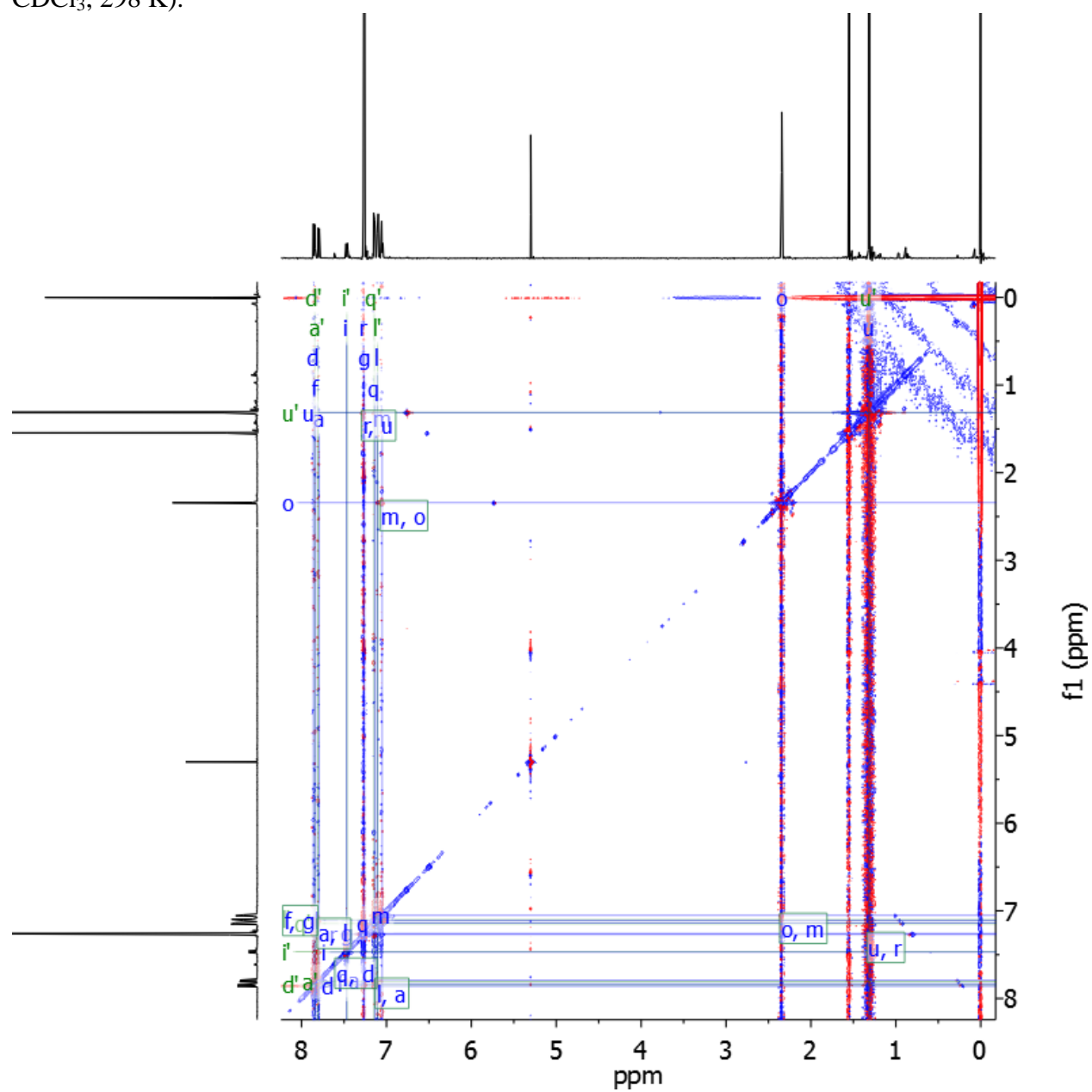


**Figure A3.60.** Partial NOESY spectrum of **9c-F** (blue) and **9d-F** (green) showing the aromatic region (600 MHz, 600 MHz, CDCl<sub>3</sub>, 298 K).

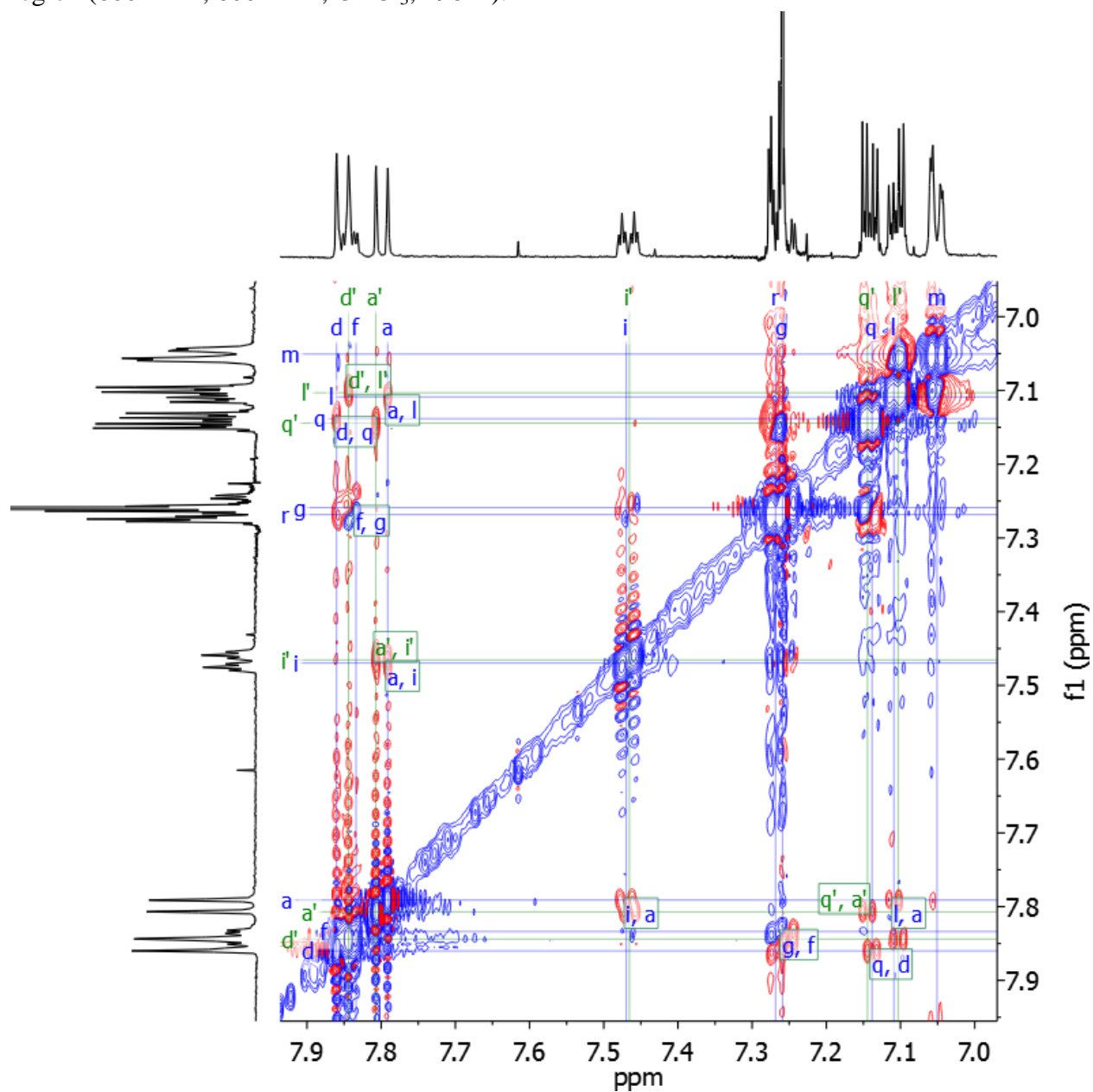


**Figure A3.61.** Full HSQC spectrum of **9c-F** (blue) and **9d-F** (green) (500 MHz, 125 MHz, CDCl<sub>3</sub>, 298 K).

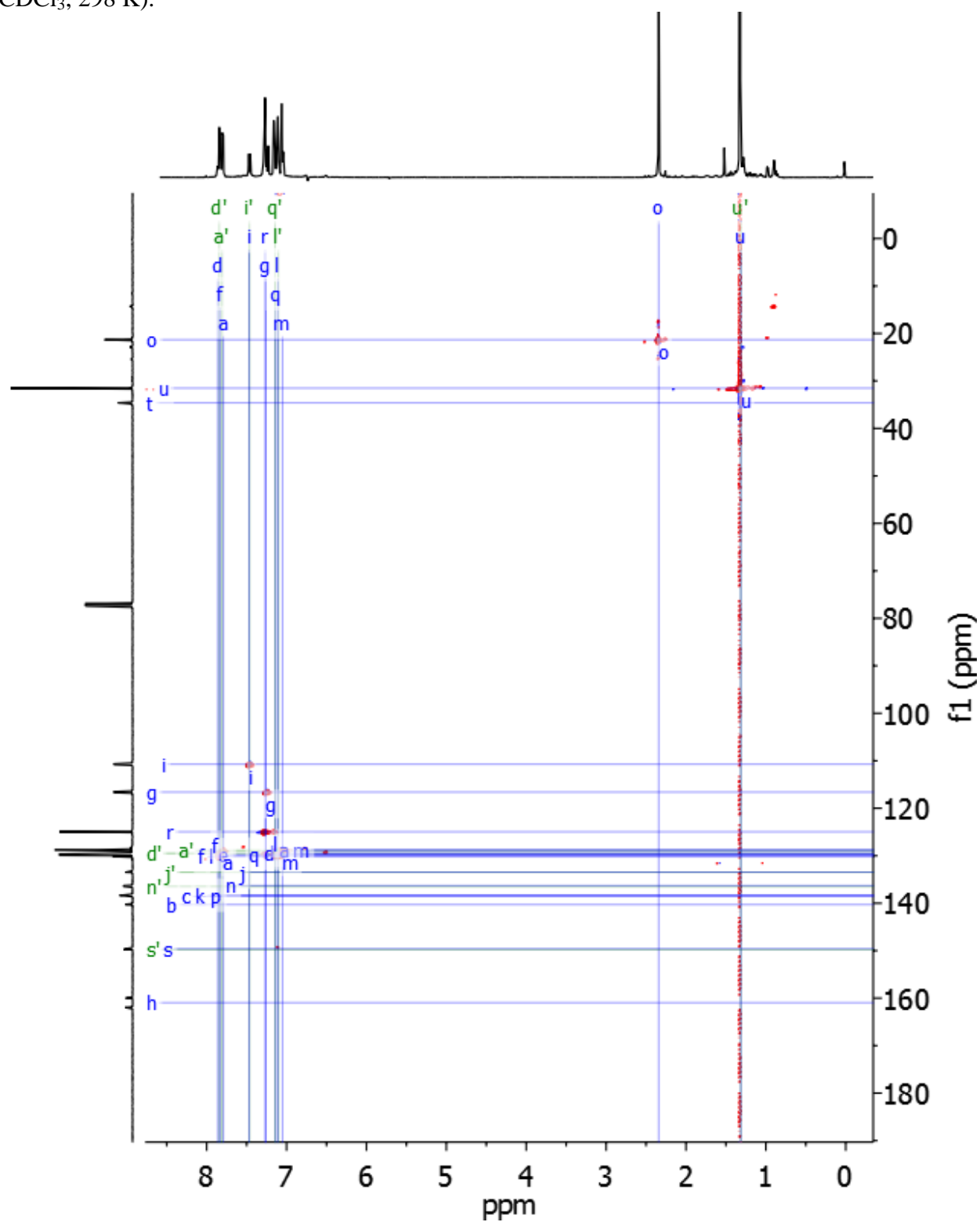


**Figure A3.62.** Partial HSQC spectrum of **9c-F** (blue) and **9d-F** (green) showing the aromatic region (500 MHz, 125 MHz, CDCl<sub>3</sub>, 298 K).

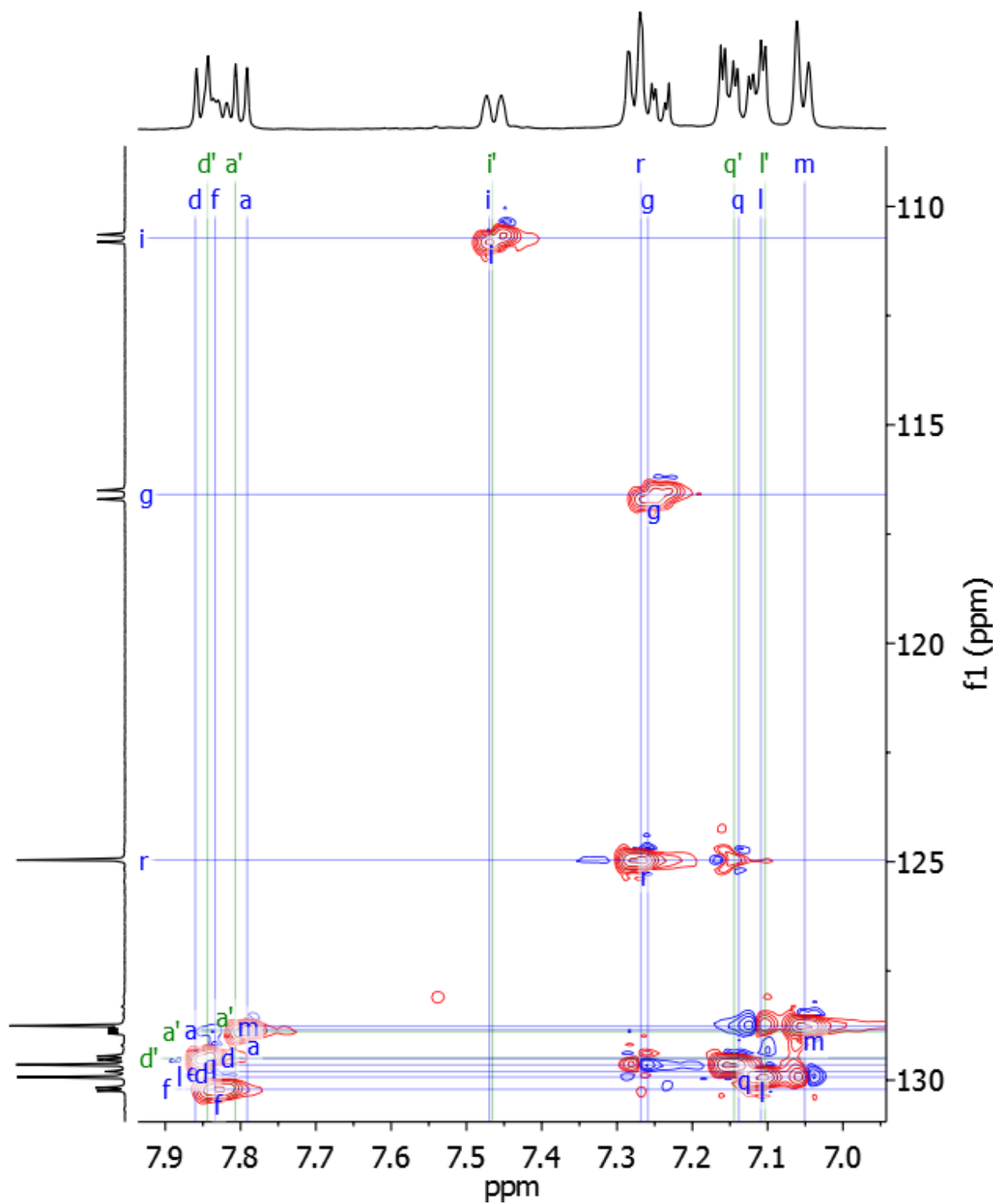


**Figure A3.63.** Full HMBC spectrum of **9c-F** (blue) and **9d-F** (green) (500 MHz, 125 MHz, CDCl<sub>3</sub>, 298 K).

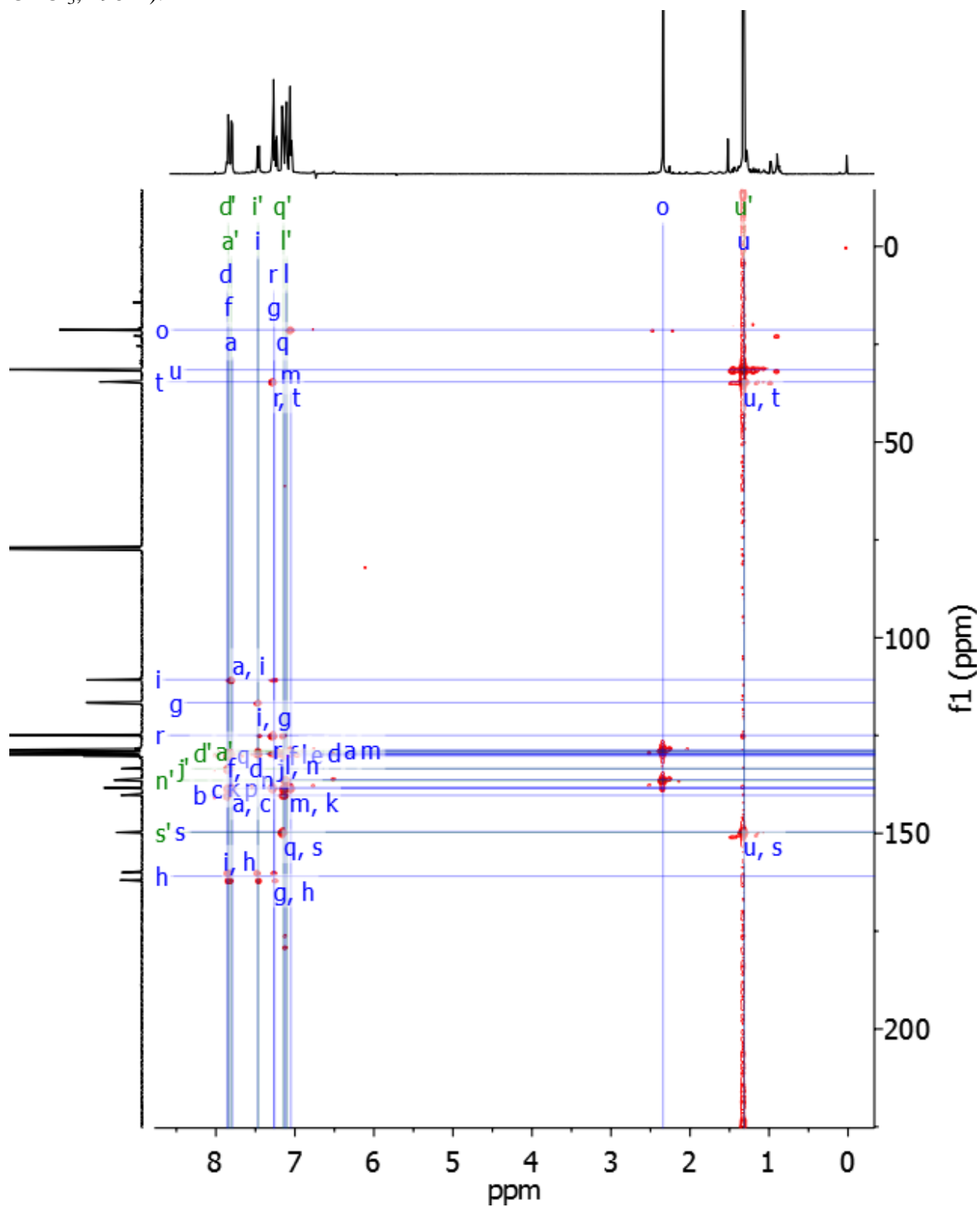
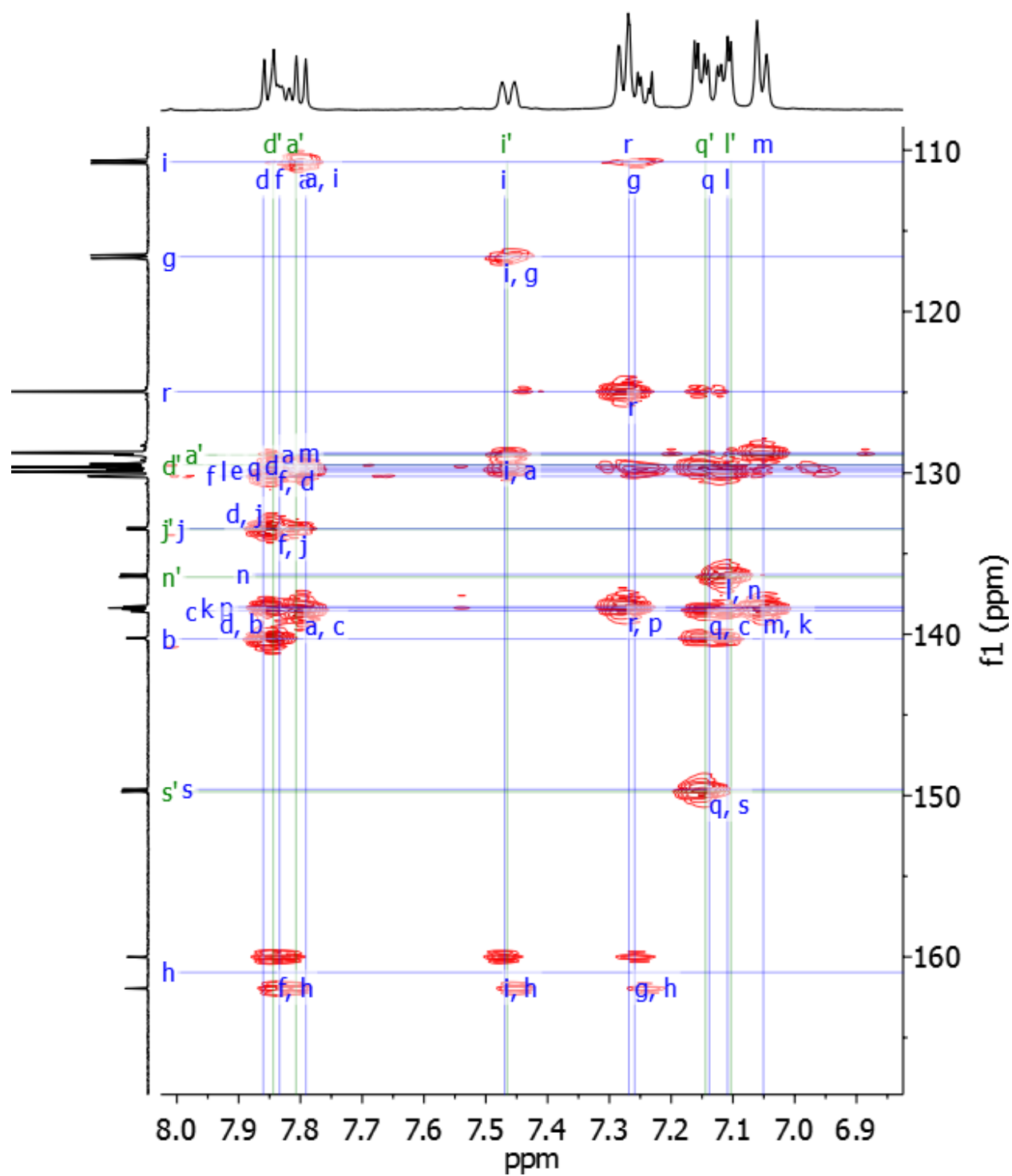


**Figure A3.64.** Partial HMBC spectrum of **9c-F** (blue) and **9d-F** (green) showing the aromatic region (500 MHz, 125 MHz, CDCl<sub>3</sub>, 298 K).





Peak assignments for the compound 10:

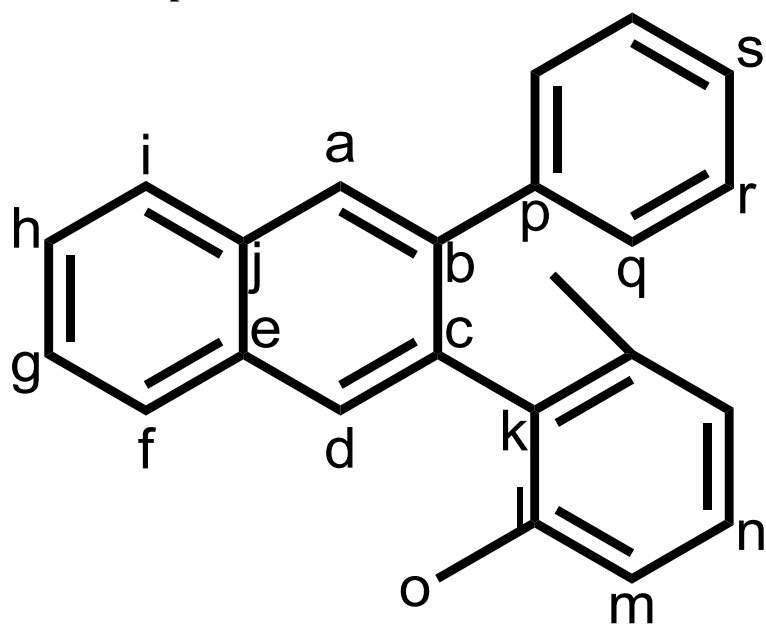


**Figure A3.65.** Full COSY spectrum of **10** (500 MHz, 500 MHz, CDCl<sub>3</sub>, 298 K).

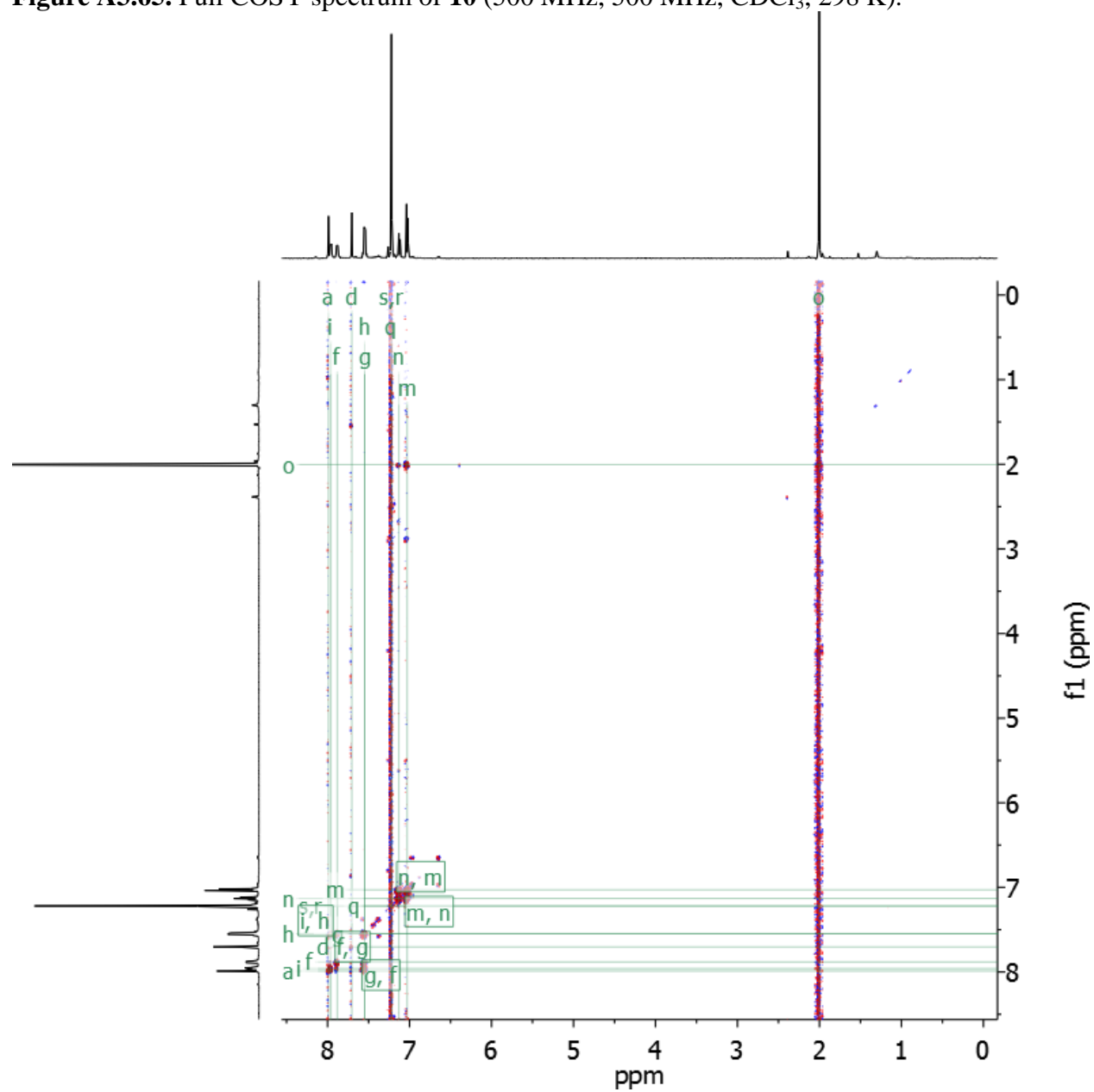


**Figure A3.66.** Partial COSY spectrum of **10** showing the aromatic region (500 MHz, 500 MHz, CDCl<sub>3</sub>, 298 K).

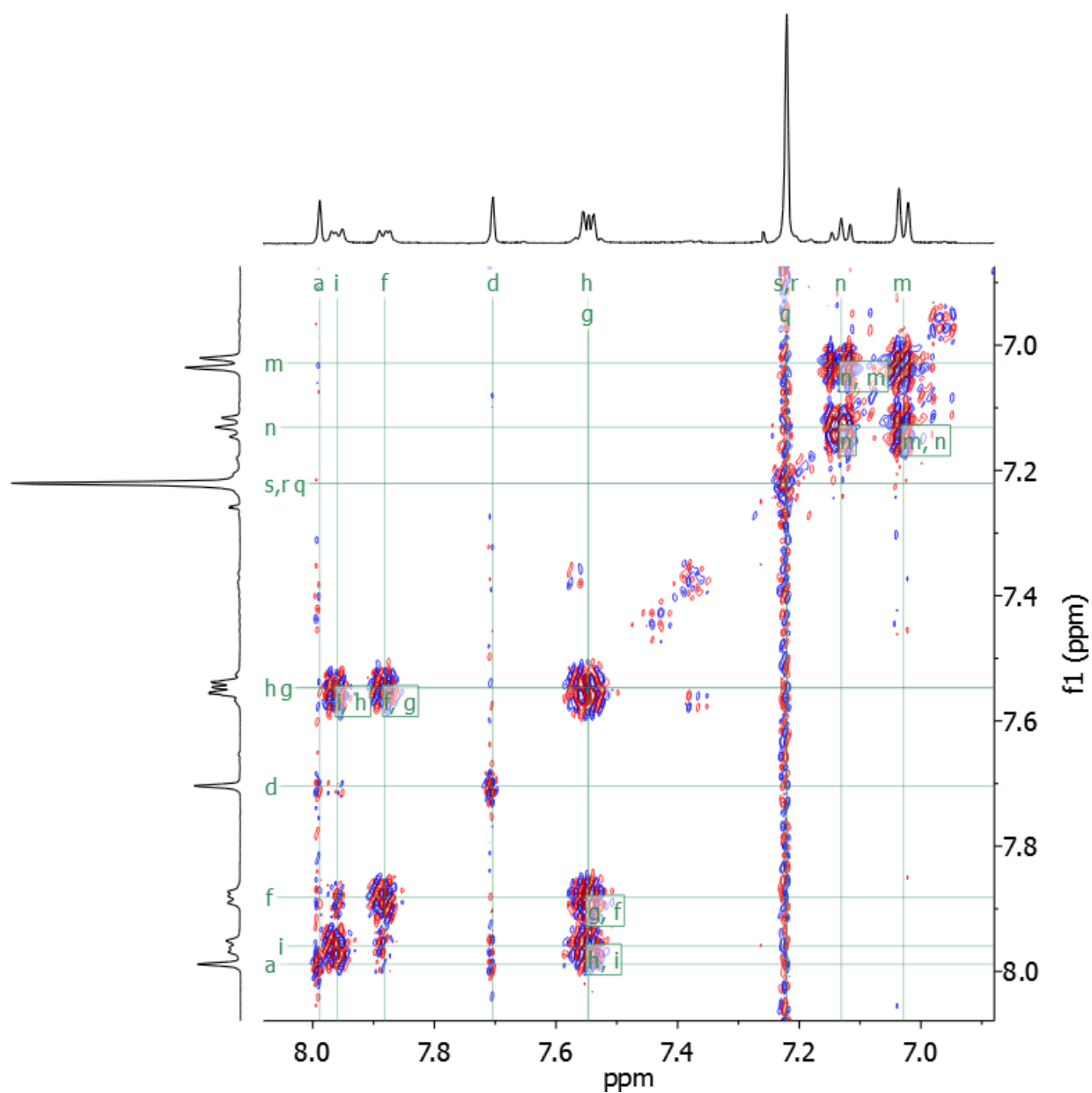


**Figure A3.67.** Full ROESY spectrum of **10** (500 MHz, 500 MHz, CDCl<sub>3</sub>, 298 K).

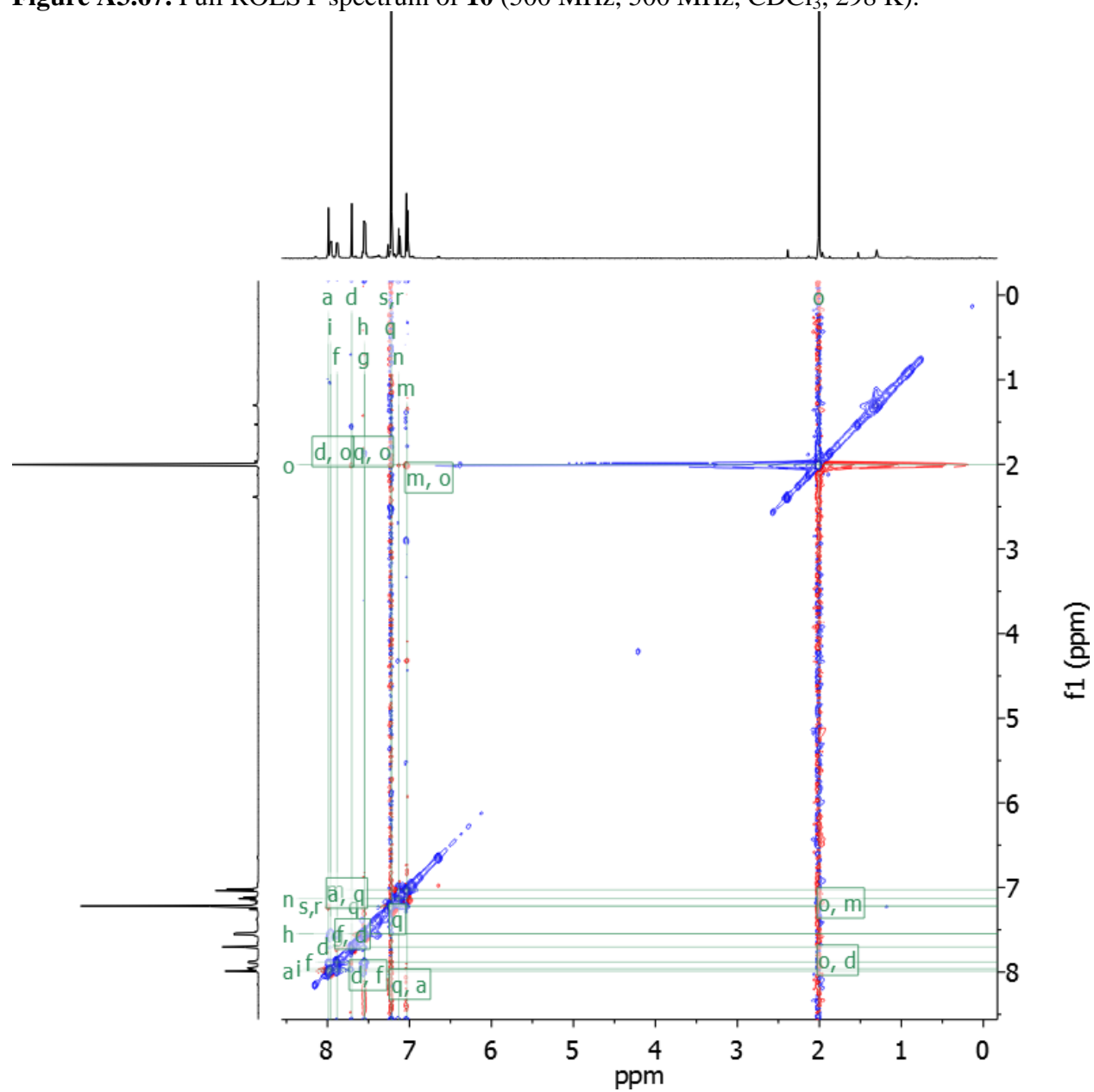


**Figure A3.68.** Partial ROESY spectrum of **10** showing the aromatic region (500 MHz, 500 MHz, CDCl<sub>3</sub>, 298 K).

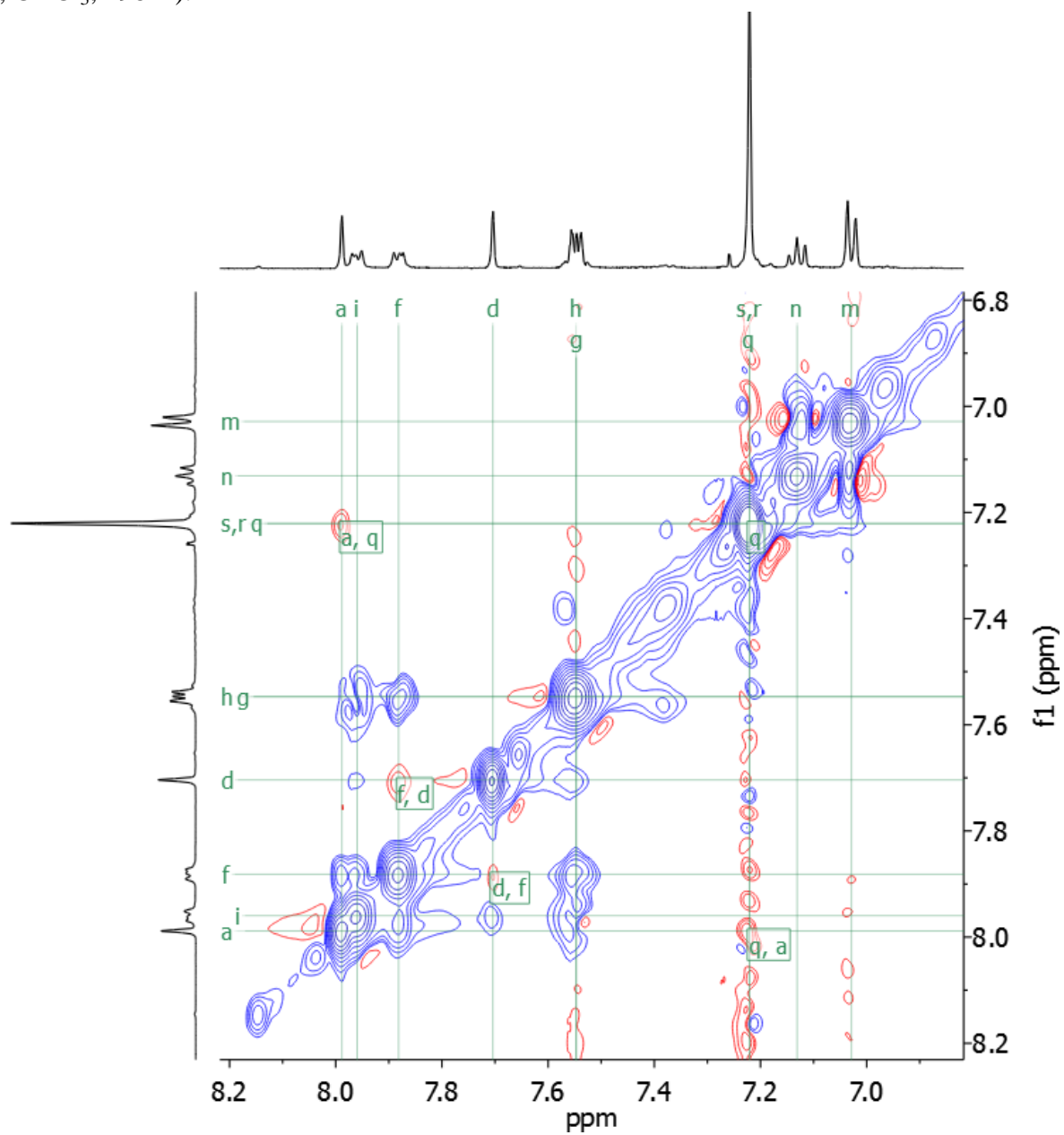


**Figure A3.69.** Full HSQC spectrum of **10** (500 MHz, 125 MHz, CDCl<sub>3</sub>, 298 K).

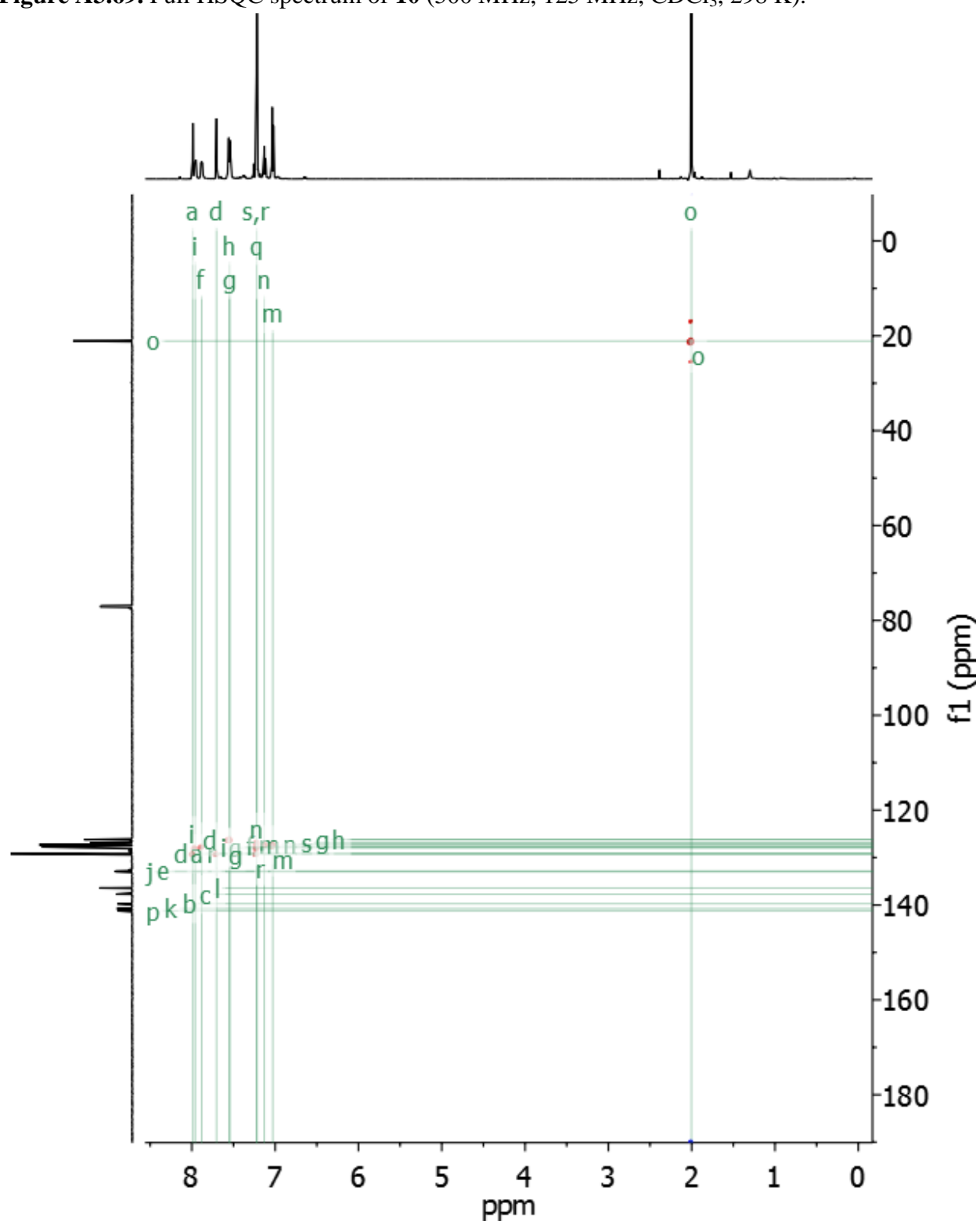


**Figure A3.70.** Partial HSQC spectrum of **10** showing the aromatic region (500 MHz, 125 MHz, CDCl<sub>3</sub>, 298 K).

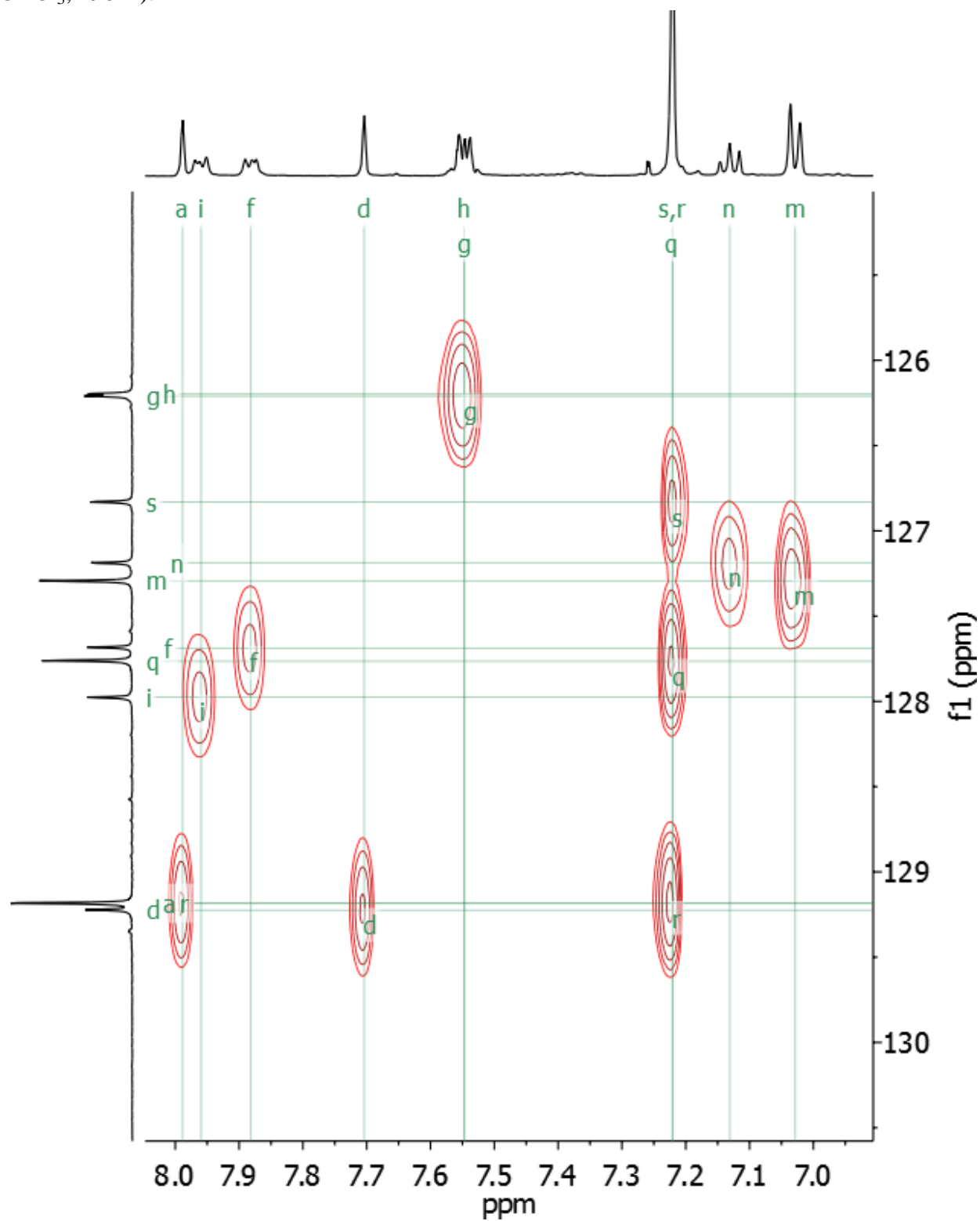


**Figure A3.71.** Full HMBC spectrum of **10** (500 MHz, 125 MHz, CDCl<sub>3</sub>, 298 K).

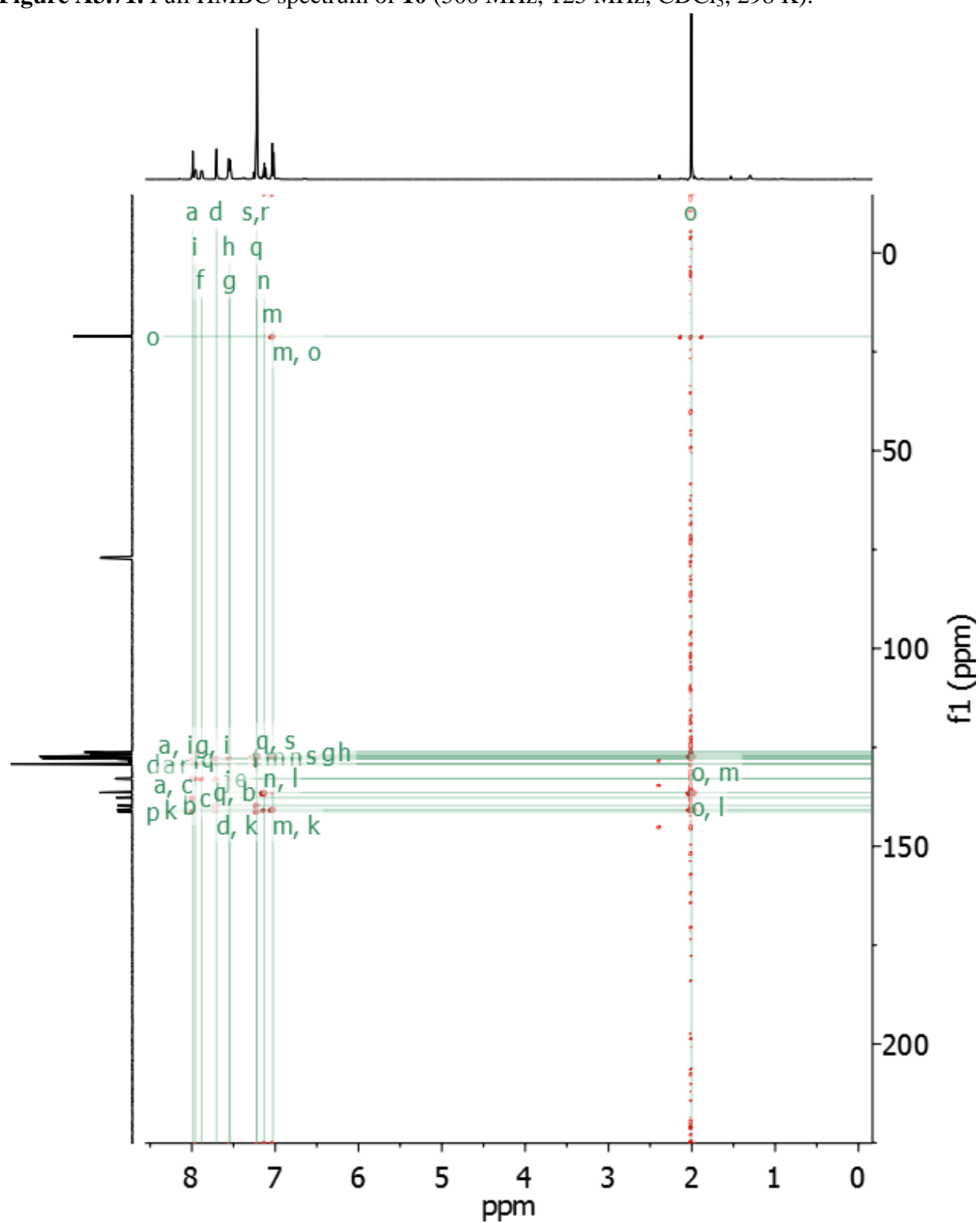
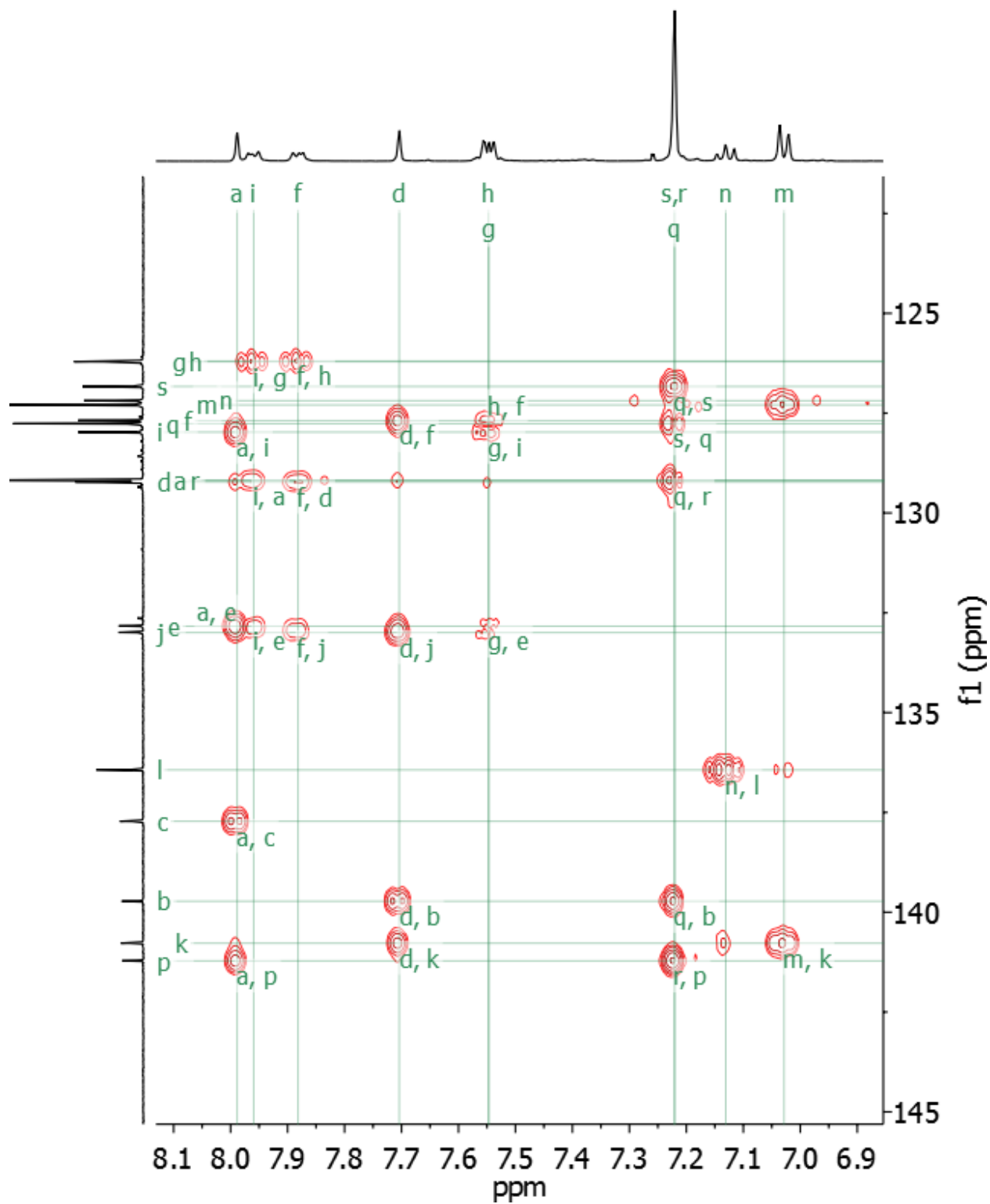




**Figure A3.72.** Partial HMBC spectrum of **10** showing the aromatic region (500 MHz, 125 MHz, CDCl<sub>3</sub>, 298 K).



Peak assignments for the compound 10c-F:

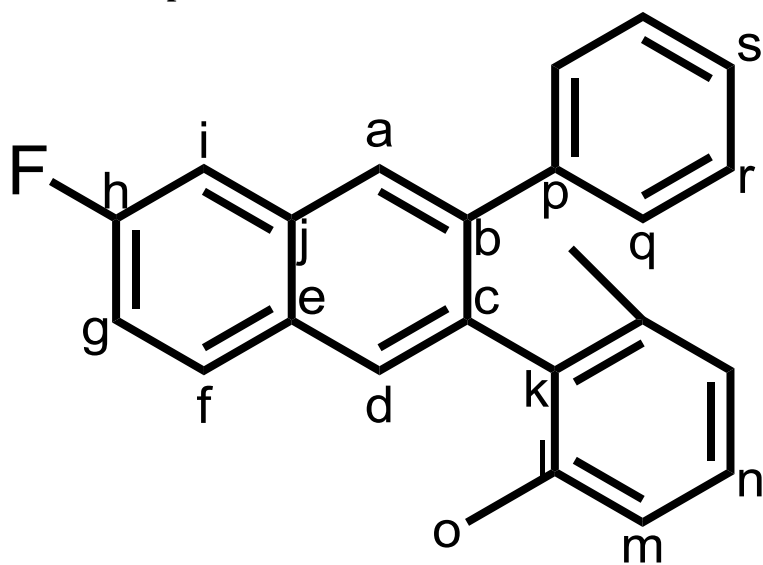


**Figure A3.73.** Full COSY spectrum of **10c-F** (500 MHz, 500 MHz, CDCl<sub>3</sub>, 298 K).

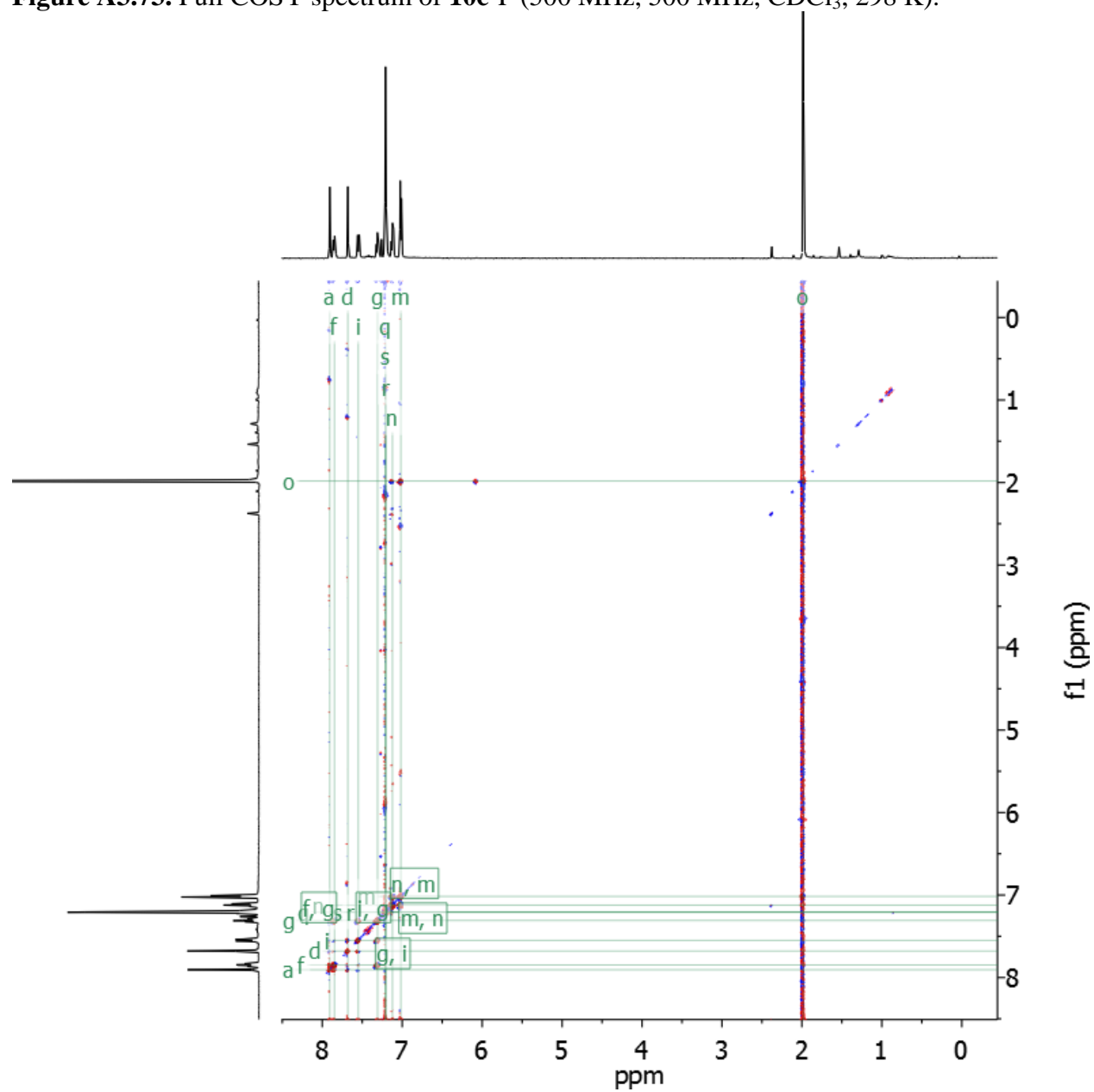


**Figure A3.74.** Partial COSY spectrum of **10c-F** showing the aromatic region (500 MHz, 500 MHz, CDCl<sub>3</sub>, 298 K).

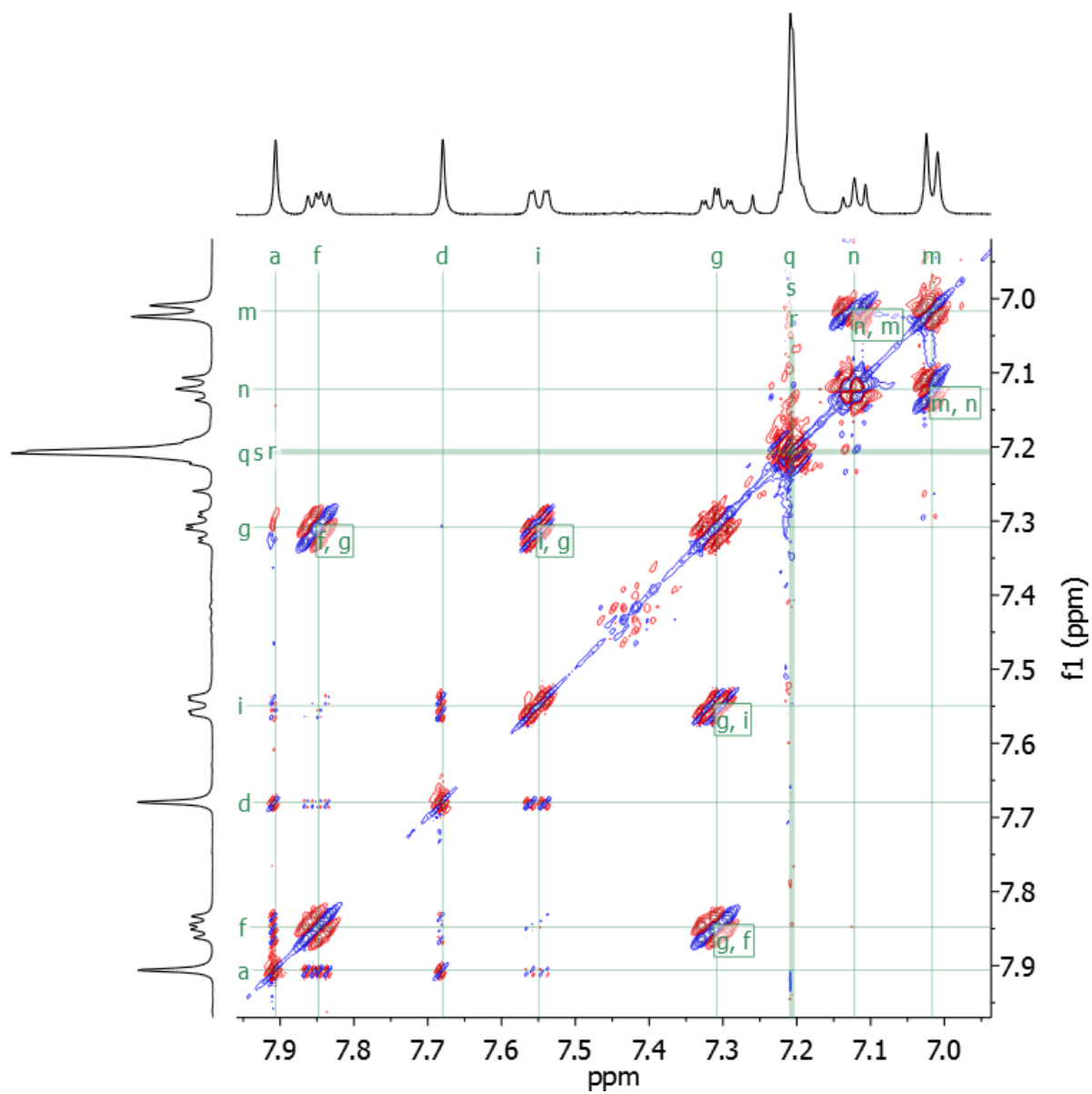


**Figure A3.75.** Full ROESY spectrum of **10c-F** (500 MHz, 500 MHz, CDCl<sub>3</sub>, 298 K).

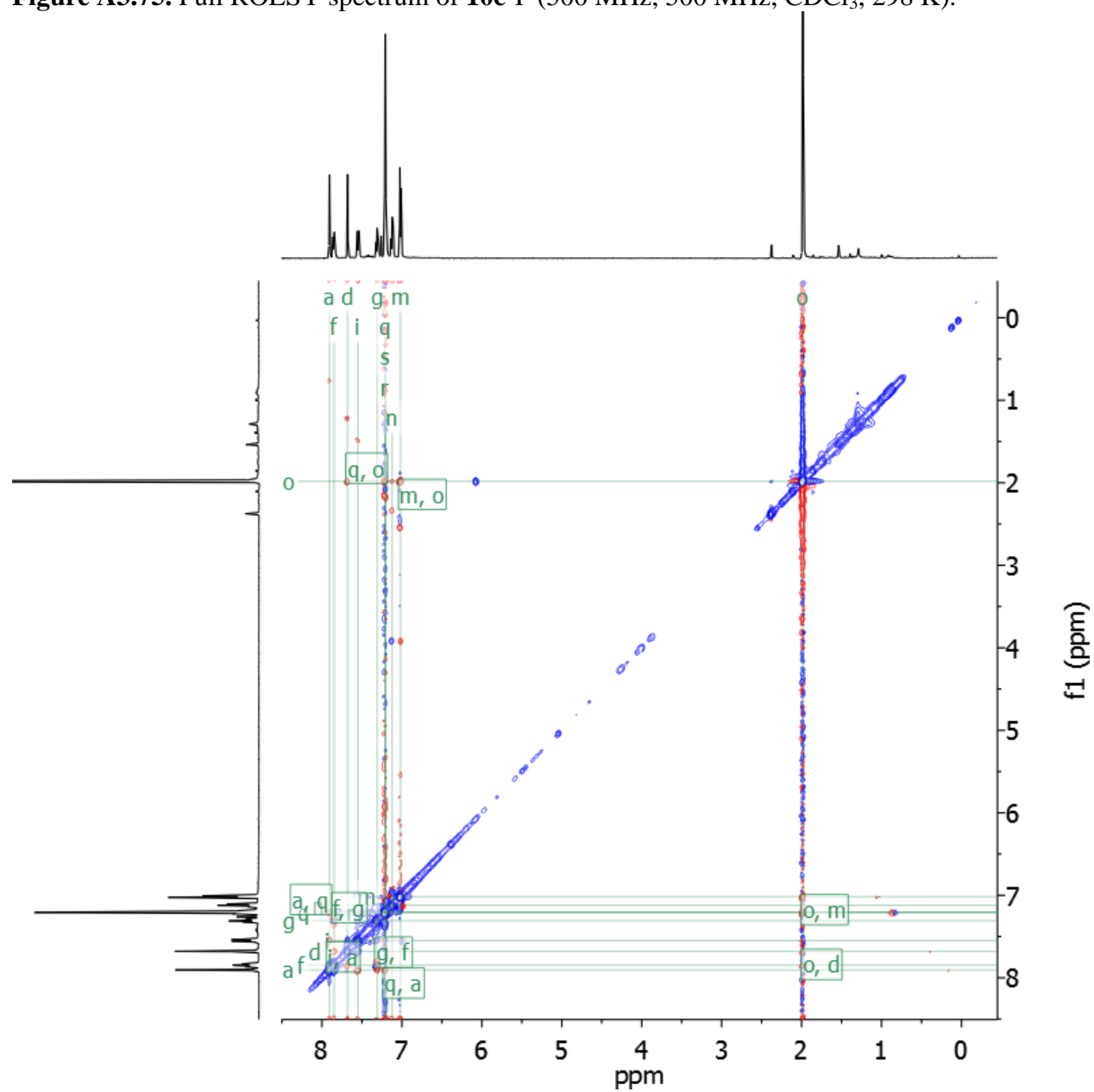


**Figure A3.76.** Partial ROESY spectrum of **10c-F** showing the aromatic region (500 MHz, 500 MHz, CDCl<sub>3</sub>, 298 K).

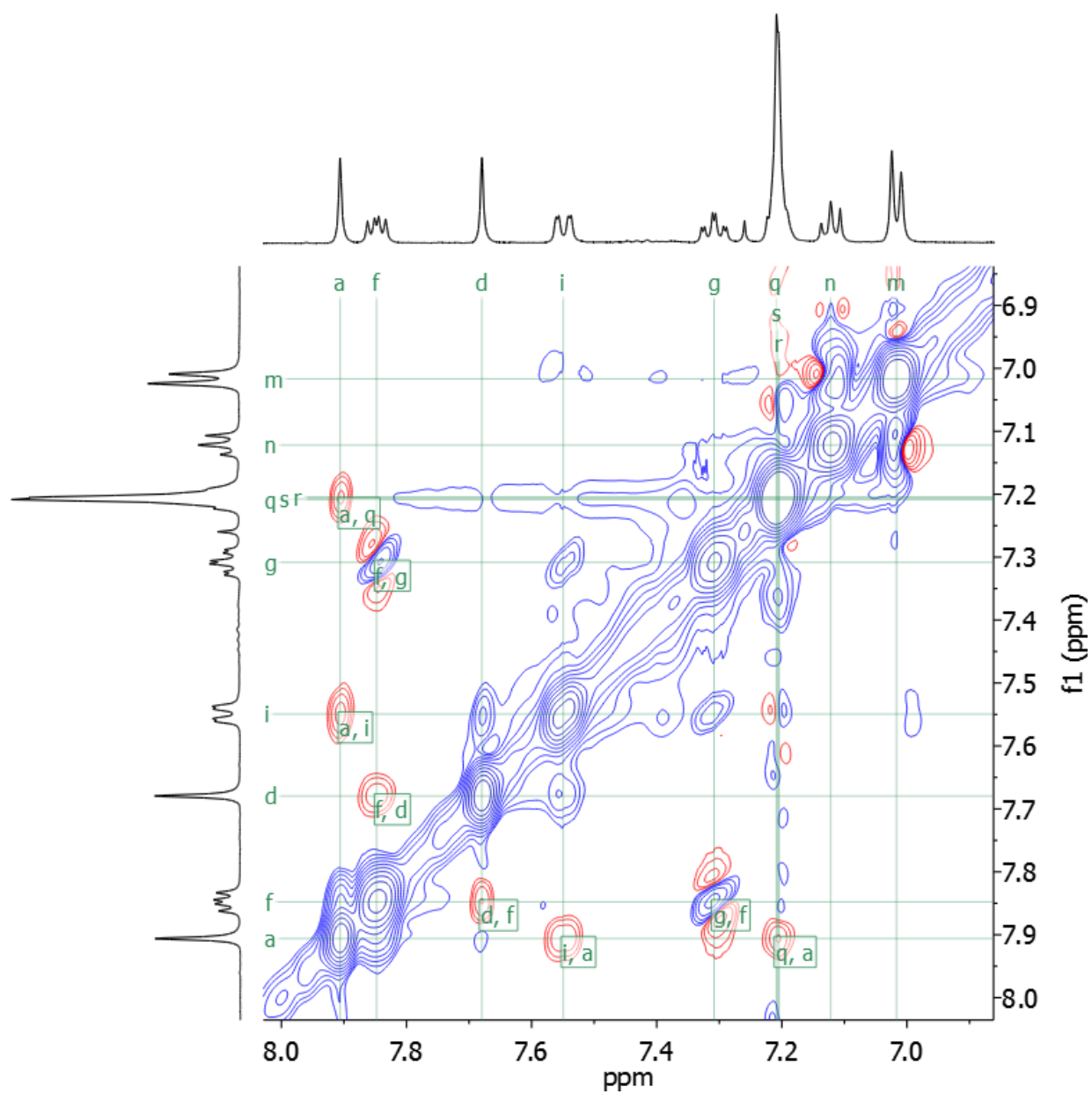


**Figure A3.77.** Full HSQC spectrum of **10c-F** (500 MHz, 125 MHz, CDCl<sub>3</sub>, 298 K).

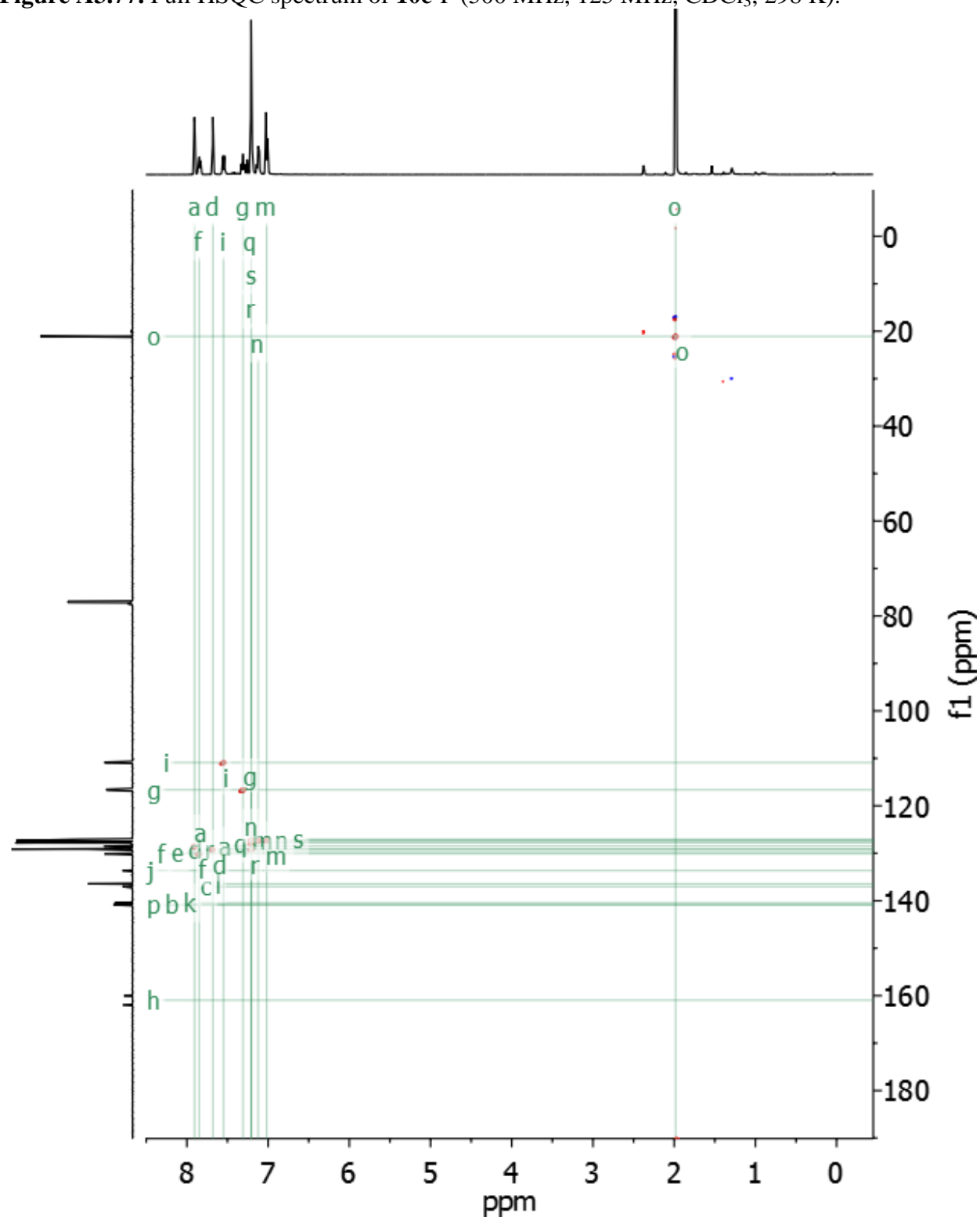


**Figure A3.78.** Partial HSQC spectrum of **10c-F** showing the aromatic region (500 MHz, 125 MHz, CDCl<sub>3</sub>, 298 K).

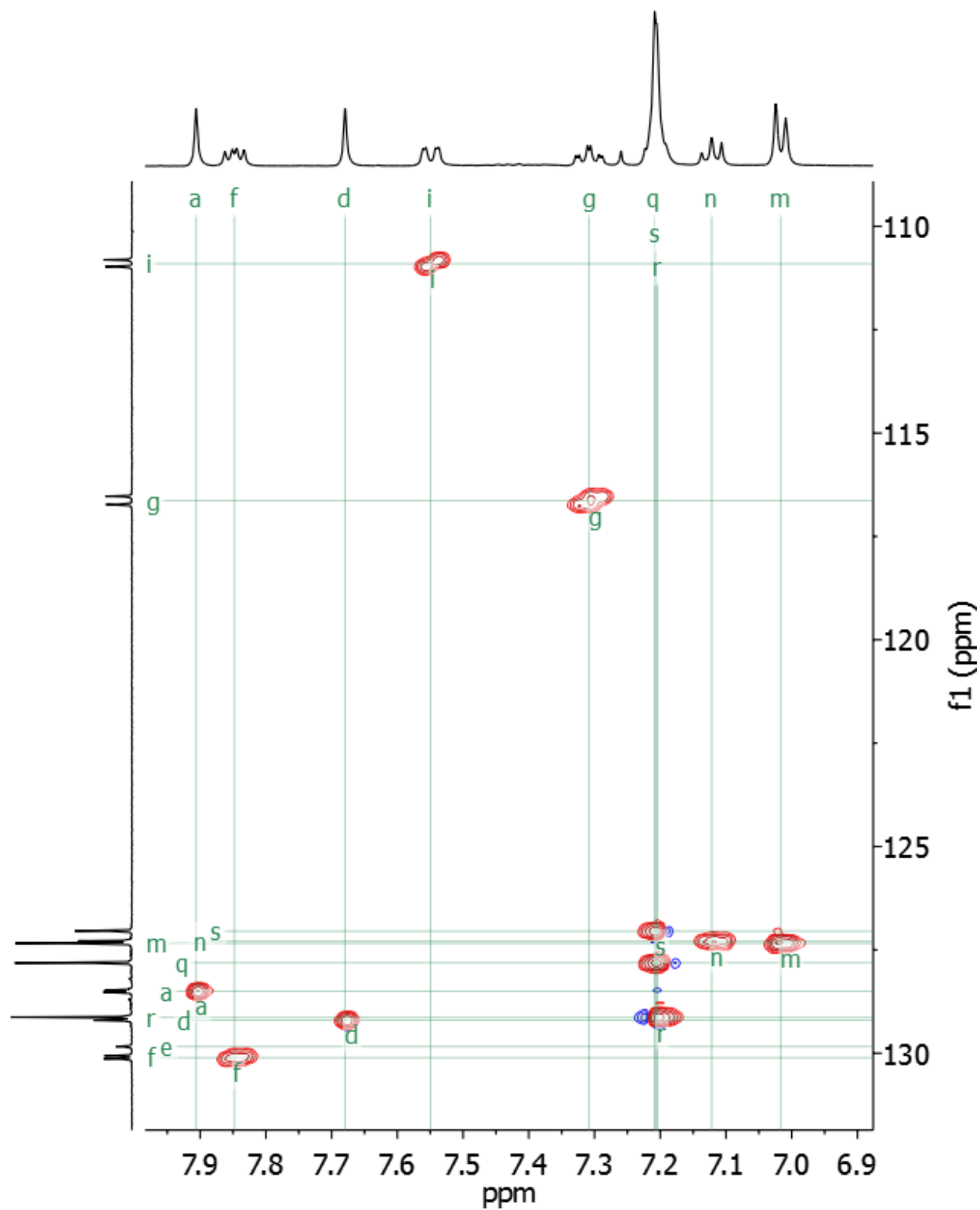




**Figure A3.79.** Full HMBC spectrum of **10c-F** (500 MHz, 125 MHz, CDCl<sub>3</sub>, 298 K).

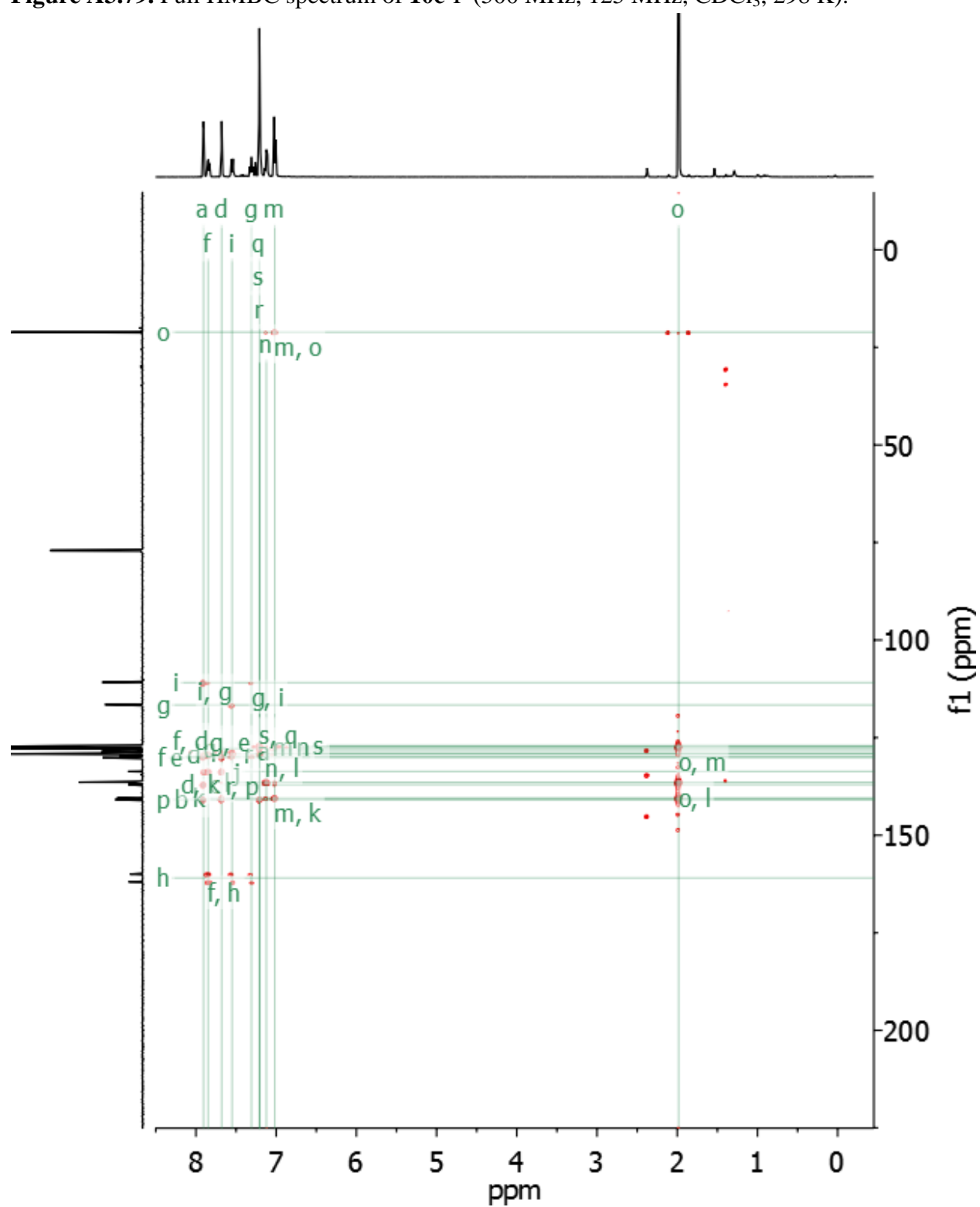
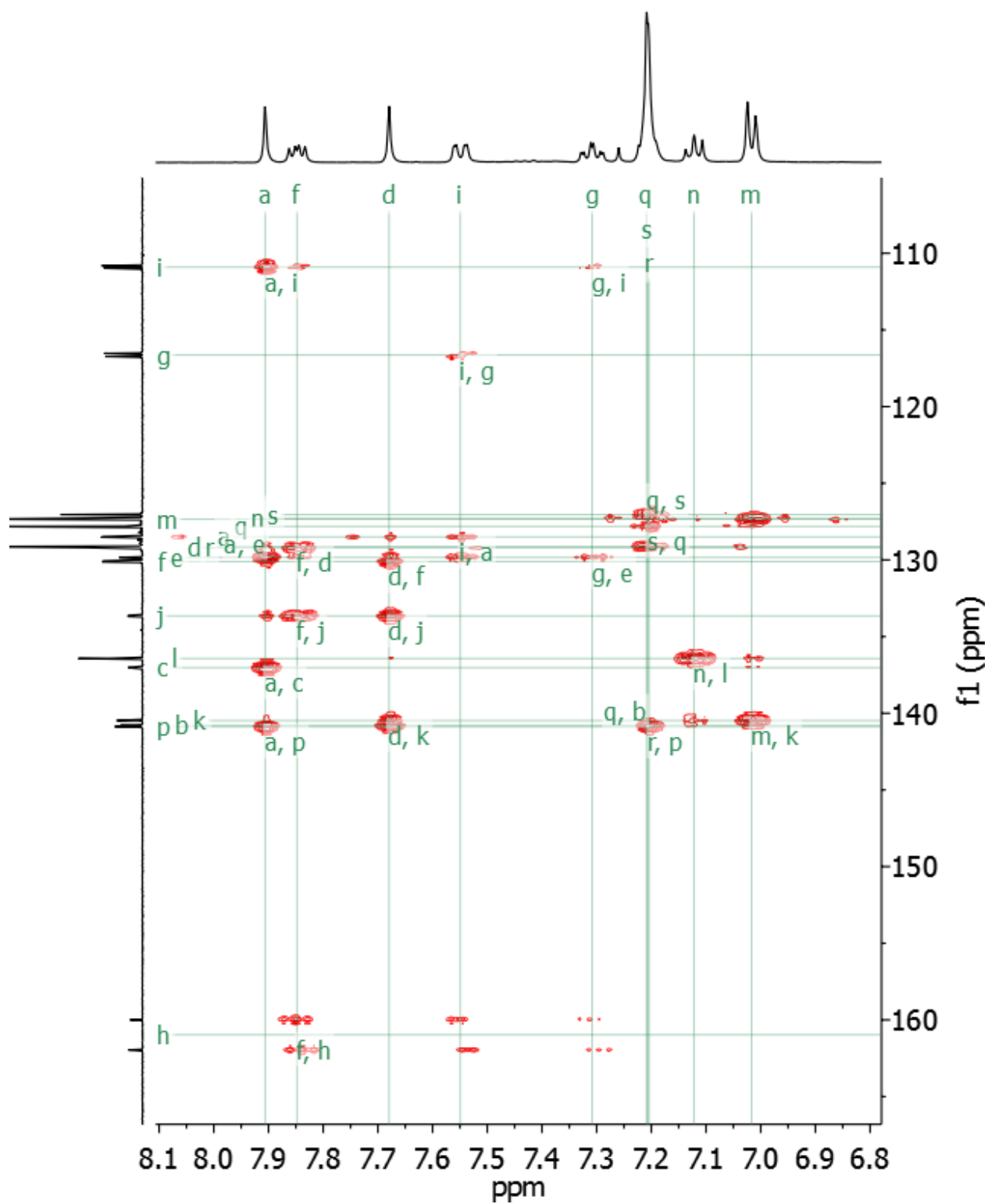


**Figure A3.80.** Partial HMBC spectrum of **10c-F** showing the aromatic region (500 MHz, 125 MHz, CDCl<sub>3</sub>, 298 K).



Peak assignments for the compound 11d-F:

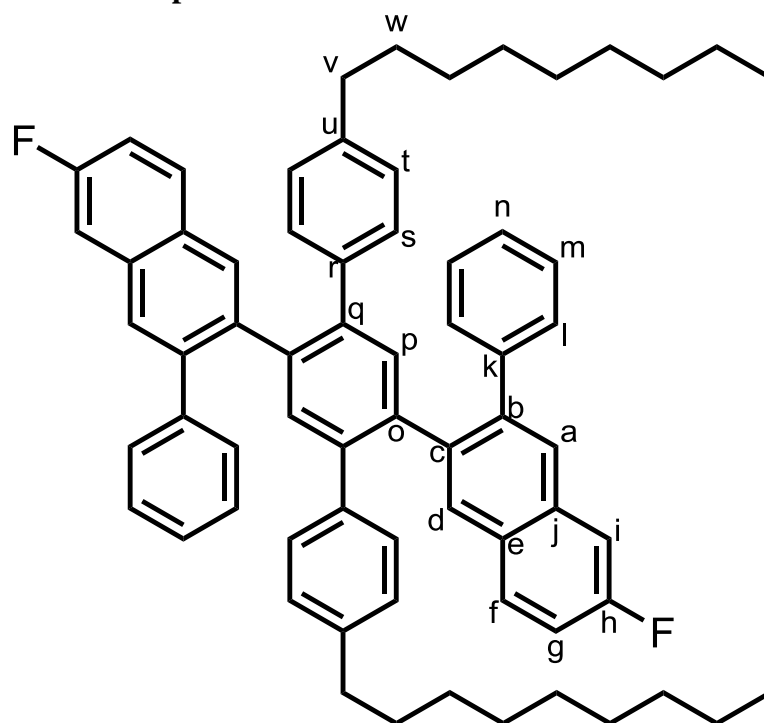


**Figure A3.81.** Full COSY spectrum of **11d-F** (500 MHz, 500 MHz, CDCl<sub>3</sub>, 298 K).

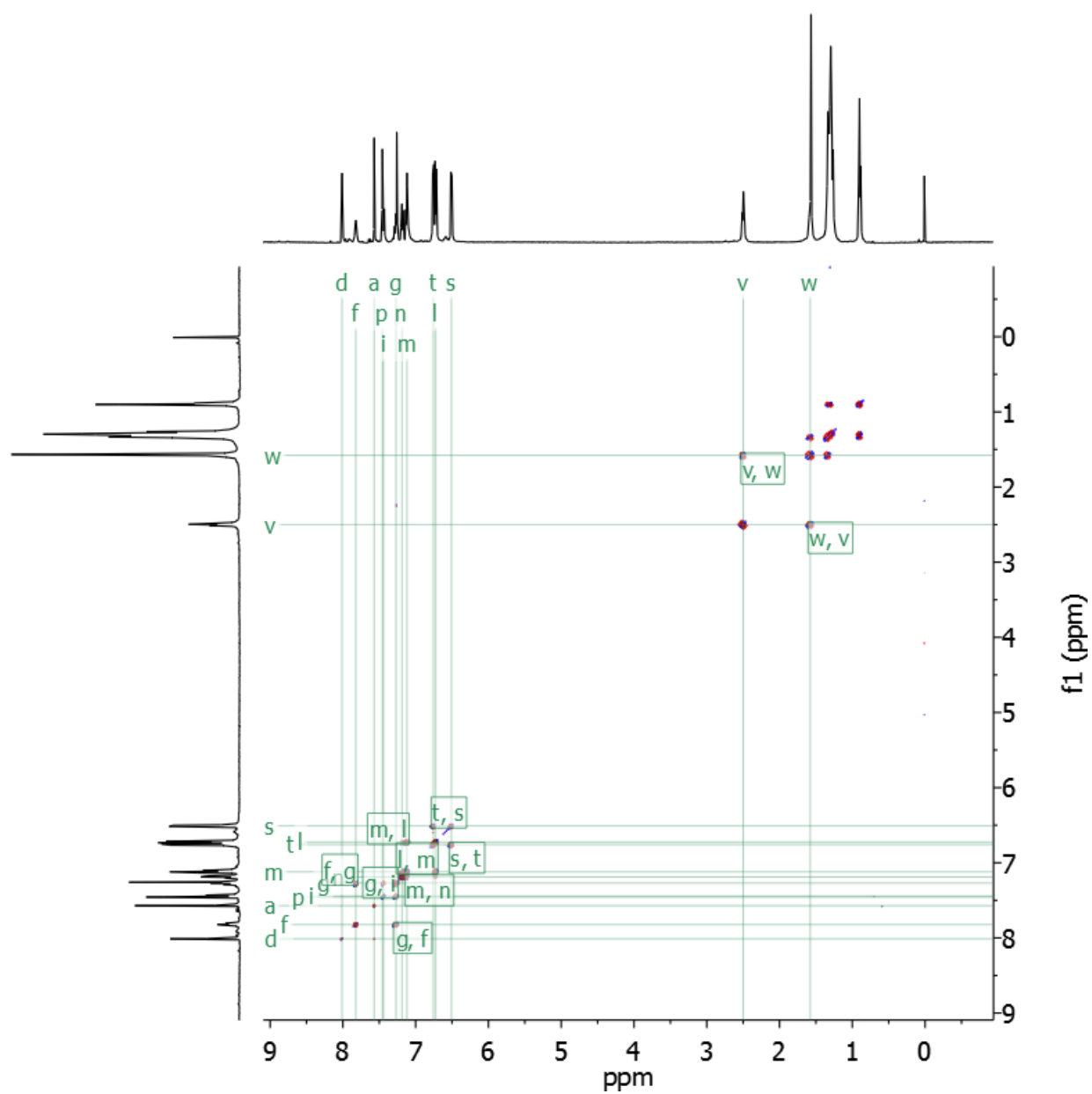


**Figure A3.82.** Partial COSY spectrum of **11d-F** showing the aromatic region (500 MHz, 500 MHz, CDCl<sub>3</sub>, 298 K).

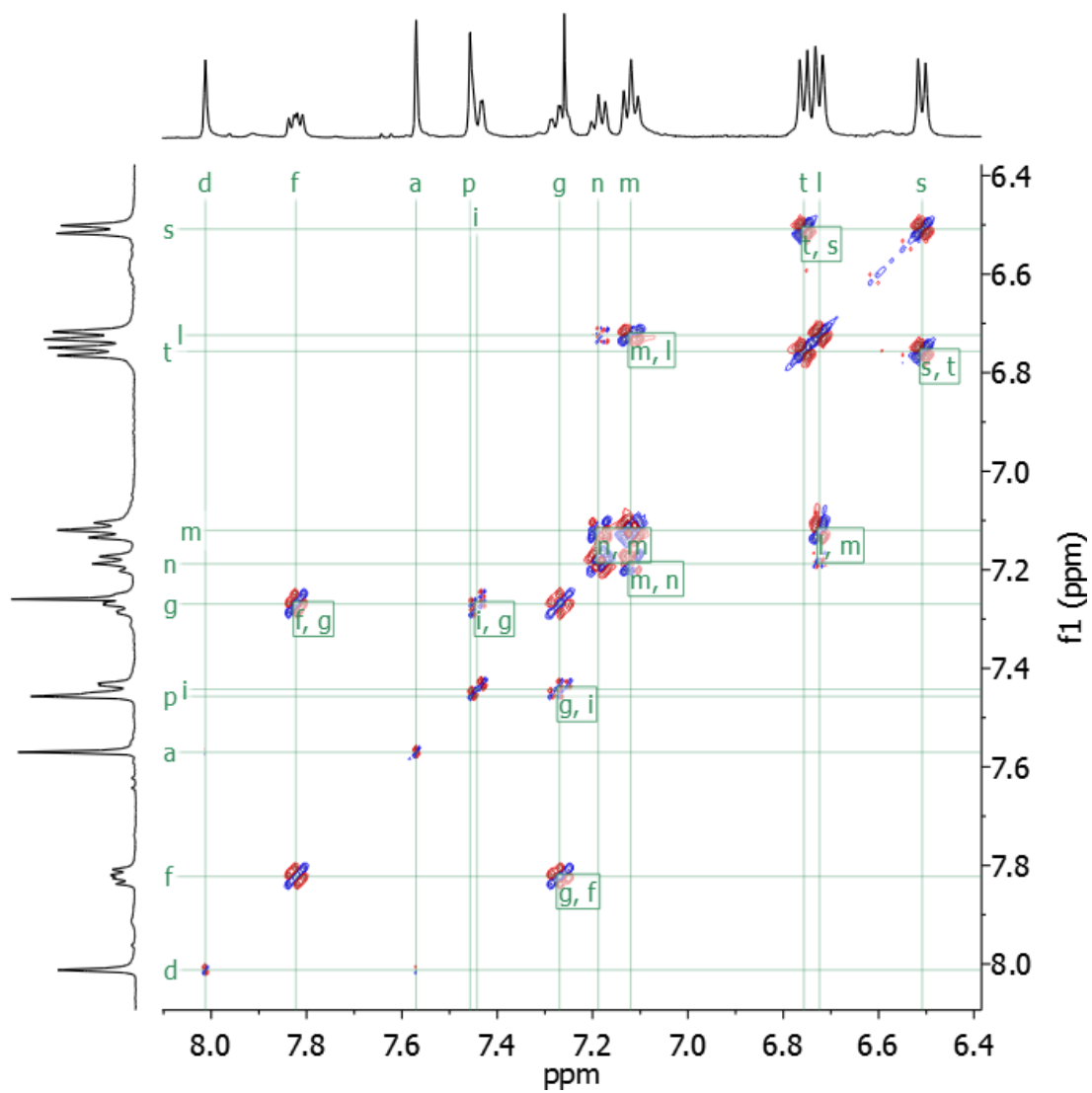


**Figure A3.83.** Full ROESY spectrum of **11d-F** (500 MHz, 500 MHz, CDCl<sub>3</sub>, 298 K).

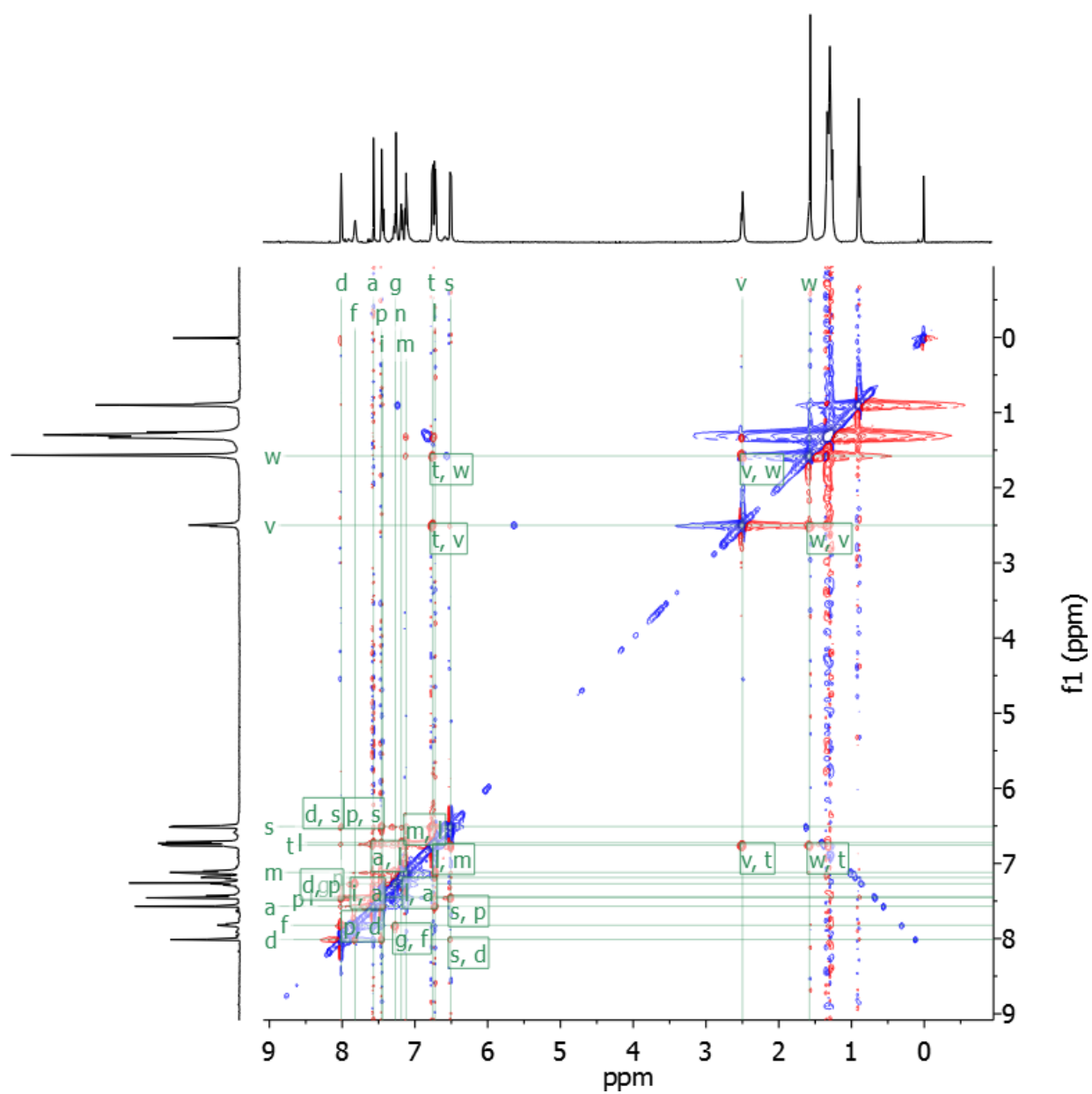


**Figure A3.84.** Partial ROESY spectrum of **11d-F** showing the aromatic region (500 MHz, 500 MHz, CDCl<sub>3</sub>, 298 K).

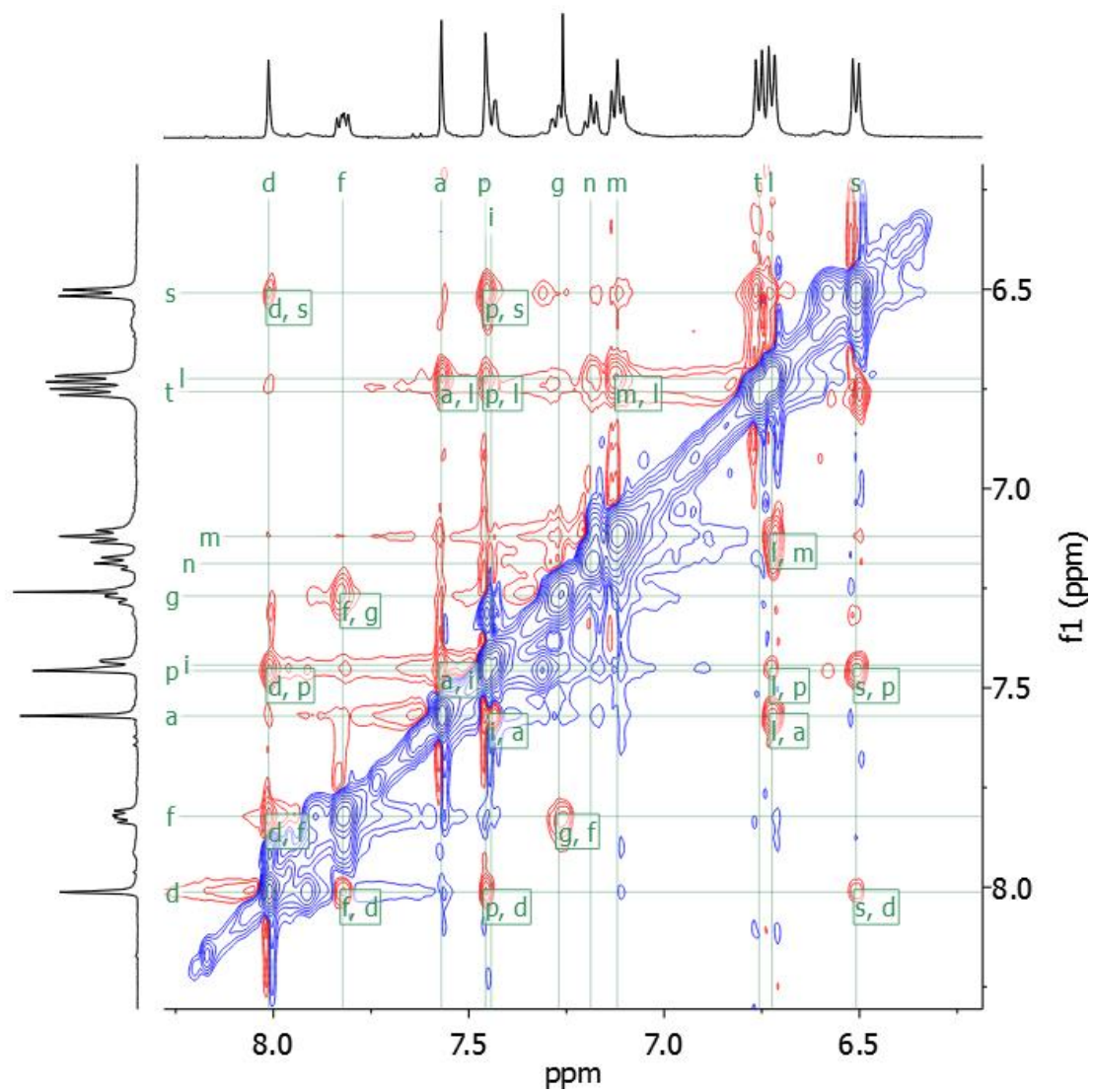


**Figure A3.85.** Full HSQC spectrum of **11d-F** (500 MHz, 125 MHz, CDCl<sub>3</sub>, 298 K).

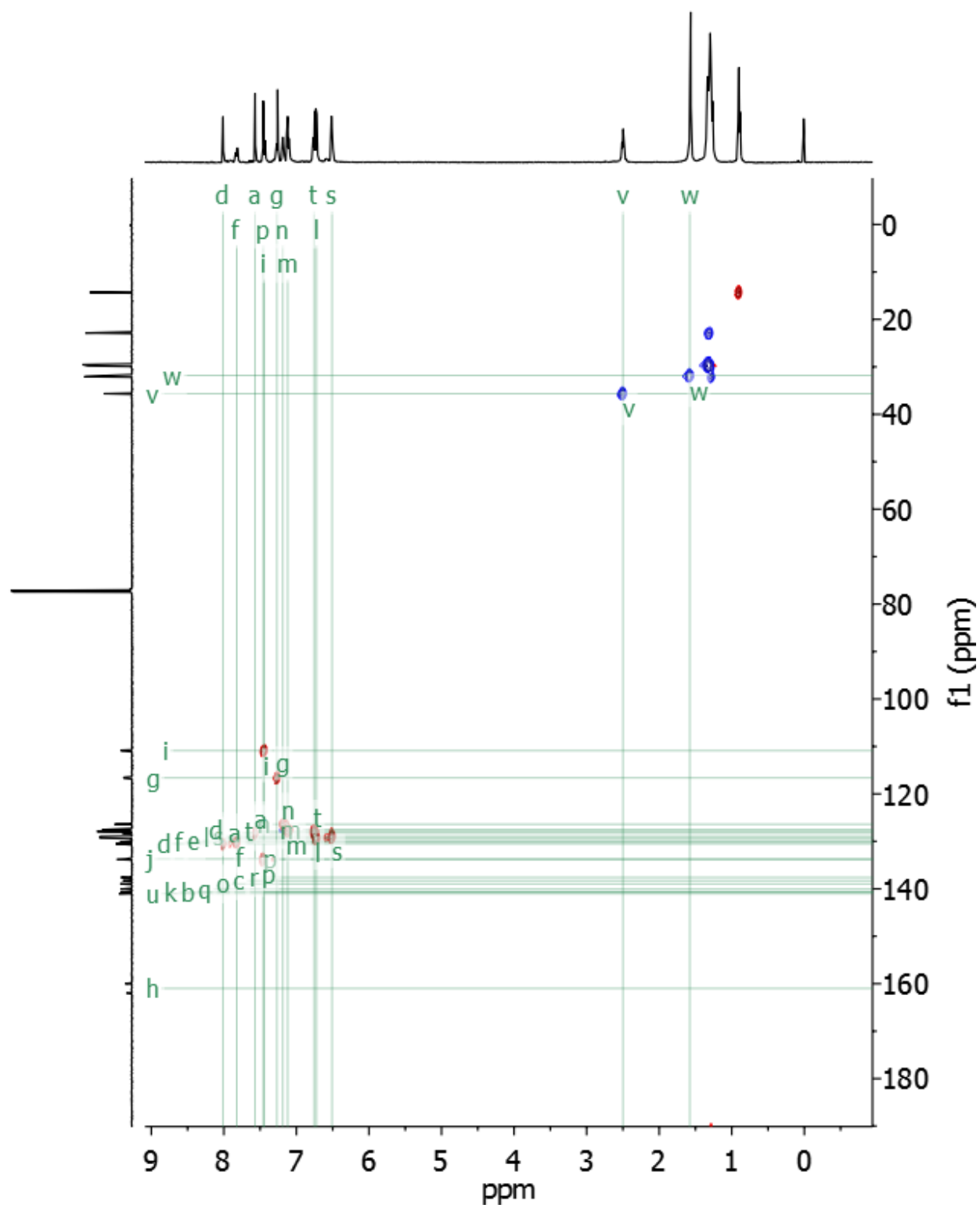




**Figure A3.86.** Partial HSQC spectrum of **11d-F** showing the aromatic region (500 MHz, 125 MHz, CDCl<sub>3</sub>, 298 K).

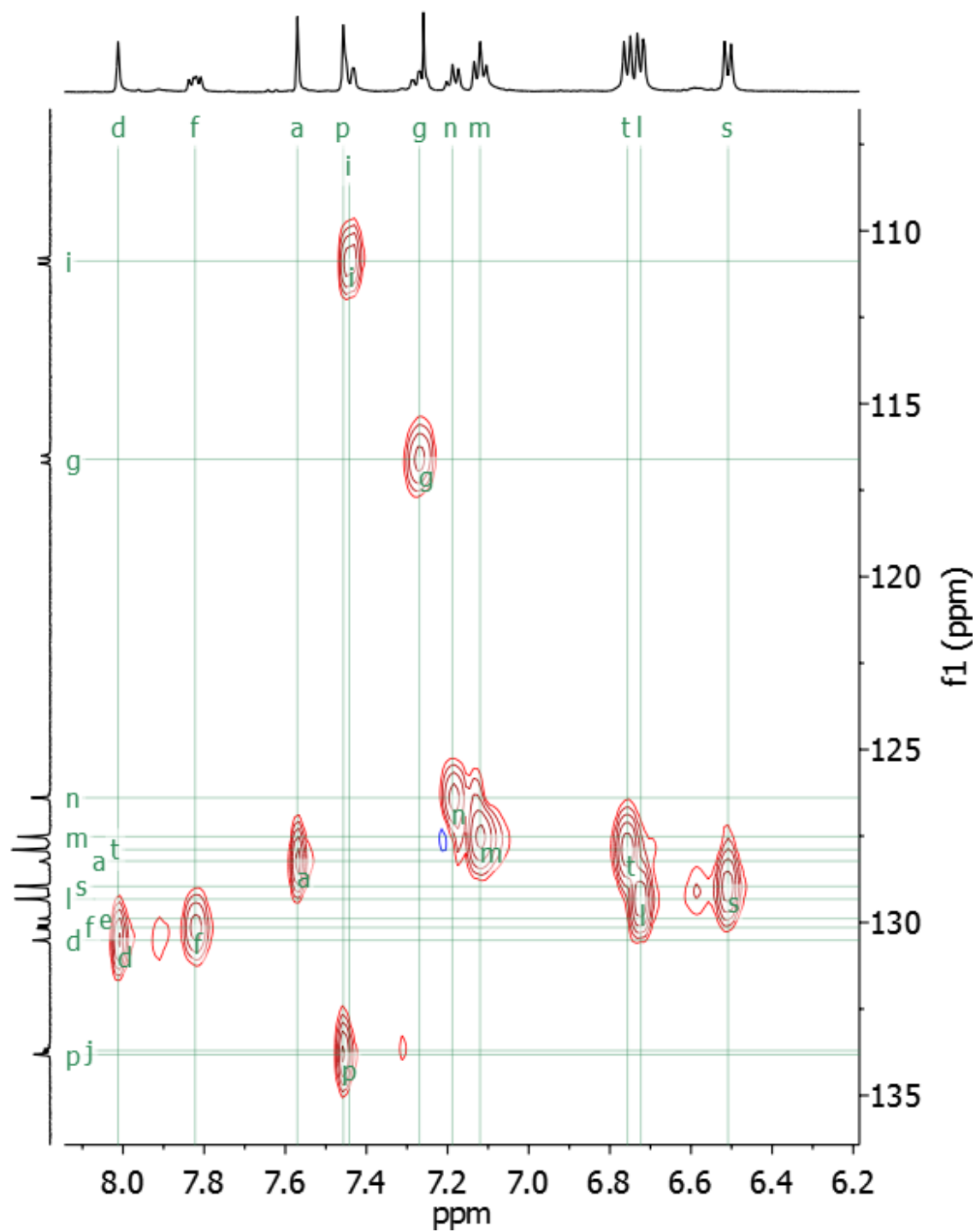


**Figure A3.87.** Full HMBC spectrum of **11d-F** (500 MHz, 125 MHz, CDCl<sub>3</sub>, 298 K).

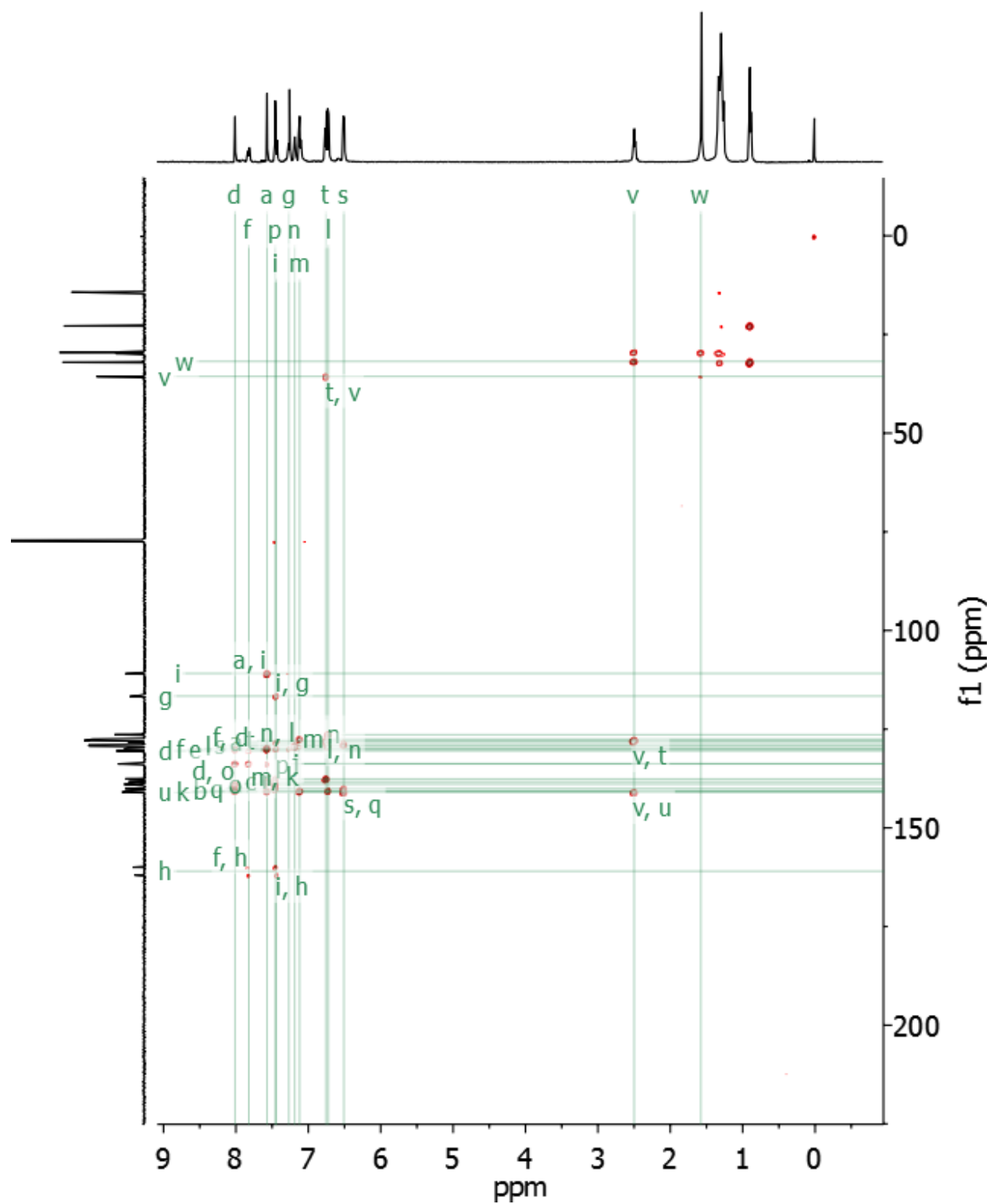
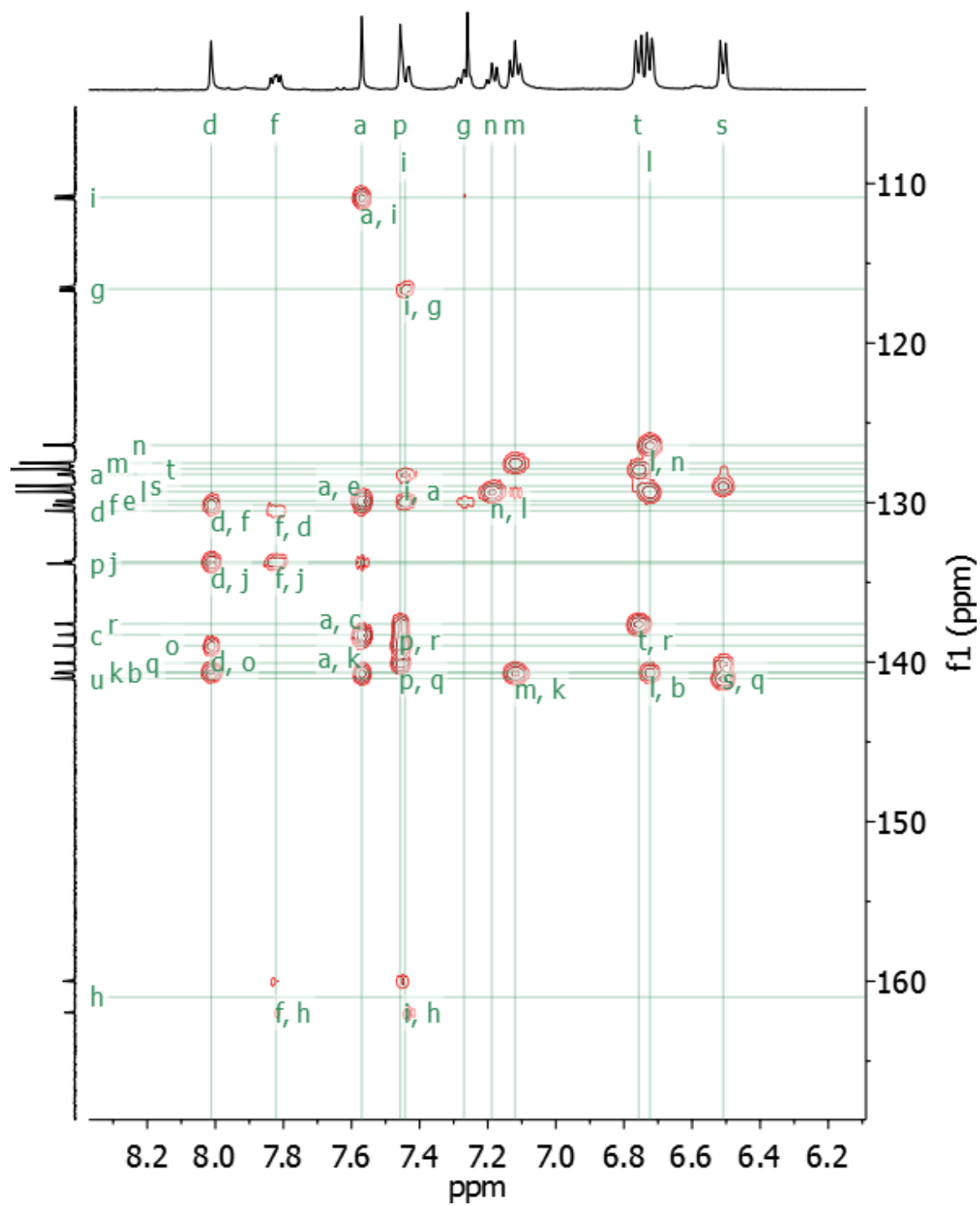


**Figure A3.88.** Partial HMBC spectrum of **11d-F** showing the aromatic region (500 MHz, 125 MHz, CDCl<sub>3</sub>, 298 K).



Peak assignments for the compounds 12b-F (blue) and 12a-F (green):

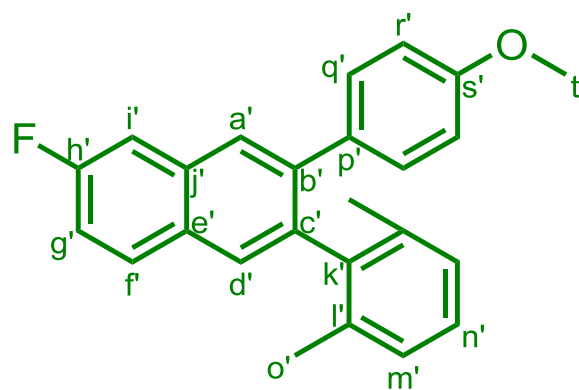
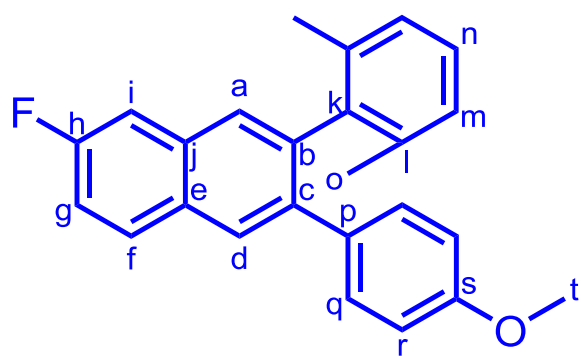


**Figure A3.89.** Full COSY spectrum of **12b-F** (blue) and **12a-F** (green) (500 MHz, 500 MHz, CDCl<sub>3</sub>, 298 K).

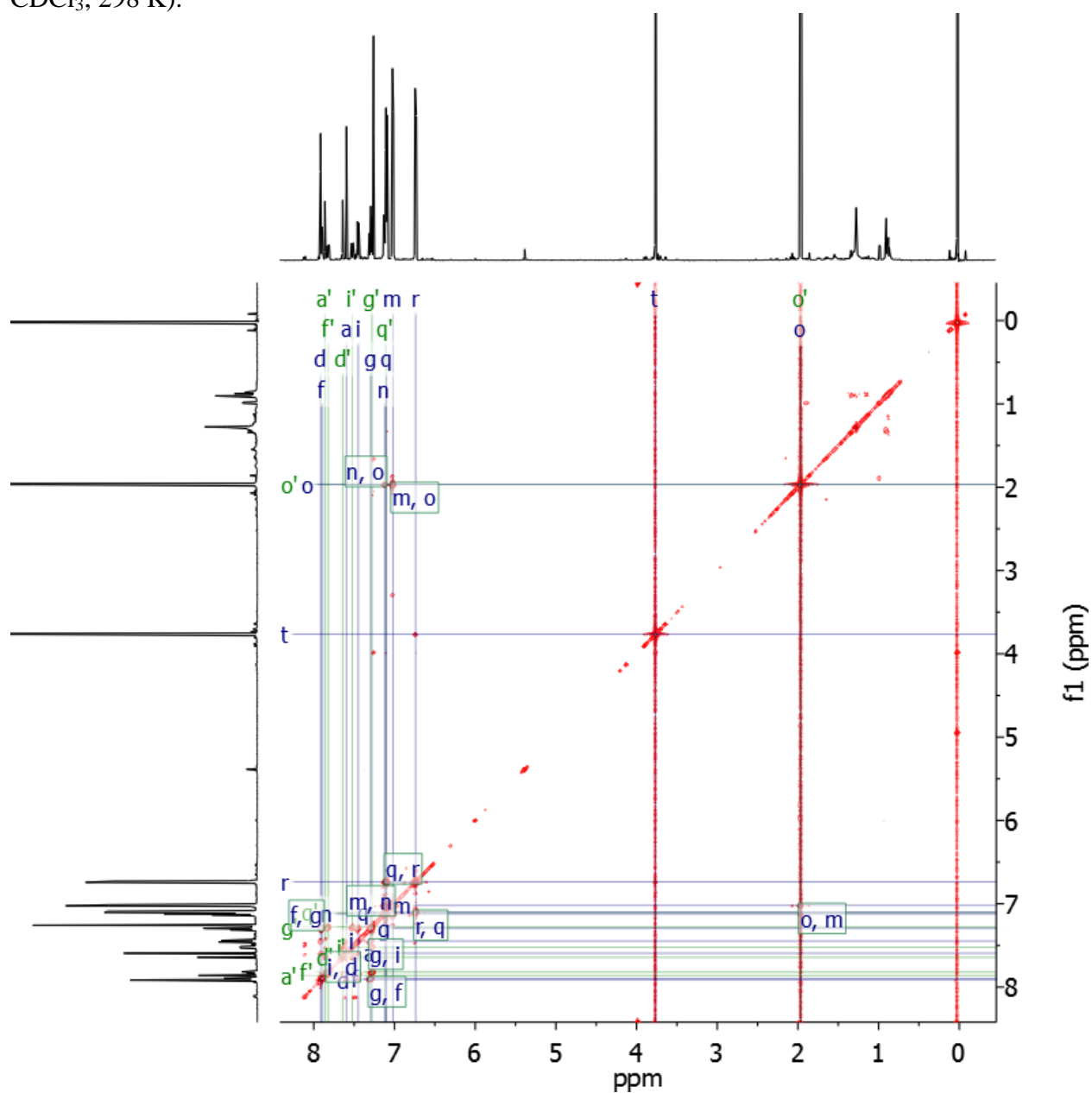


**Figure A3.90.** Partial COSY spectrum of **12b-F** (blue) and **12a-F** (green) showing the aromatic region (600 MHz, 600 MHz, CDCl<sub>3</sub>, 298 K).

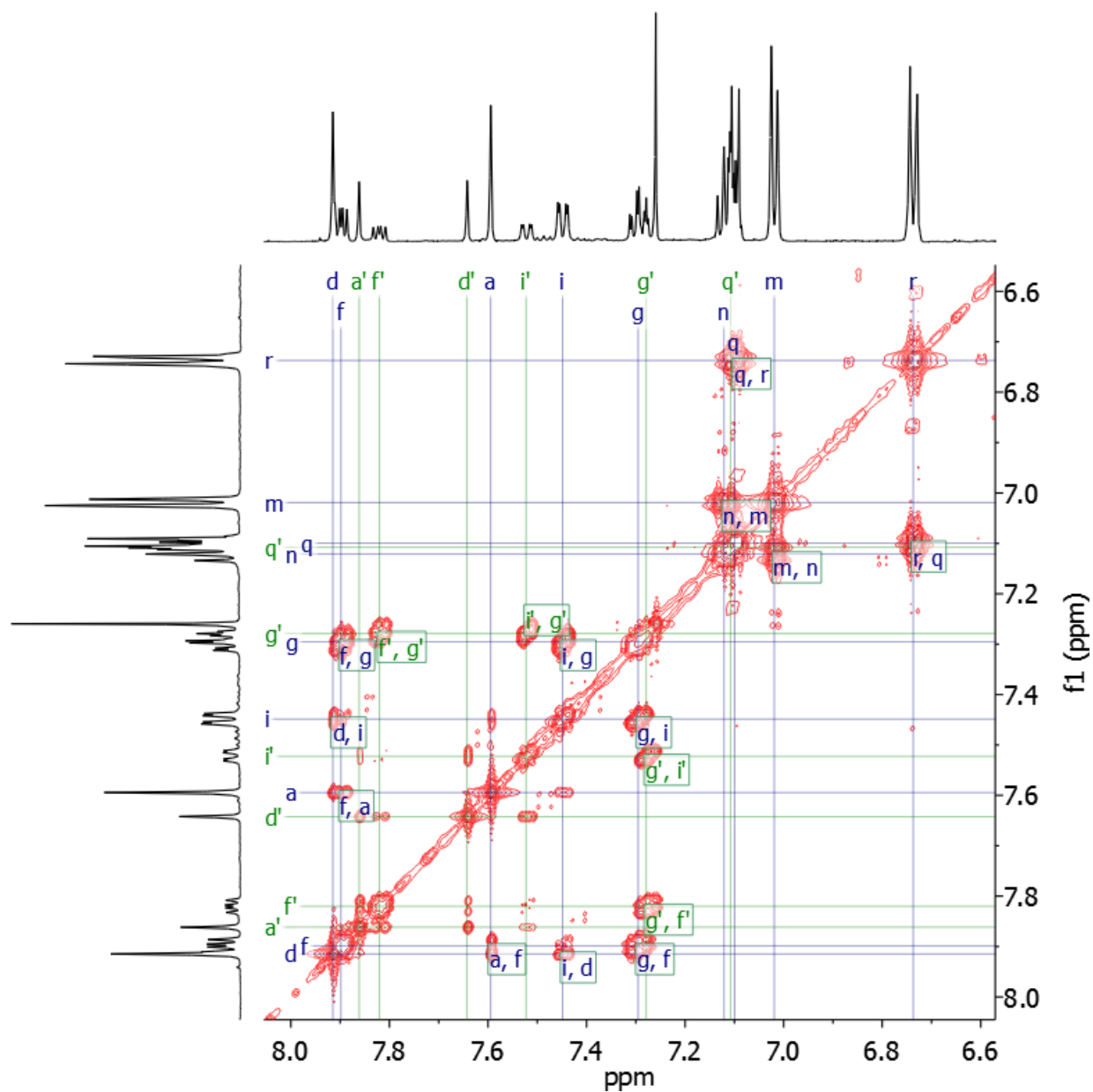


**Figure A3.91.** Full ROESY spectrum of **12b-F** (blue) and **12a-F** (green) (600 MHz, 600 MHz, CDCl<sub>3</sub>, 298 K).

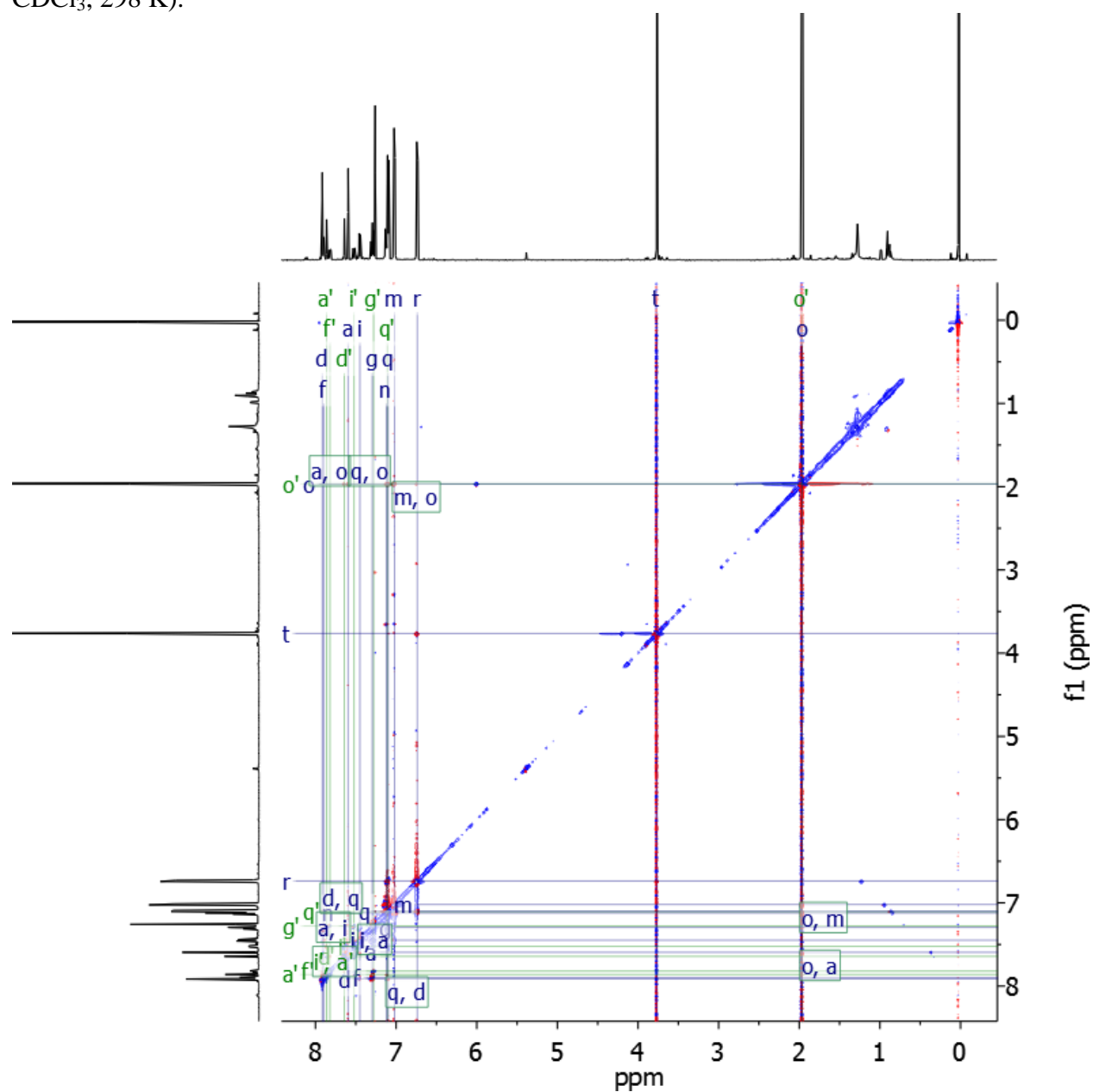


**Figure A3.92.** Partial ROESY spectrum of **12b-F** (blue) and **12a-F** (green) showing the aromatic region (600 MHz, 600 MHz, CDCl<sub>3</sub>, 298 K).

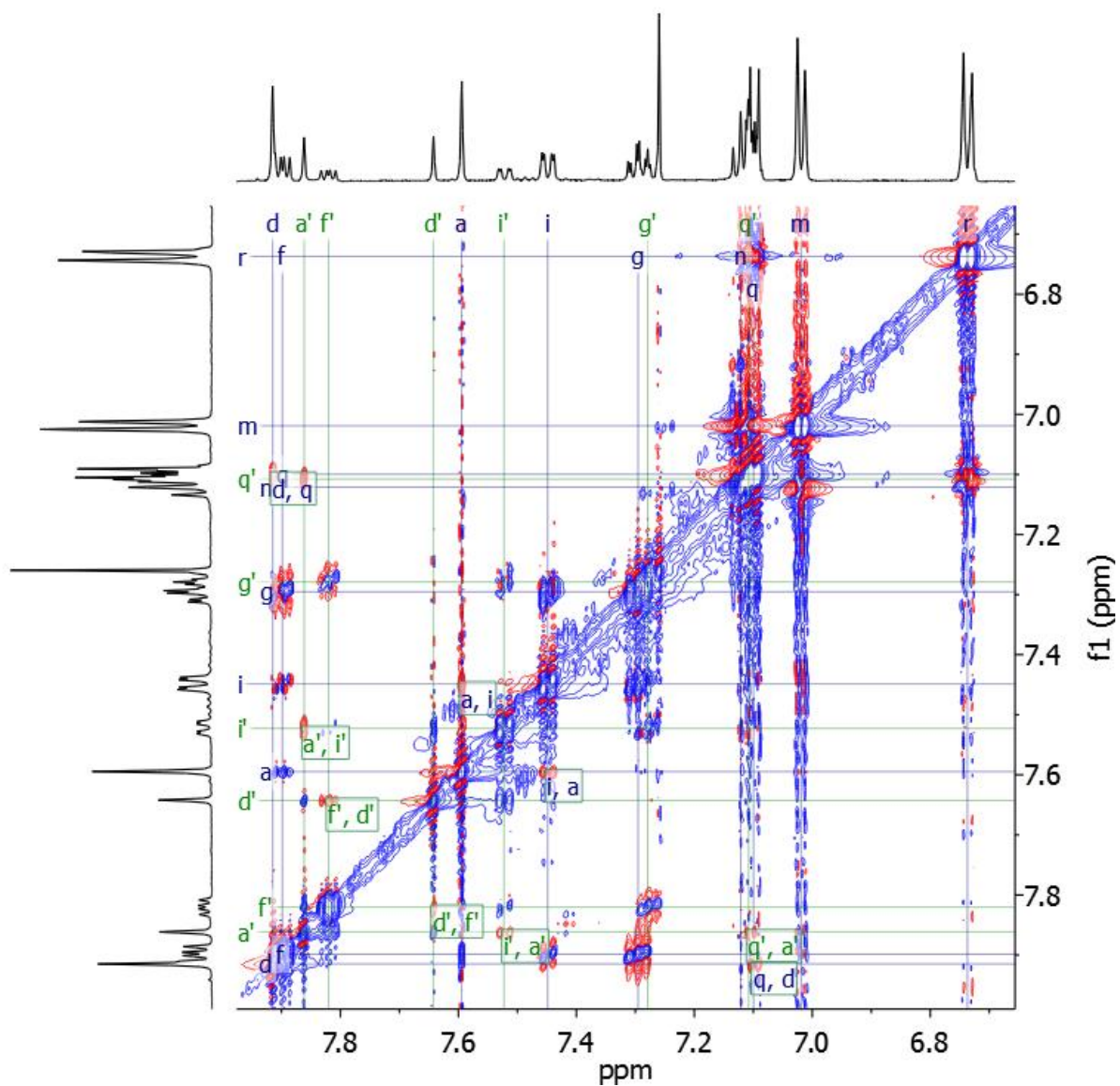




**Figure A3.93.** Full HSQC spectrum of **12b-F** (blue) and **12a-F** (green) (600 MHz, 150 MHz, CDCl<sub>3</sub>, 298 K).

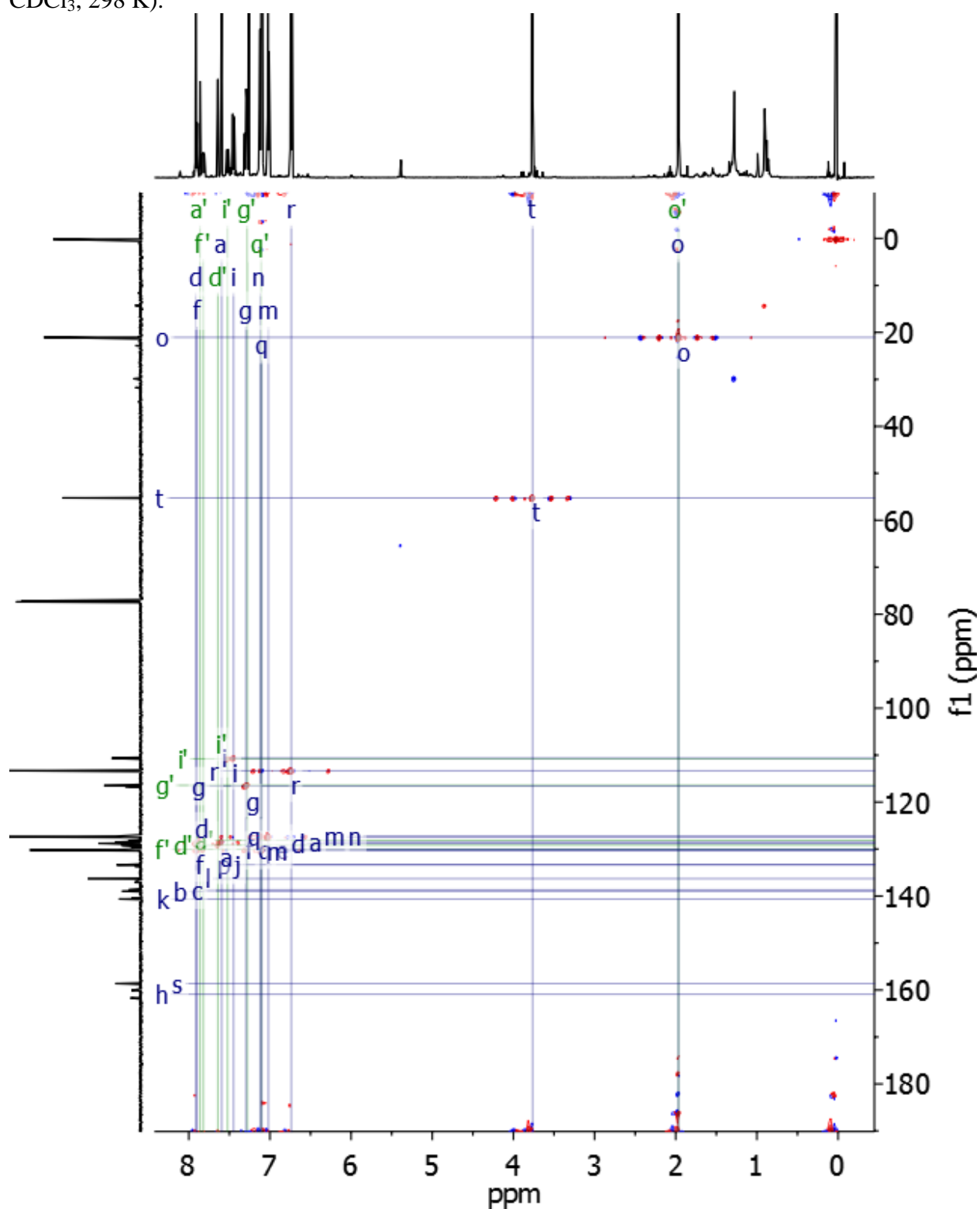


**Figure A3.94.** Partial HSQC spectrum of **12b-F** (blue) and **12a-F** (green) showing the aromatic region (600 MHz, 150 MHz, CDCl<sub>3</sub>, 298 K).

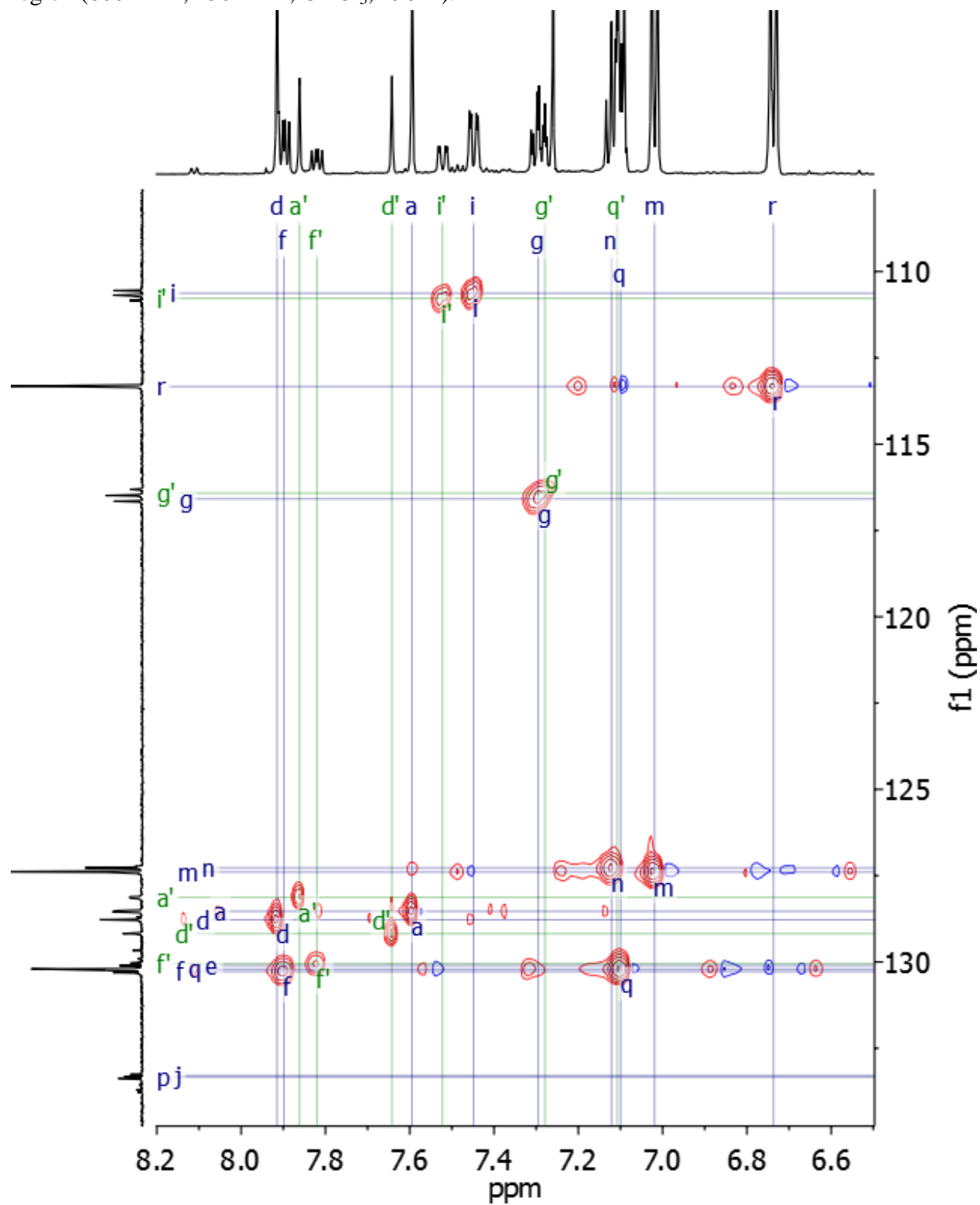


**Figure A3.95.** Full HMBC spectrum of **12b-F** (**blue**) and **12a-F** (**green**) (600 MHz, 150 MHz, CDCl<sub>3</sub>, 298 K).

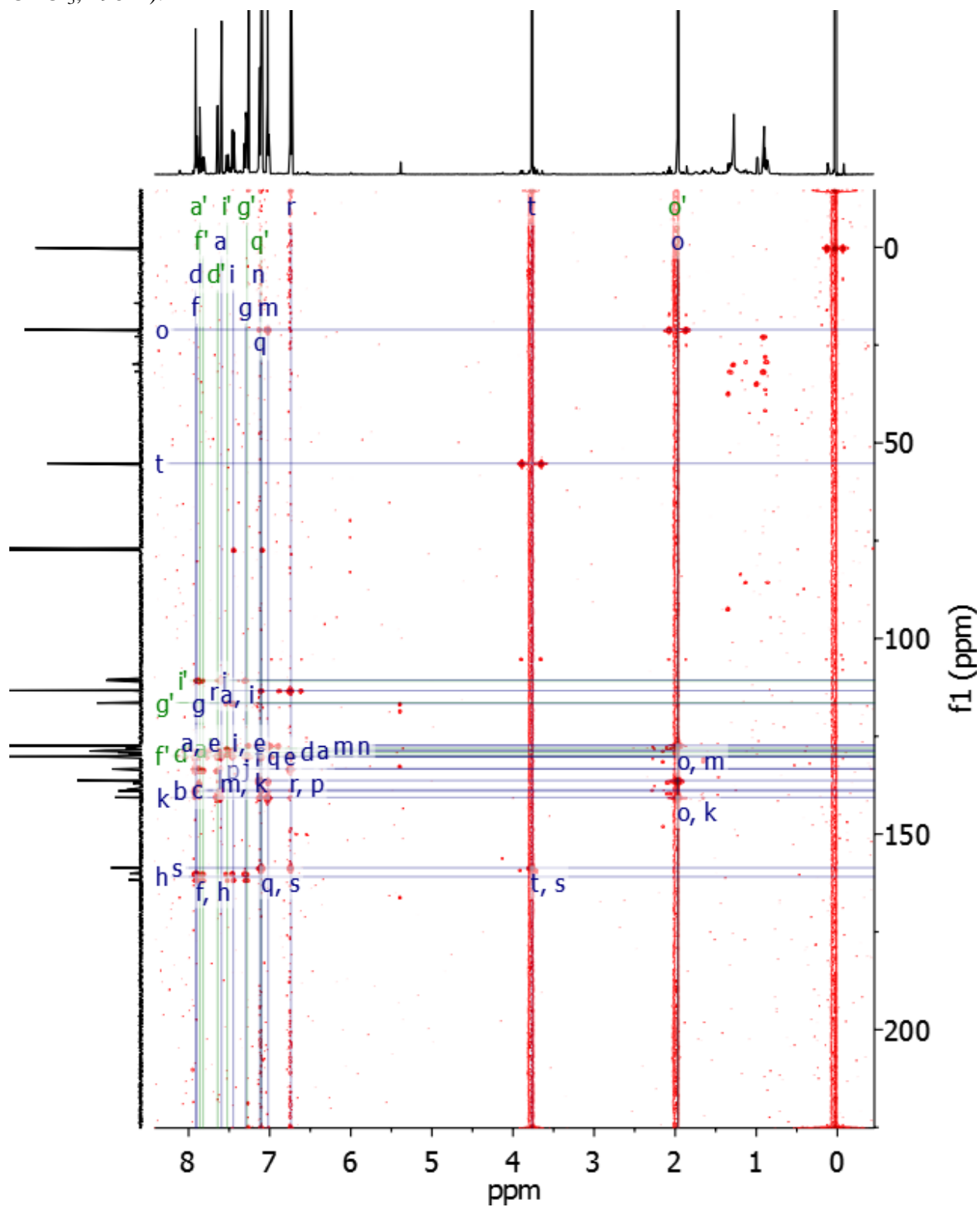
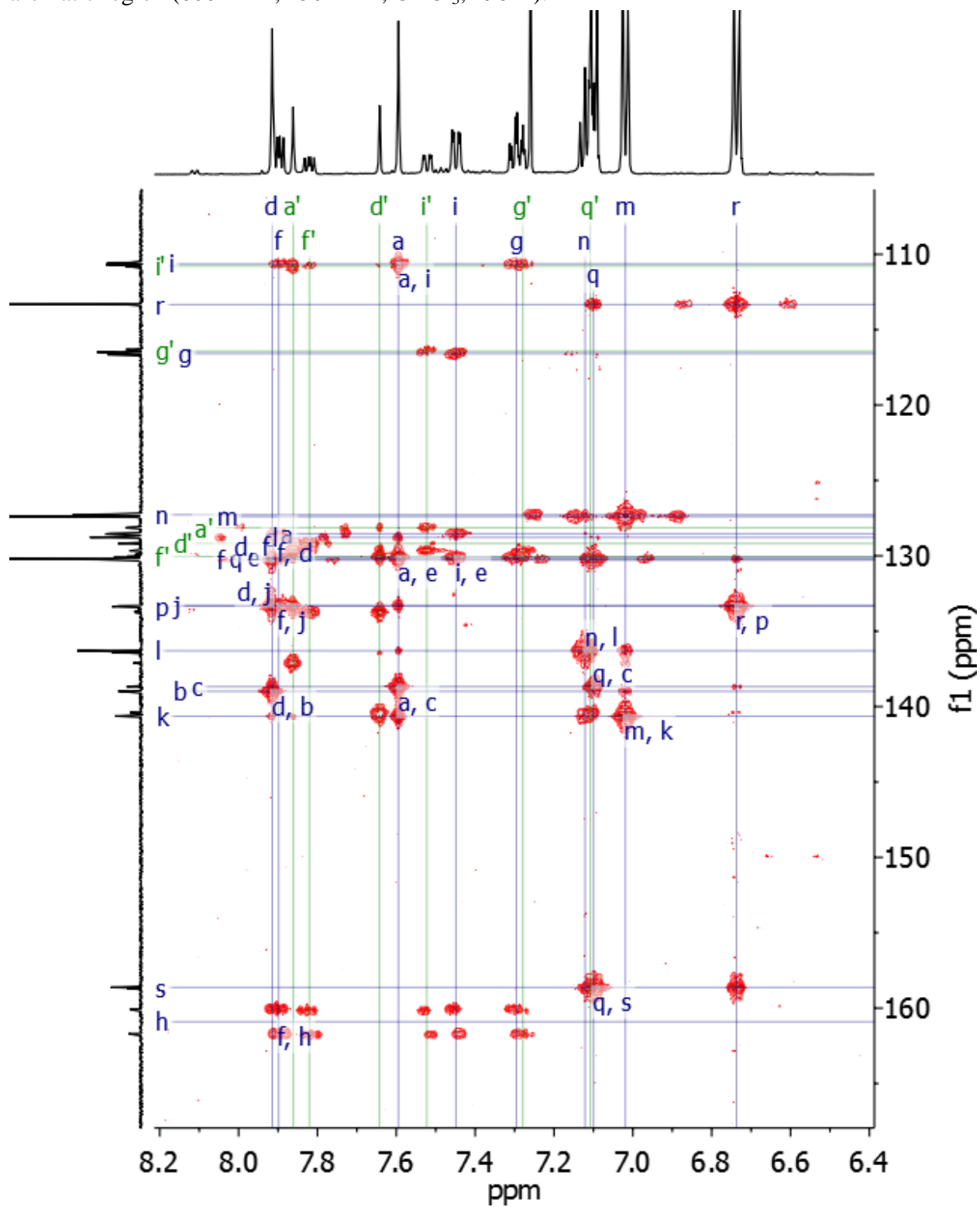


**Figure A3.96.** Partial HMBC spectrum of **12b-F** (blue) and **12a-F** (green) showing the aromatic region (600 MHz, 150 MHz, CDCl<sub>3</sub>, 298 K).



Peak assignments for the compounds 13a-F (blue) and 13b-F (green):

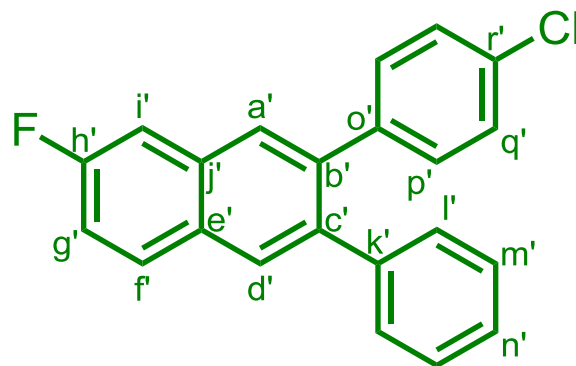
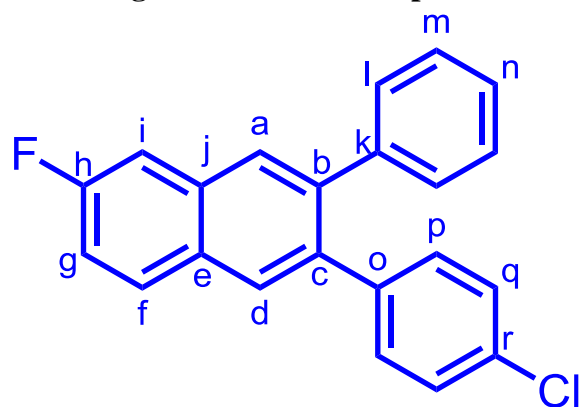


**Figure A3.97.** COSY spectrum of **13a-F** (**blue**) and **13b-F** (**green**) (600 MHz, 600 MHz, CDCl<sub>3</sub>, 298 K).

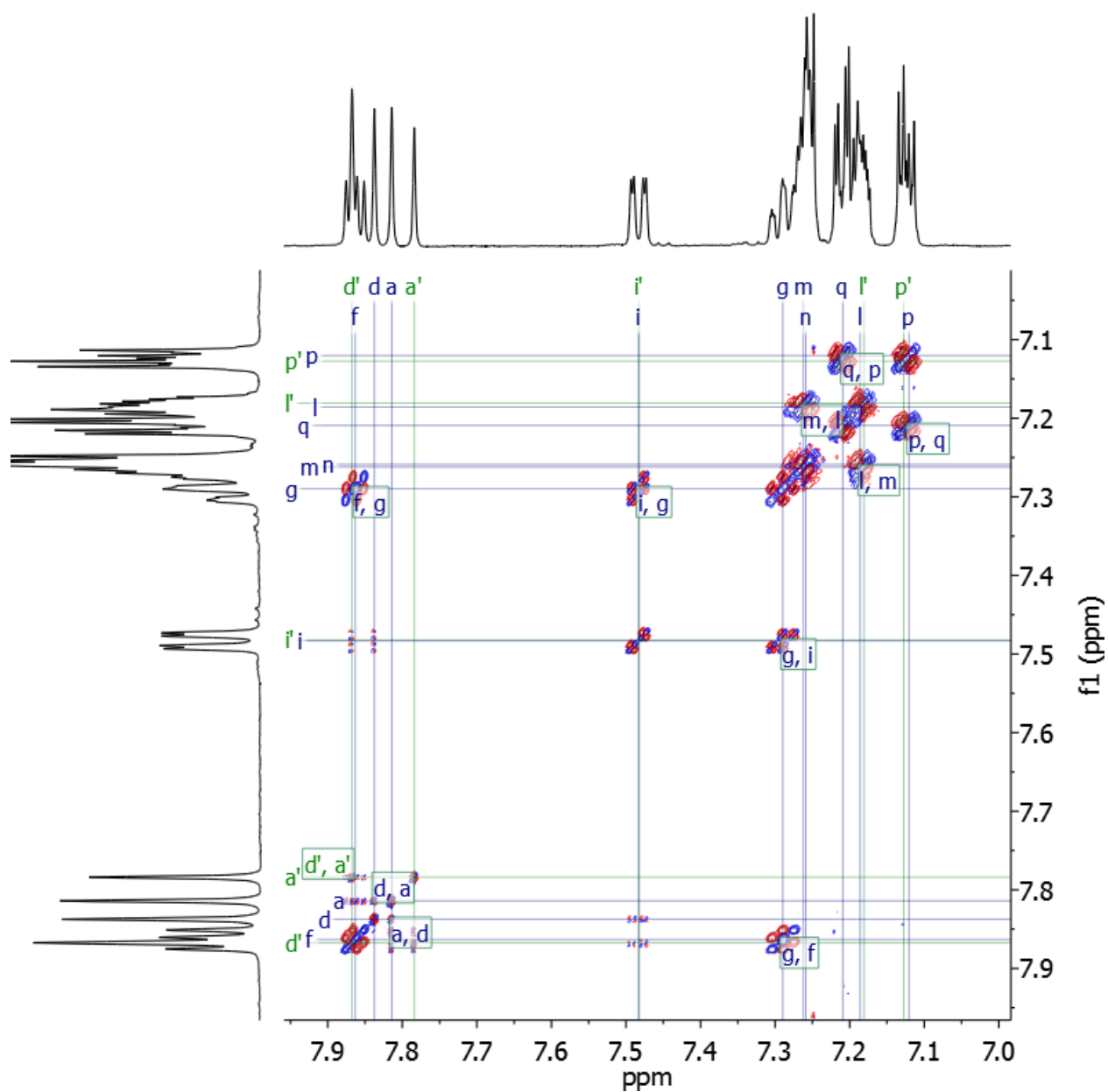


**Figure A3.98.** ROESY spectrum of **13a-F** (blue) and **13b-F** (green) (600 MHz, 600 MHz, CDCl<sub>3</sub>, 298 K).

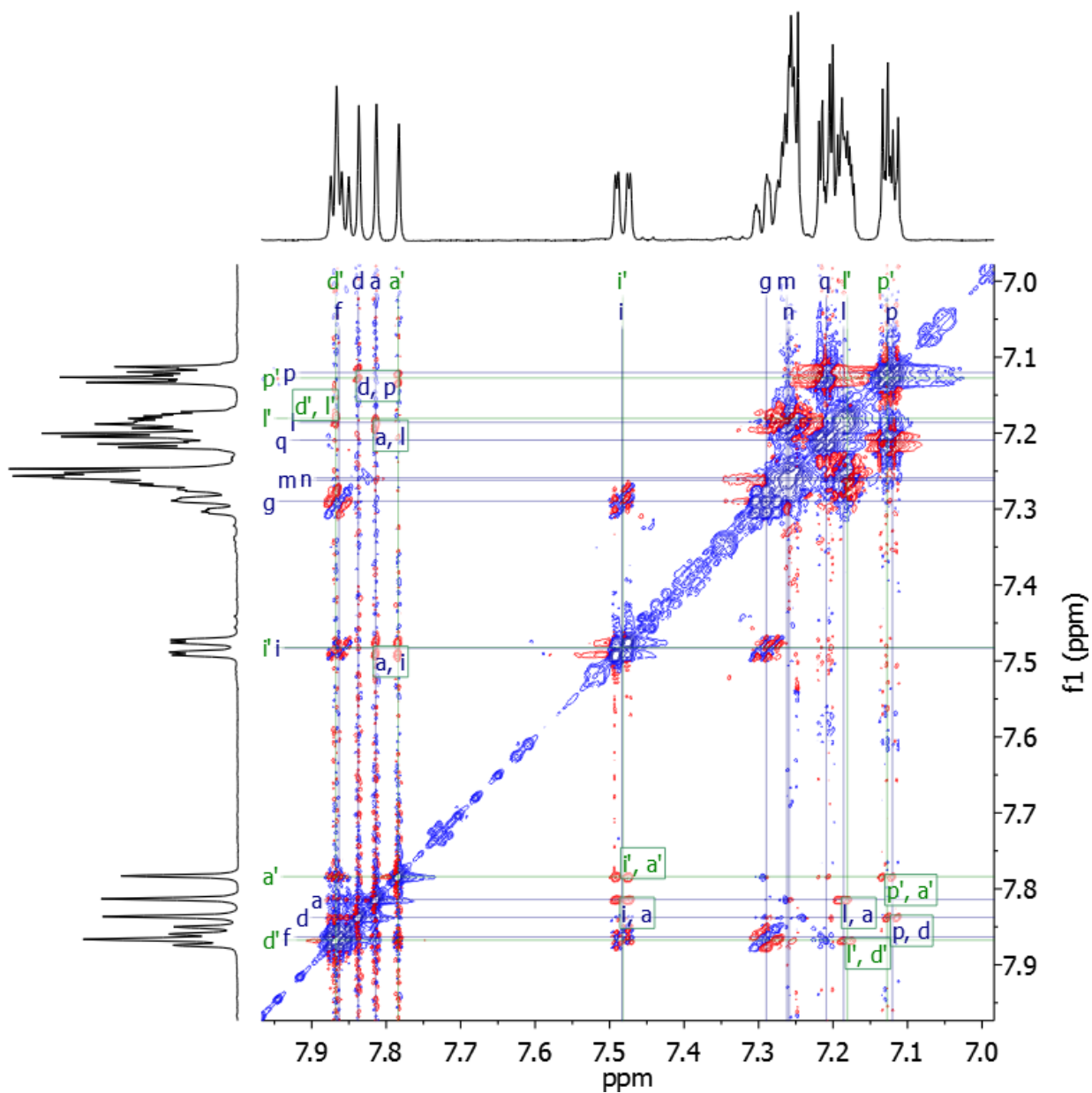


**Figure A3.99.** HSQC spectrum of **13a-F** (**blue**) and **13b-F** (**green**) (600 MHz, 150 MHz, CDCl<sub>3</sub>, 298 K).

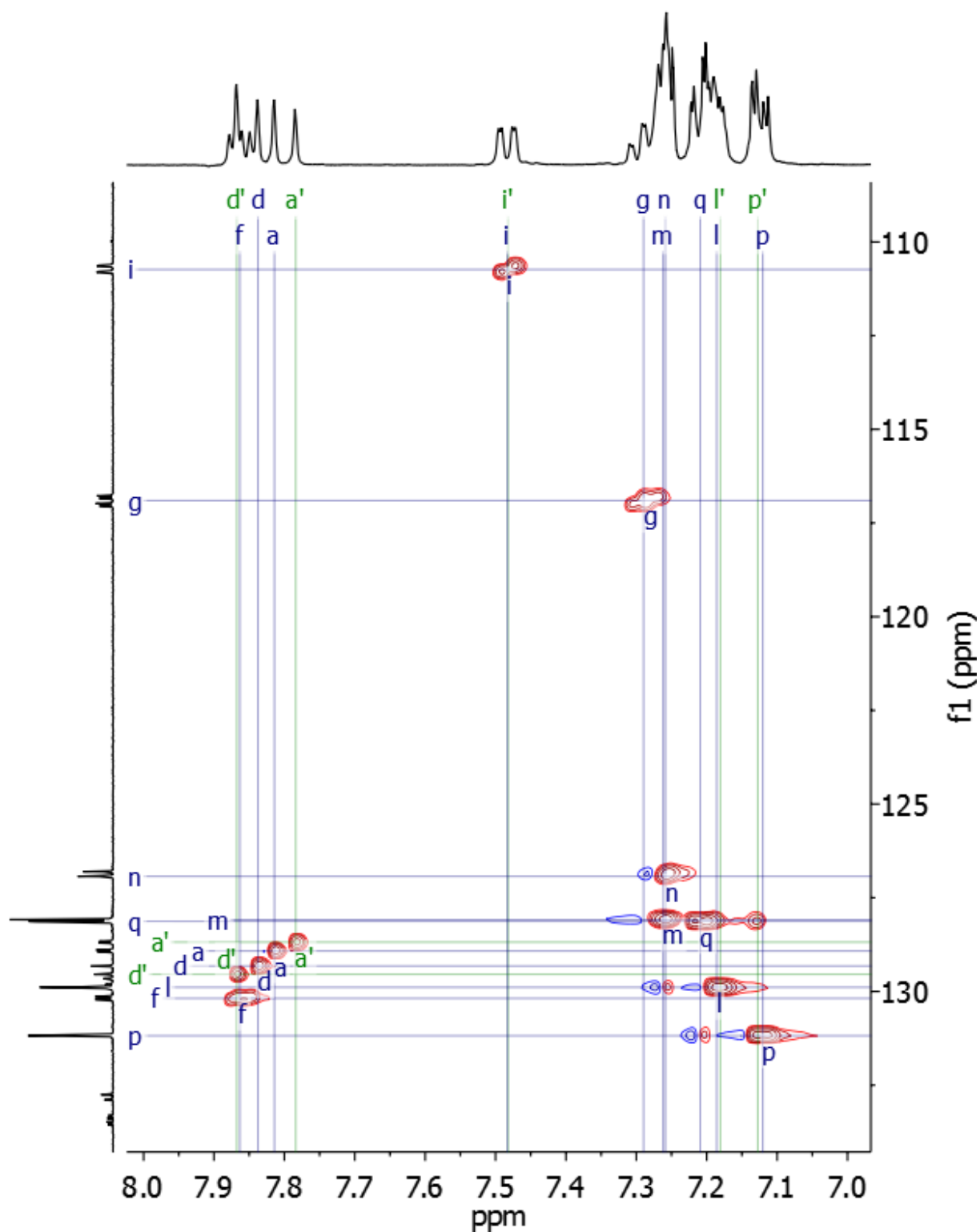
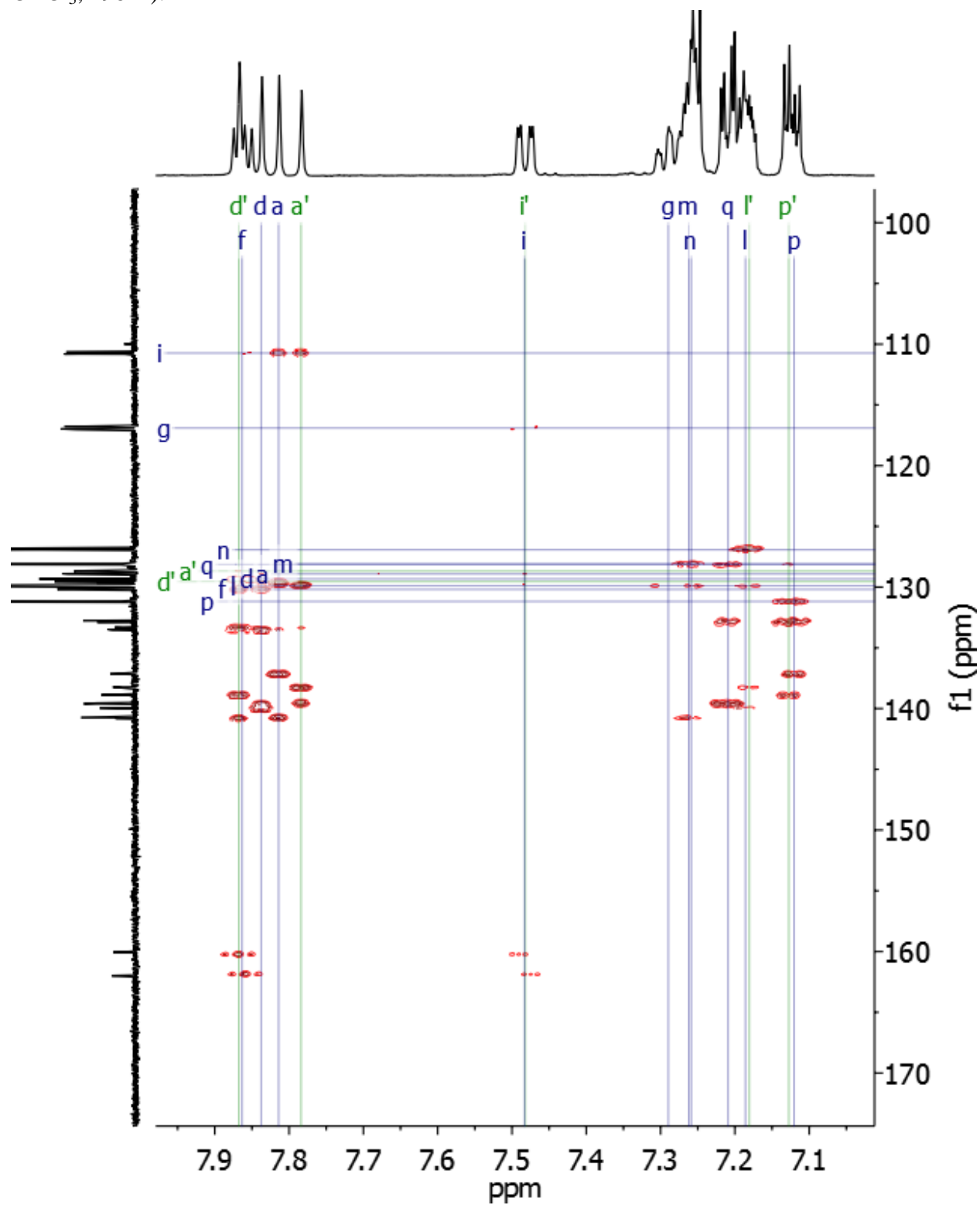




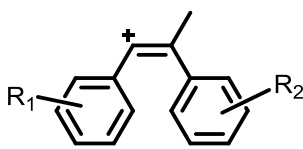
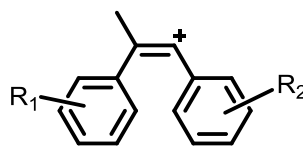
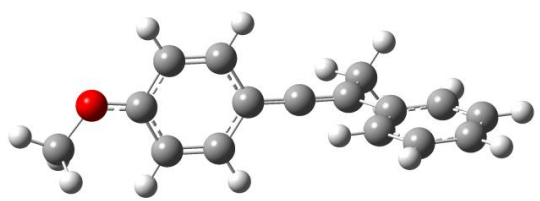
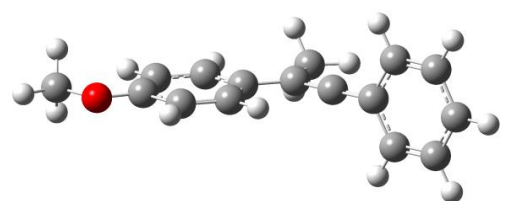
**Figure A3.100.** HMBC spectrum of **13a-F** (blue) and **13b-F** (green) (600 MHz, 150 MHz, CDCl<sub>3</sub>, 298 K).

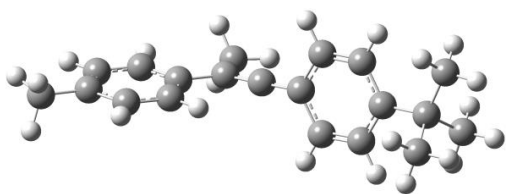


## E. DFT Calculations

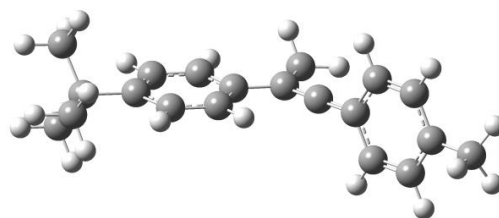
DFT calculations were performed using the Gaussian 09 program, Revision A.02.<sup>3</sup> Geometries were optimized in the gas phase using the B3LYP functional and 6-31g(d) basis set on all atoms and confirmed as stationary states using frequency calculations. We calculated the relative energies of carbocations formed at the two alkyne carbons of each substrate. These calculations indicate the relative abilities of each aromatic ring to stabilize a developing positive charge, which are predictive of the observed regioselectivity. For each pair of regioisomers, the less stable carbocation's energy was set to 0.0 kcal/mol and the more stable regioisomer is provided relative to this value.

**Table A3.1.** Calculated relative energies of carbocations **8a'**,**-10a'**,**12a'**,**13a'** and **8b'**,**-10b'**,**12b'**,**13b'**

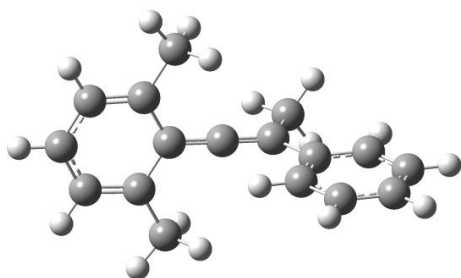
<p style="text-align: center;"><b>Isomer 1</b></p> 	<p style="text-align: center;"><b>Isomer 2</b></p> 
 <p style="text-align: center;">R<sub>1</sub> = <i>p</i>-MeO, R<sub>2</sub> = H -9.2 kcal/mol <b>8a'</b></p>	 <p style="text-align: center;">R<sub>1</sub> = <i>p</i>-MeO, R<sub>2</sub> = H 0.0 kcal/mol <b>8b'</b></p>



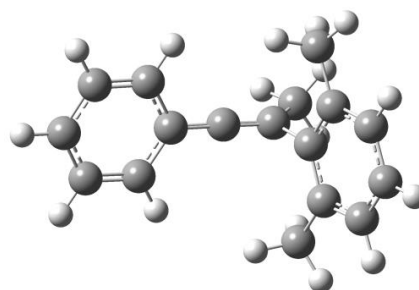
$R_1 = p\text{-(}t\text{Bu)}, R_2 = p\text{-Me}$   
 -1.0 kcal/mol  
**9a'**



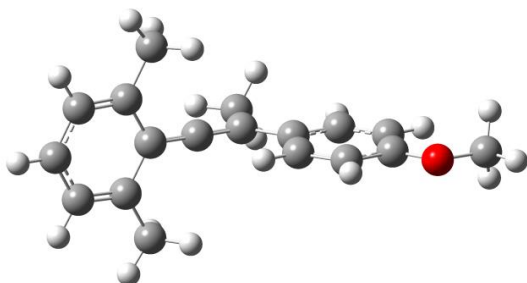
$R_1 = p\text{-(}t\text{Bu)}, R_2 = p\text{-Me}$   
 0.0 kcal/mol  
**9b'**



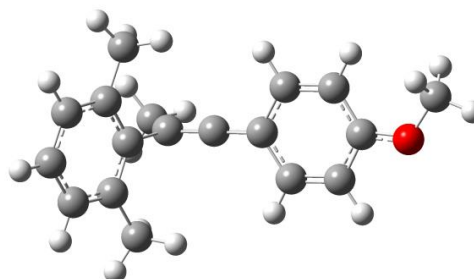
$R_1 = 2,6\text{-(Me)}_2, R_2 = \text{H}$   
 -6.7 kcal/mol  
**10a'**



$R_1 = 2,6\text{-(Me)}_2, R_2 = \text{H}$   
 0.0 kcal/mol  
**10b'**



$R_1 = 2,6\text{-(Me)}_2, R_2 = p\text{-OMe}$   
 0.0 kcal/mol  
**12a'**



$R_1 = 2,6\text{-(Me)}_2, R_2 = p\text{-OMe}$   
 -1.3 kcal/mol  
**12b'**

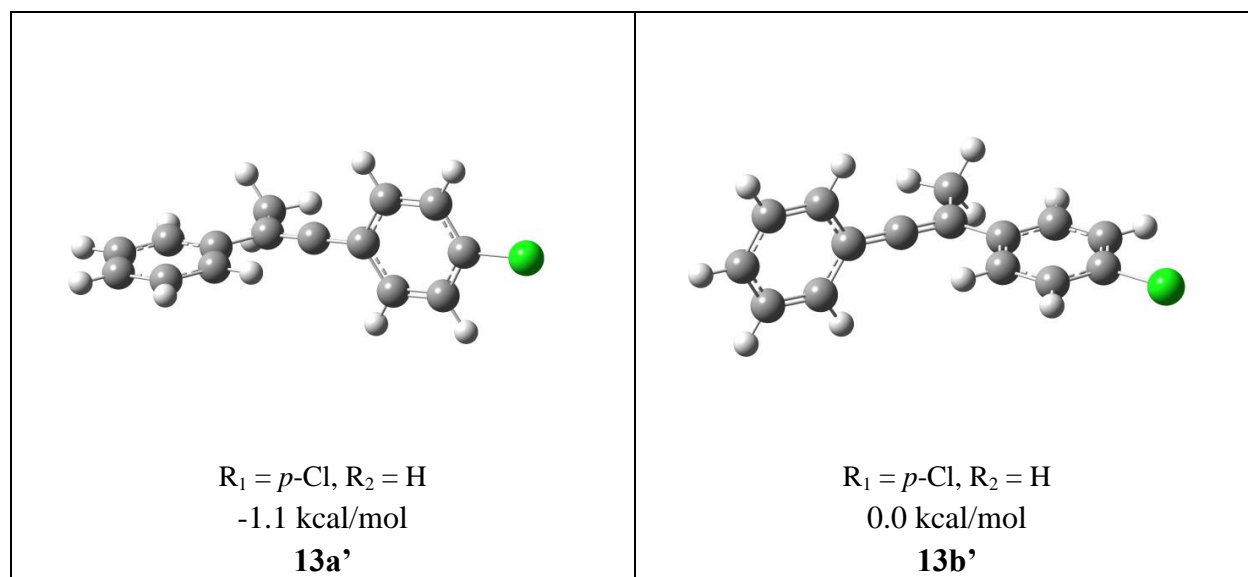


**Table A3.2.** Cartesian coordinates of DFT computed geometries

<b>8a'</b>			
C	4.05633100	0.65432000	-0.08954300
C	2.73473100	0.18476800	-0.05090400
C	2.50306300	-1.20090600	0.02665800
C	3.56796900	-2.09233100	0.06618700
C	4.88271200	-1.61622100	0.02810100
C	5.12219500	-0.24482900	-0.04986200
H	4.26513400	1.71670100	-0.14928700
H	1.48467800	-1.58060100	0.05306000
H	3.37554900	-3.15931500	0.12538500
H	5.71454500	-2.31341600	0.05833700
H	6.14005300	0.13162100	-0.08018800
C	1.59964500	1.14318500	-0.09025700
C	0.34589200	0.78952500	-0.00994400
C	-0.96763700	0.47042100	0.07911000
C	-1.73523100	0.18255900	-1.10619200
C	-1.63567000	0.41113000	1.35886600
C	-3.06587800	-0.13596500	-1.02826600
H	-1.23658500	0.22374800	-2.06927800
C	-2.96100800	0.09370100	1.43634100
H	-1.06318300	0.62476000	2.25544600
C	-3.69743800	-0.18289600	0.24696700
H	-3.62826300	-0.34900800	-1.92902800

H	-3.48708500	0.04360100	2.38348000
C	1.85844500	2.64363400	-0.22987200
H	2.45293100	2.99150000	0.62072200
H	2.41642900	2.83291000	-1.15216200
H	0.92979700	3.21684500	-0.26056500
O	-4.96792800	-0.47458400	0.43363100
C	-5.84297100	-0.77330100	-0.67747900
H	-5.49230200	-1.66317400	-1.20723600
H	-6.81420600	-0.96522800	-0.22521100
H	-5.90497400	0.08495700	-1.35198900

**8b'**

C	3.37755100	-0.19101200	1.23977100
C	2.72317700	0.11729700	0.00060100
C	3.37593800	-0.19219600	-1.23914900
C	4.62530400	-0.78123400	-1.22856400
C	5.24463500	-1.07153500	-0.00048300
C	4.62689000	-0.78009500	1.22812300
H	2.87387100	0.04604000	2.17122000
H	2.87104100	0.04396900	-2.17016500
H	5.12901000	-1.01978500	-2.15944800
H	6.22776900	-1.53442500	-0.00090100
H	5.13179600	-1.01779100	2.15857500
C	1.48239500	0.69535100	0.00111900
C	0.32452100	1.29532500	-0.00008900
C	-0.98611300	0.62237200	-0.00002400
C	-2.17454200	1.36670700	0.00009700
C	-1.07703000	-0.78764100	-0.00008000
C	-3.41781500	0.73972300	0.00015500
H	-2.14788800	2.45110100	0.00015000
C	-2.30239400	-1.41984000	-0.00000800
H	-0.17230300	-1.39106300	-0.00023900
C	-3.49268800	-0.66174400	0.00014300
H	-4.31535700	1.34616100	0.00020400
H	-2.37967100	-2.50189700	-0.00009000
C	0.42108400	2.82714300	-0.00131000
H	-0.07814000	3.21611200	0.89110500
H	1.45509600	3.17783300	-0.00166100
H	-0.07831000	3.21458900	-0.89429200
O	-4.63299400	-1.37357300	0.00014300
C	-5.88668300	-0.68582300	0.00027400

H	-5.99558700	-0.06641900	-0.89724100
H	-6.64735200	-1.46620000	0.00035000
H	-5.99539900	-0.06643900	0.89782500

**9a'**

C	1.39372000	0.51560600	1.23373000
C	0.69281600	0.66513900	-0.00923000
C	1.40590200	0.40591800	-1.22982700
C	2.72622500	0.02918500	-1.19016600
C	3.42239000	-0.11489600	0.04113600
C	2.71778700	0.13652100	1.24476800
H	3.24675800	-0.16101700	-2.12179900
H	3.22465200	0.03176100	2.19551400
C	-0.61586800	1.04104100	-0.02753200
C	-1.85435900	1.44728200	-0.04838100
C	-3.03148700	0.54659500	-0.02363500
C	-4.32694100	1.07331000	0.07489700
C	-2.87539500	-0.85072200	-0.09315700
C	-5.43147800	0.22380900	0.10481200
H	-4.48862700	2.14422600	0.13307800
C	-3.98141700	-1.68615100	-0.06308300
H	-1.88148500	-1.28415900	-0.17585300
C	-5.28453900	-1.16631300	0.03499600
H	-6.42608200	0.65374300	0.18411700
H	-3.83791300	-2.76213500	-0.11817500
C	-2.03937100	2.96657700	-0.09647500
H	-2.57048200	3.29447100	0.80237800
H	-1.08569700	3.49569800	-0.14709100
H	-2.63311400	3.22834800	-0.97751600
H	0.86186900	0.70691100	2.16033700
C	4.89068300	-0.52993900	0.02927800
H	0.88336400	0.51416800	-2.17486200
C	5.69680800	0.52250400	-0.78057500
H	6.75231200	0.23209000	-0.79033200
H	5.36394600	0.59512000	-1.82046500
H	5.62390100	1.51633900	-0.32632400
C	5.49520700	-0.63150100	1.44224400
H	4.98898100	-1.38513400	2.05570500
H	6.54454800	-0.93060400	1.36309400
H	5.47000400	0.32712300	1.97223300
C	5.00965800	-1.91576600	-0.66252600

H	6.06226000	-2.21657500	-0.67784700
H	4.44688500	-2.68216000	-0.11910100
H	4.65513600	-1.89867400	-1.69757800
C	-6.48084800	-2.08359100	0.04503300
H	-7.38694500	-1.55950400	0.36134200
H	-6.32493000	-2.93425900	0.71736200
H	-6.66629000	-2.49342900	-0.95606400

**9b'**

C	-1.90493900	1.77379200	0.00010100
C	-0.73766700	0.99443500	-0.00011000
C	-0.87075700	-0.40328700	-0.00026700
C	-2.12635100	-0.99858400	-0.00019600
C	-3.30461600	-0.23195800	0.00001500
C	-3.15544000	1.16570200	0.00013600
H	-2.18201400	-2.08070400	-0.00036600
H	-4.03424200	1.80249500	0.00023200
C	0.59698300	1.63658800	-0.00017600
C	1.73049800	0.99336600	0.00081900
C	2.94206900	0.36822300	0.00052100
C	3.59289100	0.03373900	1.23669400
C	3.59184500	0.03287700	-1.23598600
C	4.81773500	-0.59360500	1.22303400
H	3.10342600	0.28746700	2.17144300
C	4.81669700	-0.59446400	-1.22293100
H	3.10155900	0.28595900	-2.17048100
C	5.45133800	-0.92091700	-0.00010100
H	5.31109600	-0.84182300	2.15789400
H	5.30926100	-0.84334100	-2.15803700
C	0.72560500	3.16348700	-0.00105900
H	0.23393400	3.56420800	-0.89264500
H	0.23399600	3.56527600	0.89007700
H	1.76743900	3.49000100	-0.00127200
C	6.76976500	-1.63145600	-0.00042900
H	7.35773800	-1.39732600	0.89140400
H	6.59942700	-2.71826000	-0.00060300
H	7.35741800	-1.39703400	-0.89240400
C	-4.70839100	-0.85673100	0.00009600
C	-5.47163000	-0.39133500	1.26445400
H	-5.58251700	0.69731100	1.30163100
H	-6.47699200	-0.82666700	1.27406600

H	-4.95649200	-0.70964000	2.17770900
C	-4.66398000	-2.39654000	-0.00017100
H	-4.16101900	-2.79294000	-0.88966100
H	-4.16079700	-2.79325900	0.88905000
H	-5.68527500	-2.79063800	-0.00011300
C	-5.47203700	-0.39090100	-1.26383900
H	-6.47741000	-0.82621000	-1.27326900
H	-5.58292500	0.69775800	-1.30060800
H	-4.95721300	-0.70890100	-2.17738000
H	0.01443300	-1.03547100	-0.00050200
H	-1.85054100	2.85715400	0.00021300

**10a'**

C	2.30006200	-1.26551800	0.03842200
C	1.62312200	0.01661600	0.17610200
C	2.28964800	1.26137500	-0.18093600
C	3.58607100	1.18418800	-0.66117100
C	4.22543800	-0.05681800	-0.79175000
C	3.59590900	-1.26198000	-0.44931600
H	4.11362400	2.09065600	-0.94035300
H	5.24312400	-0.08561200	-1.17247400
H	4.13082000	-2.19878600	-0.56827000
C	0.34328500	0.05173000	0.62859600
C	-0.87512900	0.09202400	1.08997000
C	-2.08698600	0.01450500	0.23262400
C	-3.36390100	0.11303500	0.80537000
C	-1.97200100	-0.15730000	-1.15959400
C	-4.50092800	0.04223200	0.00013100
H	-3.48369500	0.24525700	1.87502300
C	-3.10782000	-0.22721100	-1.95684000
H	-0.98970900	-0.23892600	-1.61918500
C	-4.37754700	-0.12735700	-1.37841700
H	-5.48327300	0.11989100	0.45570400
H	-3.00563100	-0.36071000	-3.02952100
C	-1.00476200	0.22886000	2.60813900
H	-1.56887100	-0.62240100	3.00155100
H	-0.03163500	0.25996600	3.10265000
H	-1.54418200	1.15114300	2.84517700
C	1.61779100	-2.54673900	0.42284800
H	1.44395500	-2.58693600	1.50521300
H	0.64097400	-2.64637200	-0.06187600



H	2.22932200	-3.40909900	0.14894200
C	1.59601600	2.58403800	-0.02549000
H	0.61868200	2.58841900	-0.51932800
H	1.42148900	2.81174900	1.03332500
H	2.20016200	3.39031600	-0.44690700
H	-5.26475700	-0.18263100	-2.00179500

**10b'**

C	-1.98690200	-1.23900600	-0.21698800
C	-1.50751400	0.00000200	0.27169800
C	-1.98693000	1.23898900	-0.21696400
C	-3.00724400	1.21019900	-1.17070800
C	-3.51248000	-0.00001300	-1.64482100
C	-3.00720900	-1.21023000	-1.17071300
H	-3.40752200	2.14786600	-1.54526300
H	-4.30261300	-0.00003000	-2.38983500
H	-3.40747200	-2.14789400	-1.54529300
C	-0.48327100	0.00000900	1.39728300
C	0.69639700	-0.00005600	0.87819400
C	1.92605300	0.00001200	0.25891500
C	2.57428800	-1.23625400	-0.05014100
C	2.57423200	1.23629300	-0.05016700
C	3.81981600	-1.22540600	-0.65008700
H	2.07817100	-2.16908400	0.19626000
C	3.81976000	1.22545000	-0.65012200
H	2.07809600	2.16912700	0.19618500
C	4.43759600	0.00003000	-0.94856300
H	4.32092700	-2.15781300	-0.88820000
H	4.32083900	2.15786500	-0.88826600
C	-0.88103700	-0.00002300	2.85279700
H	-1.49609600	0.88196400	3.05986600
H	-1.49650300	-0.88177300	3.05968300
H	-0.01331300	-0.00027900	3.51582900
C	-1.43469300	-2.56362300	0.25585600
H	-0.44900800	-2.76686100	-0.18284200
H	-1.32062300	-2.60802900	1.34410400
H	-2.09417800	-3.38267100	-0.04165700
C	-1.43479000	2.56362300	0.25590700
H	-1.32065000	2.60795200	1.34415300
H	-0.44916000	2.76698700	-0.18286700
H	-2.09437000	3.38263600	-0.04149200

H	5.41703500	0.00004800	-1.41862000
---	------------	------------	-------------

**12a'**

C	-3.04044800	-0.22890600	-1.26672100
C	-2.40156200	0.09632100	0.00011600
C	-3.04177200	-0.22671400	1.26683600
C	-4.27593400	-0.85417900	1.22710500
C	-4.87997200	-1.16109400	-0.00008800
C	-4.27465200	-0.85630400	-1.22717800
H	-4.78106000	-1.11196200	2.15250700
H	-5.84879500	-1.65391500	-0.00016700
H	-4.77880700	-1.11569000	-2.15266200
C	-1.18362600	0.69985200	0.00024200
C	-0.03021800	1.31219600	-0.00086000
C	1.27850400	0.62844600	-0.00021100
C	2.47268200	1.36288100	-0.00118400
C	1.36163400	-0.78185100	0.00135300
C	3.71239700	0.72730300	-0.00067100
H	2.45390900	2.44745100	-0.00235800
C	2.58312200	-1.42314900	0.00187800
H	0.45312400	-1.37990600	0.00218800
C	3.77836900	-0.67400100	0.00085800
H	4.61385300	1.32802600	-0.00143800
H	2.65256300	-2.50580600	0.00308000
C	-0.10973900	2.84147000	-0.00262900
H	0.39320600	3.22948400	-0.89369400
H	-1.14116800	3.20024400	-0.00299500
H	0.39329600	3.23160400	0.88745900
O	4.91488200	-1.39440300	0.00147500
C	6.17172500	-0.71385900	0.00026400
H	6.28485400	-0.09376500	0.89693700
H	6.92854700	-1.49807500	0.00074900
H	6.28411800	-0.09557600	-0.89774900
C	-2.38629000	0.11423100	-2.57431300
H	-2.34244200	1.20117900	-2.71578200
H	-1.35685600	-0.25575300	-2.62073400
H	-2.94537300	-0.31048000	-3.41093100
C	-2.38894700	0.11869800	2.57449800
H	-1.35954600	-0.25117000	2.62258700
H	-2.34527100	1.20588600	2.71414300
H	-2.94885100	-0.30459800	3.41128400

**12b'**

C	2.73440400	1.32419200	-0.18180100
C	2.32891900	0.02119300	0.18174200
C	2.83878600	-1.12689100	-0.46331500
C	3.80251200	-0.94432500	-1.46004600
C	4.23073700	0.33210900	-1.81906400
C	3.69989400	1.45369700	-1.18492900
H	4.21873400	-1.81548200	-1.95805300
H	4.97937200	0.45332300	-2.59642600
H	4.03657800	2.44677700	-1.46889500
C	1.35254600	-0.15292300	1.32932900
C	0.10730200	-0.17111900	0.97613000
C	-1.18621800	-0.19190400	0.55561800
C	-1.94758200	1.02376900	0.47407500
C	-1.82962600	-1.42981400	0.19588900
C	-3.25567500	1.01372000	0.06020600
H	-1.46852300	1.95783900	0.74898300
C	-3.13210200	-1.44057800	-0.21663700
H	-1.26258300	-2.35249800	0.25969200
C	-3.86515900	-0.22169800	-0.29238500
H	-3.81503400	1.93949300	0.00521700
H	-3.63995300	-2.35811200	-0.49316800
C	1.85635100	-0.29012500	2.75155600
H	2.52629900	-1.15394600	2.81527500
H	2.44204100	0.59670400	3.01526200
H	1.04273800	-0.41146400	3.47032800
O	-5.11318900	-0.34462500	-0.70228200
C	-5.97634200	0.80609700	-0.82684100
H	-5.56850100	1.51029300	-1.55743100
H	-6.92570900	0.40831900	-1.18093500
H	-6.11059800	1.28755800	0.14586400
C	2.15551500	2.55972500	0.46965700
H	1.11434200	2.72707400	0.16449900
H	2.16603500	2.50210800	1.56378100
H	2.72357700	3.44803800	0.18191300
C	2.37055000	-2.52211000	-0.11635000
H	2.36965900	-2.70961700	0.96302100
H	1.35052900	-2.70632500	-0.47791600
H	3.01763300	-3.27117300	-0.57976600

**13a'**

C	-4.03946300	0.67901800	0.00015700
C	-2.72436900	0.19005000	-0.00004900
C	-2.50677600	-1.20038100	-0.00009000
C	-3.58218200	-2.07942500	0.00008900
C	-4.89101400	-1.58515500	0.00030600
C	-5.11528100	-0.20874200	0.00033200
H	-4.23553600	1.74547100	0.00019000
H	-1.49287900	-1.59319100	-0.00031200
H	-3.40306500	-3.15022500	0.00004400
H	-5.73108000	-2.27297900	0.00044400
H	-6.12874300	0.18022200	0.00048700
C	-1.57847800	1.13362600	-0.00024500
C	-0.32617600	0.77583900	0.00061300
C	0.99922300	0.45273600	0.00042200
C	1.70744100	0.27806400	1.23824600
C	1.70674400	0.27678500	-1.23762600
C	3.04355200	-0.05133700	1.23507500
H	1.17249000	0.40973600	2.17309100
C	3.04285800	-0.05259600	-1.23486100
H	1.17126600	0.40748200	-2.17230600
C	3.70716500	-0.21555800	0.00000800
H	3.59147000	-0.18592600	2.16106400
H	3.59026600	-0.18813300	-2.16101500
C	-1.81365600	2.64796500	-0.00121300
H	-2.38550100	2.92075800	-0.89333500
H	-2.38544400	2.92195100	0.89058000
H	-0.87829100	3.21104600	-0.00159300
Cl	5.37279500	-0.62656100	-0.00025500

**13b'**

C	-3.29510500	-0.23151800	-1.24077100
C	-2.65633200	0.12515200	-0.00482000
C	-3.28193600	-0.21747500	1.24187300
C	-4.48798400	-0.88949200	1.23997400
C	-5.09171200	-1.22827100	0.01569900
C	-4.50107800	-0.90333500	-1.21864000
H	-2.81389600	0.03468800	-2.17620500
H	-2.79084200	0.05912600	2.16910800
H	-4.97090100	-1.15549800	2.17439400
H	-6.04155300	-1.75609900	0.02376000

H	-4.99386900	-1.17976700	-2.14483700
C	-1.46021400	0.78416100	-0.01475600
C	-0.32919500	1.40879900	-0.01020500
C	0.99528900	0.74615900	-0.00688200
C	2.16931200	1.51480400	0.01201400
C	1.10076200	-0.65731400	-0.02183500
C	3.41882700	0.90026600	0.01645100
H	2.12632000	2.59809400	0.02376300
C	2.34125700	-1.27739400	-0.01759900
H	0.20575000	-1.27389600	-0.03812500
C	3.50072400	-0.49280200	0.00168600
H	4.32315700	1.49828600	0.03111700
H	2.41834600	-2.35891800	-0.02959300
C	-0.44012100	2.93704800	-0.01122300
H	0.06202500	3.33195600	-0.89956800
H	-1.47817600	3.27532000	-0.01969700
H	0.04705300	3.33198800	0.88544900
Cl	5.05950700	-1.26576500	0.00674400

## F. References to Appendix

- (1) H. Arslan, J. D. Saathoff, D. N. Bunck, P. Clancy and W. R. Dichtel, *Angew. Chem. Int. Ed.*, 2012, **51**, 12051-12054.
- (2) H. Arslan, F. J. Uribe-Romo, B. J. Smith and W. R. Dichtel, *Chemical Science*, 2013, **4**, 3973-3978.
- (3) G. W. T. M. J. Frisch, H. B. Schlegel, G. E. Scuseria, M. A. Robb, J. R. Cheeseman, G. Scalmani, V. Barone, B. Mennucci, G. A. Petersson, H. Nakatsuji, M. Caricato, X. Li, H. P. Hratchian, A. F. Izmaylov, J. Bloino, G. Zheng, J. L. Sonnenberg, M. Hada, M. Ehara, K. Toyota, R. Fukuda, J. Hasegawa, M. Ishida, T. Nakajima, Y. Honda, O. Kitao, H. Nakai, T. Vreven, J. A. Montgomery, Jr., J. E. Peralta, F. Ogliaro, M. Bearpark, J. J. Heyd, E. Brothers, K. N. Kudin, V. N. Staroverov, R. Kobayashi, J. Normand, K. Raghavachari, A. Rendell, J. C. Burant, S. S. Iyengar, J. Tomasi, M. Cossi, N. Rega, J. M. Millam, M. Klene, J. E. Knox, J. B. Cross, V. Bakken, C. Adamo, J. Jaramillo, R. Gomperts, R. E. Stratmann, O. Yazyev, A. J. Austin, R. Cammi, C. Pomelli, J. W. Ochterski, R. L. Martin, K. Morokuma, V. G. Zakrzewski, G. A. Voth, P. Salvador, J. J. Dannenberg, S. Dapprich, A. D. Daniels, O. Farkas, J. B. Foresman, J. V. Ortiz, J. Cioslowski, and D. J. Fox, Gaussian, Inc., Wallingford CT, 2009.

## CHAPTER FIVE

### DESIGN AND BOTTOM-UP SYNTHESIS OF DISPERSIBLE, STRUCTURALLY PRECISE GRAPHENE NANORIBBONS

#### 5.1 *Abstract*

Graphene nanoribbons (GNRs) are thin strips of graphene that exhibit technologically relevant bandgaps when their widths are less than 10 nm. Bulk-scale syntheses that simultaneously control GNR width, length, edge structure, and pendant functionality remain underdeveloped. Here we synthesize GNRs from readily accessible poly-(*p*-phenylene-ethynylene) (PPEs) conjugated polymers. PPEs with *n*-nonyl and hexa(ethylene-oxide) (OHxg) solubilizing groups, respectively, were benzannulated at each of the alkyne subunits along the polymer backbone, which were next planarized to GNRs upon oxidative cyclodehydrogenation. GNRs with OHxg solubilizing groups are dispersible in polar organic solvents. Their Raman spectra are characteristic of their graphitic structure, and they exhibit near-infrared photoemission red-shifted by more than 400 nm as compared to any previously reported GNR. The energy of this emission corresponds well to the GNR's calculated band structure. The work described in this chapter was performed in collaboration with Dr. Fernando J. Uribe-Romo, Dr. Colin Crick, and Dr. Dasari L. V. K. Prasad, under the direction of Prof. Roald Hoffmann and Prof. W. R. Dichtel.

#### 5.2 *Introduction*

Narrowing large-area graphene into few-nanometer-wide strips opens a bandgap in its electronic structure such that the resulting graphene nanoribbons (GNRs) are of interest for nanoscale electronic devices.<sup>1,2,3</sup> In contrast, the semimetallic electronic structure of large-area graphene make it unsuitable for logic circuits, despite its superior charge mobility compared to silicon. The

potential of GNRs remains largely unrealized because of synthetic limitations. Most existing methods, including subtractive lithography<sup>4</sup>, chemical etching of graphene<sup>5</sup>, chemical vapor deposition<sup>6</sup>, sonication<sup>7</sup>, spatially resolved reduction of graphene oxide<sup>8</sup>, and unzipping carbon nanotubes<sup>9</sup> do not simultaneously control the width, length, edge structure, and pendant functionality of the ribbons. Emerging bottom-up syntheses<sup>10</sup> control GNR structure by polymerizing designed molecular building blocks. These approaches have demonstrated the feasibility of GNR synthesis in solution but produce either short<sup>11</sup> and/or incomplete ribbons<sup>12</sup> or excellent structural<sup>13</sup> and energy-level control for ribbons grown as sub-monolayers on metal surfaces.

The bottom-up synthesis of GNRs in solution remains a major challenge that builds on the historical development of ladder polymers.<sup>10,14</sup> Pioneering bulk GNR syntheses link highly substituted aromatic monomers into polyphenylenes,<sup>11</sup> whose pendant phenyl rings fuse into a ribbon structure upon oxidative dehydrogenation. This final step has shown excellent efficiency in forming GNRs<sup>12</sup> and other large polycyclic aromatic hydrocarbons (PAHs),<sup>15</sup> but the polymerizations inherently rely on hindered monomers that do not polymerize efficiently, providing impractically short ribbons. Higher degrees of polymerization ( $D_p$ ) are needed in order to study well-defined GNRs as true one-dimensional semiconductors and to fabricate nanoelectronic devices. Ideal GNR syntheses will ideally employ easily synthesized and derivatized monomers to facilitate modification of the ribbons' edge functionality.

Here we report a scalable, versatile, and efficient two-step approach to prepare GNRs from easily synthesized conjugated polymers (Figure 5.1). Our method employs a benzannulation reaction at each carbon–carbon triple bond of an appropriately substituted poly(phenyleneethynylene) (PPE).<sup>16,17</sup> The resulting sterically crowded polyphenylene is



subsequently planarized to the corresponding GNR using a Scholl oxidation reaction. PPEs are attractive GNR precursors because of the structural versatility, functional group tolerance, and efficiency of their polymerizations. The alkynes of PPEs have been modified only rarely, and we recently demonstrated that their benzannulation is highly efficient<sup>17</sup> and that the Scholl oxidation of model oligophenylene motifs occurs without deleterious rearrangements.<sup>18</sup> We now apply this benzannulation/oxidation sequence to transform two PPEs into corresponding GNRs. The first PPE features a *p*-terphenyl-*alt*-phenyl structure with *n*-nonyl solubilizing groups, which provides a GNR with a rippled armchair-like edge structure (Figure 5.1b). Although the benzannulation of this polymer is highly efficient, the poor dispersibility of its graphitized products precludes unambiguous characterization of its structure. A second PPE featuring naphthalene substituents bearing hexa(ethylene-oxide) side chains is more soluble, such that high molecular weight polymers were accessed. The resulting GNRs (Figure 5.1b) exhibit a true armchair edge structure and form stable dispersions in multiple solvents. Their near-infrared photoemission and other spectroscopic characterization are consistent with the expected structure, as well as calculations of their band energies. The dispersibility of these GNRs allowed them to be imaged as individual nanometer-size objects by atomic force microscopy by drop-casting from solution. We anticipate that this approach will enable device engineering through rational chemical synthesis, and allow functionalization of well-defined GNRs with active substances or specific functionality.

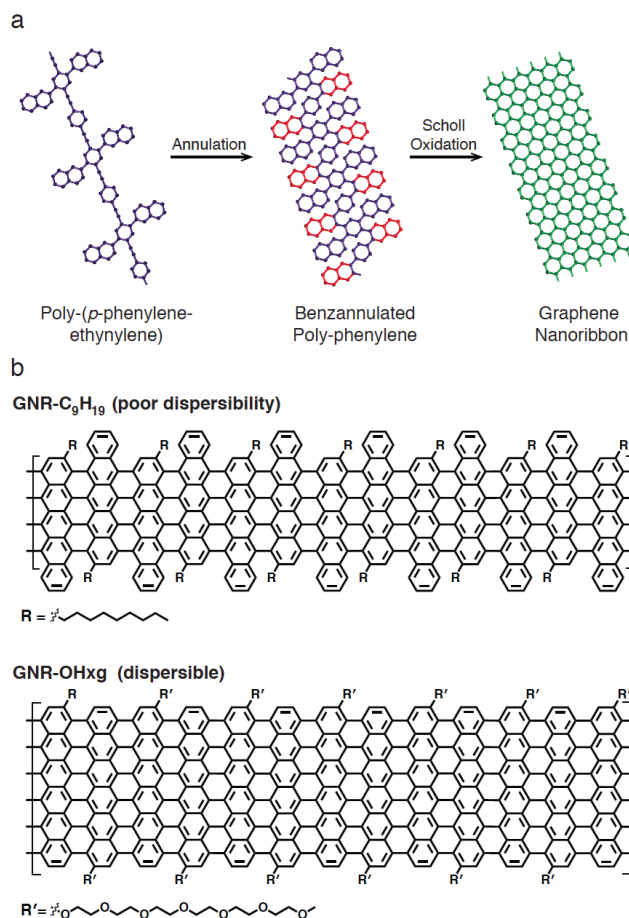
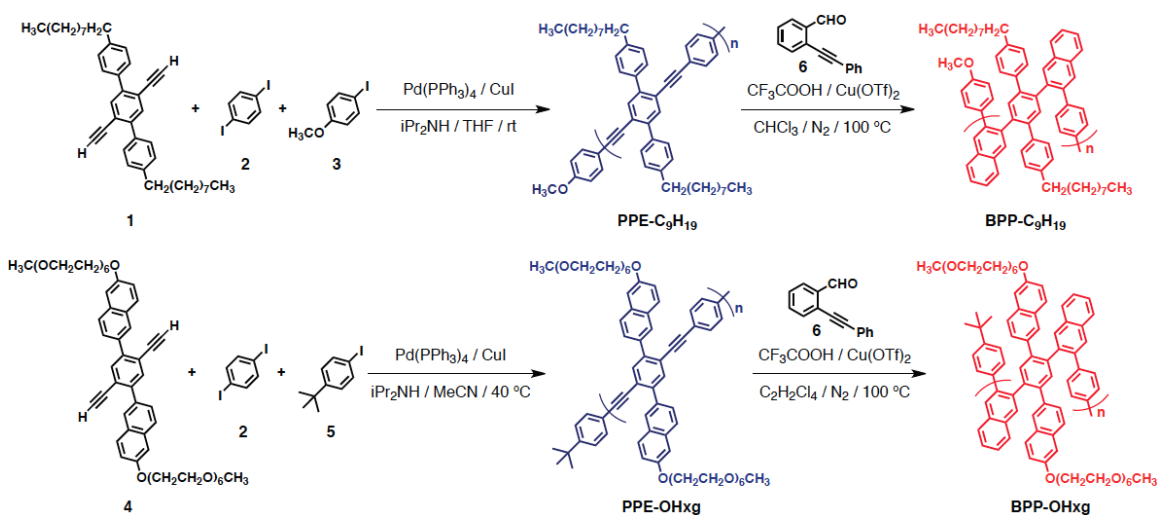


**Figure 5.1. a.** Strategy used to transform PPEs (purple) into GNRs (green) featuring the benzannulation of the alkyne subunits followed by Scholl oxidation. **b.** GNRs described in this manuscript: **GNR-C<sub>9</sub>H<sub>19</sub>** (top) is a first generation system with *n*-nonyl that confers insufficient dispersibility; **GNR-OHxg** (bottom) is fully dispersible and features an armchair edge structure.

### 5.3 Polymerization

The PPEs used in this study were prepared using a Sonogashira cross-coupling polymerization between a dialkyne monomer (**1** or **4**) and 1,4-diiodobenzene **2** (Scheme 5.1). **PPE-C<sub>9</sub>H<sub>19</sub>**, prepared from **1** and **2**, is insoluble in the THF polymerization at molecular weights of approximately 100,000 g mol<sup>-1</sup>, as observed using size-exclusion chromatography/multi-angle light scattering (SEC/MALS) measurements. Therefore a substoichiometric amount of 4-

iodoanisole **3** was used to control the molecular weight. When 10 % mol of **3** was employed, the resulting **PPE-C<sub>9</sub>H<sub>19</sub>** had an average degree of polymerization ( $D_p$ ) of 12, close to that predicted by the Carothers equation, but a bimodal molecular weight distribution. A subsequent precipitation after the benzannulation step fractionated the sample to selectively provide the high molecular weight chains; therefore, we did not attempt to fractionate the **PPE-C<sub>9</sub>H<sub>19</sub>** sample at this step.



**Scheme 5.1.** Synthesis of poly-(*p*-phenylene-ethynylene)s (PPEs) and their subsequent transformation into benzannulated polyphenylenes (BPPs).

The poor solubility of **PPE-C<sub>9</sub>H<sub>19</sub>** and its graphitized products, led us to design and investigate a second PPE system with hexa(ethylene-oxide) solubilizing groups, which effectively solubilize *m*-phenylene-ethynylene foldamers.<sup>19</sup> The dialkyne monomer **4** also features 2,6-naphthanylene rather than 1,4-phenylene substituents (Scheme 5.1), so as to provide GNRs with true armchair edge structures. Equimolar amounts of **2** and **4** were polymerized in  $\text{CH}_3\text{CN}$  under otherwise similar reaction conditions used for **PPE-C<sub>9</sub>H<sub>19</sub>**. The resulting **PPE-OHxg** remained soluble in the  $\text{CH}_3\text{CN}$  reaction mixture and high molecular weights were obtained. However, this **PPE-OHxg** sample (Table 5.1, entry A) only partially dissolved in THF,

in which SEC/MALS characterization was performed. The THF-soluble portion exhibited  $M_w$  of 134,000 g mol<sup>-1</sup>, corresponding to a  $D_p$  of 129, and a dispersity ( $D_M$ ) of 1.28 (Table 5.1, entry 1; for chromatograms, see Appendix section C). These values correspond to the lower limits of the **PPE-OHxg** molecular weight. This sample was fully soluble in chlorinated solvents used for the benzannulation reaction, such as the complete distribution of chain sizes was carried forward in the synthesis. We also targeted samples of **PPE-OHxg** with lower  $D_p$  of 80 and 40 by including 2.4 and 4.6 mol% of 4-*t*-butyl-1-iodobenzene **5**, respectively, in the polymerization. These samples were fully soluble in THF and provided  $M_w$  of 197,000 ( $D_p = 190$ ) and 36,200 g mol<sup>-1</sup> ( $D_p = 35$ ), respectively (Table 5.1, entries B and C). <sup>1</sup>H NMR end-group analysis of these samples provided similar  $D_p$  (135 and 22, respectively). These samples exhibit narrow molecular weight distributions that we attribute to fractionation that occurs upon precipitation of the benzannulated polymers from Et<sub>2</sub>O. SEC analysis of the Et<sub>2</sub>O-soluble fractions indicated the presence of low molecular weight materials that confirm this interpretation (see Appendix Figure A4.10). These combined observations indicate that high molecular weight samples of **PPE-OHxg** with narrow dispersity were accessed.

**Table 5.1.** Average molecular weights ( $M_n$ ,  $M_w$ ), dispersities ( $D_M$ ), and average degrees of polymerization ( $D_p$ ) of **PPE-OHxg** and **BPP-OHxg** samples, as determined from SEC/MALS in THF as mobile phase.

Entry	5 (mol%)	Theoretical $D_p$	PPE-OHxg				BPP-OHxg			
			$M_n^a$	$M_w^a$	$D_M$	$D_p$	$M_n^b$	$M_w^b$	$D_M$	$D_p$
			(g mol <sup>-1</sup> )	(g mol <sup>-1</sup> )			(g mol <sup>-1</sup> )	(g mol <sup>-1</sup> )		
A <sup>c</sup>	0	∞	110,000	134,000	1.22	129	186,000	190,000	1.02	152
B	2.41	80	107,00	197,000	1.85	190	158,000	167,000	1.06	134
C	4.64	40	33,400	36,200	1.26	35	39,960	50,000	1.25	40

<sup>a</sup> After one precipitation step.

<sup>b</sup> After a total of two precipitations.

<sup>c</sup> This sample was only partially soluble in THF. These masses reflect only soluble fractions.

1,3-butadiyne defects have been noted in PPEs synthesized under Sonogashira conditions, which arise from Glaser-Eglinton couplings mediated by Pd<sup>2+</sup> precatalysts or adventitious O<sub>2</sub>.<sup>20</sup> If present, these butadiynes would introduce defects into the final GNR products. Therefore, we selectively incorporated <sup>13</sup>C into the alkyne functions of **PPE-OHxg** to simplify its characterization using <sup>13</sup>C NMR and Raman spectroscopy. The <sup>13</sup>C NMR spectrum of **PPE-OHxg-<sup>13</sup>C** ( $D_p$  = 104, Figure 1a) indicated the expected intense resonances at 91 and 93 ppm, respectively, that correspond to most of the <sup>13</sup>C-labeled alkyne carbons. We assign the less intense set of resonances in this region of the spectrum to alkynes in close proximity to the 4-*t*BuPh end groups. Resonances corresponding to 1,4-diaryl-1,3-butadiyne defects would appear as coupled resonances at *ca.* 82 and 74 ppm, as shown by Tykwinski and Luu across a series of diarylpolyyne.<sup>21</sup> No such signals are observed in the spectra of **PPE-OHxg** or **PPE-OHxg-<sup>13</sup>C**.

Furthermore, the Raman spectrum of **PPE-OHxg** exhibits a characteristic alkyne symmetric stretching mode at  $2200\text{ cm}^{-1}$ , which shifts to  $2112\text{ cm}^{-1}$  in the isotopically labeled sample (Figure 5.1b). These signals appear as single, well-resolved peaks in each spectrum. No peaks corresponding to 1,3-butadiyne stretches are observed in either spectrum (*e.g.*, such as  $2214\text{ cm}^{-1}$  for 1,4-diphenyl-1,3-butadiyne<sup>22</sup>). These results indicate that PPEs with high molecular weights can be produced with minimal butadiyne defects.

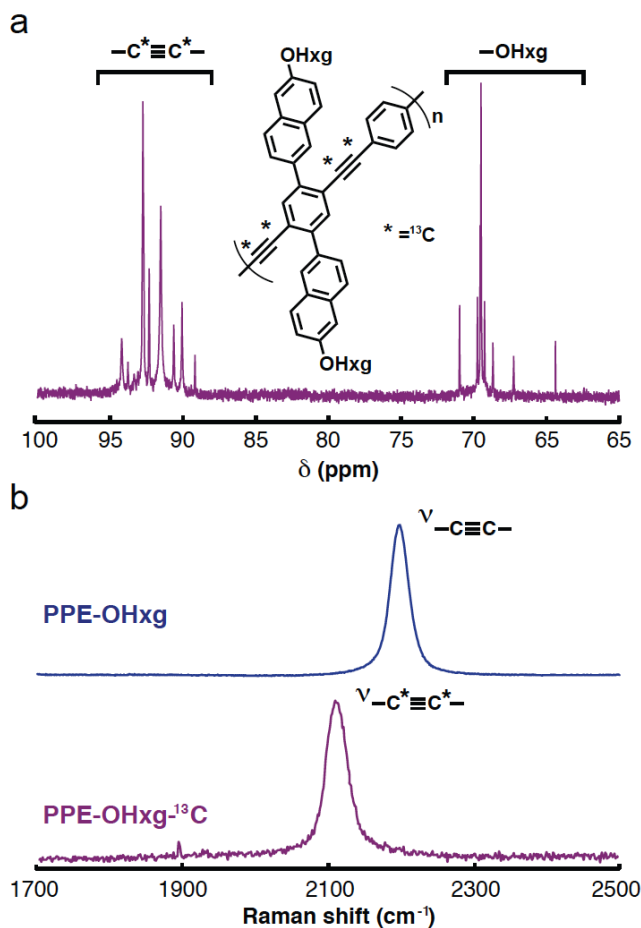


**Figure 5.2.** **a.** A partial  $^{13}\text{C}$  NMR (125 MHz, DMSO- $d_6$ , 353 K) spectrum of **PPE-OHxg- $^{13}\text{C}$**  indicates intense resonances corresponding to the alkyne carbons and the oligo-(ethylene-oxide) side chains. Signals corresponding to 1,3-butadiyne moieties are expected between 74 and 82 ppm and are not observed. **b.** Partial Raman spectra ( $\lambda_{\text{ex}} = 785\text{ nm}$ ) indicating the alkyne stretch of **PPE-OHxg** (blue) and **PPE-OHxg- $^{13}\text{C}$**  (purple).

## 5.4 Benzannulation

**PPE-OHxg** was benzannulated in similarly high efficiency as **PPE-C<sub>9</sub>H<sub>19</sub>**<sup>17</sup> using benzaldehyde **6** (7.3 equiv. per alkyne), CF<sub>3</sub>COOH (3 equiv. per alkyne), and Cu(OTf)<sub>2</sub> (0.18 equiv. per alkyne) in 1,1,2,2-tetrachloroethane (TCE) at 100 °C. The benzannulated polymers were isolated using a basic aqueous workup followed by precipitation from TCE into excess Et<sub>2</sub>O. SEC/MALS characterization of the benzannulated polymers (Table 5.1 A-C) indicated the expected increases in molecular weight corresponding to the newly installed 2,3-naphthanylene moieties. For example, the **PPE-OHxg** with  $D_p = 190$  (Table 5.1, entry B) provided **BPP-OHxg** with  $M_w = 166,900 \text{ g mol}^{-1}$  ( $D_p = 134$ ). The apparent increase in  $D_p$  and decrease in dispersity (from 1.85 to 1.18) is associated with further fractionation of the BPP during the Et<sub>2</sub>O precipitation (see Appendix Figure A4.11). This phenomenon was also observed for the **BPP-C<sub>9</sub>H<sub>19</sub>** in our initial report. The higher molecular weight sample (Table 5.1 entry A) produced a **BPP-OHxg** with  $M_n$  of  $189,000 \text{ g mol}^{-1}$ , corresponding to a degree of polymerization of 152 and a quite low dispersity of 1.02. The increase of  $D_p$  is attributed to the combined effects of fractionation (reflected in the low  $D_M$ ) and the underestimated  $M_n$  of the **PPE-OHxg** reactant. The **PPE-OHxg** of  $D_p = 35$  produced a BPP with  $M_w$  of  $50,000 \text{ g mol}^{-1}$  and a  $D_p$  of 40. Fractionation does not occur at this molecular weight and thus the  $D_p$  and  $D_M$  are almost unchanged as a result of the benzannulation. UV/vis and fluorescence spectroscopies of **BPP-OHxg** were consistent with efficient benzannulation. The absorbance of **BPP-OHxg** is blue-shifted significantly ( $\lambda_{\text{max}} = 270 \text{ nm}$ ) relative to that of **PPE-OHxg** ( $\lambda_{\text{max}} = 420 \text{ nm}$ ), which arises from the inability of the **BPP** polymers to adopt coplanar conformations along their backbones. The photoemission of **BPP-OHxg** is broadened, red-shifted, and lower quantum yield ( $\lambda_F = 1.4\%$  vs.  $7.1\%$ , see Supporting

Information) as compared to **PPE-OHxg**. These observations are consistent with the photoemission of *o*-polyphenylenes previously reported by Hartley<sup>23</sup> and Aida.<sup>24</sup>

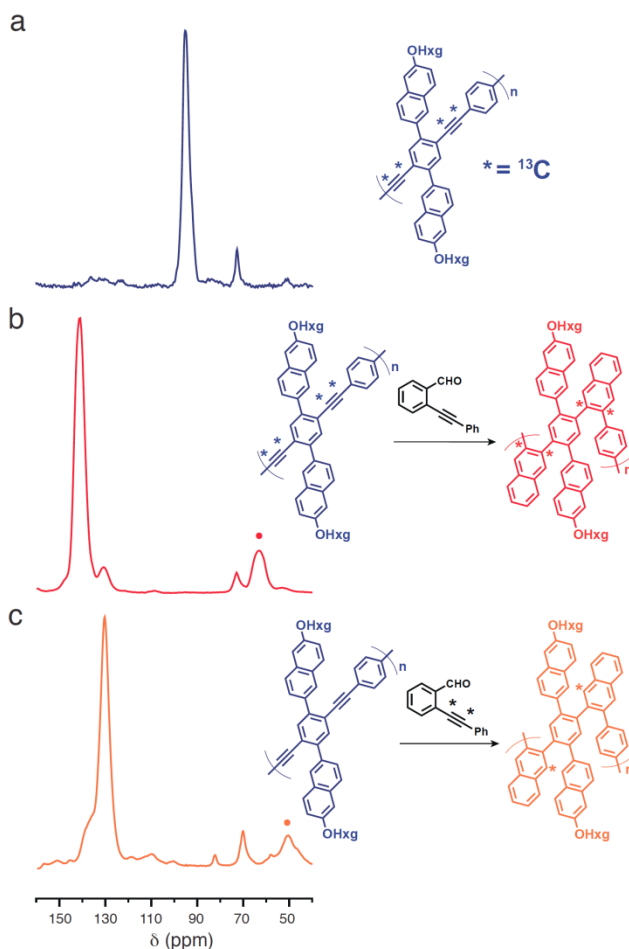


**Figure 5.3.** Partial  $^{13}\text{C}$  CP-MAS (100 MHz, 8.0 kHz MAS, rt) spectra of (a) **PPE-OHxg- $^{13}\text{C}$** , (b) **BPP-OHxg- $^{13}\text{C}(2,3)$**  and (c) **BPP-OHxg- $^{13}\text{C}(1)$** . The two isotopically labeled **BPP-OHxg** spectra both indicate efficient benzannulation of the corresponding PPE and indicate different chemical shift environments of the isotopically enriched carbons. Filled symbols indicate spinning side bands, stars indicate  $^{13}\text{C}$  labeling.

Each of the sterically crowded benzannulated polymers exhibit poorly resolved solution NMR spectra because they adopt a small number of kinetically trapped conformations whose resonances do not coalesce below 140 °C. However, significant insight into the benzannulation efficiency was obtained through two complementary  $^{13}\text{C}$  isotopic labeling studies. We first benzannulated the **PPE-OHxg- $^{13}\text{C}$**  to produce a **BPP-OHxg** with  $^{13}\text{C}$  enrichment at the 2 and 3

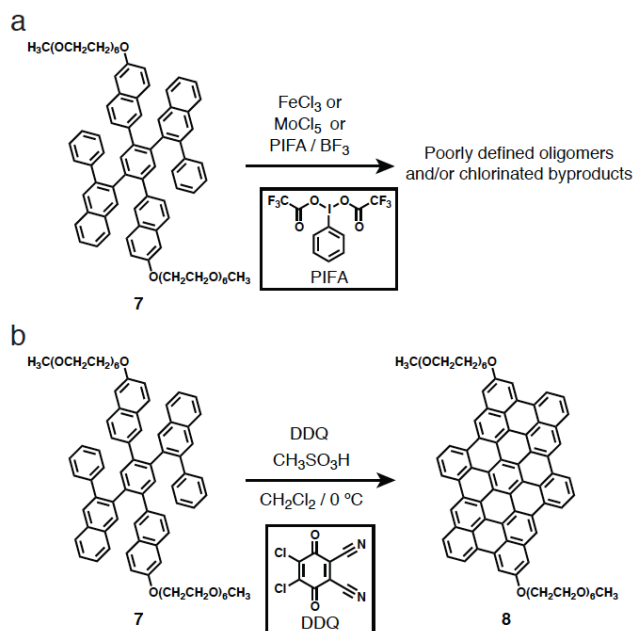


positions of the resulting naphthalene subunits [**BPP-OHxg**- $^{13}\text{C}(2,3)$ ]. We also benzannulated unlabeled **PPE-OHxg** with  $6\text{-}^{13}\text{C}_2$ , to obtain **BPP-OHxg**- $^{13}\text{C}(1)$  with isotopic labeling at the 1-position of the naphthalene subunit.<sup>25</sup> These two studies produced **BPP-OHxg** with  $^{13}\text{C}$  isotopic labels in different positions and bonding environments, which were characterized using solid-state NMR spectroscopy. Benzannulation of **PPE-OHxg**- $^{13}\text{C}$  indicated complete transformation of the labeled alkyne functions into 2,3-disubstituted naphthalenes (Figure 5.3). The cross-polarization with magic angle spinning (CP-MAS) spectrum of **PPE-OHxg** exhibited an intense resonance at 95 ppm, corresponding to the alkyne carbons. This resonance shifts to 140 ppm in the corresponding spectrum of **BPP-OHxg**- $^{13}\text{C}(2,3)$  (Figure 5.3b). No signals for residual alkynes are observed. In contrast, the spectrum of **BPP-OHxg**- $^{13}\text{C}(1)$  shows its most intense peak at 130 ppm, indicating the clear difference in the positions of the  $^{13}\text{C}$ -enriched sites in the two polymer samples (Figure 5.3c). The carbon bonding environments of each of these resonances were determined by measuring the peak intensity as a function of cross-polarization time ( $t_{\text{CP}}$ ) and interrupted decoupling time ( $t_{\text{ID}}$ ) in the CP-MAS experiment. These dependencies suggest that the 130 ppm resonance of the **BPP-OHxg**- $^{13}\text{C}(1)$  corresponds to  $^{13}\text{C}$  bound to a single hydrogen (Figures A4.47-A4.48), whereas the 140 ppm resonances of **BPP-OHxg**- $^{13}\text{C}(2,3)$  correspond to  $^{13}\text{C}$  bound only to other carbons (Figures A4.51- A4.52).<sup>26</sup> The  $^{13}\text{C}$  CP-MAS NMR spectrum of the unlabeled **BPP-OHxg** (Figure A4.44) contains both of these peaks, in addition to resolved resonances corresponding to specific aromatic carbons near the OHxg substituent (158, 107, and 94 ppm) and the side-chain methylene and methyl groups (71 ppm and 60, respectively). Taken together, these complementary spectroscopic and isotopic labeling studies indicate that the benzannulation of **PPE-OHxg** proceeds efficiently to produce well-defined polyarylenes amenable for oxidation to a GNR.

### 5.5 *Identifying Scholl conditions for GNR-OHxg*

The final synthetic operation to access GNRs is a cyclodehydrogenation (Scholl reaction) mediated by an external oxidant. A wide variety of oxidants have been employed previously, and the Scholl reaction outcome is known to be both substrate and oxidant dependent.<sup>27</sup> Examples of known side reactions include rearrangements, incomplete oxidation, oligomerization and cross-linking, and halogenation or oxygen-atom incorporation.<sup>27</sup> These deleterious processes are easily diagnosed first by studying model compounds rather than BPP polymers. We therefore prepared model compound **7** from the double benzannulation of the corresponding dialkyne (See Appendix) and subjected it to various Scholl oxidation conditions. None of the commonly employed oxidants, FeCl<sub>3</sub>, MoCl<sub>5</sub>, and [bis(trifluoroacetoxy)iodo]benzene (PIFA)/BF<sub>3</sub>OEt<sub>2</sub> oxidized **7** cleanly to the corresponding PAH **8**. A complex mixture of products was obtained in each case that included both soluble oligomers and uncharacterized insoluble byproducts. Matrix assisted laser desorption-ionization time-of-flight mass spectrometry (MALDI-TOF MS) of the soluble products also indicated many chlorinated products, even when oxidants lacking chlorine were employed. In contrast, **7** was oxidized to the fused PAH **8** using 2,3-dichloro-5,6-dicyano-1,4-benzoquinone (DDQ) in the presence of CH<sub>3</sub>SO<sub>3</sub>H.<sup>28</sup> A discrete molecule was isolated and the preliminary MALDI-TOF MS data indicates the formation of the expected product. We were not able to assign the structure unambiguously. Our work towards identifying this structure is underway. In contrast, we recently found that FeCl<sub>3</sub>-mediated conditions provide efficient planarization and no rearrangements for several model compounds of **BPP-C<sub>9</sub>H<sub>19</sub>**.<sup>18</sup> Interestingly, DDQ/CH<sub>3</sub>SO<sub>3</sub>H conditions did not oxidize these structures cleanly, indicating that these model oxidation studies should be performed for each new GNR target. Collectively, these

results indicate that DDQ/ $\text{CH}_3\text{SO}_3\text{H}$  conditions are appropriate for forming **GNR-OH<sub>9</sub>**, and  $\text{FeCl}_3$  is the best oxidant for **BPP-C<sub>9</sub>H<sub>19</sub>**.

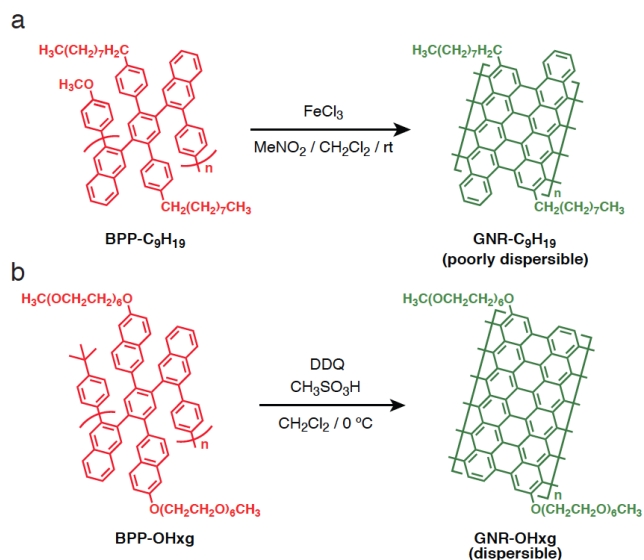


**Scheme 5.2.** Scholl oxidation of model compound.

## 5.6 GNR formation

**BPP-C<sub>9</sub>H<sub>19</sub>** was oxidized to **GNR-C<sub>9</sub>H<sub>19</sub>** using  $\text{FeCl}_3$  in a mixture of  $\text{CH}_3\text{NO}_2$  and  $\text{CH}_2\text{Cl}_2$ , from which it precipitated as a black solid. The GNR exhibits spectroscopic signatures consistent with the fusion of a planar ladder polymer. Unfortunately, the *n*-nonyl groups are insufficient for solubilizing **GNR-C<sub>9</sub>H<sub>19</sub>** in most solvents, but it was possible to disperse a small fraction of the sample in  $\text{CS}_2$  or 1,2-dichlorobenzene (Figures A4.14 and A4.15). Drop-cast films of these solutions provided Raman spectra consistent with graphitized materials as well as near-infrared (NIR) photoemission ( $\lambda_{\text{max}} = 823\text{ nm}$ , Figure S30). Transmission electron microscopy (TEM) and atomic force microscopy (AFM) of even highly diluted solutions of these dispersions showed only large aggregates. These findings suggest that the Scholl oxidation produces graphitized materials with moderate to excellent cyclodehydrogenation efficiency. However, the

intractable nature of these products precluded a more definitive assignment of their structure. These difficulties motivated our design and exploration of the **GNR-OHxg** system.



**Scheme 5.3.** Scholl oxidation of BPPs to GNRs.

In contrast, the oxidation of the **BPP-OHxg** ( $D_p = 120$ ) using DDQ/CH<sub>3</sub>SO<sub>3</sub>H in CH<sub>2</sub>Cl<sub>2</sub> provided GNR samples that were fully dispersible in *N,N*-dimethylformamide (DMF) and *N*-methyl-2-pyrrolidone (NMP) to concentrations of *ca.* 0.5 mg mL<sup>-1</sup>. In contrast, the oxidation using FeCl<sub>3</sub> provided poorly dispersible materials, as suggested by the model study. The **GNR-OHxg** derived from the DDQ/CH<sub>3</sub>SO<sub>3</sub>H oxidation were characterized by a full complement of spectroscopic and polymer characterization techniques: FTIR, Raman, X-ray photoelectron (XPS), solid-state NMR, UV-vis, and NIR photoemission spectroscopies, thermalgravimetric analysis (TGA) and AFM imaging. FTIR spectroscopy (Figure 4) indicates that the **GNR-OHxg** retains its oligo-(ethylene-oxide) side chains, as evidenced from the *sp*<sup>3</sup>-hybridized C-H vibrational modes centered at 2870 cm<sup>-1</sup>. The spectrum also shows attenuated *sp*<sup>2</sup>-hybridized C-H stretching modes at 3060 cm<sup>-1</sup>, relative to the **BPP-OHxg** precursor, a signature of the

cyclodehydrogenation process. The Raman spectrum (488 nm excitation) exhibits features of GNRs, including the *D* and *G* bands at 1365 and 1600  $\text{cm}^{-1}$ , respectively. The *2D* and the *2G* (*a.k.a G'*) overtones, as well as the *D+G* combination modes were present at 2663, 2935 and 3164  $\text{cm}^{-1}$ , respectively. These spectra are similar to those of GNRs derived from other methods.<sup>9,11,12</sup> X-ray photoemission spectroscopy of the **GNR-OHxg** solutions drop cast onto Au/Si substrates exhibited only  $\text{C}_{1s}$  and  $\text{O}_{1s}$  signals. The  $\text{C}_{1s}$  peak at 284.83 eV was fit to three Gaussian-Lorentzian-Product (GL) functions, of which the side-chain C and aromatic C signals at 286.30 and 284.69 eV, respectively, were the most intense. The small  $\text{C}_{1s}$  peak centered at 298.09 eV is assigned to a  $\pi$ -type shake up satellite that has been observed in other graphitic materials.<sup>29</sup> The  $\text{O}_{1s}$  signal was fit to a single GL function centered at 532.67 eV, consistent of that of poly(ethylene-oxide).<sup>30</sup> No peaks for  $sp^2$ -hybridized oxidized defects are observed (such as ketones, carboxylic acids, etc.), which would be expected at slightly lower binding energy.<sup>31</sup> Thermalgravimetric analysis of **GNR-OHxg** indicated thermal stability to 250 °C, followed by a 47 % mass loss from 250 – 450 °C corresponding to the side chains (48 % expected). The remainder of the sample exhibits no additional mass loss below 800 °C. This thermal response is consistent with that expected for a GNR with oligo(ethyleneoxide) side chains.

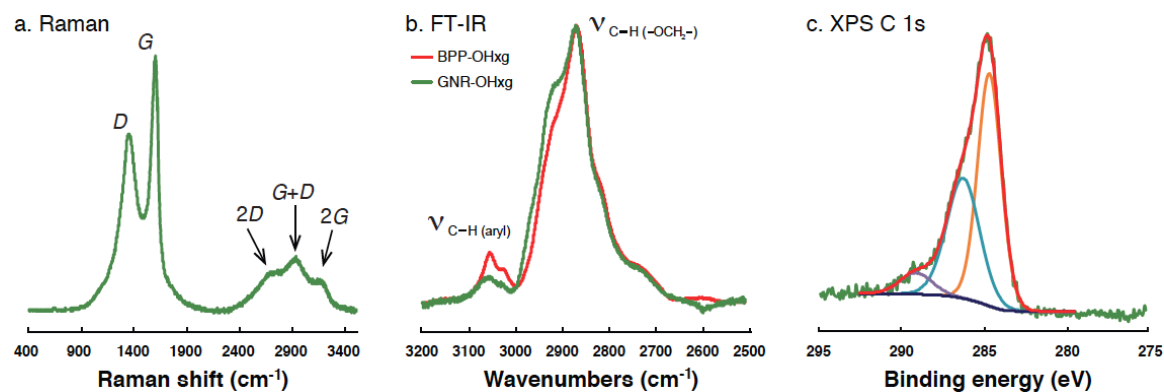


**Figure 5.4.** Spectroscopic characterization of GNR-OHxg. **a.** Raman spectrum ( $\lambda_{\text{ex}} = 488 \text{ nm}$ ) displays the *D*, *G*, and the corresponding *2D* and *2G* overtones and *D+G* combination vibrational features. **b.** Partial FT-IR spectrum of **BPP-OHxg** and **GNR-OHxg** indicate decreased intensity of the aromatic C-H stretching mode relative to the OHxg C-H stretching mode upon cyclodehydrogenation. **c.** A high resolution XPS C 1s spectrum was fit to three GL functions corresponding to the OHxg side chains (orange), graphitized carbon (blue) and a weak  $\pi$ -type satellite peak (purple).

Solid-state NMR spectroscopy of **GNR-OHxg**, including experiments performed on  $^{13}\text{C}$ -labeled **GNR-OHxg** derivatives, was also consistent with the expected ribbon structure.  $^{13}\text{C}$  CP-MAS spectra of **GNR-OHxg**, recorded at a resonance frequency of 100 MHz, and MAS rate of 8 kHz did not provide any observable signal. GNRs formed from the DDQ/ $\text{CH}_3\text{SO}_3\text{H}$  oxidation of the isotopically labelled **BPP-OHxg- $^{13}\text{C}(1)$** , and **BPP-OHxg- $^{13}\text{C}(2,3)$**  samples displayed broad signals with inconsistent drifts in chemical shifts under similar conditions. Similarly poor NMR spectra of graphitic materials had been observed previously, which were attributed either to the sample's conductivity or the presence of delocalized unpaired electrons.<sup>32</sup> Ruoff and collaborators mitigated these effects in a study of  $^{13}\text{C}$ -labelled graphite oxide by recording the spectra at higher MAS rates and reduced temperature.<sup>33</sup> Therefore, we collected the  $^{13}\text{C}$  CP-MAS spectrum of **GNR-OHxg** and both the  $^{13}\text{C}$  CP-MAS and  $^{13}\text{C}$  MAS of the isotopically labelled **GNR-OHxg- $^{13}\text{C}(1)$** , and **GNR-OHxg- $^{13}\text{C}(2,3)$**  samples under improved conditions (188 MHz  $^{13}\text{C}$  resonance frequency, MAS rate of 15 kHz,  $-5^\circ\text{C}$ ). The  $^{13}\text{C}$  CP-MAS spectrum of

unlabelled **GNR-OHxg** (Figure 5.5a) shows two signals at 120 and 70 ppm, consistent with the presence of carbons in aromatic and ethylene oxide bonding environments. Similarly, the  $^{13}\text{C}$  CP-MAS (Figures A4.54 and A4.56) and  $^{13}\text{C}$  MAS NMR (Figure 5.5b and c) spectra of the enriched **GNR-OHxg** samples exhibited signals only in the aromatic region of the spectrum, consistent with the corresponding labeling position.

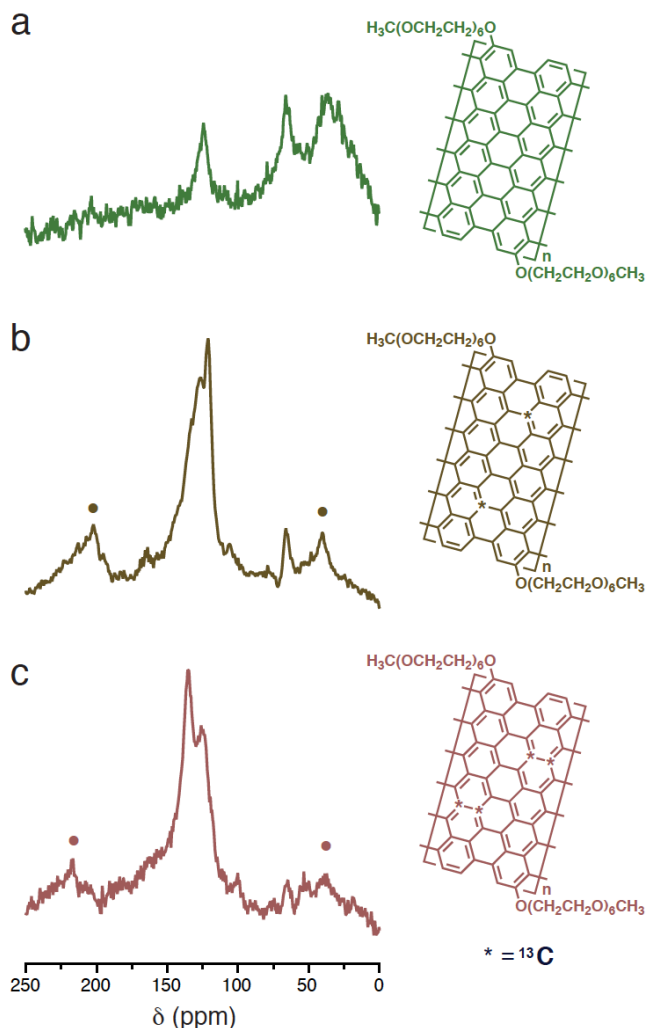


**Figure 5.5.** High-field (188 MHz, MAS rate of 15 kHz,  $-5\text{ }^\circ\text{C}$ )  $^{13}\text{C}$  CP-MAS spectra of natural abundance **GNR-OHxg** (a), and  $^{13}\text{C}$  MAS spectra of isotopically enriched **GNR-OHxg- $^{13}\text{C}(1)$**  (b) and **GNR-OHxg- $^{13}\text{C}(2,3)$**  (c), indicating the presence of carbons in oligo ethylene oxide and aromatic chemical environments. Filled symbols indicate spinning side bands, stars indicate  $^{13}\text{C}$  labeling.

The GNR exhibits solution absorbance and NIR photoemission consistent with its graphene structure and Density Functional Theory (DFT) calculations of its band structure. A DMF solution of **GNR-OHxg** exhibits a broad absorption band over much of the visible spectrum, in contrast to the distinct absorbances of **PPE-OHxg** and **BPP-OHxg** discussed above. The **GNR-OHxg** shows no observable photoemission in the visible range of the spectrum, and instead emits in the NIR with  $\lambda_{\text{max}}$  of 1409 and 1204 nm (Figure 5.6). These wavelengths correspond to photon energies of 0.88 and 1.03 eV, respectively, which are consistent with its calculated band structure (see below). The **GNR-OHxg** system is the first GNR prepared through a bottom-up approach that emits well into the NIR, consistent with the bandgap of GNRs and carbon nanotubes. In contrast, the **GNR-C<sub>9</sub>H<sub>19</sub>**, as well as other GNRs prepared previously,<sup>11b</sup> have emitted in the visible, which can arise from incomplete planarization. For example, poorly defined **GNR-OHxg** samples derived from FeCl<sub>3</sub> or MoCl<sub>5</sub>-mediated oxidations also exhibit photoemission in the visible rather than the NIR spectral region, which we attribute to partially fused and/or defective structures. NIR emission of **GNR-OHxg** was only observed in samples oxidized using DDQ/CH<sub>3</sub>SO<sub>3</sub>H.



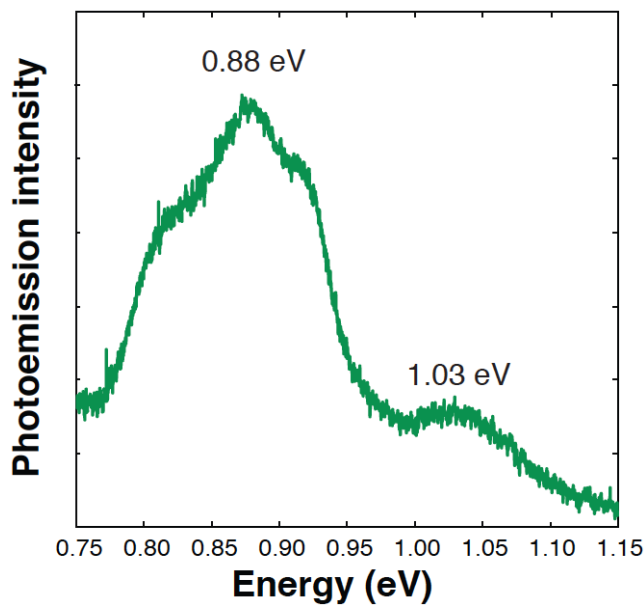


**Figure 5.6.** Near-infrared (NIR) photoemission spectrum (DMF,  $\lambda_{\text{ex}} = 450$  nm) of **GNR-OHxg**. The  $\lambda_{\text{max}}$  of 0.88 eV corresponds well to the calculated bandgap.

### 5.7 Band structure calculations of GNRs

Based on the observation of a photoemission signal in the NIR spectrum, we calculated the band structure of the **GNR-OHxg** using *ab initio* Density Functional Theory (DFT) methods in a simplified crystal model of our GNR (Figure 5.7a). A monoclinic unit cell was constructed using the **GNR-OHxg** repeating unit using the Materials Studio modeling suite,<sup>34</sup> with the point symmetry of the repeat unit ( $C_{2h}$ ) in its center of the cell, commensurate with the space group symmetry ( $P2_1/m$ ). The model assumes infinite nanoribbon length ( $c$ -axis), and no interaction with adjacent GNRs in the other two dimensions ( $a$  and  $b$ ). The hexa(ethylene oxide) solubilizing groups were also shortened to  $-\text{OCH}_3$  to reduce the computational cost. The electronic band structure and density of states (DOS) were calculated using *CASTEP* module in Materials Studio, which uses a DFT plane-wave theory method to compute electronic properties of condensed matter.<sup>35</sup> Since DFT methods tend to underestimate the bandgap of semiconductors and carbon-based nanostructures,<sup>36</sup> we performed DFT calculations using several exchange

correlation functionals, based on both local density approximation (LDA) and generalized gradient approximations (GGA). Each calculation provided similar band structures and bandgaps (see Appendix). Figure 5.7b shows the band structure and DOS of the **GNR-OCH<sub>3</sub>** (*P2/m*) model obtained from the Perdew-Burke-Ernzerhof (PBE) functional (GGA) in the energy region around the Fermi level ( $\pm 5$  eV). As expected for a quasi one-dimensional semiconducting polymer, the bands do not cross each other at the Fermi level, and display a direct bandgap at the  $\Gamma$  point of  $E_g = 0.83$  eV, very close to that observed ( $\lambda_{\text{max}} = 0.88$  eV) in the NIR photoemission spectrum. This photoemission behavior is similar to the observed in carbon nanotubes, where the  $\lambda_{\text{max}}$  of the fluorescence spectrum corresponds to the bandgap of a particular nanotube of a given width and chirality.<sup>37</sup> The calculated DOS (Figure 5.7b) shows the presence of a gap between the highest valence band state and the lowest conduction band state, supporting the validity of the calculated bandgaps and the semiconducting nature of the material.

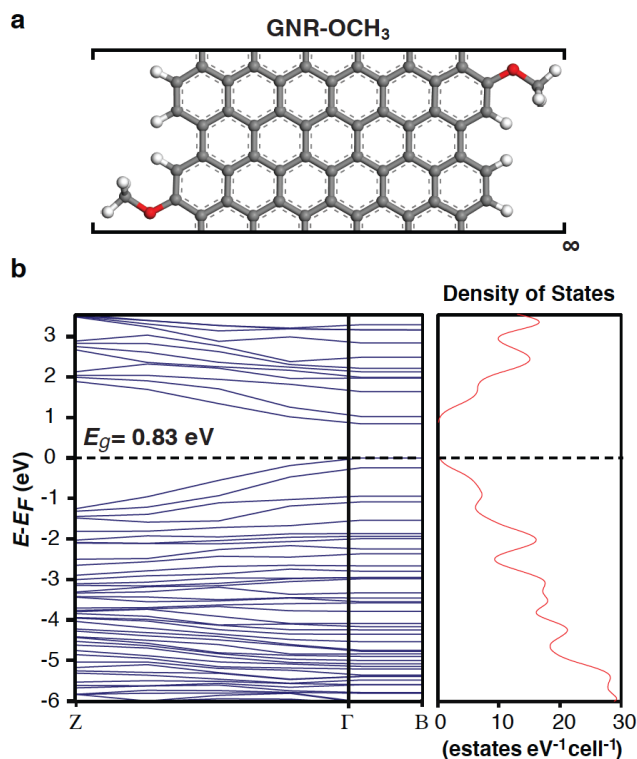


**Figure 5.7.** **a.** Repeating unit of the **GNR-OCH<sub>3</sub>** model used for the DFT calculation of the band structure and density of states (DOS) of the **GNR-OHxg**. **b.** Calculated band structure and DOS of **GNR-OCH<sub>3</sub>** near the Fermi level, indicating a bandgap of 0.83 eV.

The possibility of bending at the edges of the ribbon was explored by relaxing the structural model in a lower symmetry setting ( $P\bar{1}$ ). Although some twisting of the GNR is observed as a consequence of steric hindrance between the -OCH<sub>3</sub> and the edge -H, the calculated bandgap was unchanged (see Appendix). We also probed the effect of the alkoxy substituent by calculating the bandgap of the GNR with the OCH<sub>3</sub> replaced by H. This model of a -H terminated,  $N = 13$  GNR with  $Pmmm$  symmetry provides a calculated bandgap of 0.945 eV, which is  $\sim 0.1$  eV higher than alkoxy substituted GNRs. Moreover, the calculated  $E_g$  of the **GNR-H** model resembles those calculated<sup>36c</sup> and recently measured in submonolayer GNRs.<sup>13d</sup>

## 5.8 AFM of GNR-OHxg

We evaluated the dispersibility of the **GNR-OHxg** using AFM by drop-casting dilute DMF solutions (10 nM, 1.0 mg L<sup>-1</sup>) onto freshly cleaved mica. The resulting micrographs indicated particles whose heights correspond to individual polymer chains. Analysis of *ca.* 650 of these features provided a unimodal distribution of heights centered at 0.38 nm (3.8 Å), consistent with the height expected for a dispersed **GNR-OHxg** chain. Analysis of the lateral dimensions of the chains was complicated by the resolution limit, suggesting feature widths of < 10 nm. These features, combined with our observations that the GNRs are easily moved around the surface by higher resolution tips, suggest that their interaction with the mica substrate are weak. Further efforts will focus on improved deposition methods and alternative substrates in the hopes of unfolding GNRs onto device-relevant platforms. These micrographs indicate that high molecular weight samples of **GNR-OHxg** are dispersible and processable using solution-based techniques, such that a variety of established methods to introduce these polymers to solution might now be possible.

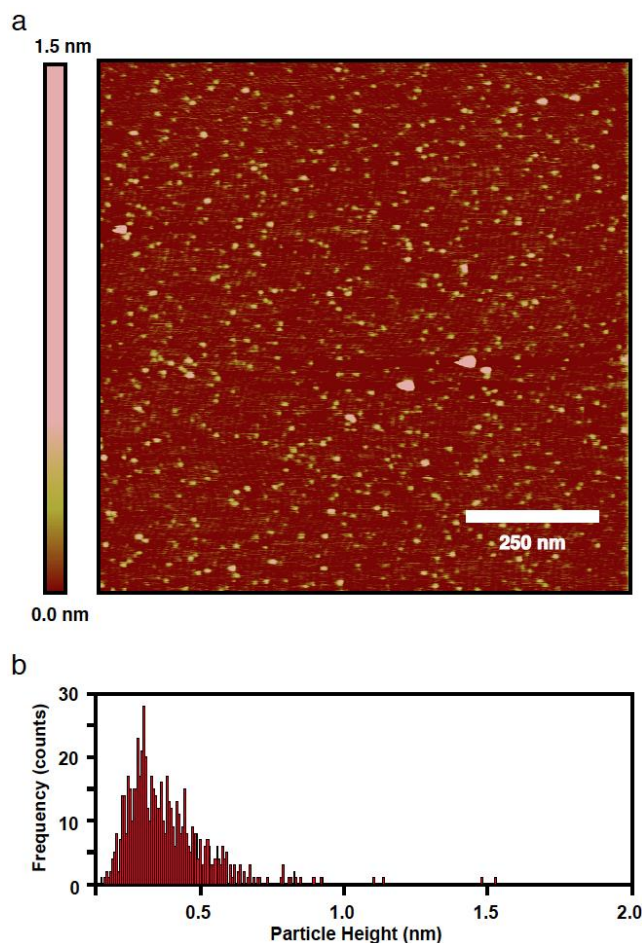


**Figure 5.8.** **a.** Representative AFM micrograph of isolated **GNR-OHxg** polymer chains deposited onto mica. **b.** A histogram of the particle height distribution produces average heights consistent with individual GNRs.

## 5.9 Conclusions

We have demonstrated a benzannulation/oxidation approach to transform PPEs, one of the most versatile classes of conjugated polymers, to structurally precise GNRs. Two distinct PPEs were prepared as high molecular weight polymers and controllable  $D_p \geq 80$  repeat units were obtained. Each of these PPEs was benzannulated efficiently, as demonstrated through their complete spectral and chromatographic characterization and two complementary isotopic labeling studies. Scholl oxidation of the **BPP-C<sub>9</sub>H<sub>19</sub>** polymer provided spectroscopic signatures that were consistent with prior observations of GNR formation but the resulting materials

suffered from poor dispersibility that prevented their unambiguous structure determination. After identifying Scholl oxidation conditions compatible with the more electron-rich **BPP-OHxg** system, fully dispersible GNRs were obtained. These GNRs showed graphitic Raman spectra and near-infrared photoemission that corresponds well to their band structure calculations. It was also possible to image these carbon nanostructure as individual polymer chains on atomically flat surfaces. We will next leverage the versatility of our synthetic approach to organize GNRs within device-relevant platforms and to establish GNR structure-property relationships.

### ***5.10 Acknowledgements***

We acknowledge Prof. Chad Lewis, Dr. Ivan Keresztes, Dr. Jimmy O'Dea for helpful discussions. This work was supported by the Beckman Young Investigator Program of the Arnold and Mabel Beckman Foundation, the NSF (CHE-1124754), the Doctoral New Investigator Program of the ACS Petroleum Research Fund (52019-DNI7), the Cottrell Scholar Program of the Research Corporation for Science Advancement, the Sloan Research Fellowship from the Alfred P. Sloan Foundation, and the Camille Dreyfus Teacher-Scholar Program of the Camille and Henry Dreyfus Foundation. This work made use of the Cornell Center for Materials Research Shared Facilities, which are supported through the NSF MRSEC program (DMR-1120296).

## REFERENCES

- (1) Schwierz, F. *Nature Nanotechnol.* **2010**, *5*, 487-496.
- (2) Jiao, L.; Wang, X.; Diankov, G.; Wang, H.; Dai, H. *Nature Nanotechnol.* **2010**, *5*, 321-325.
- (3) Shin, Y.-S.; Son, J. Y.; Jo, M.-H.; Shin, Y.-H.; Jang, H. M. *J. Am. Chem. Soc.* **2011**, *133*, 5623-5625.
- (4) (a) Chen, Z.; Lin, Y.-M.; Rooks, M. J.; Avouris, P. *Physica E* **2007**, *40*, 228-232. (b) Han, M. Y.; Özyilmaz, B.; Zhang, Y.; Kim, P. *Phys. Rev. Lett.* **2007**, *98*, 206805. (c) Tapasztó, L.; Dobrik, G.; Lambin, P.; Biró, L. P. *Nature Nanotechnol.* **2008**, *3*, 397-401. (d) Bai, J.; Duan, X.; Huang, Y. *Nano Lett.* **2009**, *9*, 2083-2087. (e) Yan, K.; Fu, L.; Peng, H.; Liu, Z. *Acc. Chem. Res.* **2013**, *46*, 2263-2274.
- (5) (a) Campos, L. C.; Manfrinato, V. R.; Sanchez-Yamagishi, J. D.; Kong, J.; Jarillo-Herrero, P. *Nano Lett.* **2009**, *9*, 2600-2604. (b) Datta, S. S.; Strachan, D. R.; Khamis, S. M.; Johnson, A. T. C. *Nano Lett.* **2008**, *8*, 1912-1915. (c) Shin, Y.-S.; Son, J. Y.; Jo, M.-H.; Shin, Y.-H.; Jang, H. M. *J. Am. Chem. Soc.* **2011**, *133*, 5623-5625. (d) Tan, X.; Zapol, P. *J. Phys. Chem. C* **2013**, *117*, 19160-19166. (e) Yan, Z.; Liu, Y.; Lin, J.; Peng, Z.; Wang, G.; Pembroke, E.; Zhou, H.; Xiang, C.; Raji, A.-R. O.; Samuel, E. L. G.; Yu, T.; Yakobson, B. I.; Tour, J. M. *J. Am. Chem. Soc.* **2013**, *135*, 10755-10762.
- (6) (a) Campos-Delgado, J.; Romo-Herrera, J. M.; Jia, X.; Cullen, D. A.; Muramatsu, H.; Kim, Y. A.; Hayashi, T.; Ren, Z.; Smith, D. J.; Okuno, Y.; Ohba, T.; Kanoh, H.; Kaneko, K.; Endo, M.; Terrones, H.; Dresselhaus, M. S.; Terrones, M. *Nano Lett.* **2008**, *8*, 2773-2778. (b) Ago H.; Tanaka I.; Ogawa Y.; Yunus R. M.; Tsuji M.; Hibino H. *ACS Nano* **2013**, *7*, 6123-6128.

- (c) Sokolov, A. N.; Yap, F. L.; Liu, N.; Kim, K.; Ci, L.; Johnson, O. B.; Wang, H.; Vosgueritchian, M.; Koh, A. L.; Chen, J.; Park, J.; Bao, Z. *Nature Commun.* **2013**, *4*, 2402.
- (7) (a) Li, X.; Wang, X.; Zhang, L.; Lee, S.; Dai, H. *Science* **2008**, *319*, 1229-1232. (b) Wu, Z.-S.; Ren, W.; Gao, L.; Liu, B.; Zhao, J.; Cheng, H.-M. *Nano Res.* **2010**, *3*, 16-22.
- (8) (a) Wei, Z.; Wang, D.; Kim, S.; Kim, S.-Y.; Hu, Y.; Yakes, M. K.; Laracuenta, A. R.; Dai, Z.; Marder, S. R.; Berger, C.; King, W. P.; de Heer, W. A.; Sheehan, P. E.; Riedo, E. *Science* **2010**, *328*, 1373-1376. (b) Mativetsky, J. M.; Treossi, E.; Orgiu, E.; Melucci, M.; Veronese, G. P.; Samorì, P.; Palermo, V. *J. Am. Chem. Soc.* **2010**, *132*, 14130-14136. (c) Sun, L.-W.; Zhao, J.; Zhou, L.-J.; Li, G.-D. *Chem. Commun.* **2013**, *49*, 6087-6089.
- (9) (a) Jiao, L.; Zhang, L.; Wang, X.; Diankov, G.; Dai, H. *Nature* **2009**, *458*, 877-880. (b) Kosynkin, D. V.; Higginbotham, A. L.; Sinitskii, A.; Lomeda, J. R.; Dimiev, A.; Price, B. K.; Tour, J. M. *Nature* **2009**, *458*, 872-876. (c) Xie, L.; Wang, H.; Jin, C.; Wang, X.; Jiao, L.; Suenaga, K.; Dai, H. *J. Am. Chem. Soc.* **2011**, *133*, 10394-10397. (d) Dhakate, S. R.; Chauhan, N.; Sharma, S.; Mathur, R. B. *Carbon* **2011**, *49*, 4170-4178. (e) Talyzin, A. V.; Anoshkin, I. V.; Krashennnikov, A. V.; Nieminen, R. M.; Nasibulin, A. G.; Jiang, H.; Kauppinen, E. I. *Nano Letters* **2011**, *11*, 4352-4356. (f) Rao, S. S.; Stesmans, A.; Kosynkin, D. V.; Higginbotham, A.; Tour, J. M. *New Journal of Physics* **2011**, *13*, 113004-113004. (g) Sun, C.-L.; Chang, C.-T.; Lee, H.-H.; Zhou, J.-G.; Wang, J.; Sham, T.-K.; Pong, W.-F. *ACS Nano* **2011**, *5*, 7788-7795. (h) Kosynkin, D. V.; Lu, W.; Sinitskii, A.; Pera, G.; Sun, Z.; Tour, J. M. *ACS Nano* **2011**, *5*, 968-974. (i) Shinde, D. B.; Degupta, J.; Kushwaha, A.; Aslam, M.; Pillai, V. K. *J. Am. Chem. Soc.* **2011**, *133*, 4168-4171. (j) James, Dustin K.; Tour, James M. *Macromol. Chem. Phys.* **2012**, *213*, 1033-1050. (k) Liu, X. H.; Wang, J. W.; Liu, Y.; Zheng, H.; Kushima, A.; Huang, S.; Zhu, T.;



Mao, S. X.; Li, J.; Zhang, S. *Carbon* **2012**, *50*, 3836-3844. (l) Genorio, B.; Lu, W.; Dimiev, A. M.; Zhu, Y.; Raji, A.-R. O.; Novosel, B.; Alemany, L. B.; Tour, J. M. *ACS Nano* **2012**, *6*, 4231-4240. (m) Wong C. H. A.; Chua Ch. K.; Khezri B.; Webster R. D.; Pumera M. *Angew. Chem. Int. Ed.* **2013**, *52*, 8685-8688. (n) Lu, W.; Ruan, G.; Genorio, B.; Zhu, Y.; Novosel, B.; Peng, Z.; Tour, J. M. *ACS Nano* **2013**, *7*, 2669-2675. (o) Vadahanambi, S.; Jung, J.-H.; Kumar, R.; Kim, H.-J.; Oh, I.-K. *Carbon* **2013**, *53*, 391-398. (p) Zhuang, N.; Liu, C.; Jia, L.; Wei, L.; Cai, J.; Guo, Y.; Zhang, Y.; Hu, X.; Chen, J.; Chen, X.; Tang, Y. *Nanotechnology* **2013**, *24*, 325604. (q) Cruz-Silva, R.; Morelos-Gomez, A.; Vega-Diaz, S.; Tristan-Lopez, F.; Elias, A. L.; Perea-Lopez, N.; Muramatsu, H.; Hayashi, T.; Fujisawa, K.; Kim, Y. A.; Endo, M.; Terrones, M. *ACS Nano* **2013**, *7*, 2192-2204. (r) James, D. K.; Tour, J. M. *Acc. Chem. Res.* **2013**, *46*, 2307-2318.

(10) Goldfinger, M. B.; Swager, T. M. *J. Am. Chem. Soc.* **1994**, *116*, 7895-7896.

(11) (a) Yang, X.; Dou, X.; Rouhanipour, A.; Zhi, L.; Räder, H. J.; Müllen, K. *J. Am. Chem. Soc.* **2008**, *130*, 4216-4217. (b) Schwab, M. G.; Narita, A.; Hernandez, Y.; Baladina, T.; Mali, K. S.; De Feyter, S.; Feng, X.; Müllen, K. *J. Am. Chem. Soc.* **2012**, *134*, 18169-18172.

(12) (a) Dössel, L.; Gherghel, L.; Feng, X.; Müllen, K. *Angew. Chem. Int. Ed.* **2011**, *50*, 2540-2543. (b) Kim, K. T.; Jung, J. W.; Jo, W. H. *Carbon* **2013**, *63*, 202-209.

(13) (a) Cai, J.; Ruffieux, P.; Jaafar, R.; Bieri, M.; Braun, T.; Blankenburg, S.; Muoth, M.; Seitsonen, A. P.; Saleh, M.; Feng, X.; Müllen, K.; Fasel, R. *Nature* **2010**, *466*, 470-473. (b) Ruffieux, P.; Cai, J.; Plumb, N. C.; Patthey, L.; Prezzi, D.; Ferretti, A.; Molinari, E.; Feng, X.; Müllen, K.; Pignedoli, C. A.; Fasel, R. *ACS Nano* **2012**, *6*, 6930-6935. (c) Bronner, C.; Stremlau, S.; Gille, M.; Brauße, F.; Haase, A.; Hecht, S.; Tegeder, P. *Angew. Chem. Int. Ed.* **2013**, *52*, 4422-4425. (d) Chen, Y.-C.; de Oteyza, D. G.; Pedramrazi, Z.; Chen, C.; Fischer, F. R.;

Crommie, M. F. *ACS Nano* **2013**, 7, 6123-6128. (e) Talirz, L.; Sode, H.; Cai, J.; Ruffieux, P.; Blankenburg, S.; Jafaar, R.; Berger, R.; Feng, X.; Mullen, K.; Passerone, D.; Fasel, R.; Pignedoli, C. A *J. Am. Chem. Soc.* **2013**, 135, 2060-2063.

(14) Schlüter, A.-D. *Adv. Mater.* **1991**, 3, 282-291.

(15) (a) Grimsdale, A. C.; Müllen, K. *Angew. Chem. Int. Ed.* **2005**, 44, 5592-5629. (b) Gille, M.; Viertel, A.; Weidner, S.; Hecht, S. *Synlett.* **2013**, 24, 259-263.

(16) Asao, N.; Nogami, T.; Lee, S.; Yamamoto, Y. *J. Am. Chem. Soc.* **2003**, 125, 10921-10925.

(17) Arslan, H.; Saathoff, J. D.; Bunck, D. N.; Clancy, P.; Dichtel, W. R. *Angew. Chem. Int. Ed.* **2012**, 51, 12051-12054.

(18) Arslan, H.; Uribe-Romo, F.J.; Smith, B. J.; Dichtel, W. R. *Chem. Sci.* **2013**, 4, 3973-3978.

(19) Stone, M. T.; Moore, J. S. *Org. Lett.* **2004**, 6, 469-472.

(20) Bunz, U. H. F. *Chem. Rev.* **2000**, 100, 1605-1644.

(21) Tykwinski, K. K.; Luu, T. *Synthesis* **2012**, 44, 1915-1922.

(22) Nyquist, R.A.; Putzig, C.L. *Vib. Spectrosc.* **1992**, 4, 35-38.

(23) (a) Hartley, C. S.; He, J. *J. Org. Chem.* **2010**, 75, 8627-8636. (b) Mathew, S.M.; Hartley, C.S. *Macromolecules* **2011**, 44, 8425-8432. (c) He, J.; Mathew, S.M.; Cornett, S. D.; Grundy, S. C.; Hartley, C. S. *Org. Biomol. Chem.* **2012**, 10, 3398-3405.

(24) (a) Ohta, E.; Sato, H.; Ando, S.; Kosaka, A.; Fukushima, T.; Hashizume, D.; Yamasaki, M.; Hasegawa, K.; Muraoka, A.; Ushiyama, H.; Yamashita, K.; Aida, T. *Nat. Chem.* **2011**, 3, 68-73. (b) Ando, S.; Ohta, E.; Kosaka, A.; Hashizume, D.; Koshino, H.; Fukushima, T.; Aida, T. *J.*

- Am. Chem. Soc.* **2012**, *134*, 11084–11087 (c) Kajitani, T.; Suna, Y.; Kosaka, A.; Osawa, T.; Fujikawa, S.; Takata, M.; Fukushima, T.; Aida, T. *J. Am. Chem. Soc.* **2013**, *135*, 14564–14567.
- (25) We previously demonstrated the regioselectivity of the benzannulation using **6**-<sup>13</sup>C<sub>2</sub> in a model system. See Reference 18.
- (26) (a) Alemany, L. B.; Grant, D. M.; Pugmire, R. J.; Alger, T. D.; Zilm, K. W. *J. Am. Chem. Soc.* **1983**, *105*, 2133–2141. (b) Alemany, L. B.; Grant, D. M.; Pugmire, R. J.; Alger, T. D.; Zilm, K. W. *J. Am. Chem. Soc.* **1983**, *105*, 2142–2147. (c) Alemany, L. B.; Grant, D. M.; Alger, T. D.; Pugmire, R. J. *J. Am. Chem. Soc.* **1983**, *105*, 6697–6704.
- (27) A comprehensive review on Scholl conditions and side reactions. Grzybowski, M.; Skonieczny, K.; Butenschön, H.; Gryko, D. T. *Angew. Chem. Int. Ed.* **2012**, *51*, 12051–12054.
- (28) Zhai, L.; Shukla, R.; Wadumethige, S. H.; Rathore, R. *J. Org. Chem.* **2010**, *75*, 4748–4760.
- (29) Leiro, J. A.; Heinonen, M. H.; Laiho, T.; Batirev, I. G. *J. Electron Spectrosc. Relat. Phenom.* **2003**, *128*, 205–213.
- (30) Shard, A. G.; Davies, M. C.; Li, Y. X.; Volland, C.; Kissel, T. *Macromolecules* **1997**, *30*, 3051–3057.
- (31) López, G. P.; Castner D. G.; Ratner B. D. *Surf. Interface Anal.* **1991**, *17*, 267–272.
- (32) Lee, K. W.; Lee, C. E. *Phys. Rev. Lett.* **2006**, *97*, 1372061–1372064.
- (33) Cai, W.; Piner, R. D.; Stadermann, F. J.; Park, S.; Shaibat, M. A.; Ishii, Y.; Yang, D.; Velamakanni, A.; An, S. J.; Stoller, M.; An, J.; Chen, D.; Ruoff, R. S. *Science* **2008**, *321*, 815–817.
- (34) Materials Studio Ver. 5.5 (Accelrys Software Inc. San Diego, CA 2010).

- (35) Clark, S.J.; Segall, M.D.; Pickard, C. J.; Hasnip, P. J.; Probert, M. I. J.; Refson, K.; Payne, M. C. Z. *Kristallogr.* **2005**, *220*, 567–570.
- (36) (a) Gillen, R., Robertson, J. *Phys. Rev. B* **2010**, *82*, 125406. (b) Hunt, M. R. C.; Clark, S. J. *Phys Rev. Lett.* **2012**, *109*, 26552. (c) Ma, F.; Guo, Z.; Xu, K.; Chu, P. K. *Solid State Commun.* **2012**, *152*, 1089.
- (37) (a) Misewich, J. A.; Martel, R.; Avouris, Ph.; Tsang, J. C.; Heinze, S.; Tersoff, J. *Science* **2003**, *300*, 783-786. (b) Chen, J.; Perebeinos, V.; Freitag, M.; Tsang, J.; Fu, Q.; Liu, J.; Avouris, P. *Science* **2005**, *310*, 1171-1174. (c) Misewich, J. A.; Martel, R.; Avouris, Ph.; Tsang, J. C.; Heinze, S.; Tersoff J. *J. Phys. Chem. B* **2006**, *110*, 17420-17424 (d) Iakoubovskii, K.; Minami, N.; Kim, Y.; Miyashita, K.; Kazaoui, S.; Nalin B. *Appl. Phys. Lett.* **2006**, *89*, 173108.

## APPENDIX FOUR

## Table of Contents

<b>A. Materials and Methods</b>	368
<b>B. Synthetic Procedures</b>	372
<b>C. Size Exclusion Chromatography</b>	393
<b>D. UV/Vis/NIR Absorption and Fluorescence Spectroscopy and Quantum Yields Determination</b>	401
<b>E. Vibrational Spectroscopy (FTIR and Raman)</b>	409
<b>F. X-Ray Photoelectron Spectroscopy</b>	413
<b>G. Solid-State NMR Spectroscopy</b>	417
<b>H. Thermalgravimetry</b>	427
<b>I. Atomic Force Microscopy.</b>	428
<b>J. Density Functional Theory Calculations</b>	431
<b>K. Solution NMR spectra</b>	443
<b>L. References to Appendix</b>	462

## A. Materials and Methods

All starting materials and solvents, unless otherwise specified, were obtained from commercial sources and used without further purification. All reactions were performed at ambient laboratory conditions, and no precautions were taken to exclude oxygen or atmospheric moisture unless otherwise specified. Anhydrous solvents: tetrahydrofuran (THF), methylene chloride, acetonitrile (MeCN), *N,N*-dimethylformamide (DMF), toluene were purified using a custom-built alumina-column based solvent purification system. *N*-methylpyrrolidone (NMP) was distilled under vacuum (10 mtorr) from molecular sieves. Diisopropylamine and 1,2-dichloroethane were distilled from CaH<sub>2</sub> under N<sub>2</sub> atmosphere. Trimethylsilylacetylene-<sup>13</sup>C<sub>2</sub> (99% atom <sup>13</sup>C) was obtained from Aldrich Chemical Co.

High-resolution <sup>1</sup>H, <sup>13</sup>C and <sup>11</sup>B nuclear magnetic resonance (NMR) spectra were recorded using Varian INOVA-400, 500 and 600 MHz spectrometers. Solid-state NMR was recorded at ambient pressure in a Varian INOVA-400 spectrometer using a magic angle-spinning (MAS) probe with 7 mm (outside diameter) silicon nitride rotors. The magic angle was adjusted by maximizing the number and amplitudes of the signals of the rotational echoes observed in the <sup>79</sup>Br MAS FID signal from KBr. Cross-polarization with MAS (CP-MAS) was used to acquire <sup>13</sup>C data at 100.7 MHz. The CP contact time varied from 100 to 7000 μs. High power two-pulse phase modulation (TPPM) <sup>1</sup>H decoupling was applied during data acquisition. The MAS sample-spinning rate was 8.2 kHz. Recycle delays between scans varied between 3 and 10 s, depending upon the compound as determined by observing no apparent loss in the <sup>13</sup>C signal from one scan to the next.

High-field solid-state NMR was measured at The New York Structural Biology Center in a Bruker using a MAS probe with 1.5 mm (outside diameter) zirconia rotors and a <sup>1</sup>H frequency of 750 MHz. <sup>13</sup>C CP-MAS and <sup>13</sup>C MAS were measured at 188.8 MHz. MAS rate, decoupling, contact time and recycle delay.

The <sup>13</sup>C chemical shifts are given relative to tetramethylsilane as zero ppm, calibrated using the methylene carbon signal of adamantane assigned to 37.77 ppm as secondary reference.

Matrix-assisted laser desorption-ionization time-of-flight mass spectrometry (MALDI-TOF MS) was performed in a Waters MALDI Micro MX, 7,7,8,8-tetracyano-quinodimethane

(TCNQ) was used as matrix and the mass ranges were calibrated using poly(ethylene-oxide) standards.

Fourier-transform infrared spectra were recorded using a Thermo Nicolet iS10 with a diamond attenuated total reflectance (ATR) attachment. A total of 64 transients were collected for each sample with a resolution of  $0.05\text{ cm}^{-1}$ . Data presented in absorbance mode was processed as follows: Raw data was converted to absorbance, smoothed ( $0.783\text{ cm}^{-1}$  level), and the baseline was subtracted with a zero-set 3200 and 2650 wavenumbers with a linear baseline in between these frequencies. Data presented in % transmittance was uncorrected.

Ultraviolet/visible/near infrared (UV/vis/NIR) absorbance spectra were recorded on a Cary 5000 spectrophotometer with a mercury lamp. Quartz cuvettes rated for transparency in the near infrared region containing the pure solvent of interest for the measurement was used for baseline.

Photoemission and excitation spectra were recorded on a Horiba Jobin Yvon Fluorolog-3 fluorescence spectrophotometer equipped with a 450 W Xe lamp, double excitation and double emission monochromators, a digital photon-counting photomultiplier and a secondary InGaAs detector for the NIR range. Correction for variations in lamp intensity over time and wavelength was achieved with a solid-state silicon photodiode as the reference. The spectra were further corrected for variations in photomultiplier response over wavelength and for the path difference between the sample and the reference by multiplication with emission correction curves generated on the instrument.

The fluorescence quantum yield ( $\Phi_F$ ) was determined using anthracene in cyclohexane as reference ( $\Phi_F = 36\% \pm 0.04\%$ ) [S<sup>38</sup>]. Integration of the total fluorescence intensity ( $I_F$ ) between 365 and 600 nm was plotted vs. the optical density (O.D.) at the excitation wavelength (350 nm) between the linear region of 0.01 and 0.15 in O.D. units. The quantum yield was obtained according to the equation:

$$F_{F, sample} = F_{F, reference} \frac{Slope_{sample}}{Slope_{reference}} \cdot \frac{n_{sample}^2}{n_{reference}^2}$$



where  $n$  is the refractive index of the solvent and *Slope* was obtained from the linear fitting of the  $I_F$  vs. O.D. plot for each collected sample and reference.

Raman spectra were recorded on a Renishaw InVia confocal Raman microscope with excitation wavelengths of 488 nm and 785 nm. Dissolved samples were drop-cast on borosilicate glass slides or silicon wafers, solid samples were compressed between borosilicate glass slides. Backgrounds were fit with a polynomial function and subtracted.

Thermalgravimetric analysis from 20-600 °C was carried out on a TA Instruments Q500 Thermogravimetric Analyzer under a N<sub>2</sub> flow using a 5 K min<sup>-1</sup> scan rate.

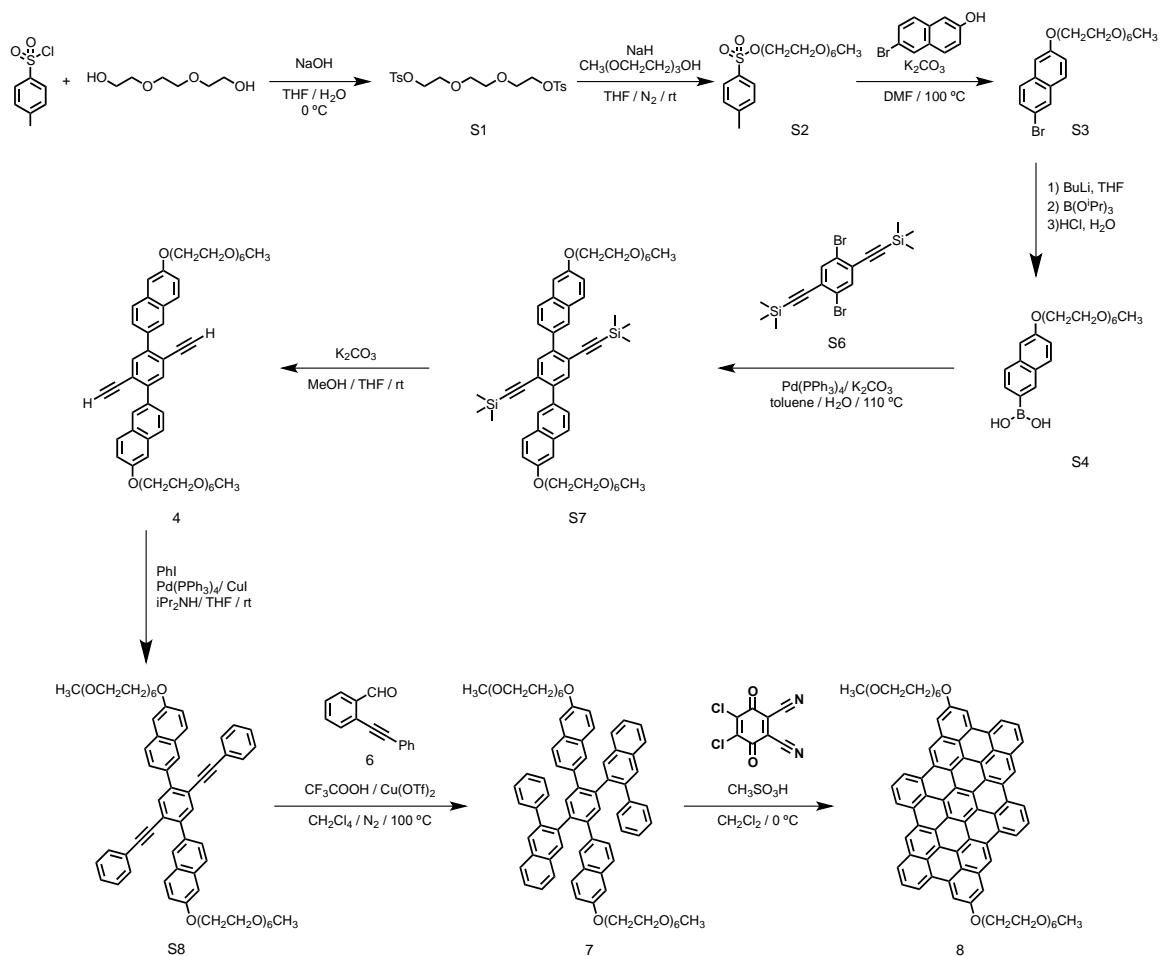
Size exclusion chromatography with multi angle laser light scattering (SEC-MALLS) with THF as mobile phase was performed on two 7.5- $\mu$ m columns (PolyPore, Varian, Inc.) connected in series. Tetrahydrofuran was used as the mobile phase at 1.0 mL min<sup>-1</sup> flow from a Shimadzu LC-20AD isocratic pump. The detector system consisted of a miniDawn S2 three angle, light-scattering system, followed downstream by an Optilab Rex differential refractometer from Wyatt Technologies. Samples were prepared in 1 mg mL<sup>-1</sup> concentration in BHT stabilized THF and filtered through a 2  $\mu$ m inorganic membrane filter previous to analysis. Average molecular weights were determined using one-point on-line  $dn/dC$ .

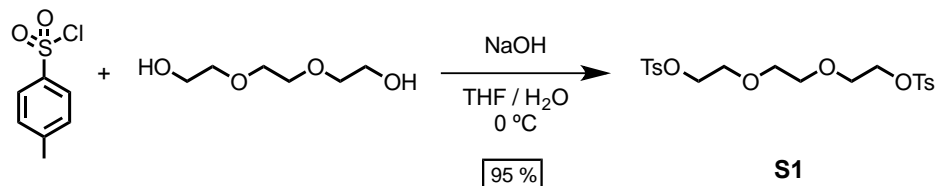
X-ray photoelectron spectroscopy (XPS) was measured in a Surface Science Instruments X-Probe SSX-100 spectrometer with operating pressure < 10<sup>-9</sup> torr using monochromatic Al K $\alpha$  X-rays at 1486.6 eV. Photoelectrons were collected at an angle of 55-degrees from surface normal in a hemispherical analyzer with pass energy of 50 V and detected with a SSI Position Sensitive, resistive anode, 40 mm x 40 mm detector, electronically defined as 128 active channels with maximum count rate of 1,000,000. Samples were prepared by drop-cast from CHCl<sub>3</sub>, DMF or NMP solutions into gold-coated silicon wafers. The wafers were cleaned with acid piranha solution previous to use. Data analysis and deconvolutions were performed in CasaXPS: Processing software for XPS (Casa Software Ltd.). Peak deconvolutions were performed with Shirley backgrounds, Gaussian-Lorentzian-Product functions with 30% Lorentzian mixing (GL(30) function). Peak position, full-width-at-half-maximum and concentration were fitted and extracted.

Ambient atomic force microscopy as performed on a Veeco Icon in tapping mode using diamond-like carbon coated silicon AFM probes (Tap190DLC, Budget Sensors). Samples were prepared by drop cast from *ca.* 0.5 - 1.0 mg L<sup>-1</sup> solutions (10 nM) in DMF or NMP (filtered through 2 µm inorganic membrane filters) into freshly cleaved mica muscovite surfaces (V-1 grade, SPI supplies). The surface was dried at room temperature and high vacuum (10<sup>-2</sup> torr) for 3 d before analysis and handled in a clean-room environment. The collected data was subjected to 0<sup>th</sup>, 1<sup>st</sup> 2<sup>nd</sup> and 3<sup>rd</sup> order flattening and the particle height statistical analysis were performed in NanoScope (Veeco, version 1.2) AFM processing software.

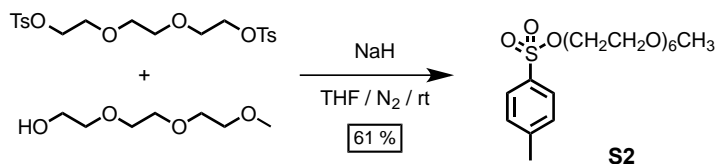
## B. Synthetic Procedures.

Synthetic scheme for the synthesis of monomer **4** and compounds **7** and **8**.



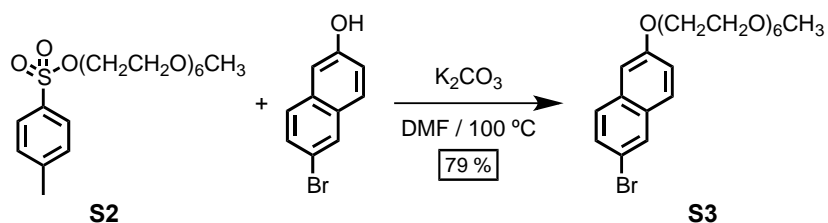


**Synthesis of S1.** NaOH (6.3 g, 158.4 mmol) was dissolved in 10 mL of water in a 100 mL round bottom flask equipped with a magnetic stirrer. Triethyleneglycol (10.0 g, 61 mmol) and THF (10 mL) were added and the mixture was cooled to 0 °C. 4-toluenesulfonyl chloride (25.5 g, 134.0 mmol) was dissolved in anhydrous THF (30 mL) and added drop wise (30 min) to the cold basic solution with stirring. The mixture was warmed to room temperature and stirred for 12 h after which the mixture was diluted with water (10 mL) and 6 M H<sub>2</sub>SO<sub>4</sub> (*aq*, 20 mL). The acidified mixture was extracted with CH<sub>2</sub>Cl<sub>2</sub> (3 x 100 mL). The combined organic extracts were rinsed with water (2 x 100 mL), dried over anhydrous Na<sub>2</sub>SO<sub>4</sub>, filtered through celite and concentrated in a rotary evaporator yielding **S1** (25.7 g, 92 % yield) as a yellow solid. Analysis matched values reported by [S<sup>39</sup>].



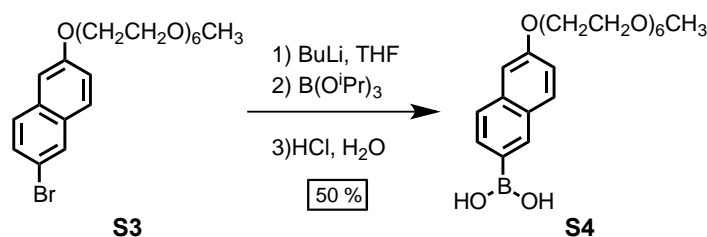
**Synthesis of S2.** **S1** (10.47 g, 22.8 mmol) was loaded in a 250 mL flame dried Schlenk flask equipped with a magnetic stirrer. The flask was evacuated under dynamic vacuum at 100 mtorr and backfilled with N<sub>2</sub> three times. Anhydrous THF (50 mL) was added via cannula and the mixture was stirred until the ditosylate was dissolved. Sodium hydride (0.400 g, 16.76 mmol) was loaded into a 100 mL flame dried Schlenk flask equipped with a magnetic stirrer and was purged three times with N<sub>2</sub>. Anhydrous THF (15 mL) was added via cannula and the mixture was stirred to dissolve the sodium hydride. Triethyleneglycol monomethyl ether (2.5 g, 15.23 mmol) was added dropwise to the hydride solution at room temperature and the mixture was stirred for 10 min after H<sub>2</sub> bubbling ceased. The triethyleneglycol/hydride/THF solution was then cannula transferred drop wise (30 min) into the **S2**/THF solution with vigorous stirring and the mixture was stirred at room temperature for 12 h under N<sub>2</sub>. Water (15 mL) was added to the

mixture and then acidified with 6 M H<sub>2</sub>SO<sub>4</sub> (*aq*, 5 mL). The acidified solution was extracted with CH<sub>2</sub>Cl<sub>2</sub> (5 x 100 mL), the combined organic extracts were dried over anhydrous Na<sub>2</sub>SO<sub>4</sub>, filtered over celite and concentrated in vacuum in a rotary evaporator. The resulting residue was purified by column chromatography (SiO<sub>2</sub>, 10% *v/v* acetone/CH<sub>2</sub>Cl<sub>2</sub>) obtaining **S2** (4.18 g, 61% yield) as an orange oil. <sup>1</sup>H NMR (400 MHz, CDCl<sub>3</sub>, 25 °C) δ (ppm) 7.77 (d, 2 H), 7.32 (d, 2 H), 4.13 (t, 2 H), 3.67–3.61 (m, br, 24 H), 3.35 (s, 3 H), 2.43 (s, 3 H). <sup>13</sup>C NMR (100 MHz, CDCl<sub>3</sub>, 25 °C) δ (ppm) 144.8, 133.0, 129.9, 128.0, 71.9, 70.8, 70.6 (br), 69.4, 66.7, 59.1, 21.7. MS: (MALDI-TOF, TCNQ) calcd for [C<sub>20</sub>H<sub>34</sub>O<sub>9</sub>S+Na]<sup>+</sup> 473.18, found 473.97. FTIR (ATR, cm<sup>-1</sup>) 3059, 3030, 2872, 1722, 1722, 1597, 1450, 1351, 1291, 1246, 1188, 1174, 1095, 1009, 1032, 1018, 916, 846, 816, 773, 706, 681, 662.



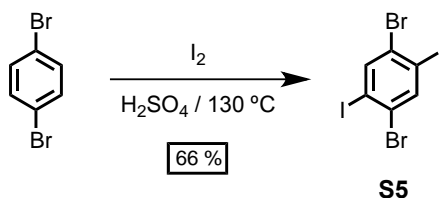
**Synthesis of S3.** K<sub>2</sub>CO<sub>3</sub> (3.6 g, 26 mmol) and 6-bromo-2-naphtol (2.1 g, 9.5 mmol) were loaded in a flame dried 25 mL Schlenk flask equipped with a magnetic stirrer. The flask was purged under dynamic vacuum to 100 mtorr and filled with N<sub>2</sub> three times. Anhydrous DMF (8 mL) was added and stirred until the solids were dissolved. **S2** (3.88 g, 8.6 mmol) was dissolved under N<sub>2</sub> in anhydrous DMF (0.5 mL) and subsequently added dropwise to the basic naphtol mixture. The mixture was stirred under N<sub>2</sub> and heated to 100 °C for 18 h, which subsequently was allowed to cool to room temperature and diluted with water (100 mL). The crude was extracted with CH<sub>2</sub>Cl<sub>2</sub> (5 x 100 mL), the organic extracts were combined and dried over anhydrous Na<sub>2</sub>SO<sub>4</sub>, filtrated over celite, and concentrated under vacuum in a rotary evaporator. The obtained dark orange oil was purified by flash column chromatography (SiO<sub>2</sub>, 50% v/v EtOAc/hexanes then 15% v/v acetone/CH<sub>2</sub>Cl<sub>2</sub>) and the desired fraction was dried under vacuum (10<sup>-2</sup> torr) in a Kugelrohr apparatus at room temperature for 18 h to provide **S3** (3.37 g, 79 % yield) as an orange oil. <sup>1</sup>H NMR (400 MHz, CDCl<sub>3</sub>, 25 °C) δ (ppm) 7.90 (d, 1 H), 7.63 (d, 2 H), 7.58 (d, 1 H), 7.48 (m, 1 H), 7.18 (m, 1 H), 7.09 (d, 1 H), 4.23 (t, 2 H), 3.91 (t, 2 H), 3.75 (m, 2 H), 3.63 (m, 16 H), 3.53

(m, 2 H), 3.36 (s, 3 H).  $^{13}\text{C}$  NMR (100 MHz,  $\text{CDCl}_3$ , 25 °C)  $\delta$  (ppm) 157.17, 133.08, 130.17, 129.74, 129.70, 128.58, 128.52, 120.19, 117.20, 110.14, 106.81, 72.05, 71.00, 70.78, 70.77, 70.73 (m), 60.64, 69.79, 67.61, 59.16. MS: (MALDI-TOF, TCNQ) calcd for  $[\text{C}_{23}\text{H}_{33}\text{BrO}_7+\text{Na}]^+$  523.13, found 523.14. FTIR (ATR,  $\text{cm}^{-1}$ ) 3064, 3007, 2875, 1627, 1590, 1500, 1451, 1409, 1349, 1332, 1260, 1207, 1123, 1097, 1063, 973, 929, 877, 851, 747, 665.

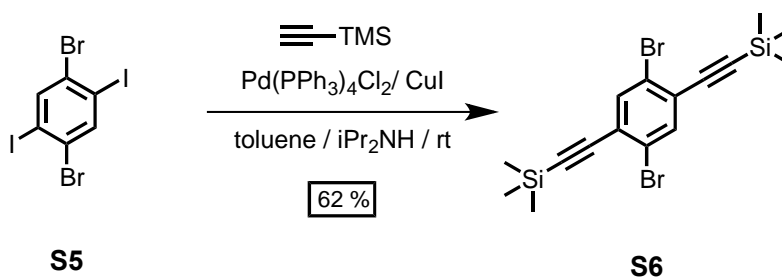


**Synthesis of S4.** **S3** (3.0 g, 5.9 mmol) was loaded in a 50 mL flame dried Schlenk flask equipped with with a magnetic stirrer. The flask was purged under dynamic vacuum to 100 mtorr and back filled with  $\text{N}_2$  three times. Anhydrous THF (12 mL) was added via cannula under  $\text{N}_2$  and the mixture was stirred and cooled to -78 °C in a  $\text{CO}_2$ /acetone bath. Butyllithium (1.6 M in hexanes, 4.12 mL, 6.58 mmol) was added drop wise via syringe with vigorous stirring under  $\text{N}_2$ . After 1 h,  $\text{B(O}^i\text{Pr)}_3$  (1.52 mL, 1.24 g, 6.58 mmol) was added drop wise at -78 °C and the mixture was stirred for 8 h allowing it to warm to room temperature. 2 M HCl (aq, 20 mL) was added to the reaction and the mixture was stirred for 2 h. The mixture was extracted with  $\text{CH}_2\text{Cl}_2$  (5 x 100 mL) and the combined organic extracts were dried with anhydrous  $\text{Na}_2\text{SO}_4$ , filtered through celite and concentrated to dryness in a rotary evaporator. The obtained orange crude was purified by  $\text{SiO}_2$  column chromatography. The silica gel was pretreated with 1% triethylamine in hexanes, and eluted with  $\text{CH}_2\text{Cl}_2$  previous to loading the crude mixture, the column was eluted with a 20% to 70% v/v gradient acetone/EtOAc, then 50% *i*PrOH/EtOAc. The purified fraction was concentrated under vacuum in a rotoevaporator and the obtained dark orange oil was dissolved in  $\text{CH}_2\text{Cl}_2$  (50 mL), and rinsed with 2 M HCl (aq, 50 mL), the organic extract was dried over  $\text{Na}_2\text{SO}_4$ , filtered over celite and the solvent was to dryness in a rotary evaporator. The obtained orange oil was dried under vacuum at  $10^{-2}$  torr at 60 °C in a Kugelrohr apparatus for 8 h obtaining **S4** (1.33 g, 50% yield) as a brown wax.  $^1\text{H}$  NMR (500 MHz, 1,4-dioxane- $d_8$ / $\text{D}_2\text{O}/\text{DCl}$  99:0.7:0.3 v/v/v)  $\delta$  9.14 (br), 8.21 (s, 1H), 7.85 - 7.66 (m, 3H), 7.21 (s, 1H), 7.16 (d,  $J$  = 8.8 Hz,

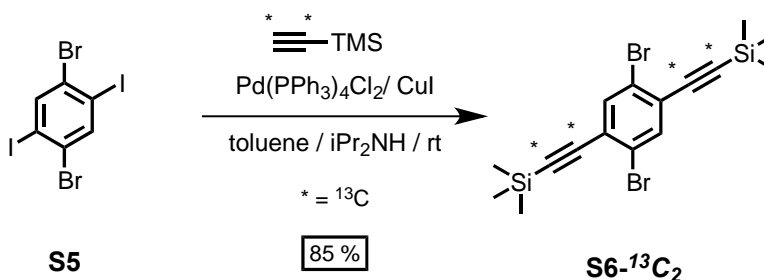
1H), 4.24 (t,  $J = 5.0$  Hz, 2H), 3.87 (t,  $J = 5.1$  Hz, 2H), 3.72 - 3.48 (br, 18H), 3.45 (t,  $J = 4.9$  Hz, 2H), 3.28 (s, 3H).  $^{13}\text{C}$  NMR (126 MHz, 1,4-dioxane- $d_8$ /D $_2$ O/DCI 99:0.7:0.3 v/v/v)  $\delta$  158.33, 136.72, 135.28, 131.50, 130.63, 129.18, 126.31, 119.46, 119.35, 107.05, 72.45, 71.26, 71.10, 71.03, 70.98, 70.85, 70.11, 68.03. MS: (EI) calcd for  $[\text{C}_{23}\text{H}_{35}\text{BO}_9 + \text{H}_2\text{O}]^+$  484.25, found 484.20. FTIR (ATR,  $\text{cm}^{-1}$ ) 3387 (br), 3054, 3030, 2870 (br), 1625, 1601, 1841, 1452, 1411, 1382, 1364, 1384, 1388, 1261, 1202, 1096, 1060, 1028, 972, 941, 853, 815, 765, 749, 717, 696.



**Synthesis of S5.** 1,4-dibromobenzene (19.5 g, 82.66 mmol) was suspended in  $\text{H}_2\text{SO}_4$  (275 mL) in a round bottom flask with a magnetic stirrer. The mixture was heated to 130  $^\circ\text{C}$  with vigorous stirring and  $\text{I}_2$  (46.2 g, 181.8 mmol) was added in portions of 0.5 g at a time. A water-cooled condenser was attached and stirred vigorously at 130  $^\circ\text{C}$  for 4 d. The flask was gently tapped each 5 h to allow the sublimated iodine at the top of the flask and condenser to return to the acid mixture. The suspension was poured into ice (700 mL) and stirred for 1 h. The mixture was extracted with  $\text{CH}_2\text{Cl}_2$  (2 x 500 mL), and the combined organic extracts were rinsed with 2 M  $\text{NaOH}$  (aq, 5 x 150 mL), saturated  $\text{NaHCO}_3$  (aq), water and brine, dried over anhydrous  $\text{MgSO}_4$ , filtered through celite and the solvent was evaporated to dryness in a rotary evaporator. The obtained solid was recrystallized twice in benzene and dried under vacuum ( $10^{-2}$  torr) affording **S5** (26.6 g, 66% yield) as a white-pink solid. Analysis matched values reported by [S<sup>40</sup>].

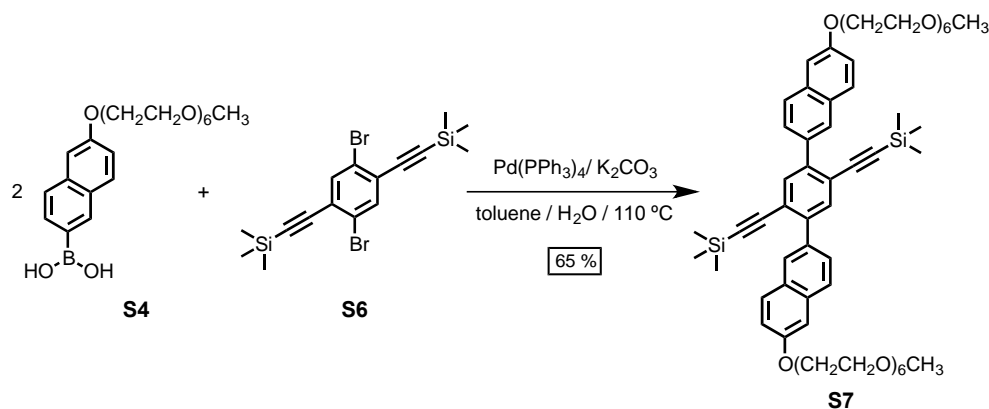


**Synthesis of S6.** S5 (6.83 g, 14.06 mmol), CuI (0.054 g, 0.28 mmol), Pd(PPh<sub>3</sub>)<sub>2</sub>Cl<sub>2</sub> (0.40 g, 0.56 mmol) were loaded in a flame dried Schlenk flask equipped with a magnetic stirrer. The flask was evacuated under dynamic vacuum to 100 mtorr and back filled with N<sub>2</sub> three times. Anhydrous toluene (45 mL) and *i*Pr<sub>2</sub>NH (13 mL) were added via syringe under N<sub>2</sub>. Trimethylsilylacetylene (4.4 mL, 3.03 g, 31.0 mmol) was added dropwise via syringe under N<sub>2</sub> and the mixture was stirred at room temperature for 10 h, after which it was quenched with saturated NH<sub>4</sub>Cl (*aq*). The mixture was extracted with toluene (3 x 100 mL), the combined organic extracts were rinsed three times with saturated NH<sub>4</sub>Cl (*aq*), water and brine, dried over MgSO<sub>4</sub>, filtered over celite and concentrated to dryness in a rotary evaporator. The crude product was purified by column chromatography (SiO<sub>2</sub>, hexanes) followed by recrystallization in DMSO obtaining S6 (3.71 g, 62% yield) as light yellow solid. Analysis matched values reported by [S<sup>41</sup>].

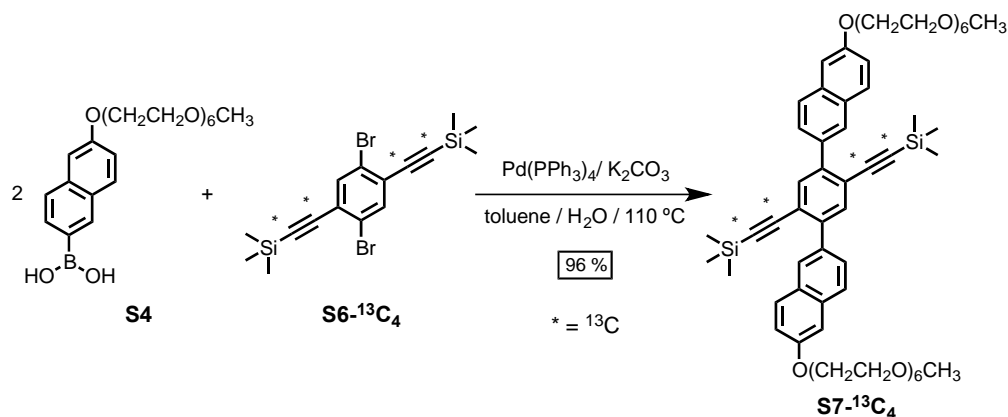


**Synthesis of S6-<sup>13</sup>C<sub>4</sub>.** Similar procedure for the synthesis of S6, but using S5 (0.160 g, 0.328 mmol), CuI (0.001 g, 0.007 mmol), Pd(PPh<sub>3</sub>)<sub>4</sub> (0.008 g, 0.007 mmol), trimethylsilylacetylene-<sup>13</sup>C<sub>2</sub> (99% atom <sup>13</sup>C, 0.100 mL, 0.069 g, 0.689 mmol), anhydrous toluene (1 mL) and *i*Pr<sub>2</sub>NH (0.3 mL). The crude product was purified by column chromatography (SiO<sub>2</sub>, pentane, gravity flow) obtaining S6-<sup>13</sup>C<sub>4</sub> (0.121 g, 85% yield) as white solid. Analysis matched values reported by [S41].

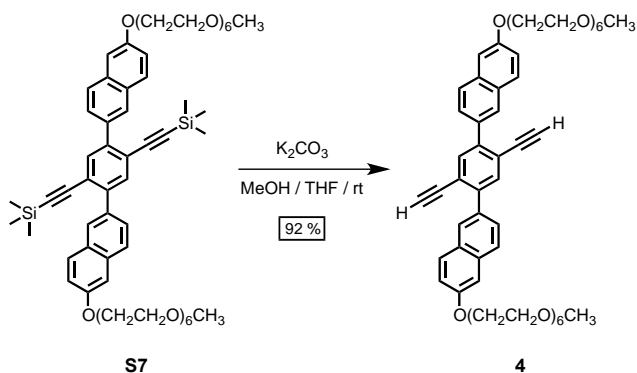




**Synthesis of S7.** **S6** (0.5 g, 1.17 mmol), **S4** (1.2 g, 2.56 mmol),  $\text{K}_2\text{CO}_3$  (0.8 g, 5.8 mmol) and  $\text{Pd(PPh}_3)_4$  (0.135 g, 0.115 mmol) were loaded in a 50 mL Schlenk flask equipped with a magnetic stirrer. The flask was evacuated under dynamic vacuum to 150 mtorr and back filled with  $\text{N}_2$  three times. Anhydrous toluene (10 mL) and  $\text{N}_2$  bubbled water (3.0 mL) were added via syringe, and the flask was attached to a water cooled condenser and a  $\text{N}_2$  inlet and oil bubbler at the top. The mixture was heated to reflux (110  $^\circ\text{C}$ ) with stirring for 18 h after which the mixture was quenched with 2 M  $\text{HCl}$  (aq), stirred for 20 minutes and subsequently extracted with  $\text{CH}_2\text{Cl}_2$  (5 x 50 mL), dried over anhydrous  $\text{Na}_2\text{SO}_4$ , filtered through celite and concentrated to dryness in a rotary evaporator. The obtained black oil was purified by column chromatography ( $\text{SiO}_2$ , 5% v/v  $\text{MeCN/EtOAc}$  then 10% to 20% v/v  $\text{MeCN/EtOAc}$ , obtaining **S7** (0.85 g, 65 %) as an orange oil.  $^1\text{H}$  NMR (500 MHz,  $\text{dmsO}-d_6$ , 25  $^\circ\text{C}$ )  $\delta$  (ppm) 8.175 (m, 2 H), 8.895 (m, 4 H), 7.785 (m, 2 H), 7.730 (s, 2 H), 7.415 (m, 4 H), 7.240 (m, 2 H), 4.260 (t, 4 H), 3.840 (t, 4 H), 3.630 (m, 4 H), 3.570 (m, 4 H), 3.50 (m, br, 28 H), 3.410 (m, 4 H), 3.220 (s, 3 H), 0.09 (s, 18 H),  $^{13}\text{C}$  NMR (125 MHz,  $\text{dmsO}-d_6$ , 25  $^\circ\text{C}$ )  $\delta$  (ppm) 156.94, 141.96, 136.64, 1334.08, 133.81, 133.12, 129.81, 128.04, 127.43, 126.30, 121.28, 119.11, 106.51, 104.28, 99.85, 71.27, 69.99, 69.84 (br), 69.79 (br), 69.57, 68.93, 67.27, 54.04, 0.41. MS: (MALDI-TOF, TCNQ) calcd for  $[\text{C}_{62}\text{H}_{86}\text{O}_{14}\text{Si}_2+\text{Na}]^+$  1133.55, found 1133.69. FTIR (ATR,  $\text{cm}^{-1}$ ) 3058, 3029, 2070, 2151, 1628, 1604, 1493, 1452, 1393, 1350, 1330, 1248, 1234, 1102 (br), 1061, 1034, 972, 938, 890, 841, 759, 731, 702.

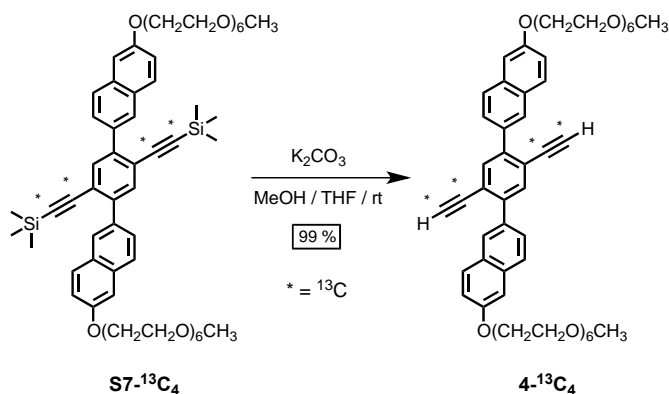


**Synthesis of S7- $^{13}\text{C}_4$ .** Similar procedure for the synthesis of **S7**, but using **S6- $^{13}\text{C}_4$** . **S6- $^{13}\text{C}_4$**  (0.121 g, 0.280 mmol), **S4** (0.522 g, 1.120 mmol),  $\text{Pd(PPh}_3)_4$  (0.016 g, 0.14 mmol),  $\text{K}_2\text{CO}_3$  (0.089, 0.644 mmol), toluene (2 mL), water (1 mL). **S7- $^{13}\text{C}_4$**  was isolated as a orange oil (0.150 g, 96% yield).  $^1\text{H}$  NMR (500 MHz,  $\text{dmsO-}d_6$ , 25  $^\circ\text{C}$ )  $\delta$  8.18 (s, 2H), 7.89 (m,  $J = 16.0$ , 8.9 Hz, 4H), 7.80 (d,  $J = 8.8$  Hz, 2H), 7.73 (d,  $J = 5.4$  Hz, 2H), 7.41 (s, 2H), 7.24 (d,  $J = 10.6$  Hz, 2H), 4.26 (t,  $J = 4.5$  Hz, 4H), 3.84 (t,  $J = 4.7$ , Hz, 2H), 3.66 – 3.36 (m, 20H), 3.22 (s, 3H).  $^{13}\text{C}$  NMR (126 MHz, 25  $^\circ\text{C}$ ,  $\text{dmsO-}d_6$ )  $\delta$  104.31 (d,  $J_{\text{C-C}} = 136.5$  Hz), 99.74 (d,  $J_{\text{C-C}} = 136.6$  Hz). MS (MALDI-TOF, TCNQ) calcd for  $[\text{C}_{58}^{13}\text{C}_4\text{H}_{86}\text{O}_{14}\text{Si}_2\text{Na}]^+$  1137.54, found 1137.32.

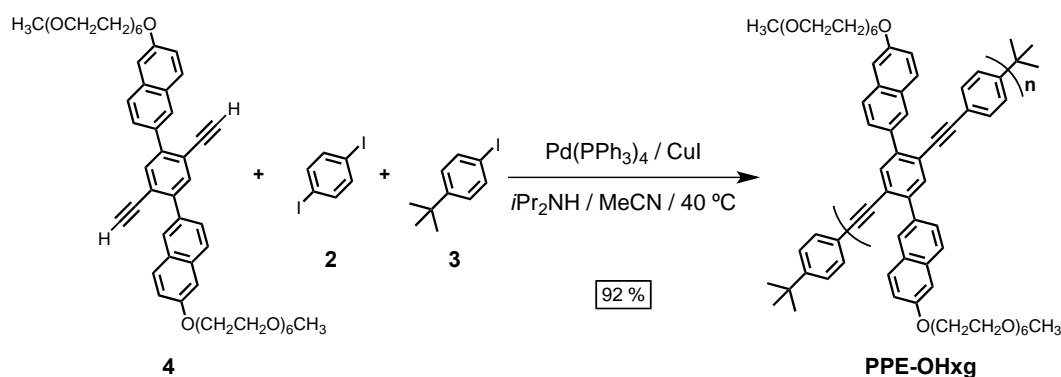


**Synthesis of monomer 4.** **S7** (150 mg, 0.135 mmol) of and  $\text{K}_2\text{CO}_3$  (187 mg, 1.35 mmol), were dissolved in THF (2.5 mL) and MeOH (0.5 mL). The suspension was stirred at 40  $^\circ\text{C}$  for 3 h. The mixture was added to 1 M  $\text{HCl}$  (aq, 3 mL), extracted with  $\text{CH}_2\text{Cl}_2$  (5 x 2 mL), the combined organic extracts were dried over anhydrous  $\text{Na}_2\text{SO}_4$ , filtered over celite and concentrated to dryness in a rotary evaporator. The obtained black wax was dried under high vacuum ( $10^{-2}$  torr) for 6 h, affording 120 mg (92% yield).  $^1\text{H}$  NMR (ppm, 500 MHz,  $\text{dmsO-}d_6$ , 80  $^\circ\text{C}$ )  $\delta$  8.107 (d, 2 H), 7.908 (dd, 4 H), 7.760 (m, 4 H), 7.415 (d, 2 H), 7.240 (dd, 2 H), 4.332 (s, 2 H), 4.254 (t, 4

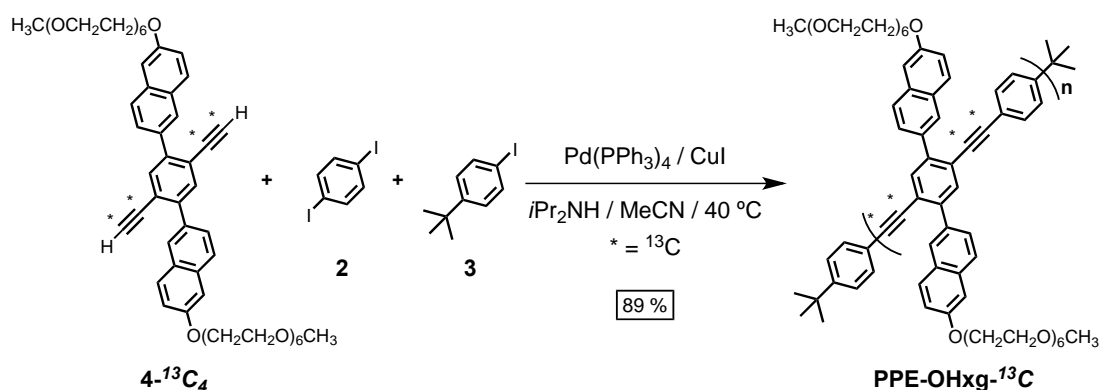
H), 3.338 (t, 4 H) 3.64-3.40 (m, br, 40 H), 3.221 (s, 6 H) 0.09 (d,  $J = 2.5$  Hz, 18H).  $^{13}\text{C}$  NMR (ppm, 126 MHz,  $\text{dms}\text{-}d_6$ , 80 °C)  $\delta$  156.94, 142.27, 134.63, 133.77, 133.47, 129.83, 128.19, 127.81, 127.41, 126.44, 120.99, 119.18, 106.55, 85.58, 82.42, 71.26, 70.00 69.83, 69.78 (br), 69.56, 68.90, 67.30, 58.04. MS: (MALDI-TOF, TCNQ) calcd for  $[\text{C}_{56}\text{H}_{70}\text{O}_{14}]^+$  966.48, found 966.26. FTIR (ATR,  $\text{cm}^{-1}$ ) 3096, 3059, 2921, 2853, 1722, 1627, 1604, 1484, 1457, 1437, 1348, 1246, 1196, 1117, 1090, 1074, 997, 937, 850, 748, 721, 695.



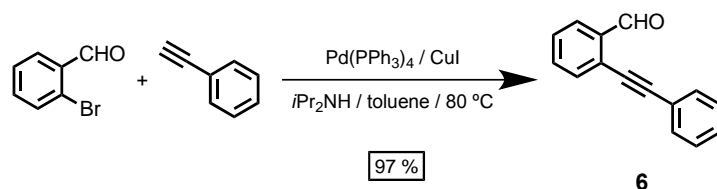
**Synthesis of monomer 4- $^{13}\text{C}_4$ .** Same procedure for the synthesis of **4**, but using **S7- $^{13}\text{C}_4$** . **S7- $^{13}\text{C}_4$** . (150 g, 0.134 mmol),  $\text{K}_2\text{CO}_3$  (0.186 g, 1.345 mmol). **4- $^{13}\text{C}_4$**  was isolated as an orange oil (0.130 g, 99% yield).  $^1\text{H}$  NMR (500 MHz,  $\text{dms}\text{-}d_6$ , 25 °C)  $\delta$  8.11 (d,  $J = 1.8$  Hz, 2H), 7.91 (dd,  $J = 15.3, 8.9$  Hz, 4H), 7.79 – 7.71 (m, 4H), 7.41 (d,  $J = 2.6$  Hz, 2H), 7.24 (dd,  $J = 8.9, 2.5$  Hz, 2H), 4.33 (dd,  $J = 245.2, 59.3$  Hz, 2H), 4.25 (t,  $J = 4.5$  Hz, 4H), 3.84 (t,  $J = 4.1$  Hz, 4H), 3.70 – 3.36 (m, 38H), 3.22 (s, 6H).  $^{13}\text{C}$  NMR (126 MHz,  $\text{dms}\text{-}d_6$ , 25 °C)  $\delta$  85.69 (d,  $J_{\text{C-C}} = 171.9$  Hz), 82.25 (d,  $J_{\text{C-C}} = 171.9$  Hz), 69.78. MS: (MALDI-TOF, TCNQ) calcd for  $[\text{C}_{52}^{13}\text{C}_4\text{H}_{70}\text{O}_{14}+\text{Na}]^+$  993.46, found 993.50. FTIR (ATR,  $\text{cm}^{-1}$ ) 3234, 3064, 3029, 2868 (br), 1632, 1604, 1491, 1459, 1453, 1447, 1415, 1395, 1356, 1345, 1334, 1305, 1275, 1257, 1242, 1235, 1218, 1198, 1176, 1167, 1125, 1112, 1098, 1068, 1057, 1033, 974, 960, 952, 940, 922, 914, 903, 896, 882, 858, 848, 831, 815, 807, 800, 752, 721, 698, 664.



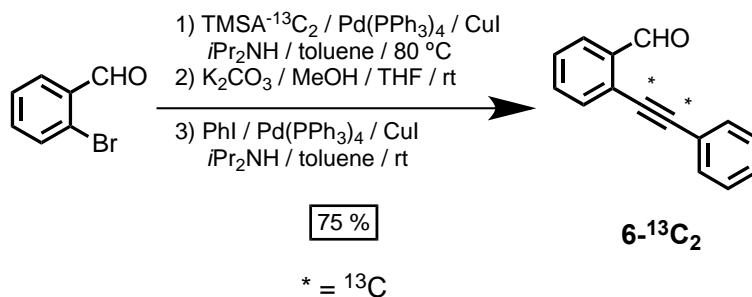
**General Synthesis of polymer PPE-OHxg.** Monomer **4** (41 mg, 0.124 mmol) 1,4-diiodobenzene **2** (41 mg, 0.124 mmol) and 4-tertbutyl-1-iodobenzene **5** (See Table S1 for amounts), Pd(PPh<sub>3</sub>)<sub>4</sub> (7 mg, 0.006 mmol) and CuI (2 mg, 0.010 mmol) were loaded in a flame dried 50 mL Schlenk flask equipped with a magnetic stirrer. The flask was evacuated under dynamic vacuum to 150 mtorr and refilled with N<sub>2</sub> three times. Under N<sub>2</sub> flow, anhydrous MeCN (12.4 mL) and anhydrous *i*Pr<sub>2</sub>NH (4.2 mL) were added via cannula. The mixture was stirred at 40 °C for 4 days covered from light, after which was transferred in air to a round bottom flask and the mixture was concentrated to dryness in a rotary evaporation. The obtained dark green oil was suspended in CH<sub>2</sub>Cl<sub>2</sub> (1 mL) and added dropwise into Et<sub>2</sub>O (500 mL) forming a brown pale precipitate in a yellow solution and the suspension was allowed to rest for 6 h. The brown precipitate was separated by vacuum filtration using a 2 μm nylon filter membrane, rinsed with water, HCl 1M (*aq*), methanol and Et<sub>2</sub>O until rinse solvent was colorless. The obtained solid was dried under dynamic vacuum (10<sup>-2</sup> torr) for 12 h to afford **PPE-OHxg** (118 mg, 92% yield) as a dark brown waxy solid. <sup>1</sup>H NMR (500 MHz, dms<sub>o</sub>-*d*<sub>6</sub>, 25 °C) δ 8.20 (br), 7.84 (br), 7.70 (br), 7.39 (br), 7.28 (br), 7.23 (br), 7.11 (br), 4.27 (br), 3.85 (br), 3.65-3.39 (br), 3.18 (br). <sup>13</sup>C NMR (126 MHz, dms<sub>o</sub>-*d*<sub>6</sub>, 25 °C) δ 156.79, 137.23, 133.56, 133.28, 132.39, 131.07, 130.91, 129.37, 128.25, 127.99, 127.50, 126.99, 126.06, 118.81, 106.89, 71.00, 69.79, 69.72, 69.60, 69.53, 69.30, 68.72, 68.69, 67.29, 57.64. FTIR (ATR, cm<sup>-1</sup>) 3058, 2867, 2205, 1627, 1603, 1493, 1389, 1349, 1261, 1232, 1196, 1098, 1005, 972, 936, 888, 852, 814, 748, 701, 669.



**Synthesis of polymer PPE-OHxg- $^{13}\text{C}$ .** Same procedure for the synthesis of **PPE-OHxg**, but using **4- $^{13}\text{C}_4$**  (90 mg, 0.091 mmol), **2** (30 mg, 0.091 mmol), **5** (109  $\mu\text{L}$  of a 5.2 mg  $\text{mL}^{-1}$  solution in anhydrous THF, 0.567 mg, 0.00218 mmol),  $\text{Pd}(\text{PPh}_3)_4$  (5 mg, 0.005 mmol),  $\text{CuI}$  (5 mg, 0.027 mmol), anhydrous  $\text{MeCN}$  (9 mL) and  $i\text{Pr}_2\text{NH}$  (3 mL). **PPE-OHxg- $^{13}\text{C}$**  was isolated as a dark brown waxy solid (85 mg, 89% yield).  $^1\text{H}$   $^{13}\text{C}$ , FTIR.

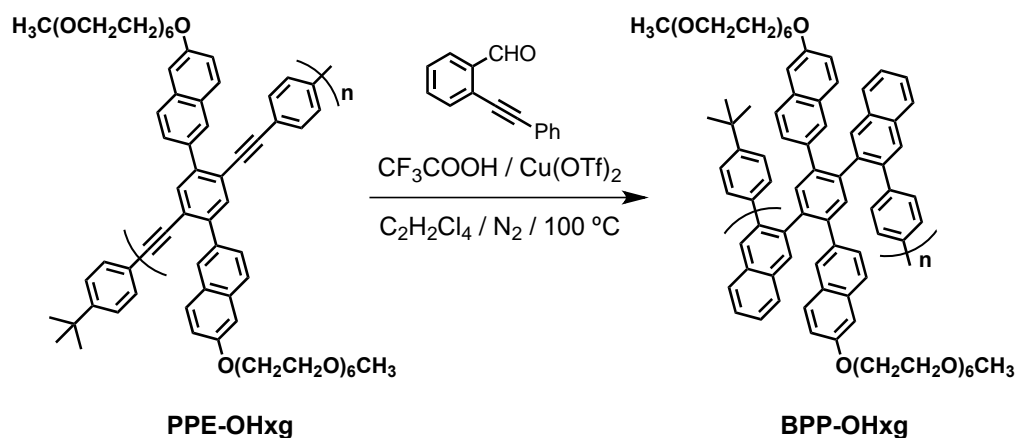


**Synthesis of 6.** 2-bromobenzaldehyde (3.0 g, 16 mmol),  $\text{CuI}$  (0.062 g, 0.32 mmol) and  $\text{Pd}(\text{PPh}_3)_2\text{Cl}_2$  (0.115 g, 0.16 mmol) were loaded in a flame dried Schlenk flask equipped with a magnetic stirrer. The flask was evacuated under dynamic vacuum to 150 mtorr and back filled with  $\text{N}_2$  three times. Anhydrous toluene (18 mL) and  $i\text{Pr}_2\text{NH}$  (6 mL) were added via syringe under  $\text{N}_2$ . Phenylacetylene (2.6 mL, 1.82 g, 18 mmol) was added dropwise via syringe under  $\text{N}_2$  and the mixture was stirred at 85  $^\circ\text{C}$  for 8 h, after which it was quenched with saturated  $\text{NH}_4\text{Cl}$  (aq). The mixture was extracted with toluene three (3 x 50 mL), the combined organic extracts were rinsed three times with saturated  $\text{NH}_4\text{Cl}$  (aq), water and brine, dried over  $\text{MgSO}_4$ , filtered through celite and concentrated to dryness in a rotary evaporator. The crude product was purified by flash column chromatography ( $\text{SiO}_2$ , 5%  $\text{Et}_2\text{O}$ /hexanes v/v) obtaining **6** (3.25 g, 97% yield) as brown oil. Analysis matched values reported by [S41].



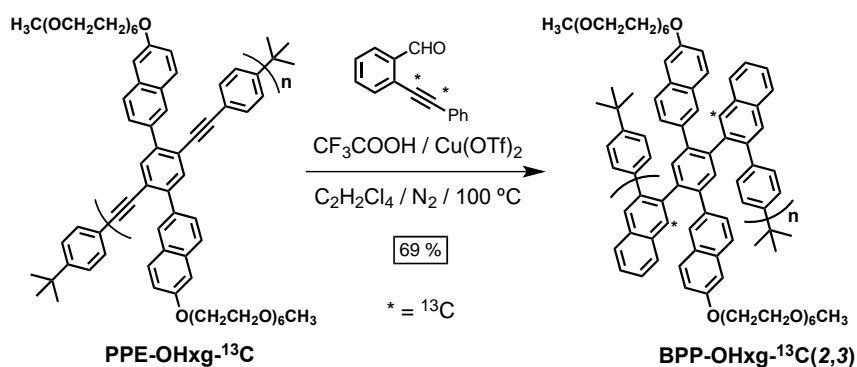
**Synthesis of 6- $^{13}\text{C}_2$ .** 2-bromobenzaldehyde (0.526 g 2.84 mmol), CuI (5 mg, 0.028 mmol), and Pd(PPh $_3$ ) $_4$  (15 mg, 0.013 mmol) were loaded in a 25 mL Schlenk flask equipped with a magnetic stirrer. The flask was evacuated under dynamic vacuum to 150 mtorr and backfilled with N $_2$  three times. Anhydrous toluene (3 mL) and anhydrous *i*Pr $_2$ NH (1 mL) were added via cannula under N $_2$ . The mixture was bubbled with N $_2$  for 20 min and trimethylsilylacetylene- $^{13}\text{C}_2$  (99% atom  $^{13}\text{C}$ , 0.435 mL, 300 mg, 2.994 mmol) was added dropwise with stirring. The mixture was heated to 80 °C and stirred for 12 h, after which it was quenched with saturated NH $_4$ Cl (aq), and extracted with CH $_2$ Cl $_2$  (3 x 10 mL). The combined organic extracts were rinsed with saturated NH $_4$ Cl (aq), water, and brine. The solution was dried over anhydrous MgSO $_4$ , filtered over celite, and concentrated to dryness. The obtained dark residue was purified by column chromatography (SiO $_2$ , 5% v/v THF/hexanes). The resulting yellow (0.554 g, 2.71 mmol), and K $_2$ CO $_3$  (3.74 g, 27.11 mmol) were suspended in THF (6 mL) and MeOH (2 mL). The suspension was stirred at rt for 30 min. The mixture was added to 1 M HCl (3 mL), extracted with CH $_2$ Cl $_2$  (3 x 2 mL), after which the combined organic extracts were dried over anhydrous MgSO $_4$ , filtered over celite, and concentrated to dryness. The resulting yellow solid (0.335 g, 2.53 mmol), CuI (5 mg, 0.027 mmol), and Pd(PPh $_3$ ) $_4$  (16 mg, 0.014 mmol) were loaded in a 25 mL Schlenk flask equipped with a magnetic stirrer. The flask was evacuated under dynamic vacuum to 150 mtorr and backfilled with N $_2$  three times. A mixture containing anhydrous toluene (5 mL), anhydrous *i*Pr $_2$ NH (2 mL), and iodobenzene (0.608 g) were added via cannula under N $_2$ . The mixture was stirred at rt for 10 h, after which it was quenched with saturated NH $_4$ Cl (aq) and extracted with toluene (3 x 10 mL). The combined organic extracts were rinsed with saturated NH $_4$ Cl (aq), water, and brine. The solution was dried over anhydrous MgSO $_4$ , filtered over celite and concentrated to dryness. The obtained dark residue was purified by column chromatography (SiO $_2$ , 5% v/v THF/hexanes) to provide 6- $^{13}\text{C}_2$  (0.506 g, 75% yield overall) as a green oil.  $^1\text{H}$

NMR (400 MHz, CDCl<sub>3</sub>)  $\delta$  10.66 (s, 1H), 7.97 (d,  $J$  = 7.27 Hz, 1H), 7.65 (m,  $J$  = 5.45, Hz, 1H), 7.61-7.56 (m, 3H), 7.46 (m,  $J$  = 7.48, 1H), 7.39 (m,  $J$  = 2.51, 3H). <sup>13</sup>C NMR (100 MHz, CDCl<sub>3</sub>)  $\delta$  96.52 (d,  $J_{CC}$  = 184.82 Hz), 84.97 (d,  $J_{CC}$  = 182.02 Hz). HRMS (EI,  $m/z$ ): calcd for [C<sub>13</sub>H<sub>10</sub>O<sup>13</sup>C<sub>2</sub>]<sup>+</sup> 208.0799, found 208.0800. FTIR (ATR, cm<sup>-1</sup>) 3079, 3061, 3031, 3020, 2957, 2842, 2745, 1692, 1663, 1598, 1591, 1571, 1564, 1490, 1471, 1449, 1442, 1387, 1286, 1264, 1191, 1160, 1142, 1086, 1069, 1025, 1014, 997, 958, 914, 874, 849, 815, 753, 753, 720, 709, 688, 668, 654.



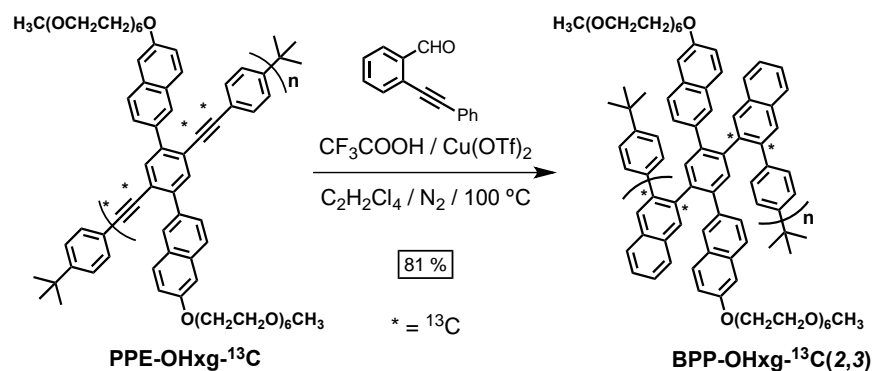
**General synthesis of polymer BPP-OHxg.** PPE-OHxg (80 mg of, 0.080 mmol, based on repeating unit) and Cu(CF<sub>3</sub>SO<sub>3</sub>)<sub>2</sub> (10 mg, 0.027 mmol) were loaded in a 5 mL round bottom flask equipped with a magnetic stirrer. C<sub>2</sub>H<sub>2</sub>Cl<sub>4</sub> (2 mL) was added and the mixture was degassed by three cycles of freeze-pump-thaw, backfilled with N<sub>2</sub> and heated to 90 °C with stirring. 2-(2-phenylethynyl)-benzaldehyde **6** (206 mg, 1.152 mmol) and CF<sub>3</sub>COOH (30  $\mu$ L, 44 mg, 0.046 mmol) were added at 90 °C with stirring in portions of 80 mg of **6** and 10  $\mu$ L of acid each 3 hours. After 9 h, the mixture was cooled to room temperature, quenched with saturated NaHCO<sub>3</sub> (aq). After effervescence stopped, the mixture was extracted with CH<sub>2</sub>Cl<sub>2</sub> (3 x 50 mL), dried over anhydrous Na<sub>2</sub>SO<sub>4</sub>, filtered through celite and concentrated to dryness. The obtained brown oil was dissolved in C<sub>2</sub>H<sub>2</sub>Cl<sub>4</sub> (1 mL) and precipitated into Et<sub>2</sub>O (250 mL), forming a brown solid in a pale yellow suspension. The mixture was allowed to rest 8 h after which the solid was isolated by vacuum filtration using a 2  $\mu$ m nylon filter paper, rinsed with HCl 2 M (aq), water, MeOH and Et<sub>2</sub>O until rinse liquors were colorless. The obtained dark brown solid was dried

under dynamic vacuum ( $10^{-2}$  torr) for 12 h affording 118 mg (92% yield).  $^1\text{H}$  NMR (500 MHz,  $\text{dmso-}d_6$ , 25 °C)  $\delta$  7.95 (br), 7.52-7.06 (br), 4.15 (br), 3.43 (br), 3.16 (br).  $^{13}\text{C}$  NMR (126 MHz,  $\text{dmso-}d_6$ , 25 °C)  $\delta$  138.79, 135.74, 132.68, 128.34, 71.80, 70.33, 70.10, 69.39, 67.96. FTIR (ATR,  $\text{cm}^{-1}$ ) 3055, 2867, 1627, 1602, 1487, 1447, 1394, 1348, 1244, 1197, 1100, 937, 888, 851, 751, 698.

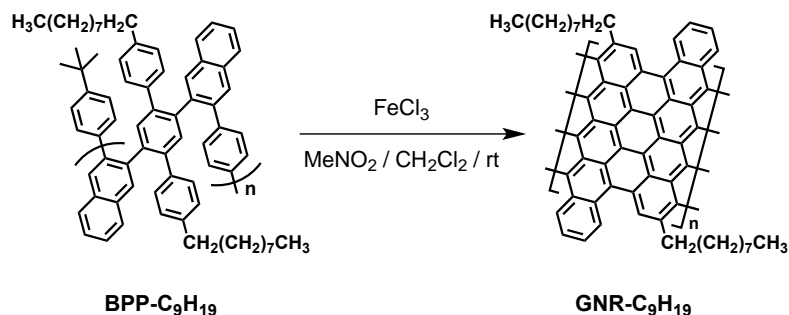


**Synthesis of polymer BPP-OHxg- $^{13}\text{C}(I)$ .** Similar procedure for the synthesis of **BPP-OHxg**, but using **PPE-OHxg** (60 mg, 0.058 mmol, based on repeating unit),  $\text{Cu}(\text{CF}_3\text{SO}_3)_2$  (7 mg, 0.020 mmol), **6- $^{13}\text{C}_2$**  (180 mg, 0.864 mmol) and  $\text{CF}_3\text{COOH}$  (22  $\mu\text{L}$ , 33 mg, 0.346 mmol) and  $\text{C}_2\text{H}_2\text{Cl}_4$  (1.5 mL). **BPP-OHxg- $^{13}\text{C}(I)$**  was isolated as a brown powder (40 g, 69% yield).  $^1\text{H}$  NMR (500 MHz, 1,1,2,2-tetrachloroethane- $d_2$ )  $\delta$  7.93 (br), 7.57 (br), 7.26 (br), 7.17 (br), 7.03 (br), 4.27 (br), 3.95 (br), 3.65 (br), 3.57 (br), 3.37 (br).  $^{13}\text{C}$  NMR (126 MHz, 1,1,2,2-tetrachloroethane- $d_2$ )  $\delta$  136.53, 130.78, 128.78, 72.17, 70.77, 70.74, 70.53. FTIR (ATR,  $\text{cm}^{-1}$ ) 3053, 2866 1690, 1697, 1602, 1486, 1447, 1390, 1348, 1245, 1197, 1099, 937, 883, 851, 750, 702.



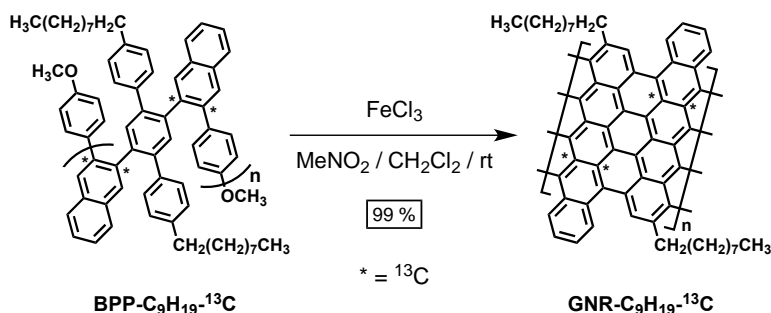


**Synthesis of polymer BPP-OHxg- $^{13}\text{C}$ (2,3).** Similar procedure for the synthesis of **BPP-OHxg**, but using **PPE-OHxg- $^{13}\text{C}$**  (75 mg, 0.072 mmol, based on repeating unit),  $\text{Cu}(\text{CF}_3\text{SO}_3)_2$  (9 mg, 0.025 mmol), **6** (222 mg, 1.076 mmol) and  $\text{CF}_3\text{COOH}$  (27  $\mu\text{L}$ , 44 mg, 0.431 mmol) and  $\text{C}_2\text{H}_2\text{Cl}_4$  (2 mL). **BPP-OHxg- $^{13}\text{C}$ (I)** was isolated as a brown powder (73 mg, 81 % yield).  $^1\text{H}$  NMR (599 MHz,  $\text{CDCl}_3$ )  $\delta$  7.85 (br), 7.43 (br), 7.09 (br), 6.83 (br), 4.15 (br), 3.88 (br), 3.60 (br), 3.32 (br), 1.60 (br).  $^{13}\text{C}$  NMR (126 MHz,  $\text{CDCl}_3$ )  $\delta$  144.31, 139.97, 139.48, 138.81, 138.36, 132.93, 131.27, 129.70, 127.91, 126.38, 72.03, 70.94, 70.69, 70.59, 69.89, 67.40. FTIR (ATR,  $\text{cm}^{-1}$ ) 3051, 2869, 1627, 1602, 1495, 1447, 1394, 1348, 1244, 1198, 1101, 936, 887, 849, 750, 701.

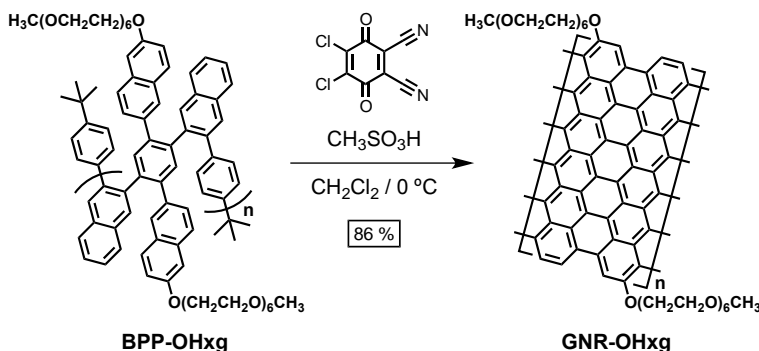


**Synthesis of graphene nanoribbon GNR-C $_9\text{H}_{19}$ .** **BPP-C $_9\text{H}_{19}$**  (50 mg, 0.056 mmol based on repeat unit) was loaded in a 100 mL Schlenk flask equipped with a magnetic stirrer. The flask was evacuated under dynamic vacuum to 150 mtorr and the filled with  $\text{N}_2$  three times. Anhydrous  $\text{CH}_2\text{Cl}_2$  (40 mL) was added via cannula, and the solution was stirred.  $\text{FeCl}_3$  (0.300 g, 1.85 mmol) was dissolved in 2 mL of  $\text{CH}_3\text{NO}_2$  and the mixture was bubbled with  $\text{N}_2$  for 5 min. The  $\text{FeCl}_3$  solution was added drop wise via syringe to the dichloromethane solution under  $\text{N}_2$ , and the mixture was stirred at room temperature for 24 h. After which it was poured into MeOH (50 mL) yielding a black precipitate. The black solid was separated by centrifugation, rinsed with MeOH three times. The obtained black solid was extracted with acetone in a Soxhlet apparatus

for 24 h affording **GNR-C<sub>9</sub>H<sub>19</sub>** (44 mg, 90% yield) as a black powder. FTIR (ATR, cm<sup>-1</sup>) 2950, 2919, 2850, 1730, 1654, 1463, 1377, 1265, 1118, 1073, 796, 749.

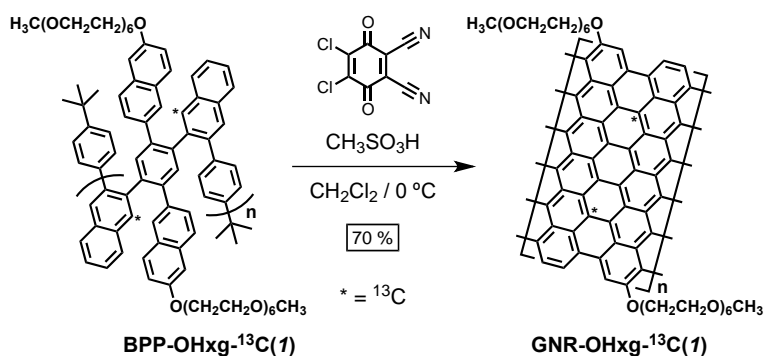


**Synthesis of polymer GNR- C<sub>9</sub>H<sub>19</sub>-<sup>13</sup>C.** Similar procedure for the synthesis of **GNR- C<sub>9</sub>H<sub>19</sub>**, but using **BPP-C<sub>9</sub>H<sub>19</sub>-<sup>13</sup>C** (20 mg, 0.025 mmol, based on repeating unit),  $\text{FeCl}_3$  (119 mg, 0.736 mmol),  $\text{CH}_3\text{NO}_2$  (1.2 mL) and  $\text{CH}_2\text{Cl}_2$  (25 mL). **GNR-C<sub>9</sub>H<sub>19</sub>-<sup>13</sup>C(I)** was isolated as a black powder (18 mg, 99 % yield). FTIR (ATR, cm<sup>-1</sup>) 3055, 2919, 2849, 1732, 1634, 1505, 1462, 1455, 1373, 1207, 1158, 1106, 887, 822, 748, 719, 699.

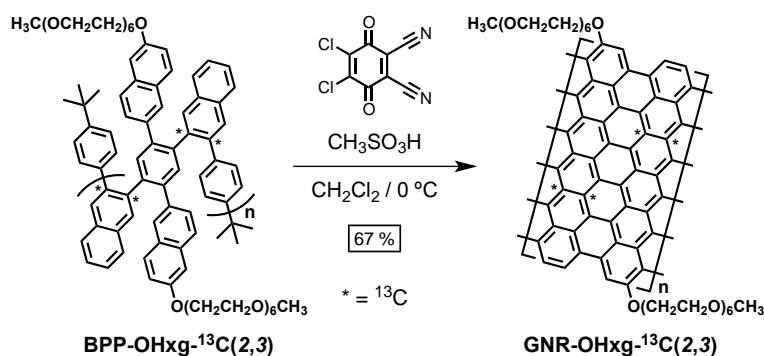


**Synthesis of graphene nanoribbon GNR-OHxg.** **BPP-OHxg** (21 mg, 0.017 mmol based on repeat unit) was loaded in a 500 mL Schlenk flask equipped with a magnetic stirrer. The flask was evacuated under dynamic vacuum to 150 mtorr and the filled with  $\text{N}_2$  three times. Anhydrous  $\text{CH}_2\text{Cl}_2$  (80 mL) and  $\text{CH}_3\text{SO}_3\text{H}$  (10 mL) were added via cannula, and the solution was stirred and cooled to 0 °C in an ice/water bath. 2,3-dichloro-5,6-dicyano-1,4-benzoquinone, (DDQ, 0.114 g, 0.506 mmol) was dissolved in 2.5 mL of anhydrous  $\text{CH}_2\text{Cl}_2$  and the mixture was bubbled with  $\text{N}_2$  for 5 min. The DDQ solution was added drop wise via syringe to the  $\text{CH}_2\text{Cl}_2$

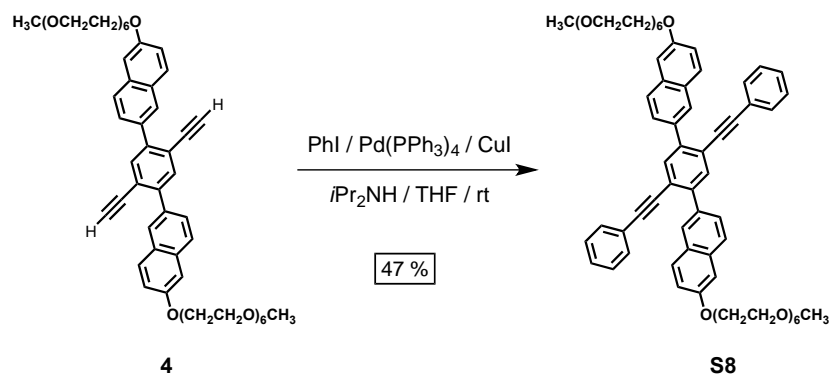
solution under N<sub>2</sub>, and the mixture was stirred at 0 °C for 1 h. The mixture was warmed up to room temperature and stirred for 48 h to form a dark solution. The mixture was quenched with saturated NaHCO<sub>3</sub> (aq) yielding a black precipitate suspended in the organic phase. After effervescence stopped, the mixture was extracted with CH<sub>2</sub>Cl<sub>2</sub> (3 x 100 mL). The black solid (present in both aqueous and organic phases) was separated by filtration from each phase and combined. The obtained black solid was rinsed with water, MeOH, EtO<sub>2</sub> and CH<sub>2</sub>Cl<sub>2</sub>, and dried under dynamic vacuum (10<sup>-2</sup> torr) for 8 h affording **GNR-OHxg** (18 mg 70% yield). FTIR (ATR, cm<sup>-1</sup>) 3064, 2865, 1717, 1447, 1348, 1240, 1198, 1095, 948, 880, 829, 756, 701.



**Synthesis of polymer GNR-OHxg-<sup>13</sup>C(I).** Similar procedure for the synthesis of **GNR-OHxg**, but using **BPP-OHxg-<sup>13</sup>C(I)** (27 mg, 0.016 mmol, based on repeating unit), DDQ (47 mg, 0.482 mmol), CH<sub>3</sub>SO<sub>3</sub>H (10 mL) and CH<sub>2</sub>Cl<sub>2</sub> (100 mL). **GNR-OHxg-<sup>13</sup>C(I)** was isolated as a black powder (18 mg, 70 % yield). FTIR (ATR, cm<sup>-1</sup>) 3064, 2865, 1575, 1447, 1348, 1240, 1198, 1095, 944, 880, 842, 829, 756, 691.

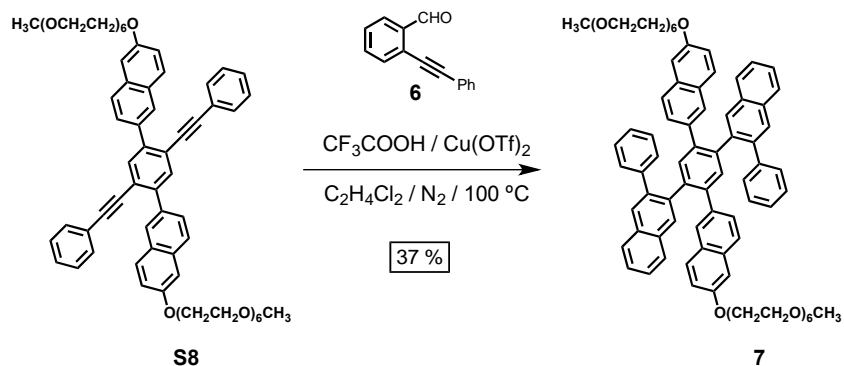


**Synthesis of polymer GNR-OHxg- $^{13}\text{C}(2,3)$ .** Similar procedure for the synthesis of **GNR-OHxg**, but using **BPP-OHxg- $^{13}\text{C}(2,3)$**  (15 mg, 0.012 mmol, based on repeating unit), DDQ (82 mg, 0.361 mmol),  $\text{CH}_3\text{SO}_3\text{H}$  (6 mL) and  $\text{CH}_2\text{Cl}_2$  (60 mL). **GNR-OHxg- $^{13}\text{C}(2,3)$**  was isolated as a black powder (10 mg, 67 % yield). FTIR (ATR,  $\text{cm}^{-1}$ ) 3058, 2870, 1699, 1634, 1581, 1457, 1348, 1243, 1174, 1095, 953, 832, 755, 700.



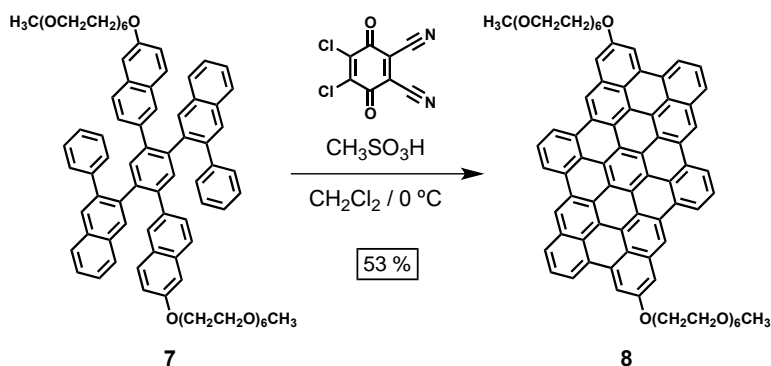
**Synthesis of S8.** **4** (105 mg, 0.109 mmol), iodobenzene (0.131 mL, 50 mg, 0.239 mmol), CuI (2 mg, 0.01 mmol) and  $\text{Pd}(\text{PPh}_3)_4$  (6 mg, 0.005 mmol) were loaded in a 50 mL Schlenk flask equipped with a magnetic stirrer. The flask was evacuated under dynamic vacuum to 150 mtorr and back filled with  $\text{N}_2$  three times. Anhydrous toluene (1 mL) and  $i\text{Pr}_2\text{NH}$  (0.5 mL) were added via syringe. The mixture was heated to  $45\text{ }^\circ\text{C}$  with stirring for 3 h after which the mixture was quenched with saturated  $\text{NH}_4\text{Cl}$  (aq), and subsequently extracted with  $\text{CH}_2\text{Cl}_2$  (3 x 50 mL). The combined organic extracts were dried over anhydrous  $\text{Na}_2\text{SO}_4$ , filtered through celite and concentrated to dryness. The obtained brown oil was purified by column chromatography ( $\text{SiO}_2$ , 20% v/v acetone/EtOAc), obtaining **S8** (57 mg, 47 %) as a yellow oil.  $^1\text{H}$  NMR (500 MHz, 60

°C,  $\text{dmso-}d_6$ )  $\delta$  8.28 (d,  $J = 1.6$  Hz, 2H), 8.01 – 7.89 (m, 8H), 7.44 (d,  $J = 2.5$  Hz, 2H), 7.38 (s, 10H), 7.26 (dd,  $J = 8.9, 2.4$  Hz, 2H), 4.27 (dd,  $J = 5.8, 3.5$  Hz, 4H), 3.85 (dd,  $J = 5.8, 3.4$  Hz, 4H), 3.64 (dd,  $J = 5.9, 3.6$  Hz, 4H), 3.60 – 3.45 (m, 32H), 3.40 (dd,  $J = 5.8, 3.6$  Hz, 4H), 3.21 (s, 6H).  $^{13}\text{C}$  NMR (126 MHz, 60 °C,  $\text{dmso-}d_6$ )  $\delta$  156.97, 141.82, 133.84, 133.59, 131.10, 129.81, 129.02, 128.78, 128.25, 128.02, 127.53, 126.39, 122.14, 121.29, 119.26, 106.59, 93.86, 89.05, 71.26, 69.99, 69.84, 69.78, 69.76, 69.56, 68.92, 67.28, 58.03. MS (MALDI-TOF, TCNQ) calcd for  $[\text{C}_{68}\text{H}_{78}\text{O}_{14}+\text{Na}]^+$  1141.53, found 1141.45, FTIR (ATR,  $\text{cm}^{-1}$ ) 3057, 3030, 2919, 2870, 1724, 1628, 1604, 1497, 1489, 1453, 1437, 1390, 1349, 1260, 1230, 1196, 1169, 1118, 1100, 1028, 1014, 996, 971, 938, 890, 854, 811, 757, 721, 691.



**Synthesis of 7.** **S8** (0.050 g, 0.045 mmol),  $\text{Cu}(\text{CF}_3\text{SO}_3)_2$  (0.003 g, 0.009 mmol), **6** (0.023 g, 0.112 mmol) were loaded in a 25 mL round bottom flask equipped with a magnetic stirrer. 1,2-dichloroethane (0.5 mL) and  $\text{CF}_3\text{COOH}$  (0.01 mL, 0.015 g, 0.131 mmol) were added via syringe and the mixture was degassed by three cycles of freeze-pump-thaw, backfilled with  $\text{N}_2$  and heated to 95 °C with stirring for 4 h after which the mixture was quenched with saturated  $\text{NaHCO}_3$  (aq). After effervescence stopped, the mixture was extracted  $\text{CH}_2\text{Cl}_2$  (3 x 50 mL), the combined organic extracts were dried over anhydrous  $\text{Na}_2\text{SO}_4$ , filtered through celite and concentrated to dryness. The obtained brown oil was purified by column chromatography ( $\text{SiO}_2$ , 15% v/v MeCN/EtOAc, atmospheric pressure), obtaining **7** (0.022 g, 37 %) as an orange oil.  $^1\text{H}$  NMR (600 MHz, 25 °C,  $\text{dmso-}d_6$ )  $\delta$  8.16 (s, 2H), 7.92 (m, 4H), 7.70 (s, 2H), 7.54 - 7.46 (m, 6H), 7.41 (d,  $J = 9.1$  Hz, 2H), 7.33 (d,  $J = 8.7$  Hz, 2H), 7.24 (t,  $J = 7.4$  Hz, 2H), 7.17 (d,  $J = 2.6$  Hz, 2H), 7.10 - 7.03 (m, 4H), 6.98 (s, 2H), 6.74 (d,  $J = 8.5$  Hz, 2H), 6.64 (d,  $J = 7.7$  Hz, 4H), 4.16 (t,  $J = 3.0$  Hz, 4H), 3.79 (t,  $J = 4.6$  Hz, 4H), 3.64 - 3.58 (m, 4H), 3.57 - 3.43 (m, 32H), 3.41 - 3.37

(m, 4H), 3.33 (s, 6H).  $^{13}\text{C}$  NMR (126 MHz, 25 °C,  $\text{dms}\text{-}d_6$ )  $\delta$  166.94, 156.28, 146.92, 140.26, 139.50, 138.84, 138.77, 137.86, 135.26, 133.62, 133.22, 132.61, 132.46, 132.24, 131.69, 131.58, 131.55, 131.41, 130.75, 130.37, 130.28, 129.86, 129.52, 128.77, 128.68, 128.63, 128.39, 127.65, 127.57, 127.31, 127.25, 126.30, 126.27, 126.23, 125.35, 120.91, 120.79, 119.58, 118.46, 106.14, 71.24, 69.94, 69.80, 69.76, 69.71, 69.61, 69.54, 68.89, 67.38, 67.08, 58.00, 40.11, 40.02, 39.95, 39.85, 39.78, 39.69, 39.61, 39.52, 39.44, 39.35, 39.26, 39.19, 39.02. MS (MALDI-TOF, TCNQ) calcd for  $[\text{C}_{84}\text{H}_{90}\text{O}_{14}]^+$  1322.63, found 1322.61, FTIR (ATR,  $\text{cm}^{-1}$ ) 3056, 2919, 2851, 1724, 1628, 1602, 1489, 1456, 1422, 1350, 1250, 1201, 1107, 1025, 1002, 957, 914, 889, 851, 816, 760, 698.



**Synthesis of model compound 8.** **7** (15 mg, 0.011 mmol) was loaded in a 500 mL Schlenk flask equipped with a magnetic stirrer. The flask was evacuated under dynamic vacuum to 150 mtorr and the filled with  $\text{N}_2$  three times. Anhydrous  $\text{CH}_2\text{Cl}_2$  (5.5 mL) and  $\text{CH}_3\text{SO}_3\text{H}$  (0.5 mL) were added via cannula, and the solution was stirred and cooled to 0 °C in an ice/water bath. DDQ (51 mg, 0.480 mmol) was dissolved in anhydrous  $\text{CH}_2\text{Cl}_2$  (1 mL) and the mixture was bubbled with  $\text{N}_2$  for 5 min. The DDQ solution was added dropwise via syringe to the acidified  $\text{CH}_2\text{Cl}_2$  solution under  $\text{N}_2$ , and the mixture was stirred at 0 °C for 1 h. The mixture was warmed to rt and was stirred for 12 h, during which time it darkened. The suspension was quenched with saturated  $\text{NaHCO}_3$  (aq), and after bubbling stopped, the mixture was extracted with  $\text{CH}_2\text{Cl}_2$  (3 x 100 mL). The combined organic extracts were washed with saturated  $\text{NaHCO}_3$  (aq, 3 x 100 mL), dried over anhydrous  $\text{Na}_2\text{SO}_4$  filtered over celite and concentrated to dryness. The obtained dark red

crude was purified by column chromatography (1% TEA/hexanes neutralized SiO<sub>2</sub>, 30% v/v MeCN/EtOAc). The obtained dark red solid was dried under dynamic vacuum (10<sup>-2</sup> torr) for 8 h affording **8** (8 mg, 53% yield). Compound **8** decomposes after a few hours of isolation, even when kept under N<sub>2</sub> and away from light. This instability precluded collection of <sup>13</sup>C and heteronuclear correlation 2D NMR data. <sup>1</sup>H MS (MALDI-TOF, TCNQ) calcd for [C<sub>84</sub>H<sub>74</sub>O<sub>14</sub>+Na]<sup>+</sup> 1329.49, found 1329.57 FTIR (ATR, cm<sup>-1</sup>) 3063, 2919, 2869, 1720, 1637, 1599, 1449, 1408, 1344, 1244, 1175, 1095, 1018, 953, 872, 848, 799, 763, 726, 703.

### C. Size Exclusion Chromatography.

**Figure A4.1.** Size-exclusion chromatogram of polymers with  $D_{p,\text{theor}} = \infty$  (entry A Table S1), as detected by their differential refractive index on the THF mobile phase.

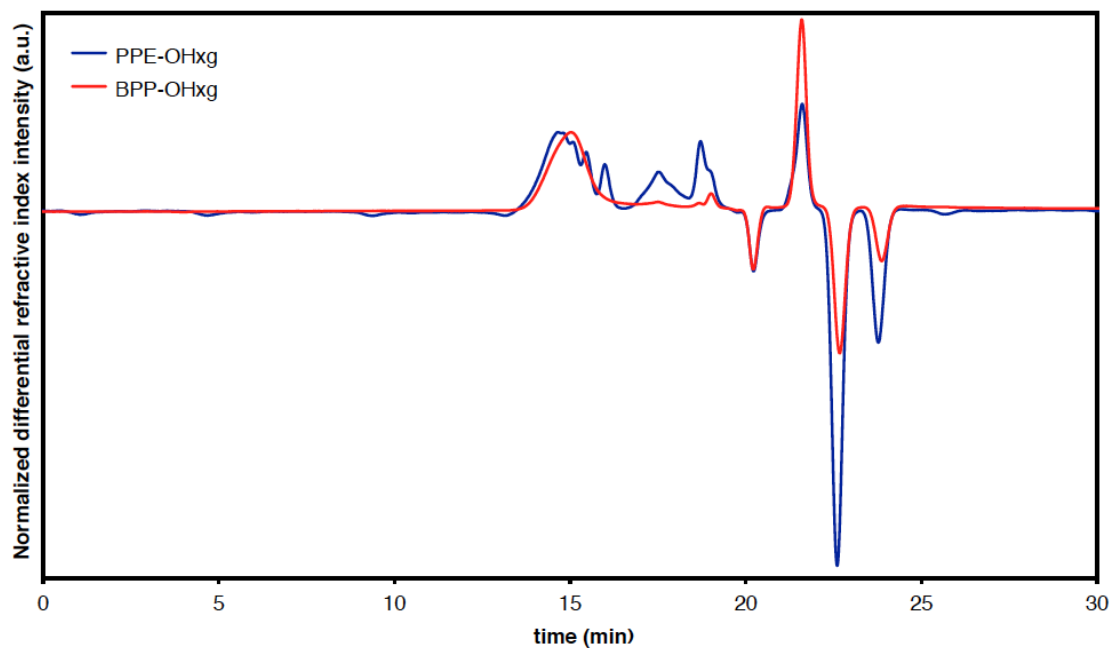


**Figure A4.2.** Size-exclusion chromatogram of polymers with  $D_{p,\text{theor}} = \infty$  (entry A Table S1), as detected by their light scattering intensity.

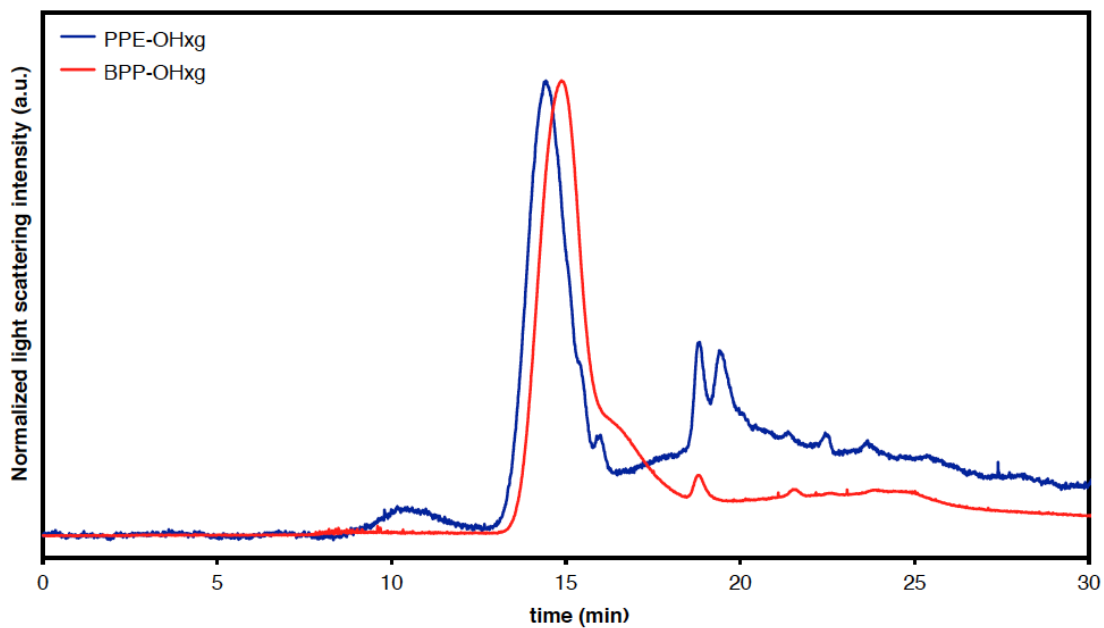




**Figure A4.3.** Size-exclusion chromatogram of polymers with  $D_{p,\text{theor}} = 80$  (entry B Table S1), as detected by their differential refractive index on the THF mobile phase.

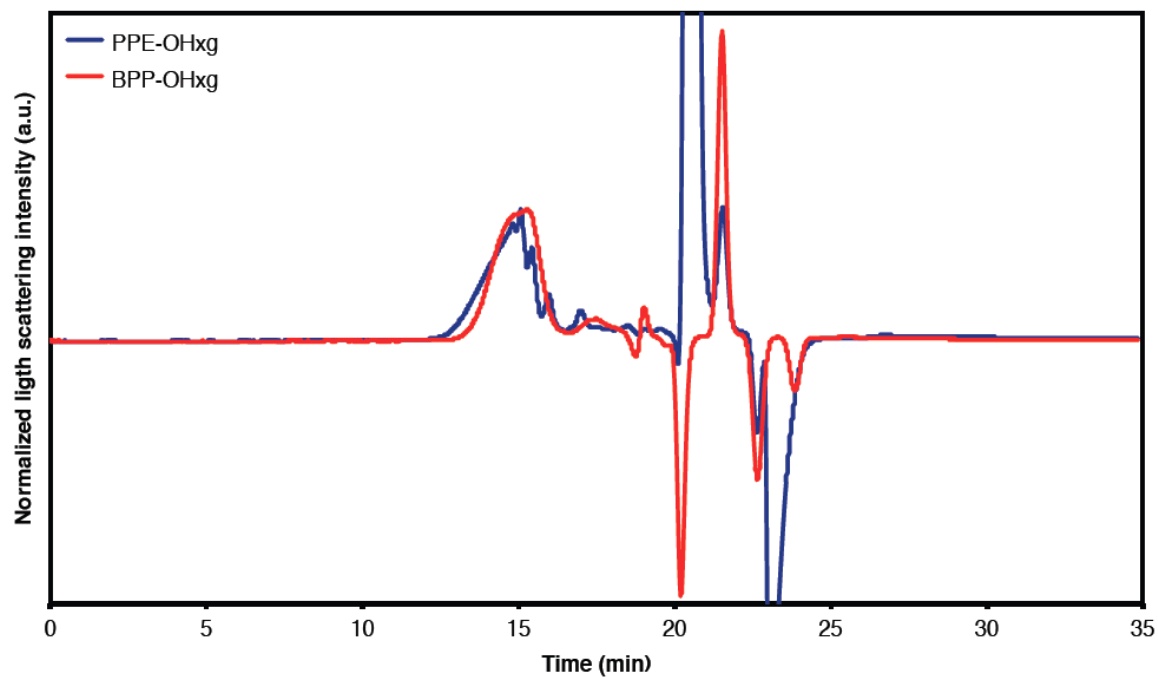


**Figure A4.4.** Size-exclusion chromatogram of polymers with  $D_{p,\text{theor}} = 80$  (entry B Table S1), as detected by their light scattering intensity.

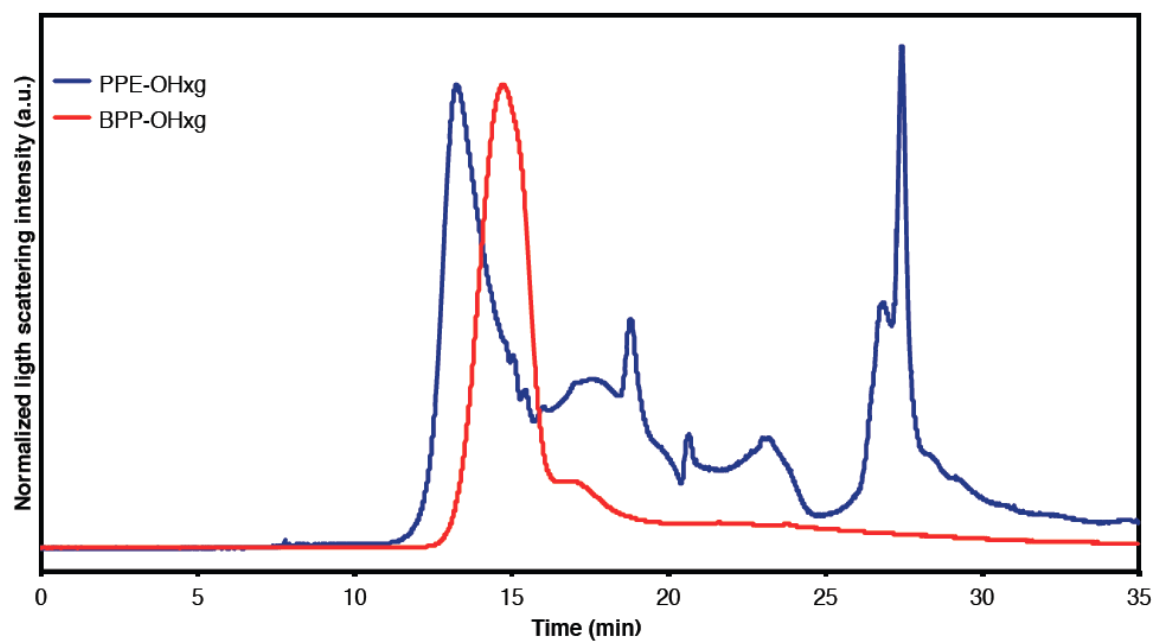


**Figure A4.5.** Size-exclusion chromatogram of polymers with  $D_{p,\text{theor}} = 40$  (entry C Table S1), as detected by their differential refractive index on the THF mobile phase.

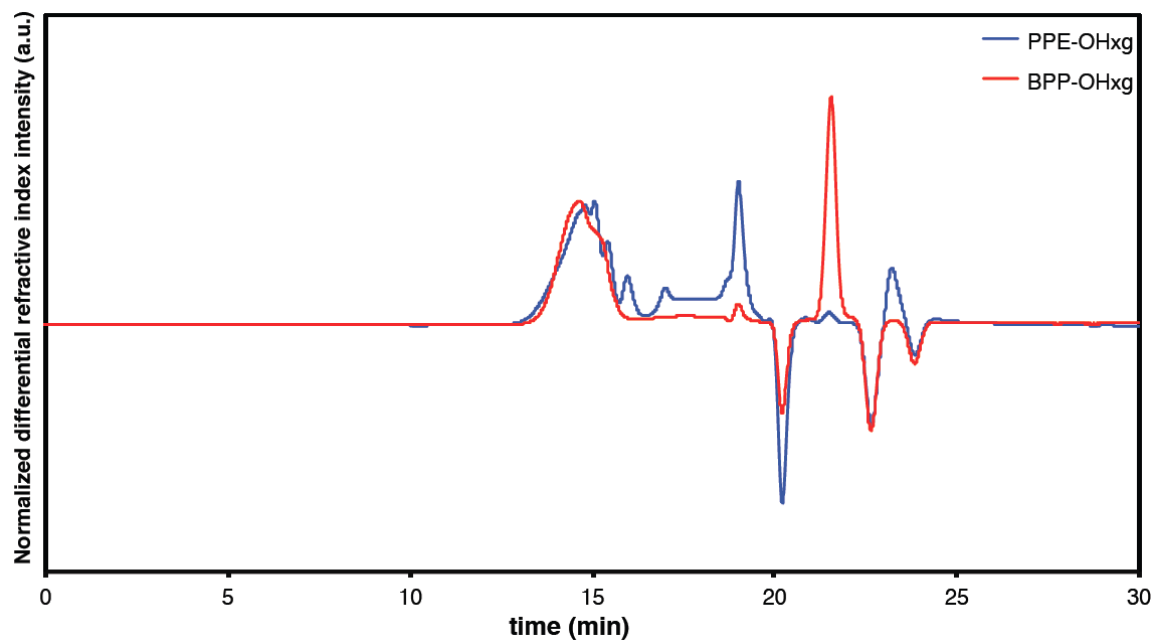


**Figure A4.6.** Size-exclusion chromatogram of polymers with  $D_{p,\text{theor}} = 40$  (entry C Table S1), as detected by their light scattering intensity.

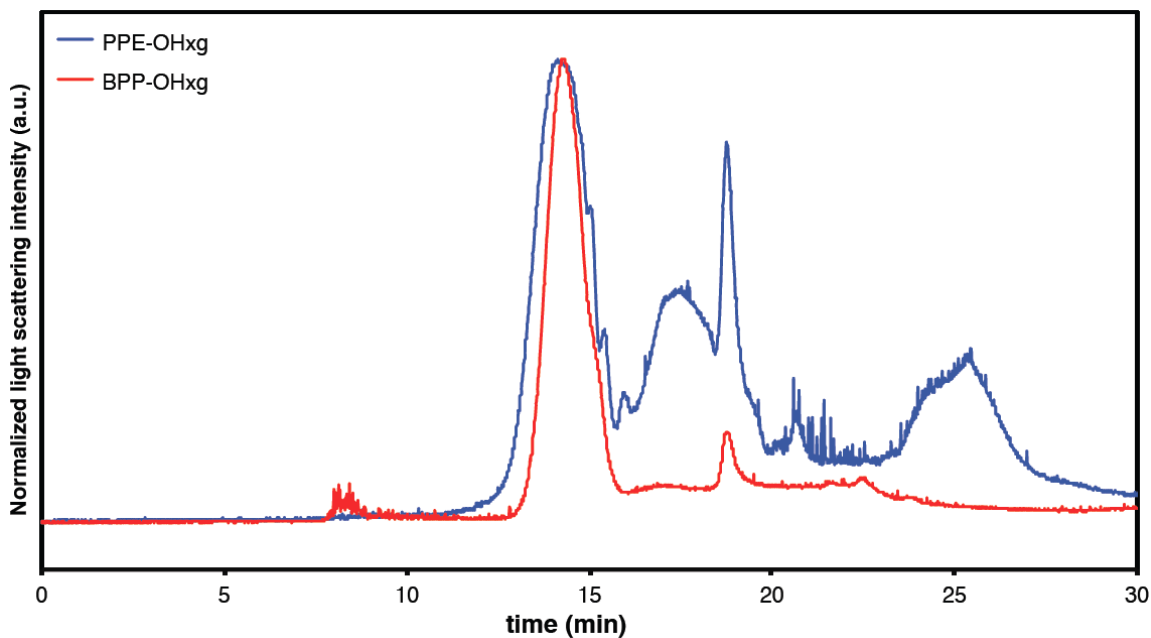


**Figure A4.7.** Size-exclusion chromatogram of isotopically enriched polymers with  $D_{p,\text{theor}} = 80$  (entry D Table S1), as detected by their differential refractive index on the THF mobile phase.

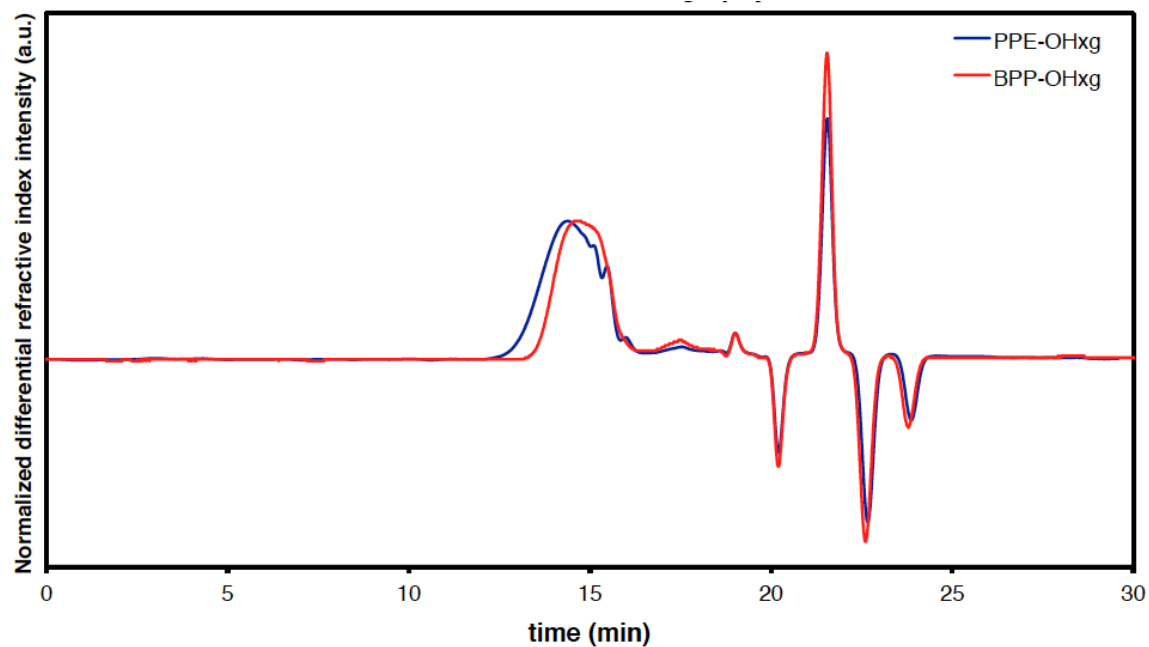


**Figure A4.8.** Size-exclusion chromatogram of isotopically enriched polymers with  $D_{p,\text{theor}} = 80$  (entry D Table S1), as detected by their light scattering intensity.

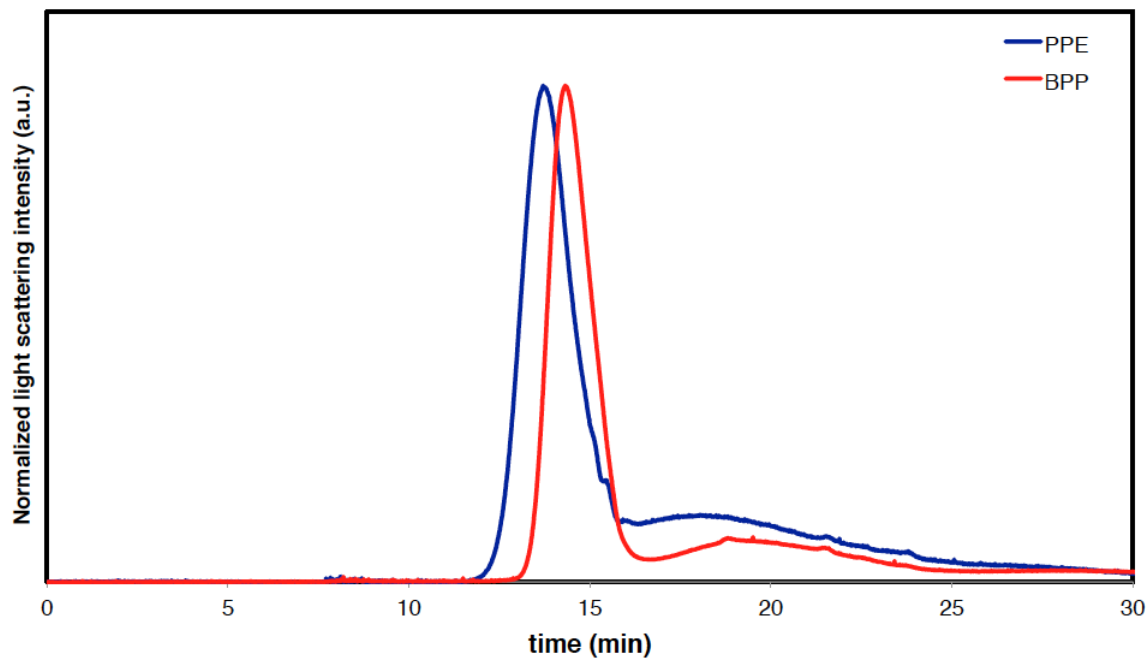


**Figure A4.9.** Size-exclusion chromatogram of isotopically enriched polymers with  $D_{p,theor} = 80$  (entry E Table S#), as detected by their light scattering and differential refractive index on the THF mobile phase.

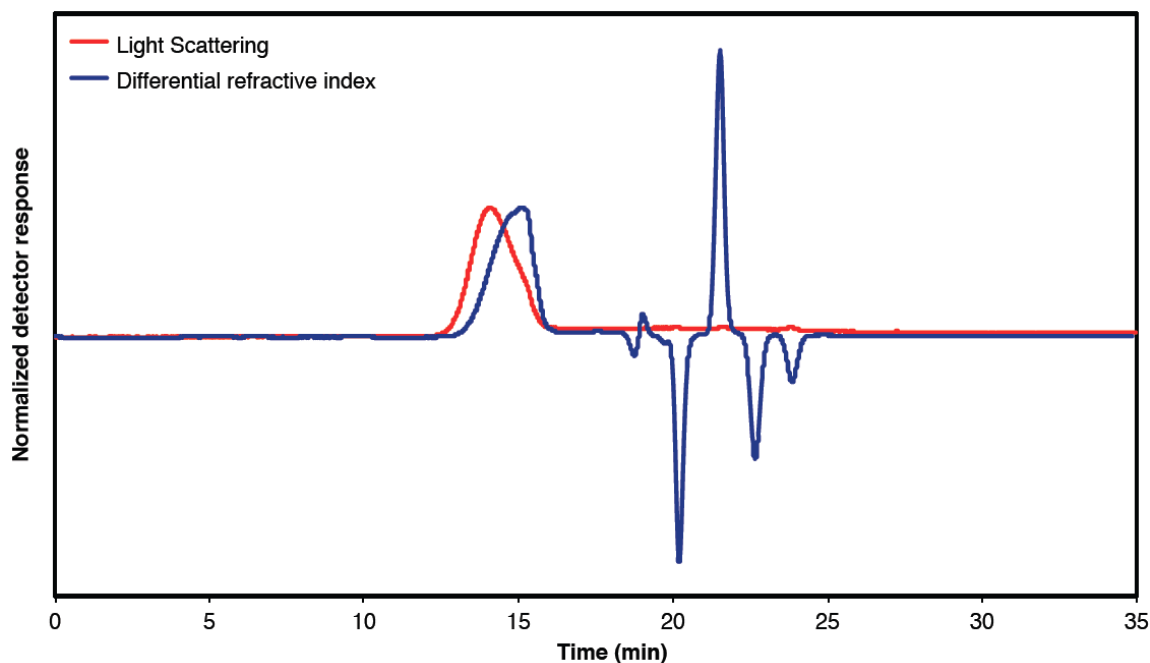


**Table A4.1.** Molecular weight determinations of synthesized polymers as determined by SEC-MALLS.  $D_p$  was calculated from  $M_w$ .

Entry	3 (mol%)	$D_p$ <i>Theor.</i>	Polymer	$M_n$ (g mol <sup>-1</sup> )	$M_w^a$ (g mol <sup>-1</sup> )	$\bar{D}$	$D_p$	$dn/dC$
A	0	$\infty$	PPE-OHxg	110,400 <sup>a,c</sup>	134,200 <sup>a,c</sup>	1.275 <sup>a,c</sup>	129 <sup>c</sup>	0.040
A'			BPP-OHxg	185,600 <sup>b,c</sup>	189,900 <sup>b,c</sup>	1.023 <sup>b,c</sup>	152 <sup>c,d</sup>	0.124
B	2.41	80	PPE-OHxg	106,500 <sup>a</sup>	197,300 <sup>a</sup>	1.852 <sup>a</sup>	190	0.052
B'			BPP-OHxg	157,500 <sup>b</sup>	166,900 <sup>b</sup>	1.060 <sup>b</sup>	134	0.183
B''			GNR-OHxg <sup>e</sup>	<sup>e</sup>	<sup>e</sup>	<sup>e</sup>	<sup>e</sup>	<sup>e</sup>
C	4.64	40	PPE-OHxg	33,420 <sup>a</sup>	36,220 <sup>a</sup>	1.260 <sup>a</sup>	35	0.053

C'			<b>BPP-OHxg</b>	39,960 <sup>b</sup>	50,000 <sup>b</sup>	1.252 <sup>b</sup>	40	0.120
D	2.41	80	<b>PPE-OHxg-<sup>13</sup>C</b>	72,650 <sup>a</sup>	108,100 <sup>a</sup>	1.488 <sup>a</sup>	104	0.058
D'			<b>BPP-OHxg-<sup>13</sup>C(2,3)</b>	103,100 <sup>b</sup>	121,800 <sup>b</sup>	1.181 <sup>b</sup>	90	0.133
E	2.41	80	<b>BPP-OHxg-<sup>13</sup>C (I)</b>	96,440 <sup>b</sup>	109,100 <sup>b</sup>	1.131 <sup>b</sup>	88	0.137
F <sup>d</sup>	10	17	<b>PPE-C<sub>9</sub>H<sub>19</sub></b>	7,850	27,700	3.53	12	0.265
F <sup>d</sup>			<b>BPP-C<sub>9</sub>H<sub>19</sub></b>	39,600	65,300	1.65	50	0.130

<sup>a</sup> After one precipitation step.

<sup>b</sup> After a total of two precipitations.

<sup>c</sup> Polymers partially soluble in THF. These masses reflect only soluble fractions.

<sup>d</sup> From reference [S41]

<sup>e</sup> SEC measured in DMF (0.1 M LiBr) as mobile phase, after a total of three precipitations.

**Table A4.2.** Average Molecular weight and degree of polymerization of **PPE-OHxg** as determined by end group intensity from  $^1\text{H}$  NMR (spectra in section K).

Entry	$D_p$ (Theor.)	$D_p$ (SEC-MALLS)	$D_p$ (endgroup)	$M_n$ (endgroup)
B	80	102	135	140,500
C	40	35	22	22,900

**Figure A4.10.** SEC detail of **PPE-OHxg** (entry D) before, after precipitation, and the resulting residue, as detected by the differential refractive index response.

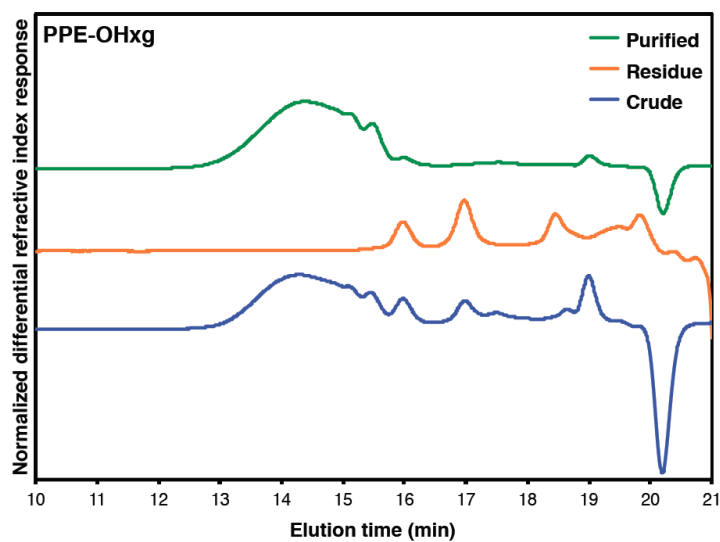
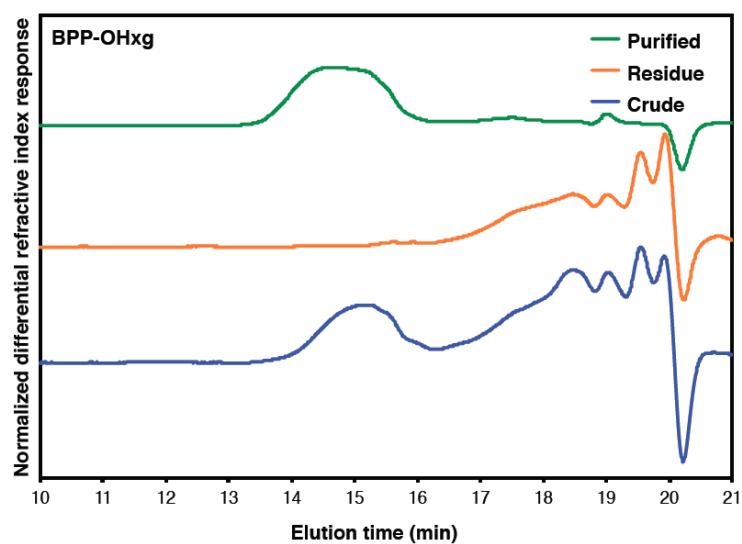


**Figure A4.11.** SEC detail of **BPP-OHxg** (entry D') before, after precipitation, and the resulting residue, as detected by the differential refractive index response.



#### D. UV/Vis/NIR Absorption and Fluorescence Spectroscopy and Quantum Yields Determination

**Figure A4.12.** UV-Visible photoabsorption spectra of **PPE-OHxg**, **BPP-OHxg** (1,2-dichloroethane) and **GNR-OHxg** (NMP).

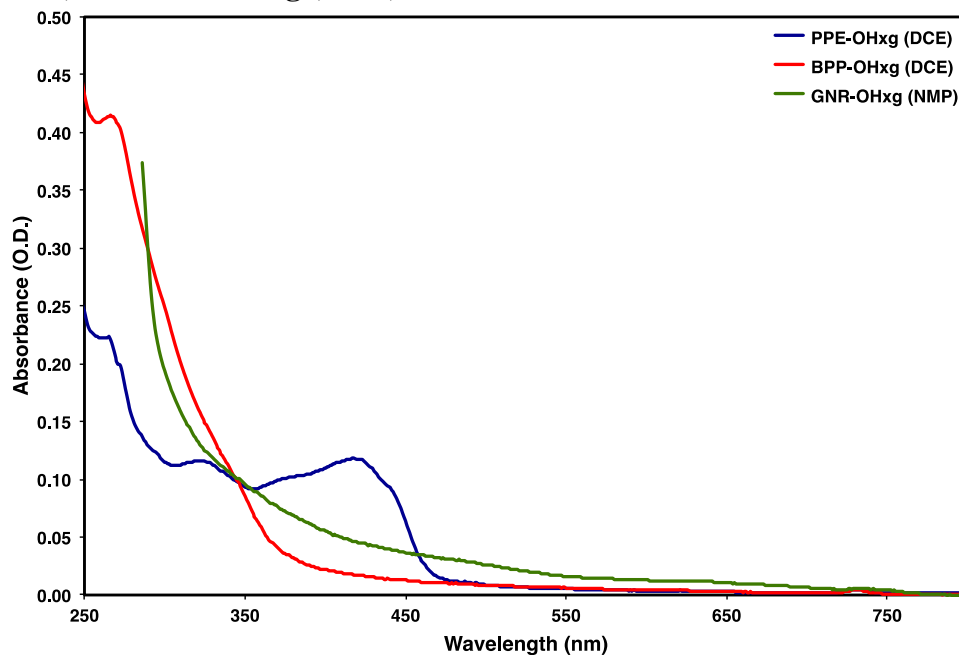


**Figure A4.13.** UV-vis photoemission spectra of **PPE-OHxg**, **BPP-OHxg** (1,2-dichloroethane) and **GNR-OHxg** (NMP). Spectra recorded with a  $\lambda_{\text{ex}} = 350$  nm at an optical density  $A = 0.10$ .

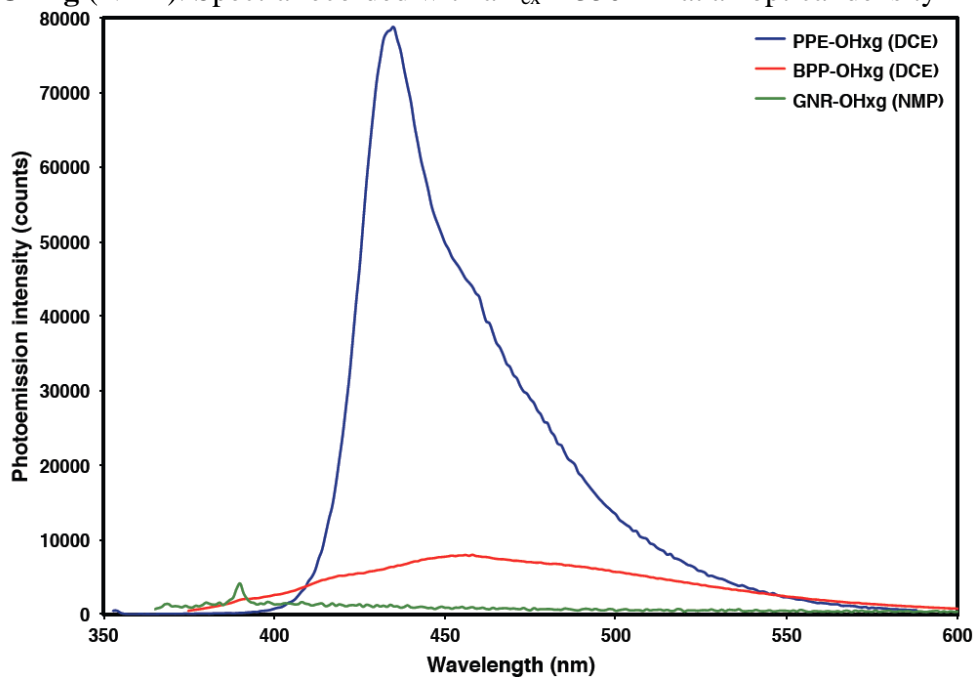




**Figure A4.14.** UV-vis-NIR photoabsorption spectrum of **GNR-C<sub>9</sub>H<sub>19</sub>** (black trace) in CS<sub>2</sub>.

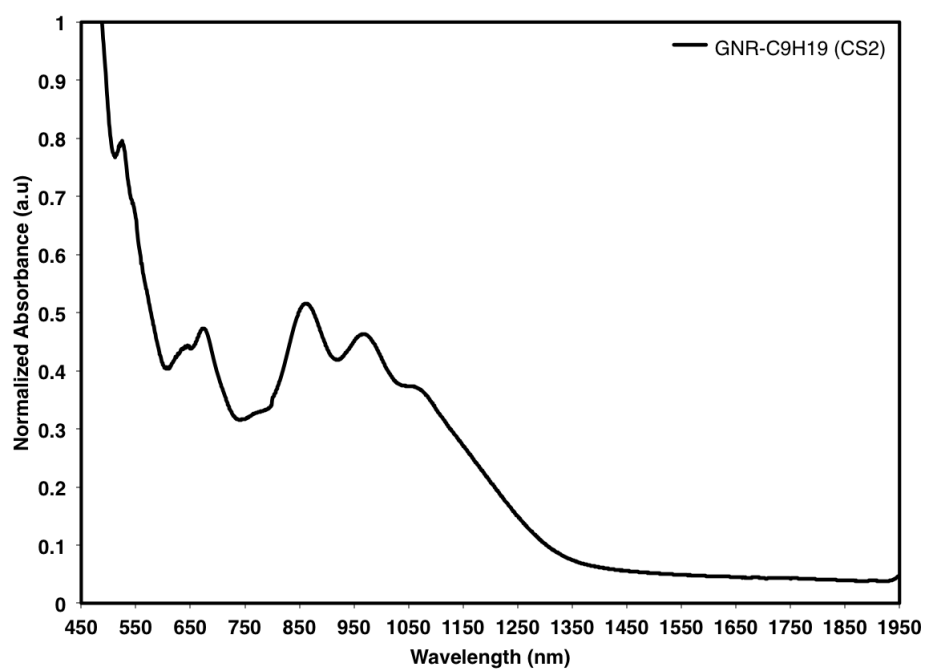


**Figure A4.15.** UV-vis photoemission spectrum of **GNR-C<sub>9</sub>H<sub>19</sub>** (black trace) in 1,2-dichlorobenzene (oDCB). Spectrum recorded with a  $\lambda_{\text{ex}} = 400$  nm.

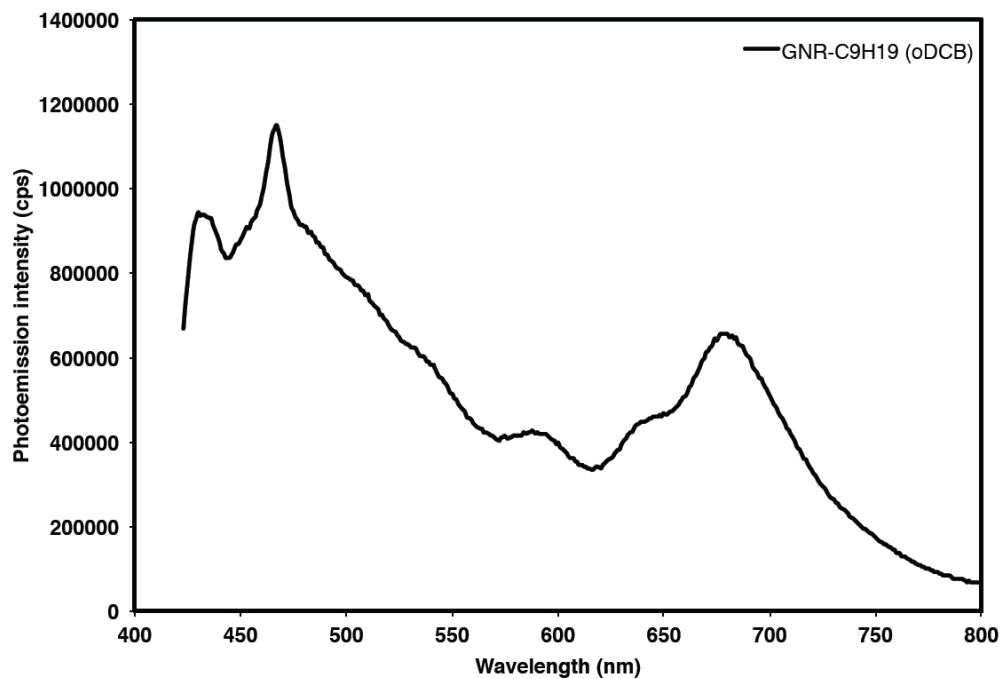


**Figure A4.16.** UV-Visible photoabsorption spectra of **7** (purple trace) and **8** (orange trace) in CHCl<sub>3</sub>.

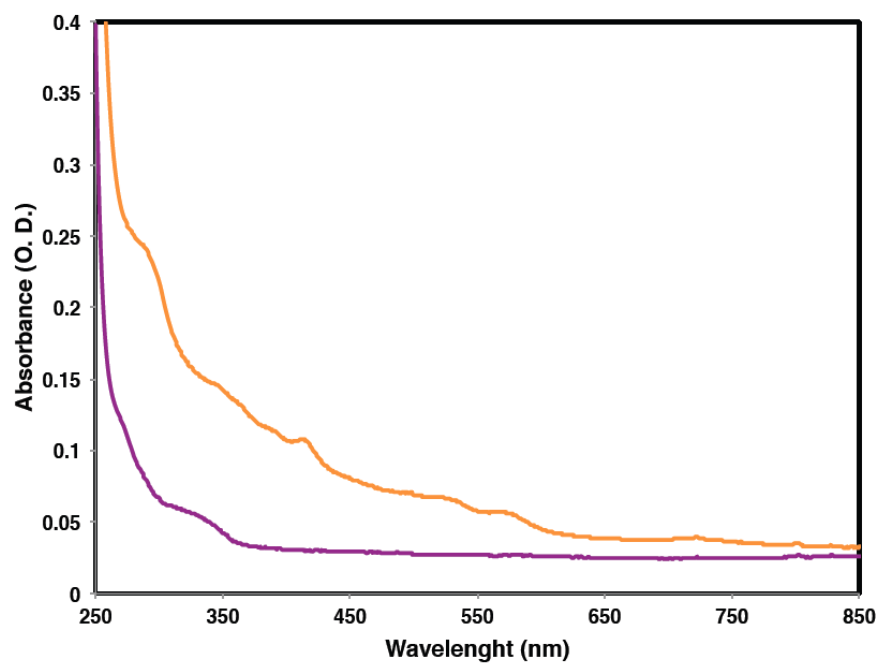


**Figure A4.17.** Photoemission spectra of **7** (purple trace) and **8** (orange trace) in  $\text{CHCl}_3$ . Spectra recorded with a  $\lambda_{\text{ex}} = 285$  nm and 400 nm, respectively, at an optical density  $A = 0.10$ .

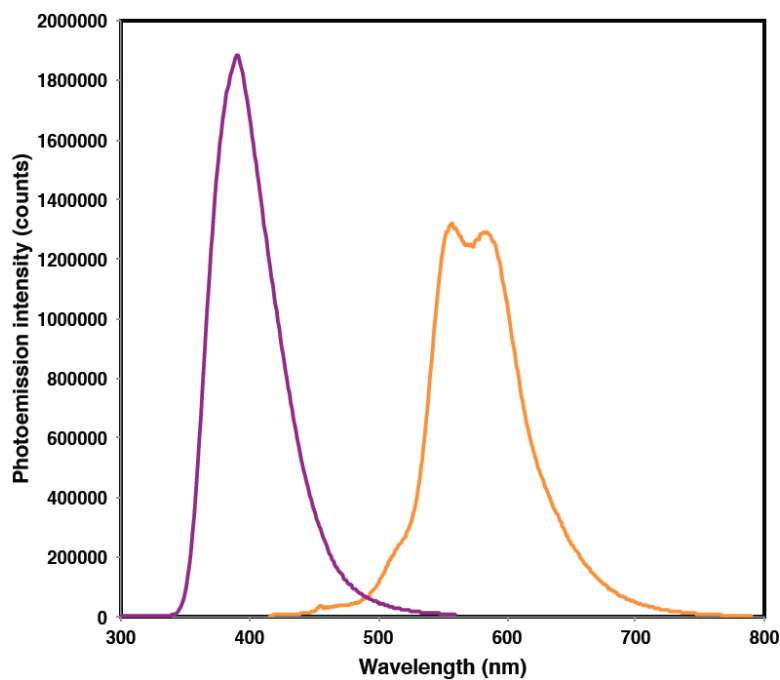


**Figure A4.18.** Near-IR photoabsorption spectrum of **GNR-OHxg** in DMF. Spectra recorded at a concentration of *ca.*  $0.5 \text{ mg mL}^{-1}$ .

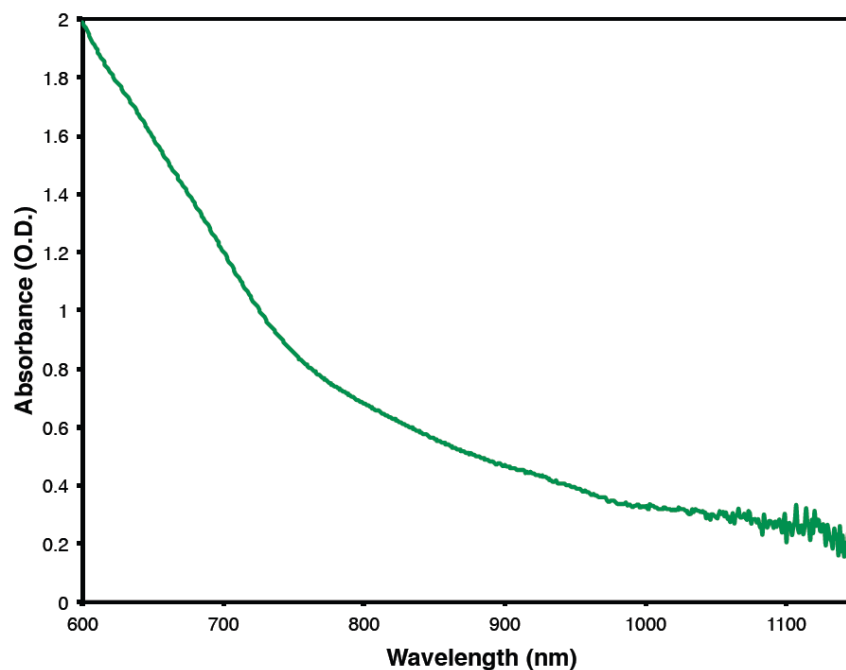


**Figure A4.19.** NIR photoemission spectra of **GNR-OHxg** in DMF vs. photon wavelength. Spectra recorded with a  $\lambda_{\text{ex}} = 450$  nm and a concentration of *ca.*  $0.5 \text{ mg mL}^{-1}$ .

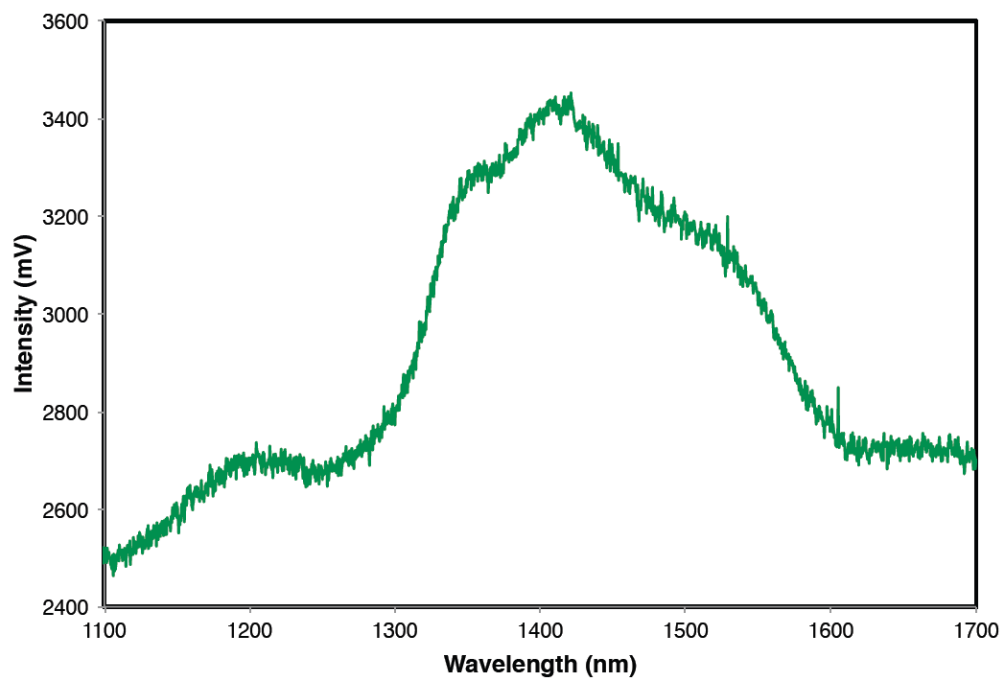


**Figure A4.20.** NIR photoemission spectra of **GNR-OHxg** in DMF vs. photon energy. Spectra recorded with a  $\lambda_{\text{ex}} = 450$  nm and a concentration of *ca.*  $0.5 \text{ mg mL}^{-1}$ .

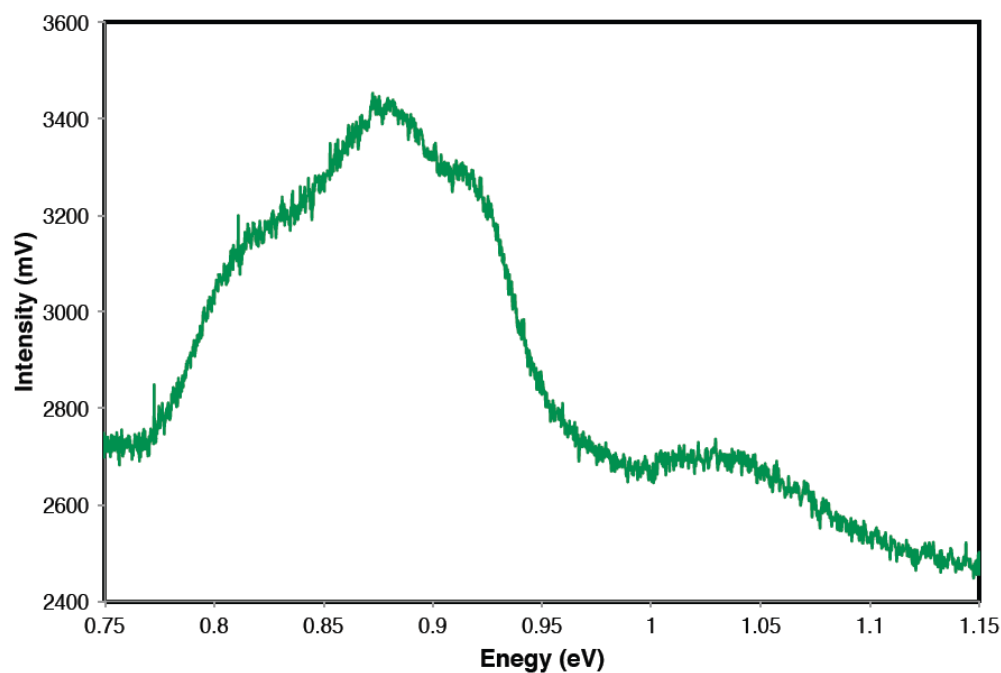


**Figure A4.21.** NIR photoemission spectrum of **GNR-C<sub>9</sub>H<sub>19</sub>** in CS<sub>2</sub> vs. photon wavelength. Spectra recorded with a  $\lambda_{\text{ex}} = 823$  nm.

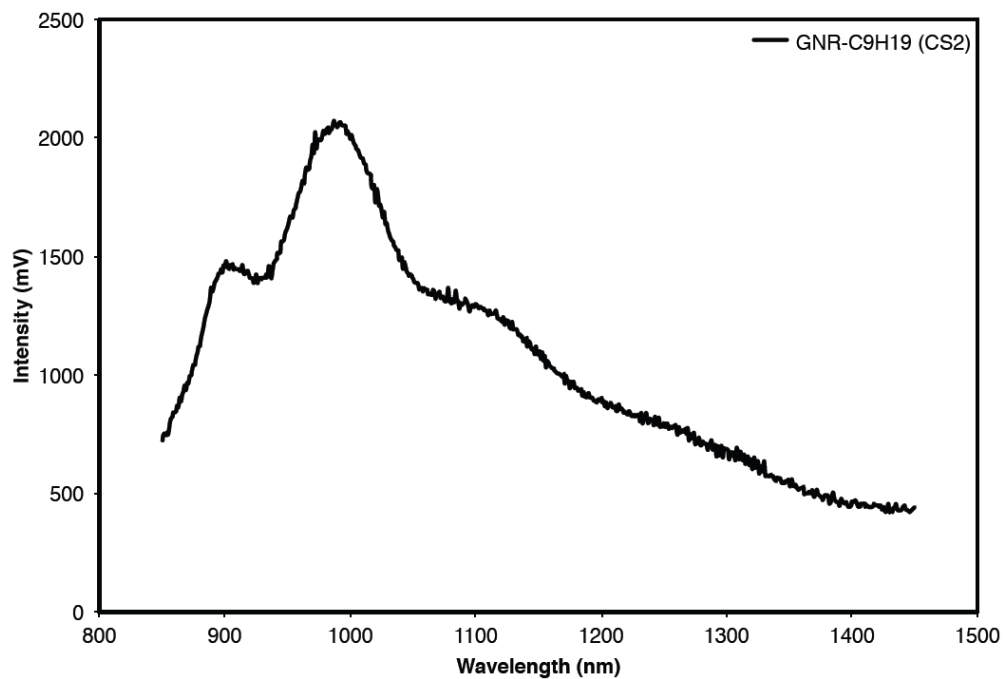
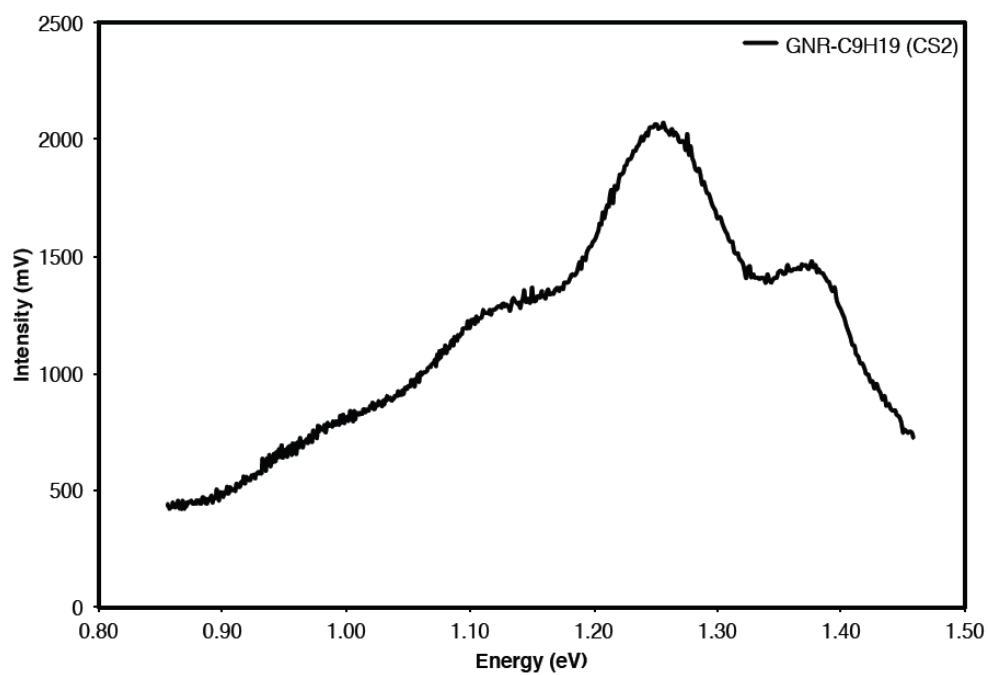


**Figure A4.22.** NIR photoemission spectrum of **GNR-C<sub>9</sub>H<sub>19</sub>** in CS<sub>2</sub> vs. photon energy. Spectra recorded with a  $\lambda_{\text{ex}} = 823$  nm.



### Fluorescence quantum yield determination.

**Figure A4.23.** Integrated total emission intensity vs. optical density plot of anthracene in cyclohexane (yellow), **PPE-OHxg** (blue) and **BPP-OHxg** (red) in 1,2-dichloroethane, **GNR-OHxg** (green) in NMP, **7** (purple) **8** (orange) in  $\text{CHCl}_3$ .

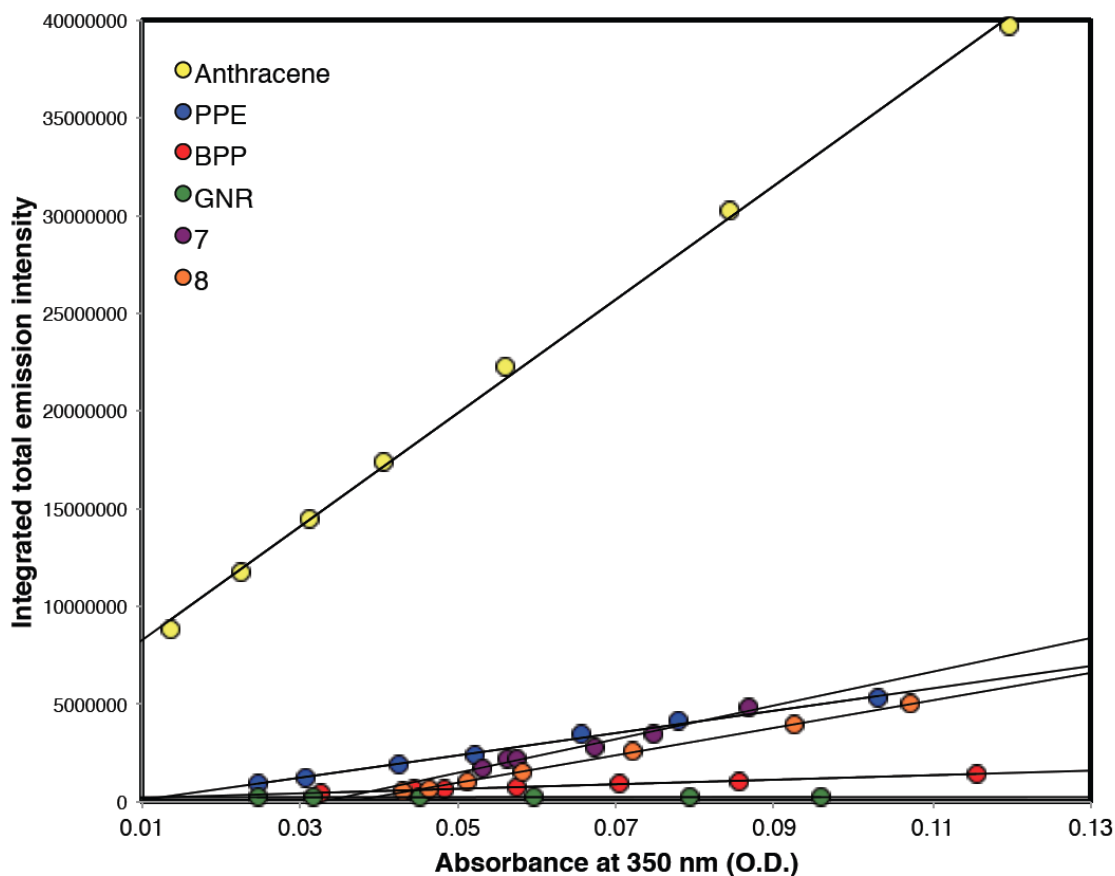


**Table A4.3.** Slope and correlation coefficient of the linear fit and quantum yields for the synthesized compounds.

Sample	Solvent	Slope	$R^2$	$n^2$	$\phi_F$
Anthracene	$\text{C}_6\text{H}_{12}$	291031937	0.9985	2.0815	$36\% \pm 0.4\%$
<b>PPE-OHxg</b>	DCE	57150430	0.9951	2.0799	7.1%
<b>BPP-OHxg</b>	DCE	11624691	0.9990	2.0799	1.4%

<b>GNR-OH<sub>x</sub>g</b>	NMP	67903	0.9598	2.1561	< 0.01%
<b>7</b>	CHCl <sub>3</sub>	86173653	0.9839	2.0906	9.2%
<b>8</b>	CHCl <sub>3</sub>	70223032	0.9998	2.0906	7.5%

### E. Vibrational Spectroscopy (FTIR and Raman)

**Figure A4.24.** Raman spectrum of **PPE-OHxg** natural abundance (green) and  $^{13}\text{C}$  enriched at the alkynes (blue). Note the shift from 2200 to 2112  $\text{cm}^{-1}$  of the  $\text{-C}\equiv\text{C-}$  symmetric stretching mode as result of the change in mass.  $\lambda_{\text{ex}} = 785 \text{ nm}$ .

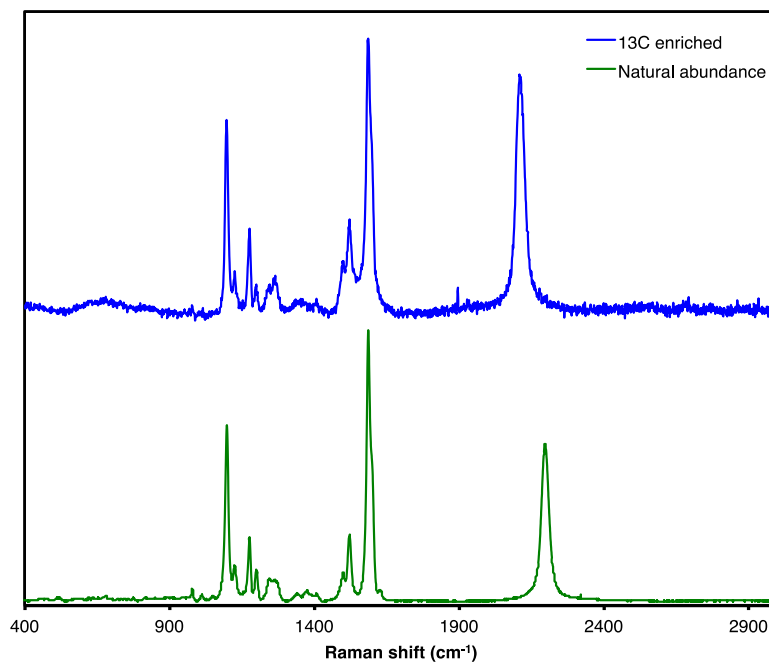


**Figure A4.25.** Featureless Raman spectrum of **BPP-OHxg** natural abundance.  $\lambda_{\text{ex}} = 488 \text{ nm}$ .

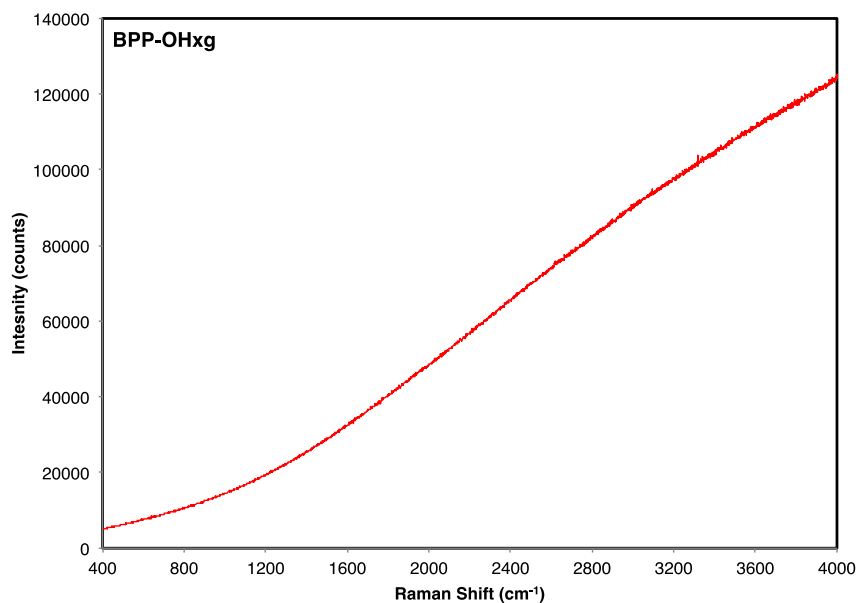




**Figure A4.26.** Raman spectrum of **GNR-OHxg** natural abundance.  $\lambda_{\text{ex}} = 488$  nm.

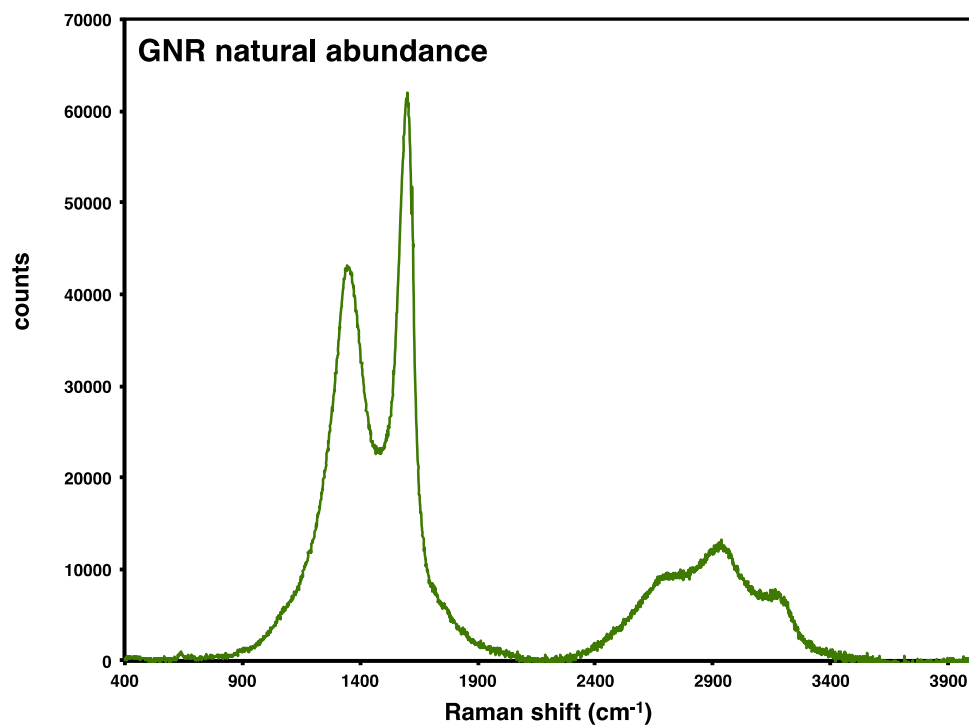


**Figure A4.27.** Raman spectrum of **GNR-OHxg-<sup>13</sup>C(*I*)**.  $\lambda_{\text{ex}} = 488$  nm.

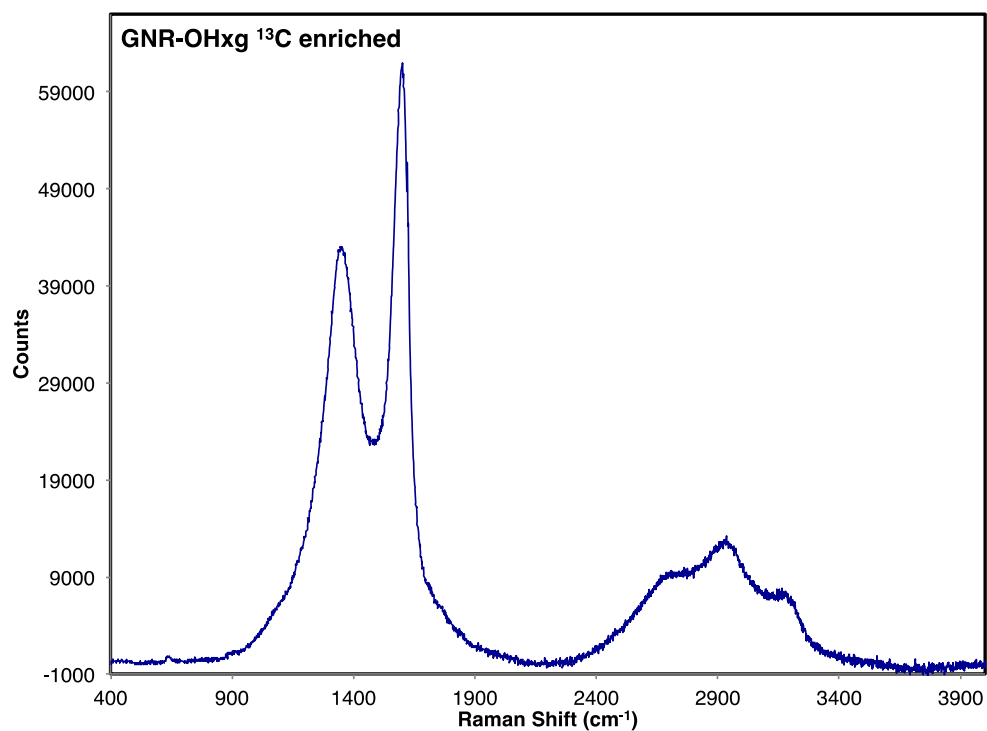


**Figure A4.28.** Raman spectrum of **GNR-OHxg- $^{13}\text{C}(2,3)$** .  $\lambda_{\text{ex}} = 488 \text{ nm}$ .

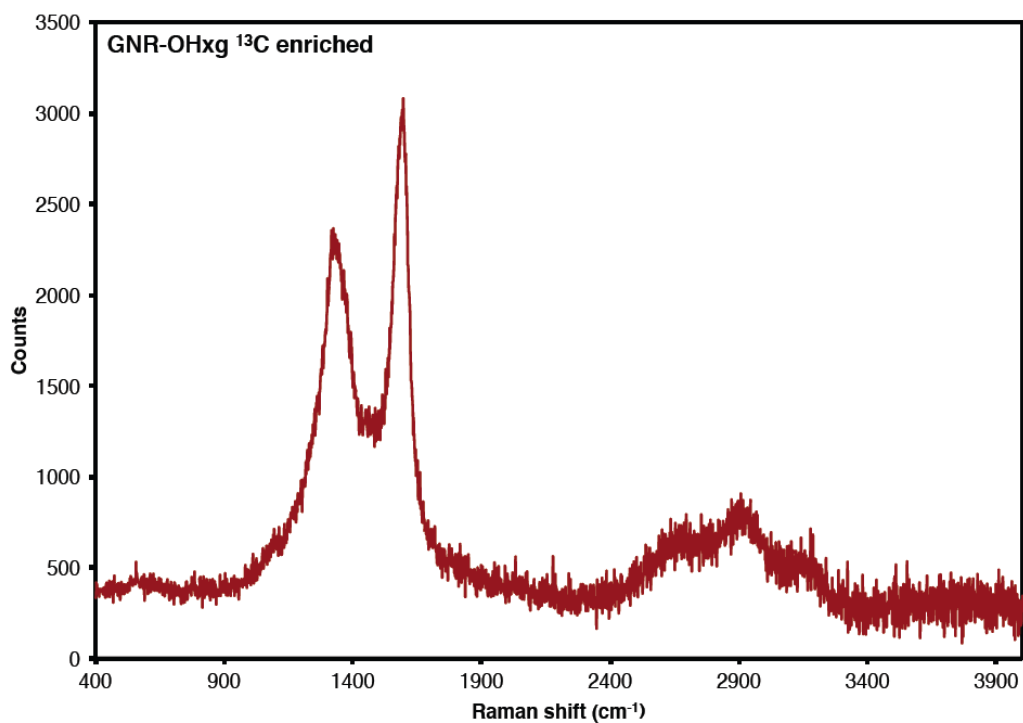


**Figure A4.29.** Raman spectrum of  $\text{CS}_2$  extract of **GNR- $\text{C}_9\text{H}_{19}$** .  $\lambda_{\text{ex}} = 488 \text{ nm}$ . Signals at 520 and 998  $\text{cm}^{-1}$  correspond to Si and  $\text{SiO}_2$  from substrate, respectively.

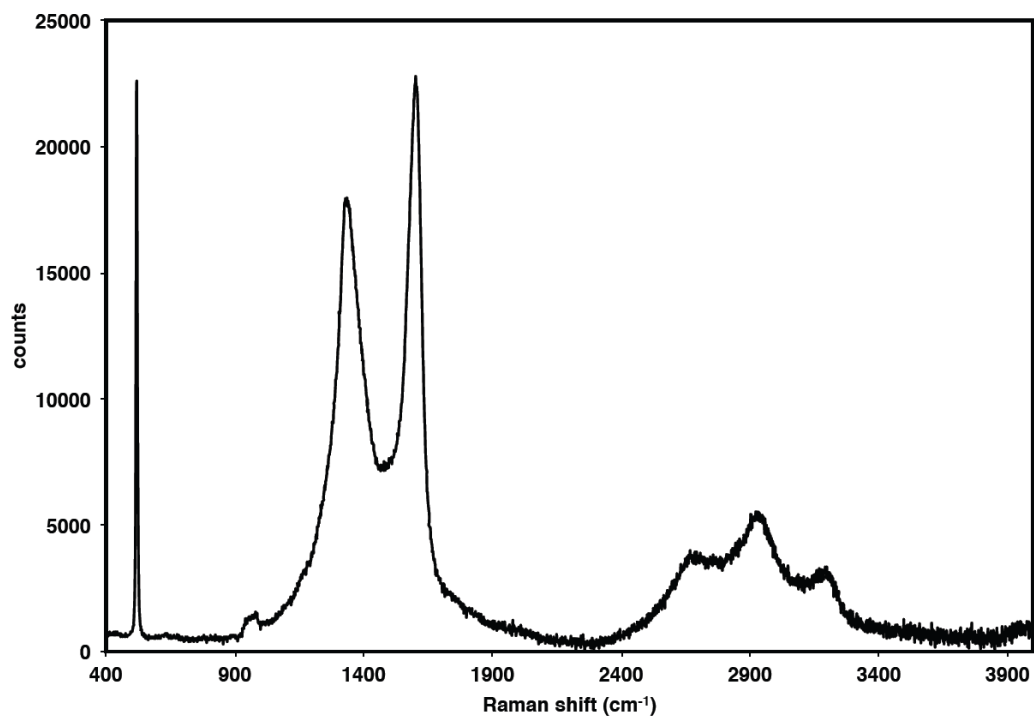


**Figure A4.30.** FTIR spectra of natural abundance **PPE-OH<sub>xg</sub>**, **BPP-OH<sub>xg</sub>** and **GNR-OH<sub>xg</sub>** in transmittance mode (offset by 20% for clarity).

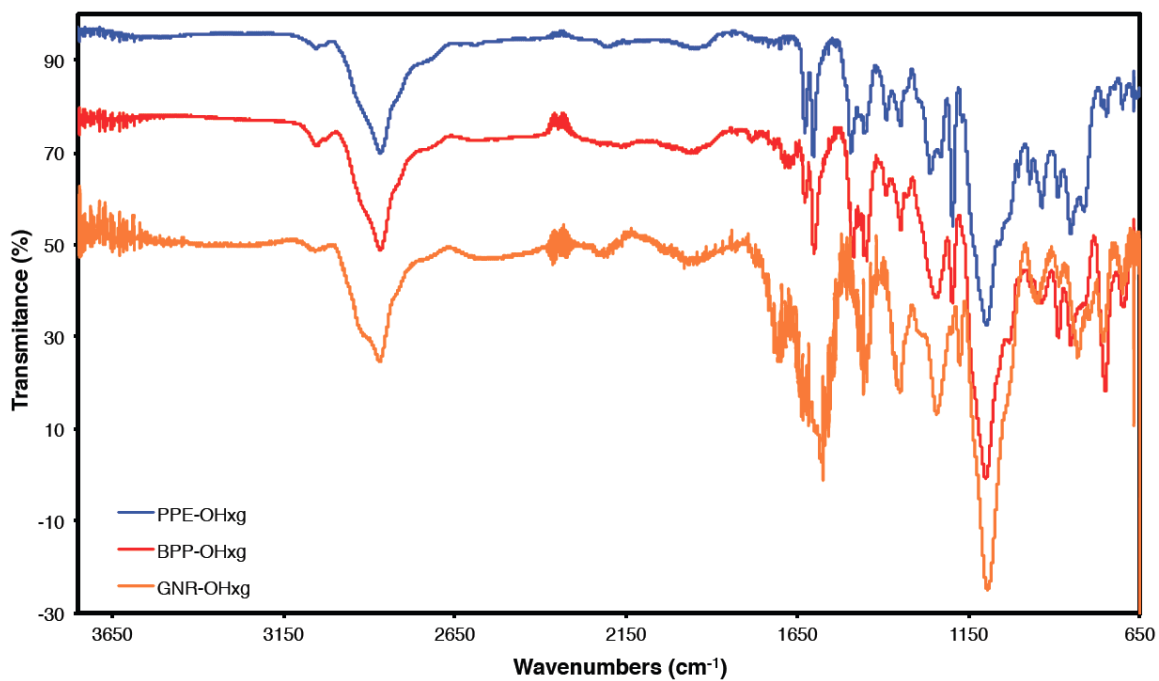
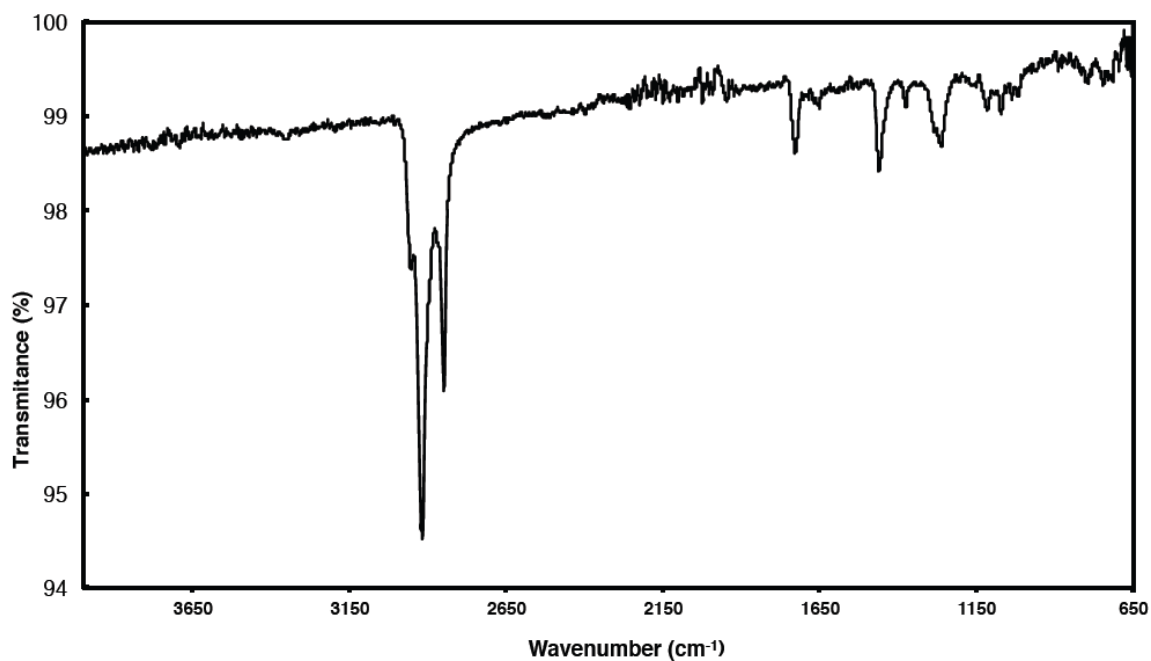


**Figure A4.31.** FTIR spectra of  $\text{CS}_2$  extract of **GNR-C<sub>9</sub>H<sub>19</sub>** in transmittance mode.



## F. X-Ray Photoelectron Spectroscopy

**Figure A4.32.** XPS spectrum of **BPP-OHxg**. Note the sole presence of Si 1s (substrate), Au (substrate), C 1s and O 1s.

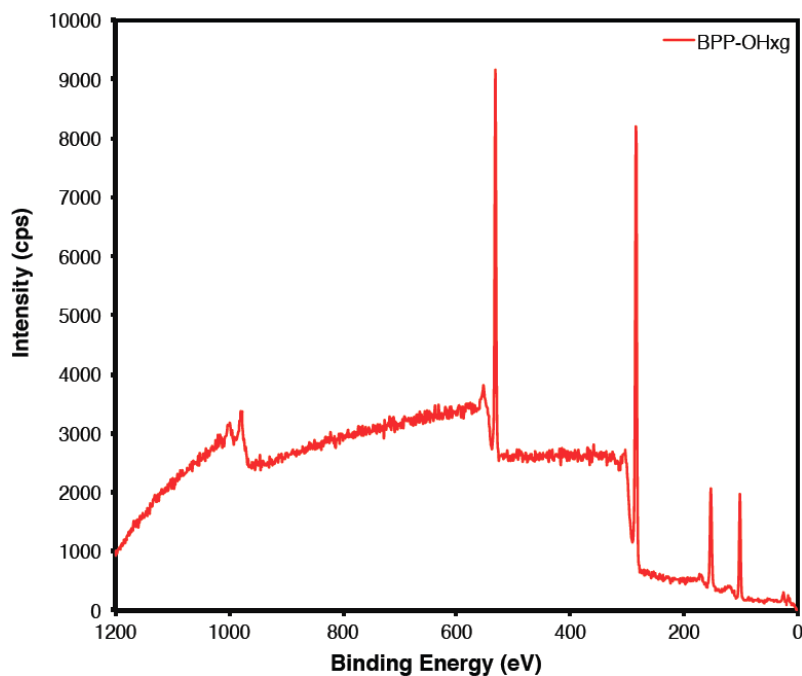


**Figure A4.33.** XPS spectrum of **GNR-OHxg**. Note the sole presence of Si 1s (substrate), Au (substrate), C 1s and O 1s.

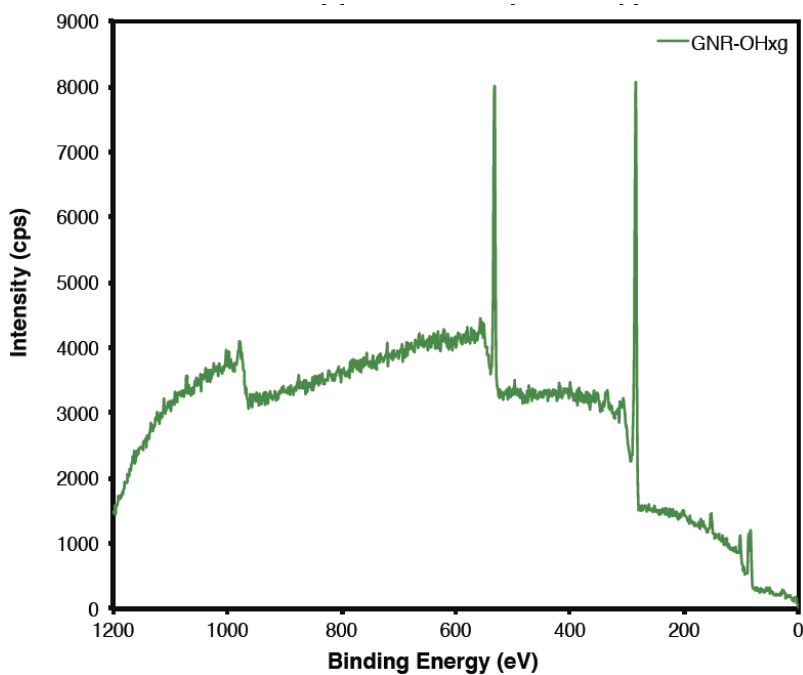


**Figure A4.34.** XPS C 1s spectrum of **BPP-OHxg**.

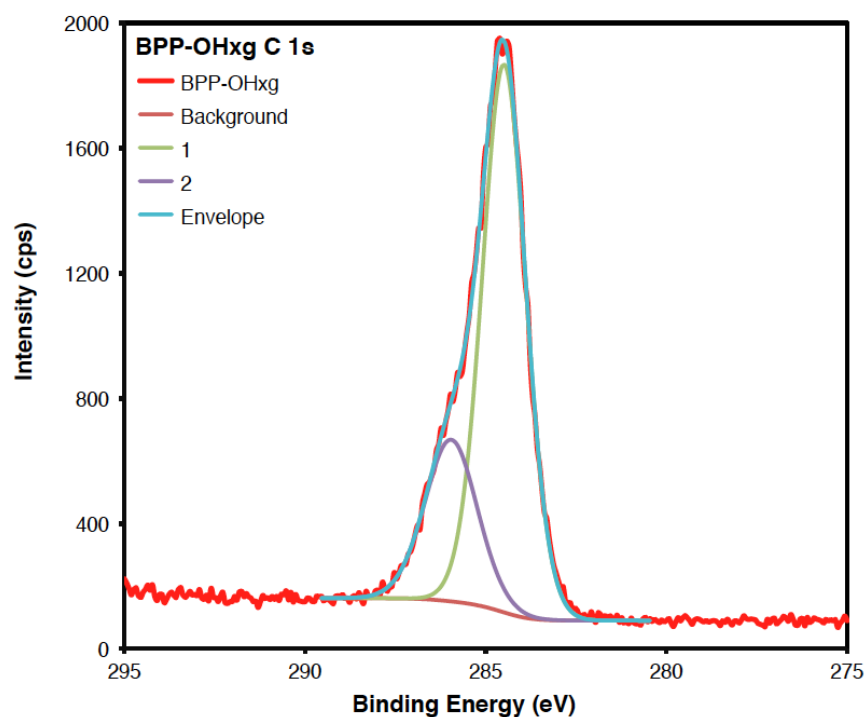


**Figure A4.35.** XPS C 1s spectrum of **GNR-OHxg**.

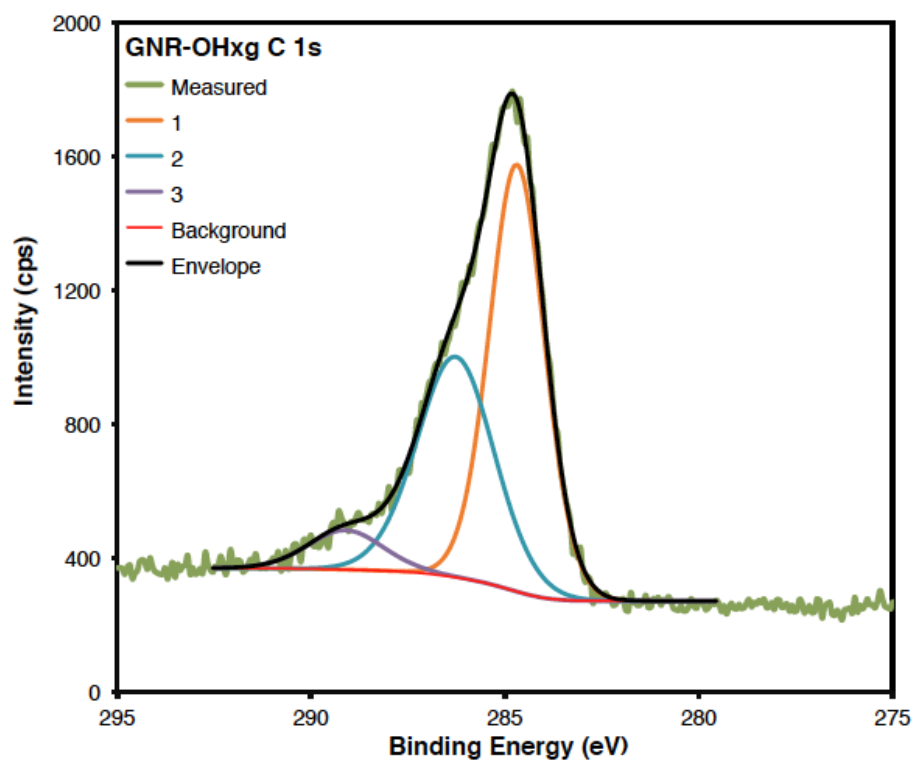


**Figure A4.36.** XPS O 1s spectrum of **BPP-OHxg**.

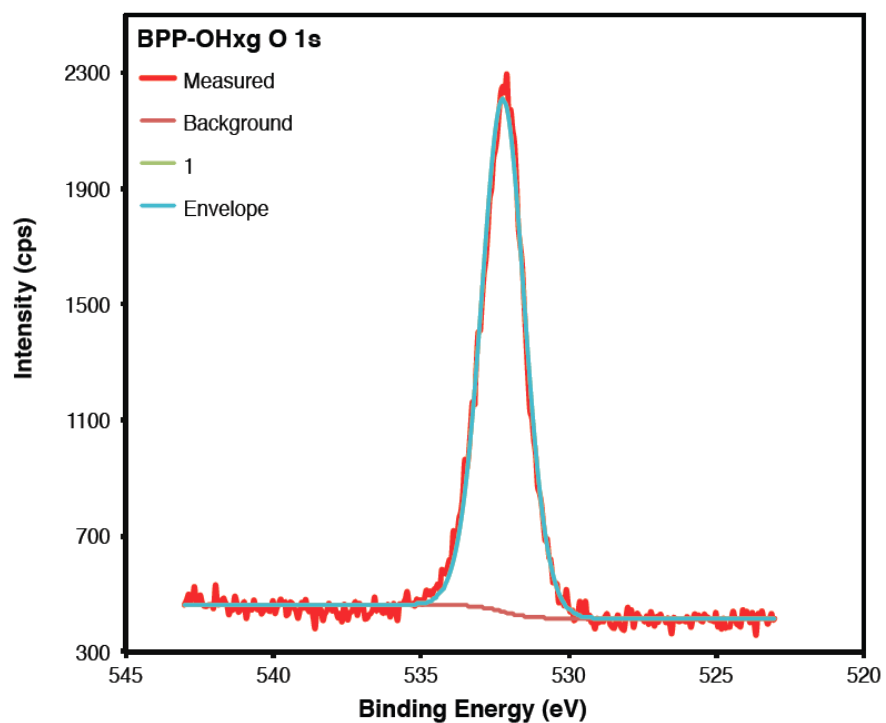


**Figure A4.37.** XPS O 1s spectrum of **GNR-OHxg**.

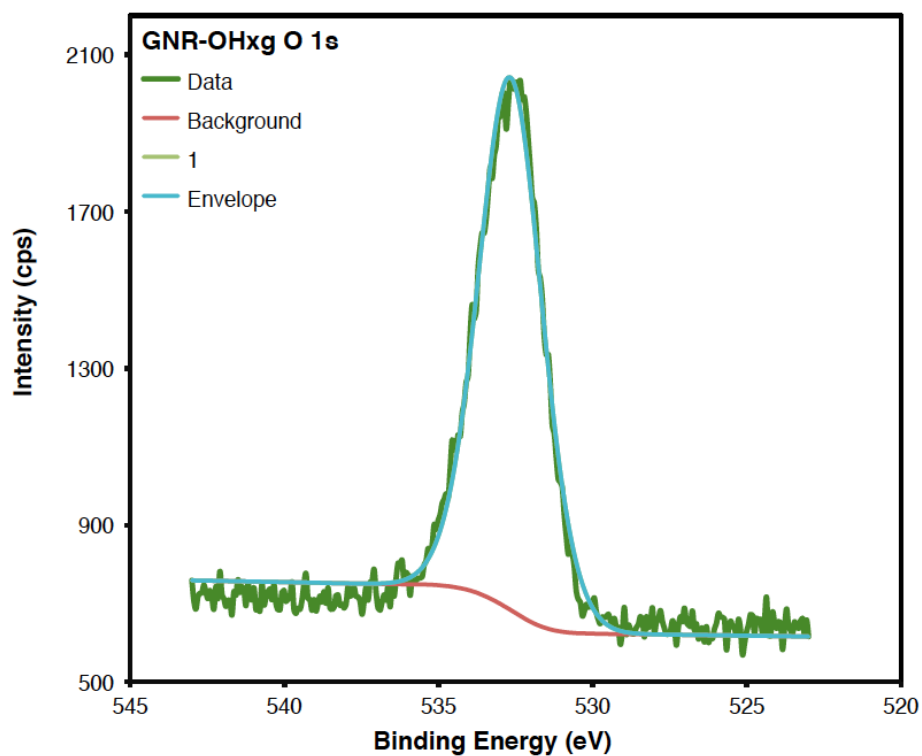


**Figure A4.38.** Refined C 1s XPS overlay spectra of **GNR-OHxg** and **BPP-OHxg**.

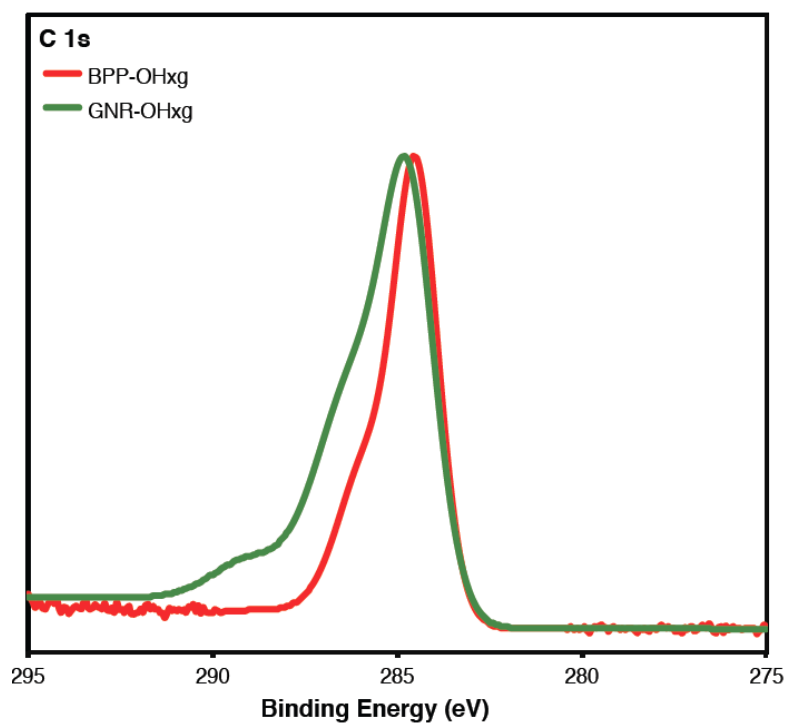
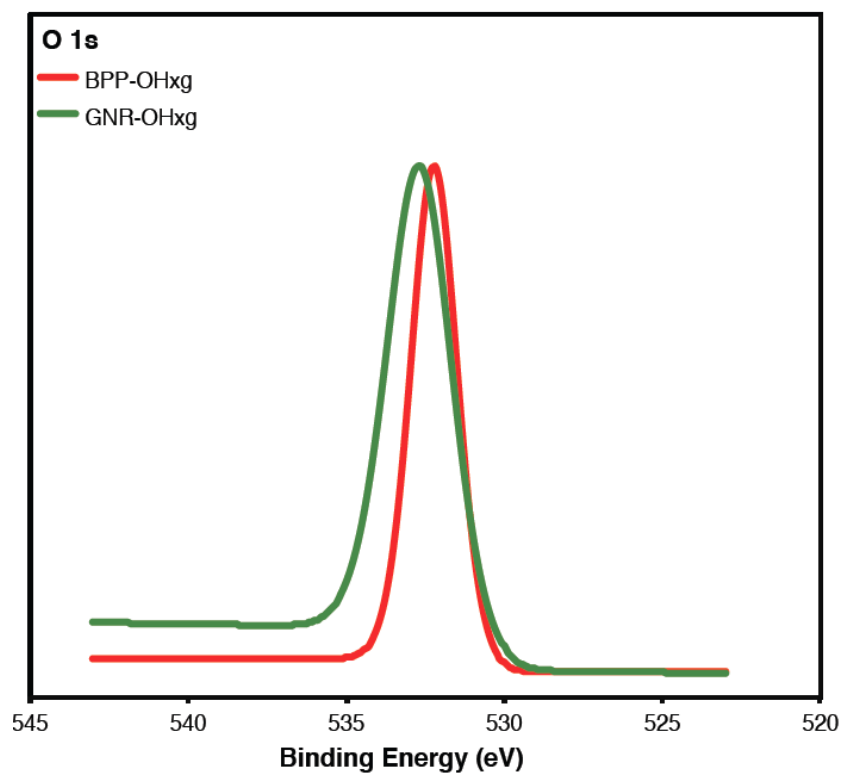


**Figure A4.39.** Refined O 1s XPS overlay spectra of **GNR-OHxg** and **BPP-OHxg**.



## G. Solid-State NMR Spectroscopy

**Figure A4.40.**  $^{13}\text{C}$  CPMAS NMR spectrum of **PPE-OH<sub>x</sub>g** (natural abundance).

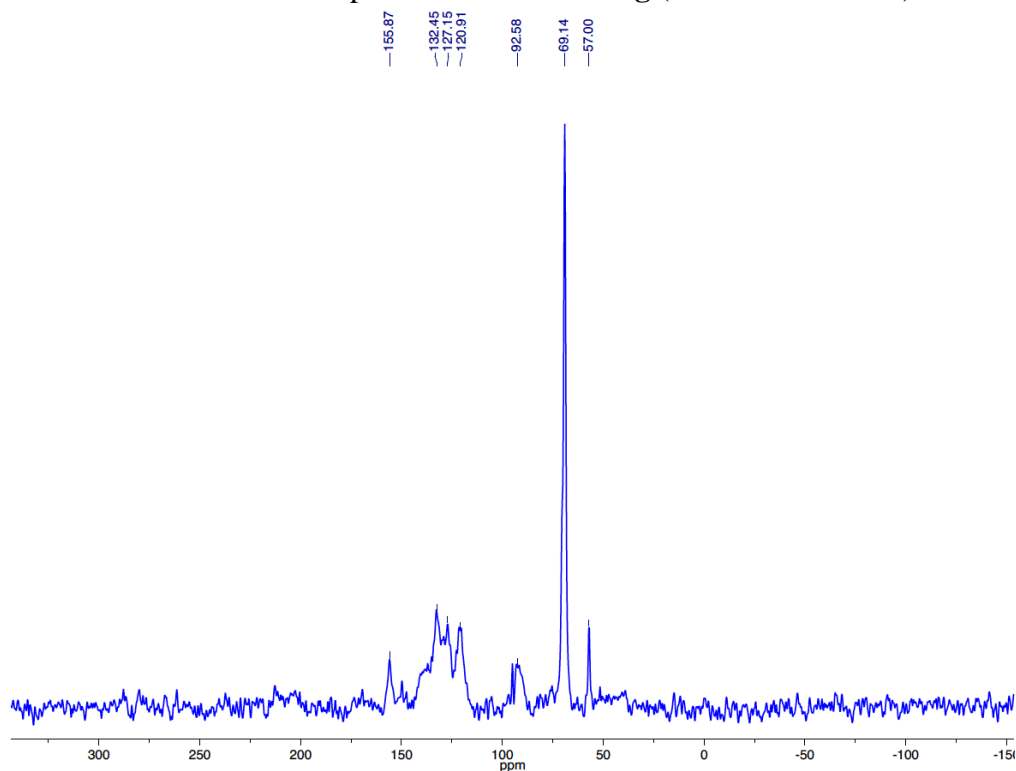


**Figure A4.41.**  $^{13}\text{C}$  CPMAS NMR spectrum of **PPE-OH<sub>x</sub>g- $^{13}\text{C}$** .

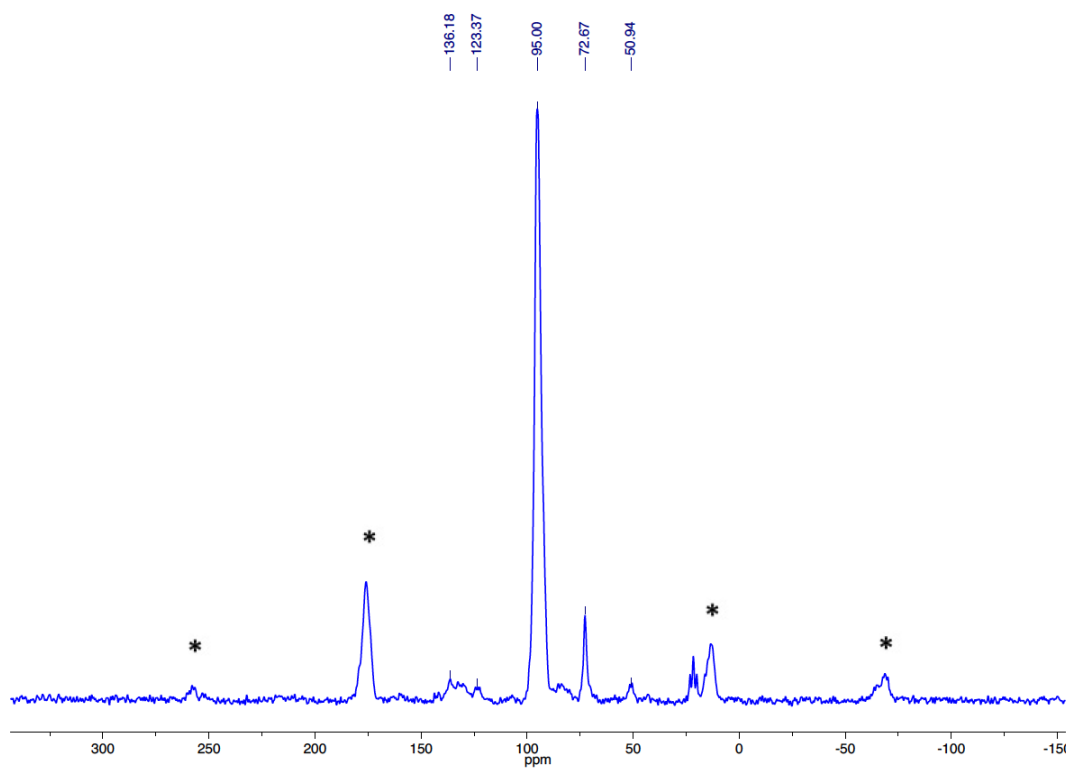




**Figure A4.42.**  $I$  vs.  $t_{CP}$  plot of PPE-OHxg- $^{13}C$ .

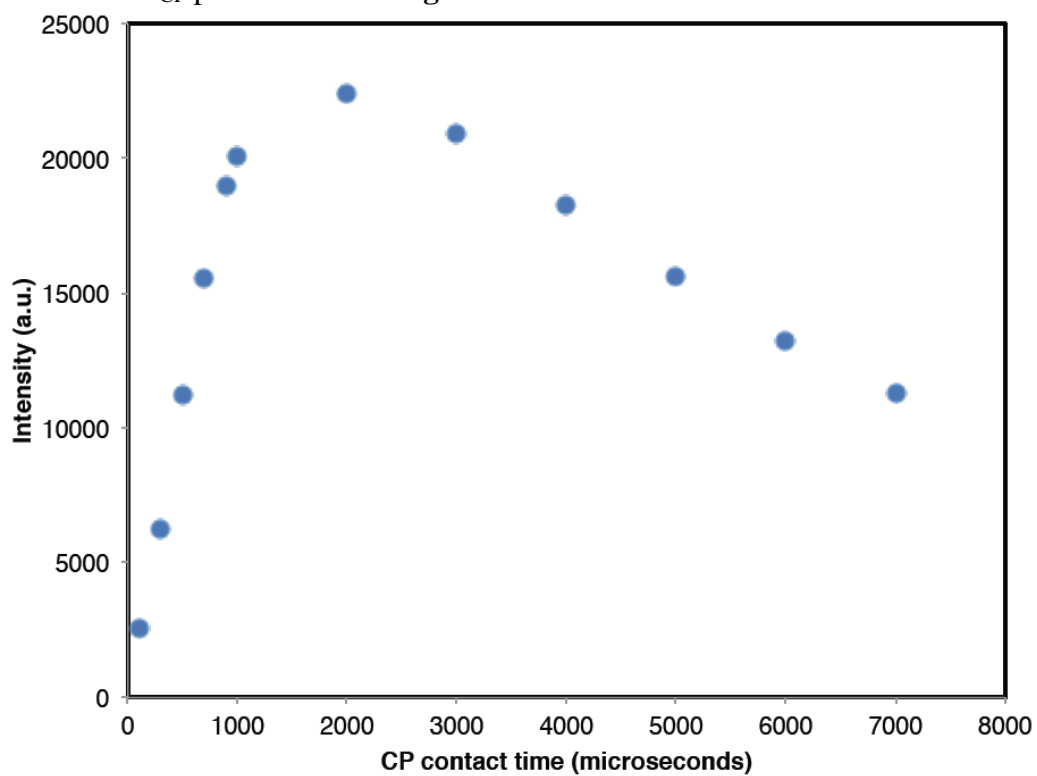


**Figure A4.43.**  $^{13}C$  MAS NMR spectrum of PPE-OHxg- $^{13}C$ .

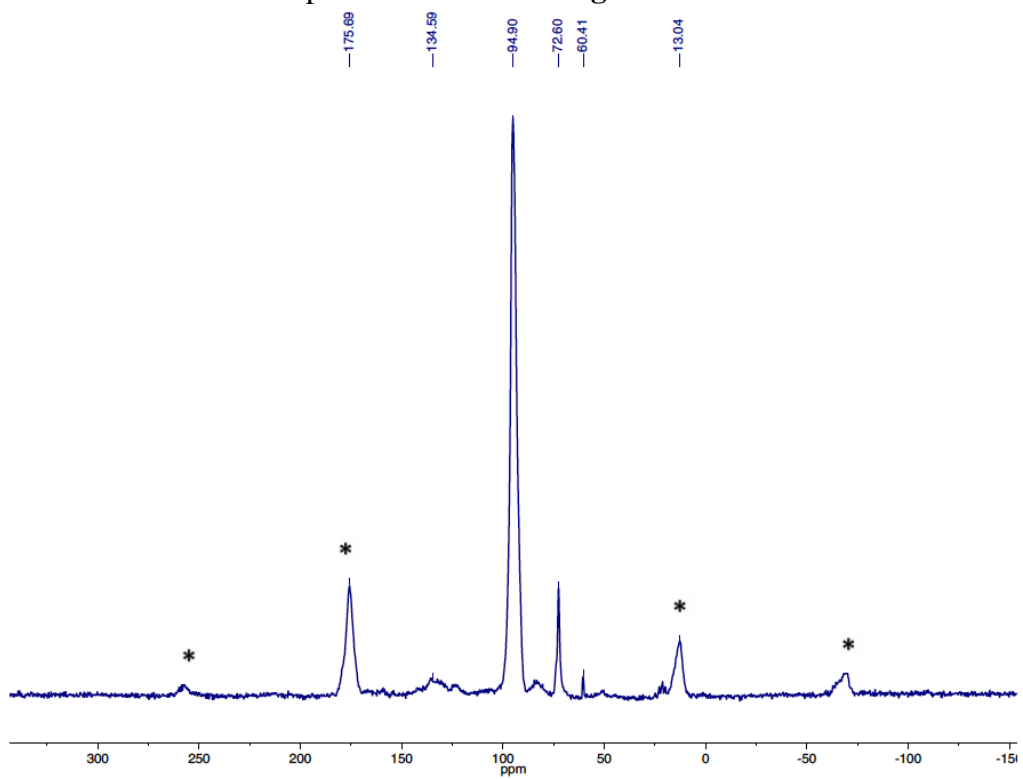


**Figure A4.44.**  $^{13}\text{C}$  CPMAS NMR spectrum of **BPP-OHxg** (natural abundance).

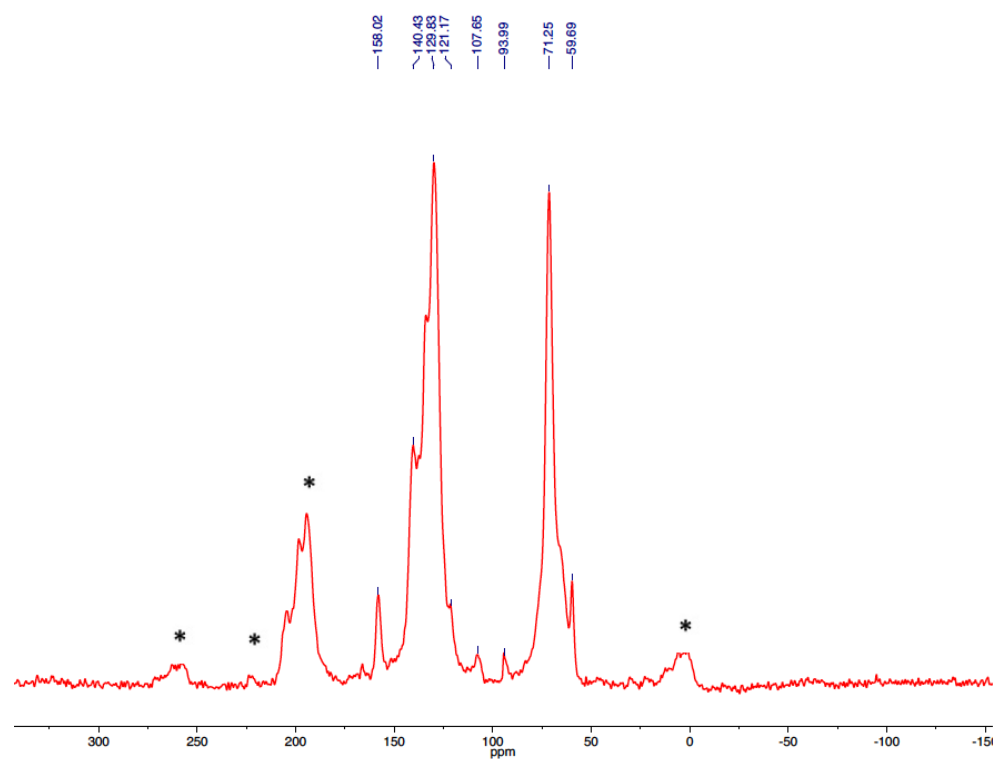


**Figure A4.45.**  $^{13}\text{C}$  CPMAS NMR spectrum of **BPP-OHxg- $^{13}\text{C}(I)$** .

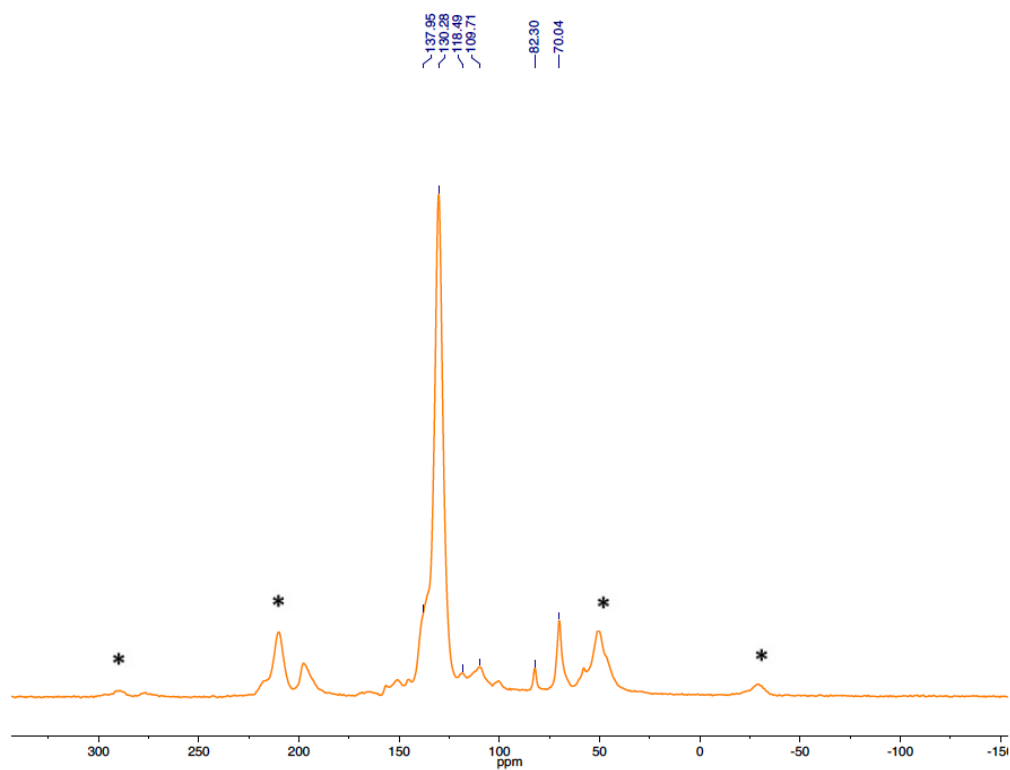


Figure A4.46.  $^{13}\text{C}$  MAS NMR spectrum of **BPP-OHxg- $^{13}\text{C}(I)$** .

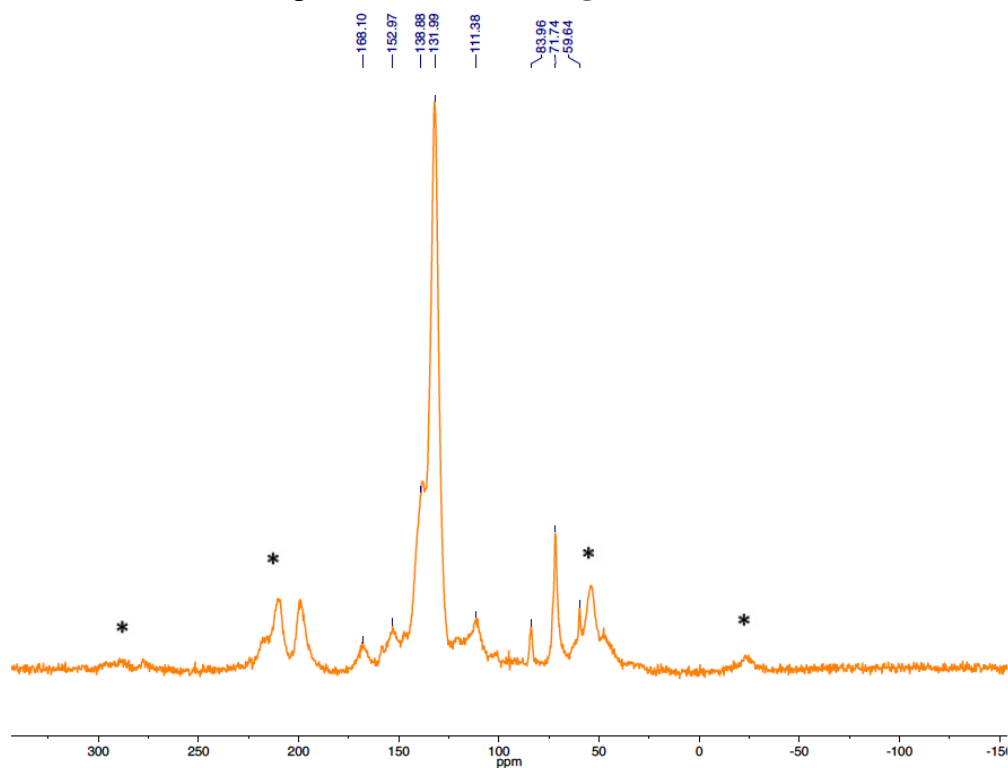
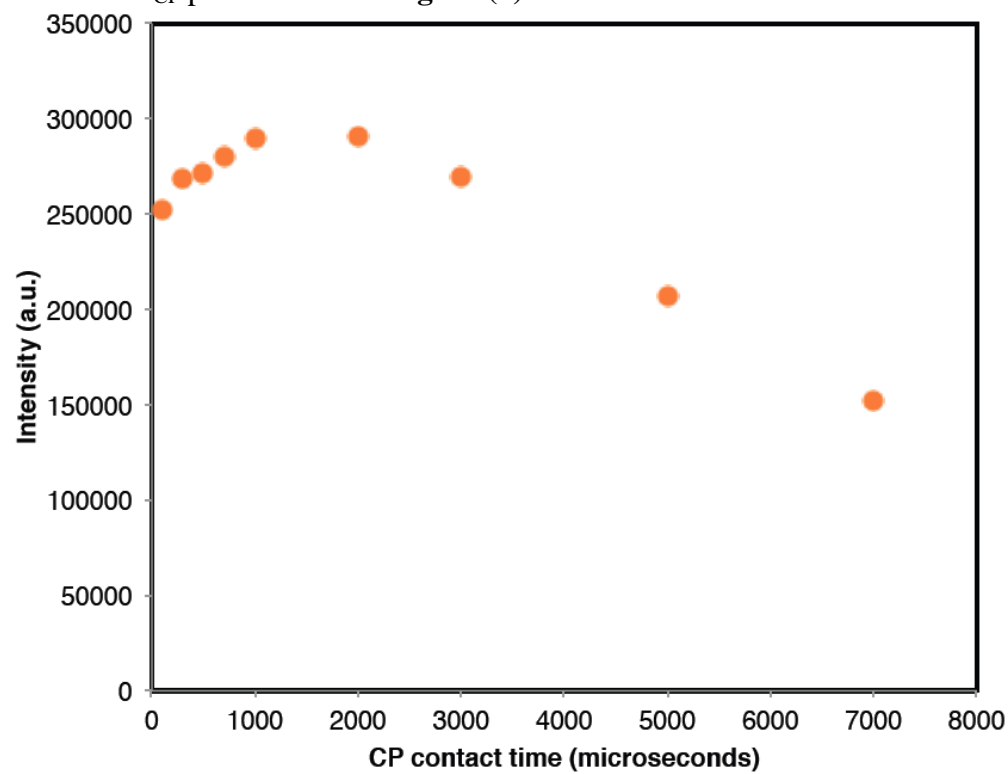
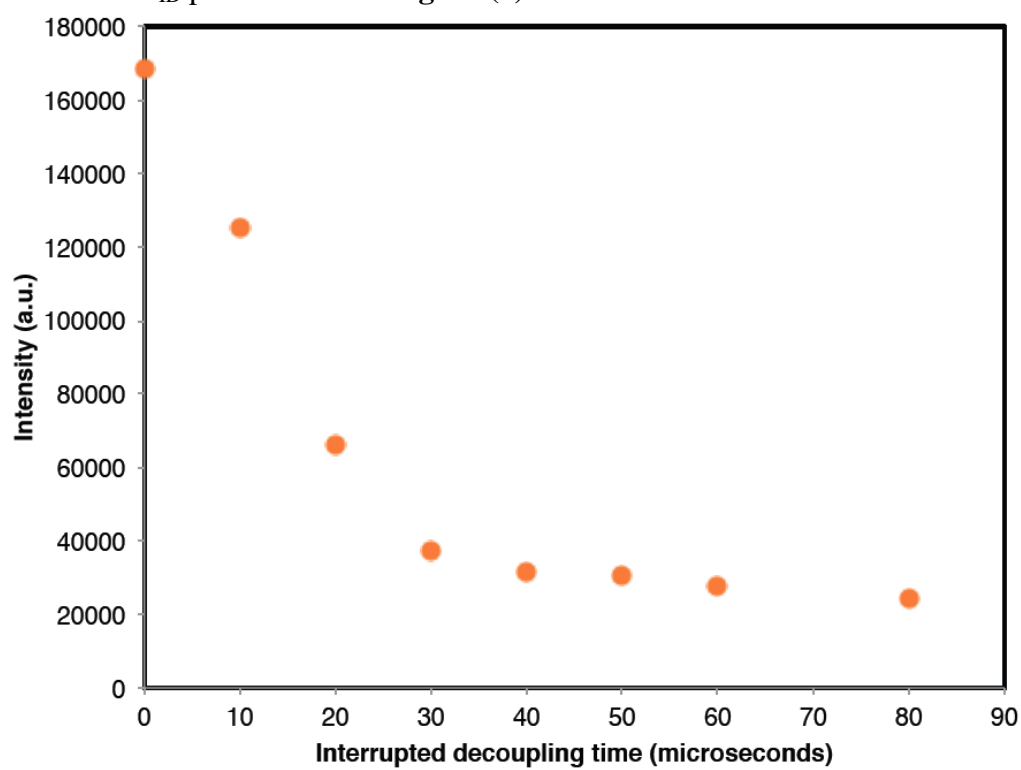


Figure A4.47.  $I$  vs.  $t_{\text{CP}}$  plot of **BPP-OHxg- $^{13}\text{C}(I)$** .



**Figure A4.48.**  $I$  vs.  $t_{ID}$  plot of **BPP-OHxg- $^{13}\text{C}(I)$** .



**Figure A4.49.**  $^{13}\text{C}$  CPMAS NMR spectrum of **BPP-OHxg- $^{13}\text{C}(2,3)$** .

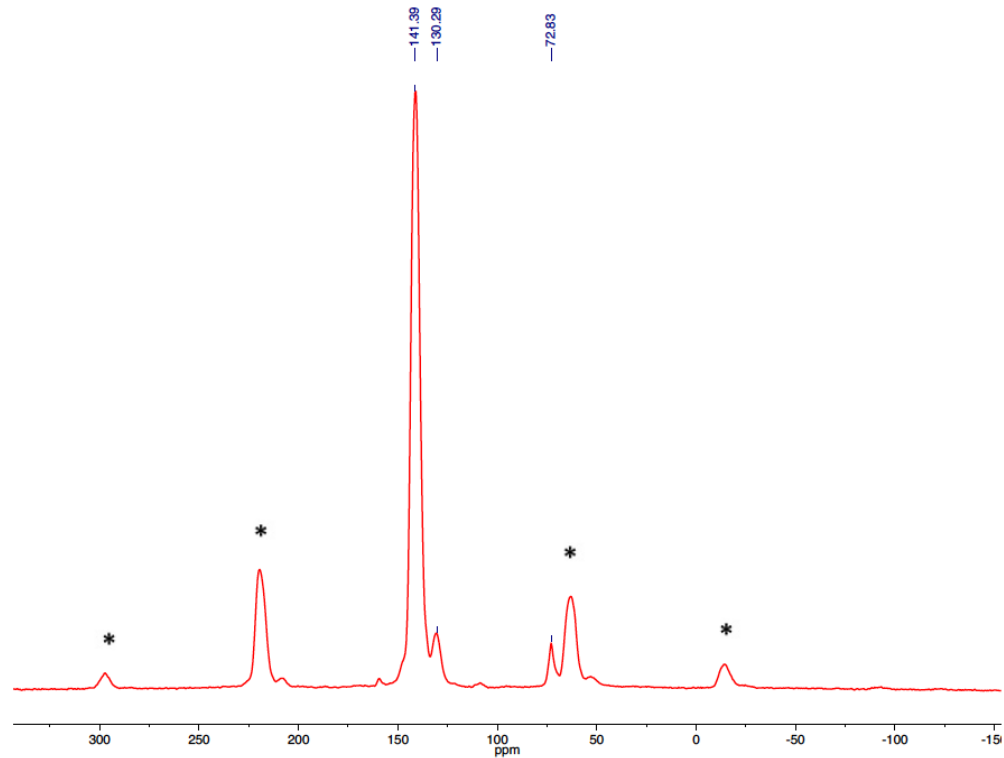


Figure A4.50.  $^{13}\text{C}$  MAS NMR spectrum of **BPP-OHxg**- $^{13}\text{C}(2,3)$ .

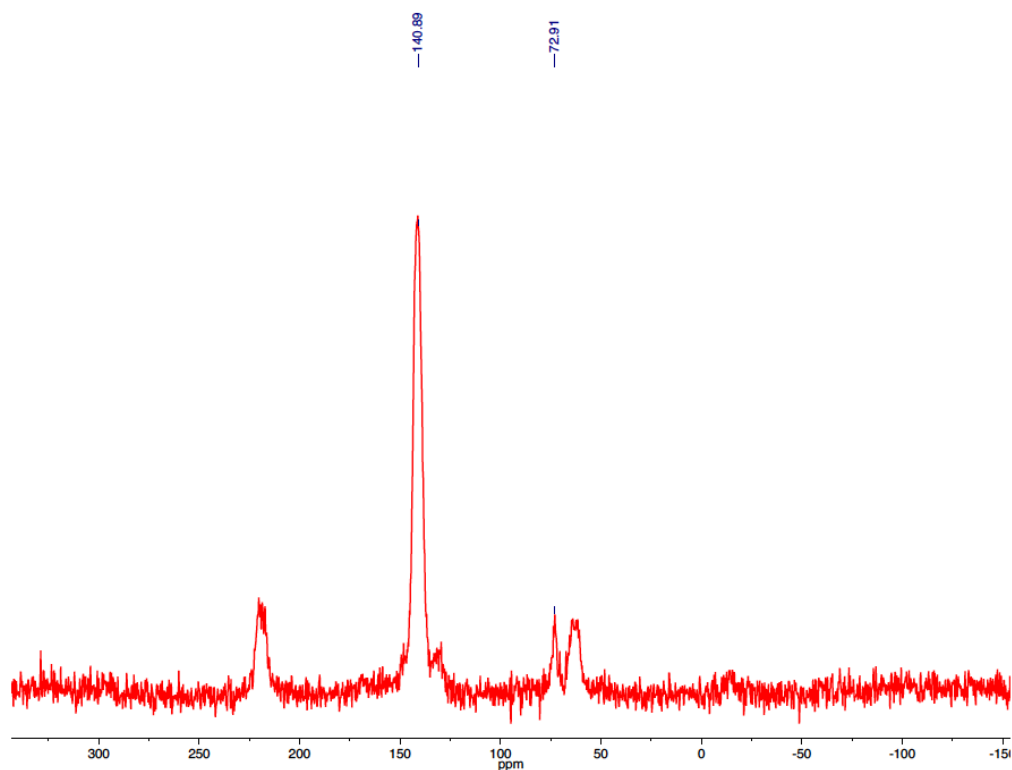
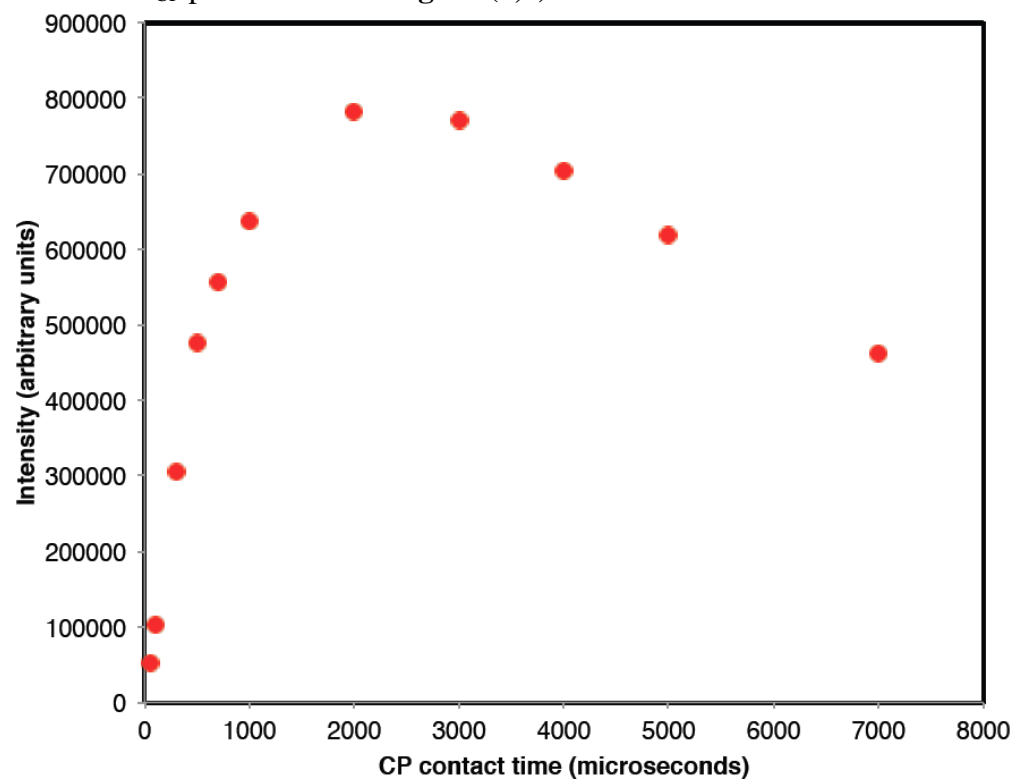
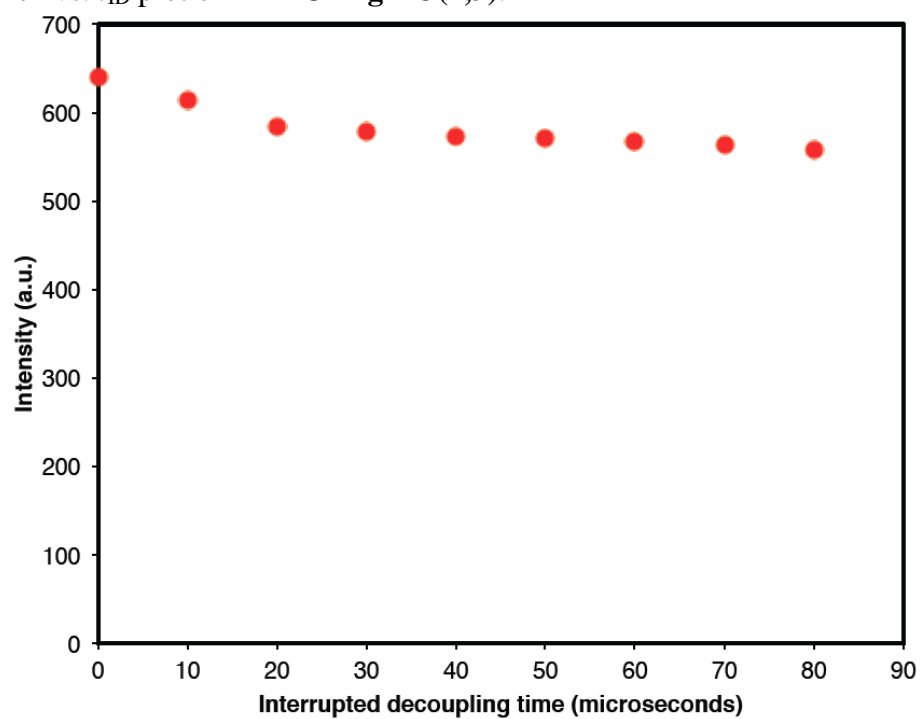


Figure A4.51.  $I$  vs.  $t_{\text{CP}}$  plot of **BPP-OHxg**- $^{13}\text{C}(2,3)$ .



**Figure A4.52.**  $I$  vs.  $t_{ID}$  plot of **BPP-OHxg**- $^{13}\text{C}(2,3)$ .



**Figure A4.53.**  $^{13}\text{C}$  CPMAS NMR spectrum of **GNR-OHxg** (natural abundance).

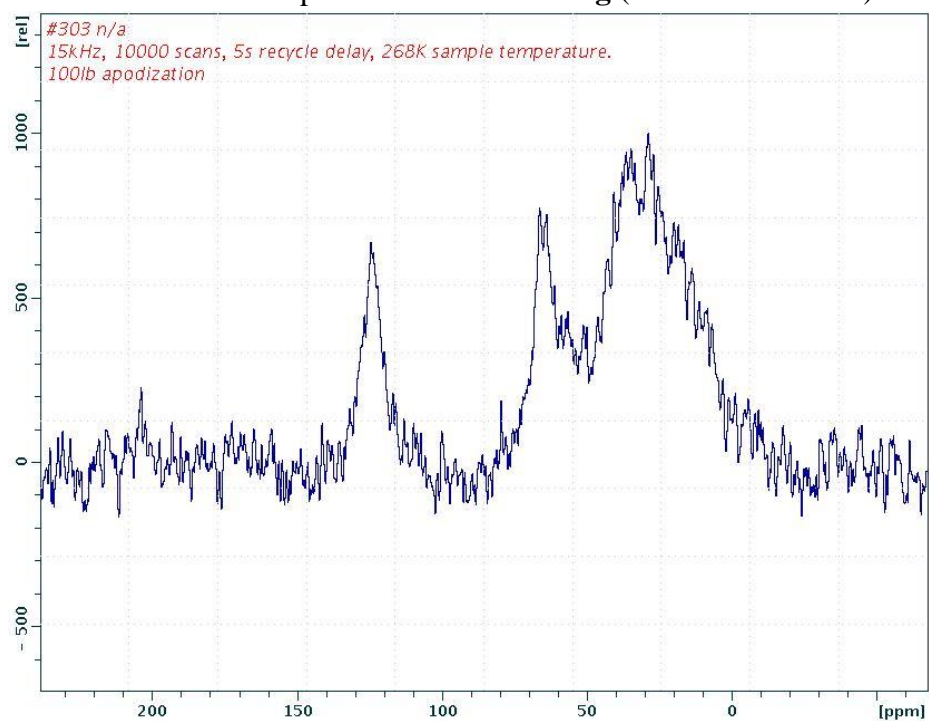


**Figure A4.54.**  $^{13}\text{C}$  CPMAS NMR spectrum of **GNR-OHxg- $^{13}\text{C}(I)$** .

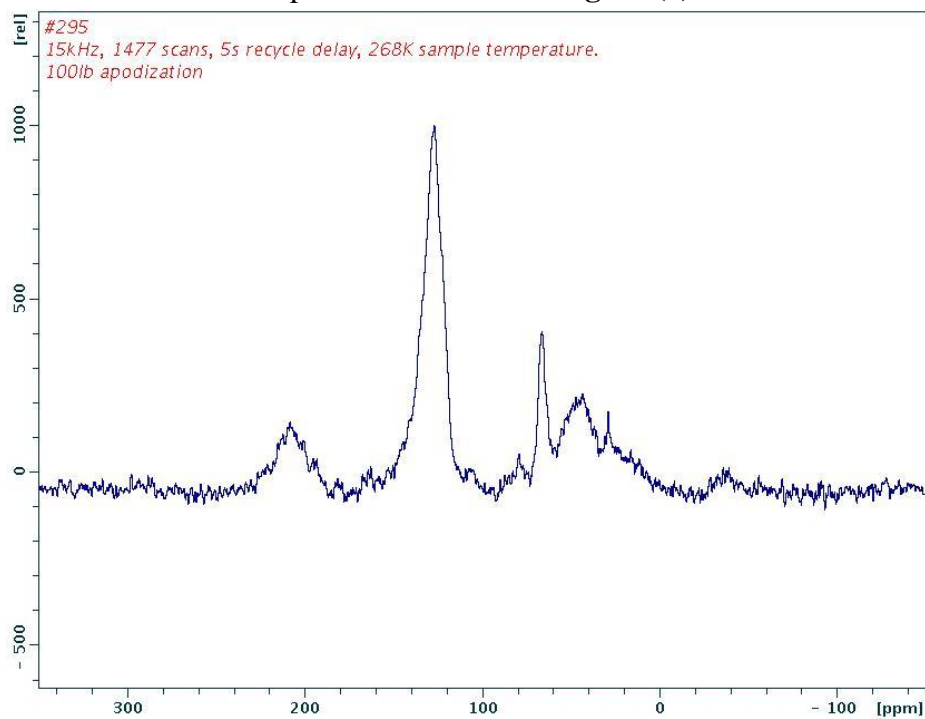


**Figure A4.55.**  $^{13}\text{C}$  MAS NMR spectrum of **GNR-OHxg- $^{13}\text{C}(I)$** .

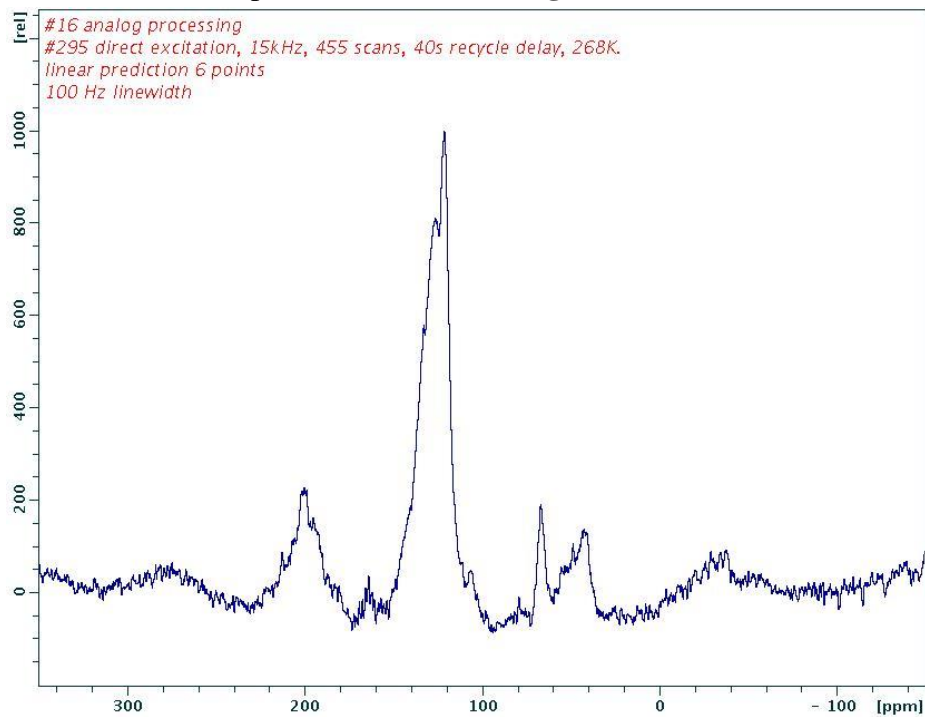


**Figure A4.56.**  $^{13}\text{C}$  CPMAS NMR spectrum of **GNR-OHxg- $^{13}\text{C}(2,3)$** .

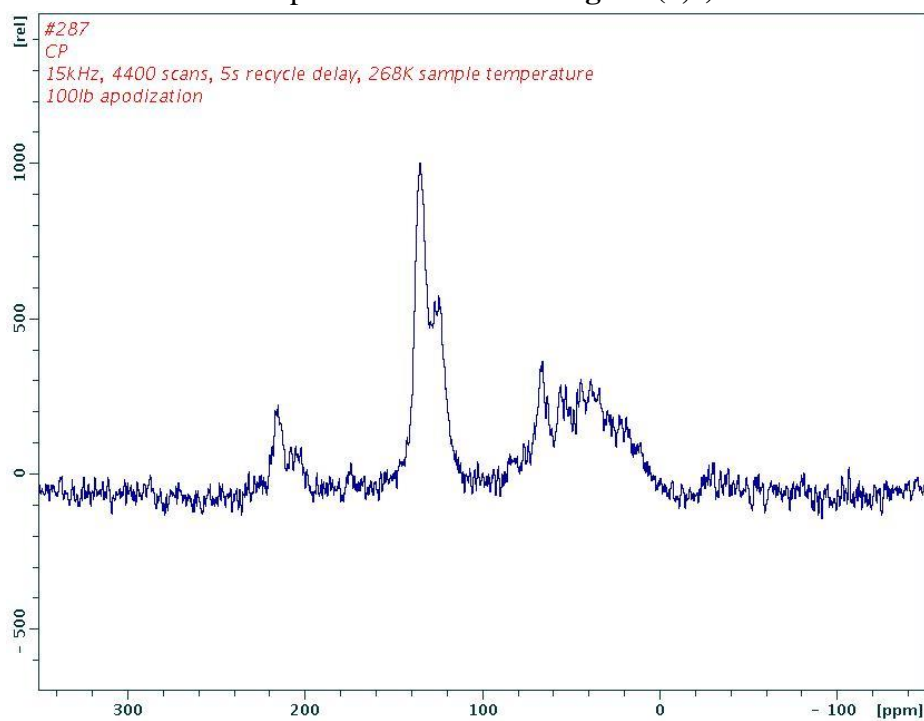


**Figure A4.57.**  $^{13}\text{C}$  MAS NMR spectrum of **GNR-OHxg- $^{13}\text{C}(2,3)$** .

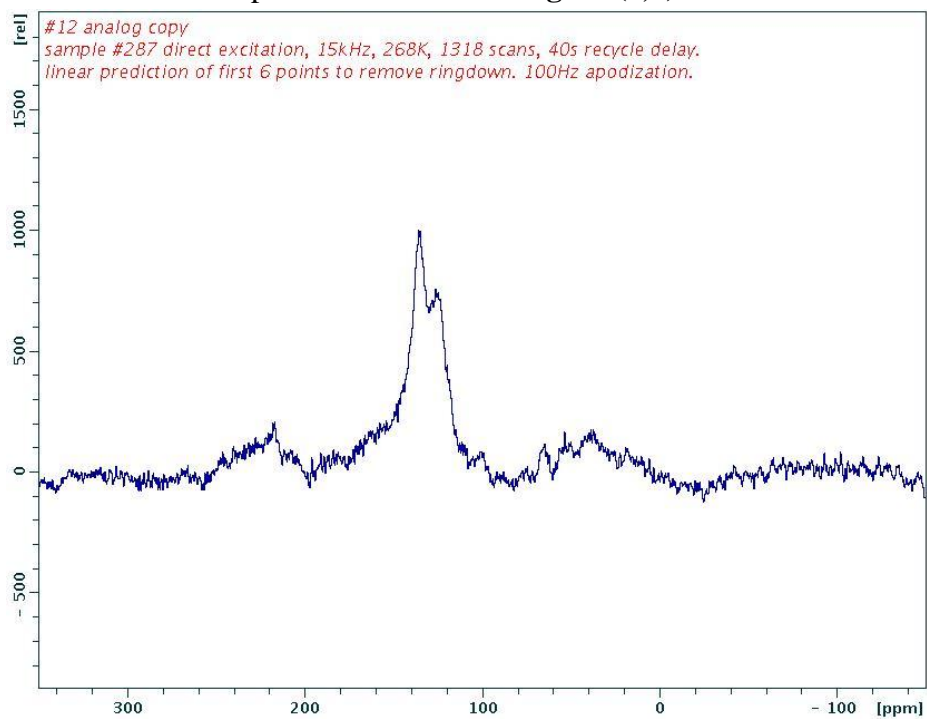
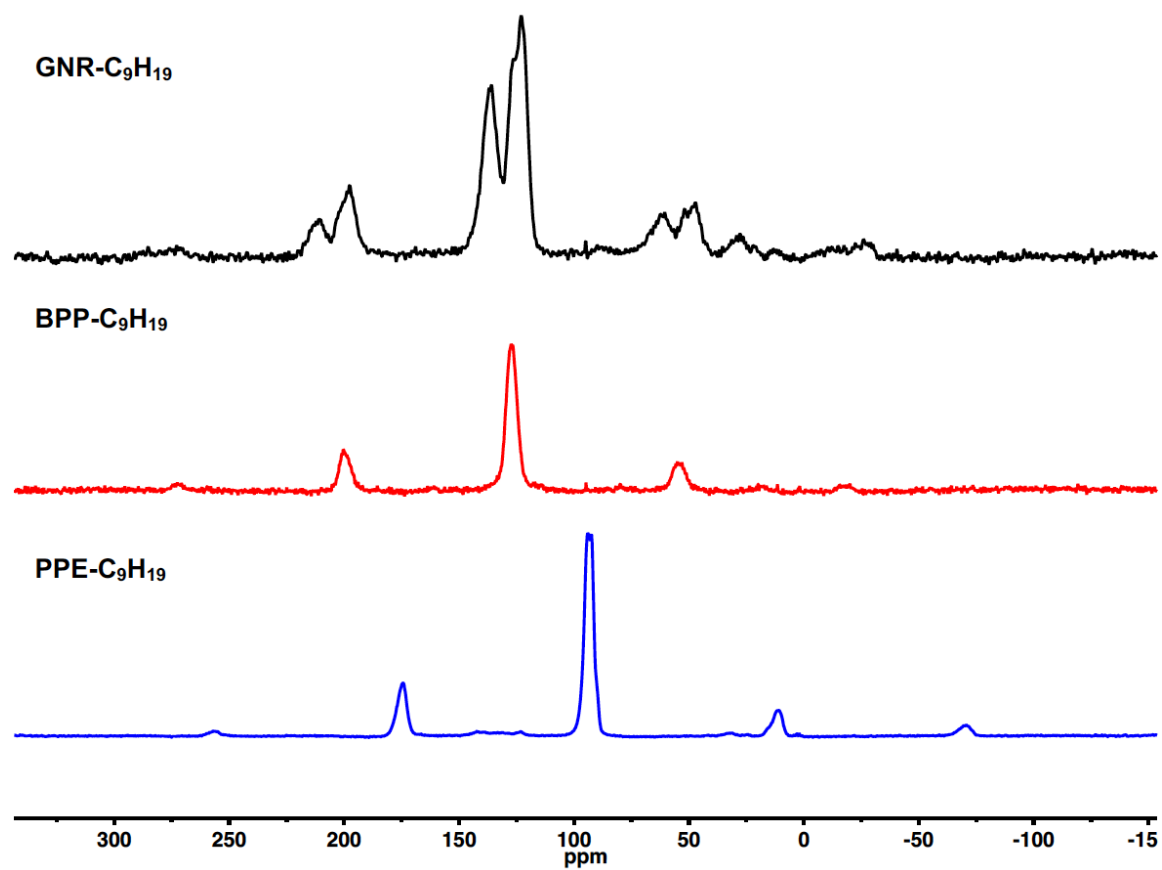




**Figure A4.58.**  $^{13}\text{C}$  MAS NMR spectra of **PPE- $\text{C}_9\text{H}_{19}$ - $^{13}\text{C}$**  (blue) **BPP- $\text{C}_9\text{H}_{19}$ - $^{13}\text{C}$  (2,3)** (red) and **GNR- $\text{C}_9\text{H}_{19}$ - $^{13}\text{C}$  (2,3)** (black).



## H. Thermalgravimetry

**Figure A4.59. PPE-OHxg** (blue trace). Loss of HxgO side chains corresponds to a 56.7% mass loss. **BPP-OHxg** (red trace) Loss of HxgO side chains corresponds to at 47.7% loss. **GNR-OHxg** (black trace) HxgO side chains corresponds to a 48.2% mass loss.

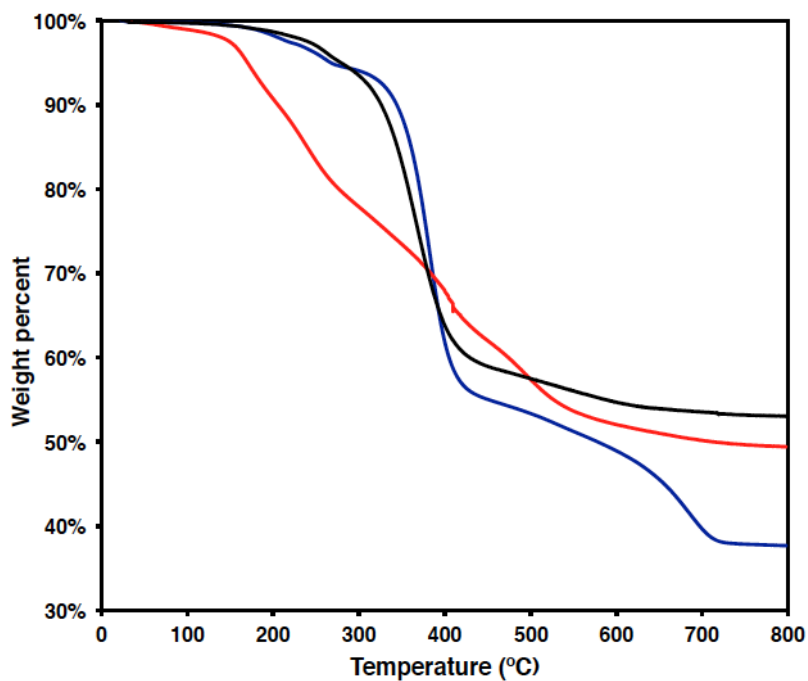
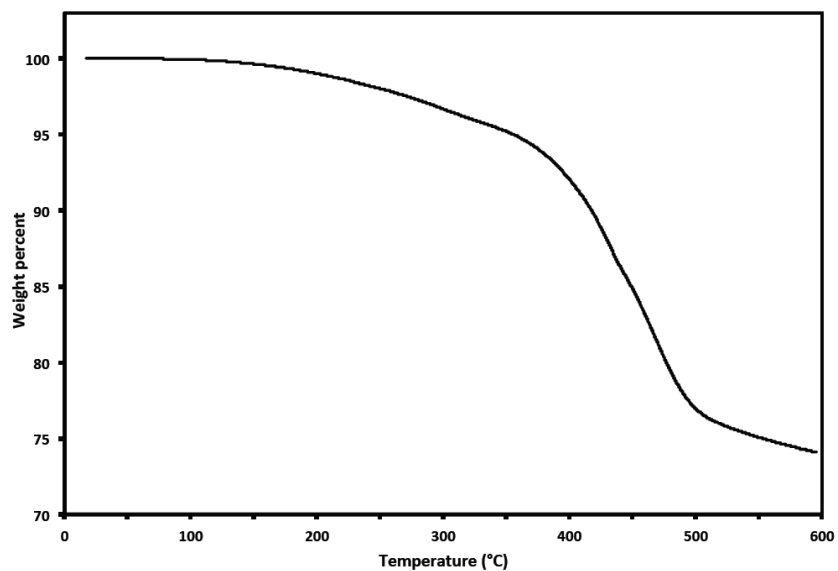


**Figure A4.60. GNR-C<sub>9</sub>H<sub>19</sub>**



## I. Atomic Force Microscopy

**Figure A4.61.** AFM micrograph of **BPP-OH<sub>x</sub>g** mica substrate.

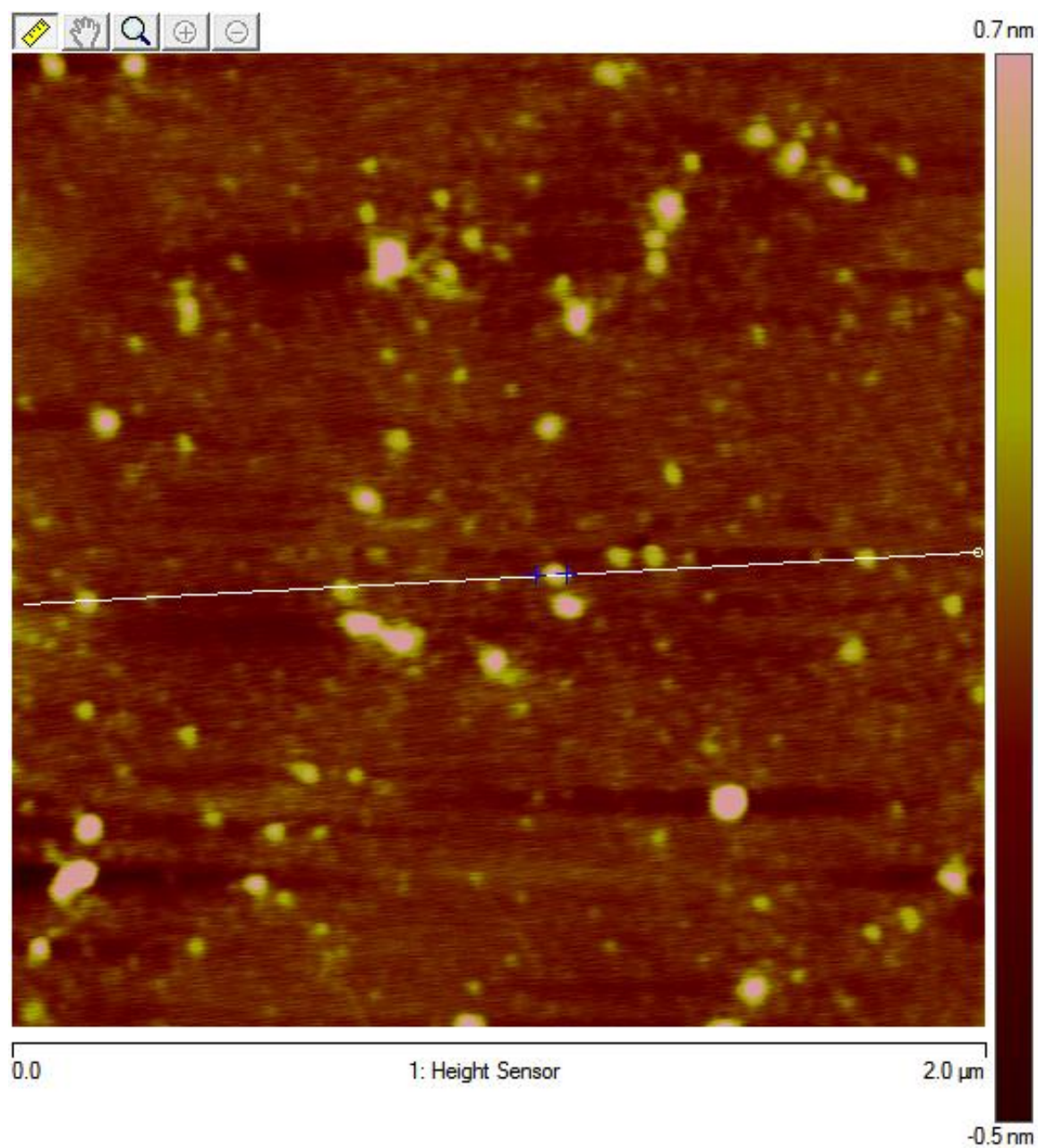


**Figure A4.62.** AFM micrograph of **GNR-OHxg** from DMF dropcast on mica substrate.

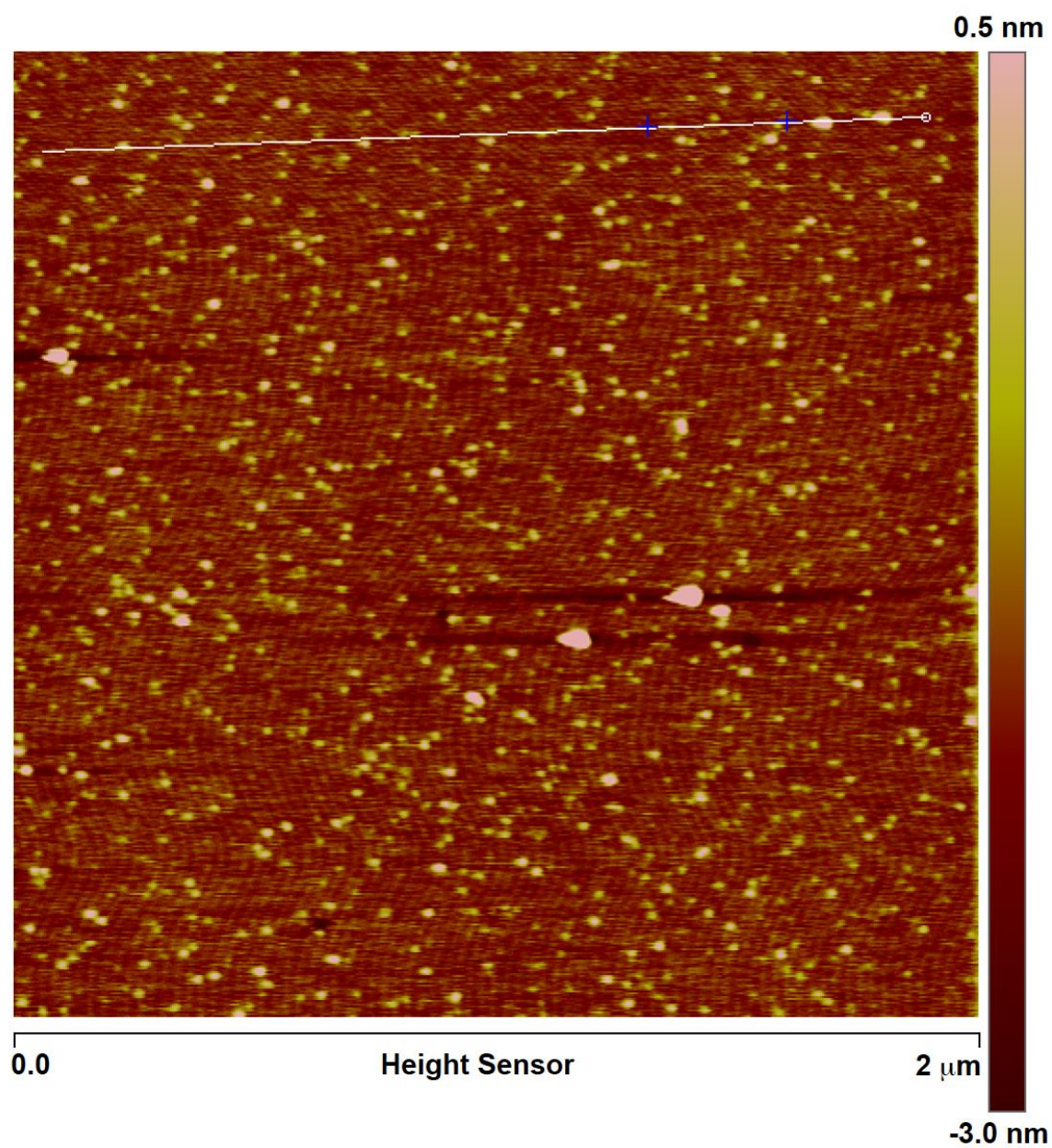


**Figure A4.63.** Particle height histogram of **GNR-OHxg** DMF dropcast deposited over mica as obtained from Figure S64.

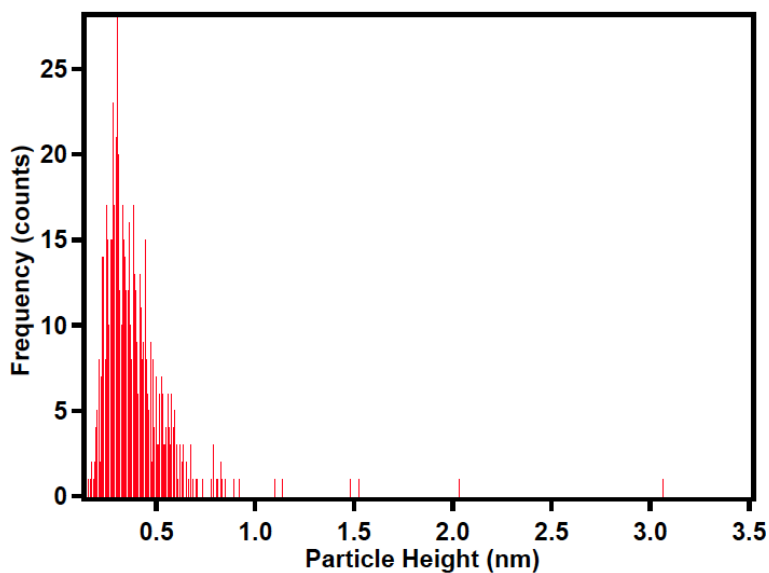
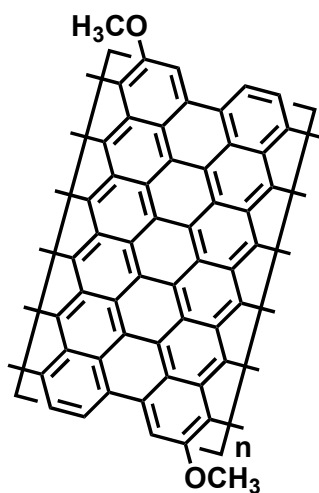


**Table A4.4.** Statistics of **GNR-OHxg** DMF dropcast deposited over mica as obtained from Figure S64.

Parameter	Value
Total number of particles	642
Density	160 particles $\mu\text{m}^{-1}$
Average height	0.39 nm (3.9 Å)
Standard deviation (height)	0.23 nm (2.3 Å)
Median height	0.34 nm (3.4 Å)
Mode (height)	0.29 nm (2.9 Å)
Minimum (height)	0.15 nm (1.5 Å)
Maximum (height)	3.50 nm (35.0 Å)

## J. Density Functional Theory Calculations

The band structure, density of states (DOS), phonon dispersion, IR and Raman spectra were calculated using the Density Functional theory (DFT) plane-wave pseudopotential method from the *CASTEP* module [42] in Materials Studio [43]. The initial graphene nanoribbon structure was sketched in an Atomistic Simulation canvas inside a of monoclinic unit cell ( $P2/m$ ) with arbitrary  $a$ ,  $b$  and  $c$  cell parameters ( $\alpha = 90^\circ$ ), placing all but one H atom from the methyl in the  $2n$  special position (along the  $m$  plane, perpendicular and with center at the 2-fold axis) to contain one GNR repeating unit, the OHxg was simplified to a methoxy group:



The piecewise constructed structure and formal charges were optimized with the geometry optimization routine in the MS Forcite module using a SMART algorithm and the Universal Force Field [44]. The nanoribbon model resulted in GNR width along the  $a$  parameter, stacking in  $b$  and length in  $c$  (optimized cell parameters  $a = 20.33 \text{ \AA}$ ,  $b = 3.22 \text{ \AA}$ ,  $c = 8.55 \text{ \AA}$ ,  $\alpha = 91.57^\circ$ ). The  $a$  and  $b$  parameters were readjusted to 80 and 32  $\text{\AA}$ , respectively, to reduce any effect on packing and the structure was further optimized keeping the cell parameters constant. A DFT geometry optimization was performed using the *CASTEP* module with constant cell parameters. A Broyden-Fletcher-Goldfarb-Shanno (BFGS) algorithm using *ab initio* forces was utilized with the Generalized Gradient Approximation Perdew-Burke-Ernzerhof (GGA-PBE) exchange and correlation functional; a plane-wave energy cut-off of 400 eV; a self-consistent field (SCF) of 100 cycles with a  $2.0 \times 10^{-6}$  eV/atom tolerance; a norm-conserving pseudopotential represented in reciprocal space; a Pulay energy mixing scheme with a 0.5 charge

mixing amplitude; and a maximum residual force of 0.05 eV/Å. Once the calculations achieved convergence, electronic energy minimizations were performed, followed by band structure and DOS calculations using the indicated exchange correlation functionals in Table S7 with  $k$ -point set at  $\square$ .

To observe the effect of the non-planarity of the side chains, the cell symmetry was reduced to  $P\bar{1}$ , the missing atoms added, and the geometry structure was UFF relaxed, and the electronic energy was optimized in the same method as described above.

The effect of the heteroatom of the side chains on the GNR was calculated as follows, the -OMe group was converted into a -H atom, the space group was expanded to  $Pmmm$ , and the geometry structure was UFF relaxed, and the electronic energy was optimized in the same method as described above.

A model of the **GNR-C<sub>9</sub>H<sub>19</sub>** system was constructed in a similar manner, but reducing the alkyl chain to CH<sub>3</sub> and using space group  $P\bar{1}$ .

**Table A4.5.** Calculated electronic bandgaps.

Side Group	Space group	XC functional	Bandgap $E_g$ (eV)
-OMe	$P2/m$	LDA	0.838
-OMe	$P2/m$	GGA-PBE	0.836
-OMe	$P2/m$	GGA-PW91	0.836
-OMe	$P\bar{1}$	GGA-PBE	0.836
-H	$Pmmm$	GGA-PBE	0.945
-Me (from C <sub>9</sub> H <sub>19</sub> )	$P\bar{1}$	GGA-PBE	0.654

**Figure A4.64.** Arbitrary views of the **GNR-OMe** ( $P2/m$ ) unit cell model. Axes are indicated.

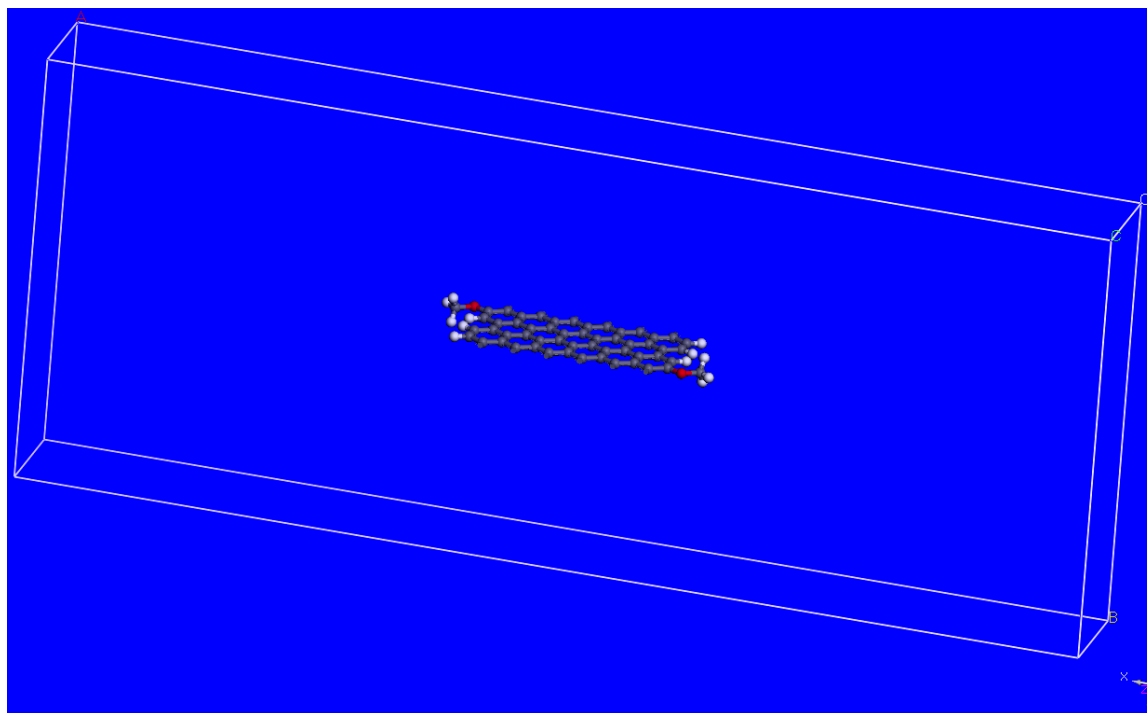


**Table A4.6.** Atomic coordinates of **GNR-OMe** ( $P2/m$ ) model.

Space Group:  $P2/m$

Cell Parameters

$$a = 80.0000 \text{ \AA}$$

$$b = 32.0000 \text{ \AA}$$

$$c = 8.5517 \text{ \AA}$$

$$\alpha = 90.0000^\circ$$

$$\beta = 91.5727^\circ$$

$$\gamma = 90.0000^\circ$$

Atom Positions

Label	$x/a$	$y/b$	$z/c$	Occupancy
-------	-------	-------	-------	-----------



H1	0.37626	0.52858	0.70357	1
O2	0.60794	0.5	0.12614	0.5
C3	0.62276	0.5	0.22133	0.5
C4	0.59269	0.5	0.19793	0.5
C5	0.57745	0.5	0.10413	0.5
C6	0.59216	0.5	0.35845	0.5
C7	0.57677	0.5	0.43495	0.5
C8	0.59209	0.5	0.68997	0.5
C9	0.59231	0.5	0.85005	0.5
C10	0.57725	0.5	0.93424	0.5
C11	0.56174	0.5	0.85032	0.5
C12	0.57681	0.5	0.60347	0.5
C13	0.56158	0.5	0.68164	0.5
C14	0.56158	0.5	0.34934	0.5
C15	0.56194	0.5	0.18116	0.5
C16	0.54636	0.5	0.0948	0.5
C17	0.54611	0.5	0.42848	0.5
C18	0.5461	0.5	0.59467	0.5
C19	0.54624	0.5	0.92857	0.5
C20	0.53072	0.5	0.84181	0.5
C21	0.53067	0.5	0.67362	0.5
C22	0.53068	0.5	0.34176	0.5
C23	0.53081	0.5	0.1734	0.5
C24	0.51545	0.5	0.91979	0.5
C25	0.5154	0.5	0.58797	0.5
C26	0.50001	0.5	0.66719	0.5
C27	0.48449	0.5	0.91207	0.5
C28	0.49997	0.5	0.83339	0.5
C29	0.48459	0.5	0.58044	0.5
H30	0.3669	0.5	0.86301	0.5
H31	0.39608	0.5	0.57273	0.5
H32	0.39582	0.5	0.36875	0.5
H33	0.39555	0.5	0.08837	0.5

**Figure A4.65.** Band structure and density of states plot of **GNR-OMe** ( $P2/m$ ) model using LDA-CA-PZ functional.

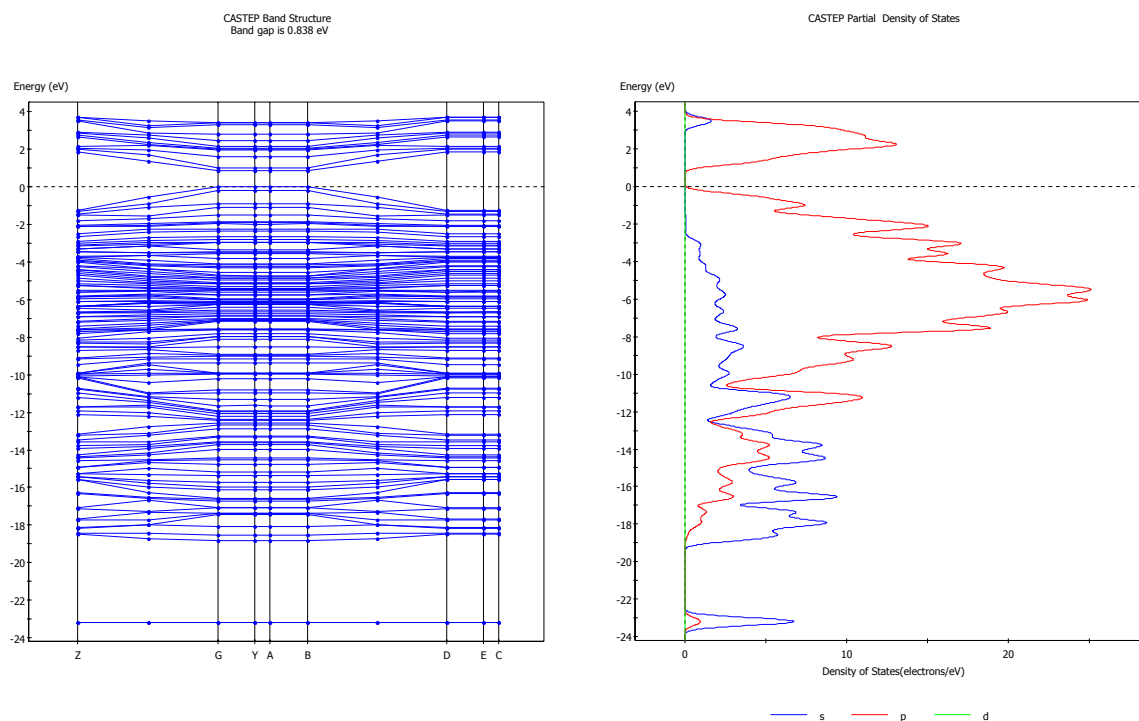


**Figure A4.66.** Band structure and density of states plot of **GNR-OMe** ( $P2/m$ ) model using GGA-PBE functional.

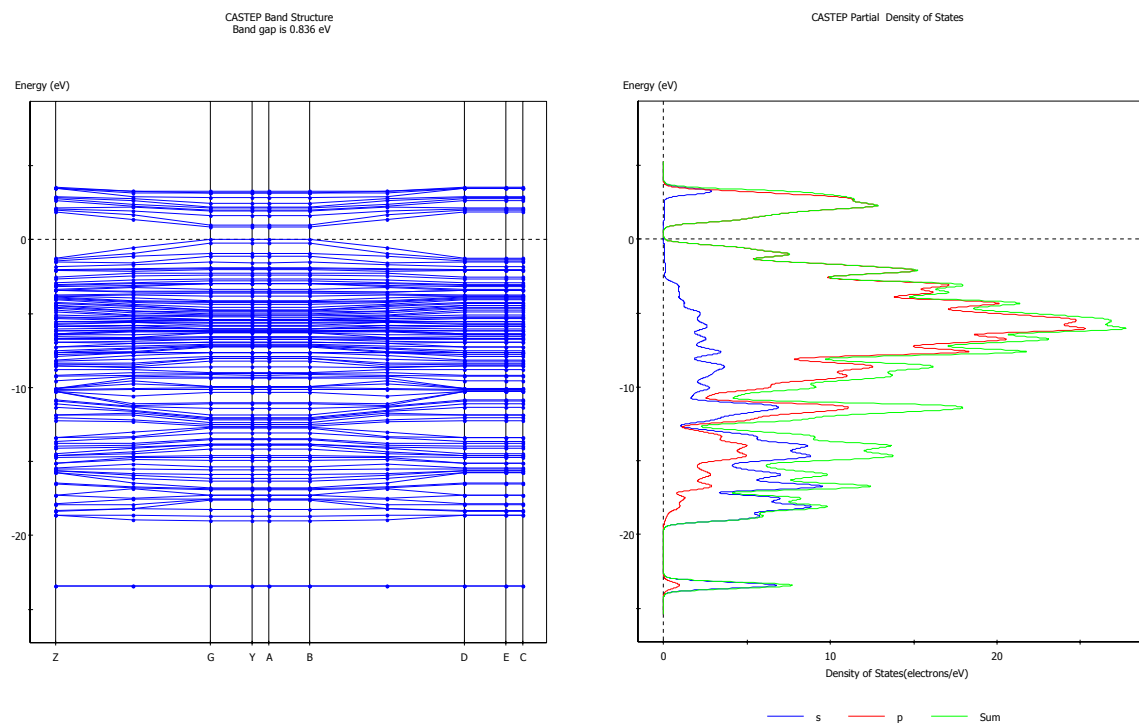


**Figure A4.67.** Band structure and density of state plot of **GNR-OMe** ( $P2/m$ ) model using GGA-PW91 functional.

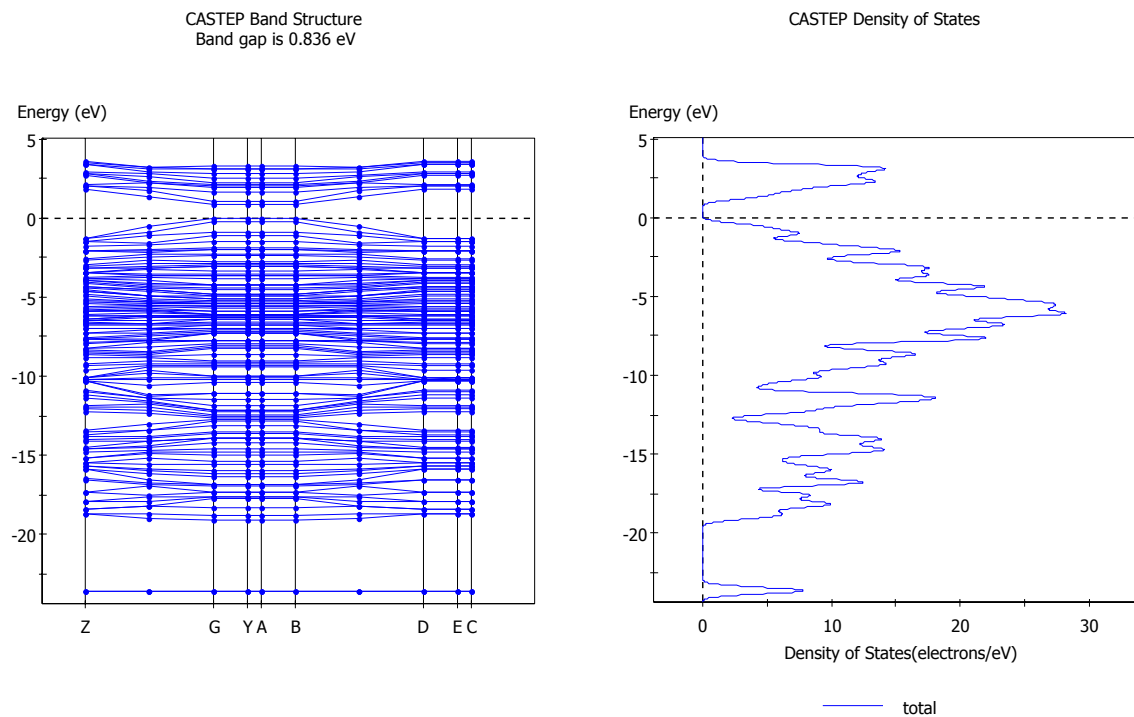


**Figure A4.68.** Arbitrary views of the **GNR-OMe** ( $P\bar{1}$ ) model.

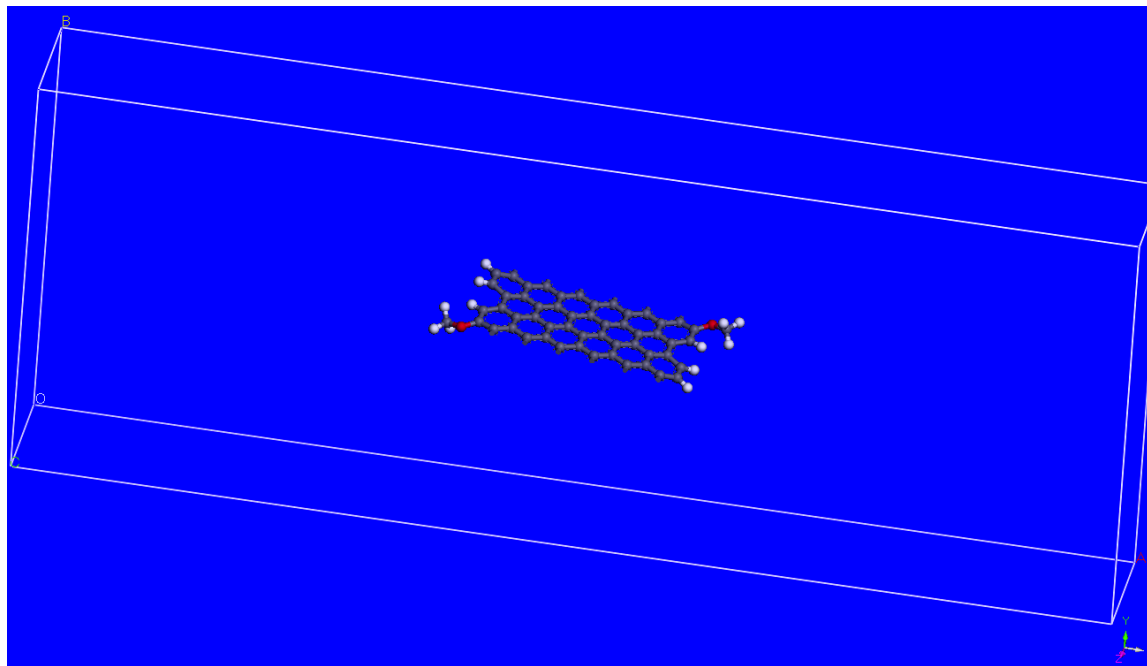


**Table A4.7.** Atomic coordinates of **GNR-OMe** ( $P\bar{1}$ ) model.

Space Group:  $P\bar{1}$

Cell Parameters

$$a = 80.0000 \text{ \AA}$$

$$b = 32.0000 \text{ \AA}$$

$$c = 8.5516 \text{ \AA}$$

$$\alpha = 90.0000^\circ$$

$$\beta = 91.5727^\circ$$

$$\gamma = 90.0000^\circ$$

Atom positions

Label	$x/a$	$y/b$	$z/c$	occupancy
H1	0.38100	0.47875	0.71115	1
O2	0.60644	0.48510	0.11906	1
C3	0.62102	0.49394	0.21097	1
C4	0.59194	0.47809	0.19689	1
C5	0.57672	0.47630	0.10444	1
C6	0.59164	0.47463	0.3576	1
C7	0.57632	0.47386	0.43566	1
C8	0.59065	0.45877	0.69278	1
C9	0.59072	0.45878	0.85337	1
C10	0.57647	0.47211	0.93543	1
C11	0.56131	0.47874	0.85062	1
C12	0.57619	0.47087	0.60453	1
C13	0.56121	0.47820	0.68206	1
C14	0.56122	0.47914	0.35037	1

C15	0.56144	0.47966	0.18215	1
C16	0.54604	0.48467	0.09521	1
C17	0.54592	0.48455	0.42921	1
C18	0.54594	0.48477	0.59521	1
C19	0.54603	0.48520	0.92910	1
C20	0.53067	0.49082	0.84223	1
C21	0.53064	0.49073	0.67397	1
C22	0.53062	0.49034	0.34239	1
C23	0.53068	0.49027	0.17387	1
C24	0.51546	0.49571	0.91986	1
C25	0.51544	0.49574	0.58845	1
C26	0.49999	0.49998	0.66704	1
C27	0.48450	0.50434	0.91179	1
C28	0.49997	0.49992	0.83331	1
C29	0.48456	0.50432	0.58008	1
H30	0.36917	0.49847	0.87357	1
H31	0.39662	0.52529	0.57309	1
H32	0.39820	0.55238	0.36714	1
H33	0.39813	0.55223	0.08174	1
H34	0.37485	0.53332	0.71675	1

**Figure A4.69.** Band structure and density of state plot of **GNR-OMe** ( $P\bar{1}$ ) model using GGA-PBE functional.

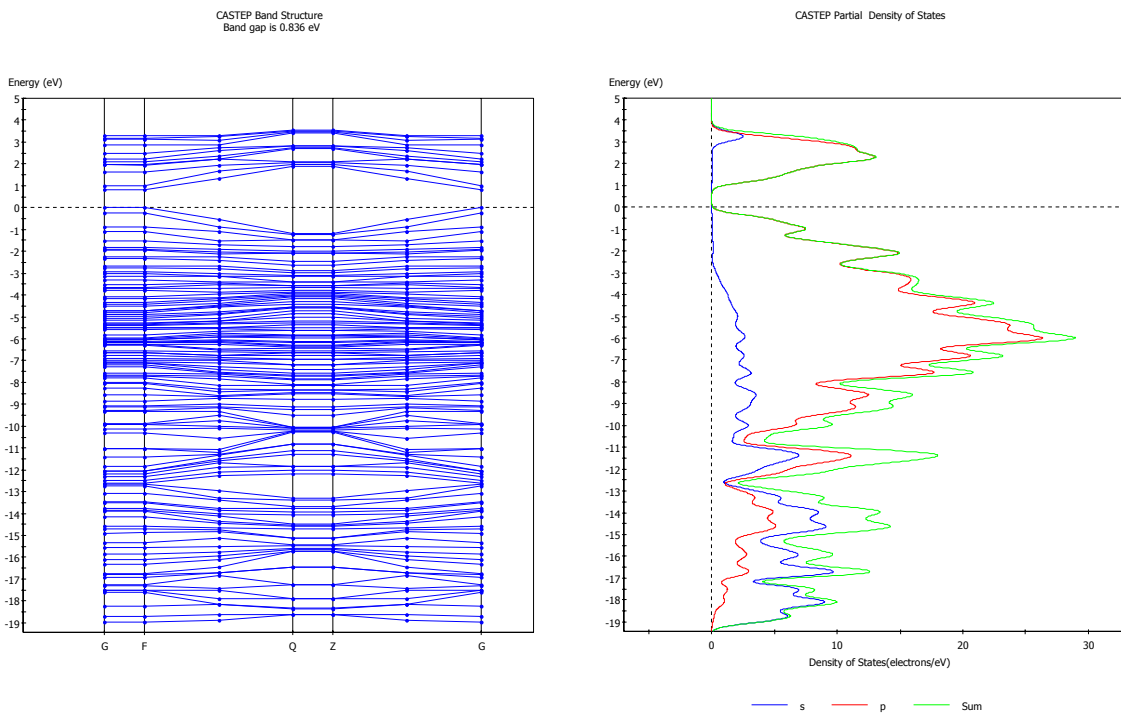


**Figure A4.70.** Arbitrary views of the **GNR-H** ( $Pmmm$ ) model.

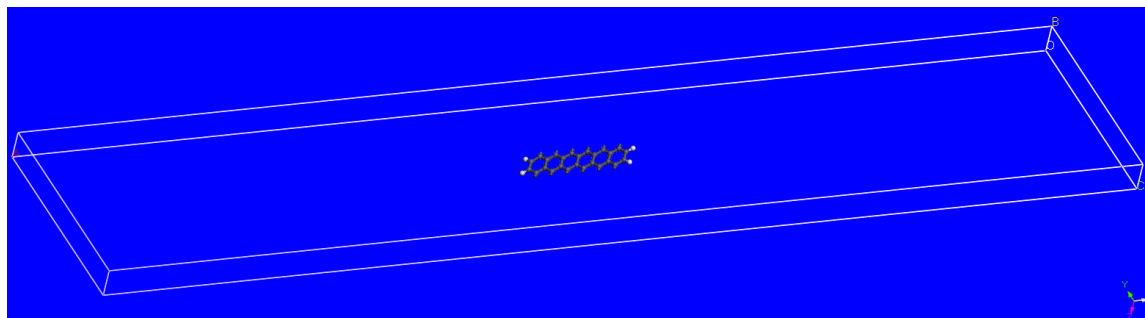


**Table A4.8.** Atomic coordinates of **GNR-H** ( $Pmmm$ ) model.

Space Group:  $Pmmm$

Cell Parameters

$$a = 159.94 \text{ \AA}$$

$$b = 4.276 \text{ \AA}$$

$$c = 32.00 \text{ \AA}$$

$$\alpha = 90.0000^\circ$$

$$\beta = 90.0000^\circ$$

$$\gamma = 90.0000^\circ$$

Label	$x/a$	$y/b$	$z/c$	occupancy
H1	-0.55195	-0.21759	-0.50000	0.50
C2	-0.54589	-0.33846	-0.50000	0.50
C3	-0.53829	-0.16454	-0.50000	0.50
C4	-0.53064	-1.66676	-0.50000	0.50
C5	-0.52297	-0.16629	-0.50000	0.50
C6	-0.51526	-1.66612	-0.50000	0.50
C7	-0.50766	-1.83278	-0.50000	0.50
C8	-0.50000	-1.33388	-0.50000	0.25

**Figure A4.71.** Band structure and density of states plot of **GNR-H** (*Pmmm*) model using GGA-PBE XC functional.

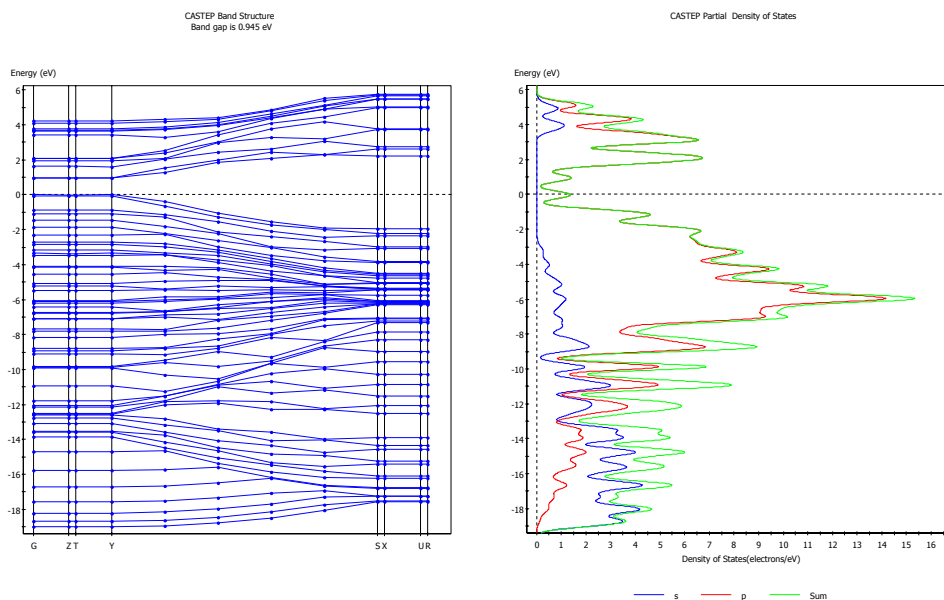


**Figure A4.72.** Arbitrary views of the **GNR-Me** ( $P\bar{1}$ ) model.

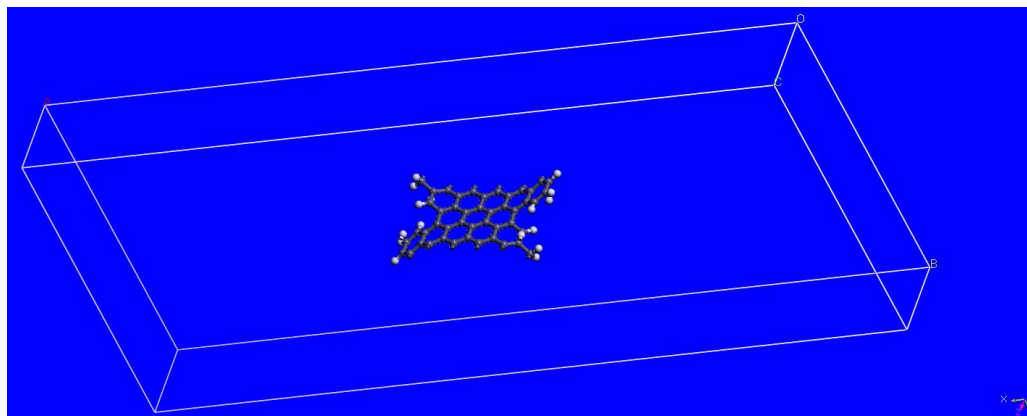


**Table A4.9.** Atomic coordinates of **GNR-Me** ( $P\bar{1}$ ) model

Space Group:  $P\bar{1}$

Cell Parameters

$$a = 80.0 \text{ \AA}$$

$$b = 32.0 \text{ \AA}$$

$$c = 8.4217 \text{ \AA}$$

$$\alpha = 90.0000^\circ$$

$$\beta = 91.5727^\circ$$

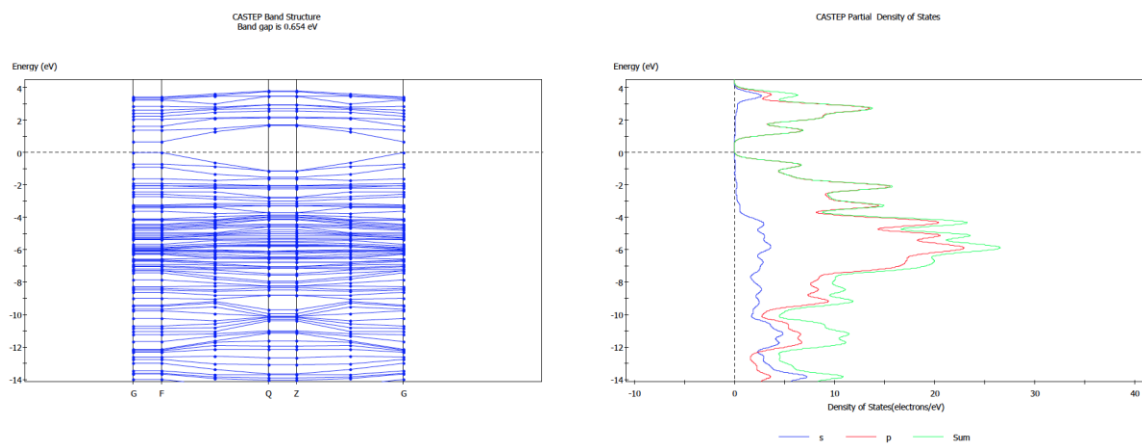
$$\gamma = 90.0000^\circ$$

Label	$x/a$	$y/b$	$z/c$	Occupancy
H1	0.42849	0.60291	0.83003	1
H2	0.57531	0.51234	0.06852	1
H3	0.56881	0.44498	0.41885	1
C4	0.57134	0.42799	0.10962	1
C5	0.59016	0.52184	0.69561	1
C6	0.58986	0.52234	0.86211	1
C7	0.57569	0.50979	0.93887	1
C8	0.5612	0.49599	0.85286	1
C9	0.57618	0.50932	0.60839	1
C10	0.56135	0.4963	0.68298	1
C11	0.55844	0.45895	0.34857	1



C12	0.55841	0.45538	0.18399	1
C13	0.54546	0.47625	0.09735	1
C14	0.54552	0.47906	0.42735	1
C15	0.54611	0.48735	0.59661	1
C16	0.54599	0.48523	0.92849	1
C17	0.5308	0.48858	0.84317	1
C18	0.53086	0.48963	0.67344	1
C19	0.53059	0.48843	0.34233	1
C20	0.53066	0.48747	0.17429	1
C21	0.51515	0.49234	0.92025	1
C22	0.51522	0.49327	0.58802	1
C23	0.49987	0.49703	0.66477	1
C24	0.48466	0.50455	0.91201	1
C25	0.49981	0.49691	0.8353	1
C26	0.48471	0.50395	0.57983	1
H27	0.41577	0.5592	0.87824	1
H28	0.39866	0.46717	0.36536	1
H29	0.39922	0.46602	0.06875	1
H30	0.42371	0.48843	0.52128	1
H31	0.43125	0.57748	1.01785	1

**Figure A4.73.** Band structure and density of states plot of **GNR-Me** ( $P\bar{1}$ ) model using GGA-PBE XC functional.



**K. Solution NMR Spectra.**

**Figure A4.74.**  $^1\text{H}$  NMR spectrum of **S2**. 25 °C,  $\text{CDCl}_3$ .

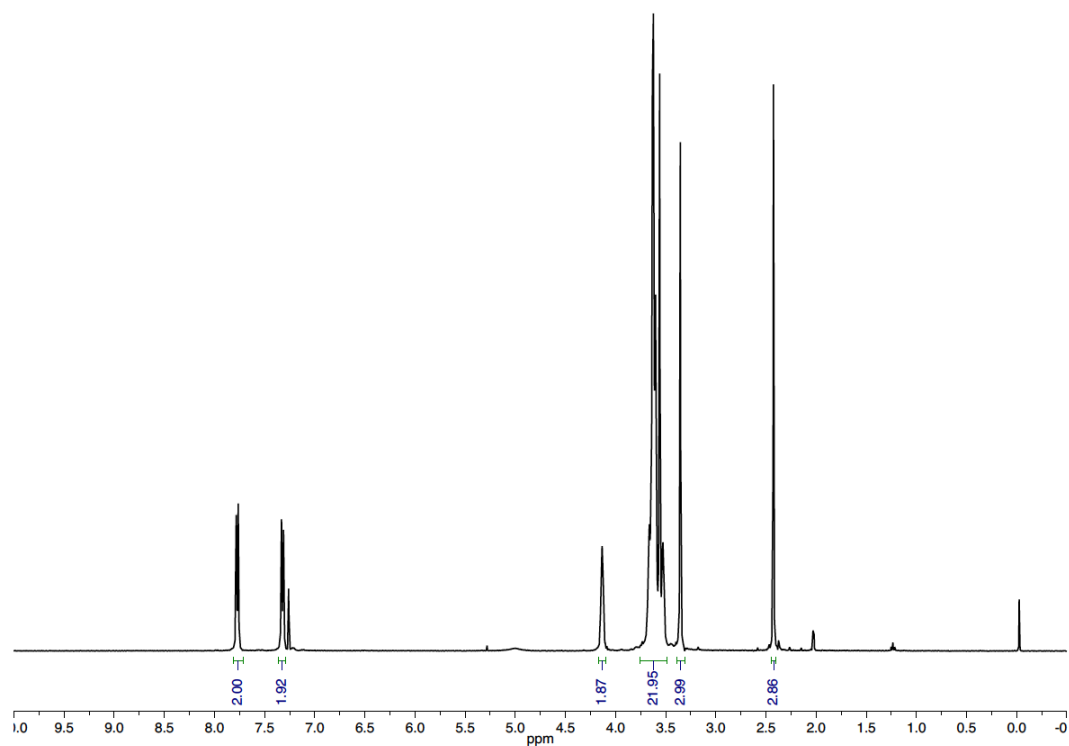


**Figure A4.75.**  $^{13}\text{C}$  NMR spectrum of **S2**. 25 °C,  $\text{CDCl}_3$ .

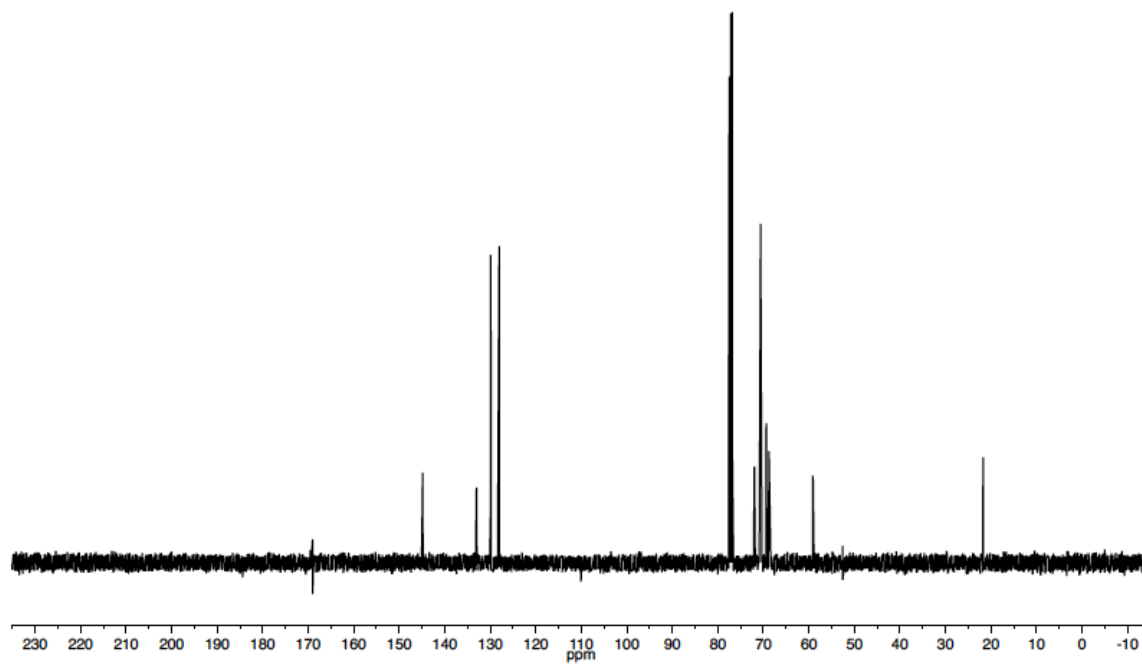


**Figure A4.76.**  $^1\text{H}$  NMR spectrum of **S3**. 25 °C,  $\text{CDCl}_3$ .

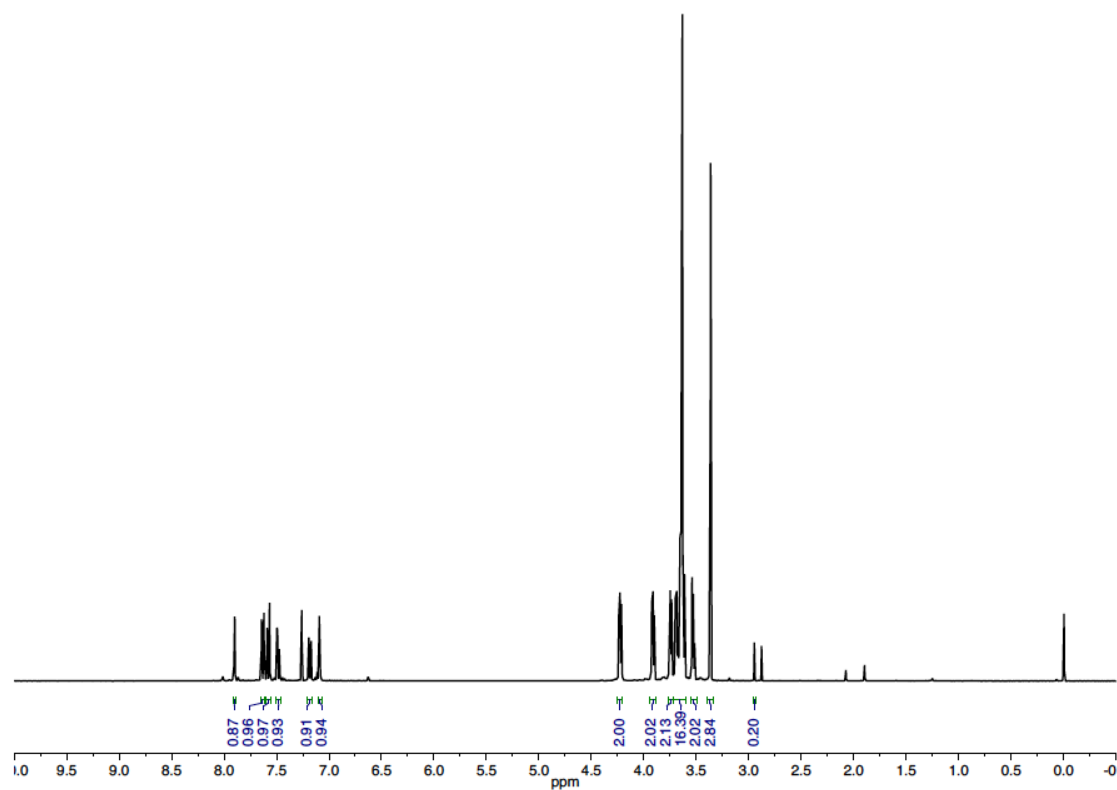


**Figure A4.77.**  $^{13}\text{C}$  NMR spectrum of **S3**. 25 °C,  $\text{CDCl}_3$ .

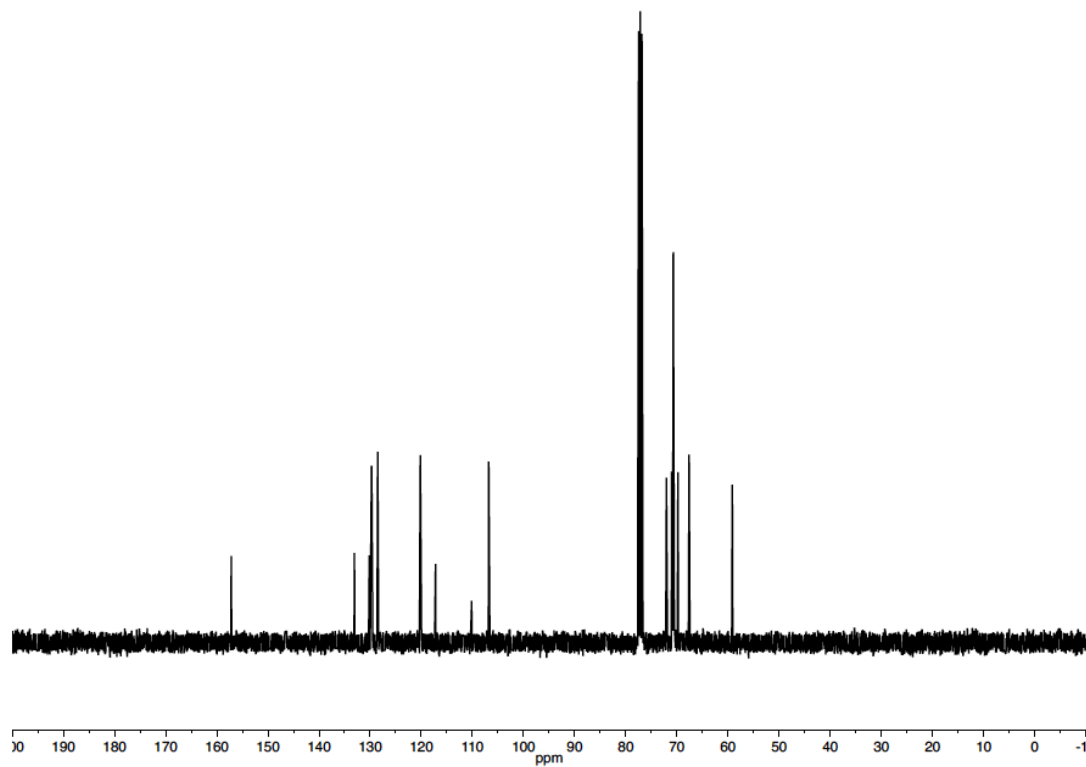


**Figure A4.78.**  $^1\text{H}$  NMR spectrum of **S4**. 25 °C, dioxane- $d_8$ /D $_2$ O/DCI 99:0.7:0.3 (v/v/v).

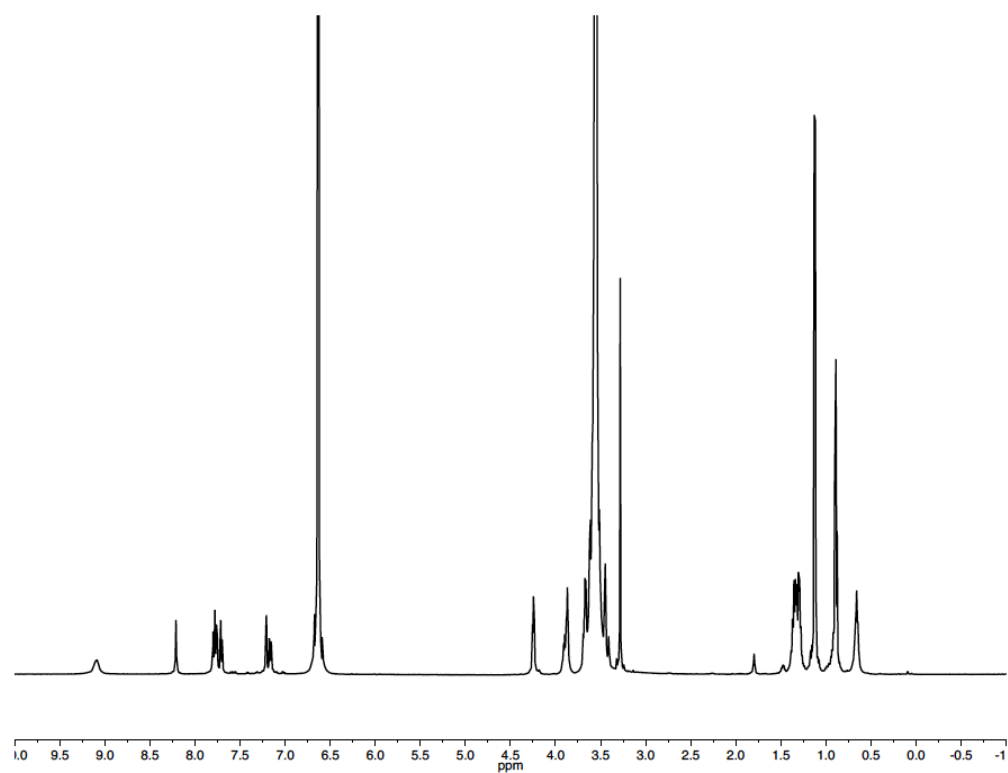


**Figure A4.79.**  $^{13}\text{C}$  NMR spectrum of **S4**. 25 °C, dioxane- $d_8$ /D $_2$ O/DCI 99:0.7:0.3 (v/v/v)

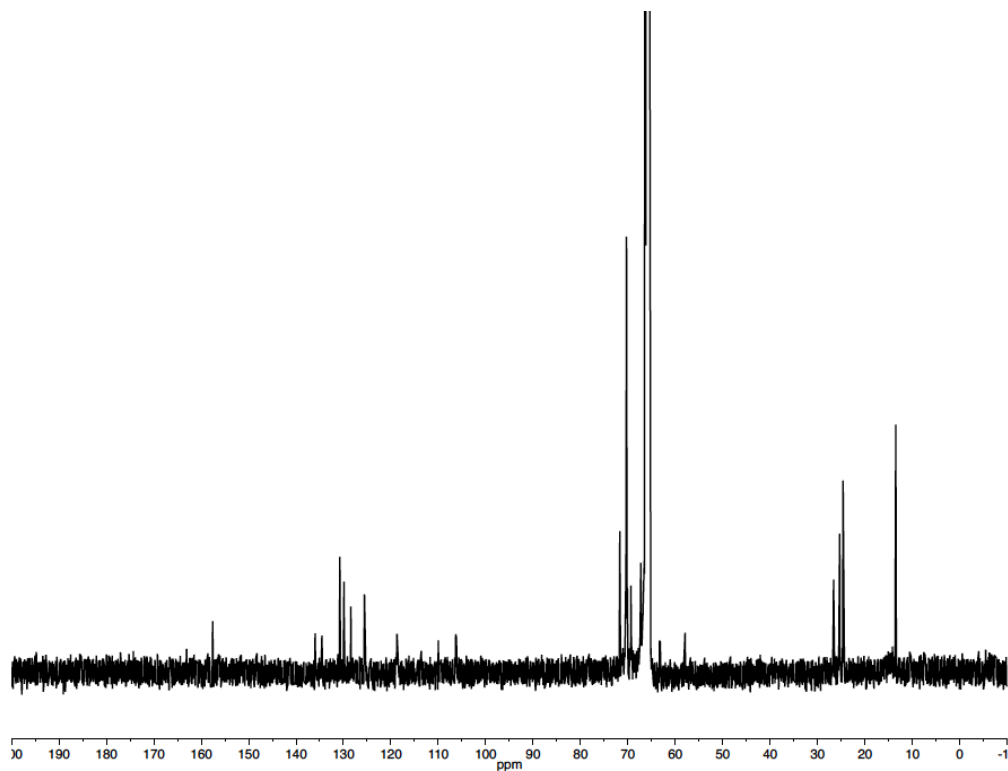


**Figure A4.80.**  $^1\text{H}$  NMR spectrum of **S7**. 25 °C,  $\text{dms}\text{-}d_6$ .

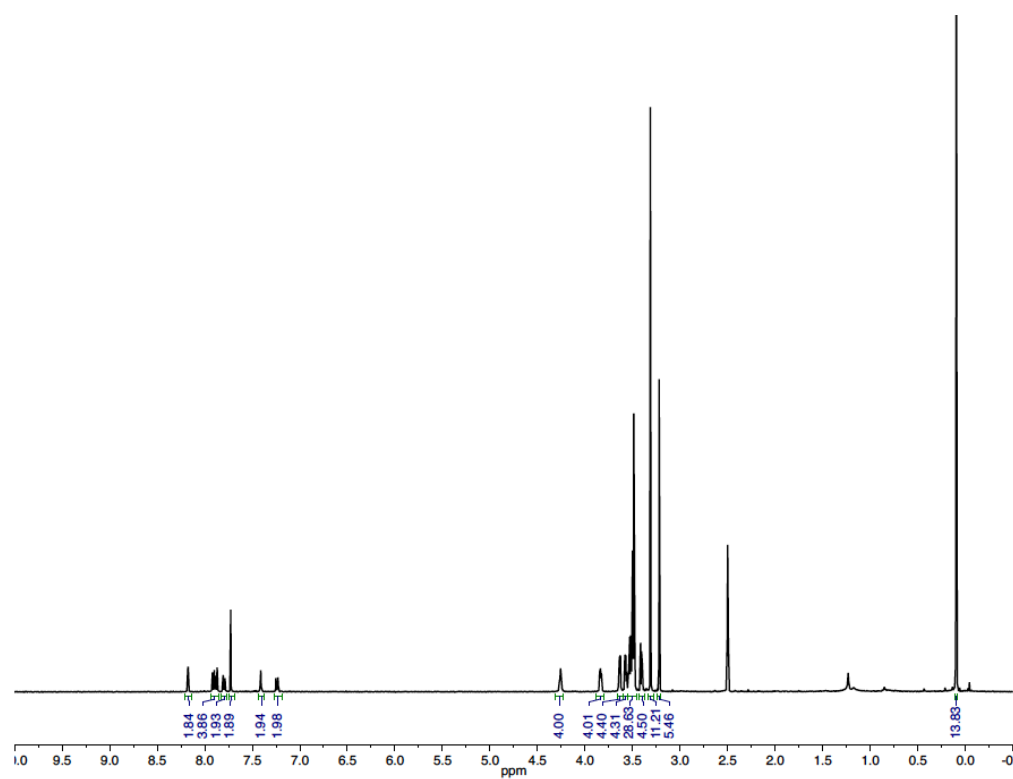


**Figure A4.81.**  $^{13}\text{C}$  NMR spectrum of **S7**. 25 °C,  $\text{dms}\text{-}d_6$ .

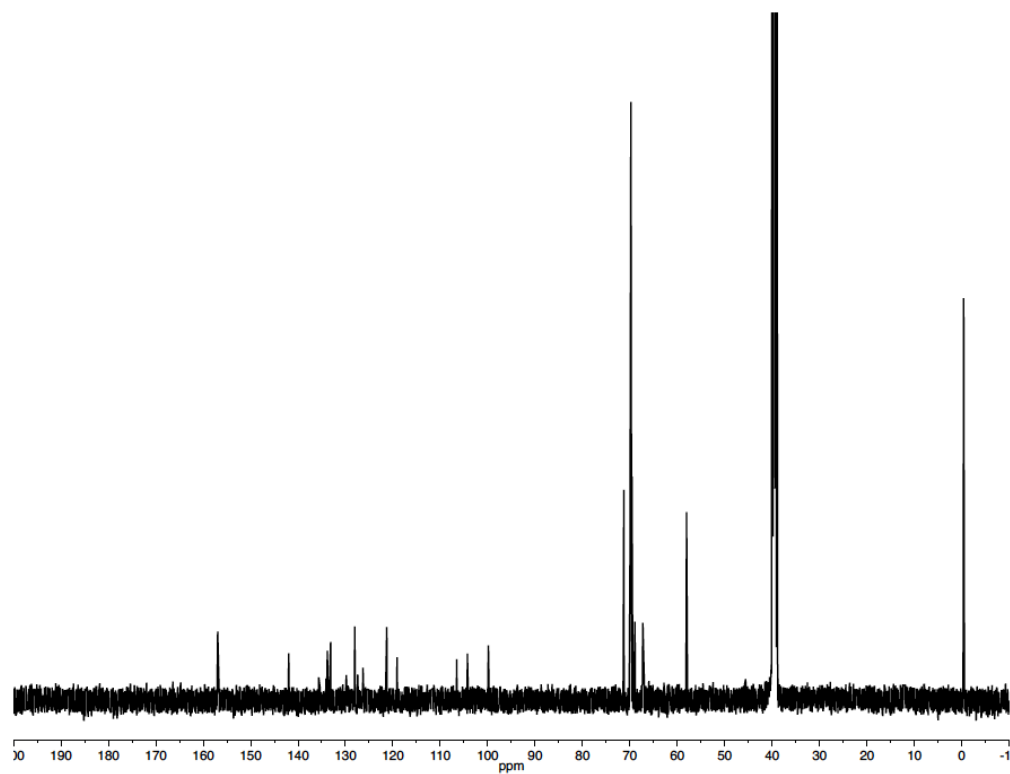


**Figure A4.82.**  $^1\text{H}$  NMR spectrum of **S7- $^{13}\text{C}_4$** . 25 °C,  $\text{dms-}d_6$ .

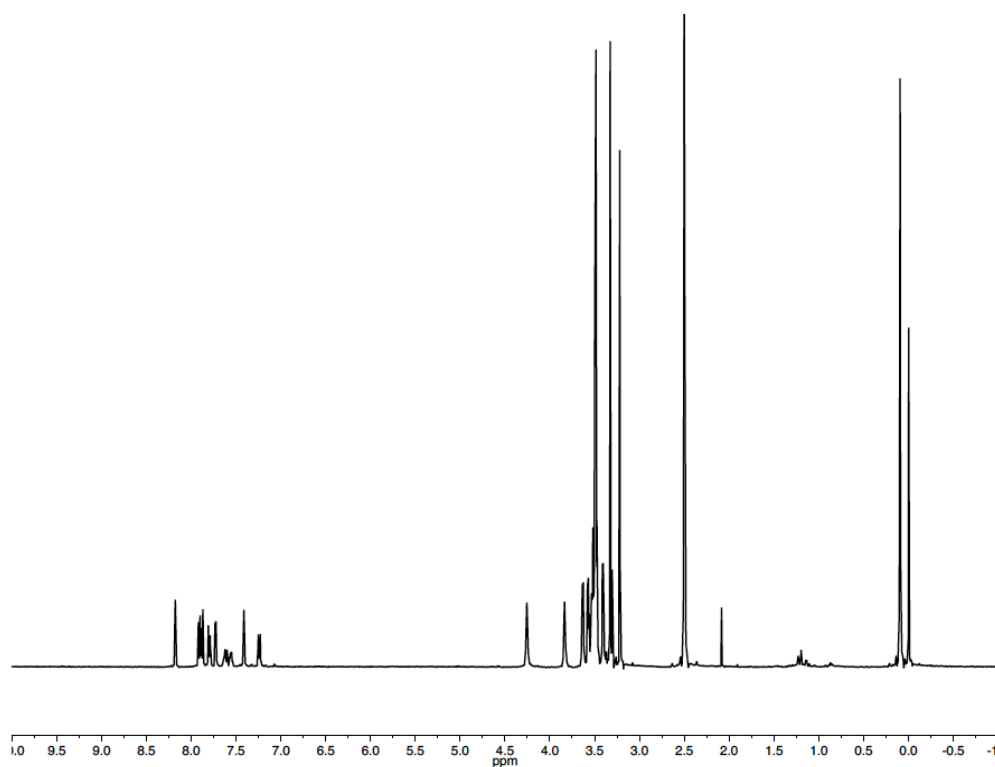


**Figure A4.83.**  $^{13}\text{C}$  NMR spectrum of **S7- $^{13}\text{C}_4$** . 25 °C,  $\text{dms-}d_6$ .

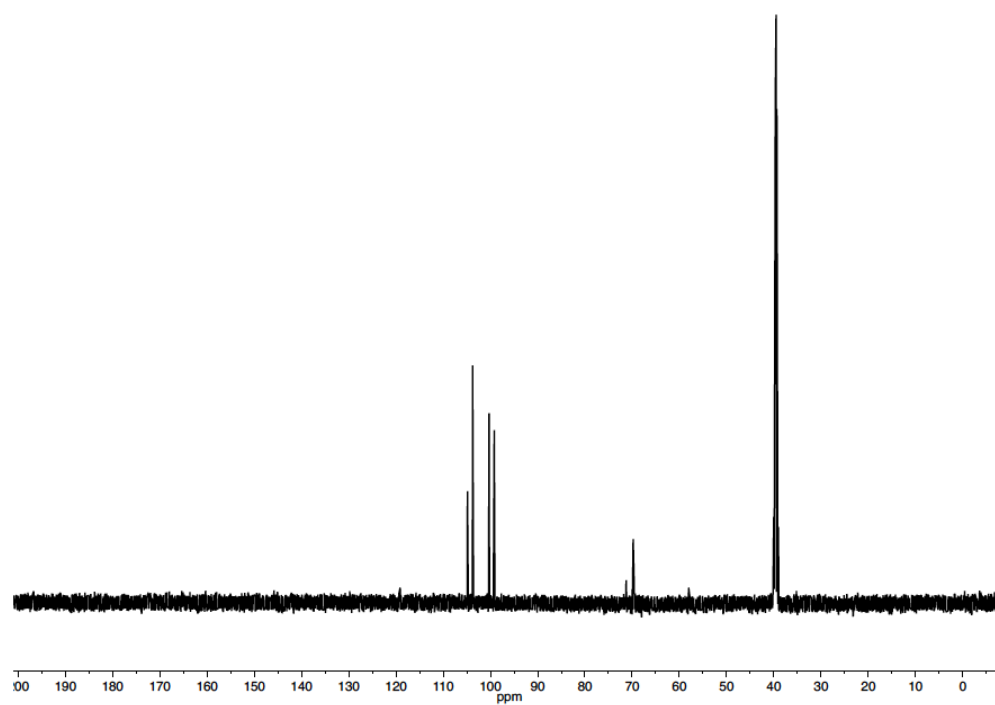


**Figure A4.84.**  $^1\text{H}$  NMR spectrum of **4**. 80 °C,  $\text{dms}\text{-}d_6$ .

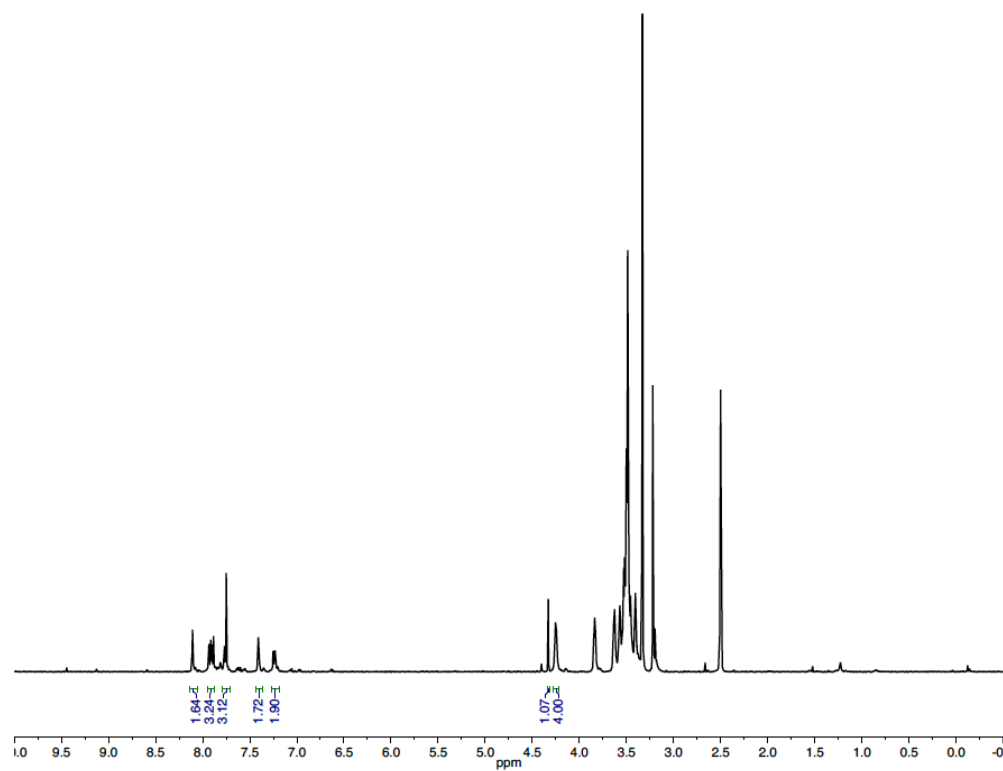


**Figure A4.85.**  $^{13}\text{C}$  NMR spectrum of **4**. 80 °C,  $\text{dms}\text{-}d_6$ .

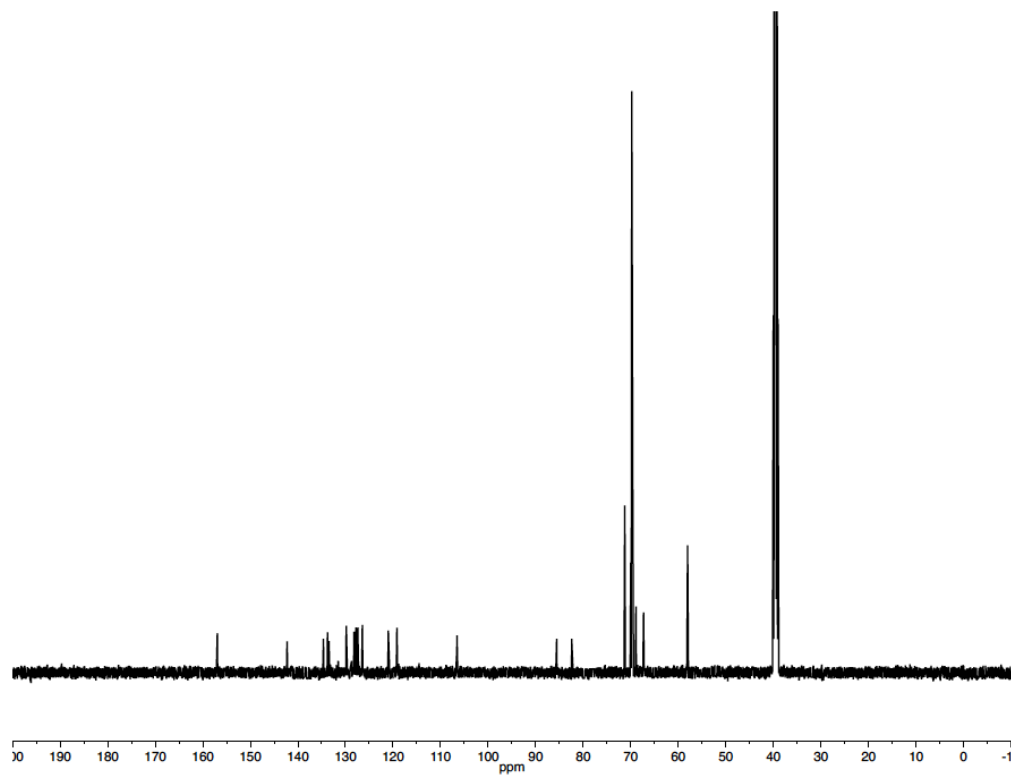


**Figure A4.86.**  $^1\text{H}$  NMR spectrum of  $4\text{-}^{13}\text{C}_4$ . 25 °C,  $\text{dms}\text{-}d_6$ .

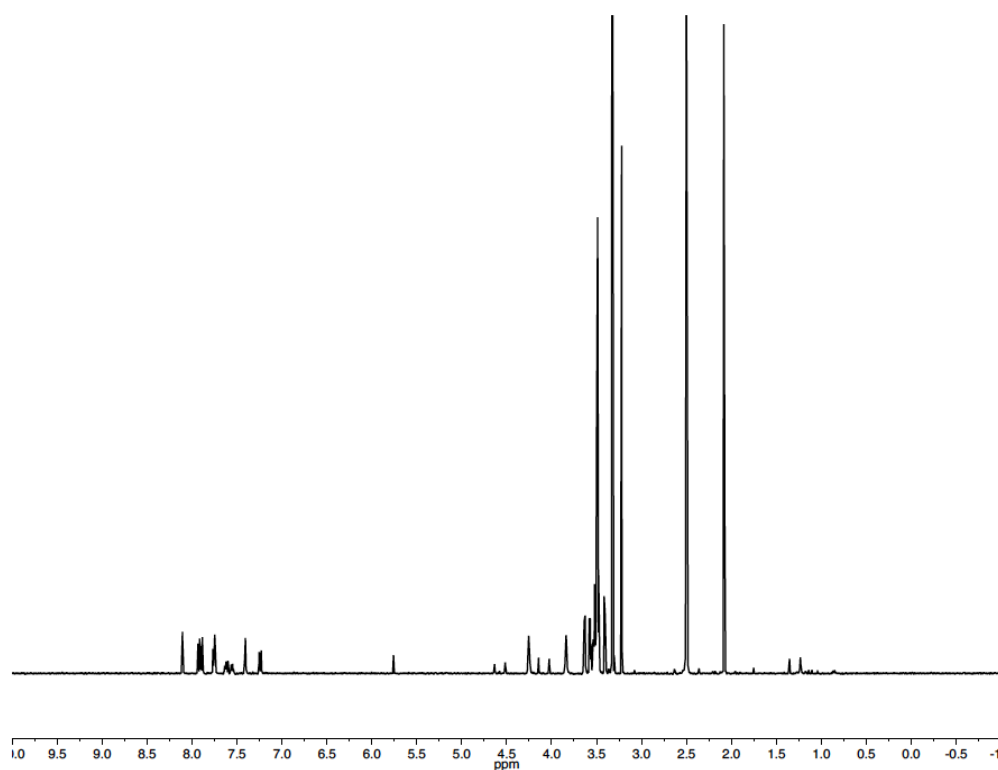


**Figure A4.87.**  $^{13}\text{C}$  NMR spectrum of  $4\text{-}^{13}\text{C}_4$ . 25 °C,  $\text{dms}\text{-}d_6$ .

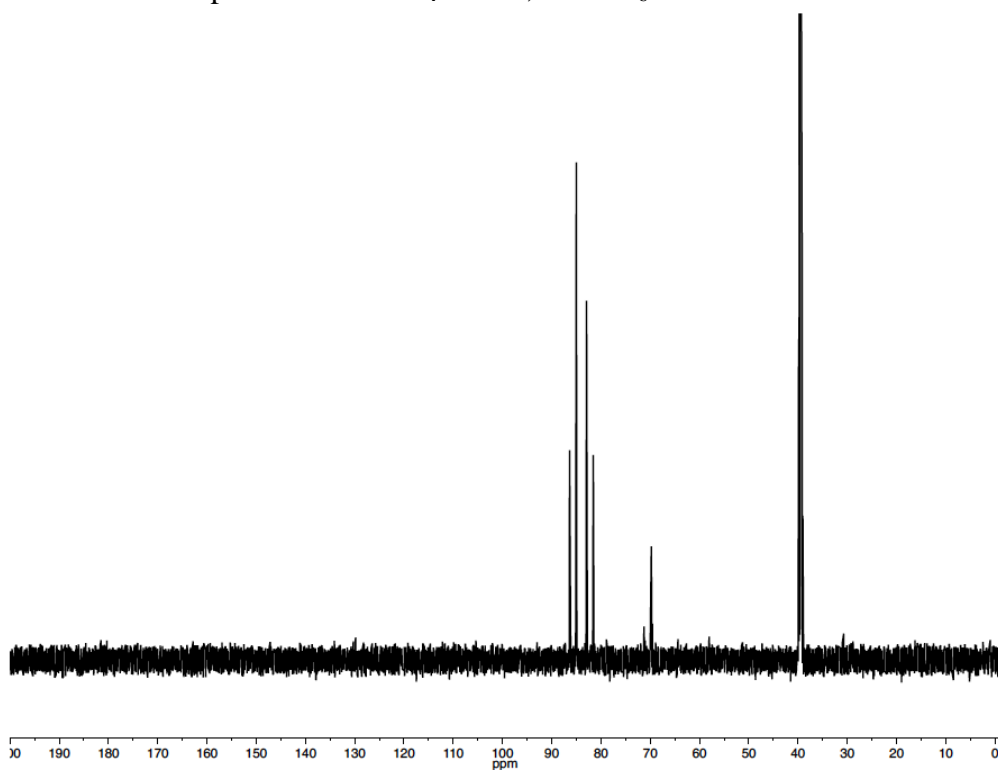




**Figure A4.88.**  $^1\text{H}$  NMR spectrum of **PPE-OHxg**. Entry A Table A4.1 ( $D_p = \infty$ ). 80 °C,  $\text{dms-}d_6$ .

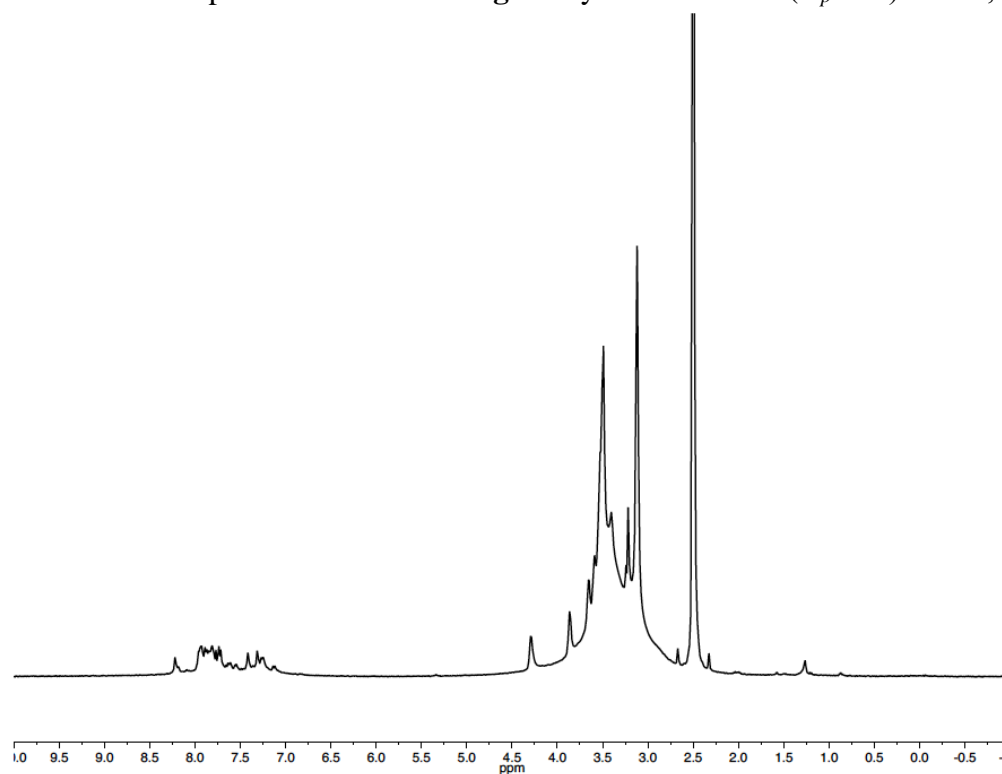


**Figure A4.89.**  $^1\text{H}$  NMR spectrum of **PPE-OHxg**. Entry B Table A4.1 ( $D_p = 80$ ). 80 °C,  $\text{dms-}d_6$ .

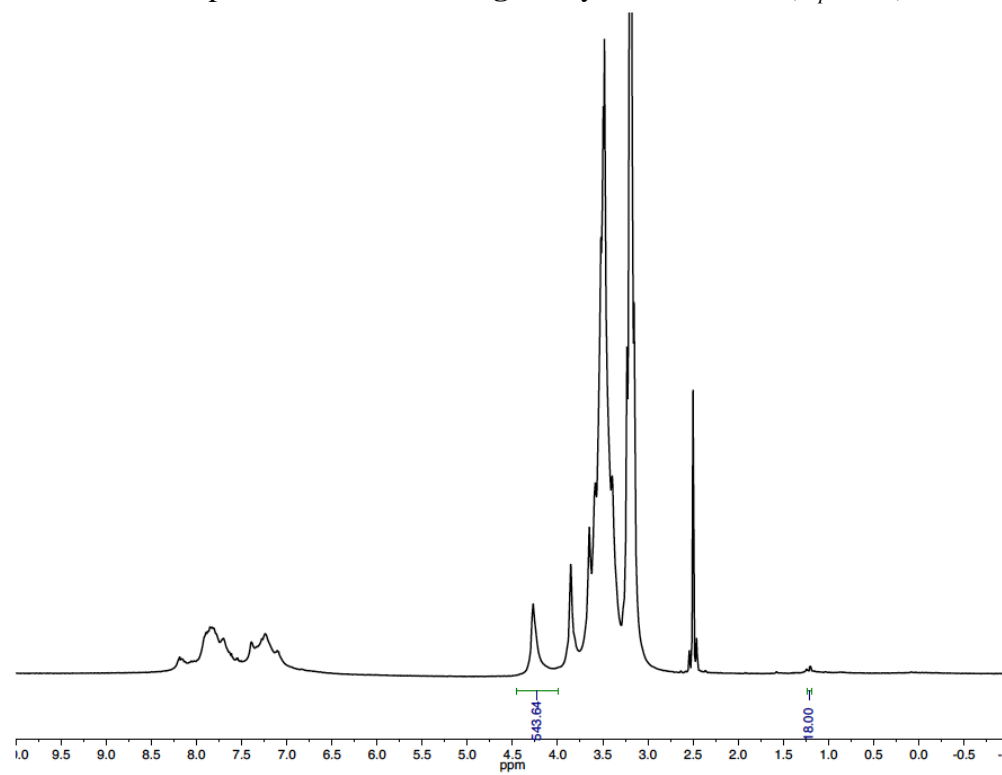


**Figure A4.90.**  $^1\text{H}$  NMR spectrum of **PPE-OH**vg. Entry C Table A4.1 ( $D_p = 40$ ). 80 °C,  $\text{dms-}d_6$ .

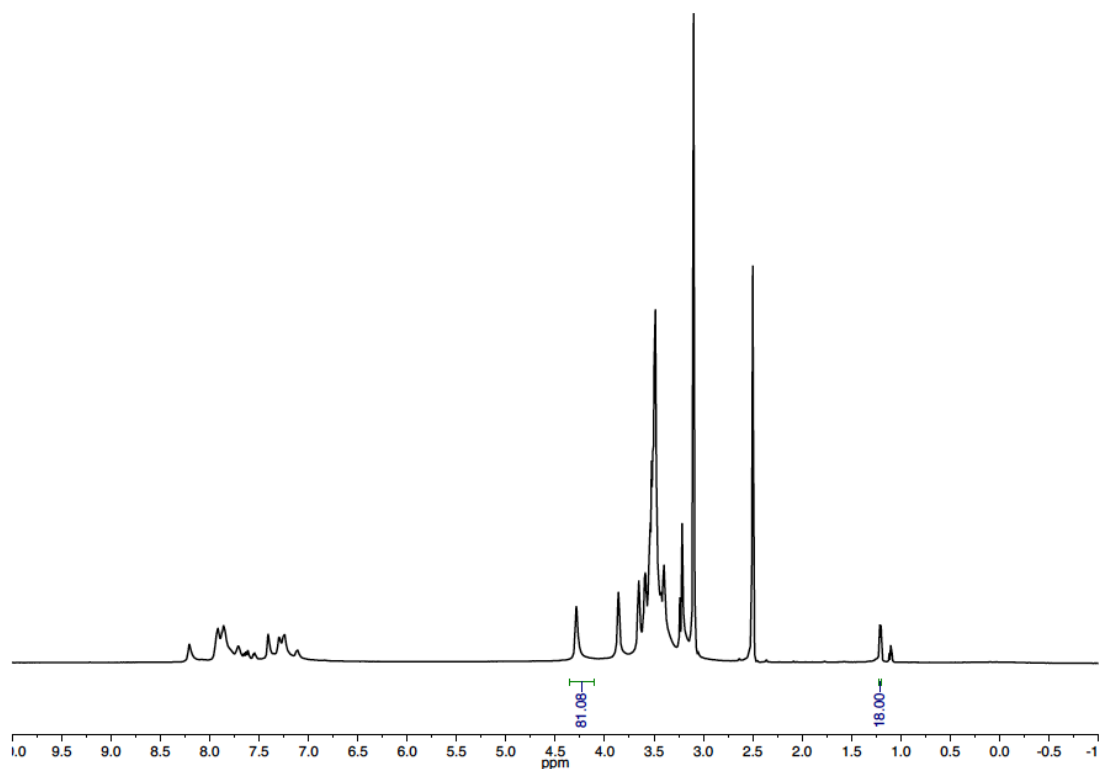


**Figure A4.91.**  $^{13}\text{C}$  NMR spectrum of **PPE-OH**vg. 80 °C,  $\text{dms-}d_6$ .

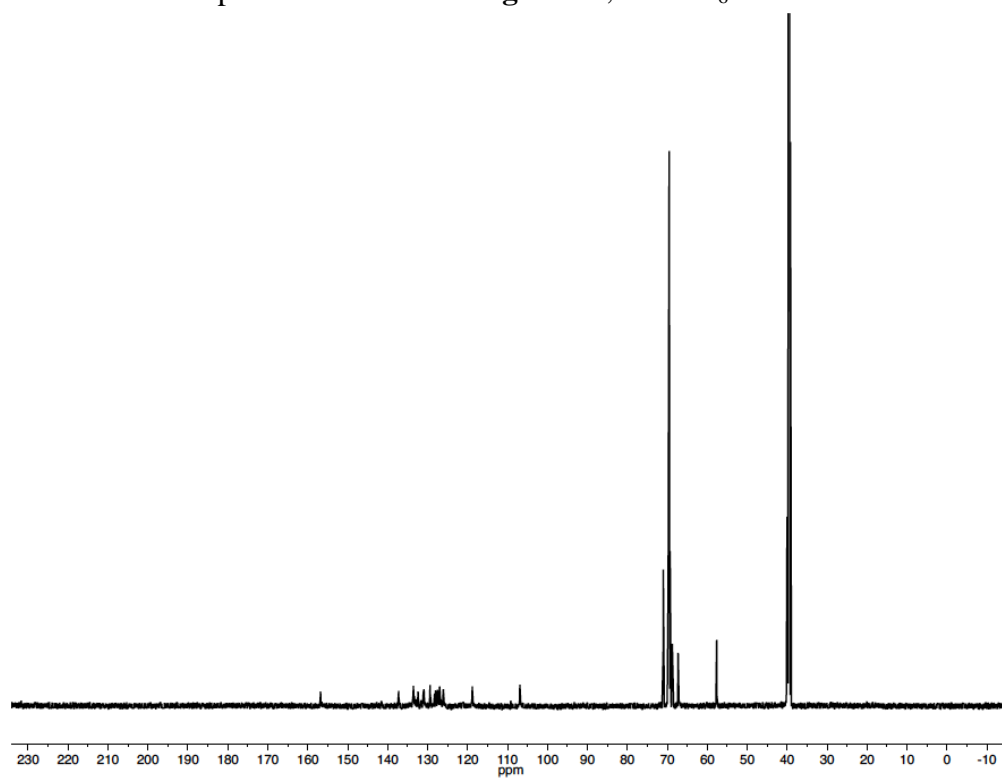


**Figure A4.92.**  $^1\text{H}$  NMR spectrum of **PPE-OHxg- $^{13}\text{C}$** . 80 °C,  $\text{dms-}d_6$ .

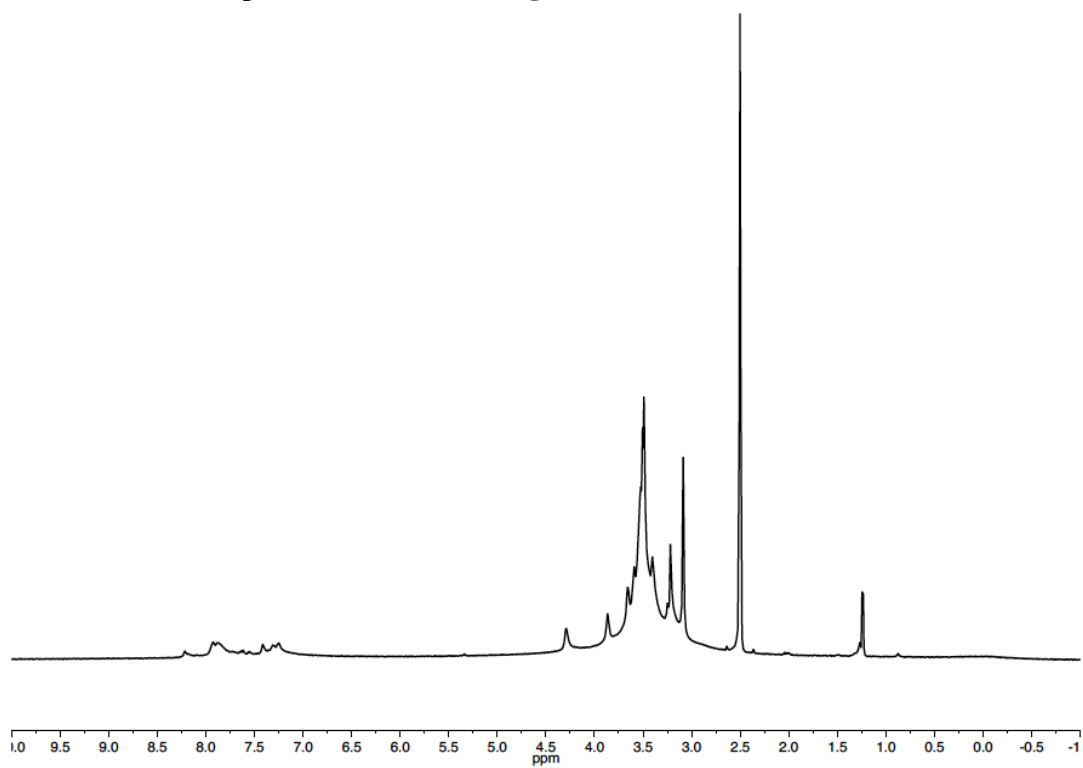


**Figure A4.93.**  $^{13}\text{C}$  NMR spectrum of **PPE-OHxg- $^{13}\text{C}$** . 80 °C,  $\text{dms-}d_6$ .

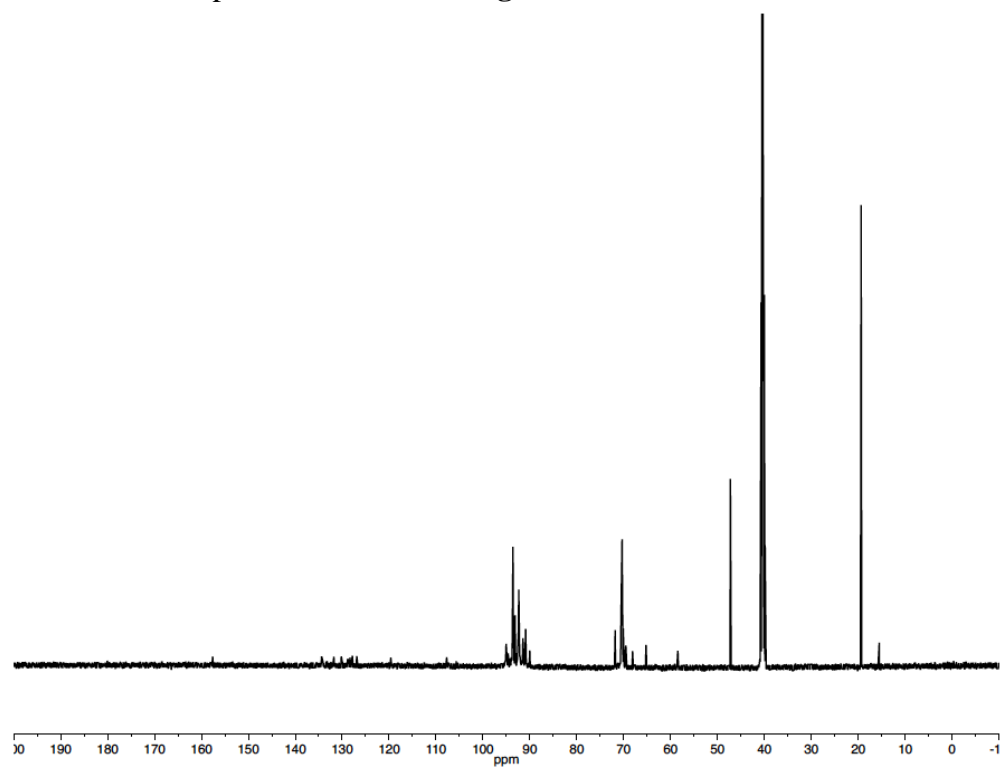


**Figure A4.94.**  $^1\text{H}$  NMR spectrum of **6**- $^{13}\text{C}_2$ . 25 °C,  $\text{CDCl}_3$ .

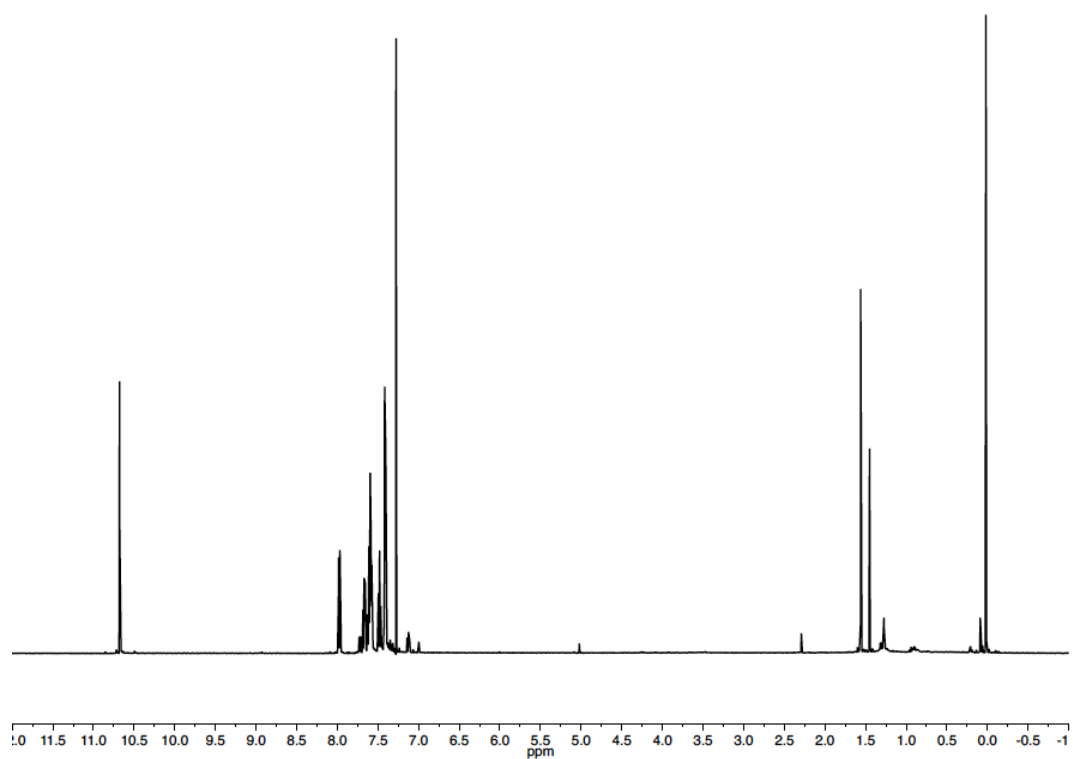


**Figure A4.95.**  $^{13}\text{C}$  NMR spectrum of **6**- $^{13}\text{C}_2$ . 25 °C,  $\text{CDCl}_3$ .

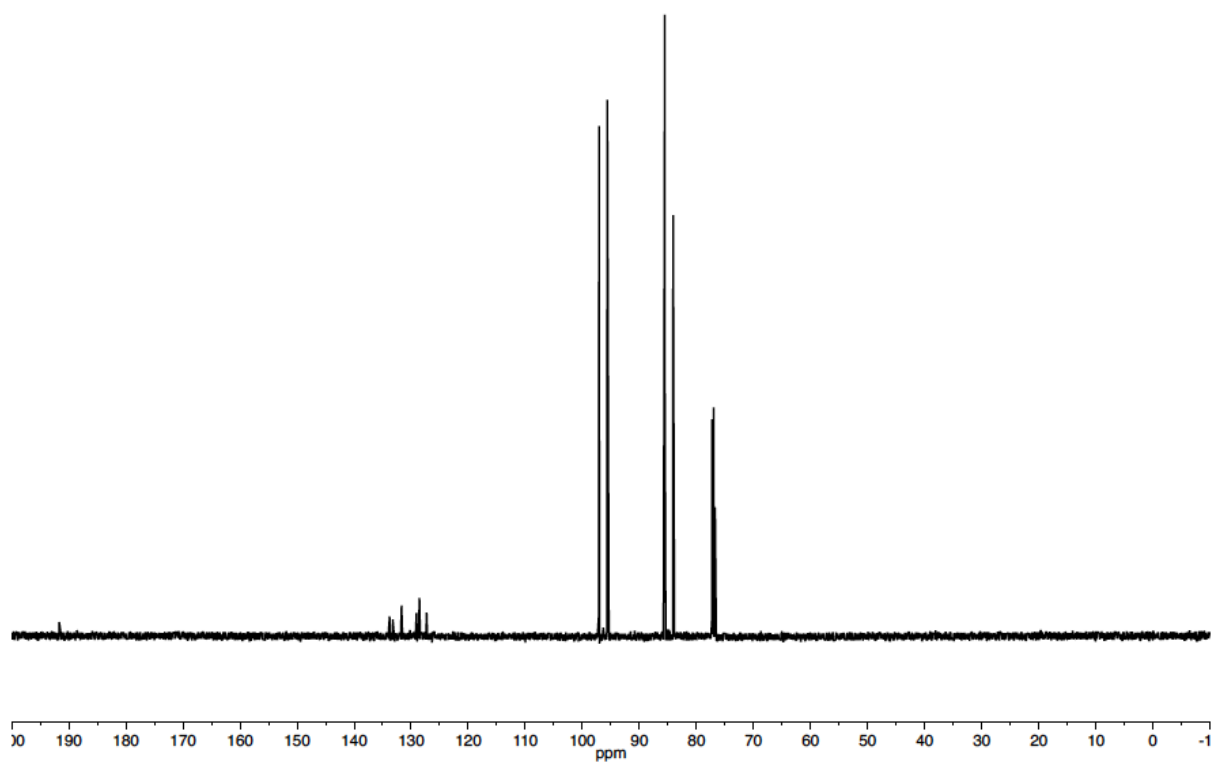


**Figure A4.96.**  $^1\text{H}$  NMR spectrum of **BPP-OHxg**. 80 °C,  $\text{dms-}d_6$ .

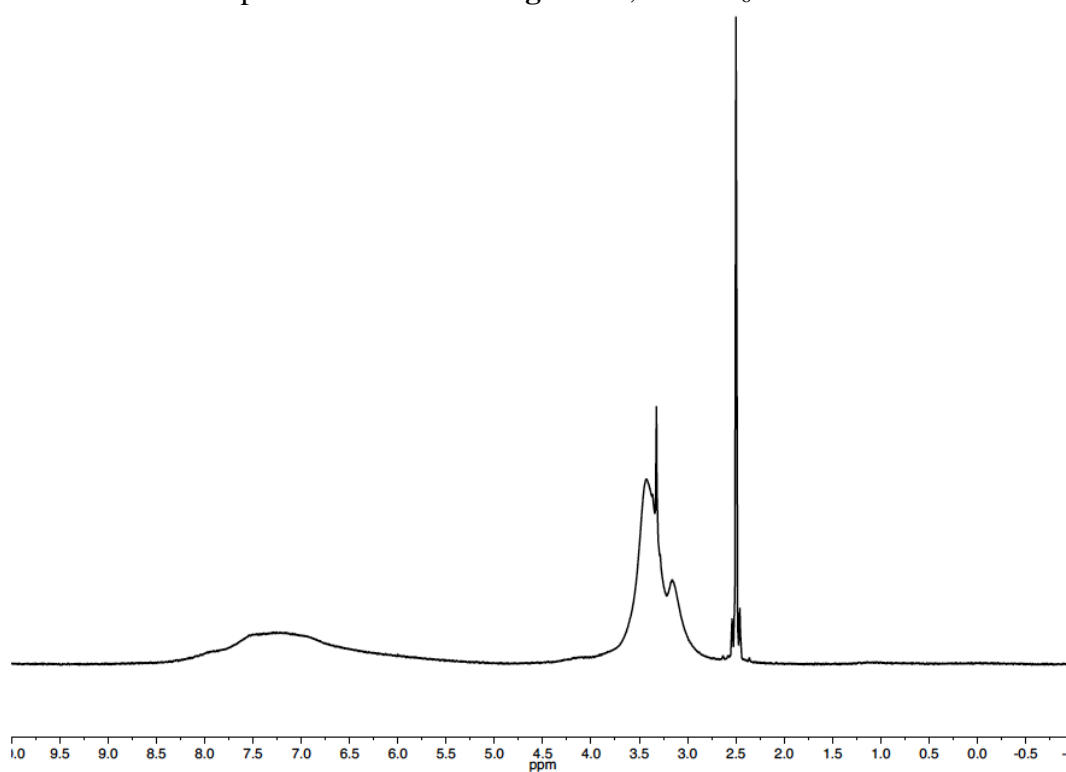


**Figure A4.97.**  $^{13}\text{C}$  NMR spectrum of **BPP-OHxg**. 80 °C,  $\text{dms-}d_6$ .

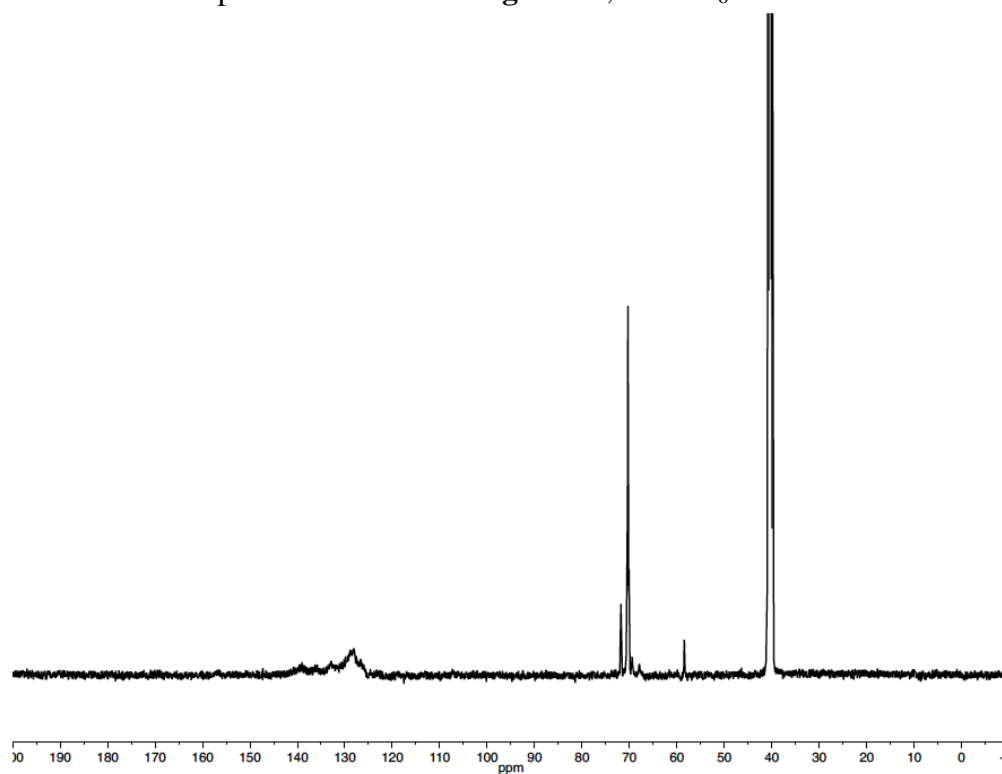


**Figure A4.98.**  $^1\text{H}$  NMR spectrum of **BPP-OHxg- $^{13}\text{C}(I)$** . At 135 °C in  $\text{C}_2\text{D}_2\text{Cl}_4$ .

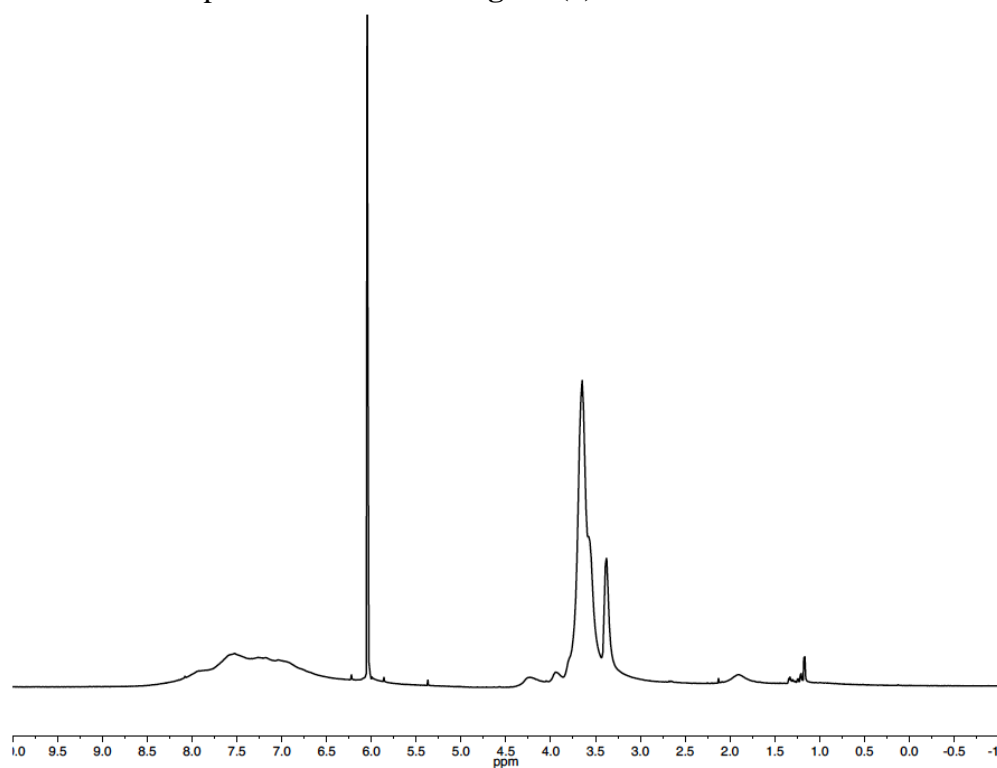


**Figure A4.99.**  $^{13}\text{C}$  NMR spectrum of **BPP-OHxg- $^{13}\text{C}(I)$** . At 135 °C in  $\text{C}_2\text{D}_2\text{Cl}_4$ .

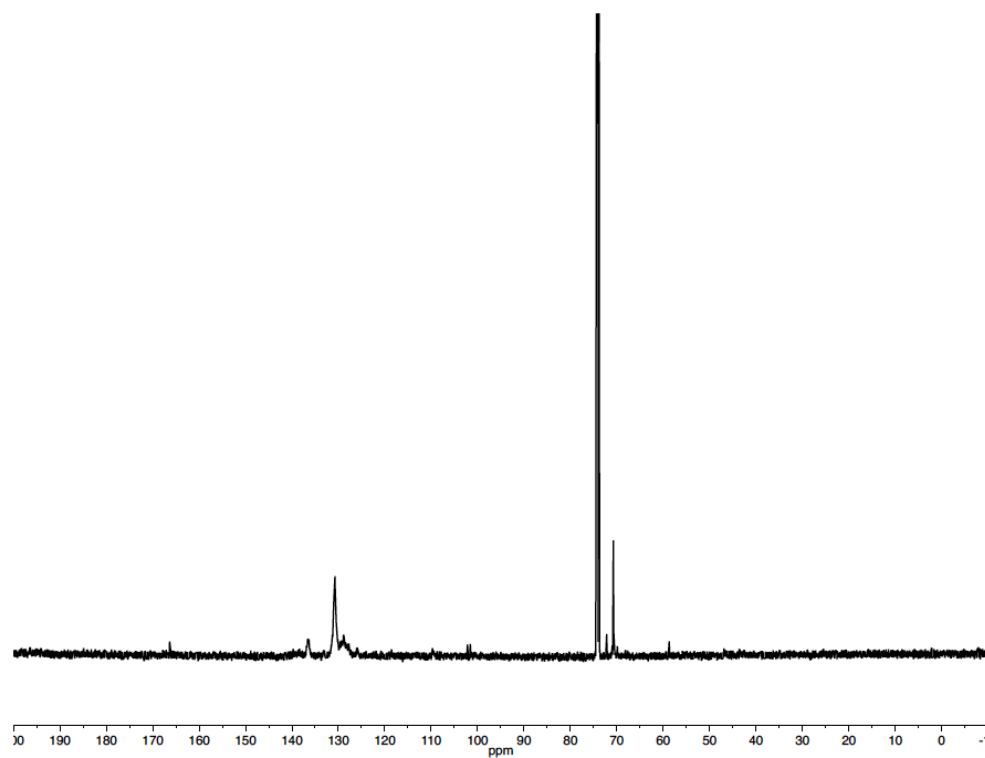


**Figure A4.100.**  $^1\text{H}$  NMR spectrum of **BPP-OHxg- $^{13}\text{C}(2,3)$** . 25 °C,  $\text{CDCl}_3$ .

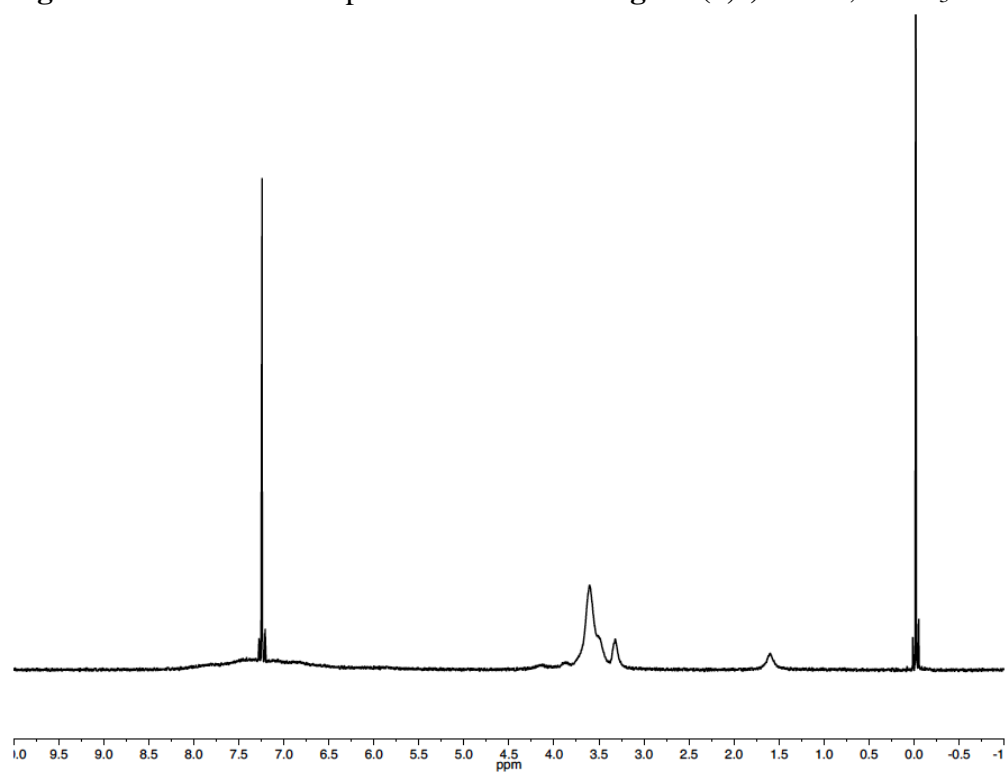


**Figure A4.101.**  $^{13}\text{C}$  NMR spectrum of **BPP-OHxg- $^{13}\text{C}(2,3)$** . 25 °C,  $\text{CDCl}_3$ .

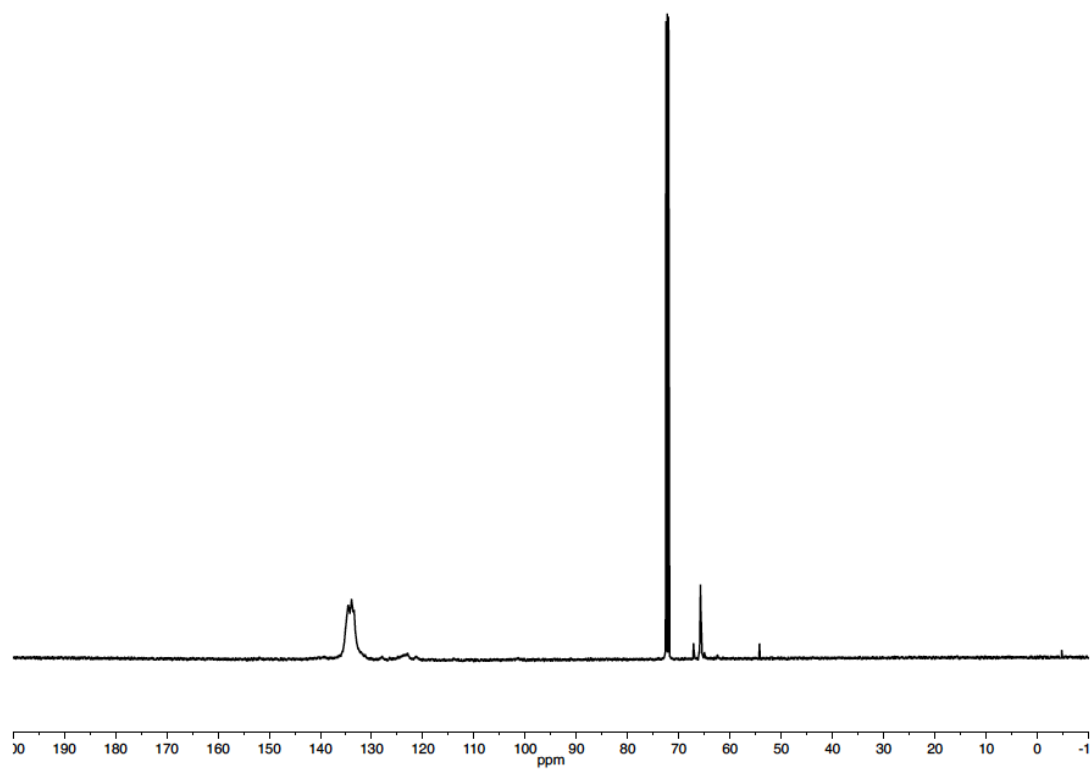


**Figure A4.102.**  $^1\text{H}$  NMR spectrum of **S8**. 60 °C,  $\text{dms-}d_6$ .

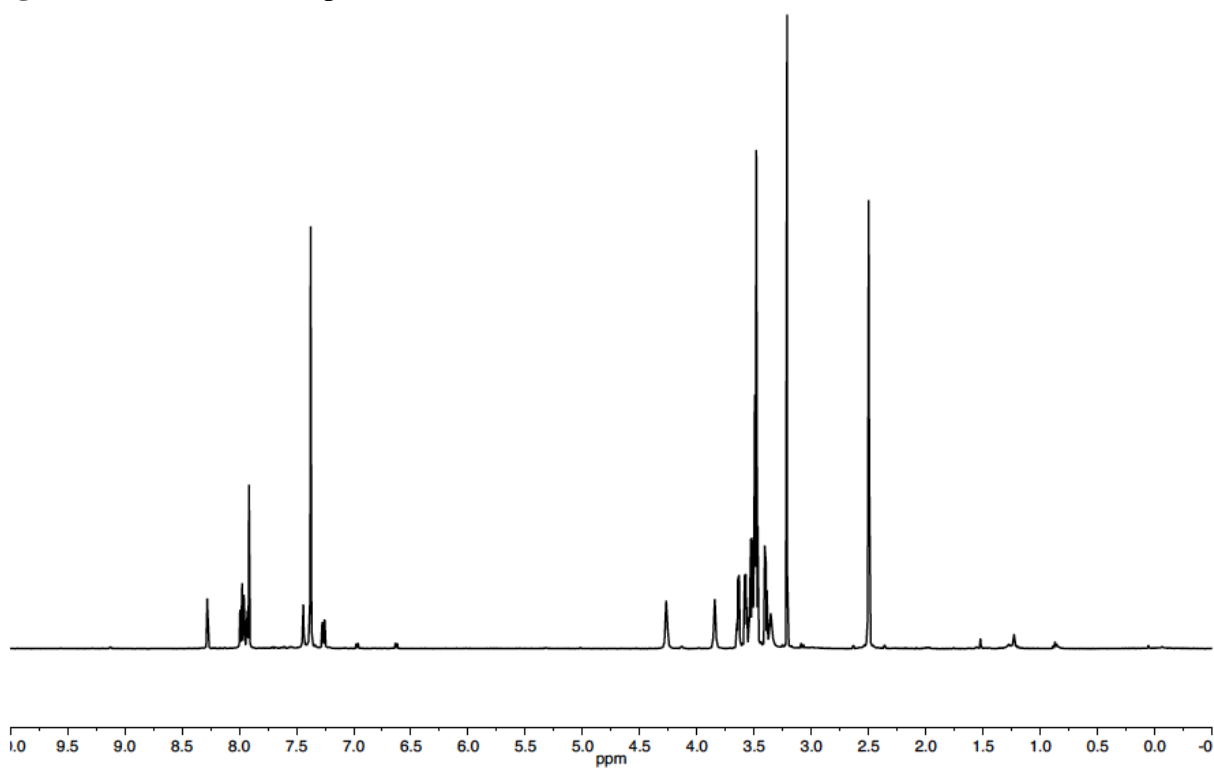


**Figure A4.103.**  $^{13}\text{C}$  NMR spectrum of **S8**. 60 °C,  $\text{dms-}d_6$ .

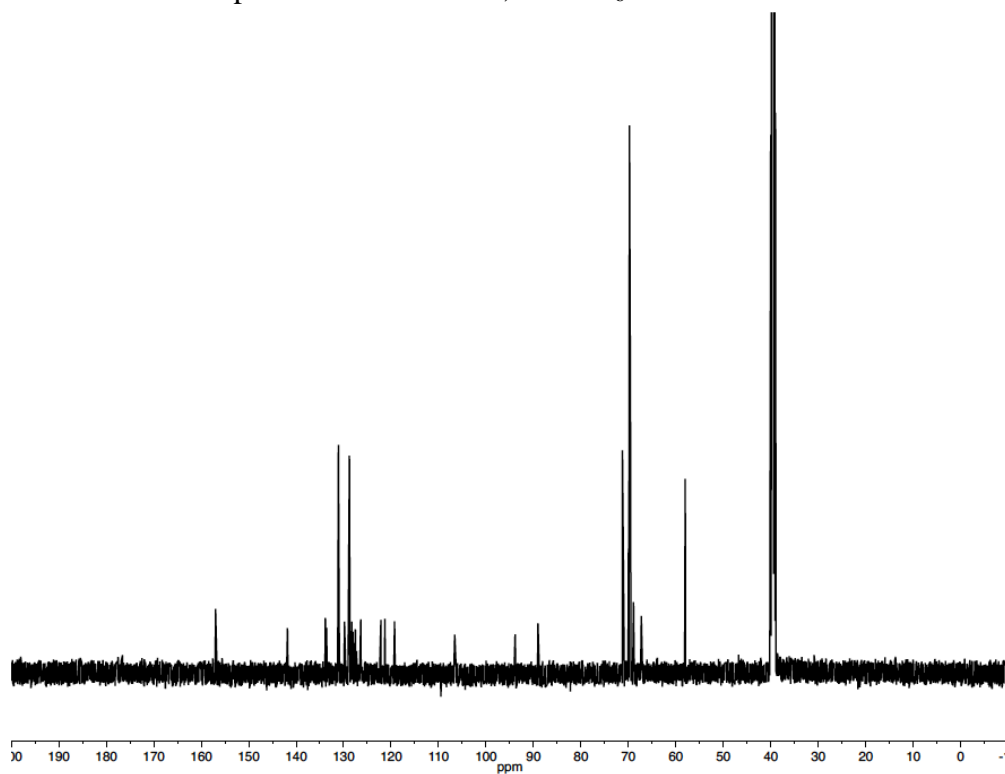




**Figure A4.104.** COSY spectrum of **S8**. 60 °C, dms $\text{-}d_6$ .

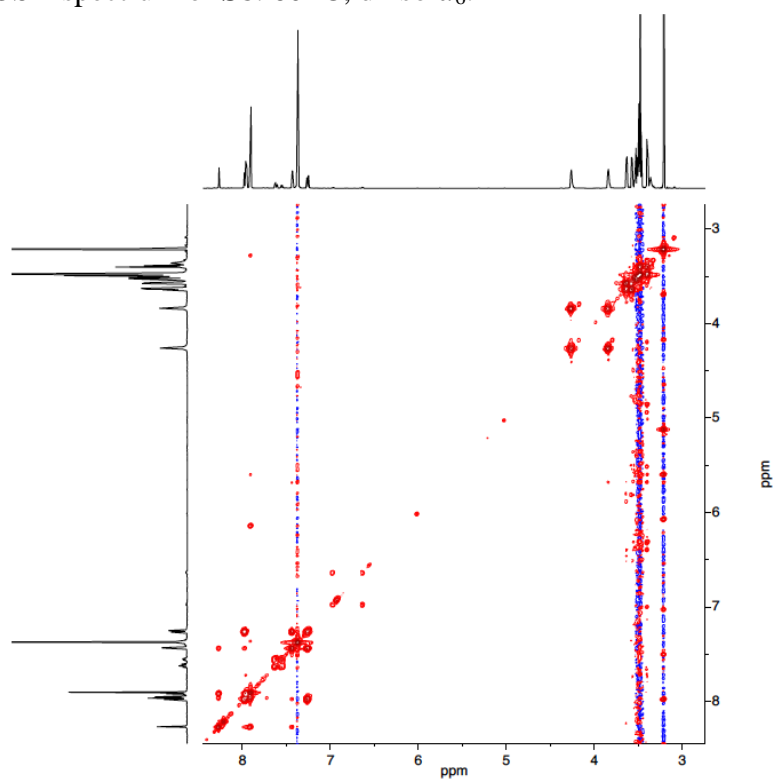


**Figure A4.105.** ROESY spectrum of **S8**. 60 °C, dms $\text{-}d_6$ .

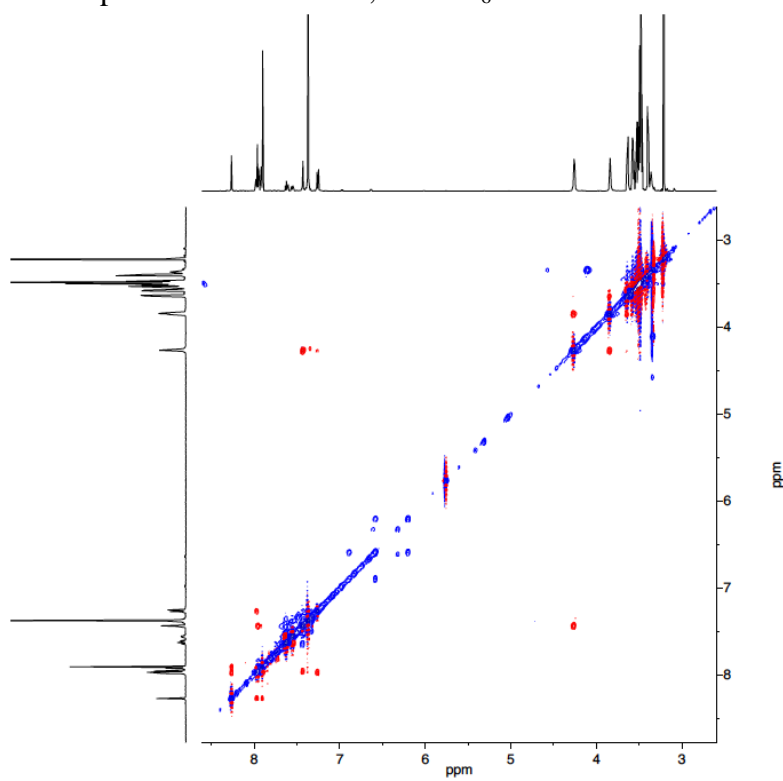


**Figure A4.106.**HSQC spectrum of **S8**. 60°C, dms $o$ - $d_6$ .

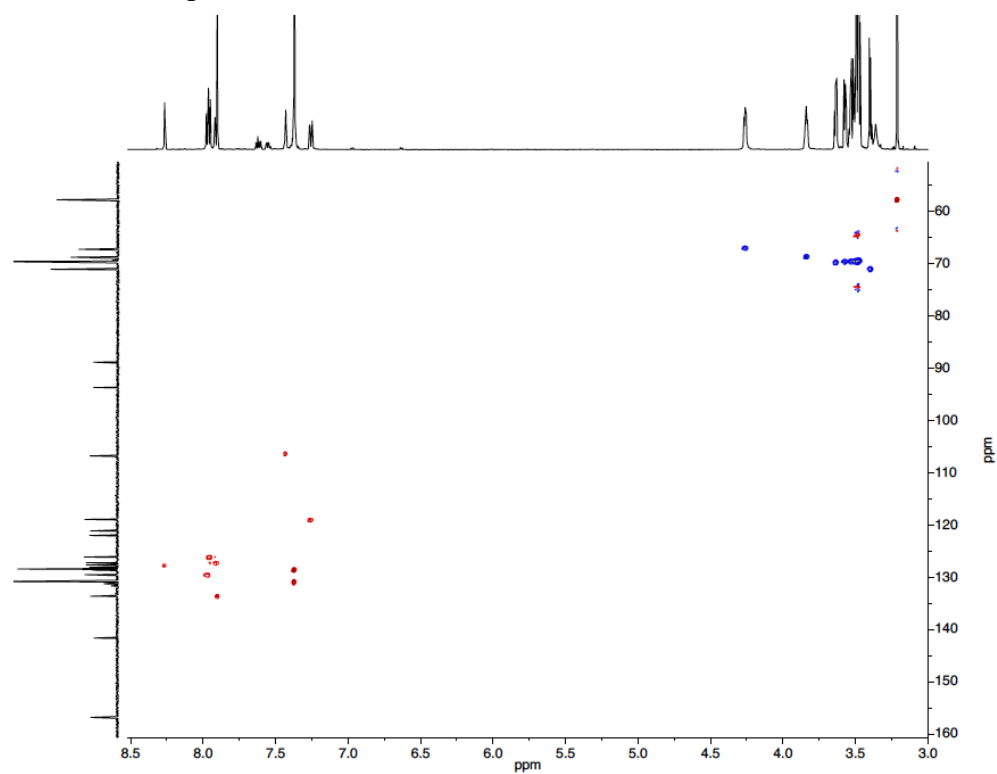


**Figure A4.107.**HMBC spectrum of **S8**. 60 °C, dms $o$ - $d_6$ .

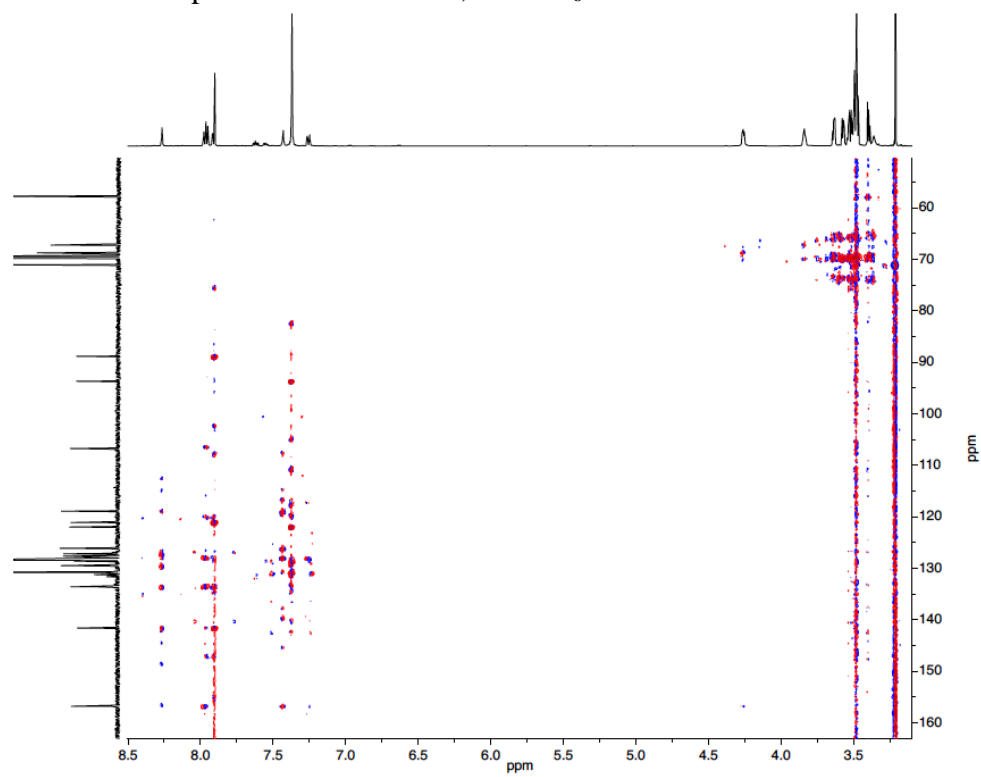


**Figure A4.108.**  $^1\text{H}$  NMR spectrum of **7**. 25 °C,  $\text{dms}\text{-}d_6$ .

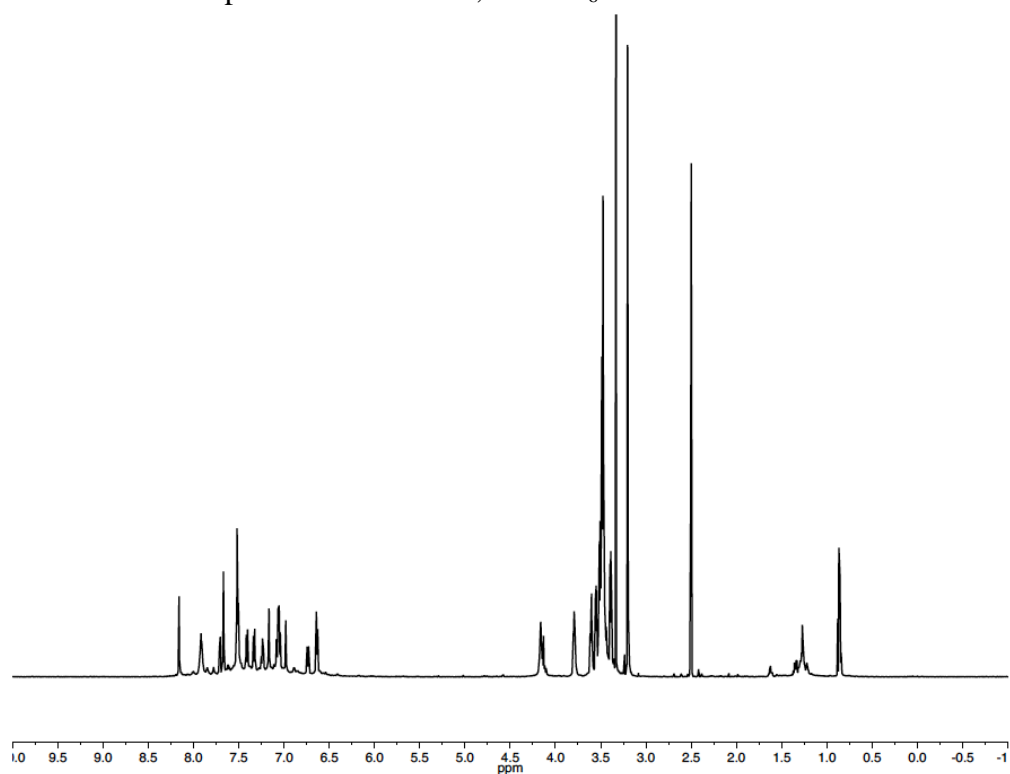


**Figure A4.109.**  $^{13}\text{C}$  NMR spectrum of **7**. 25 °C,  $\text{dms}\text{-}d_6$ .

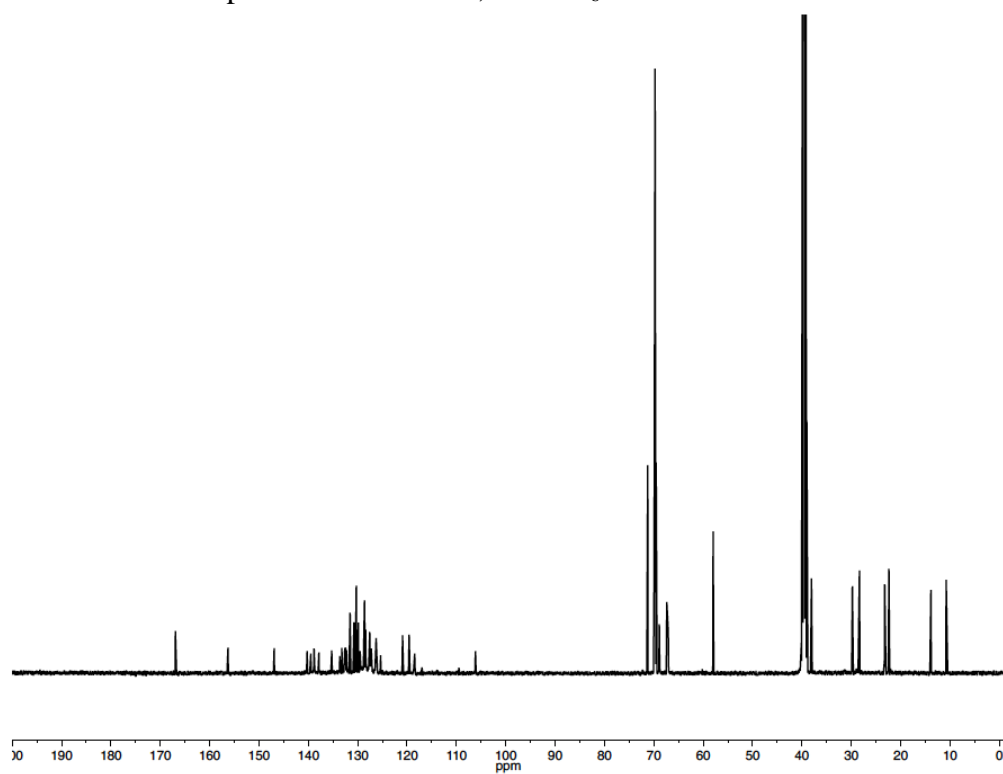


**Figure A4.110.** COSY spectrum of **7**. 25 °C, dms $\text{-}d_6$ .

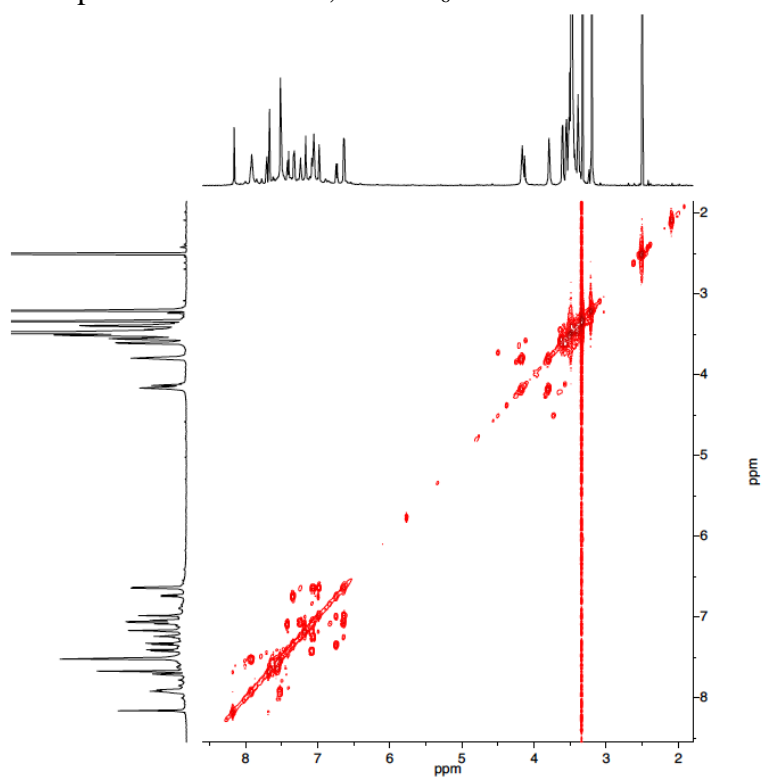


**Figure A4.111.** ROESY spectrum of **7**. 25 °C, dms $\text{-}d_6$ .

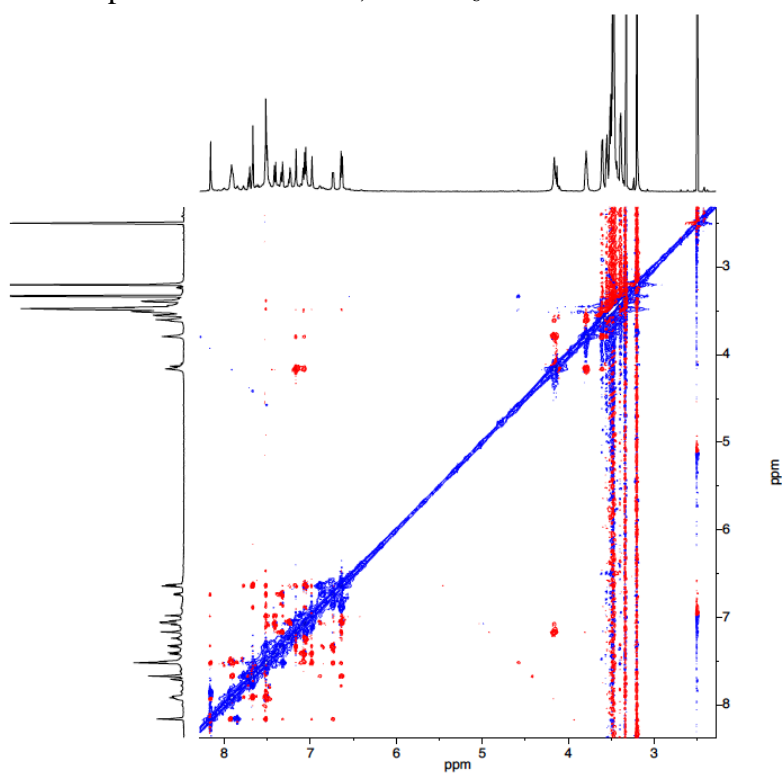
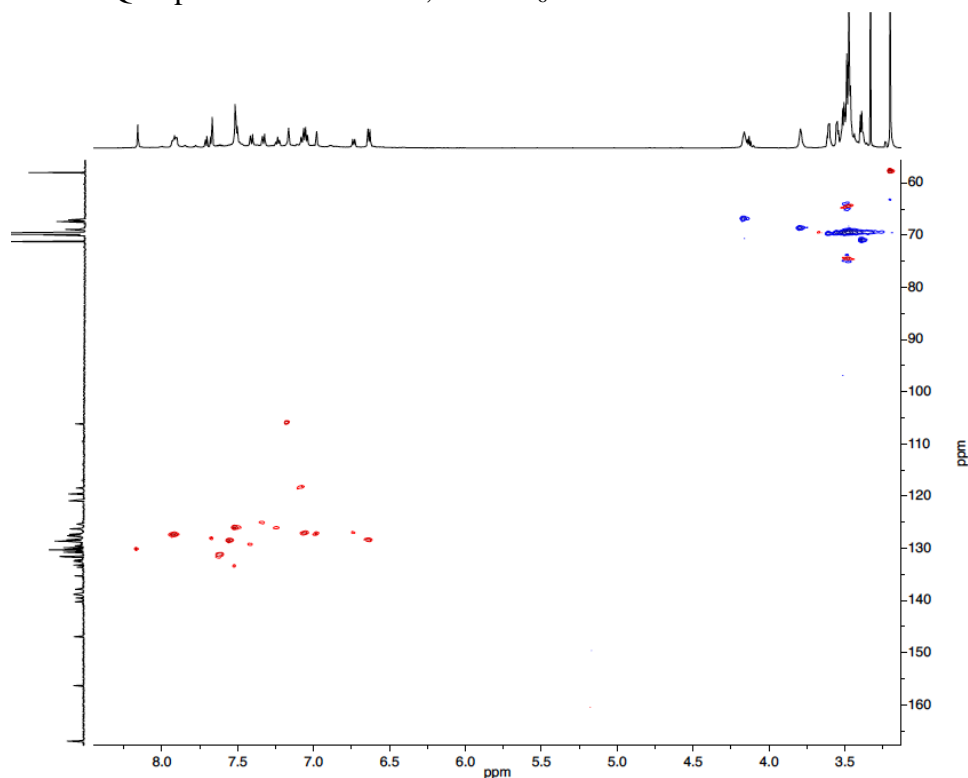


**Figure A4.112.**HSQC spectrum of **7**. 25 °C, dms-*d*<sub>6</sub>.



#### **L. References to Appendix**

- (38) Brower, A. M. *Pure Appl. Chem.* **2011**, 83, 2213-2228.
- (39) Friscourt, F.; Fahrni, C. J.; Boons, G.-J. *J. Am. Chem. Soc.* **2012**, 134, 18809-18815.
- (40) Hart, H.; Harada, K.; Du, C. J. F. *J. Org. Chem.* **1985**, 50, 3104-3110.
- (41) Arslan, H.; Saathoff, J. D.; Bunck, D. N.; Clancy, P.; Dichtel, W. R. *Angew. Chem. Int. Ed.* **2012**, 51, 12051-12054.
- (42) Clark, S.J.; Segall, M.D.; Pickard, C. J.; Hasnip, P. J.; Probert, M. I. J.; Refson, K.; Payne, M. C. *Z. Kristallogr.* **2005**, 220, 567–570.
- (43) Materials Studio Ver 5.5 (Accelrys Software Inc. San Diego, CA 2010)
- (44) Rappe, A. K.; Casewit, C. J.; Colwell, K. S.; Goddard-III, W. A.; Skiff, W. M. *J. Am. Chem. Soc.* **1992**, 114, 10024-10035.